UNIVERSITAT POLITÈCNICA DE CATALUNYA BARCELONATECH

Experimental and numerical study of the effect of stress on ASR expansions in concrete

Joaquín Liaudat

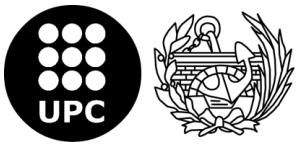

School of Civil Engineering of Barcelona
UPC BARCELONATECH

Experimental and numerical study of the effect of stress on ASR expansions in concrete

Doctoral Thesis submitted by

Joaquín Liaudat

Supervised by

Ignacio Carol & Carlos M. López

Doctoral Program in Geotechnical Engineering
Division of Geotechnical Engineering and Geosciences
Department of Civil and Environmental Engineering
Universitat Politècnica de Catalunya

Barcelona, May 2018

Abstract

This thesis aims at deepening in the understanding of the mechanisms by which the stress state affects the development of concrete expansions and cracking due to the Alkali-Silica Reaction (ASR). With this purpose, a combined experimental-numerical study has been undertaken.

For the experimental part of the study, two new experimental setups have been developed and used in an extensive experimental campaign. The first setup has made it possible to measure, seemingly for the first time, ASR expansion curves at the level of a single interface between a reactive aggregate and a cementitious matrix (mortar or cement paste), as well as to study the formed ASR products by means of SEM images and EDS analyses. The thesis includes results from various series of Interfacial Expansion Tests under different conditions, in order to assess their influence on the kinetics of the measured expansions.

For the second experimental setup, an existing triaxial testing machine has been adapted. With this machine, experimental ASR expansion curves from cubical concrete specimens subjected to three different triaxial stress states have been obtained. The results seem to indicate that the volumetric ASR expansion rate is reduced as the applied volumetric compressive stress is increased. Additionally, there seems to be an increase in the expansion rate in the less compressed direction in detriment of the expansion rates in the most compressed ones.

Based on the results obtained in the experimental study, as well as on published results from other authors, a reaction-expansion mechanism has been proposed that may explain the effects of the stress state on the ASR expansions of concrete. This reaction-expansion mechanism has been theoretically formulated and implemented in a coupled Chemo-Mechanical Finite Element (FE) model. In this model, the chemical and the mechanical problems are solved by means of two different FE codes, coupled via a staggered implementation. Both codes are used to analyse the same FE mesh in which the reactive aggregates are explicitly represented, embedded in a matrix phase representing non-reactive mortar or cement paste.

This mesh includes zero-thickness interface elements which are inserted a priori along all the aggregate-matrix contacts and also along some predefined matrix-matrix and aggregate-aggregate inter-elements boundaries in order to represent the main potential crack paths. In the case of the aggregate-matrix contacts, the interface elements also make it possible to represent the specific properties of the Interfacial Transition Zones.

The chemical formulation consists of three primary diffusion/reaction fields for aqueous silicate, calcium and alkalis in the pore solution, complemented by a number of chemical kinetics and chemical equilibrium equations. The dissolution/precipitation reactions involved in ASR expansions are considered to occur only within the zero-thickness interface elements representing fractures and aggregate-matrix contacts, while diffusion of primary species may occur within interface as well as continuum finite elements. The volume fraction distribution of the solid chemical species (reactive silica, portlandite, and ASR products) associated to the interface elements evolve with the progress of the reactions.

From a mechanical point of view, the interface elements are equipped with an elasto-plastic constitutive model based on concepts and parameters of non-linear fracture mechanics. In contrast, the continuum elements are assumed to behave linear elastically. Thus, the mechanical non-linearity of the overall model is due exclusively to the zero-thickness interface elements.

The model has been used for simulating a number of ideal and real cases, demonstrating its ability to reproduce experimental observations regarding the effects of concrete stress state on the development of the ASR expansions.

Resumen

Esta tesis tiene como objetivo principal profundizar en la comprensión de los mecanismos por los cuales el estado tensional del hormigón afecta el desarrollo de las expansiones y fisuras debido a la Reacción de Álcali-Sílice (RAS). Con este propósito, se ha realizado un estudio combinado numérico-experimental del fenómeno.

Para la parte experimental del estudio, se han desarrollado dos nuevas configuraciones experimentales, que posteriormente han sido utilizadas en una extensa campaña experimental. La primera configuración ha permitido medir, aparentemente por primera vez, curvas de expansión por RAS a nivel de una única interfaz entre un árido reactivo y una matriz cementosa (pasta de cemento o mortero), así como estudiar los productos formados por la RAS mediante imágenes SEM y análisis EDS.

Para la segunda configuración experimental, se ha adaptado una máquina existente para ensayos triaxiales. Con esta máquina, se han obtenido curvas experimentales de expansión por RAS de probetas cúbicas de hormigón sometidas a tres estados distintos de tensión triaxial. Los resultados obtenidos parecen indicar que la tasa volumétrica de expansión por RAS se reduce a medida que se aumenta la tensión volumétrica de compresión aplicada. Además, parece haber un aumento en la tasa de expansión en la dirección menos comprimida en detrimento de las tasas de expansión en las direcciones más comprimidas.

Con base en los resultados obtenidos en el estudio experimental, así como en los resultados publicados por otros autores, se ha propuesto un mecanismo de reacción-expansión que podría explicar los efectos del estado tensional en las expansiones por RAS del hormigón. Este mecanismo de reacción-expansión se ha formulado teóricamente e implementado en un modelo acoplado Quemo-Mecánico de Elementos Finitos (EF). En este modelo, los problemas químico y mecánico se resuelven mediante dos códigos de EF diferentes, acoplados mediante una implementación escalonada. Ambos códigos usan la misma malla de EF en la que los áridos reactivos se representan explícitamente rodeados de una matriz cementosa no reactiva. Esta malla incluye elementos junta sin espesor que se insertan a priori a lo largo de todos los contactos matriz-árido y también a lo largo de algunos contactos predefinidos matriz-matriz y árido-árido para representar los principales caminos potenciales de fractura. En el caso de los contactos de matriz-árido, los elementos junta también permiten representar las propiedades específicas de las Zonas de Transición.

La formulación del problema químico consiste en tres campos de difusión/reacción primarios correspondientes a silicato, calcio y álcalis en la solución de poros, complementados por una serie de ecuaciones de cinética química y equilibrio químico. Las reacciones de disolución/precipitación involucradas en las expansiones por RAS pueden ocurrir únicamente en los elementos junta que representan fracturas y contactos árido-matriz, mientras que la difusión de las especies primarias puede ocurrir tanto en elementos junta como continuos. La distribución de las fracciones volumétricas de las especies sólidas (sílice reactiva, portlandita y productos de las RAS) asociadas a los elementos junta evoluciona con el progreso de las reacciones.

Desde un punto de vista mecánico, los elementos junta están equipados con un modelo constitutivo elasto-plástico basado en conceptos y parámetros de la teoría no lineal de la mecánica de fractura. Por el contrario, los elementos del continuo se asumen linealmente elásticos. En consecuencia, la no linealidad mecánica del modelo se logra exclusivamente por medio de los elementos junta.

El modelo se ha utilizado para simular una serie de casos ideales y reales, en los que ha demostrado su capacidad para reproducir observaciones experimentales con respecto a los efectos del estado tensional del hormigón en el desarrollo de las expansiones por RAS.

Acknowledgements / Agradecimientos

Quisiera comenzar esta página agradeciendo a Ignacio Carol y Carlos López, directores de esta tesis, el apoyo, el estímulo y la dedicación que me han brindado durante los siete años que ha demandado esta investigación.

El trabajo experimental en esta tesis se ha desarrollado mayormente en el Laboratorio de Geotecnia del Departamento de Ingeniería Civil y Ambiental (UPC). Mi agradecimiento a su director Enrique Romero y a todo su personal, por la buena disposición y el asesoramiento. En particular, quisiera mencionar a Tomás Pérez por ayudarme a resolver multitud problemas técnicos en los montajes experimentales. También he recurrido al Laboratorio de Tecnología de Estructuras y Materiales del mismo departamento para la elaboración y preparación de probetas de hormigón. Agradezco a su director Tomás García por permitirme usar las instalaciones y al resto del personal técnico (en especial a Camilo Bernard y Robert McAloon) por la ayuda y el asesoramiento que me han prestado. En estos trabajos experimentales he contado con la colaboración de estudiantes de grado (Jonathan Stokes, Iván Acosta, Alejandro González, y Edgar Vacas) y de compañeros de doctorado (Rodrigo Gómez y Ariadna Martínez, entre otros).

The testing machine used in one of the experimental setups presented in this thesis was originally designed and constructed by Prof. Victor Saouma at the U. of Colorado-Boulder. Prof. Saouma has also helped the author with valuable comments in the process of interpreting the experimental results. The author would also like to thank Dr Andreas Leemann from the EMPA (Switzerland) for performing some of the SEM/EDS analyses used in this thesis.

Un especial agradecimiento a Daniel Garolera por haberme acompañado en el proceso de implementar el modelo numérico propuesto en esta tesis, asesorándome en programación y resolviendo muchos de los problemas implementación que surgieron. Puntualmente también me han ayudado en el trabajo de modelación Mariana Rodríguez y Adrià Pérez.

Muchas muchas gracias a Lola Zavala por haberme ayudado tantas veces a sortear los laberintos burocráticos de la UPC.

Agradezco a mis hermanos y a mi madre en Argentina por el apoyo y el cariño que me han brindado a la distancia. Y a mi compañera, Regine, por la paciencia y por cuidar de mí todos estos años. Many thanks also to Gundl and Michael Zoelch for their loving support over these years.

Finalmente, agradezco al Ministerio de Economía, Industria y Competitividad del Gobierno de España por el financiamiento recibido duramente la primera etapa de este trabajo mediante una ayuda FPI (BES-2010-030515).

Contents

A mi compañera, Regine,
y a nuestros hijos, Teo y Nora.

Chapter 1

Introduction

1.1 Motivation and scope

Alkali-Silica Reaction (ASR) can be described as a particular type of chemical reaction in concrete involving the alkaline pore solution of the Hydrated Cement Paste (HCP) and various metastable forms of silica present in many natural and synthetic aggregate particles used in concrete [173, 185]. The silica structure is dissolved by the attack of hydroxyl anions, passing to the pore solution in aqueous forms which later recombine with calcium and alkali cations (always present in concrete pore solution) to form silicate hydrates of variable stoichiometric composition, the so-called 'ASR gel'. This reaction product is usually hygroscopic and swells as it absorbs water. The degree of hygroscopy and the associated volume change of the ASR gel depends mainly on its chemical composition and the Relative Humidity (RH) in the concrete pores. If the space available at the reaction site, i.e. pores, cracks, etc., is not enough to allocate the ASR gel, the 'swelling pressures produced by the gel induce the formation of microcracks close to the reaction sites, and these propagate and coalesce to produce cracking within the fabric of the concrete and overall expansion of the structural element affected' [166]. Since ASR was first identified in the late 1930s by T.E. Stanton [198, 199], extensive knowledge has been accumulated 'regarding the mechanisms of the reactions, the aggregate constituents that may react deleteriously, and precautions that can be taken to avoid resulting distress' [1]. However, the ASR expansion of concrete is a complex phenomenon and some aspects of it are still a matter of controversy. One of these aspects is the influence of the stress state of concrete on the development of the ASR expansions, as well as the underlying mechanisms that determine this influence.

Since the early investigations, it was noticed that the stress state has an influence on the kinetics and distribution of ASR-induced cracking and expansions [148]. However,

it was not until recent years that this topic became of particular interest for researchers and practitioners. This interests is motivated by the need of introducing the effect of the stress state in the numerical models used for the prediction of the evolution of the serviceability and strength of ASR-affected concrete structures. In the last 20 years a number of experimental studies on the effect of the stress state on ASR concrete expansions have been published, but, nevertheless, the nature and magnitude of these effects, as well as the basic mechanisms behind them, have not been totally clarified.

In this context, this thesis aims at deepening in the understanding of the mechanisms by which the stress state of affects the development of ASR concrete expansions. With this purpose, a combined experimental-numerical study is undertaken. For the experimental part of the study, two new experimental setups are developed and used in an extensive experimental campaign. The first one for studying ASR expansions at the level of a single aggregate-cementitious matrix (HCP or mortar) interface, and the second one for studying ASR expansions of concrete specimens under triaxial stress states.

Based on the results obtained in the experimental study, as well as on published results from other authors, a reaction-expansion mechanism that may explain the effects of concrete stress state on ASR expansions is proposed. This reaction-expansion mechanisms is theoretically formulated and implemented in a coupled Chemo-Mechanical (C-M) Finite Element model, along the line of a pre-existing model for External Sulphate Attack developed by the group of Mechanics of Materials of UPC (MECMAT) [98]. Finally, this model is used to demonstrate the ability of the proposed reaction-expansion mechanism to qualitative and/or qualitatively reproduce the experimental observations.

1.2 Objectives

The main objective of this thesis is to propose a reaction-expansion mechanism capable of explaining the effects of the stress state on the development of ASR concrete expansions. In order to achieve this goal, various requirements and intermediate objectives had to be fulfilled:

- Development of a new experimental setup and the associated testing methodology for measuring ASR expansions at the level of a single aggregate-cementitious matrix interface.
- Development of a new experimental setup and the associated testing methodology for measuring of ASR expansions of concrete specimens under triaxial confinement.

- Experimental study of ASR expansions in concrete made with soda-lime glass (SL glass) as reactive aggregate, using the new methodologies mentioned above, as well as complementary conventional tests.
- Characterization via Scanning Electron Microscopy (SEM) and Energy Dispersive Spectroscopy (EDS) of the ASR products formed at different locations within the specimens tested.
- Proposal of a reaction-expansion mechanism, capable of explaining the effects of concrete stress on ASR expansions, based on the results obtained in the experimental campaign, as well as on published results from other authors.
- Theoretical and numerical formulation of a general framework for modelling diffusion-dominated durability problems in cement-based materials.
- Implementation of this modelling framework in the pre-existing codes `DRAC`, `DRACFLOW`, and `STAG`, developed within the MECMAT research group. In the case of `DRACFLOW`, this implementation required major improvements in the structure of the code, namely: extension of the number of field variables, computation of the mass balance of solid chemical species, time integration of arbitrary chemical kinetic laws, implementation of advanced iteration strategies (Newton-Raphson, Line Search), implementation of an iterative solver, among others.
- Theoretical and numerical formulation of the reaction-expansion mechanism for ASR in concrete within the general modelling framework. Implementation in `DRAC`, `DRACFLOW` and `STAG`.
- Use of the resulting ASR model for the simulation of real and ideal cases. Comparison with experimental results in order to demonstrate the ability of the proposed reaction-expansion mechanism of reproducing the effect of concrete stress on the development of ASR expansions.

1.3 Methodology

The research work in this thesis has involved both experimental and numerical modelling work. The experimental work was oriented, on one hand, to achieve a phenomenological macroscopic description of the effect of triaxial confining stresses on the development of ASR expansions in concrete and, on the other hand, to understanding the mechanisms occurring at lower scales (mesoscopic or microcopic) that may explain these effects. For these purposes, two new experimental setups were developed. The first setup was devoted to the study of the ASR expansions at the level of single aggregate-cementitious

matrix interface. To do so, small sandwich-like specimens, with cement paste or mortar on top and bottom of a disc of reactive aggregate in the middle were used. These specimens were placed in airtight containers with an alkaline solution and they were then introduced in an oven at 60 °C. In these conditions, ASR products were formed rapidly in between the aggregate disc and the HCP or mortar, inducing length changes in the specimen which were measured regularly.

The second setup was aimed at measuring ASR expansions in concrete specimens under triaxial confinement. To do so, an ad hoc testing machine, called 'Alkali-Aggregate Reaction Triaxial Machine' (AARTM), which had been originally designed and constructed by Prof. Saouma at the U. of Colorado - Boulder, was transferred to UPC in 2010 where a number of modifications were introduced by the author to the original setup. The AARTM consists of a triaxial loading frame which can deliver 0 to 9 MPa confining stress on each axis of a $150 \times 150 \times 150$ mm cubical specimen. Specimen deformation is measured using three displacement sensors on each of the three axes. The apparatus is designed to be capable of raising and maintaining the specimen temperature at a pre-set value between 30 to 70 °C, and the faces of the loading plates in contact with the specimens are crossed by grooves for a solution to circulate in order to keep the specimen wet and supply reactants (alkalis). A computer control and data acquisition system maintains the desired confining stress and specimen temperature while logging all relevant data points.

These two setups, complemented with other conventional tests, were employed to carry out an experimental campaign for which SL glass was used as reactive aggregate. SL glass was chosen because of its very high reactivity, its homogeneity as an industrial material and the availability of many published experimental studies about concrete made with it.

Based on the results obtained and those of other researchers found in the literature, a reaction-expansion mechanism was proposed, which accounts for the interplays between the transport processes, the reaction kinetics, and the mechanical actions at the microscopic/mesoscopic level in order to explain the effects of the stress state on the development of ASR expansions in concrete.

The validation of this reaction-expansion mechanism requires to prove its ability to reproduce the observed experimental behaviour. For this purpose, the governing equations of this mechanism were theoretical and numerically formulated, and they were subsequently implemented in Finite Element (FE) code. This task was divided in two steps. First, a general framework for modelling diffusion-dominated durability problems in cement-based materials was formulated and numerically implemented. This modelling framework can also be used to model durability problems other than ASR, as for

instance has been done recently by the author and co-workers for modelling Acid Attack of oilwell cement exposed to carbonated brine [128]. And second, this framework was developed specifically for the particular case of ASR expansions in concrete made with SL glass aggregates.

The resulting formulation consists of two parts, one dealing with the mechanical problem and one dealing with the diffusion-reaction problem. A number of coupling terms link together both formulations. These two formulations were implemented in two different codes, called `DRAC` and `DRACFLOW`, respectively. Both codes are used to analyse the same FE mesh, in which the reactive aggregates are explicitly represented and they are embedded in a cementitious matrix phase representing non-reactive mortar or HCP. This mesh includes zero-thickness interface elements which are inserted a priori along all the aggregate-matrix contacts and also along some predefined matrix-matrix and aggregate-aggregate inter-elements boundaries in order to represent the main potential crack paths. In the case of the aggregate-matrix, the interface elements also make it possible to represent the specific properties of the Interfacial Transition Zones (ITZ). The coupling between the two codes is achieved by updating the coupling terms of each problem in an iterative process. To do so, each code exchanges data with the other one, in the context of a 'staggered procedure' which is administrated by a third code called `STAG`.

The diffusion-reaction formulation consists of three primary diffusion/reaction fields for the concentrations of aqueous silicate, calcium and alkalis in the pore solution, complemented by a number of chemical kinetics and chemical equilibrium equations. The dissolution/precipitation processes associated with ASR only occur within zero-thickness interface elements representing cement-glass contacts and opened fractures. The volume fraction distribution of the solid chemical species (reactive silica, portlandite, and ASR products) associated to these interface elements evolve with the progress of the reactions.

From a mechanical point of view, the interface elements are equipped with an elasto-plastic constitutive model based on concepts and parameters of non-linear fracture mechanics. The continuum elements are assumed to behave linear elastically. Thus, the non linearity of the overall model is due exclusively to the zero-thickness interface elements.

The coupling between the diffusion-reaction formulation and the mechanical formulation is bidirectional. On one hand, the volume balance of solid chemical species within the interface elements may lead to the development of internal mechanical pressures. This occurs if the volume of formed ASR products is higher than the available pore space. On the other hand, the development of 'plastic' apertures of interface elements (which in this model represent the crack apertures) modifies the transport properties of the material and allows the dissolution/formation of solid species within them.

The model has been used for simulating a number of ideal and real cases of increasing complexity. The simplest cases were intended to prove the numerical implementation and to show the implications of the adopted modelling assumptions. The rest of the cases were intended to demonstrate the ability of the model to reproduce experimental observations regarding the effects of concrete stress state on the development of the expansion.

Although presented in a sequential order, the experimental and numerical modelling work were developed in parallel. In such a way that preliminary modelling results oriented the experiments, and preliminary experimental results oriented the formulation of the model.

1.4 Organization of the thesis

The thesis is structured as described in the following paragraphs.

Chapter 2 summarizes the different aspects of ASR expansions in concrete, beginning with the observed symptoms on field structures, continuing with the current understanding of the reaction-expansion mechanisms, and finalizing with the mathematical models proposed in the last two decades to simulate the phenomenon.

Chapter 3 describes in detail the test setup and the testing methodology proposed for the study of ASR expansions at the level of a single aggregate-matrix (HCP or mortar) interface. Subsequently, test results obtained using different reactive aggregates (SL glass and Borosilicate glass), different cementitious matrices, different alkali contents, and different lateral sealing of the specimens, are presented and discussed. Complementarily, the ASR products formed between the reactive aggregate and the cementitious matrix are characterized by means of SEM images and EDS analyses.

Chapter 4, describes first a new testing machine and the associated testing methodology for performing ASR expansion tests with cubic concrete specimens under triaxial confining stress. Second, the ASR expansion curves of SL glass concrete for three different triaxial stress states obtained with this machine are presented, together with a series of free expansion test results performed in parallel to the tests under loading, in order to asses the effect of the applied stress. Results of mechanical tests performed to characterize the ASR concrete, both before and after the ASR expansion tests, are also presented, as well as SEM images and EDS analyses performed to characterize the ASR products in the specimens and the corresponding cracking patterns. As a side result, a modification to the phenomenological model by Saouma and Perotti [183] is proposed in order to reproduce the obtained ASR confined expansion rates.

In Chapter 5, a general framework for numerical modelling of diffusion-dominated durability problems in cement-based materials is proposed. This framework consists of two separated theoretical and numerical formulations, one for the diffusion-reaction problem and the other for the mechanical problem. The numerical formulations are based in both cases on the Finite Element Method (FEM). These formulations have the distinctive feature of explicitly considering discontinuities (cracks, cement paste-aggregate interfaces, etc.) which in both formulations are represented via zero-thickness interface elements. Coupling effects are introduced by implementing a staggered scheme in which each FE model interacts with the other. Finally, various coupling mechanisms which can be reproduced with the proposed modelling framework in order to simulate different durability problems in cementitious materials, are discussed.

Chapter 6 proposes a reaction-expansion mechanism capable of explaining experimental observations on ASR expansions in SL glass concrete, both found in the literature and presented in previous Chapters 3 and 4. In particular the proposed mechanism is capable of explaining the effect of the stress state on the magnitude and distribution of ASR concrete expansions. Later, assuming some simplifying hypotheses, the proposed mechanism is mathematically formulated within the modelling framework presented in Chapter 5. The most significant of those simplification consists of considering that the dissolution/precipitation processes associated with ASR only occur within zero-thickness interface elements representing cement-glass contacts and fractures, while the continuum between them only hosts diffusion phenomena.

In Chapter 7, the model proposed in Chapter 6 for simulating expansions due to ASR in SL glass concrete, is used for analysing a number of real and ideal cases of increasing complexity. The cases analysed are considered as fundamental required steps for validating the proposed model. Wherever possible, the simulation results are quantitative and/or qualitatively compared with experimental results from Chapters 3 and 4, and from the literature.

Chapter 8 summarizes the main conclusions that can be drawn from this thesis. It also proposes several directions that can be taken to further develop the research work presented, as well as new research areas that could be now tackled.

Appendix A gathers details and complementary results of the experimental tests presented in Chapters 3 and 4.

Appendix B gathers details of the formulations presented in Chapters 5 and 6 that have been removed from the main body of the document for the sake of brevity. Additionally, simulation results complementary to those presented in Chapter 7 are also included.

Chapter 2

Alkali-Silica Reaction in concrete: a summary

2.1 Introduction

In this chapter, different aspects of ASR expansions in concrete are briefly summarized, beginning with the observed symptoms on field structures, continuing with the current understanding of the reaction mechanisms, and finalizing with the mathematical models proposed in the last two decades to simulate the phenomenon. The approach used follows very much the reviewing works by Lindgård [133], Rajabipour et al. [173] and Pan et al. [162], as well as the book by Saouma [181] and the one edited by Swamy [166].

2.2 The Alkali-Silica Reaction in concrete

'ASR is a deleterious reaction between the alkaline pore solution of concrete and various metastable forms of silica contained in many natural and synthetic aggregates' [173]. The silica structure is dissolved by the attack of hydroxyls ions passing to the pore solution in aqueous forms which later recombine with calcium and alkali ions (always present in concrete pore solution) into silicate hydrates of variable stoichiometric composition, i.e. the ASR gel. This reaction product is usually hygroscopic and swells as absorbs water. The degree of hygroscopy and the associated volume change of the ASR gel depends mainly on its chemical composition and RH in concrete pores. If the space available in the reaction site, i.e. pores, cracks, etc., is not enough to allocate the produced ASR gel, the 'swelling pressures produced by the gel induce the formation of microcracks close to the reaction sites, and these propagate and coalesce to produce cracking within the fabric of the concrete and overall expansion of the structural element affected'[166].

2.2.1 The observed effects of ASR

ASR affected structures typically show at least one of the following defects [212]:

- **Cracking** - Cracking ranges from map cracking for relatively unrestrained elements (Fig. 2.1) to aligned cracking where expansion is limited along the direction of highest restraint resulting in increased expansion in the less restricted direction. In such cases, the cracks become oriented in the same direction as the confining stresses (e.g. vertical cracks in columns and horizontal cracks in beams, Fig. 2.2).
- **Expansion or relative dislocation** - ASR-induced expansion may have a significant effect on the serviceability of a given structure, whether the entire structure is expanding or certain elements are expanding relative to adjacent non-expanding elements (Fig. 2.3).
- **Gel exudation** - ASR gel can precipitate in cracks reaching the concrete surface. When fresh, this gel will be colorless with jelly-like texture. On dehydration, it becomes white (Fig. 2.4).
- **Popouts** - The development of gel at a particular reactive aggregate near the surface can cause conical spalls from the concrete surface.

FIGURE 2.1: Map cracking on bridge abutment. From Ref. [212].

Other defects such as efflorescence, staining and joint spalling can be associated with ASR expansions. It shall be noticed that none of these features by itself can be used to unambiguously diagnose ASR, since the same symptoms may be due to other distress mechanisms. Therefore, the confirmation of ASR being present relies on laboratory investigation of samples taken from the structure [166, 212].

FIGURE 2.2: Aligned cracking on columns and beams. From Ref. [212].

FIGURE 2.3: Relative dislocation or misalignment. From Ref. [212].

2.2.2 Historical perspective

ASR was first identified in the late 1930s in concrete pavements of California, U.S.A., by T. E. Stanton [198, 199]. His early laboratory work demonstrate that expansion and cracking occur when certain combinations of high-alkali cement and aggregate where mixed in mortar bars stored in containers at high relative humidity. He further showed that expansion was negligible when the alkali content of the cement, expressed in terms of Na_2O_e (see Section 2.5.1), was below 0.60%, and that expansion could be reduced by pozzolans, thus setting the groundwork for preventive measures. This work also formed the basis for the mortar-bar test procedure, e.g. ASTM C227 [12].

In 1941, shortly after Stanton had published his work, Blanks [22] and Meissner [150] conducted investigations of abnormal cracking in concrete dams, generally confirming

FIGURE 2.4: Gel exudation. From Ref. [212].

Stanton's findings in relation with the importance of cement alkali level, aggregate composition and environmental condition in the development of expansion due to ASR. One result of this work was the development of the quick chemical test by Mielenz et al. [151], e.g. ASTM C289 [11].

Other researchers during 1940s and 1950s concentrated on clarifying the mechanisms of ASR expansions. In particular, Hansen [87] in 1944 and later Powers and Steinour [168] in 1955 proposed that osmotic pressure developed during swelling of ASR gel were responsible for the observed expansions.

In 1957, Swenson [205] was the first to recognize alkali-aggregate reactions which involved carbonate aggregate instead of siliceous one. 'Because rock susceptible to this type of reaction is relatively rare, and is often unacceptable for use as concrete aggregate for other reasons, reported occurrences of deleterious ACR in actual structures are relatively few' [1].

In the 1970s and 1980s, important improvements in the comprehension of ASR chemical mechanisms was achieved by the work of authors such as Struble, Diamond, Chatterji and Thaulow [41, 55, 56, 108].

The first mathematical models of ASR expansions were proposed in the early 1980s [91]. Since then, a wide range of theoretical and empirical models from micro to macro scale have been proposed. Lately, focus has been in modelling coupled chemo-mechanical, chemo-hygro and chemo-thermal mechanisms.

By far, the most widely cited ASR tests of the last two decades have been conducted at the *Laboratoire Central des Ponts et Chauses* (LCPC) in Paris. According to Saouma

[181], the work of Larive [109] and Multon [153] 'actually sparked the development of "modern" computational tools for AAR, and models went from "empirical" to "chemo-mechanical"'.

Since 1974, fourteen international conferences on alkali-aggregate reaction (ICAAR) have been held, attracting increasing numbers of researchers and engineers. 'The series of published proceedings of these conferences perhaps provides the most important source of research information available' [166].

2.3 Reaction mechanisms

ASR in concrete is a very complex phenomenon that involves a number of simultaneous reaction mechanisms that are not completely understood, in spite of how much has been learned since it was first reported 70 years ago. The available research work on the basic mechanisms mainly focus on partial aspects and an effort have to be made to formulate a comprehensive, coherent explanation of ASR mechanisms. In this sense, the recent reviewing article by Rajabipour et al. [173] is a step forward and its approach will be followed in the present section.

According to Rajabipour et al. [173], ASR damage is the result of a number of sequential reactions, including: (1) dissolution of metastable silica, (2) formation of nano-colloidal silica sol, (3) gelation of the sol, and (4) swelling of the gel:

$$(SiO_2)_{solid} \xrightarrow{1} (SiO_2)_{aqueous} \xrightarrow{2} (SiO_2)_{sol} \xrightarrow{3} (SiO_2)_{gel} \xrightarrow{4} \text{swelling of gel} \tag{2.1}$$

The slowest of these reactions is often the silica dissolution, and thus primarily controlling the rate of ASR in concrete. Factors that accelerate the silica dissolution (e.g. high alkalinity, temperature) usually accelerate the ASR in concrete. Additionally, swelling of gel depends on moisture availability, which could limit ASR damage in dry concrete.

2.3.1 Dissolution of metastable silica

Silicates are primarily composed of tetrahedral silica units (SiO_2), with one silica atom in the centre and four oxygen atoms surrounding it. This tetrahedral units are connected through oxygen vertex forming siloxane ($\equiv Si-O-Si\equiv$) bonds. While the $O-Si-O$ bond angle is fixed in 109°, the angle of $Si-O-Si$ bonds can vary between 100° and 170°, allowing thus a wide variety of structures that can be macro-crystalline (Fig. 2.5a), micro-crystalline or amorphous (Fig. 2.5b) [194]. In addition to pure silica, silica minerals often contain hydrogen or metallic elements (e.g. Na, K, Ca) connected to oxygen

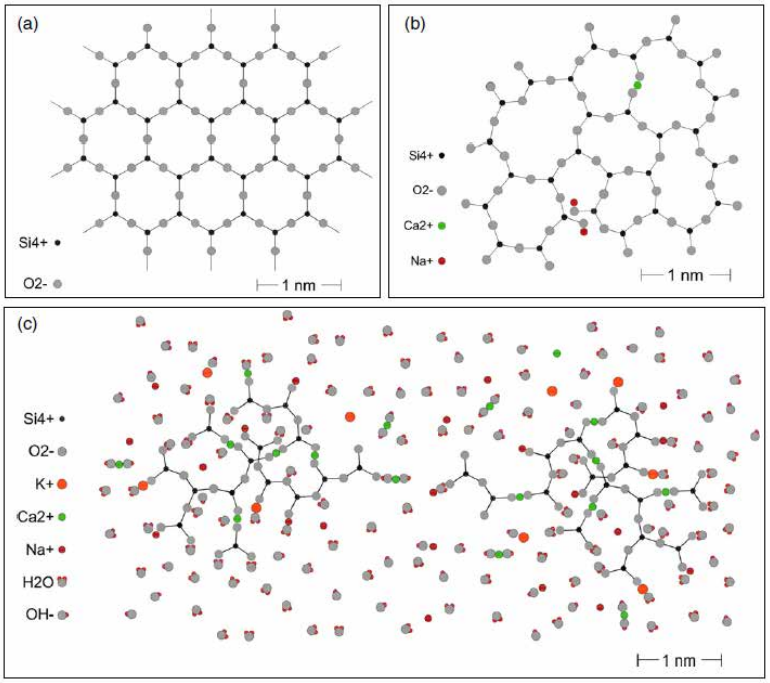

FIGURE 2.5: (a) 2D ball and stick representation of quartz (a common form of crystalline solid SiO_2) composed of uniformly sized silica rings where all oxygens are bridging silicon atoms; (b) amorphous solid SiO_2, showing non-uniform rings and the contribution of alkalis and Ca in forming non-bridging oxygens; (c) alkali-silica (ASR) gel composed of clustering of colloidal silica particles surrounded by the gel's pore solution; the silica structure is highly degraded with lots of non-bridging oxygens. From Ref. [173].

atoms. The dissolution and deposition of silica in water involves hydration and dehydration reactions catalyzed by hydroxyl ions (OH^-) [101]:

$$x(SiO_2)_s + 2H_2O \longleftrightarrow (x-1)(SiO_2)_s + (Si(OH)_4)_{aq} \tag{2.2}$$

In addition to monosilicic $Si(OH)_4$, the dissolution products can be oligomers of the form [101]:

$$x(SiO_2)_s + (y+1)H_2O \longleftrightarrow (x-1)(SiO_2)_s + (Si_yO_{y-1}(OH)_{2y+2})_{aq} \tag{2.3}$$

The solubility product of Reaction (2.2) increases with temperature and with reduction of silica crystallinity, as it is shown for quartz and amorphous silica in neutral water in Fig. 2.6.

While the solubility limit of $(Si(OH)_4)_{aq}$ does not change significantly with the pH, the apparent solubility of silica (i.e. the summation of the solubility limits of all the aqueous silica species) increases rapidly in highly alkaline solutions due to the ionization Reactions (2.4) and (2.5).

$$(Si(OH)_4)_{aq} \longleftrightarrow (H_3SiO_4^-)_{aq} + H^+ \tag{2.4}$$

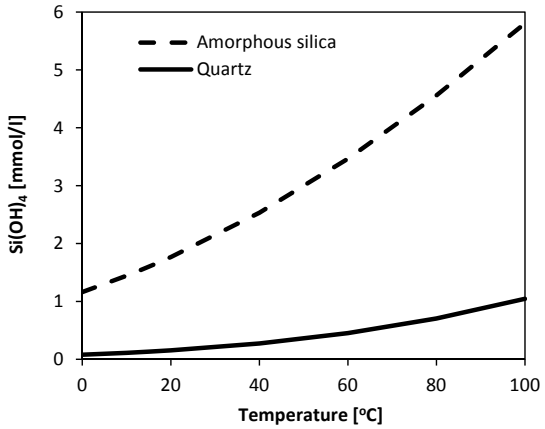

FIGURE 2.6: Solubility limit in neutral water of quartz and amorphous silica as a function of temperature, using best fit expressions proposed in Refs. [72, 132].

$$(H_3SiO_4^-)_{aq} \longleftrightarrow (H_2SiO_4^{2-})_{aq} + H^+ \tag{2.5}$$

The equilibrium equations of these reactions are given in Eqs. (2.6) and (2.7) [195], where the equilibrium constants are valid in a 0.6M NaCl medium at 25 °C and $\{X\}$ stands for the thermodynamic activity of species X.

$$\frac{\{H_3SiO_4^-\}\{H^+\}}{\{Si(OH)_4\}} = 10^{-9.473} \tag{2.6}$$

$$\frac{\{H_2SiO_4^{2-}\}\{H^+\}}{\{H_3SiO_4^-\}} = 10^{-12.647} \tag{2.7}$$

Using Eqs. (2.6) and (2.7), it is possible to calculate the solubility limit of each silica species in aqueous solution as a function of pH, as it is shown in Fig. 2.7. It can be observed that above pH 9 (the pH of concrete pore solution usually range between 12 and 13.5), the apparent solubility of silica increases by several orders, being the predominant species in the solution $H_3SiO_4^-$ and $H_2SiO_4^{2-}$. At lower concentration, other polymeric silicic ions can also be present [195]. In this sense, alkali ions in pore solution play a decisive role by raising the OH^- concentration to a level at which: (1) the silica solubility limit is high enough to allow the formation of ASR gel, and (2) the solid silica is dissolved at a significant rate. It is important to note that, at high pH, Reactions (2.4) and (2.5) proceed in the direction of reducing pH. In addition, ion exchange reaction could further decrease pH, e.g.:

$$(Si(OH)_4)_{aq} + Na^+_{aq} \longleftrightarrow ((HO)_3 \equiv Si - O^- ... Na)_{aq} + H^+_{aq} \tag{2.8}$$

$$(Si(OH)_4)_{s} + Na^+_{aq} \longleftrightarrow ((HO)_3 \equiv Si - O^- ... Na)_{s} + H^+_{aq} \tag{2.9}$$

where $O^-...Na$ indicates a strong Van der Waals bond.

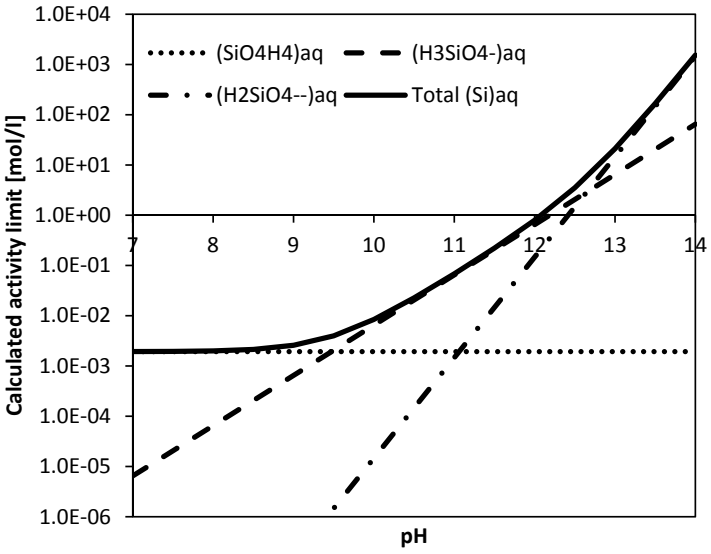

FIGURE 2.7: Calculated solubility limit of amorphous silica in 0.6 M NaCl solution as a function of pH (T = 25 °C), assuming unitary activity coefficients for all species. Adapted from Ref. [140].

Beside the solubility limits of silica dissolution reaction, special attention should be paid to its kinetics, since it can largely control the overall rate of ASR. However, 'literature on this subject is limited and significant knowledge gaps exist with respect to quantifying the dissolution rate as a function of aggregate composition, mineralogy, and surface properties, pore solution composition, temperature and pressure' [173]. The influence of these factors can be illustrated with Fig. 2.8, corresponding to experimental measurements in batch reactors of silica dissolution rates for quartz and amorphous silica at different temperatures and solution compositions.

2.3.2 Formation and gelation of colloidal silica

If pH and temperature are high enough to avoid supersaturation, and in the absence of calcium ions, dissolved silica will remain in solution. At high pH, most aqueous silica species are negatively charged (Fig. 2.7) and the resulting electrostatic repulsion prevents gelation. In concrete pore solution, however, the Ca^{2+} (and other polivalent metal ions. e.g Al^{3+}) present can link silica ions forming poly-metal-silicates allowing a condensation reaction even in a strongly basic medium [73, 101], e.g.

$$2((HO)_3{\equiv}Si{-}O^-)_{aq} + (Ca^{2+})_{aq} \longleftrightarrow ((HO)_3{\equiv}Si{-}O...Ca...O{-}Si{\equiv}(HO)_3)_{sol} \quad (2.10)$$

where the right hand side compound can be written as CS_2H_3, using the cement chemistry notation. Additionally, alkali-silicate monomers (formed accordingly with Reaction (2.8)), may also react with Ca^+ (Reaction (2.11)). The resulting calcium deficiency

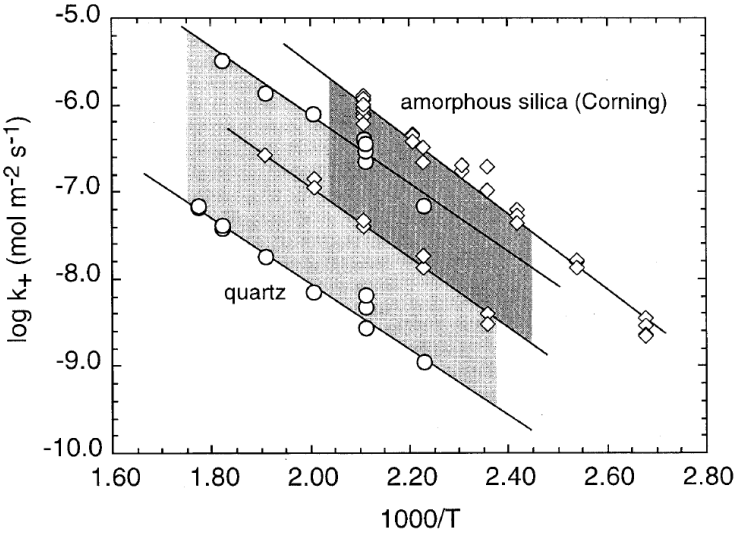

FIGURE 2.8: Comparison of measured amorphous silica and quartz dissolution rates. A similar, but offset, temperature dependence is exhibited. Open circles denote quartz dissolution rates measured in deionized water (lower trend) and 0.05 molar NaCl (higher trend). Open diamonds indicate amorphous silica dissolution rates in same solutions. Shaded areas illustrate the change in dissolution rate with the addition of sodium. From Ref. [95].

promotes further dissolution of solid portlandite maintaining the Ca^{+} concentration (Reaction 2.12).

$$2((HO)_3 \equiv Si - O^{-} ... Na)_{aq} + Ca^{2+} \longleftrightarrow 2Na^{+} + ((HO)_3 \equiv Si - O ... Ca ... O - Si \equiv (HO)_3)_{sol} \quad (2.11)$$

$$(Ca(OH)_2)_{sol} \longleftrightarrow (Ca^{2+})_{aq} + (OH^{-})_{aq} \quad (2.12)$$

As condensation reactions proceed, the initial nucleus grows to nano-colloidal silica sol. Aggregation of these colloidal particles results in large metal silicate structures in the form of space-filling silicate gel or more compact macro-scale precipitates [94, 186] (Fig. 2.9). The presence of soluble calcium is essential to form ASR gel [23, 112], otherwise silica species remain in solution. Fig. 2.5c is a schematic representation of the structure of alkali-silica gels, which are composed of clustering colloidal particles surrounded by gel pore solution. The distance between the particles is a function of the water content of the gel [173].

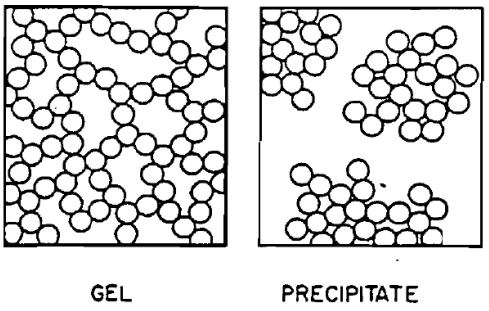

FIGURE 2.9: Two-dimensional representation of the difference between a gel and a precipitate. From Ref. [101].

2.3.3 Swelling of the gel

The swelling of ASR gels has been explained appealing to a number of different phenomena. The most accepted explanation, first proposed by Powers and Steinour [168], attribute the absorption of water and the associated swelling of the gel to an osmotic mechanism, in which the insoluble silica gel acts as a semi-permeable membrane (Fig. 2.10). This diffusion mechanism derives fundamentally from the difference in the free energy (or activity) of the water already in the gel and the surrounding water being drawn into the gel [55]. In this context, the osmotic pressure may be defined as the minimum pressure that needs to be exerted on the gel water to prevent the absorption of outer water. Swelling have been also attributed to electric double-layer repulsion forces that form on the charged surface of the gel solid particles [171]. Other authors, focused on the micro or meso-scale, attribute the swelling to differential kinetics of fast inward diffusion of alkali and hydroxyl ions into the reactive sites and slow outward diffusion of silica ions from this sites [40, 96]. Finally, Garcia-Diaz et al. [76] attribute the swelling to change of volume of the aggregate during the $Q_4 \rightarrow Q_3$ depolymerization of silica by hydroxyl attack. It shall be noted that the above-mentioned mechanisms are not mutually exclusive, and, therefore, simultaneous manifestation of two or more of them could be expected.

2.3.4 Mass transport

In concrete, the above-mentioned reactions are accompanied by mass transport processes of chemical species in solution, which may determine both the rate and the extent of ASR expansions. In Fig. 2.11, the mass transport pathways are shown schematically. The pore solution is in intimate contact with cement hydration products as well as with aggregates particles and it serves as the main agent of transport [82]. Although capillary absorption and permeation (i.e. the transport of fluid under a pressure gradient) can in

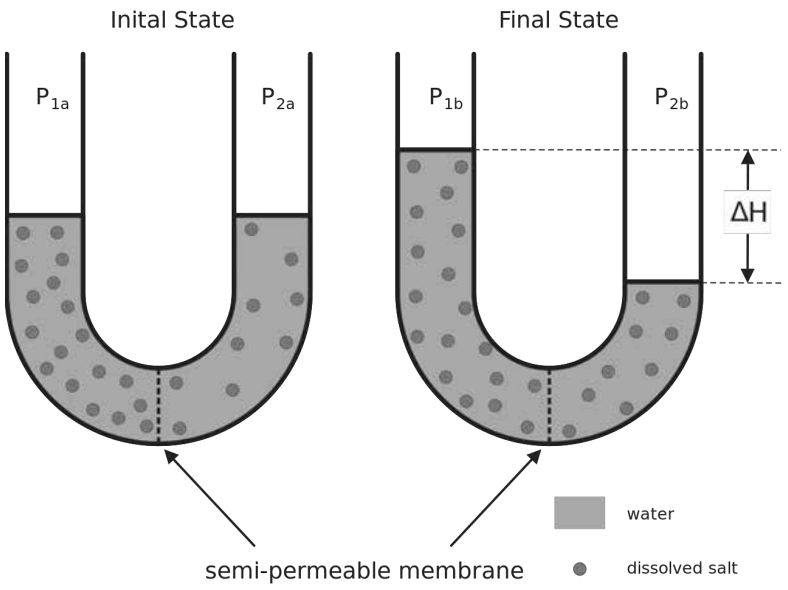

FIGURE 2.10: An example of osmosis: dissolved salt forcing water to pass through a semi-permeable membrane. From ©Hans Hillewaert / Wikimedia Commons / CC-BY-SA-4.0.

certain cases be of significant importance, numerous studies have clearly indicated that ions are mainly transported through the concrete pore structure and microcracks by a diffusion process [180].

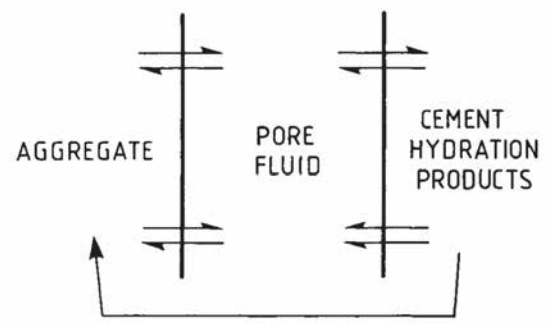

FIGURE 2.11: Mass transport initiates the ASR. Transfer pathways are shown between pore solution and aggregate, but secondary pathways may also occur between solids: aggregate and cement paste. From Ref. [82].

The solid and solution phases in concrete are in a dynamic chemical equilibrium. The solid phases that form the HCP are an assemblage of hydrated compounds that may be crystalline or gel-like in character. A change in the composition of the solution affects the amount and composition of the solid [175]. Not considering any external source, the composition of both solid and solution phases depends mainly on the composition of the binder (cement and pozzolans) and on the water:binder ratio. All the major elemental constituents present in cement (Ca, Mg, Na, K, Fe, Al, Si, S, C and Cl) can be found in the pore solution after hydration [8]. However, cement pore water at normal

temperatures can be described principally as a solution of Na^+, K^+, Ca^{2+} and OH ions, where portlandite ($Ca(OH)_2$) solubility controls Ca^{2+} concentrations (SO_4^{2-} is an important ion in cement pore water only at early time or high temperature) [60].

Due to the concentration gradient (Fick's law), the ions in HCP pores tend to diffuse into the aggregates, dissolving the reactive silica into silicate ions which pass to the pore solution. The dissolved silica may combined with the incoming ions from the HCP to form ASR gel, or well diffuse towards the HCP.

2.4 Effect of aggregate properties

The presence of some form of 'reactive silica' in the aggregates is a necessary but insufficient condition for the development of deleterious ASR in concrete. Other aggregate properties, such as the composition and texture of the source rock, grading and size of the particles, and the reactive aggregate content, may play a decisive role in the rate at which aggregates containing potentially reactive forms of silica react.

2.4.1 Aggregate composition

To identify a potentially reactive aggregates, attention is focused on the mineral constituents of the source rock. As little as 2% of reactive components in the aggregates is needed to produce deleterious ASR [166]. Although most rock are capable of containing reactive forms of silica, the number of types of silica that exhibit reactivity is quite small. The potential reactivity of a silica mineral increases with the degree of microstructural disorder, i.e. the different forms of amorphous, glassy or poorly crystalline silica, as well as strained or intensely fractured crystalline forms are expected to be reactive. A comprehensive list of potentially reactive silicate minerals is shown in Table 2.1.

Strictly speaking, depending on time, temperature, and particle size, all silicate or silica minerals can react with alkaline solutions, although a large number of minerals react only to a negligible degree [149]. In the context of ASR studies or design codes and regulations, referring to a particular siliceous mineral as 'reactive', means that this aggregate constitutive mineral could lead to the development of deleterious ASR expansions in concrete within engineering time scales. Moreover, microstructural parameters such as the silica micro-porosity, the rock matrix porosity or the presence of microcracks, which control the diffusion of reactants into the aggregate particles, may be determinant of the reactivity of a given aggregate.

TABLE 2.1: Some silicates susceptible to ASR. From Refs. [1, 149, 165, 166].

Name	Chemical Composition	Description
Opal	SiO_2nH_2O	Amorphous
Chalcedony	SiO_2	Microcrystalline to cryptocrystalline; commonly fibrous
Certain forms of quartz	SiO_2	Microcrystalline to cryptocrystalline; Crystallines, but intensely fractured, strained, and/or inclusion-filled
Cristobalite	SiO_2	Crystalline
Tridymite	SiO_2	Crystalline
Rhyolitic, dacitic, latitic, or andesitic glass or cryptocrystalline devitrification products	Siliceous, with less proportions of Al_2O_3, Fe_2O_3, alkaline earths, and alkalis	Glass or cryptocrystalline material as the matrix of volcanic rocks or fragmented in tuffs
Synthetic siliceous glasses	Siliceous, with less proportions of alkalis, alumina, and/or other substances	Glass

2.4.2 Aggregate size and grading

The influence of aggregate grading on concrete expansion has been studied since the very first report of ASR [198], but it is still not fully understood. Since ASR starts with a topochemical reaction (silica dissolution), ASR expansions should be expected to increase with reduced particle size, because of the increased specific surface area of reactive aggregates [198, 217]. However, experimental observations have showed that the maximum expansion may vary non-monotonically as a function of aggregate size, and the most deleterious effect may occur for aggregates of some intermediate size [173] (Fig. 2.12). The pessimum size depends on the nature and composition of the aggregate [154]. This effect of aggregate size on the ASR-induced expansion can be attributed to various causes of either chemical or mechanical origin:

- Different mineralogy of aggregates at different sizes. In natural sands it is likely that certain reactive minerals dominate in certain sieve sizes [173].
- Pozzolanic effect. Very fine reactive aggregates aggregates may reduce or even suppress the expansion due to pozzolanic reactions [57, 193].
- Diffusion process of aqueous species in pore solution to the core of larger aggregates. Different diffusivities may imply a gradual modification of the pore solution composition towards the interior of the aggregate which may modify the ASR rate and/or ASR gel composition.
- Residual cracks in crushed aggregates. Maraghechi et al. [142] observed that the reactivity of glass aggregates depends significantly on the size/width of residual

cracks formed during aggregate crushing. They found that the fraction with wider cracks show higher ASR reactivity.

- Fracture mechanics size effects. The pressure exerted by the ASR gel which is needed to propagate a pre-existing crack in an aggregate particle depends on the particle size [176], i.e. given two aggregates of different size but same pre-existing crack, the amount of ASR gel required to propagate the crack will be greater for the bigger aggregate.

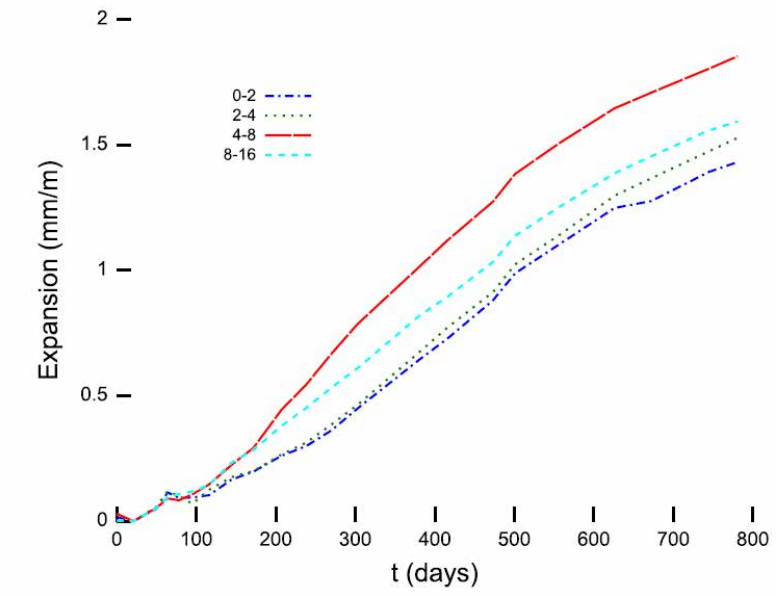

FIGURE 2.12: Expansion of concrete with a single fraction of reactive aggregate. Mortar bars of 70×70×280mm in 0.15 M NaOH solution at 38 °C. From Ref. [62].

2.4.3 Reactive aggregate content

Certain aggregates containing highly-reactive forms of silica have a pessimum effect: for a given level of alkalis, the swelling of concrete based on these aggregates increases first with the reactive aggregate content to reach a maximum value and finally decreases for a reactive aggregate content greater than the pessimum [75] (Fig. 2.13). Hobbs [92] distinguished 4 areas on the pessimum curve (Fig. 2.13):

- Areas A and D: the reaction occurs but is too weak because of a lack in reactive silica (area A) or in alkalis (area D) to induce a swelling phenomenon.
- Area B: the reaction occurs with an excess of alkalis. The swelling increases with the reactive silica content.
- Area C: the reaction occurs with an excess of reactive silica. The swelling decreases with the reactive silica content.

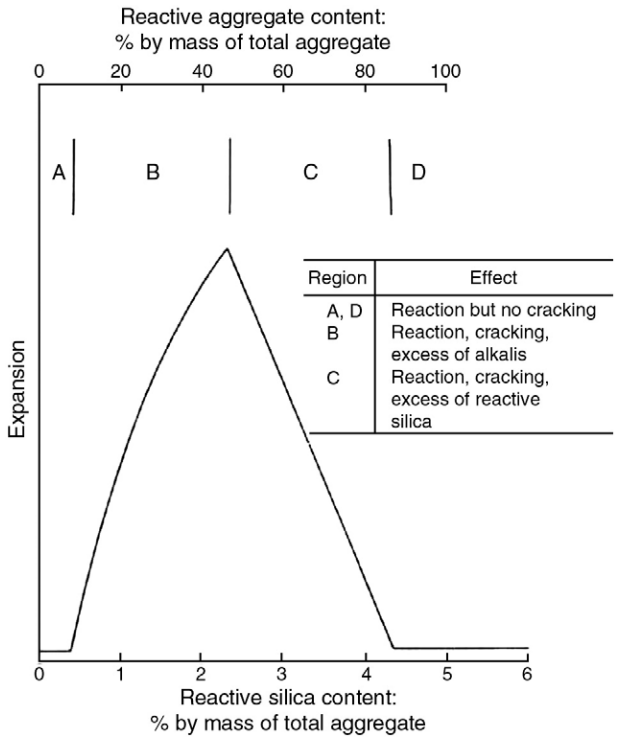

FIGURE 2.13: Pessimum effect of pure siliceous aggregate according with Hobbs [92].

The pessimum aggregate content varies with the alkali content of concrete, with higher alkalis resulting in a larger pessimum aggregate content [173]. For this reason, some authors suggest that both alkali and silica concentration should be considered together, and that there is a certain 'pessimum proportion' of water-soluble alkali to reactive silica in order to produce the maximum expansion [57, 83, 92].

2.4.4 Surface versus intra-particle reactions

An important factor influencing aggregate reactivity is the accessibility of the alkaline pore solution to reactive silica [173]. If the reactive aggregate is composed entirely of reactive silica (e.g. volcanic or synthetic glasses), the aggregate may react quickly with the pore solution to form ASR gel at the surface. However, if the reactive silica is finely disperse in the non-reactive matrix of the aggregate (e.g. siliceous limestones) it takes time for the pore solution to reach the reactive silica and, therefore, the reaction proceeds more slowly and the gel is formed within the aggregate [173]. In addition, the composition of ASR gel varies with the location of the reaction site. In general, ASR gel formed at the aggregate surface, where the calcium sources of the HCP are readily available, is richer in calcium than the one formed in the interior of the aggregate, where calcium ions have to diffuse from the outside [206]. This may have a major influence in

the development of the internal pressures, since the calcium content of ASR gel determine its hygroscopic and mechanical properties [111, 112, 114, 203].

In addition, the presence of pre-existing microcracks in the aggregate may play an important role by increasing the exposed surface of aggregate to pore solution and by altering the diffusion pattern of calcium and alkali ions into the aggregate [142, 174].

2.5 Alkalis

Sodium and potassium ions in pore solution play a double role in the development of ASR. On one hand, they raise the pH of the pore solution to a level at which the reactive silica is dissolved at a significant rate and the solubility limit is high enough to allow the formation of ASR gel. On the other hand, alkali ions neutralize part of the silicate ions in solution in the gelation process, increasing the hygroscopic capacity of the ASR gel [107].

2.5.1 Alkali requirement

The ASR cannot proceed in concrete if the alkali concentration is below a certain threshold value [166]. Although this threshold value cannot be establish a priori for every concrete mixture, permissible alkali contents between 2.5 and 4.5 kg of Na_2O_e per m^3 of concrete have been specified by various countries and agencies, sometimes varying depending on aggregate reactivity [71]. Some authors establish this limit in terms of OH^- concentration in pore solution, e.g. according with Diamond [54] the threshold OH^- concentration is above 0.25 M. Empirical linear relationships between the Na_2O_e content of the binder and OH^- concentration in pore solution has been proposed by several authors [55, 89, 211], e.g. Fig. 2.14.

In order to assess the total alkalis present in a cement or concrete, it has become a standard practice to express the alkali content in terms of 'sodium oxide equivalent' (Na_2O_e), which is calculated as Na_2O_e wt% = Na_2O wt% + 0.658 K_2O wt%, where 0.658 is the ratio between de molar mass of Na_2O and K_2O. Fig. 2.15 illustrates the effect of alkali content of concrete on the expansions of concrete prisms, for concrete with a range of cement contents (and w/c), cement alkali levels and with and without alkali boosting. Data indicates that expansion is primarily a function of the alkali content and, to some extent, independent of the cement content, the alkali content of the cement, and whether or not the alkali content was artificially boosted [133].

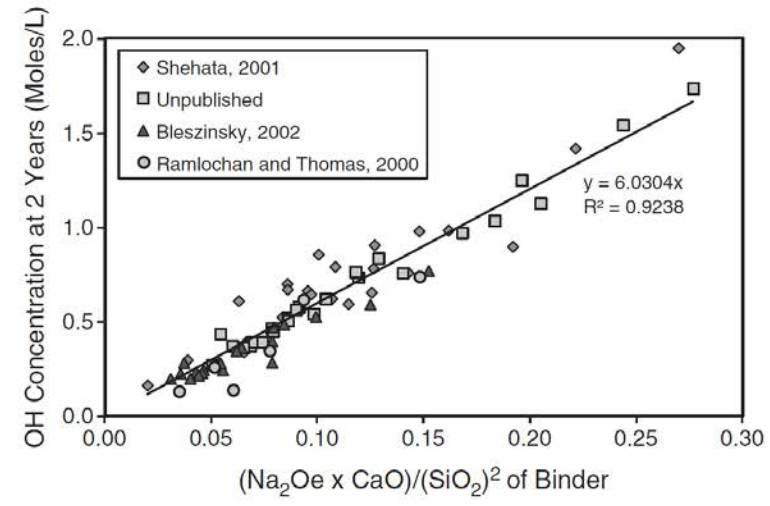

FIGURE 2.14: Relationship between pore solution composition and the chemical composition of the binder. Pore solution extracted from 2-years-old sealed pastes with w/cm=0.50. From Ref. [211].

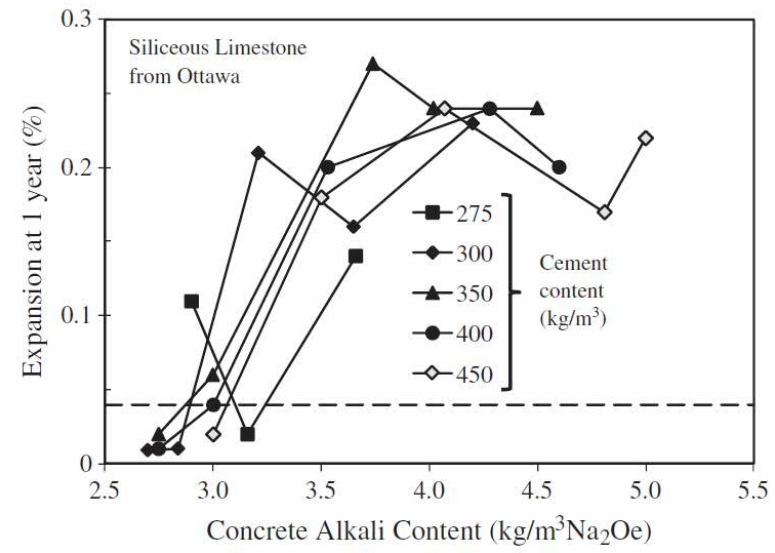

FIGURE 2.15: Expansion of concrete prisms as a function of alkali content. The dashed line represents the adopted critical 1 year expansion limit. From Ref. [133].

Even though, by using Na_2O_ewt% as a general indicator of alkali content, sodium and potassium alkalis are treated indistinctly, some authors have reported that concrete mixtures with equal Na_2O_ewt% but different K/Na ratios can expand considerably differently [113].

2.5.2 Alkali sources

Usually the main source of alkalis in concrete is the binder (i.e. Portland cement and SCMs) used. When Portland cement is mixed with water, the alkali sulphates pass into

solution almost immediately, whereas alkali locked into the crystal structures of clinker minerals only pass into solution as the hydration proceeds [82]. The alkali release rate, therefore, varies from one cement to the other depending on the distribution of alkalis between rapid-release and slow-release sources. However, since ASR proceeds slowly under site exposure conditions, over the period of time required for its action virtually all the cement alkali, irrespective of the source, is likely to become potentially available for release [82]. This may not be the case with SCMs, which hydration may need longer time for hydration.

Even though SCMs are known to control ASR mainly by their capability to reduce the alkalinity of the pore solution by binding alkalis in the hydration products [133], certain SCMs (primarily some high-Ca fly ashes) include significant content of alkalis that are slowly released to the pore solution as hydration proceeds. In some cases, this alkali contribution may exceed the benefit of using SCMs [173].

Some aggregate types containing certain minerals, e.g. micas, clay minerals, alkali feldspars, zeolites and volcanic glass, may gradually release significant quantities of Na^+ and K^+ to the concrete pore water [18, 19, 47]. According with Bérubé et al. [18], aggregate contribution to the total alkali content of concrete can be as significant as 3.4 kg of Na_2O_e per m^3 of concrete.

In addition to alkalis coming from the concrete constituents, external sources such as seawater, some ground waters and de-icing salts, may also contribute to the total alkali content. The absorption of alkalis from such sources will depend primarily on the porosity and permeability of the concrete, as well as on the nature of the exposure to alkali-containing fluids [166].

2.5.3 Alkali binding

The C–S–H formed in cement and SCMs hydration has variable composition. In Portland cements, the typical Ca/Si ratio is about 1.8, but the addition SCMs tends to decrease it. SCMs with high calcium contents lead in general to only a slight reduction in Ca/Si ratios, which may decrease to 1.4-1.5. However, SCMs with low calcium content can lead to ratios as low as 1.0 [82]. The surface charge of C–S–H clusters depends on its Ca/Si ratio: at high ratios its charge is positive, with the result that C–S–H tends to adsorb anions but not cations. Hence, incorporation of Na^+ and K^+ into C–S–H is rather limited; alkalis preferentially concentrate in pore solution. But as the Ca/Si ratio decreases the surface charge of C–S–H drops to zero, eventually becoming negative below Ca/Si $\sim$ 1.2-1.3 [93]. Negatively charged C–S–H shows enhanced alkali-binding power for cations, especially alkalis. Thus the alkali-binding power of C–S–H is enhanced by

the addition of SCMs, leading to a reduction of alkali and hydroxyl concentration in the pore solution [211].

2.6 Role of calcium

The content of CaO of ordinary Portland cements ranges between 45 and 60 percent in solid weight. During hydration this calcium content is mainly distributed in portlandite crystals and C–S–H. In terms of volume of solids, portlandite constitute 20 to 25 percent of the hydrated paste [149]; and it may be found as isolated crystals or in solid solution in C–S–H gels with high Ca/Si ratio [196].

In an aqueous medium, portlandite dissolves according to Reaction 2.12. Its solubility limit, however, is relatively small and is reduced even more by increasing alkali concentration and temperature. In relation with silica dissolution kinetics, portlandite dissolution is practically instantaneous, i.e. pore solution in contact with portlandite remains calcium saturated during ASR.

As already described in Section 2.3.2, calcium ions react with silica species in solution causing the gelation of alkali and silicate species, which otherwise would remain in the solution. Once the gel is formed, part of the alkali ions fixed in the ASR gel may be replaced by Ca^{2+} (Reaction 2.11), increasing the cross-linking of the silica structure (Fig. 2.5c) and recycling alkalis to the pore solution. This calcium enrichment has been reported by several authors [66, 108, 206] who have found that gel formed within or close to aggregates has a low calcium content and high content in alkali, but as the distance from the aggregate increases the calcium content of the gel increases (Fig. 2.16).

The composition of ASR gels found in concretes is highly variable, but, accordingly with Helmut and Stark [88], it is possible to regard them as belonging to one of several relatively simple compositional categories: (1) partially reacted and swollen silica, (2) relatively pure alkali silicate solutions or gels of various alkali and water contents, and (3) simple mixtures of two components of nearly constant composition (except for their water contents), one rich in calcium and the other with little or no calcium at all. Considering this later possibility, by fitting composition data from natural [108] and synthetic [104] silico-calco-alkaline gels, they found that the composition of the first compound should be $C_{1.4}N_{0.16}SH_x$ and that of the second one $N_{0.2}SH_x$ (if sodium is the only alkali present).

As the calcium content increases, the microstructure of the ASR gel changes due to the increasing amount of internal restrictions (cross-linking) [73, 101], resulting in increasing

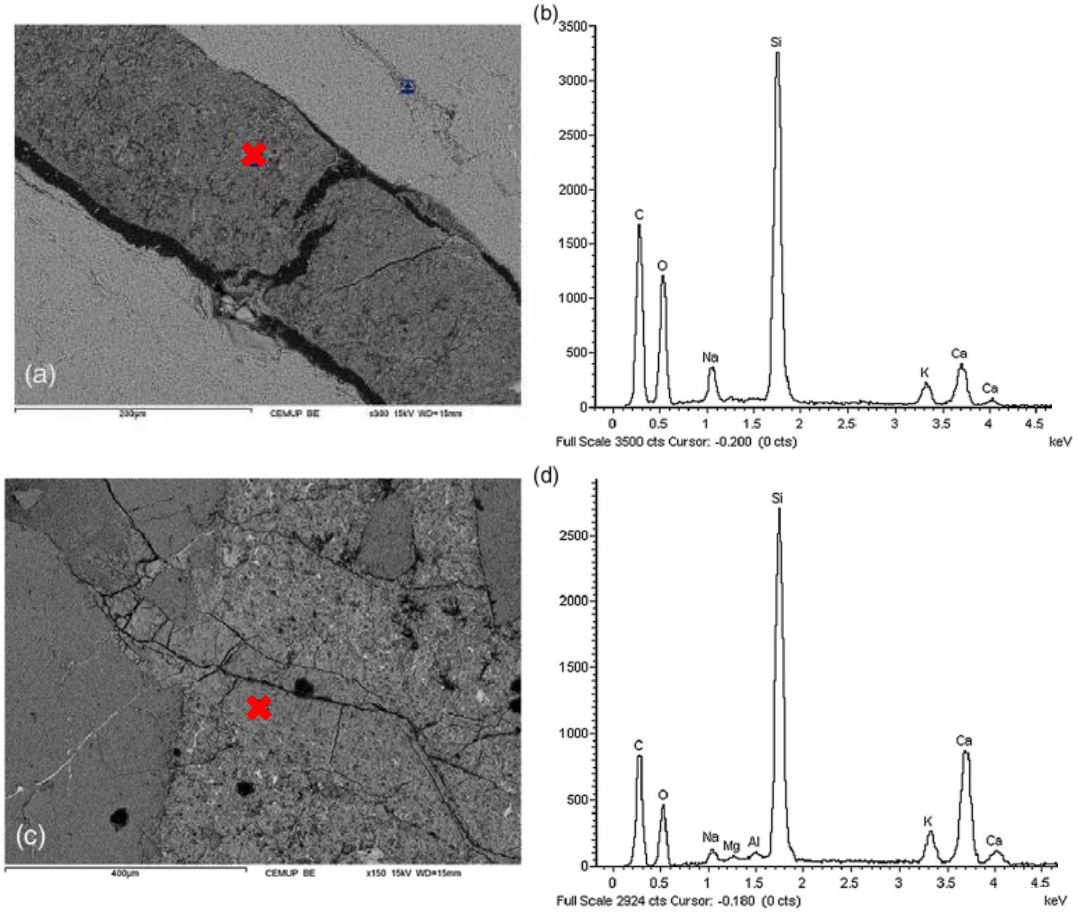

FIGURE 2.16: SEM images and EDS analysis (at the points indicated with a cross) of ASR gel in concrete from a bridge in service. (a-b) Gel filling a crack crossing a quartz particle. (c-d) Gel filling a crack expanding to the cement paste. Adapted from Ref. [66].

stiffness and mechanical strength [114]. Simultaneously, the hygroscopic capacity of the gel, linked to the alkali content, is reduced, resulting in less volume change [111, 112, 171].

2.7 Effect of exposure conditions

2.7.1 Moisture

ASR expansion is significantly dependent on the availability of moisture, usually measured in percent of relative humidity (RH) in the concrete pore space. The type of relationship is illustrated in Fig. 2.17. It can be seen that below a certain critical value of RH (usually around 80% at 23 °C [170]) ASR expansion is negligible, but above that value the expansion increases dramatically [166]. Critical RH have been reported to decrease with temperature [170], but this effect has not been studied systematically.It is important to note that concrete, even in dry conditions, will retain some amount of pore water. In general, and with the exception of a dried outer layer of up to a few tens of millimetres, the RH within concrete may remain at 80-90% [166]. Therefore, significant ASR swelling can develop even without external water supply.

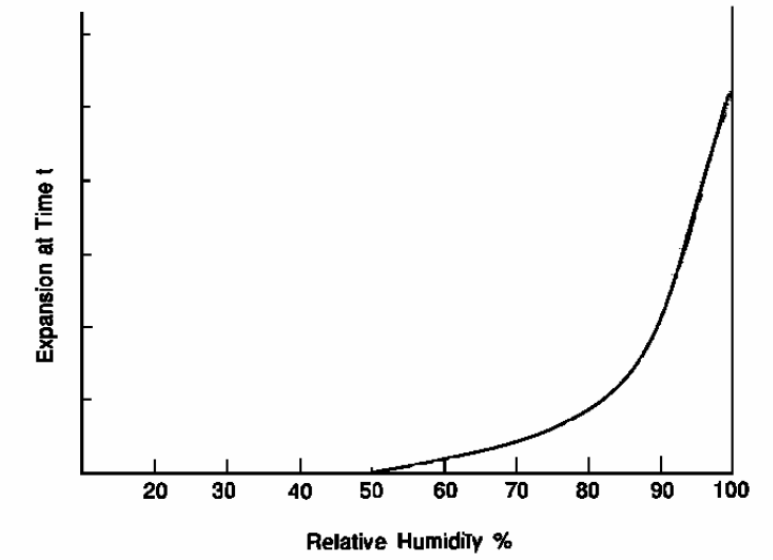

FIGURE 2.17: Effect of relative humidity on the ASR expansion of concrete. From Ref. [166].

The effect of RH cycles is well illustrated in Fig. 2.18 taken from the experimental work of Poyet et al. [170], with concrete samples at 60 °C. In this figure, ASR expansion curves of concrete samples for four different external RH conditions are plotted together: constant 96% RH, constant 59% RH, alternated 14 days cycles (short cycle) and 28 days cycles (long cycle) between these constant values. As expected the sample exposed to 96% RH expanded far more than the sample exposed to 59% RH. Final expansions of long and short cycle curves are quite similar. For each drying part an extra shrinkage attributed to water loss of the ASR gel was recorded (shrinkage of drying HCP was already discounted in Fig. 2.18). These drying shrinkages were readily recovered in the

following wetting cycle. As it was previously found by Larive et al. [110], irregular external RH seems to irreversibly affect concrete expansion.

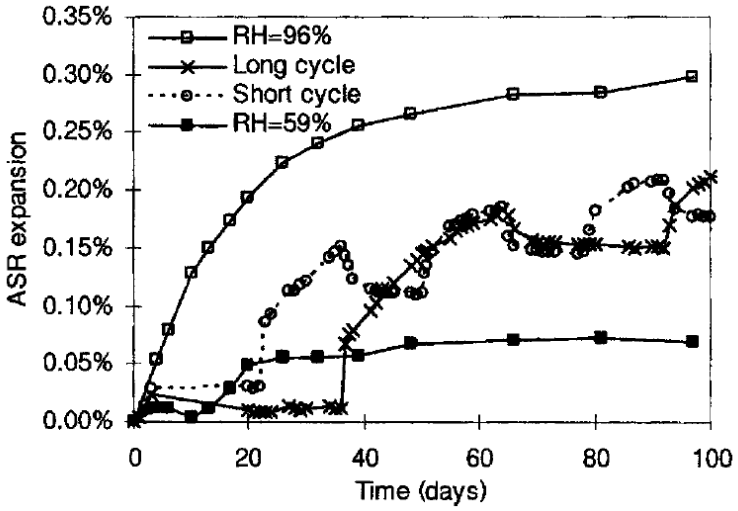

FIGURE 2.18: ASR swelling comparison: between constant and cyclic relative humidity. From Ref. [170].

The mechanisms by which moisture availability affects ASR expansions are still unclear. According to Larive et al. [110], water osmosis or imbibition is not the main cause of swelling. Therefore, water only increases concrete expansion when it is available during formation of the ASR gel. This implies that the lack of sufficient water alters in some way the amount or characteristics of the gel formed and not only its water content.

2.7.2 Temperature

Temperature affects both the rate and the final magnitude of ASR expansions in concrete, as it is illustrated in Fig. 2.19. At high temperature the expansion is initiated early and developed rapidly, but as reaction continues the expansion rate slows down. At lower temperatures, expansion starts later and more slowly but eventually reaches the same level and then exceeds the expansion attained at higher temperatures [166]. The illustration given is for expansions at 20 °C and 40 °C but similar comparisons in the range of 8 °C to 60 °C can be found in the literature, e.g. Ref. [70].

The effect of temperature in the expansion rate is readily explained by its effect on silica dissolution rate (Fig. 2.8), which is believed to control the overall ASR rate [173]. Considering the Arrhenius equation and an apparent activation energy for amorphous silica dissolution of 74.5 kJ/mol [95], the silica dissolution rate is expected to increase 12 times when temperature is raised 20 °C.

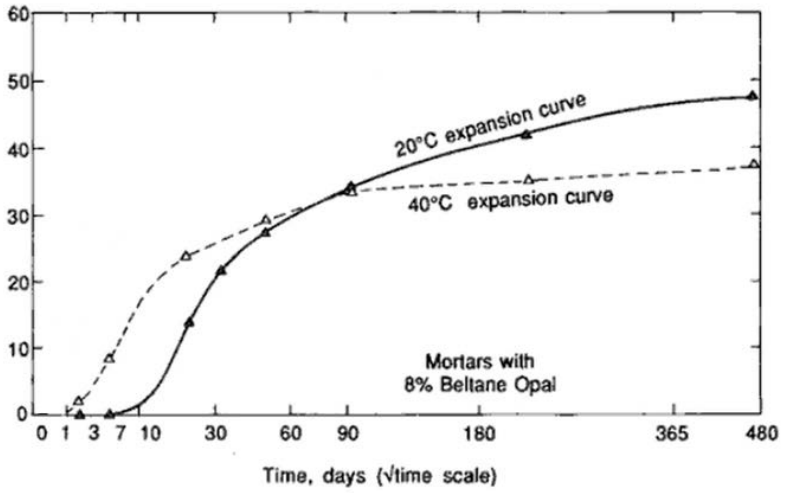

FIGURE 2.19: Expansion curves for sealed mortar specimens at 20 °C and 40 °C. Adapted from Ref. [56].

The reason why final expansion is reduced with increasing temperature, however, is not so clear. On one hand, the raise of silica solubility with temperature (around 50% in pure water from 20 °C to 40 °C) would be expected to raise the extent of silica dissolution within the aggregates with consequent increase in the amount of ASR gel. Additionally, the raise of ionic diffusivity with temperature may also play a role by increasing the income of alkali and hydroxyl ions into the reactive aggregates, thus increasing the rate and extent of silica dissolution. On the other hand, several mechanisms can be attributed to reduce concrete expansion with increasing temperature, e.g.:

- Temperature reduces portlandite solubility (around 20% in pure water from 20 °C to 40 °C), thus smaller content of calcium in ASR gel can be expected, with consequent modification of ASR gel properties.
- When concrete temperature is elevated the concentration of sulphates in the pore solution is increased at the expense of hydroxyl ions (Fig. 2.20) [138, 188], thus lowering pore solution pH and resulting in lower silica solubility.
- Provided there is no change in the concrete internal water content, the internal RH in concrete will decrease with increasing internal temperature. This reduction could reach 5% for temperature increasing from 20 °C to 40 °C for a concrete with w/c ratio of 0.40 [133].

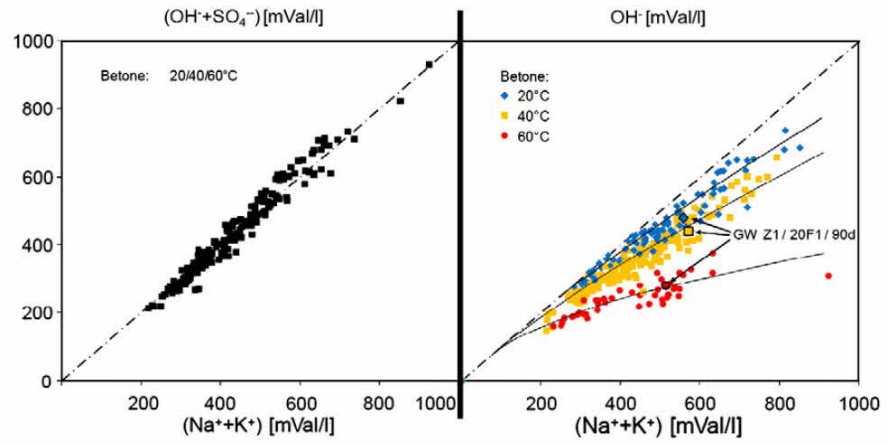

FIGURE 2.20: Concentration of anions OH^- and SO_4^{2-} versus concentration of cations (Na^+ and K^+) in pore solution at different temperatures. From Ref. [188]. Note: mVal is the German notation for meq, a unit of electrical charge.

2.8 Effect of mechanical restraints

Since the early investigations on ASR in concrete, it was noticed that the stress state has an influence on the magnitude and distribution of ASR-induced cracking and expansions [148]. Stresses may be due to external loads applied to the structure or the reaction to constrained expansion due to internal (rebars) or external restraints.

As a general rule, the orientation of the cracks in unreinforced concrete with none or small loads tends to be random (map cracking). In reinforced concrete or in concrete under significant load, the larger cracks tend to become oriented in the direction of the main compressive stress. Typically, in 'linear' structural elements such as beams and columns, the cracks tend to become oriented in the direction of the main rebars (Fig. 2.2).

Experimental studies of the effect of mechanical restraints on the development of ASR expansions have been carried out both at the level of ASR gel, and at the level of mortar/concrete. The first tests performed at the level of ASR gel were reported by Struble and Diamond [202, 203]. For these tests, Struble and Diamond prepared synthetic alkali-silica and alkali-calcium-silica gels with compositions similar to ASR gels found in real concrete structures. These gels were then placed in contact with water in the device sketched in Fig. 2.21a. Measurements included, first, the volume increase of the gels without any mechanical restriction (named 'free swelling'), and, second, the pressure developed in the gel when the expansion is prevented (named 'swelling pressure'). The measured free swelling ranged from as little as 0.5 to as much to 80%, and the maximum swelling pressures varied from as little as 0.1 to almost 11 MPa. No clear relationship

was observed between gel composition and its free swelling or swelling-pressure, nor between free swelling and swelling-pressure.

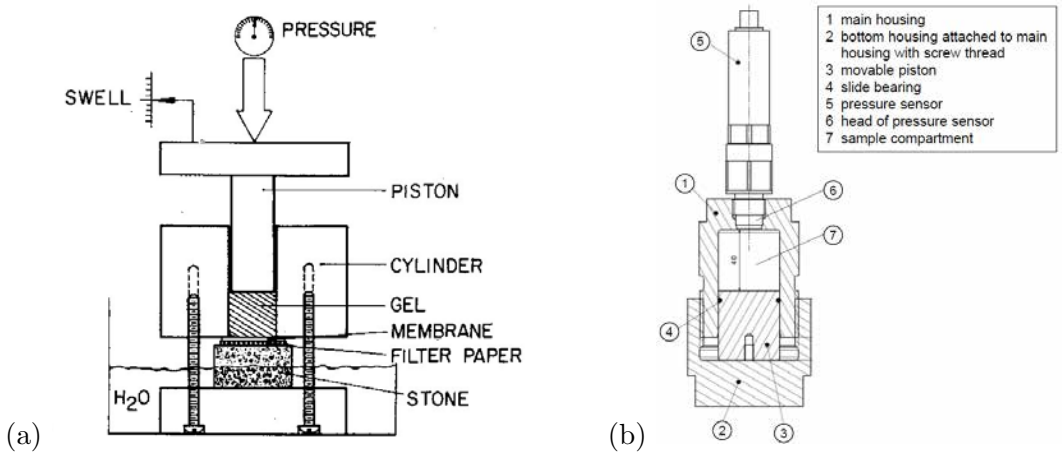

FIGURE 2.21: Testing devices used by (a) Strbule and Diamond (1981) and (b) Leemann (2012). From Refs. [111, 202, 203].

More recently, Leemann [111] measured autogenous strains and swelling pressure developed due to ASR in closed model systems, consisting of 1M NaOH solution, solid portlandite and microsilica in different proportions. Autogenous strains ranged from -0.1 to 0.3%, while swelling-pressure ranged from -0.4 to 0.2 MPa (model system where pressurized to 0.5 MPa before test). Portlandite content of the system correlates well with autogenous strains and swelling pressures but only for low content values. For higher amounts of portlandite, the relationship is not straightforward.

Studies at mortar or concrete level are more representative of the conditions at which ASR expansions develop in concrete structures. A first group of experimental studies to deal with this problem consisted of impeding the longitudinal expansion of mortar or concrete bars via very stiff loading frames [21, 67, 68, 105]. This setup makes it possible to measure what is called 'expansive' or 'swelling pressure', i.e. the stress developed in the specimen in the restrained direction. Kagimoto et al. [103], introduced a variation to this scheme by performing tests with loading frames of different stiffnesses. Refer to Fig. 2.22a for a schematic representation of this kind of tests. Swelling pressure and ultimate free expansion usually correlates well, as it is shown in Fig. 2.23. The results obtained in this setup are difficult to interpret since the evolution of the swelling pressure will not only depend on the ASR mechanisms, but also on the rheological behaviour of concrete due to the development of internal pressures.

A second group of studies consisted of applying a constant axial load on cylindrical specimens (Fig. 2.22b), usually via creep frames, e.g. [62, 109, 157]. To isolate ASR expansions, creep deformations due to the applied load are deducted from the overall

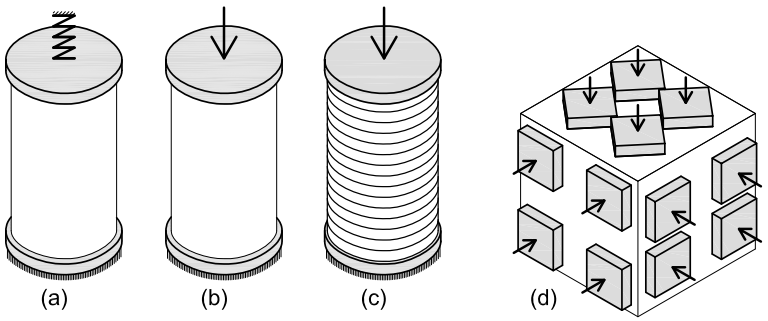

FIGURE 2.22: Schematic representation of ASR expansion tests under different mechanical restraints.

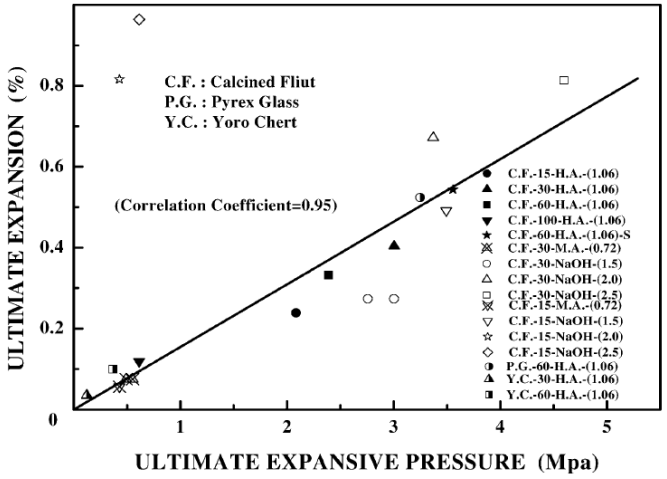

FIGURE 2.23: Relation between ultimate expansive pressure and ultimate free expansion in mortar bars. From Ref. [105].

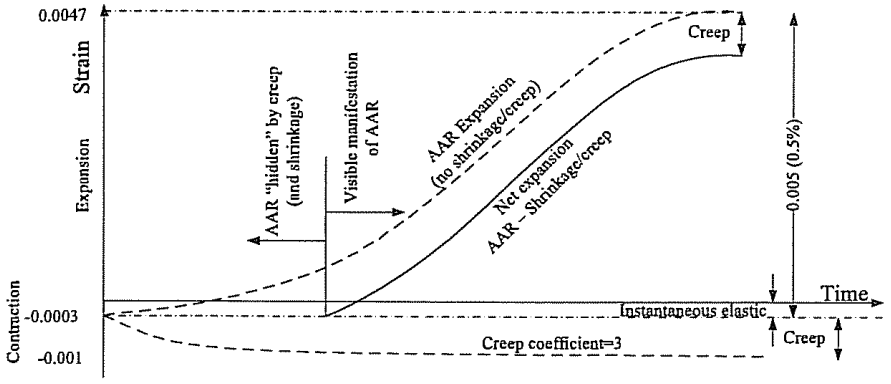

FIGURE 2.24: ASR and creep interaction. From Ref. [181].

expansion curve obtained, as indicated in Fig. 2.24. Since, for obvious reasons, it is not possible to directly measure creep on reactive concretes, creep strains had to be assessed on concretes with similar characteristic but with non-reactive aggregates or by means of analytical expressions from the literature. A similar approach is followed to deduct shrinkage strains when they are significant.

As a general rule, in this test setup, axial ASR expansion is reduced with increasing values of axial load, in some cases until completely inhibiting the swelling (Fig. 2.25a). On the other hand, the reported tendency for ASR radial expansions is not uniform among authors (Fig 2.25b). Larive found that, at least for axial stresses under 10 MPa, ASR radial expansion increased as axial load was increased, keeping the final value of volumetric ASR expansion relatively constant. These results led her to conjecture that under low compressive stresses exists a 'expansion transfer' from the most compressed direction (axial in her tests) to the less compressed directions (radial). The trend change for higher axial stresses is attributed to the development of microcracks as the UCS of concrete is approached. These microcracks would be capable of accommodate ASR gel without exerting internal pressure in the concrete. Later, Multon and Toutlemonde [157] supported this conjecture based on their own experimental results of ASR expansion tests of cylindrical specimens under triaxial stress states. The experimental set-up used by Multon and Toutlemonde consisted also in applying a constant axial load with creep frame, but in this case radial restraint to expansion is added by means of steel rings 3- or 5-mm-thick, which were not connected to each other, so that they would not exert any longitudinal restriction to expansion(Fig. 2.22c). This setup has the drawback that the radial stresses are not constant but linearly dependent on the expansion in this direction, making the interpretation of the results troublesome. In addition, both in the tests of Larive and those of Multon&Toutlemonde, the fact that tested specimens developed markedly anisotropic ASR expansions in free expansion conditions make the interpretation of the results even more difficult. This anisotropy, which can be appreciated in Fig. 2.25a and 2.25b, means that ASR expansions in the casting (axial) direction can be twice as large as in the radial (transversal) direction [155].

In the author's opinion, the 'expansion transfer' conjecture cannot be confirmed in base of these results. Moreover, later results reported by Dunant and Scrivener [63] are completely incongruent with the conjecture of constant volumetric ASR expansions (Fig. 2.25c).

In a recent paper, Gautam and Panesar [78] have proposed an ingenious test setup for measuring ASR expansions in concrete under constant triaxial stress states. For these tests, cubic specimens of $254 \times 254 \times 254$ mm were loaded by means of post-tensioning bolts (Fig. 2.22d). The bolts were stressed close to the yield limit of steel, in such a way that any additional elongation of the bolt induced by ASR expansion in the concrete will not induce any significant increase of the reaction exerted by the bolts on the specimen. The main drawback of this setup is that the stress distribution in the specimens is highly non-uniform, since the stresses concentrate under the bolt anchors. Therefore, the interpretation of the results requires estimation of the real distribution of stresses in the specimen via numerical modelling.

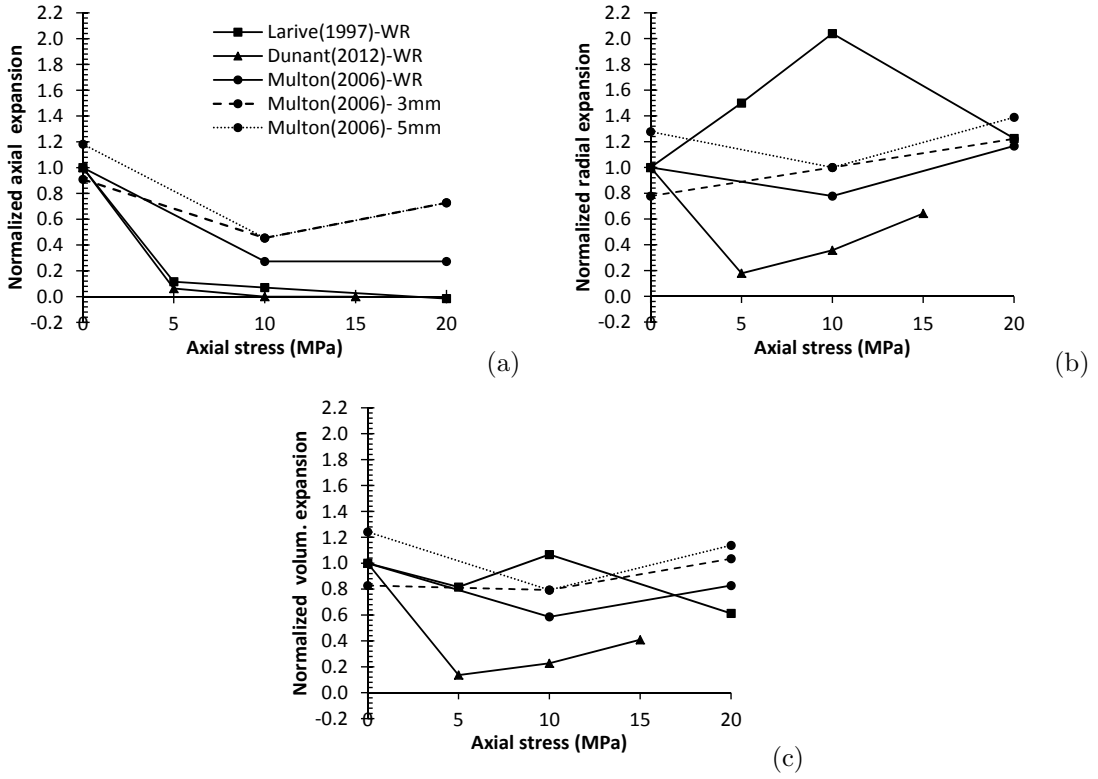

FIGURE 2.25: Final (a) axial, (b) radial and (c) volumetric ASR expansions of cylindrical concrete specimens under axial load and different radial restraint: 3- and 5-mm-thick steel rings and without restraint (WR). Expansions have been normalized by the corresponding free expansion value. Both creep and elastic deformation have been discounted. Data from Refs. [63, 109, 157].

With regard to the effect of internal restraint due to reinforcing bars, the available experimental studies seems to be consistent with the results of unreinforced concrete under load: ASR expansions are reduced in the direction of the reinforcement bars, i.e. in the direction of main compressive stresses, and increased in the unrestrained (transversal) directions [152, 155].

Finally, the effect of the mechanical restraint exerted by the cement matrix around the reactive aggregate has been studied by Song et al. [197], by comparing the ASR evolution around a glass inclusion for two concrete mixtures, one with and the other without steel microfibers. In Fig. 2.26 it can be appreciated how the increase of internal restraint introduced by the steel microfibers reduced the extent of the ASR rim around the glass.

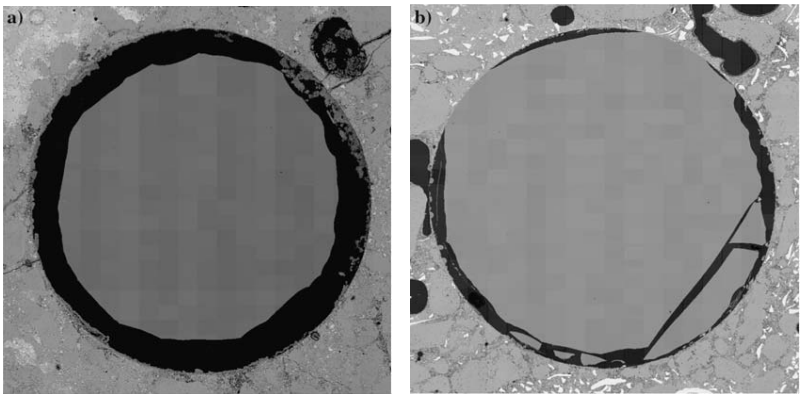

FIGURE 2.26: Backscattered (SEM) images of the remaining cross-section of a glass rod inclusion in concrete after exposure to 1 N NaOH(aq) for 42 days (actual area size: 6mm×6mm); (a) specimen without microfibers, (b) specimen reinforced with steel microfibers (visible as white regions in mortar matrix). From Ref. [197].

2.9 Mechanical deterioration

Reduction of elastic modulus, UCS and UTS of concrete as ASR expansions develop, have been reported by several a authors [e.g. 81, 146, 152]. However, it is not easy to associate the changes in the mechanical properties with a level of expansion as these changes depend on the materials and mechanisms involved in the reaction such as the mineralogy of the rock, the size of the aggregate (coarse or fine reactive aggregates) and kinetics of reaction (rate of expansion) [81].

2.10 Modelling of ASR expansions in concrete

In the last three decades several mathematical models have been proposed for ASR expansions in concrete, which, in one way or another, dealt with two distinct aspects of the phenomenon: (1) The mechanics of fracture that affects volume expansion and causes loss of strength, with possible disintegration of the material; and (2) the kinetics of the chemical reactions and diffusion processes involved [15]. These models can be classified according to their modelling scale in micro-, meso- and macro-scale models. In macro-scale models, concrete is considered as a homogeneous material, while in micro- and meso-scale models concrete heterogeneities (aggregates, voids, etc.) are explicitly accounted for. While micro- and meso- scale models aim at elucidating the underlying mechanisms of ASR expansions, macro-scale models are focused on structural analysis of ASR-affected structures.

The micro-scale models generally examine a Representative Volume Element (RVE) which is comprised of a spherical aggregate particle and the surrounding cement paste

[e.g. 14, 15, 156, 169, 172, 204]. These models deal with the chemical mechanisms of ASR including diffusion processes, kinetics of silica dissolution and gel formation and its swelling which induces deterioration of concrete. Even though this scale of analysis is essential to understand the kinetics of ASR, the assessment of ASR expansions at macro-level requires to consider mechanical phenomena (creep, shrinkage, fracture propagation) and transport processes which are very dependent on the Particle Size Distribution (PSD) of aggregates in concrete and, therefore, cannot be properly simulated by these models.

Meso-scale models, in turn, represent explicitly the PSD and the reactive aggregate fraction [e.g. 6, 43, 61, 220]. In the referenced models, macro expansions are the result of monotonically increasing local strains imposed to the aggregate particles or in 'gel pockets' within the aggregates particles, according to empirical or theoretical ASR kinetics law. These models are capable of reproducing the effects of concrete meso-strucuture as internal constraints in the development of stress-strain fields due to the imposed local expansions, as well as their consequences in the initiation and propagation of cracks. However, in none of them the influence of the meso-scale heterogeneities (aggregates, ITZ, cracks) in the transport processes involved in ASR expansions is considered explicitly, while this aspect may be expected to play a significant role in some cases.

Finally, macro-scale models focus on determining the strain-stress fields and damage (cracking) patterns of concrete structures affected by ASR. Most of the existing models were implemented in the FEM framework, treating concrete as a homogeneous material and combining chemical aspects with their mechanical effects. According to Saouma [181], five groups of macro-scale models can be distinguished:

- Empirical models [39, 90, 115, 213]. In this approach ASR expansions are estimated through empirical kinetic laws as a function of stresses, temperature, and RH, to be later imposed as pseudo-thermal expansions. It should be emphasized that these models are the most popular among practitioners [185].
- Models developed at *Laboratoire Central des Ponts et Chaussès* (LCPC) [64, 65, 116, 200, 214]. These models considered the sigmoidal kinetics law deduced by Larive [109] and, in most cases, are rooted in the Theory of Plasticity.
- Models developed in collaboration by *Université de Toulouse* and *Électricité de France* (EdF) [30, 85, 86, 169, 170, 192]. As opposed to the LCPC model, the Toulouse/EdF developments are rooted in Damage Mechanics, with various proposals for ASR kinetics, from empirical to theoretical.
- Model developed at *Politecnico di Milano* by Comi and coworkers [44–46]. Similar to those propose by Toulouse/EdF, it has been tested with some complex problems.

- Model developed at University of Colorado by Saouma and coworkers [181–184]. The model developed by Saouma and coworkers also adopted the ASR kinetics law proposed by Larive [109], but introducing additional empirical terms in order to considered the effect of concrete stress state and RH in the development of the expansions. The mechanical response is obtained by coupling the proposed chemical law with different mechanical models (linear elasticity, smeared cracking, localized cracking).

In all these models, some kind of coupling between the amount and/or the kinetics of imposed ASR strains and the stress tensor at the integration point is explicitly considered. However, heat and water diffusion processes, when considered, are completely decoupled from the mechanical deterioration process.

In the following sections, relevant models of ASR expansions in concrete at each level (micro-,meso-, macro-) of analysis are briefly described.

2.10.1 Micro-scale model by Bažant and coworkers (2000)

A paradigmatic example of the micro-scale approach is the mathematical model proposed by Bažant and Steffens [14] for concrete elaborated with ground waste glass. The model was developed based on a cubic RVE containing one spherical glass particle of diameter D (Fig. 2.27). A spherical layer of ASR gel is assumed to grow radially inward into the particle, controlled by diffusion of water toward the reaction front, which is assumed to be governed by a linear Fick's law. Considering additional assumptions and simplifications, the following differential equation for the velocity of the reaction front is reached:

$$\dot{z} = -\frac{2w_s D F'(\bar{x})}{r\rho_s \tau_w} \tag{2.13}$$

in which

$$F'(\bar{x}) = \frac{dF(\bar{x})}{d\bar{x}} = \frac{1}{[(D/2z)-1]\,\bar{x}^2} \quad (z/D \leq \bar{x} \leq 1); \quad \tau_w = D^2/a_s; \quad \bar{x} = \frac{2x}{D} \tag{2.14}$$

where w_s is the concentration of water in the concrete surrounding the particle, ρ_s is the mass density of the reactive silica, τ_w represents the halftime of diffusion of water through the gel layer, and a_s is Fick's permeability.

The mass of basic gel gel produced per m^3 of concrete (ξ_g) is determined by the volume of the glass that has reacted according to

$$\xi_g = \frac{4\pi}{3}\left(\frac{D^3}{8} - z^3\right)\rho_s \frac{m_g}{m_s}\frac{1}{s^3} \quad (0 \leq z \leq D/2) \tag{2.15}$$

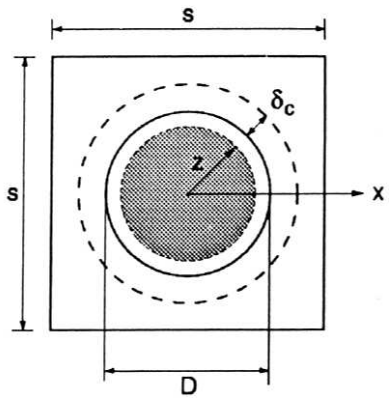

FIGURE 2.27: Idealized repetitive cubical cell with one reactive particle of original diameter D (the remaining unreacted particle of radius z is marked gray; δ_c = thickness of layer with capillary pores and cracks into which pressurized ASR gel formed intrudes by diffusion. From Ref. [14].

where m_g and m_s are the molar weights of silica (SiO_2) and silicate ions ($H_2SiO_4^{2-}$), respectively. It is assumed that the formation of this basic gel per se causes no significant volume increase, and that any swelling of the ASR gel is caused solely by the intake of additional water, i.e. $\Delta V = w_i/\rho_w$, denoting w_i the mass of water imbibed by the basic gel and ρ_w the mass density of water. The imbibition of water is described as a second diffusion process, limited by the development of pressure due to resistance of concrete to expansion. Then, the rate of imbibition of water into gel is formulated as

$$\dot{w}_i = \frac{1}{\tau_i}(n(p)m(h)\xi_g - w_i) \tag{2.16}$$

In this expression, the effect of the pressure in the gel (p) and the RH in pores of concrete (h) is introduced by empirical functions $n(p)$ and $m(h)$ (Fig. 2.28). Finally, the water used up to form the basic ASR gel and imbibed to cause its swelling appears as a sink term in the non-linear diffusion equation for the global water transport through a concrete structure.

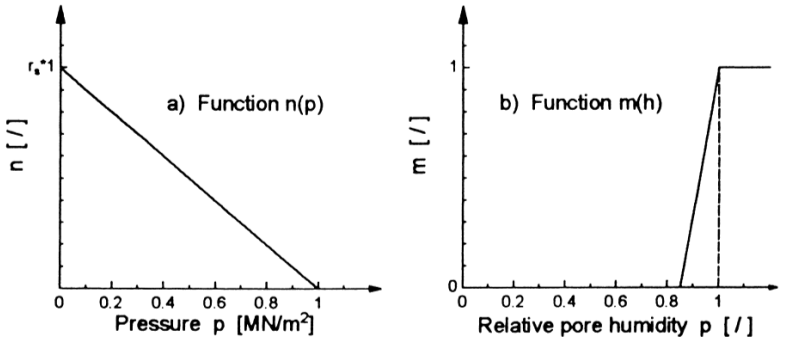

FIGURE 2.28: Empirical functions describing the influence of (a) gel pressure and (b) relative pore humidity on the equilibrium content of water imbibed by the gel. From Ref. [14].

The mechanics of fracture due to gel swelling have been addressed by Bažant in a second paper [15], in this case in collaboration with Zi and Meyer. In this second work, the kinetics of chemical reaction and diffusion processes is left aside, in order to explain by fracture mechanics alone the pessimum particle size effect. In this model, a regular array of cubical cells, each containing one spherical glass particle embedded in the matrix of hardened cement mortar, was considered for the fracture analysis (Fig. 2.29). The ASR proceeds from the surface of the particle inward. The expanding layer of the solid ASR gel at the surface of the particle applies radial pressure p on the surrounding cement mortar.

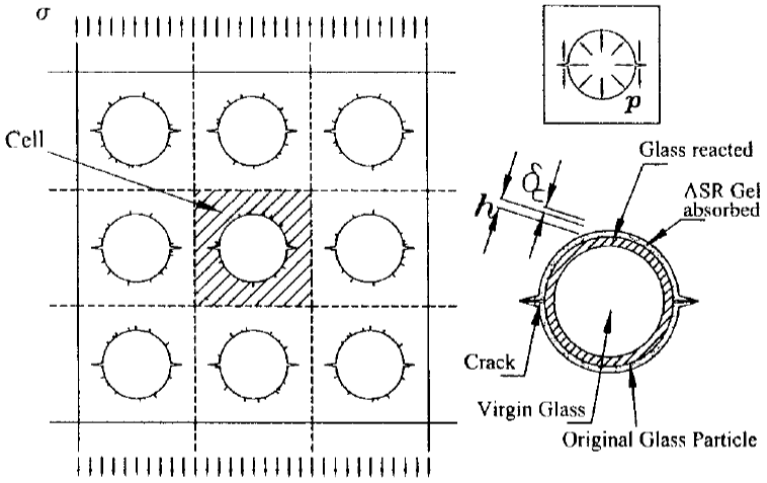

FIGURE 2.29: (Left) Idealized cubic array of expanding spherical glass particles surrounded by flaws, and dominant growing cracks filled by pressurized ASR gel; (Right Top) one cell with glass particle and crack; (Right Bottom) layer of reacted glass (ASR gel layer growing into glass particle) and layer of ASR gel forced into capillary pores of concrete. From Ref. [15].

The pressure causes cracks to initiate from pre-existing flaws at the surface of the particle (Fig. 2.29, left). The ASR gel also penetrates into cracks and applies pressure p on their surfaces. Restricting the analysis to a single cubical cell and realizing that the stress field caused by the gel-induced pressure p on the crack and void surfaces is a superposition of the stress field caused by the volumetric (hydrostatic) stress p applied by the gel onto the void and crack surfaces and the stress field caused by externally applied tensile stress $\sigma = -p$ (Fig. 2.30b), the authors derived the stress intensity factor at the pre-existing flaws at the surface of the particle as

$$K_I = (\sigma + p)\sqrt{s}k(\omega), \quad \omega = A_c/s^2 \tag{2.17}$$

where $k(\omega)$ is a dimensionless function which accounts for the geometry of crack front (Fig. 2.30a) and A_c is the area of the crack and the spherical void. Knowing K_I, it is possible to obtain the material compliance $C(\omega)$, which increases with fracture growth

and depends on the damage parameter ω. Then, the relative volume change due to fracture is $\Delta V_{fr} = C(\omega)(\sigma + p)$. Finally, considering volume compatibility conditions, an expression of macroscopic volume expansion due to ASR in the cubic cell as a function of the volume of gel formed is obtained.

By means of this theoretical model, the authors were able to explain the pessimum particle size effect as the result of two opposing mechanisms: (1) The extent of chemical reaction as a function of surface area, which causes the strength to decrease with a decreasing particle size; and (2) the size effect of the cracks produced by expansion of the ASR gel, which causes the opposite.

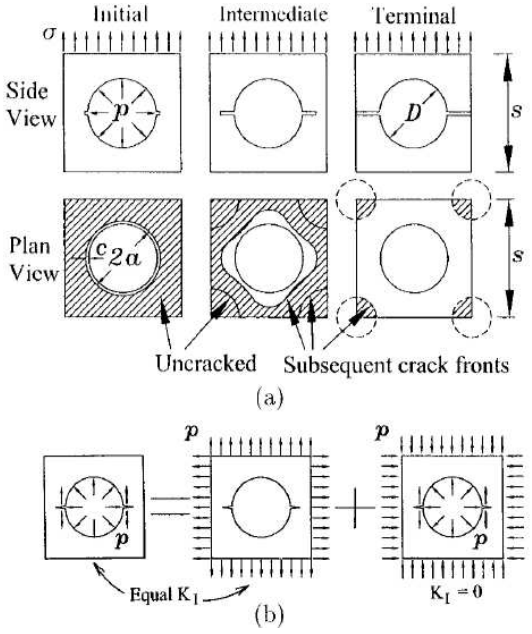

FIGURE 2.30: (a) Idealized evolution of crack front from initial stage of shallow annular cracks around glass particle to terminal stage of small circular uncracked ligaments; (b) superposition argument revealing equivalence of crack pressurization and stress externally applied on one cell. From Ref. [15].

2.10.2 Meso-scale model by Alnaggar and coworkers (2013)

The model proposed by Alnaggar and coworkers [6] implemented the ASR effect within the framework of the Lattice Discrete Particle Model (LDPM), which has been formulated and validated by Cusatis and coworkers [49, 50]. LDPM is a meso-scale discrete model that simulates the mechanical interaction of coarse aggregate particles. Concrete mesostructure is constructed through the following steps: (1) the coarse aggregate particles, whose shapes are assumed to be spherical, are introduced into the concrete volume by a try-and-reject random procedure; (2) zero-radius segregate particles (nodes) are randomly distributed over the external surfaces to facilitate the application of the

boundary conditions; (3) a three-dimensional domain tessellation, based on Delaunay tetrahedralization of the generated aggregate centers, creates a system of polyhedral cells interacting through triangular facets and a lattice system composed by line segments connecting the particle centers.

In LDPM, particle rigid body kinematics is used to describe the deformation of the lattice/particle system and the displacement jump at the centroid of each facet is used to define measures of strain. Next, a vectorial constitutive law governing the mechanical behavior of the material is imposed at the centroid of each facet. Finally, the governing equations of the LDPM framework are completed through the equilibrium equations of each individual particle.

To account for ASR, the reaction model proposed by Bažant and Steffens [14] (see Section 2.10.1) has been adopted and extended. As in the original model and consistently with LDPM formulation, the aggregate particles are assumed to have spherical shape and the whole volume of each particle is assumed to be reactive. Under these conditions, the dissolution of silica, the gel formation, and the water imbibition are assumed to evolve in the radial direction inward from the surface towards the particle center, as a consequence of water diffusion. As an additional simplification, the mortar matrix around the aggregates is assumed to remain water saturated at all times, i.e. macro-level diffusion processes are not explicitly considered.

Finally, the volume variation of the ASR gel layer is assumed to be equal to the volume of water imbibed. This swelling is introduce in LDPM as a radius variation Δr of each aggregate particle of radius r which produces an imposed enlargement of the lattice connected to the center of the aggregate particle. The radius variation of a given aggregate particle is calculated as follow:

$$\Delta r = \left(\frac{3M_i}{4\pi\rho_w} + r^3)^{1/3} \right) - r \tag{2.18}$$

where M_i is the mass of water imbibed by the basic gel and ρ_w is the water mass density. A expression of M_i as a function of time, the particle diameter, temperature, alkali content of concrete is given by the authors. However, since temperature, and alkali content are assumed to be uniform and constant during the simulations, M_i is primarily a function of particle diameter and time, i.e. the swelling rate of each particle depends only on its diameter.

In order to introduce creep and shrinkage effects, a simplified approach was taken by adding basic creep and shrinkage strains macroscopically to the LDPM averaged response of the simulated specimens. More specifically, with reference to a specimen subject to macroscopic stress $\sigma(t)$, the corresponding macroscopic strain was calculated as $\varepsilon =$

$\varepsilon^{LDPM} + \varepsilon^{sh} + \varepsilon^{ve}$, where ε^{LDPM}, ε^{sh} and ε^{ve} are averaged macroscopic LDPM strain, shrinkage strain, and viscoelastic strain, respectively. This last simplification may not be acceptable since the ASR-induced cracking of concrete is expected to modified the internal stress field of specimens and, consequently, their internal creep strains.

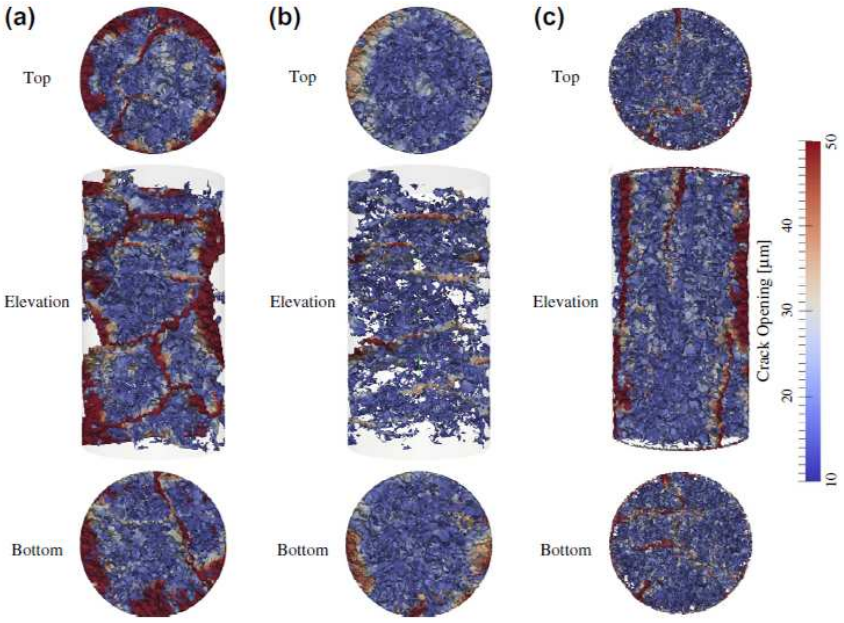

FIGURE 2.31: Crack patterns simulated in one cylindrical specimen for (a) free expansion case, (b) 0 MPa and 5-mm-restraint case, and (c) 20 MPa unrestrained case. From Ref. [6].

To verify the ability of the model to predict correctly ASR expansions under different loading conditions, the authors simulated the experimental results obtained by Multon and Toutlemonde [157] (see Section 2.8). The ASR-LDPM seems capable to qualitatively reproduce the observed crack patterns (Fig. 2.31) and the 'expansion transfer' to the less compressed direction. It is remarkable that the expansion transfer effect is obtained automatically in the ASR-LDPM as a result of the redirection of cracking due to the external load applied. However, for some loading conditions the fitting error is very high, which may indicate that the main governing mechanisms have not been completely captured.

2.10.3 Macro-scale model by Ulm and coworkers (2000)

Ulm and coworkers [214] developed a chemo-elastic model that accounted for ASR kinetics and consequent concrete swelling. They assumed that once the free expansion space in pores and micro-cracks is filled with the expansive ASR product, the swelling is restrained, and the product phases exert locally a pressure on the surrounding concrete skeleton (Fig. 2.32a). Under stress free conditions, the internal swelling pressure p_g of

the expansive products is self balanced by the tension σ_μ in the skeleton. Consequently the overall material swells.

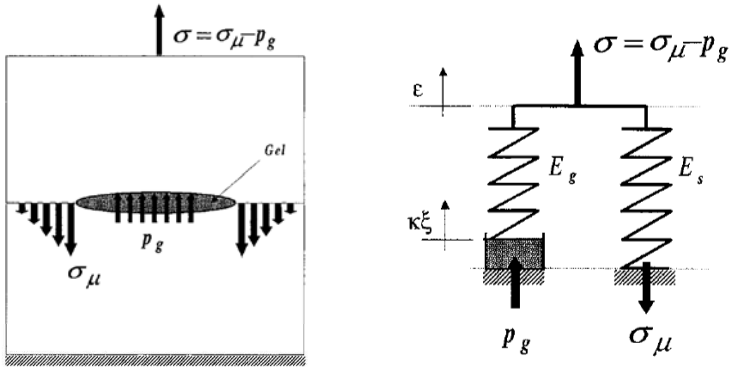

(a) (b)

FIGURE 2.32: (a) Mesocopic mechanism of ASR swelling, (b) chemoelastic pressure-spring device of ASR swelling. From Ref. [214].

Assuming an elastic material behavior of the skeleton and of the ASR product, the macro-expansion mechanism is idealized in the 1D model shown in Fig. 2.32b, where σ is the macroscopic stress due to external forces, and ε is the corresponding overall strain. The stress equilibrium in this chemo-elastic device is given by

$$\sigma = \sigma_\mu - p_g = E_s\varepsilon + E_g(\varepsilon - \kappa\xi) \tag{2.19}$$

where E_g and E_s are the spring moduli, $\xi \in [0, 1]$ is the extent of the ASR, and κ is the intrinsic dilatation coefficient of the reaction products. It is assumed that the volume increase of the products is proportional to the reaction extent.

To extend the model to 3D, an energy approach is proposed by the authors. For the original 1D system considered, the expression of the free energy is given by

$$\psi = \frac{1}{2}\left[E_s\varepsilon^2 + E_g(\varepsilon - \kappa\xi)^2\right] + g(\xi) \tag{2.20}$$

The first term in brackets represents the free energy of the springs, and function $g(\xi)$ corresponds to the free energy in the chemical pressure cell. Introducing Eq. (2.20) in the expression of dissipation $\varphi dt = \sigma d\varepsilon - d\psi \geq 0$ yields

$$\varphi dt = \left[\sigma - (E_s\varepsilon + E_g(\varepsilon - \kappa\xi))\right] d\varepsilon + \left[\kappa E_g(\varepsilon - \kappa\xi) - \frac{\partial g}{\partial \xi}\right] d\xi \geq 0 \tag{2.21}$$

From Eq. (2.19) and (2.20) it is trivial that

$$\sigma = \frac{\partial \psi}{\partial \varepsilon} = E_s\varepsilon + E_g(\varepsilon - \kappa\xi) \tag{2.22}$$

The extension to 3D is thus obtained by replacing the scalar quantities by their tensorial counterparts. Hence, the state Eq. (2.22) becomes in the isotropic case

$$\sigma_{ij} = \left(K - \frac{2}{3}G\right)\epsilon\delta_{ij} + 2G\varepsilon_{ij} - 3\beta K\xi\delta_{ij} \tag{2.23}$$

where $\epsilon = \varepsilon_{ii}$; $K = K_s + K_g = E/3(1-2\nu)$ and $G = E/2(1+\nu)$ are the overall bulk modulus and shear modulus; $E_s + E_g$ is the overall Young's modulus; ν is the Poisson's ratio; and $\beta = \kappa E_g/E$ is the chemical expansion coefficient.

The second term in Eq. (2.21) represents the driving force of the reaction, i.e. the chemical affinity of the reaction,

$$A_m = -\frac{\partial\psi}{\partial\xi} = -\kappa p_g - \frac{\partial g}{\partial\xi} \tag{2.24}$$

The first term $-\kappa p_g$ is neglected, assuming that the chemical affinity depends mainly on the reaction extent ξ. Then, the time evolution of the reaction extent ξ is defined by a linear kinetics law, a rate equation relating the reaction affinity $A_m = A_(\xi)$ to the reaction rate $\dot{\xi} = d\xi/dt$:

$$A_m(\xi) = k_d\frac{d\xi}{dt} \tag{2.25}$$

A_m decreases progressively from then initial value $A_m(\xi = 0) = A_{m0}$, which starts the reaction, to the equilibrium $A_m(\xi = 1) = 0$, at which the reaction stops. Assuming a first-order reaction kinetics, $A_m(\xi)$ has to vary linearly with respect to ξ:

$$1 - \xi = t_c(\theta_0, \xi)\frac{d\xi}{dt} \tag{2.26}$$

where $t_c = t_c(\theta, \xi) = k_d/A_{m0}$ defines a characteristic time of the reaction, which has been found to depend on temperature θ and on the ASR extent ξ. For an isothermal stress-free expansion test, the later equation can be rewritten as

$$\epsilon(\infty) - \epsilon(t) = t_c(\theta_0, \xi)\frac{d\epsilon}{dt} \tag{2.27}$$

According to Larive [109], for a given concrete and moisture content

$$t_c = \tau_c(\theta)\frac{1 + \exp[-\tau_L(\theta)/\tau_c(\theta)]}{\xi + \exp[(-\tau_L(\theta)/\tau_c(\theta)]} \tag{2.28}$$

Substituting Eq. (2.28) into Eq. (2.27), after integration, leads to

$$\epsilon(t) = \epsilon(\infty)\xi(t); \quad \xi(t) = \frac{1 - \exp(-t/\tau_c)}{1 + \exp(-t/\tau_c + \tau_L/\tau_c)} \tag{2.29}$$

The shape of Eq. (2.29), together with the physical interpretation of time constants τ_c and τ_L, are shown in Fig. 2.33. These time constants can be directly determined from stress-free ASR expansion tests. Larive's experiments have shown that there is temperature dependence of the time constants τ_c and τ_L in agreement with the Arrhenius relation

$$\tau_c(\theta) = \tau_c(\theta_0)\exp[U_c(1/\theta - 1\theta_0)] \tag{2.30}$$

$$\tau_L(\theta) = \tau_L(\theta_0)\exp[U_L(1/\theta - 1\theta_0)] \tag{2.31}$$

By analogy with the Arrhenius equation, U_c and U_L can be considered as activation energy constants of τ_c and τ_L, respectively.

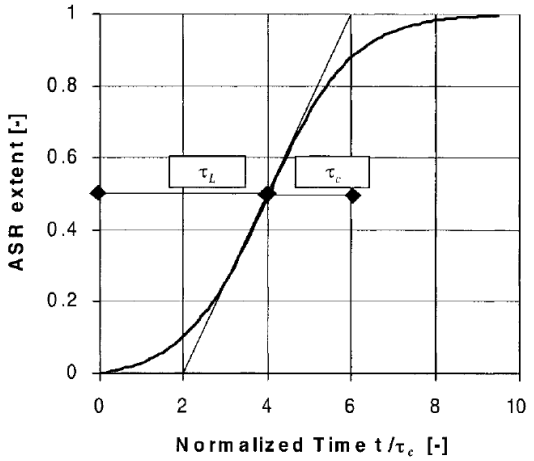

FIGURE 2.33: Definition of Latency Time τ_L and Characteristic Time τ_c in normalize isothermal expansion curve. From Ref. [214].

As the authors themselves recognized, considering an elastic material behaviour is a first-order engineering approach which does not correspond to reality. However, the approach proposed in this model has been broadly adopted to combine with various nonlinear mechanical constitutive models [e.g. 64, 65, 183].

Chapter 3

Interfacial Expansion Tests

3.1 Introduction

As discussed in Section 2.4.2, ASR expansion in concrete depends strongly on the aggregate size and grading. This effect can be attributed to various mechanisms of either chemical or mechanical origin, usually acting simultaneously, which are very difficult to isolate in order to assess their real significance. Additionally, the complexity of concrete meso-structure, determined by the irregular geometry and big range of sizes of the aggregates, make the study and modelling of the ASR mechanisms particularly difficult.

In this context, a new test setup for studying ASR is proposed. The aim of this new methodology is to ease the study of ASR-induced expansions by reducing the complexity of concrete meso-structure. For this purpose, instead of studying ASR in regular concrete specimens, a new type of specimen with a single, disc-shaped reactive aggregate is used. In these specimens, the reactive aggregate disc is placed as a sandwich in between of cementitious matrix at both sides. In this way, two plane, symmetrical and geometrically defined interfaces between the reactive aggregate and the cementitious matrix are obtained. In this configuration, ASR products mainly precipitate at these interfaces tending to separate the aggregate disc from the cementitious matrix. Then, it is possible to have an estimate of the expansion developed at a single interface by measuring the length change of the specimen. Furthermore, the simplicity of the geometry allow us to relate the measured expansion to the thickness and composition (measured by means of SEM and EDS analysis) of the layer of ASR products.

In a previous paper, Carles-Gibergues et al. [31] have proposed to use specimens with a similar configuration to study ASR. However, the authors limited their work to the study of the composition and morphology of the ASR reaction products at the aggregate-cement interface, without doing any measurement of the developed expansions. Later,

Schlangen and Çopuroglu [187] proposed other test setup with a single aggregate-cement interface which, in principle, should have allowed them to measure the localized expansion due to ASR. To the best of the author's knowledge, however, they have never presented any results since then.

In the following section, the test setup and the proposed testing methodology are described in detail. Subsequently, test results obtained using glass as reactive aggregate are presented and discussed. The results are grouped by 'Series' of tests, consisting of group of tests that were performed simultaneously. These results do not constitute a systematic parametric study and, hence, they shall be considered only as a preliminary exploration of influencing parameters, in the framework of the on-going development of a testing methodology.

3.2 General description

The aim of the proposed test is to study expansions at the level of a single interface aggregate-matrix due to the precipitation of ASR products. For this purpose, two kinds of cylindrical specimens of approximately 33 mm diameter and 66 mm height are elaborated. The first type, named 'reactive specimens', involves sandwich-like specimens, with cement paste or mortar on top and bottom of a disc of reactive aggregate in the middle (see Fig. 3.1). At both ends of the specimen, steel gauge inserts are embedded for length change measurements. The second type, called 'control specimens', involves purely mortar or cement paste specimens without reactive aggregate. Control specimens are used to assess the deformations of the matrix of cement paste or mortar, solely caused by phenomena such us drying shrinkage or thermal expansions.

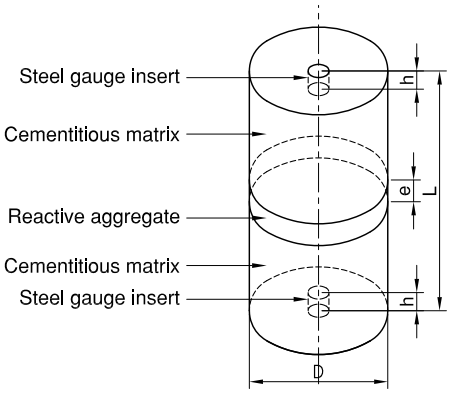

FIGURE 3.1: Scheme of reactive specimens.

After casting, the specimens are kept in the moulds for 24h in a humid chamber. Once unmoulded, they are cured in airtight containers with a solution of sodium hydroxide of

1 mol per kg of water at room temperature during 27 days. Additionally, a small amount of $Ca(OH)_2$ is added to the solution to prevent calcium leaching from the specimens. Finally, the containers are introduced in an oven at 60 °C until the end of the test. The sodium hydroxide solution keeps the specimens saturated of water and prevents the leakage of alkali ions from the cement paste. During both stages, specimen length and mass changes are measured regularly until the end of the test.

Once in the oven at 60 °C, the reactive specimens start to expand and to expel a whitish reaction product at the interfaces, until the moment when the amount of reaction product at the interface is high enough to separate the disc aggregate from the matrix, which can happen in a matter of days, weeks, or months depending on the dosage of the matrix and the type of reactive aggregate. Before the separation, scanning electron microscopy coupled with energy dispersive spectroscopy (SEM/EDS) is employed to analyze the reaction products in the specimens.

From the length change measurements of the reactive and the control specimens, the expansion curves corresponding to the ASR reaction products precipitated in a single interface matrix-aggregate can be obtained, assuming that the strains developed in the matrix of reactive specimen is the same as the one developed in the control specimens.

3.3 Method

3.3.1 Specimen preparation

Reactive aggregate discs

In this thesis, soda-lime (SL) glass and borosilicate (BS) glass have been used as reactive aggregates because of their homogeneity as industrial materials. Once the methodology will be demonstrated, natural reactive aggregates may be used for more realistic studies. The glass discs were cut from flat glass by means of a ∅35 mm diamond holesaw. The SL glass thick was 6 mm and the BS glass thick was 3.2 mm. The parallelism and the smoothness of the faces of the discs is guaranteed by industrial origin of the flat glass. In case of testing natural aggregates, special attention will have to be paid to the cutting and polishing process in order to reach similar geometrical precision.

Moulds and gauge inserts

The moulds and accessory pieces used for elaborating both reactive and control specimens were made in grey PVC accordingly with the dimensions given in Fig. 3.2. The different uses of each piece in the elaboration process is described below. For the gauge

inserts, standard M4 nickel-plated screw union, consisting of a male screw and a threaded sleeve, have been used. See Fig. 3.3 for dimensions. Before casting, a thin layer of mineral oil was applied to the interior of the moulds to facilitate the removal of the hardened specimens. Special care was taken in keeping the gauge inserts free of oil.

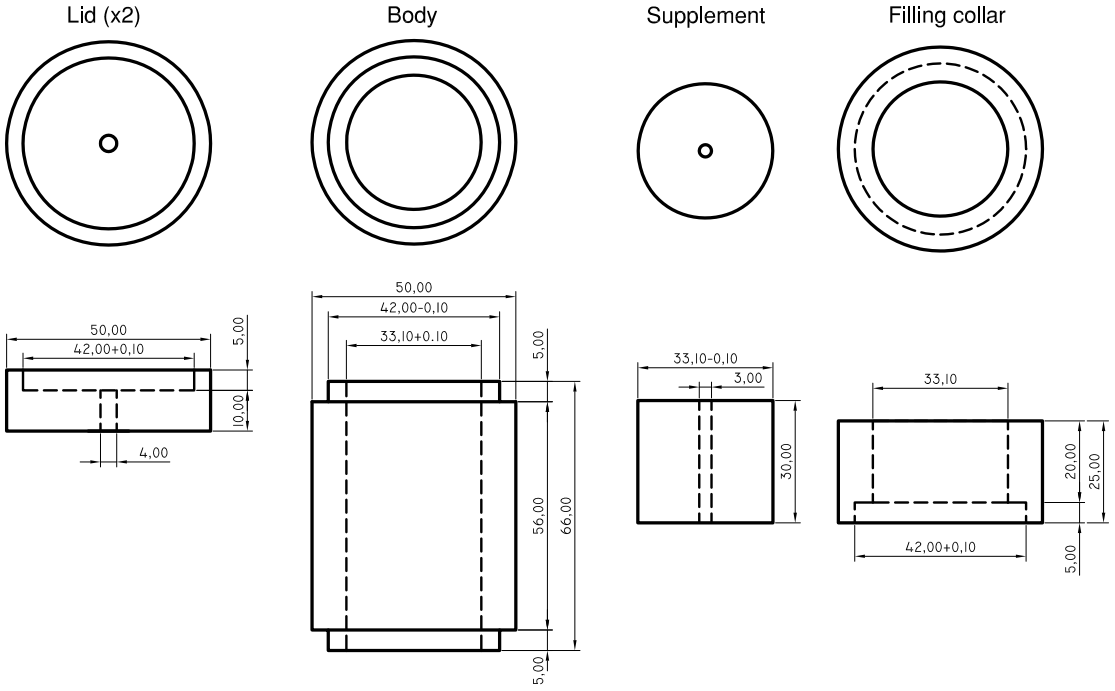

FIGURE 3.2: Dimensions (in mm) of PVC moulds and accessory pieces used for elaborating specimens for interfacial expansion tests.

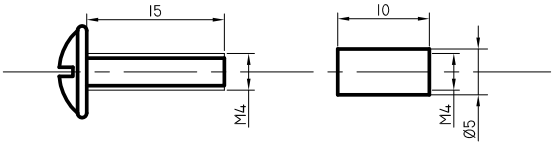

FIGURE 3.3: Dimensions (in mm) of the steel gauge inserts.

Cementitious matrix

The proportions of the cementitious matrix is one of the study variables and, therefore, may change from one test to the other. However, once established the composition to be tested, the following general procedures have been followed for the elaboration the mixture:

- Estimating the volume of cementitious matrix needed accordingly with the number of specimens to be elaborated, and increase this amount by 20%.
- Calculating the absolute amount of each component necessary to obtain the desired volume.

- For cement paste:
  - Pour the water into the mixing bowl.
  - If applicable, add alkali hydroxide (NaOH or KOH) to the water and mix it until complete dissolution.
  - Pour the cement into the mixing bowl and mixed it with the water for a minute.
  - Remove the cement paste added to the bowl using a spatula and mix for another minute.
- For cement paste with microsilica (MS):
  - Pour 2/3 of the water into the mixing bowl.
  - If applicable, add alkali hydroxide (NaOH or KOH) to the water and mix it until complete dissolution.
  - In another mixing bowl, mix manually using a spatula the cement with the MS.
  - Pour the cement with the MS into the mixing bowl and mixed it with the water for one minute.
  - Add the remaining water together with the plasticizer additive and mix for 30 seconds.
  - Remove the cement paste added to the bowl using a spatula and mix for another minute.
- For Mortars:
  - Pour all the water into the mixing bowl.
  - If applicable, add alkali hydroxide (NaOH or KOH) to the water and mix it until complete dissolution.
  - Pour the cement in the mixing bowl and mixed it with the water for 30 seconds.
  - Add the sand and mix all for 1 minute.
  - Remove the mortar added to the bowl using a spatula and mix for another minute.

Unless stated otherwise, the mixing was done mechanically using a 175 W cooking mixer.

Moulding of specimens

Control and reactive specimens require different moulding procedures. The main difference is that each control specimen was completely cast in one single operation with cementitious matrix from the same batch, while the reactive specimens had to be cast by halves, the second half filled 24h after the first one, therefore using cementitious matrix from two different batches.

The moulding procedure for control specimens, illustrated in Figs. 3.4, was the following:

(a) Place the mould bottom lid with the measurement terminal in position at the lower end of the mould. Place the filling collar at the upper end of the mould.

(b) Fill the first half of the mould with two approximately equal layers of cementitious matrix, each layer being compacted with a tamper (a cylindrical steel rod of ∅5 mm and 150 mm length). Give a few strokes to the mould with the tamper to remove trapped air and smooth the surface. Repeat the procedure for the second half of the mould.

(c) Remove the filling collar, cut off the mortar flush with the top of the mould and smooth the surface with a few strokes of the tamper.

(d) Place the second mould lid with the gauge insert in position, and give a few strokes to the mould with the tamper to help the cementitious matrix to wet the terminal. Introduce the mould in a humid chamber (RH $>$ 95%) for 24 $\pm$2 h.

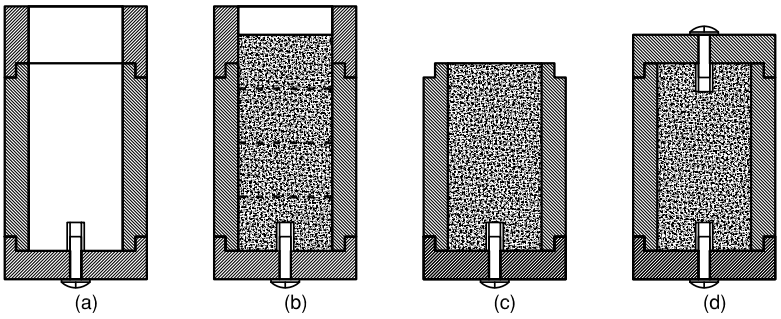

FIGURE 3.4: Schematic elaboration sequence of control specimens.

On the other hand, for moulding reactive specimens the following procedure, illustrated in Fig. 3.5, was followed:

(a) At the lower end of the mould place the mould bottom lid and the supplement. Above the supplement, place the disc of reactive aggregate, with care so as not to dirty the glass with oil. Place the filling collar at the top end of the mould.

(b) Fill the mould with two approximately equal layers of cementitious matrix, each layer being compacted with the tamper. Give a few strokes to the mould with the tamper to remove trapped air and smooth the surface.

(c) Remove the filling collar, cut off the mortar flush with the top of the mould and smooth the surface with a few strokes of the tamper.

(d) Place the second mould lid with the gauge insert in position, and give a few strokes to the mould with the tamper to help the cementitious matrix to wet the terminal. Introduce the mould in a humid chamber (RH $>$ 95%) for 24 $\pm$2 h.

(e) Take the mould out of the humid chamber. Invert the mould and remove the (now) upper tap and the supplement. Place the filling collar.

(f) Proceed as described in (b).

(g) Proceed as described in (c).

(h) Proceed as described in (d).

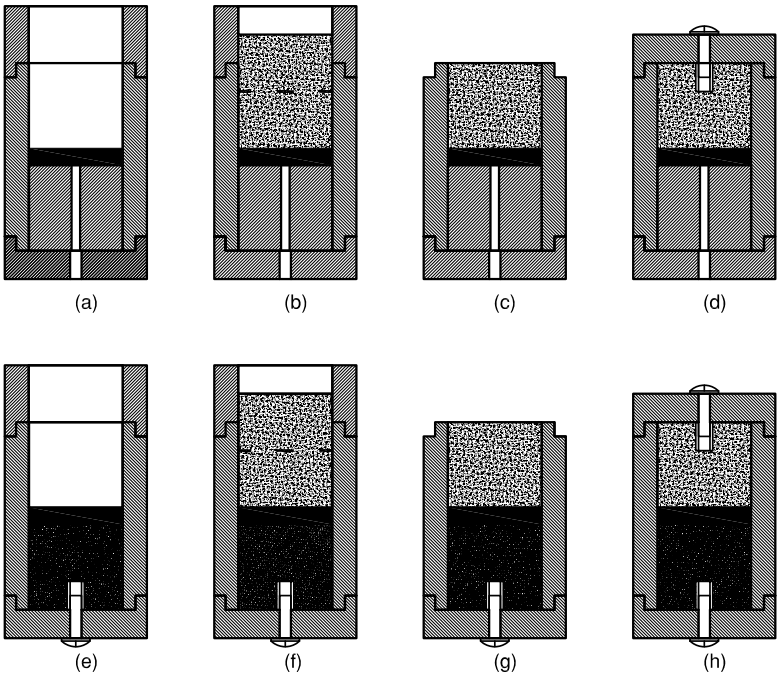

FIGURE 3.5: Schematic elaboration sequence of reactive specimens.

The filling of the moulds was always completed within the first 10 minutes after preparing the mix.

In order to unmould the specimens, first the screws of the gauge terminals and, then, the top and bottom lids had to be removed. Next, the hardened specimens were extracted by means of the device schematically described in Fig. 3.6. Note that the pressure is

not applied on the gauge terminal but on the outer corona of the specimen, preventing in that way a punching action.

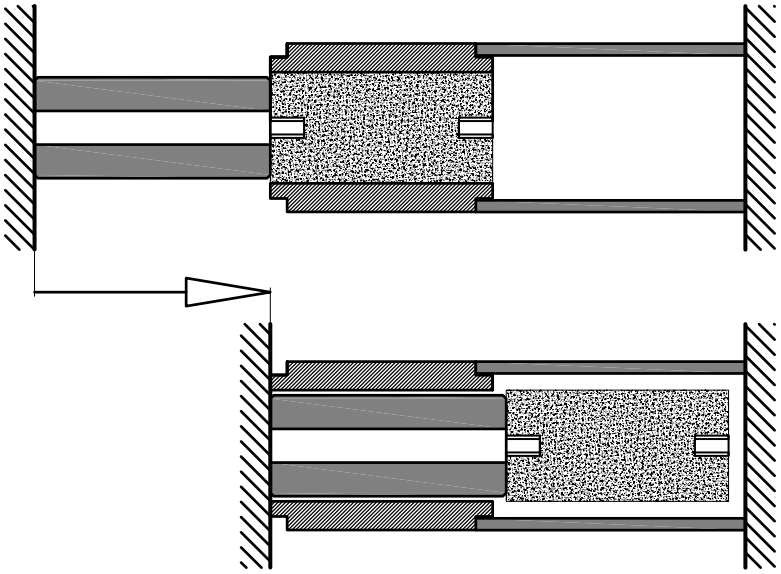

FIGURE 3.6: Specimen extraction device.

3.3.2 Alkaline bath

Once unmoulded the specimens were identified with a permanent marker and introduced by pairs in airtight containers with alkaline solution. The containers were standard Gastronorm size GN 1/9 (1 L capacity) and made of polypropylene. The resulting volume proportion of alkaline solution to specimens in the container was then greater than 6. The specimens were placed in ad-hoc manufactured supports made of methacrylate and stainless steel, thought to ensure free access of the alkaline solution to the entire surface of the specimens and, therefore, to ensure that the specimens do not touch the sides of the container or each other. A view of a container and a specimens support is given in Fig. 3.7.

The air tightness of the type of container used was tested by measuring the mass loss of a container full of water after keeping it in an oven at 80 °C for 13 days. In these conditions the measured mass loss was 1.3 %, which was considered acceptable for the purposes of the test.

The alkaline solution used for the exposure stage in all the tests performed for this thesis was prepared with 40 g (1 mol) of NaOH and 2 g of $Ca(OH)_2$ per kg of water, using tap water and USP grade NaOH and $Ca(OH)_2$. This solution was also used for the curing stage, with the exception of the tests performed for Series C in which limewater was used.

FIGURE 3.7: Specimens support and airtight container for alkaline bath.

For the curing stage, the containers were kept at room temperature. For the exposure stage, the containers were placed in an oven set at 60 °C, with a standard deviation of ±1.2 °C.

3.3.3 Length comparator

The device used for determining the length change of the specimens is shown in Fig. 3.8. It is made of steel and features a dial micrometer with 0.002 m resolution. The terminals of the device are tapered tips with an angle of 20° with respect to the vertical, which are introduced in the gauge inserts of the specimen to be measured. A reference bar made of Invar (nickel-iron alloy with a coefficient of thermal expansion of about 1.2×10^{-6} K^{-1}) is used for checking the device at regular intervals. The reference bar is 66 mm length and has two aligned longitudinal holes of 4 mm diameter to place the tapered terminals of the length comparator. The length comparator and the scale were placed beside the oven, in order to minimize the time needed for measuring.

3.3.4 Measuring procedure

After unmoulding and before doing the first readings (zero readings), the specimens were kept for 30 minutes in the containers with alkaline solution in order to guarantee that the specimens were at room temperature. Otherwise the specimens temperature could have been somewhat higher due to the heat released by the cement hydration.

The general procedure for measuring length and weight changes of the specimens was the following:

FIGURE 3.8: Length comparator.

- Place the reference bar in the length comparator. If necessary, reset the dial gauge of the micrometer.
- Remove the containers from the storage location (the oven for the exposure stage) one at a time.
- Remove the first specimen from the water and dry its surface with absorbent paper.
- Place the specimen in the length comparator and take the reading immediately. Left the specimen on a tray, and repeat for the second specimen.
- Take the first specimen and weight it; repeat for the second one. Complete the process of drying and reading both specimens within 60 s.
- Return both specimens to the container. Verify that the specimens are completed cover with alkaline solution before returning the container to the storage location; otherwise, refill it.

3.3.5 Calculations

The current strain ε of each control specimen is calculated according to the following expression:

$$\varepsilon = \frac{l - l_0 - 2h\alpha_{steel}(T - T_0)}{L_0 - 2h} \tag{3.1}$$

where L_0 [m] is the initial distance between inserts (see Fig. 3.1), h [m] is the length of the gauge inserts, l_0 and l[m] are the initial and the current lecture of the dial indicator,

respectively, α_{agg} [1/ °C] is the linear thermal expansion coefficient of the gauge inserts steel, T and T_0 [°C] are the current and initial temperature of the specimen, respectively. Then, the interfacial expansion at each interface of a reactive specimen, d_I [m], can be calculated as

$$2d_I = (l - l_0) - \bar{\varepsilon}\,(L_0 - 2h - e) - (e\alpha_{agg} + 2h\alpha_{steel})\,(T - T_0) \tag{3.2}$$

where $\bar{\varepsilon}$ is the averaged strain measured in the corresponding control specimens set, e [m] is the thickness of the aggregate disc, and α_{agg} [1/ °C] is the linear thermal expansion coefficient of the aggregate.

The relative mass variation of each specimen, π, is calculated, depending of the type of the specimen, as follows

$$\text{Control specimens: } \pi = \frac{w - w_0}{w_0 - 2w_{ins}} \tag{3.3a}$$

$$\text{Reactive specimens: } \pi = \frac{w - w_0}{w_0 - w_{agg} - 2w_{ins}} \tag{3.3b}$$

where w_0 and w are the initial and the current mass of the specimen, respectively, w_{agg} is the mass of the disc aggregate and w_{ins} is the mass of one gauge insert.

3.3.6 SEM images and EDS analyses

With the exception of the samples from Series C, which were gently analysed by Dr. A. Leemann at the EMPA (Switzerland), all the remaining SEM/EDS analysis were performed at the *Centres Cientifics i Tecnològics* of the *Universitat de Barcelona* (CCiTUB) with scanning electron microscope FEI Quanta 200 equipped with EDS-EDAX Genesis. The samples were prepared at the *Servei de Làmina Prima* of the *Facultat de Ciències de la Terra* of *Universitat de Barcelona*. The samples were cut with a diamond saw with a width of approximately 1 cm and then put in vacuum desiccator for two days. After drying, the samples were impregnated with a low viscosity epoxy resin. Once the epoxy was cured, the upper 1-2 mm were cut with a low speed precision diamond saw. The new exposed surfaces were ground and polished with abrasive grains successively finer, starting with 15 μm and finishing with 1 μm. In order to avoid leaching, all the grinding and polishing operations were done using polishing oil instead of water.

3.4 Series C

The tests included in this series were the first to offer acceptable results. Previous tests (Series A and B) were used for the development of the methodology and are not presented in this document. The series includes two sets of specimens, one made with mortar and the other with plain cement paste. In both cases, SL glass discs were used for the reactive specimens. Part of the tests in this series were performed as part of a bachelor's thesis of A. González [84] under the supervision of the author.

3.4.1 Description

The specimens tested in this series are listed in Table 3.1. Two types of cementitious matrix were used: mortar with crushed limestone sand (set #1) and plain cement paste(set #2a). The Portland cement was type CEM I 42,5 N-SR5 according to the Spanish standard UNE-EN 197-1 [3]. The oxide composition of the cement is given in Table A.1, cement PC01, of Appendix A.1. The same water/cement weight ratio of 0.47 was adopted for both mixtures. The PSD of limestone sand used for the mortar is given in Table 3.2. The specific weight of the limestone sand was of 2.675 g/cm^3. The weight ratio sand/cement in the mortar was 2.25 wt%, resulting in a sand/mortar volume ratio of 0.52. The reactive discs for reactive specimens were of colourless SL glass.

Table 3.1: List of specimens tested in Series C.

Set #	Type	Specimens	Cementitious matrix
1a	Reactive	C01 to C03	Mortar w/ limestone sand
1c	Control	C04 to C06	
2a	Reactive	C07 to C09	Cement paste
2c	Control	C10 to C12	

Table 3.2: Particle size distribution of calcareous sand used for series C.

Sieve size (mm)	Passing (wt%)
4.750	100
2.000	77
1.180	52
0.430	25
0.150	14
0.075	10

Curing of the specimens was done in limewater at room temperature, ranging between 19 to 23 °C. During the exposure stage, the oven temperature had a mean value of 60.7 °C and a standard deviation of 0.3 °C.

3.4.2 Results

Strain curves corresponding to control specimens of set #1c are presented in Fig. 3.9. The vertical dashed line indicates the end of the curing stage and the beginning the exposure stage. The thickest continuous line indicates the average strain of the three specimens. This average strain was used for the calculation of the interfacial expansions in reactive specimens of set #1a, according to Eq. 3.2, which are presented in Fig. 3.10. During the curing stage there was practically no length change in both control and reactive mortar specimens. During the exposure stage, the mortar steadily shrunk to an asymptotic value of -0.10%. The interfaces of the reactive specimens, in contrast, exhibited small expansions ranging between 3 and 13 μm.

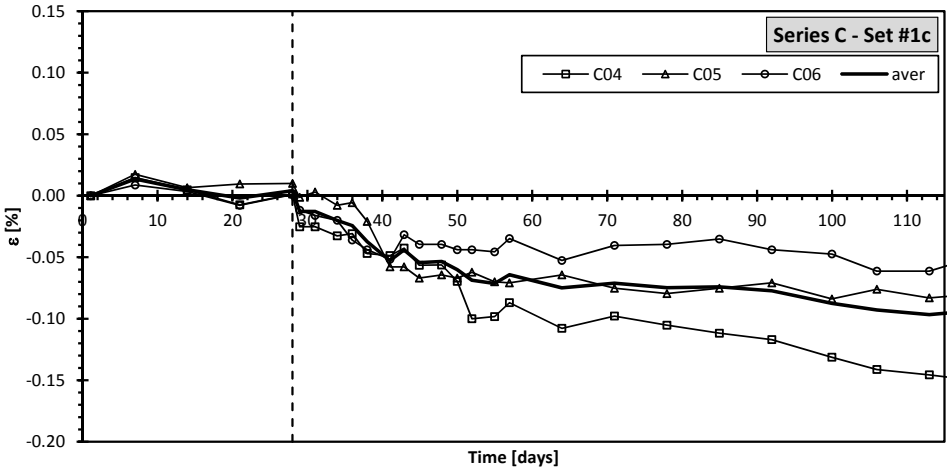

FIGURE 3.9: Strain curves corresponding to Series C - Set #1c.

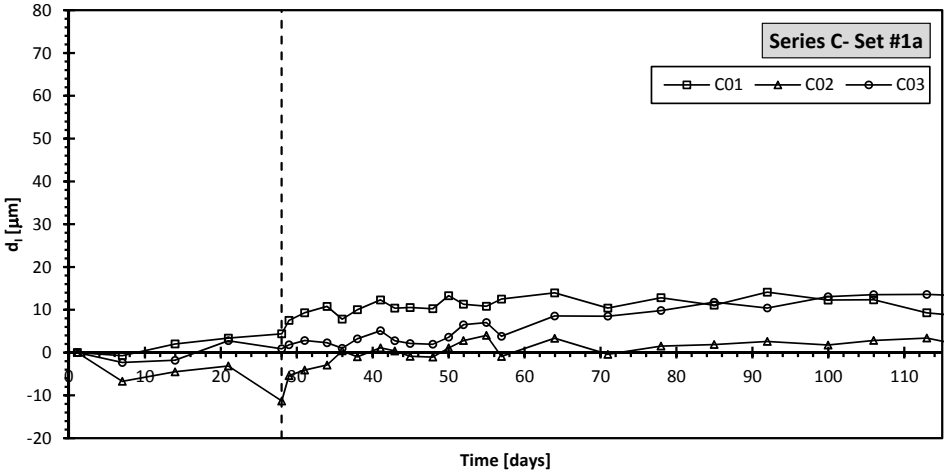

FIGURE 3.10: Interfacial expansion curves corresponding to Series C - Set #1a.

The relative mass change curves of the mortar control specimens, calculated according to Eq. 3.3, is presented in Fig. 3.11. During the curing stage there was a mass increase of

1.3% mainly developed in the first week. When the temperature was raised to 60 °C, the specimens lost mass but not enough to recover the original weight. The relative mass change curves of the reactive specimens, which is given in Appendix A.3, Fig. A.15, exhibit a similar pattern, but with a smaller increase of the mass during the curing stage. This difference is probably due to the fact that the reactive specimens were moulded by halves, with 24 h in between. That means that when a reactive specimen was weighed for the first time, half of the specimen was 24 h old and other half was 48 h old, while the control specimens were always 24 h old. In that way, the weight gained by the older half of a reactive specimens in the second 24 h was not measured.

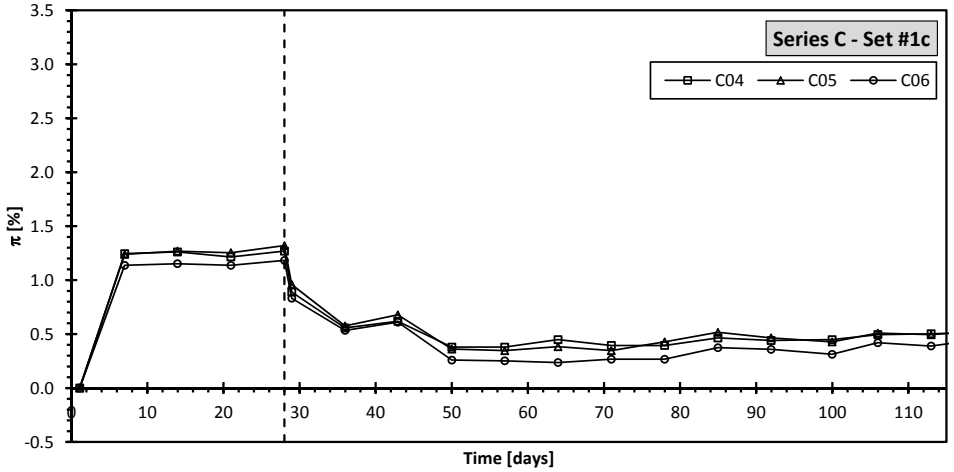

FIGURE 3.11: Relative mass change curves corresponding to Series C - Set #1c.

From here on, in order to make the reading easier, all the remaining relative mass change and strain curves will be included in the Appendices A.3 and A.2, respectively.

The interfacial expansion curves of the cement paste specimens are given in Fig. 3.12. During the curing stage there were small expansions ranging between 4 to 7 μm. Once in the oven, the specimens interfaces expanded steadily reaching values over 40 μm at day 106. After that, interfaces of specimens C07 and C08 opened up, physically separating the specimens in two parts, while specimen C09 continued expanding for another three weeks before one its interfaces also opened up for a expansion of 53 μm (not plotted). In the strain curves of the control specimens (Appendix A.2, Fig. A.2), it can be appreciated that cement paste shrunk less than mortar. In contrast with the mortar, cement paste curves exhibit a jump when heated to 60 °C due to thermal expansion.

With regard to the mass change, cement paste specimens exhibited a pattern similar to that of the mortar specimens, but with a mass increase that was practically twice the one of the mortar. Note that this ratio is the same as the ratio between the volume of cement paste in the cement paste specimens (set #1c) and the volume of cement

paste in the mortar specimens (set #2c), probably indicating that the mass change was proportional to the amount of cement paste in the specimen.

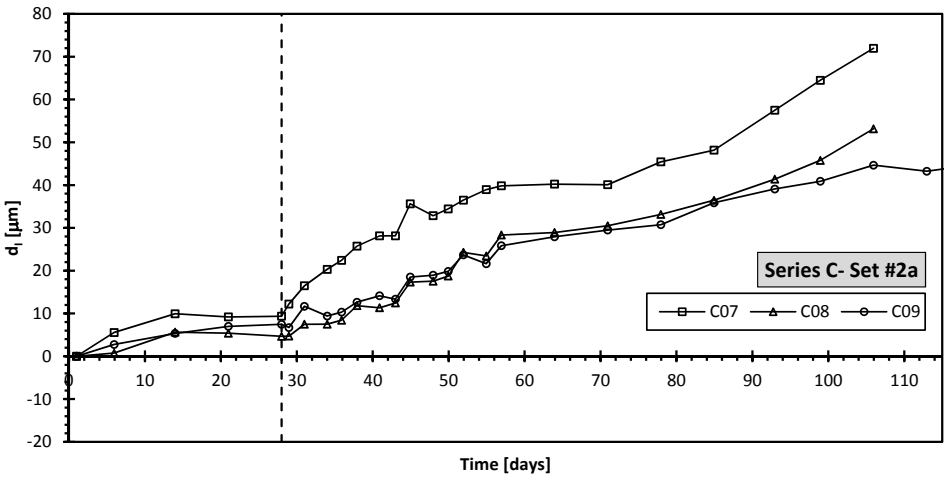

FIGURE 3.12: Interfacial expansion curves corresponding to Series C - Set #2a.

After 64 days in the oven, a whitish reaction product was detected exuding from the interfaces of the reactive cement paste specimens (set #2a), as it can be seen in Fig. 3.13, left. Immediately after the separation, the reaction products at the interface formed a continuous layer with a waxen texture. A few minutes later, after exposure to the air, the surfaces got dry and took a scaly appearance (Fig. 3.13, right). In the mortar specimens, no exuding of reaction product was detected.

FIGURE 3.13: Reaction products in specimens from Series C. Left: whitish reaction product leaching at from specimen C07. Right: reaction products at the separated interface of specimen C08.

After the test, the reacted zones of two specimens (from sets #1a and #2a), were studied by means of SEM/EDS analysis. The analyses were gently performed at EMPA (Switzerland) by Dr. A. Leemann.

In Fig. 3.14, a set of images of the interfacial zone of the reactive specimen C08 (CP and SL glass, set #2a) can be seen. In the left image, the upper part corresponds to

the glass, the bottom part to the HCP, and the middle part, a region of about 80 μm width, to the reaction products. The reaction products themselves can only be seen at the borders of this zone, just beside the HCP and the glass. The rest is plain black due to the epoxy used in the preparation of the sample. It is assumed that reaction products had been there but due to the cutting and polishing processes they were lost. A similar configuration can be seen in the SEM images obtained by Yi and Ostertag [221] for mortar-BS glass interfaces. In the upper-right image, the corrosion process of the glass can be appreciated in detail, from the intact glass to the ASR product. In the bottom-right image, the original position of the interface can be clearly distinguished as a straight line separating the mortar from the ASR products. Note that the morphology of the reaction products beside the HCP is quite different from that observed beside the glass.

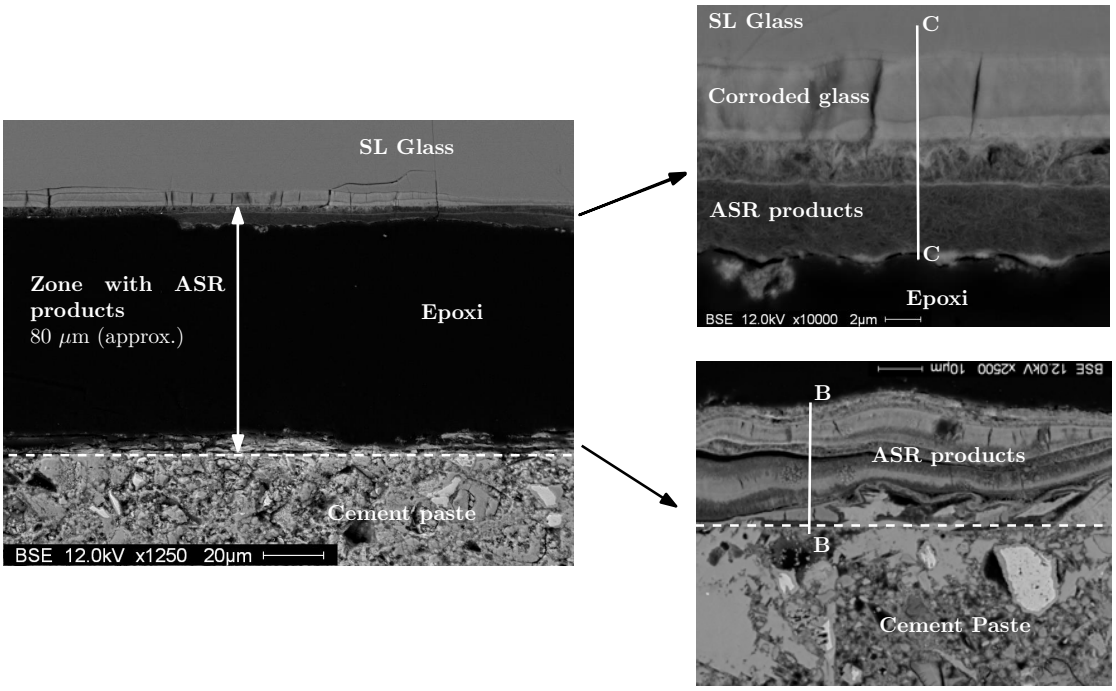

FIGURE 3.14: SEM images from the reacted interfacial zone of a CP-SL glass specimen (C08).

Similarly, in Fig. 3.15, two images of the reactive specimen C01 (mortar and SL glass, set #1a) are presented. The pattern is the same described for the HCP specimen, but in this case the width of reaction product layer is about 9.5 μm. The degraded glass and the reaction products beside it (right image) look similar to those observed in the HCP specimen. Unfortunately, no image of the reaction products beside the mortar was obtained. As expected, the width of the ASR products layer was bigger in the specimen C08, which developed higher interfacial expansion than specimen C01. However, this relation is not proportional.

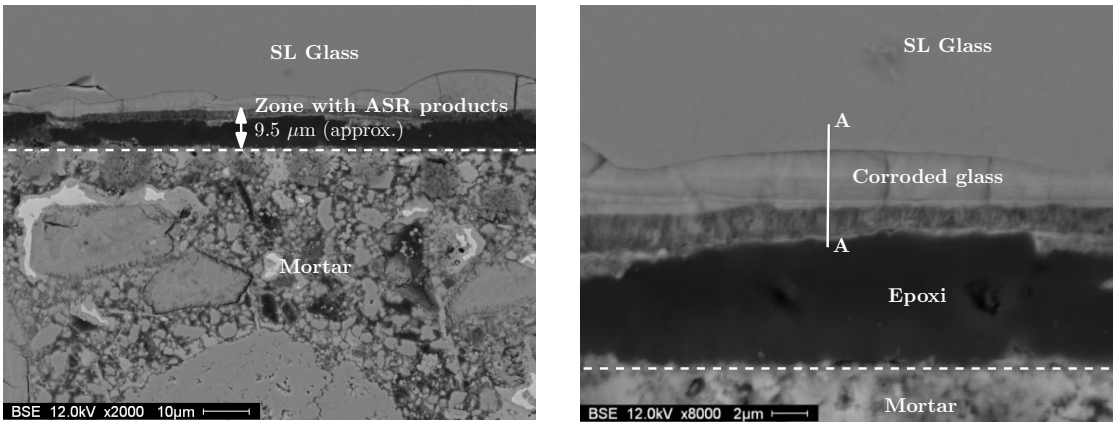

FIGURE 3.15: SEM images from the reacted interfacial zone of a mortar-SL glass specimen (C01).

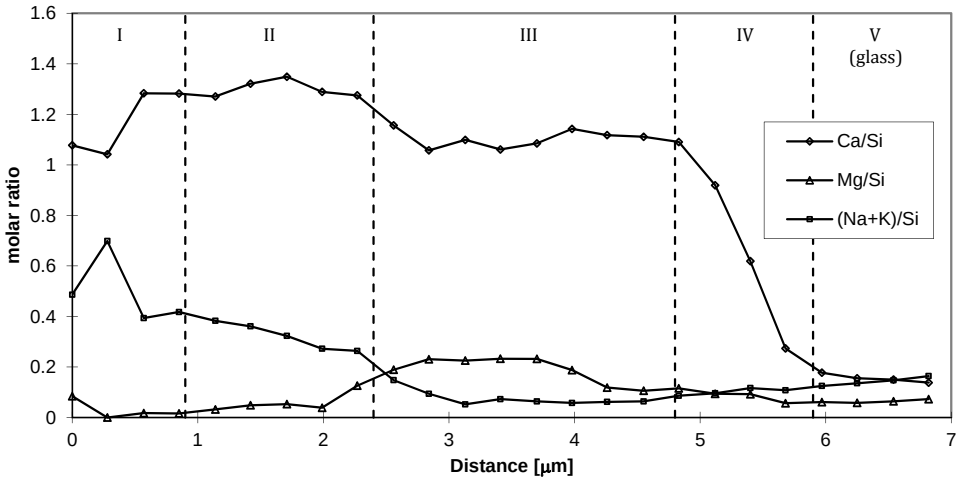

FIGURE 3.16: Profile of the molar Ca/Si-, Mg/Si- and (Na+K)/Si-ratios along line A-A of Fig. 3.15.

The composition of the reaction products was investigated by means of EDS analysis performed in equally separated points along the lines A-A (Fig. 3.15), B-B and C-C (Fig. 3.14). In Figs. 3.16 to 3.18, the profile obtained of the molar Ca/Si-, Mg/Si- and (Na+K)/Si-ratio are presented. The profiles A-A and C-C (ASR products beside the glass) exhibit a similar pattern which can be divided in five sectors: (I) points on the epoxy layer with an erratic composition; (II) Ca/Si≈1.3 and (K+Na)/Si≈0.2–0.3; (III) Ca/Si≈1.0–1.1 and (K+Na)/Si≈0.1; (IV) transition between composition of sector III and V; (V) glass composition.

In the profile B-B (ASR products beside the HCP) we can also distinguish different sectors: (I) HCP composition, Ca/Si≈1.7 and (Na+K)/Si≈0.25; (II) Ca/Si≈1.2–1.4 and (K+Na)/Si≈0.2–0.3; (III) Ca/Si≈1.2–1.4 and (K+Na)/Si≈0.3–0.8; (IV) Ca/Si≈1.3–1.1 and (K+Na)/Si≈0.2–0.4; (V) Ca/Si≈1.2 and (K+Na)/Si≈0.1–0.2; (VI) points on the epoxy layer with a erratic composition.

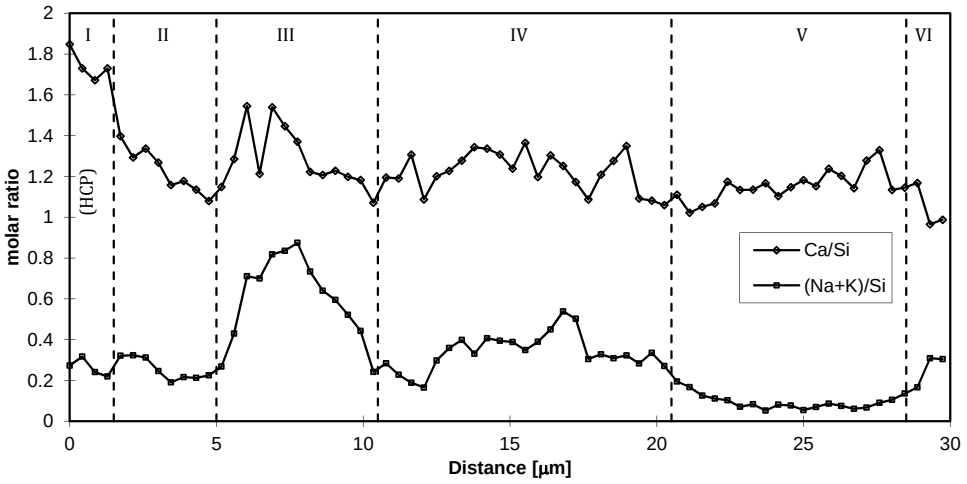

FIGURE 3.17: Profile of the molar Ca/Si- and (Na+K)/Si-ratios along line B-B of Fig. 3.14.

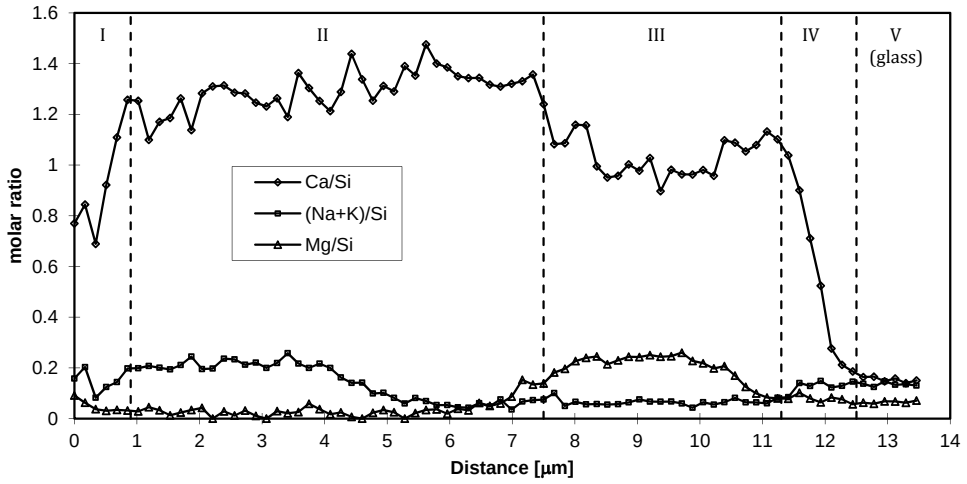

FIGURE 3.18: Profile of the molar Ca/Si-, Mg/Si- and (Na+K)/Si-ratios along line C-C of Fig. 3.14.

The complete compositional profiles are given in Appendix A.4, Figs. A.44 to A.46. The increase of the Mg/Si-ratio in sector III of profiles A-A and C-C is probably due to the loss of Si atoms in the corroded glass layer rather than the fixation of Mg atoms coming from cement. This is confirmed by the practical absence of Mg in the profile B-B. Interestingly, the presence of K is negligible in all the profiles despite the fact that it was the major alkali of the cement (see Table A.1, cement CP01).

3.5 Series D

In the previous Series C, the concentration of alkalis in the pore solution of the cementitious matrix was estimated, based on the experimental results reported in Refs. [55, 133],

to have been in between 0.40 to 0.70 mol/L. With this concentration, during the curing stage there probably was some leaching of alkalis to the lime-water curing bath. During the exposure stage the concentration of alkalis in the curing bath was higher and, hence, the flux of alkalis presumably reversed.

In the present series the intention was to reduce these alkali movements, keeping its concentration in the pore solution as constant as possible. To do so, first, the alkali content of the cementitious matrix was raised to a level in which the expected concentration of alkalis in the pore solution was the same than that in the exposure bath, and, second, the same solution was used for both curing and exposure stages. The series included three sets of specimens, one elaborated with plain cement paste, one with calcareous mortar, and one with siliceous mortar.

3.5.1 Description

The specimens tested in this Series D are listed in Table 3.3. Three different cementitious matrices were used: cement paste, mortar with crushed limestone sand and mortar with normalized siliceous sand. The Portland cement was type CEM I 42,5 N-SR5 according to the Spanish standard UNE-EN 197-1 [3]. The oxide composition of the cement is given in Table A.1, cement PC01, of Appendix A.1. The same water/cement weight ratio of 0.47 was adopted for the three mixtures. Sodium hydroxide was added to the mixing water in order to rise the alkali content in terms of equivalent sodium oxide (Na_2O_e) up to 1.1 wt% of the cement weight. This ratio of Na_2O_e was estimated in order to have a similar concentration of alkalis in the pore solution of the hydrated cement paste and in the alkaline bath, based on the experimental results reported in Refs. [55, 133]. The PSD of the sands used for the mortars is given in Table 3.4. The specific weight of the calcareous and siliceous sands were of 2.675 g/cm^3 and 2.570 g/cm^3, respectively. The amount of sand in the mortars was fixed in 63 wt% of the cement weight, resulting in an aggregate/mortar volume ratio of 0.23 for the calcareous mortar and of 0.24 for the siliceous one. In all cases, the reactive discs for reactive specimens were of colourless SL glass.

TABLE 3.3: List of specimens tested in Series D.

Set #	Type	Specimens	Cementitious matrix
1a	Reactive	D01 to D03	Mortar w/ calcareous sand
1c	Control	D04 to D06	
2a	Reactive	D07 to D09	Cement paste
2c	Control	D10 to D12	
3a	Reactive	D19 to D21	Mortar w/siliceous sand
3c	Control	D22 to D24	

TABLE 3.4: Particle size distribution of sands used for mortar specimens.

Sieve size (mm)	**Passing (wt%)**	
	Calcareous	Siliceous
2.000	100	100
1.180	100	81
0.430	49	28
0.150	27	12
0.075	19	3

During the curing stage the room temperature was not controlled, ranging between 20 to 30 °C. During the exposure stage, the oven temperature had a mean value of 59.5 °C and a standard deviation of 1.2 °C. Unlike the previous series, in this cases the curing solution was the same used for the exposure stage (40 g NaOH and 2 g of $Ca(OH)_2$) per kg of water), in order to avoid alkali leaching during the curing stage.

3.5.2 Results

The interfacial expansion curves obtained from the three tested sets are presented in Figs. 3.19 to 3.21. The strain curves of control specimens and the relative mass change curves of both reactive and control specimens are given in Appendixes A.2 and A.3, respectively.

The limestone mortar specimens (set #1a) have in average a final expansion of 14 μm, which developed mainly in the first 3 weeks in the oven. After two months in the oven some ASR product was expelled at the interfaces. The test ended without interface separations.

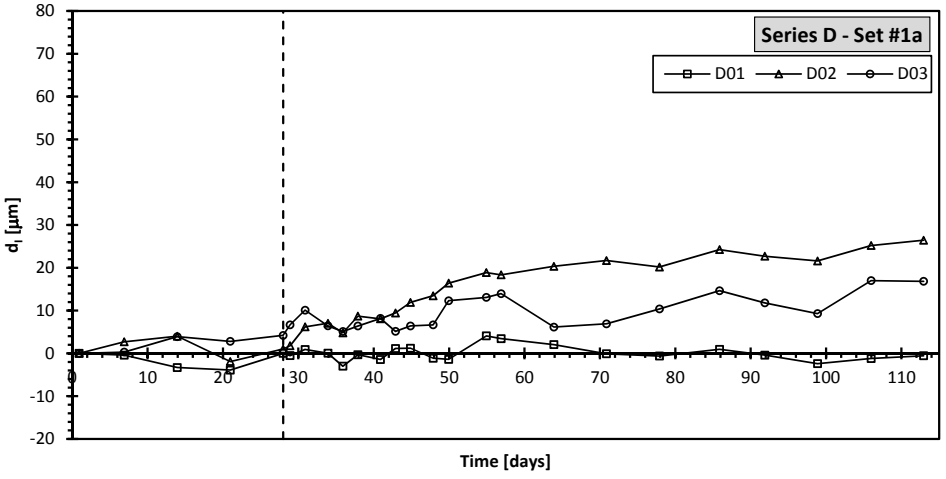

FIGURE 3.19: Interfacial expansion curves corresponding to Series D - Set #1a.

The curves of the cement paste specimens (set #2a) exhibit rather less scatter than the mortar ones. The expansion developed mainly in the first two weeks in the oven reaching a mean value of 27 μm. After that, the expansion continued until the separation of the glass-matrix interfaces, but at a lower rate.

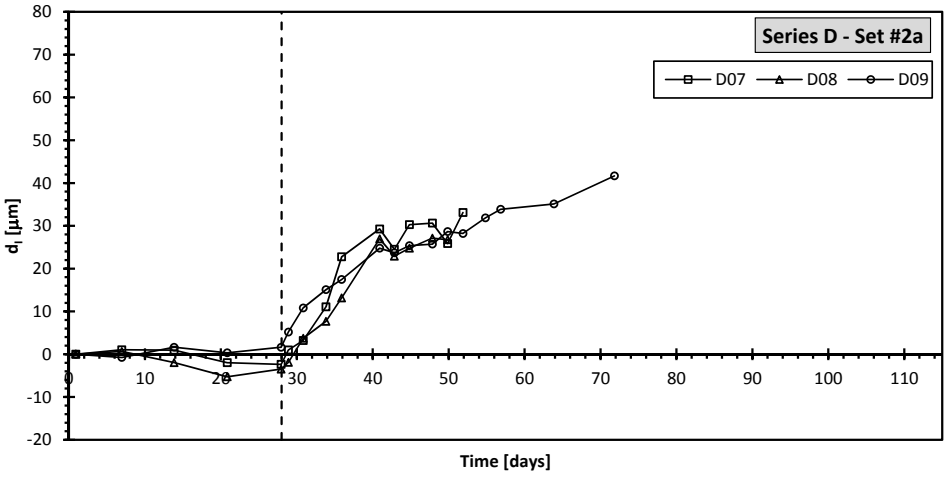

FIGURE 3.20: Interfacial expansion curves corresponding to Series D - Set #2a.

The siliceous mortar specimens (set #3a) reached in average an interfacial expansion of 40 μm before separation. The expansion rate decreased steadily as the maximum expansion was reached. The scatter is similar to the one obtained for the limestone mortar specimens.

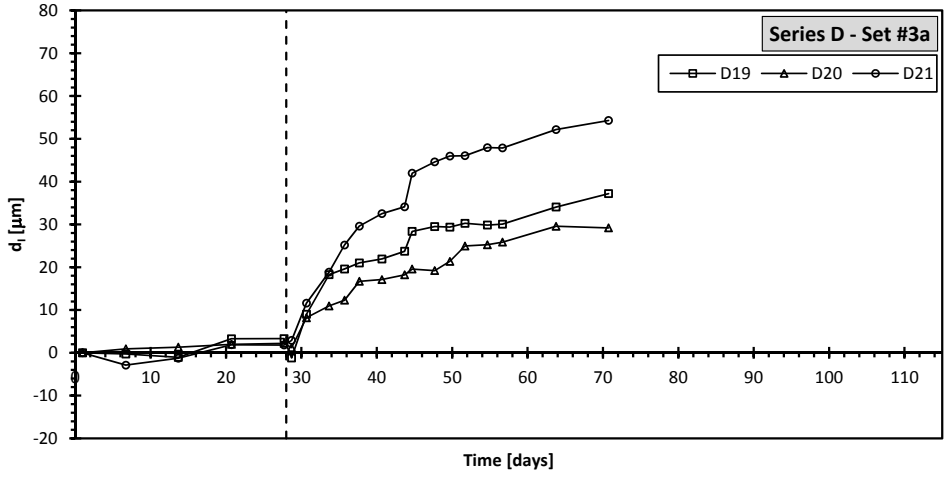

FIGURE 3.21: Interfacial expansion curves corresponding to Series D - Set #3a.

The strain curves of the control specimens (Appendix A.2) exhibit the same patterns for the three tested sets: a general trend to shrinkage with a jump due to thermal expansion when the specimens were heated up to 60 °C. However, the shrinkage of the siliceous mortar specimens was approximately two times larger than that of the cement paste and calcareous mortar specimens.

The relative mass change curves (Appendix A.3) have the same pattern described for Series C, an initial mass gain during the curing stage followed by a progressive loss once in the oven, until reaching a constant value in a matter of 2 or 3 weeks. Again, mortar specimens gain less mass than the cement paste ones.

In Fig. 3.22, SEM images of the interfacial zone of specimen D07 (cement paste reactive specimen) are presented. In the left image, the upper part corresponds to the cement paste, the lower part to the glass and in between the zone with ASR products of about 90 μm width. The reaction products can only be seen at the borders of this zone, just beside the HCP, as it can be appreciated more clearly in the right image. As discussed for the previous series, the rest of the ASR products were lost and replaced by epoxy resin during the preparation of the sample. The crack in the HCP may have been produced by the cutting process of the sample. EDS analysis of the reaction products indicated in the right image of Fig. 3.22 yield molar Ca/Si- and (Na+K)/Si-ratios of 1.25 and 0.12–0.14, respectively.

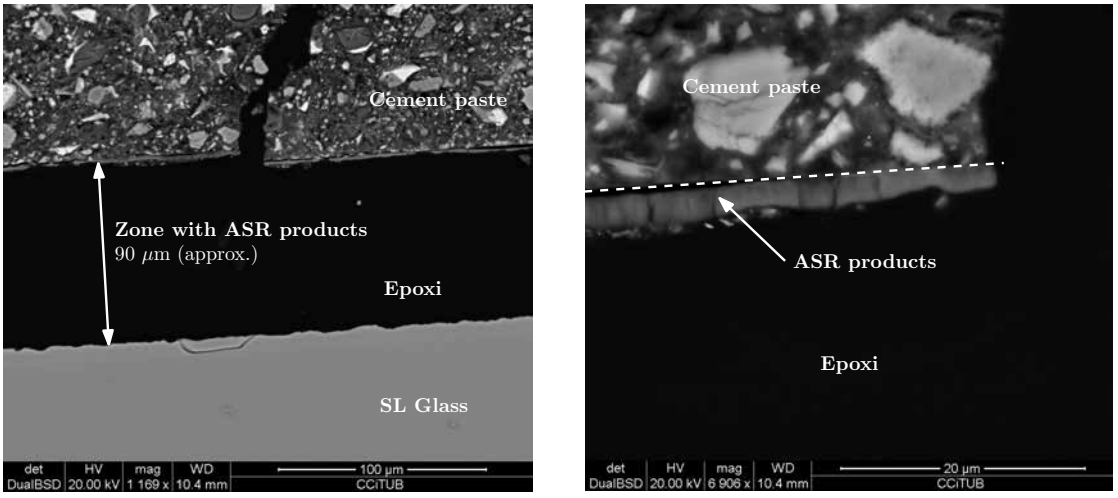

FIGURE 3.22: SEM images of the reacted interfacial zone of a CP-SL glass specimen (D07).

3.6 Series E

Series E of tests was focused on the study of the effects of:

- the type of glass used as reactive aggregate.
- replacing part of the cement of the matrix with Micro Silica (MS).
- pre-existing cracks.
- sealing the lateral surface of the specimens.

As discussed in Sections 2.5 and 2.6, calcium and alkalis play a determinant role in the development of ASR expansions. Both reactants are generally coming from the cementitious matrix, but can also come from the aggregates. For instance, the SL glass used in previous Series D has 10 wt% of CaO and 14 wt% of Na_2O. When the glass is degraded by the alkaline pore solution, calcium and sodium are released and immediately consumed in the formation of ASR products. In the present Series E, the effect of the release of calcium and sodium present in the aggregate is assessed by testing some reactive specimens made with borosilicate glass, which has low content of alkalis and no calcium.

MS is known to control the ASR expansions in concrete, mainly by its 'capability to reduce the alkalinity of the pore solution by binding alkalis in the hydration products' [133]. In addition, when MS is used as partial replacement of the Portland cement, 'there is a dilution of the alkalis available from the clinker', and a 'reduction of $Ca(OH)_2$ in the paste, restricted ingress of water into the concrete caused by reduced permeability and an increase in the resistance to cracking by increasing the strength of concrete' [133].

In tests with mortar specimens prepared with SL glass, Rajabipour et al. [174] found that the composition of the reaction products formed in pre-existing cracks inside the glass particles was substantially different from that of those formed at the glass-cement interfaces. The first one exhibited much lower content of calcium and, consequently, a higher swelling capacity. The authors suggested that this difference was due to the lower availability of calcium at the interior of the cracks. With the intention of studying ASR products formed within cracks, some reactive specimens of the present series were prepared with the glass discs intentionally pre-cracked.

Finally, the effect of the mass exchange (mainly water and/or alkalis) through the lateral surface of the specimen was assessed by testing some specimens with complete lateral sealing.

3.6.1 Description

The specimens tested are listed in Table 3.5. Three different cementitious matrices were used: plain cement paste, cement and MS paste, and mortar with normalized siliceous sand. The Portland cement was type CEM I 42,5 N-SR5 according to the Spanish standard UNE-EN 197-1 [3]. The microsilica was BASF Meyco® MS610. The oxide composition of the cement and of the MS are given in Table A.1, PC02 and MS01 respectively, of Appendix A.1. The same water/binder (cement plus MS, if applicable) weight ratio of 0.47 was adopted for the three mixtures. For the cement and MS paste a MS/cement weight ratio of 0.15 was adopted. To improve the workability of the

cement and MS paste, superplasticizer BASF Glenium® C303 SCC was added to the mixing water in a proportion of 0.90% of the weight of binder. Sodium hydroxide was added to the mixing water of the three mixtures in order to rise the alkali content in terms of equivalent sodium oxide (Na_2O_e) up to 1.1 wt% of the binder weight. As discussed above (Section 3.5), this amount of Na_2O_e was estimated in order to have a similar concentration of alkalis in the pore solution of the hydrated cement paste as in the alkaline bath, based on the experimental results reported in Refs. [55, 133]. The siliceous sand was the same used for the Series D tests, with a specific weight of 2.570 g/cm^3 and the PSD given in Table 3.4. The amount of sand in the mortar was fixed as 63 wt% of the cement weight, resulting in a aggregate/mortar volume ratio of 0.24.

TABLE 3.5: List of specimens tested in Series E.

Set #	Type	Specimens	Reactive aggregate	Cementitious matrix	Other treatments
1a1	Reactive	E01 to E04	BS glass	Cement and MS paste	none
1a2	Reactive	E05 to E07	SL glass		
1c	Control	E08 to E10	None		
2a	Reactive	E14 to E17	BS glass	Cement paste	None
2c	Control	E18 to E21	None		
3a	Reactive	E25 to E28	SL glass	Cement paste	Lateral sealing w/silicone
3c	Control	E29 to E32	None		
4a1	Reactive	E33 to E36	BS glass	Cement paste	Pre-cracked
4a2	Reactive	E37 to E40	SL glass		
5a	Reactive	E41 to E44	BS glass	Mortar w/siliceous sand	None
5c	Control	E45 to E48	None		
6a	Reactive	E52 to E55	SL glass	Cement paste	Lateral sealing w/rubber
6c	Control	E56 to E59	None		

Two different glasses were tested as reactive discs for reactive specimens: soda-lime glass (SL glass) and borosilicate glass (BS glass). For the specimens of set #4, the glass discs were split into two parts and carefully put together again inside the moulds before pouring the cement.

Once the curing period was completed, the specimens of set #3 were removed from the curing bath, dried superficially with a towel, and let dry exposed to air for half an hour. Then, a thin layer of silicon thread sealant Loctite® SI 5331™ was applied to the lateral surface of the specimens, and was let cure for 4 hours before returning to the alkaline bath for the exposure stage. The specimens were weighted before and after the application of the sealant layer in order to discount the weight increase in the assessment of the mass evolution of the specimens. For set #6, the procedure was similar but using self-curing rubber tape ATMOS® instead of silicon sealant. The rubber tape was overlapped at least 10 mm at every turn.

During the curing stage, the room temperature ranged between 18 to 20 °C for sets #1 to #5, and between 22 to 24 °C for set #6. During the exposure stage, the oven temperature had a mean value of 59.5 °C and a standard deviation of 1.2 °C. As in the previous series, the same solution (40 g NaOH and 2 g of $Ca(OH)_2$ per kg of water) was used for the curing and exposure baths.

3.6.2 Results

Set #2

The reactive specimens made with plain cement paste and BS glass discs (set #2a, Fig. 3.23) exhibited practically no interfacial expansion during the curing stage, followed by a roughly linear expansion during the exposure stage, reaching an average value of 38 μm after two weeks at 60 °C. Afterwards, all specimens experienced the separation of one of their interfaces, with the exception of the E17 which remained in a plateau until the end of test. Views of the interfacial zone of specimen E15 before and after the separation are given in Fig. 3.24. In contrast with previous tests done with SL glass, the BS glass discs cracked due to the ASR. Moreover, the amounts of expelled ASR products was higher than those observed in specimens with SL glass for similar interfacial expansions. The counterpart control specimens (set #2c, Fig. A.7, Appendix A.2) showed the same behaviour previously observed in Series C and D: continuous shrinkage, only altered by the thermal expansion step when heated. The relative mass change curves (Figs. A.28 and A.29, Appendix A.3) also show the expected behaviour.

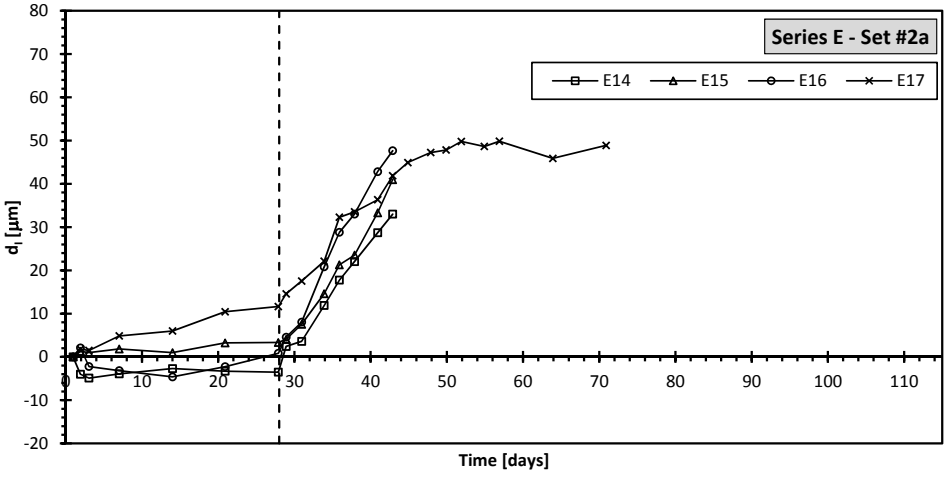

FIGURE 3.23: Interfacial expansion curves corresponding to Series E - Set #2a.

Set #5

The reactive specimens made with siliceous mortar and BS glass discs (set #5a, Fig. 3.25)

FIGURE 3.24: Reaction products in specimen E15 (Series E-set #2a). Left: whitish reaction product expelled from the specimen. Right: reaction products and cracked BS glass disc at the detached interface.

developed a smaller rate of interfacial expansions than those made with cement paste and the same glass (set #2a). Moreover, the interfacial expansions of specimens of set #5a stopped after two weeks at 60 °C, without reaching the separation of the interfaces. The strain curves of the siliceous mortar control specimens (set #5c, Fig. A.9, Appendix A.2) are similar to the cement paste ones (set #2c) but with higher shrinkage rate. The relative mass change curves (Figs. A.34 and A.35, Appendix A.3) are also similar to previous ones.

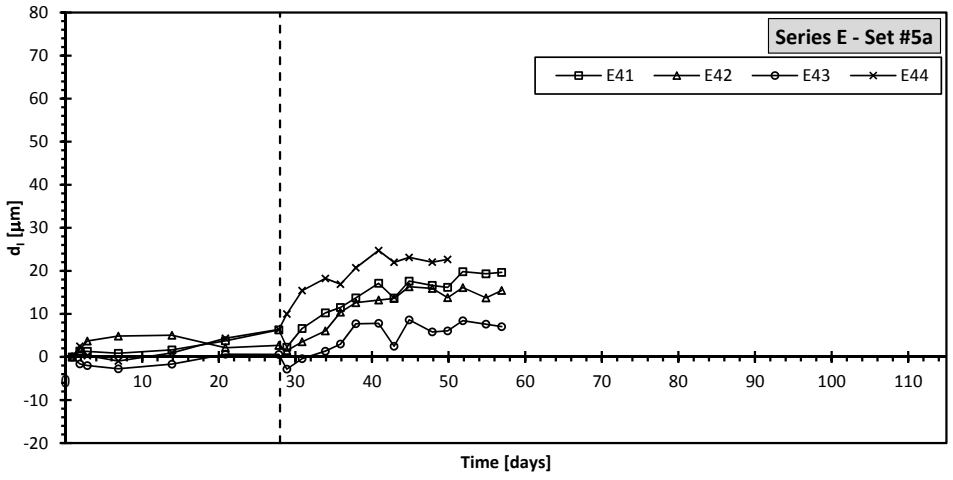

FIGURE 3.25: Interfacial expansion curves corresponding to Series E - Set #5a.

The reactive specimen E44 was removed from the solution before the end of the test for EDS/SEM analysis. In Fig. 3.26, some SEM images of the reacted interfacial zone are shown. Two different morphologies of ASR products can be distinguished in Figs. 3.26a and b: one relatively thin layer of 'massive' gel in contact with the mortar, and one thicker layer of 'spongy' gel, which is partially visible due to the impregnation of the epoxy resin used for the preparation of the sample. The total thickness of the ASR layer

was about 150 μm. A better view of the morphology of the spongy gel was obtained in Fig. 3.26c using a ETD detector. EDS analysis of massive gel lead to molar Ca/Si- and (Na+K)/Si- ratios of 0.55–1.32 and 0.33–0.70, respectively. In Fig. 3.26d, cracks induced in the BS glass disc by the ASR can be observed. It is interesting that there is no separation between the two glass pieces in the middle and the mortar matrix, while at the left and right ends of the image there are significant separations that indicate the presence of ASR products. It seems that, somehow, the ASR was inhibited at the interface of the two glass pieces. This may be attributed to the pressure exerted by the ASR products in the cracks surrounding the two pieces, since the ASR products formed within aggregate cracks (with low calcium content) developed higher swelling pressures than ASR products formed in contact with the cement paste (with high calcium content), as discussed in Section 2.8. A priori, the fact that no ASR products were detected inside the glass cracks does not invalidate this conjecture since most of the ASR products were removed or impregnated with epoxy resin in the preparation of the sample.

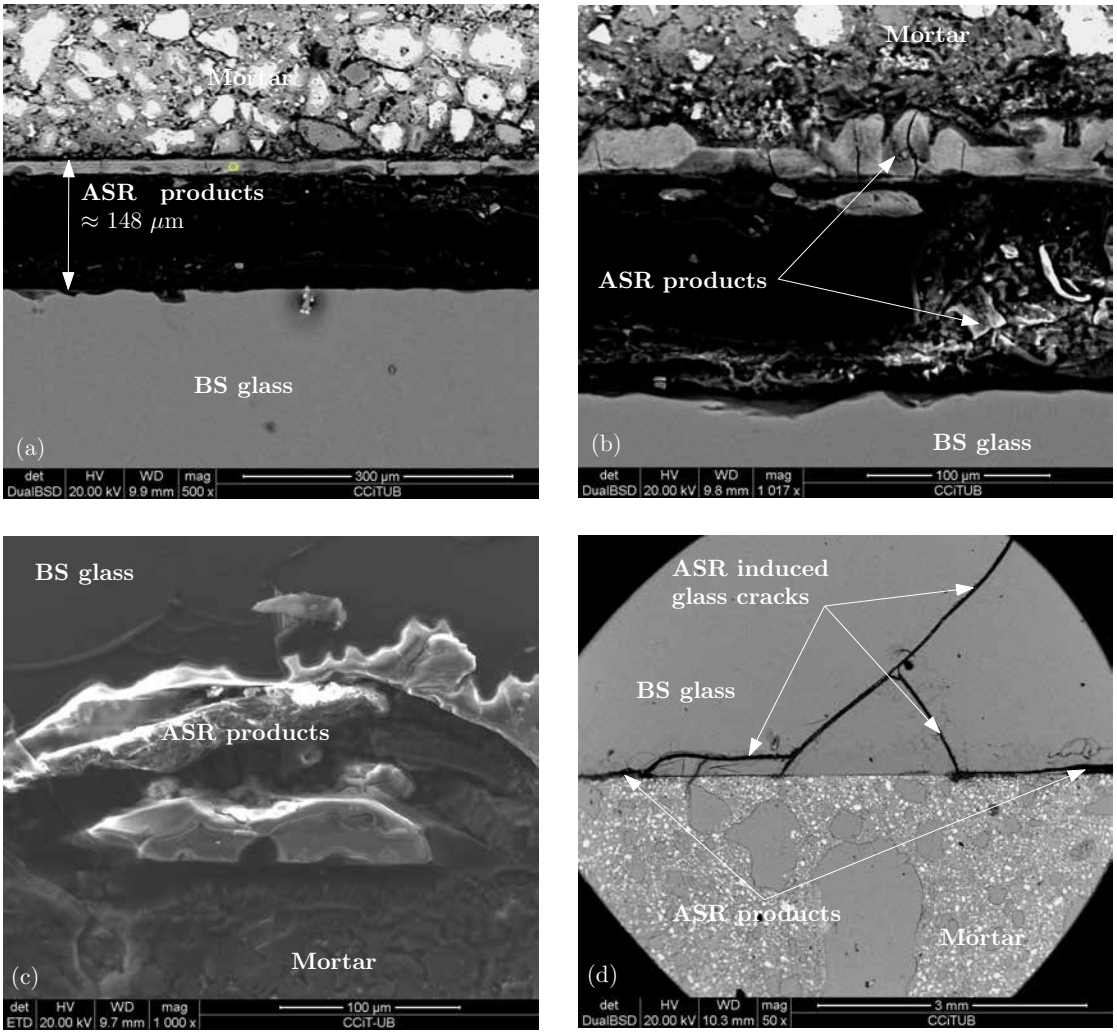

FIGURE 3.26: SEM images from the reacted interfacial zone of a mortar-BS glass specimen (E44).

Sets #1

In contrast with the specimens made with plain cement paste (in this series and in previous ones), the control specimens made with cement and MS paste (set #1c, Fig. A.6, Appendix A.2) exhibited practically no shrinkage during the curing stage nor during the exposure stage. Moreover, the thermal expansion when the specimens were heated to 60 °C is significantly greater than the ones corresponding to plain cement paste or mortar.

The use of MS as partial replacement of cement also affected the development of the interfacial expansions. During the curing stage, the reactive specimens with SL glass discs (set #1a2, Fig. 3.28) developed average interfacial expansions of 5 μm, which suddenly raised to 35 μm in the first 24 h at 60 °C, leading in all cases to the separation of the interfaces shortly after. In the case of the specimens made with BS glass discs (set #1a1, Fig. 3.27), the behaviour was more erratic during the curing stage, when two of the specimens developed very high interfacial expansions, while the other two remained practically inactive. When heated up to 60 °C, the two lagging specimens expanded suddenly reaching the same level of accumulated expansion as the other two. After a few days in the oven, the interfaces of all the specimens separated for average accumulated expansion of approximately 35 μm. The amount of ASR products observed on the separated interfaces of specimens of both sets was much lower than that observed for similar interfacial expansions in previous tests.

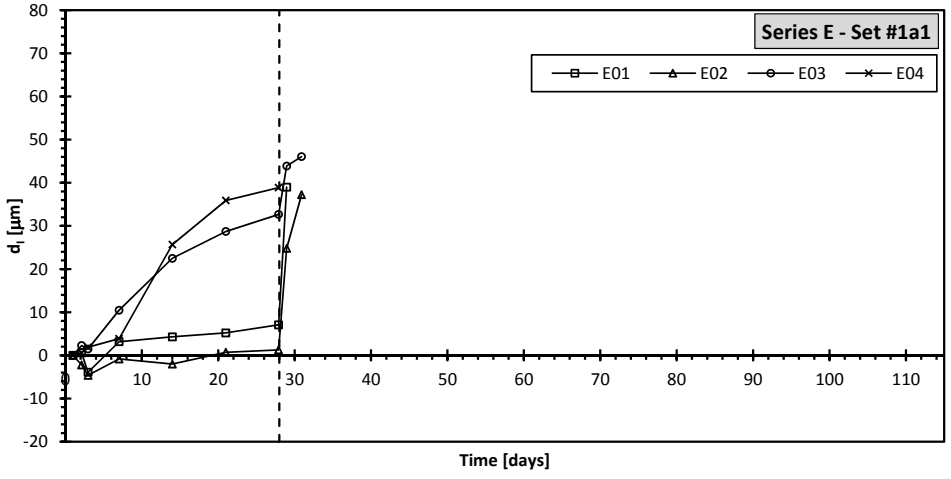

FIGURE 3.27: Interfacial expansion curves corresponding to Series E - Set #1a1.

The relative mass change curves of sets #1 (Figs. A.25 to A.27, Appendix A.3) exhibit the same pattern observed in previous series. The only difference is that after the mass drop due to the heating, instead of continuing loosing mass one can observe a progressive mass gain. Additionally, compared with the plain cement paste specimens of the present series and previous ones, the amount of mass gained during the curing

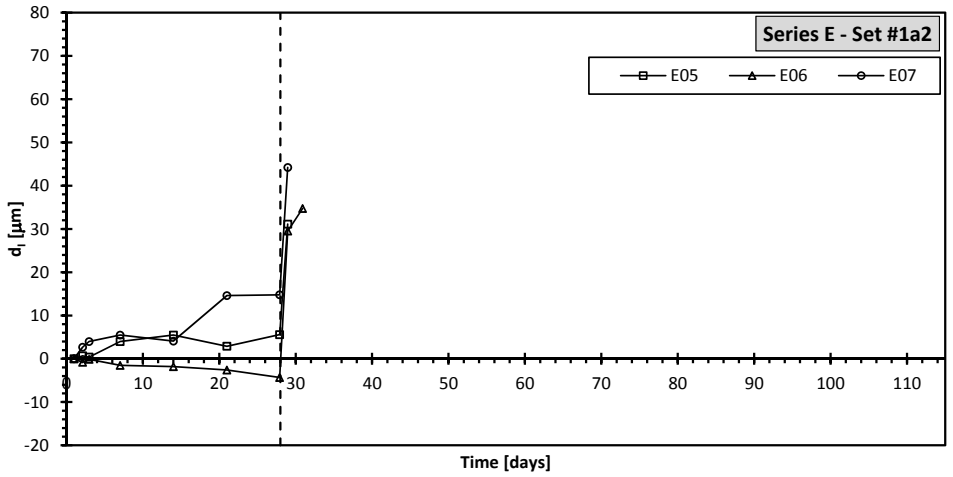

FIGURE 3.28: Interfacial expansion curves corresponding to Series E - Set #1a2.

stage is significantly greater. Both behaviours may be related to the slower hydration rate of MS in comparison with clinker.

Sets #3 and #6

Two different kinds of lateral sealing were tested in sets #3 and #6. The silicone sealant (set #3) did not work as expected. After three days in the alkaline bath at 60 °C it partially detached from the specimens, as it is discussed below. On the other hand, the self-curing rubber remained unaltered throughout the test.

In set #6 with the lateral sealing, the weight drop due to heating that had been observed in all the previous weight change curves did not take place (Figs. A.36 and A.37, Appendix A.3). In sets #3, due to the imperfection of the silicone sealing, the weight loss did not disappear but was reduced significantly (Figs. A.30 and A.30, Appendix A.3).

When comparing the interfacial expansion curves of sets #3a and #6a (Figs. 3.29 and 3.30) with those of Series D-set #2a (Fig. 3.20), i.e. specimens of the same type but with and without lateral sealing, it seems clear that the application of a lateral sealing after the curing stage had reduced the expansion rates. This effect cannot be attributed to a difference in the shrinkage behaviour of the cement paste matrix since both sealed and not-sealed control specimens exhibit similar strain curves (compare Figs. A.8 and A.10, sets #3c and #6c, with Fig. A.7, set #2c). This issue is further discussed below for Series F (Section 3.7), which was completely dedicated to the study of the lateral sealing effect.

At the end of test, the specimens of this series had not developed enough expansions to cause the separation of the interfaces, with the exception of specimen E25 which separated prematurely, probably due to a fault in the elaboration process. Expansion

curves of specimens E54 and E55 are not given in Fig. 3.30 since they exhibited an inconsistent development.

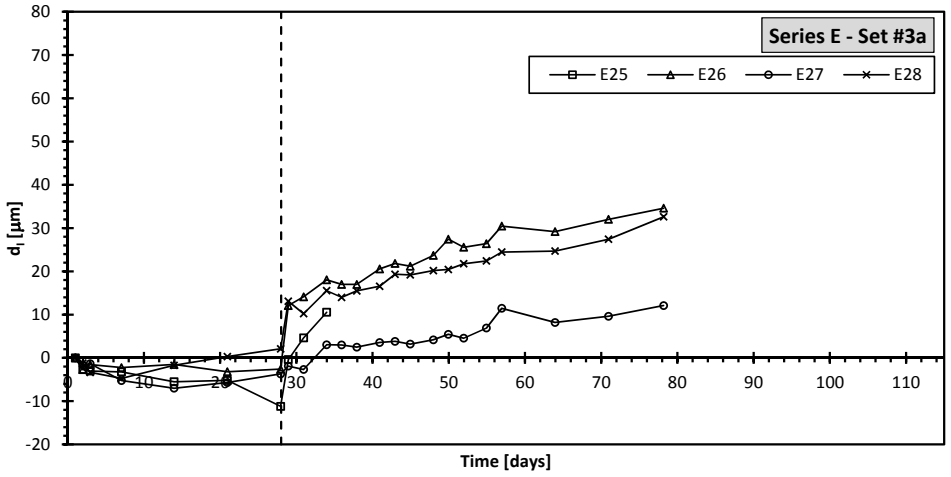

FIGURE 3.29: Interfacial expansion curves corresponding to Series E - Set #3a.

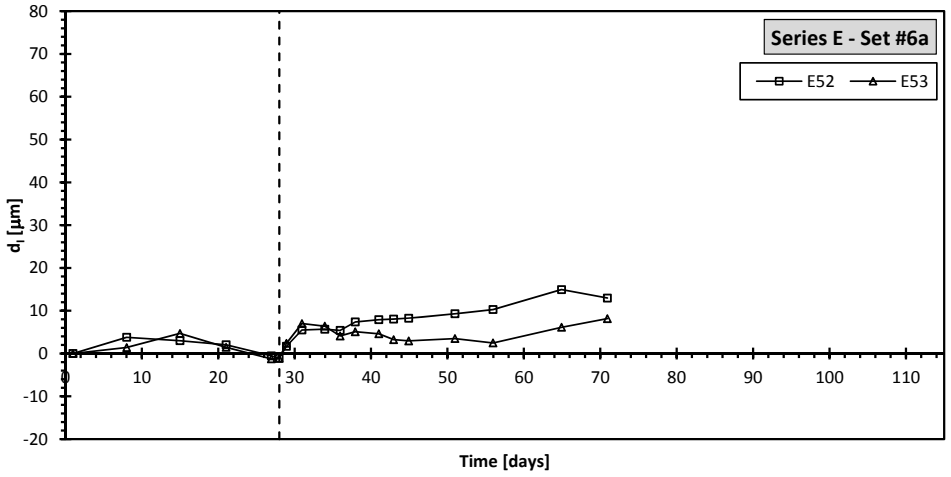

FIGURE 3.30: Interfacial expansion curves corresponding to Series E - Set #6a.

Set #4

The reactive specimens of set #4, made with pre-cracked glass discs, exhibited a reduced interfacial expansion rate (Figs. 3.31 and 3.32) in comparison with similar specimens made with sound glass discs, such as sets #2a (Fig. 3.23) and Series D-set#2a (Fig. 3.20). In addition, the specimens made with pre-cracked SL glass discs (set #4a2) exhibited a greater scatter. The calculation of the interfacial expansion curves of set #4 was made using the strain measured on the cement paste control specimens of set #2c (Fig. A.7). One of the interfaces of specimen E33 separated before the end of the tests. Specimens E34 and E37 were removed from the bath before the end of the test for SEM/EDS analysis.

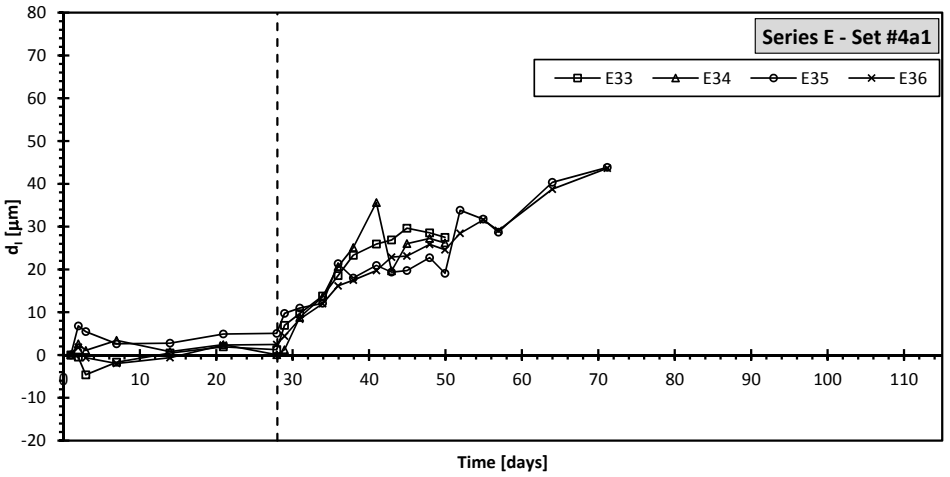

FIGURE 3.31: Interfacial expansion curves corresponding to Series E - Set #4a1.

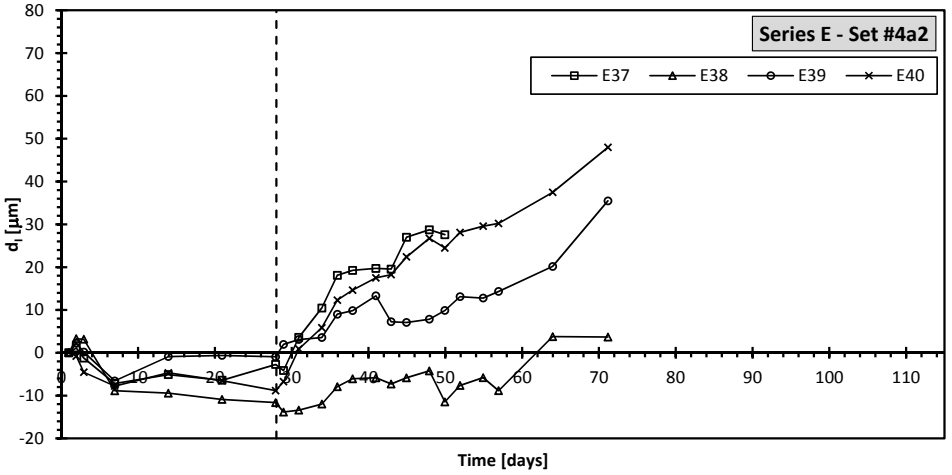

FIGURE 3.32: Interfacial expansion curves corresponding to Series E - Set #4a2.

The SEM images obtained from specimen E34 (set #4a1) revealed the presence of layer of ASR products of about 130 μm of thickness (Fig. 3.33a). As in the SEM images presented for set #5 (Fig. 3.26), two different morphologies of ASR products can be observed, bot located in between the cement paste and the glass, in Figs. 3.33b and c: relatively thin layers of 'massive' gel in between thicker layers of 'spongy' gel, which is partially visible due to the impregnation of the epoxy resin used for the preparation of the sample. EDS analysis performed on the massive ASR gel lead to molar Ca/Si- and (Na+K)/Si-ratios of 0.06–0.28 and 0.18–0.34, respectively.

In the SEM images of specimen E37 (set #4a2) the observed layer of ASR product was only of 21 μm of thickness (Fig.3.34a). The two different morphologies of ASR products observed in the previous SEM images are no clearly distinguished in this case (Fig.3.34a and b). Figure 3.34c shows that the pre-existing crack was filled with cement paste in the elaboration process, indicating that the original goal of having a glass crack with limited

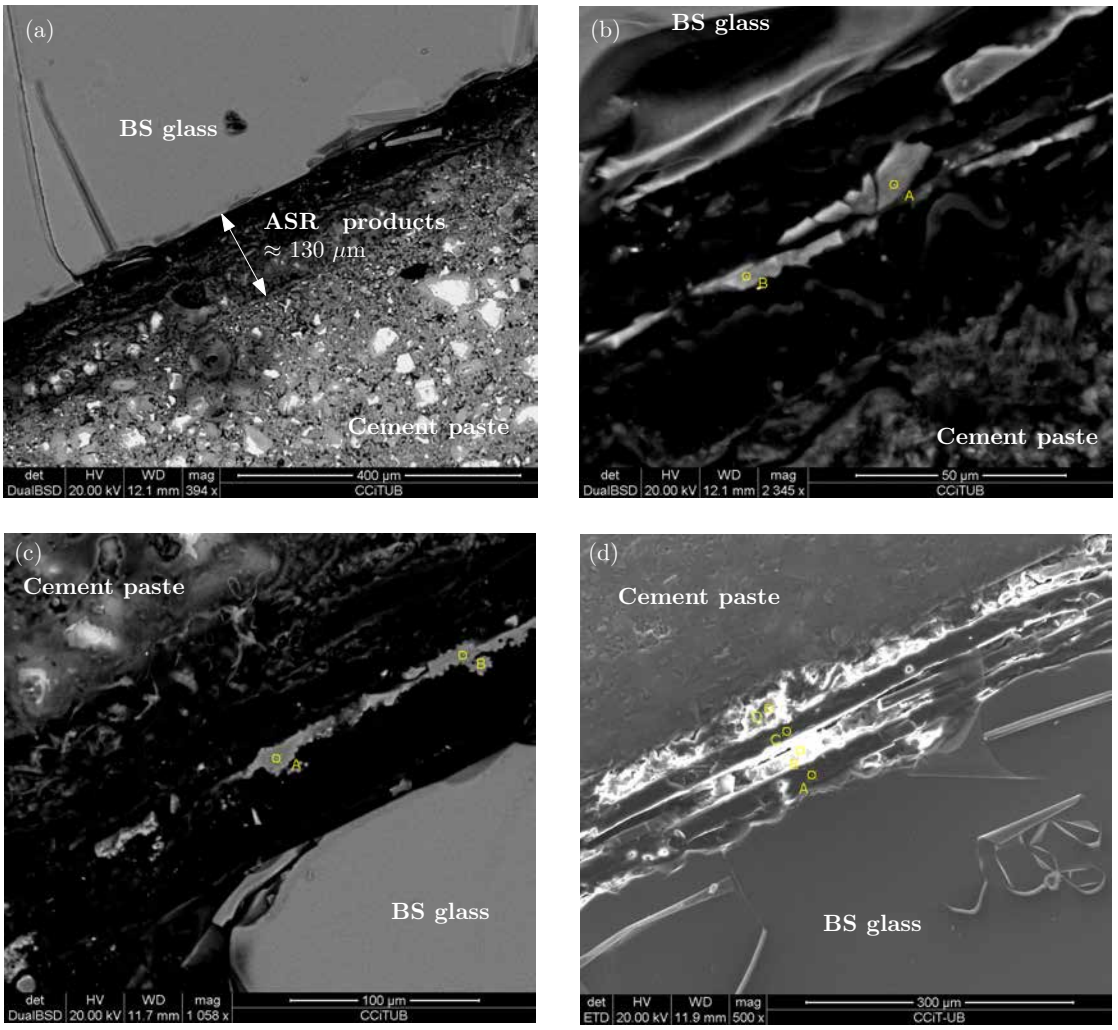

FIGURE 3.33: SEM images from the reacted interfacial zone of a CP-BS glass specimen (E34). The glass disc was cracked before testing.

access of calcium was not accomplished. Presumably, the conditions within the pre-existing crack are the same as at the CP-glass interfaces out of the crack. However, no evidence of ASR products was found within the pre-existing glass cracks. Again, we may resort to the mechanical constraint of the surroundings to explain why ASR products were not formed in sites that a priori seemed to had the appropriate conditions. In this case, the formation of ASR products within the pre-existing crack would have required, due to kinematic compatibility, to develop a swelling pressure high enough to propagate the crack towards the cement paste matrix. In change, the formation/swelling of ASR products at the main cement paste-glass interfaces could develop without mechanical restrictions. Finally, in Fig. 3.34d, cracks induced in the cement paste at the mouth of the pre-existing glass crack by the formation of ASR products are indicated with dashed lines.

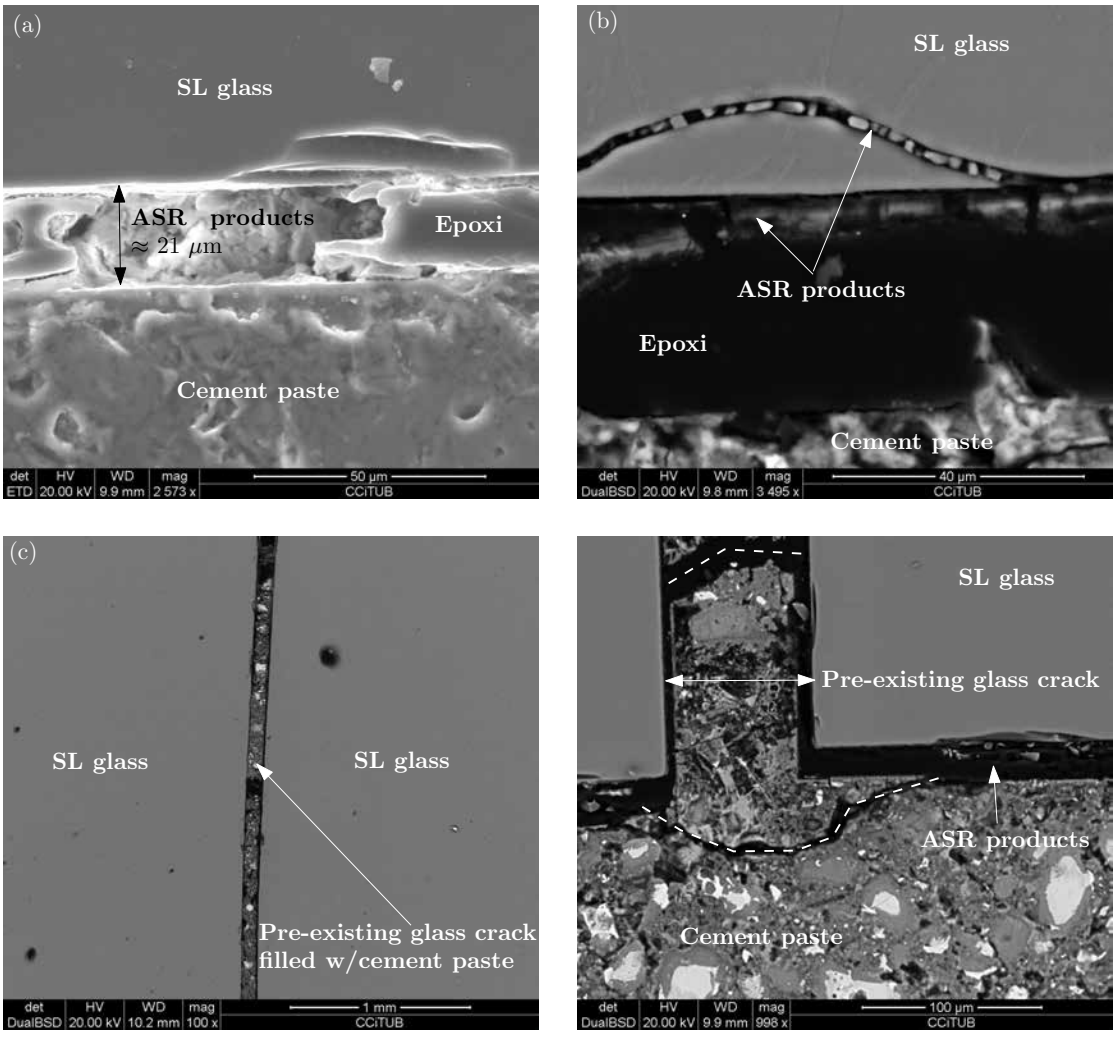

FIGURE 3.34: SEM images from a CP-SL glass specimen (E37). The glass disc was cracked before testing.

3.7 Series F

The results of Series E, sets #3 and #6, indicated that the mass exchange between the alkaline bath and the specimens plays a significant role on the development of the interfacial expansions. In order to further assess this issue, another series of tests was performed in which two different sealing schemes were tested (Fig. 3.35), one completely sealing the lateral surface of the specimens and the other only covering the interfacial zone. The underlying assumption in this proposal was that the glass-matrix interfaces constitute preferential paths for the mass exchange due to the higher permeability of the Interfacial Transition Zone (ITZ) [190]. Then, one would expect that the specimens with the interfacial zone sealed expand similarly to those with complete lateral sealing. The results obtained in this series are relevant for the calibration of meso-scale numerical models for ASR expansion that considered the differentiated transport properties of the

ITZs, as the one proposed in Chapter 6. The tests in this series were performed as part of the bachelor's thesis of A. Martínez [143] under the supervision of the author.

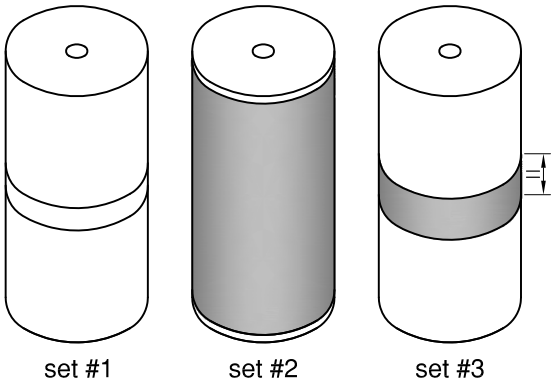

FIGURE 3.35: Schematic representation of the lateral sealing applied to specimens of Series F. The grey shading indicates the position of the self-curing rubber tape.

3.7.1 Description

The specimens tested in this series are listed in Table 3.6. Plain cement paste was used as cementitious matrix for all the specimens. The Portland cement was type CEM I 42,5 N-SR5 according to the Spanish standard UNE-EN 197-1 [3]. The oxide composition of the cement is given in Table A.1, PC02, Appendix A.1. A water/cement weight ratio of 0.47 was adopted. Sodium hydroxide was added to the mixing water in order to rise the alkali content in terms of equivalent sodium oxide (Na_2O_e) up to 1.1 wt% of the cement weight, as in previous series. For the reactive discs of reactive specimens, SL glass was used.

TABLE 3.6: List of specimens tested in Series F.

Set #	Type	Specimens	Lateral Sealing
1a	Reactive	F01 to F04	None
1c	Control	F05 to F08	
2a	Reactive	F09 to F12	Complete
2c	Control	F13 to F16	
3a	Reactive	F17 to F20	Only the interfacial zone
3c	Control	F21 to F24	

Once the curing period was completed, the specimens were retired from the curing bath, dried superficially with a towel, and let dry exposed to air for half and hour. Then, the specimen were sealed laterally, accordingly with the scheme given in Fig. 3.35, using the same self-curing rubber tape ATMOS® as in Series E - Set #6.

During the curing stage, the room temperature ranged between 22 to 24 °C. During the exposure stage, the oven temperature had a mean value of 59.6 °C and a standard

deviation of 1.2 °C. As in the previous series, the same solution (40 g NaOH and 2 g of $Ca(OH)_2$) per kg of water) was used for the curing and exposure baths.

3.7.2 Results

Set #1

The interfacial expansion curves of the specimens without lateral sealing are given in Fig. 3.36. During the curing stage there were in average practically no expansions. Once in the oven, the specimen interfaces expanded steadily reaching an average value 33 μm after a week at 60 °C. After that, interfaces of specimens F01 and F04 detached, while specimen F02 continued expanding for another two weeks before one its interfaces detached for a expansion of 51 μm. Length change measurements of specimen F03 were discard since one of its steel gauge inserts was loose. The strain curves of the control specimens (Fig. A.11, Appendix A.2), show the usual shrinking behaviour. The relative mass change curves (Figs. A.38 and A.39, Appendix A.3) exhibit the usual pattern, but the mass gained during the curing period was smaller than in previous tested cement paste specimens.

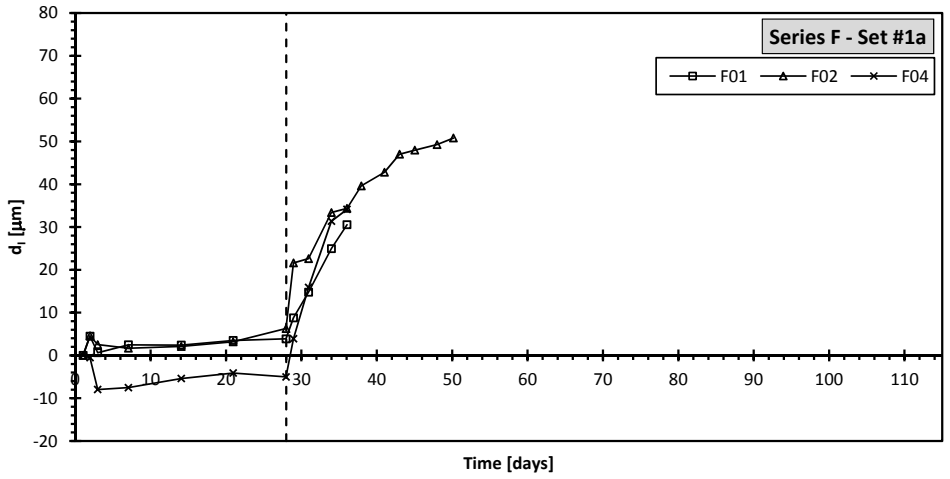

FIGURE 3.36: Interfacial expansion curves corresponding to Series F - Set #1a (specimens with no lateral sealing).

Set #2

The interfacial expansion curves of the specimens with complete lateral sealing are given in Fig. 3.37. During the curing stage there were in average practically no expansions. In the exposure stage, the specimen interfaces expanded steadily but with decreasing rate. At the end of the test, after 70 days in the oven, the specimens reached an average interfacial expansion of 25 μm without inducing the separation of any interface. The strain curves of the control specimens (Fig. A.12, Appendix A.2), exhibit the usual shrinking

behaviour. During the curing period, the relative mass change curves (Figs. A.40 and A.41, Appendix A.3) show mass increments similar to specimens of set #1, but the mass loss during the exposure stage was significantly smaller.

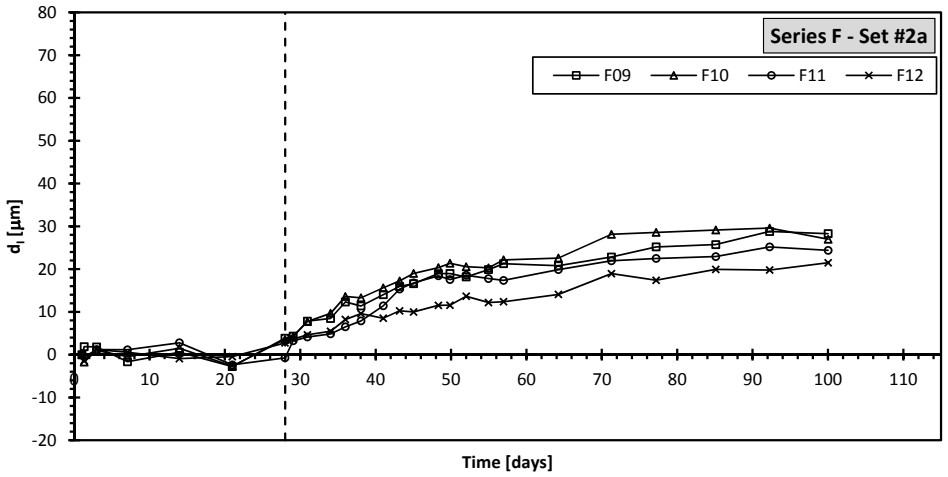

FIGURE 3.37: Interfacial expansion curves corresponding to Series F - Set #2a (specimens with complete lateral sealing).

Set #3

The interfacial expansion curves of the specimens with lateral sealing only on the interfacial zone are given in Fig. 3.38. During the curing stage there were in average practically no expansions. In the exposure stage, the specimen interfaces expanded steadily but with decreasing rate. Between days 48 and 50, the lateral sealing of specimen F17 got loose, exposing the interfacial zone to the alkaline solution. As a consequence, a sudden interfacial expansion was developed ending in the separation of one of the specimen interfaces. The rest of the specimens reached the end of the test, after 64 days in the oven, with an average interfacial expansion of 36 μm, and without inducing the separation of any interface. The strain curves of the control specimens (Fig. A.13, Appendix A.2), exhibit the usual shrinking behaviour. During the curing period, the relative mass change curves (Figs. A.42 and A.43, Appendix A.3) show similar mass increments to specimens of set #1. The mass loss during the exposure stage was in between of the ones measured for sets #1 and #2.

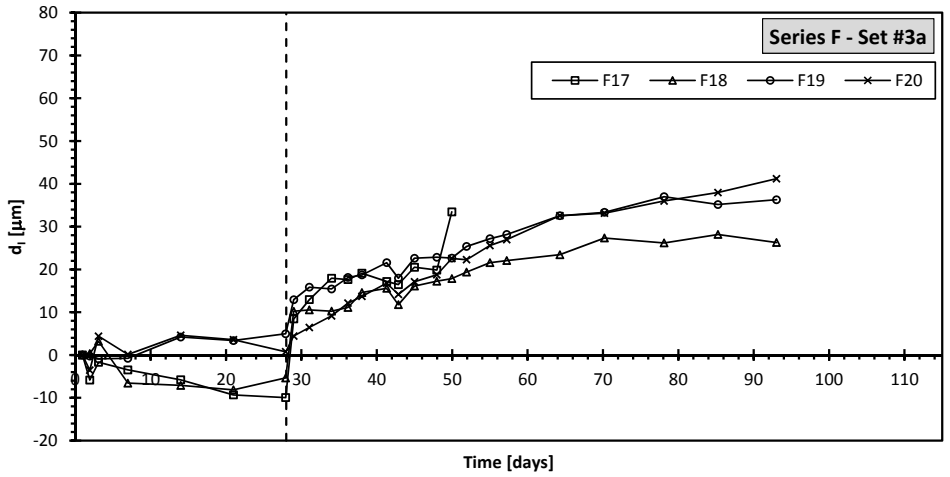

FIGURE 3.38: Interfacial expansion curves corresponding to Series F - Set #3a (specimens with partial lateral sealing).

3.8 Discussion

3.8.1 The testing methodology

The proposed testing methodology is based in the assumption that the cementitious matrix at both ends of a reactive specimens exhibit the same strain as the the one of the counterpart control specimen. This assumption may not be strictly valid since the geometries and the boundary conditions are not the same. For instance, the presence of the glass discs in the reactive specimens introduce a mechanical restriction to the shrinkage of the cementitious matrix that may affect the strain field inside the specimen. However, the fact that, in most cases, during the curing stage the interfacial expansions remain practically null while the counterpart control specimen shrunk, seems to indicate that this assumption is acceptable.

One remaining concern, however, is the magnitude of the scatter of the expansion curves. Big scatters are characteristic of ASR expansion tests performed on concrete. However, this scatter is attributed to the heterogeneous meso- and micro-structure of concrete, an aspect that in the proposed interfacial expansion tests disappeared or was reduced significantly. Therefore, the cause(s) of the scatter must be attributed to factors affecting the repeatability of the measurements, for instance:

- The oscillations of the room/oven temperature may have induced thermal strains in the specimens.

- Small variations in the time spent in the steps of the measurement sequence may have induced differences in the thermal contractions due to cooling when the specimens were exposed to air.
- Given the small magnitude of the measured length changes, false contact or bad placement of the tapered terminals of the length comparator in the hollow steel inserts of the specimens may have induced significant errors.
- The resolution of the dial micrometer (2 μm) may have been too coarse for the range of measured length changes. This issue could also have made relevant the magnitude of parallax errors.

With regard to the reproducibility of the test, no systematic study has been carried out. However, the comparison of the results obtained from analogous tests performed in different series may give an approach to the problem. For instance, by plotting together the strain curves obtained from cement paste control specimens tested in Series D, E and F (Fig. 3.39), it can be appreciated that the strain curves are fairly well replicated from test to test. In contrast, when comparing the interfacial expansion curves obtained from reactive cement paste-SL glass specimens from Series D and F (Fig. 3.40), we notice that the coincidence is not as good. The origin of this discrepancy could be found in small differences in the elaboration process of the specimens and/or in the curing temperature.

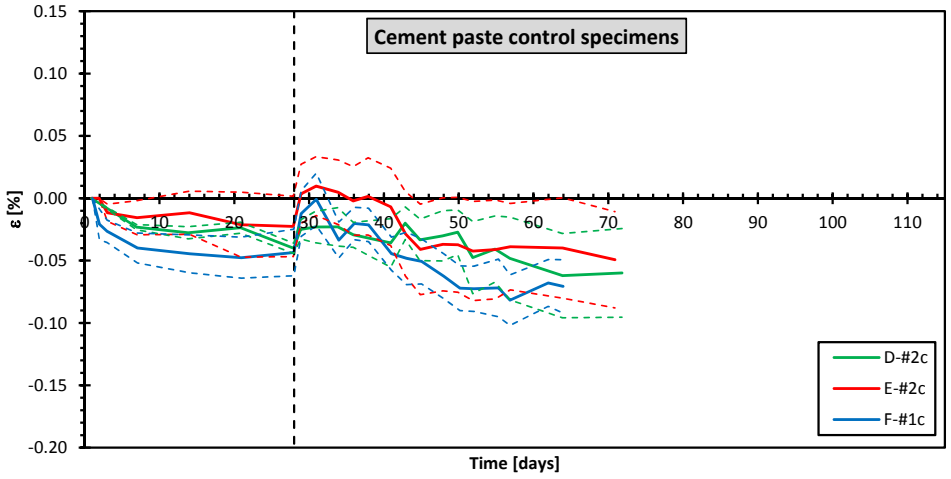

FIGURE 3.39: Comparison of average strain curves of control specimens made of plain cement paste. Dashed lines indicate the standard deviation of the measurements.

With a view to future experiments, both the repeatability and reproducibility of the test results could be improved by establishing more strict methodologies for the specimen casting and measurement steps, as well as a better control of the environmental conditions of the laboratory.

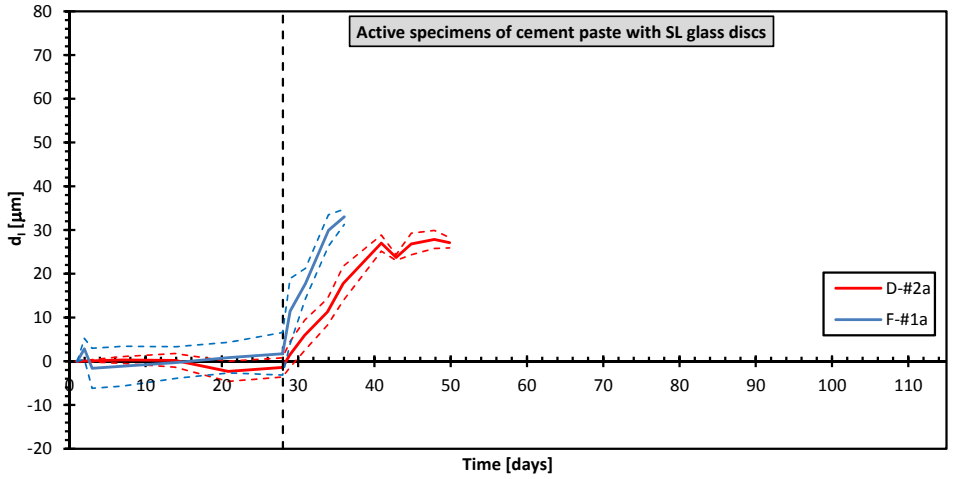

FIGURE 3.40: Comparison of average interfacial expansion curves of reactive specimens made of cement paste and SL glass. Dashed lines indicate the standard deviation of the measurements.

The performed SEM images gave interesting insights into the nature of the ASR products. However, the fact that most of the ASR products were lost and replaced by epoxy resin during the preparation process of the samples, made it difficult to interpret the images. For future tests, attention should be paid to improving the sample preparation procedure.

Finally, despite the above-mentioned aspects to be improved, it must be emphasized that the proposed methodology meets the objective of measuring ASR expansions at the level of a single interface between a reactive aggregate and the cementitious matrix.

3.8.2 The effect of the type of cementitious matrix

The effect of the type of cementitious matrix on the development of the interfacial expansions can be appreciated in Figs. 3.41 and 3.42 for SL and BS reactive discs, respectively. In both cases, the replacement of part of the Portland cement by MS resulted in an increase of the expansion rate, while the addition of inert aggregates resulted in a reduction of the expansion rate.

MS is known to control ASR expansion in concrete mainly by its capability to reduce the alkalinity of the pore solution which is caused by the binding of alkalis to the hydration products [133]. In the case of our tests, however, this effect may be insignificant given the superabundance of alkalis both in the cementitious and in the curing bath. Other effects of MS, in contrast, may have influenced the results through the modification of the material microstructure. For instance, when MS is used as partial replacement of the Portland cement the packing of cementitious particles in the ITZs is densified

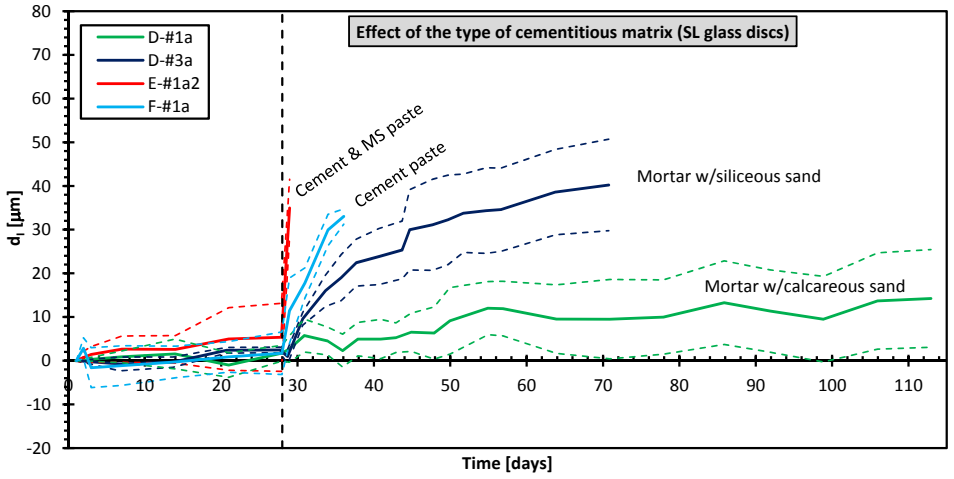

FIGURE 3.41: Comparison of average interfacial expansion curves of reactive specimens made with SL glass discs and different cementitious matrices. Dashed lines indicate the standard deviation of the measurements.

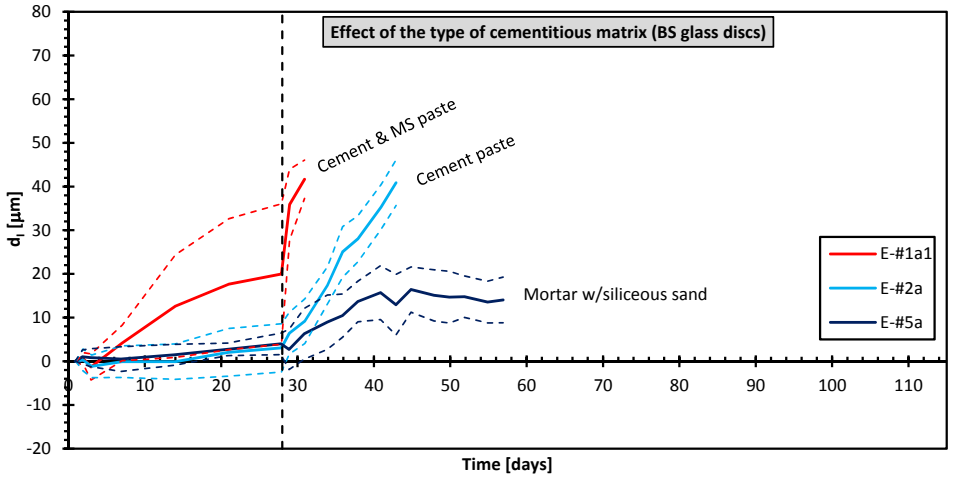

FIGURE 3.42: Comparison of average interfacial expansion curves of reactive specimens made with BS glass discs and different cementitious matrices. Dashed lines indicate the standard deviation of the measurements.

resulting in a significant reduction of the porosity in these regions [189]. This reduction of the porosity of the ITZ may have induced two competing effects. On one hand, it may have slowed down interfacial expansion by hindering the access of reactants due to a reduction of the material permeability. On the other hand, it may have accelerated the expansion by reducing the available 'empty' space to be filled with reaction products before inducing internal pressure. It is significant, in this sense, that the amount of ASR products visible at detached interfaces was much lower for the specimens with MS than in the specimens made with plain cement paste.

With regard to mortars, experimental studies [e.g. 51, 52] in which the aggregate content has been varied keeping the water/cement ratio constant, indicate that the transport

properties are lower for higher aggregate contents. This may explain, at least in part, the lower interfacial expansion rates observed in our tests. The lower expansion rate of the specimens with calcareous aggregates with respect to the ones with siliceous aggregates is attributed to the differences in the PSD (Tables 3.2 and 3.4) rather than to the chemical/mineralogical nature of the aggregates. Being of smaller size, the calcareous aggregates probably induced a greater reduction of the transport properties by generating a greater increase of the tortuosity of the paths for transport.

3.8.3 The effect of the type of glass

The effect of the type of glass used for the reactive discs can be observed by comparing Fig. 3.41 with Fig. 3.42. The specimens with BS glass developed lower expansion rates than the ones with equal cementitious matrix but with SL glass discs. This difference can be attributed to the much lower content of alkali and calcium of the BS glass with regard to the SL glass. The dissolution of glass due to the attack of the hydroxyl ions in the pore solution, not only releases silica but also calcium and alkalis [141], and, hence, the specimens with SL glass discs has higher input of reactants at the ITZ than the ones with BS glass discs.

3.8.4 The effect of alkali boosting

To assess the effect of the initial content of alkalis, average interfacial expansions curves from specimens made with (Series D-#2a and Series F-#1a) and without (Series C-#1a) addition of NaOH to the mixing water ('alkali boosting') are plotted together in Fig. 3.43. The cement paste of specimens of Series C-#1a had a Na_2O_e content of 0.61% of cement weight, while those from Series D-#2a and Series F-#1a had a 1.1%. Additionally, specimens of Series D-#2a and Series F-#1a were cured in 1 m NaOH solution saturated with $Ca(OH)_2$, while specimens of Series C-#1a were cured in limewater. As expected, the specimens with higher initial alkali content developed the greatest interfacial expansion rates. However, it seems that lower alkali content allows the development of higher expansion before the interface separation. One possible explanation is that the alkali boosting may have affected the mechanical characteristics of the cement-glass interfaces.

3.8.5 The effect of the lateral sealing

The effect of the degree of lateral sealing on the development of the interfacial expansion is shown in Fig. 3.44, where the average expansion curves of all specimens from Series F

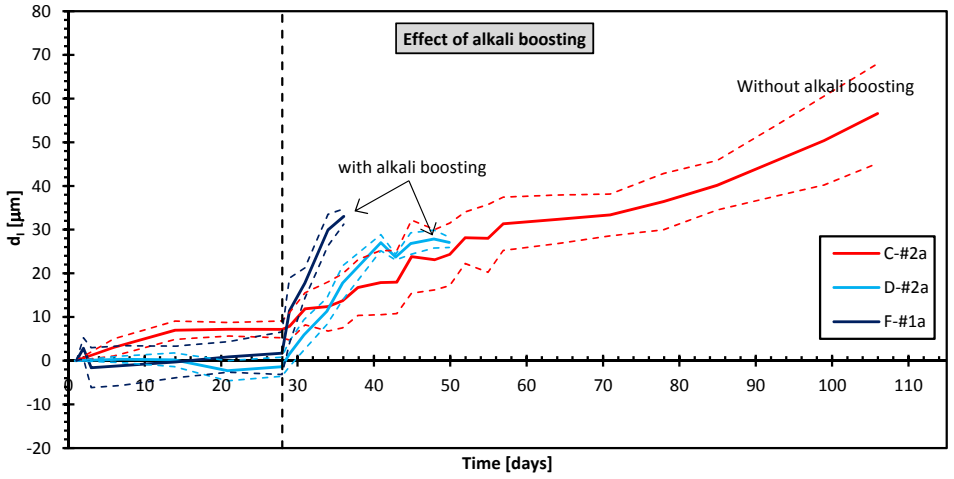

FIGURE 3.43: Comparison of average interfacial expansion curves of reactive specimens with and without alkali boosting. Dashed lines indicate the standard deviation of the measurements.

are plotted together. As the degree of lateral sealing increases, the expansion rate decreases. This may be attributed to the restriction imposed to the access of alkali and/or water from the alkaline bath into the reaction site.

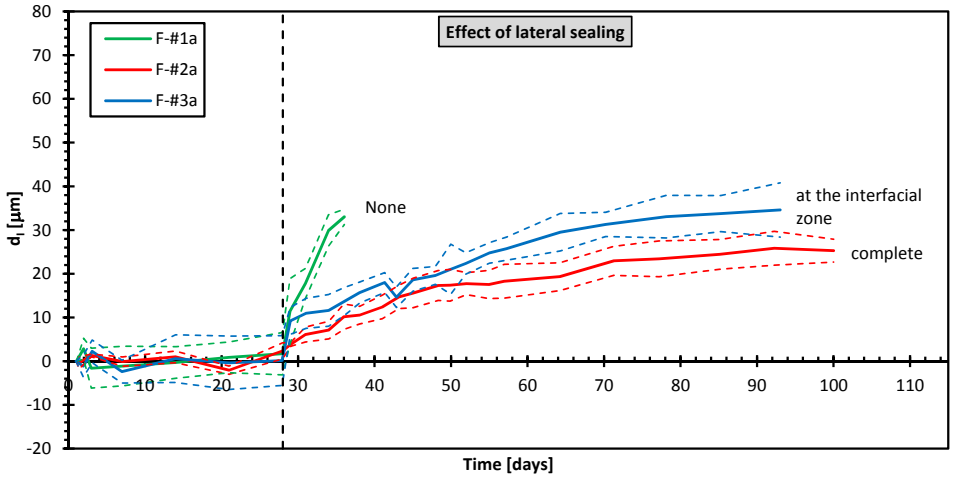

FIGURE 3.44: Comparison of average interfacial expansion curves of reactive specimens made with different degrees of lateral sealing. Dashed lines indicate the standard deviation of the measurements.

It may be argued that, besides sealing the lateral surface of the specimens, the self-curing rubber imposed a mechanical constraint to the interfacial expansions that may have influenced the results. In order to asses this possibility, lets consider the specimens with complete lateral sealing. Assuming that there is no sliding of the rubber over the cement paste, the development of the interfacial expansions will induce an axial enlargement of rubber covering the glass disc. The reaction of the rubber over the cement paste will induce, in turn, a normal pressure on the interfacial surfaces. The

average value of this pressure (σ_N) can be estimated by

$$\sigma_N = \frac{8aE_{rub}}{eD} d_I \tag{3.4}$$

where D [m] is the diameter of the specimen, e [m] is the width of the glass disc, a [m] is the thickness of the rubber tape, E_{rub} [MPa] is the linear elastic module of the rubber, and d_I [m] is the developed expansion in one interface. Considering E_{rub} = 1.0–2.5 MPa [42], $a \approx 2$ mm, $D = 33$ mm, $e = 6$ mm and $d_I = 30$ μm, the average normal pressure developed ranged in between 0.002 to 0.006 MPa. This pressure is 3 to 4 orders lower than the pressure that can be developed in concrete under restraint due to ASR expansions [20, 67]. Such a small pressure is not likely to have any significant effect on the development of the interfacial expansions.

3.8.6 Composition and morphology of the ASR products

In the SEM images presented (Figs. 3.14, 3.15, 3.22, 3.33, 3.34, and 3.26), the original position of the interfaces is clearly distinguished as a straight line dividing the 'unaltered' cementitious matrix from the zone with reaction products. At the glass side, in contrast, the limit is more diffuse, with a layer of about 5 to 10 μm in which the glass exhibited cracks and a degraded aspect. The reaction products observed in between the glass and the cementitious matrix via SEM images and EDS analysis are summarized in Table 3.7.

In general, the observed ASR products exhibited a layered structure, i.e. reaction products of different morphology and/or composition appeared alternated in layers parallel to the original glass-matrix interface. This indicates that, as the reaction products precipitate, the conditions for the formation of new products change, probably due to the formation of diffusion barriers that altered the supply of reactants. Layered ASR products have also been observed by other authors. In a study on the reactivity of Pyrex (BS glass) rods embedded in mortar, Yi and Ostertag [221] reported distinctively banded distributions of Ca- and Na-rich gels around the Pyrex rods. In another study, Bleszynski and Thomas [23] found a layered structure of reaction products with different morphology and composition in concretes made with reactive flint aggregates.

The range of compositions of the reaction products observed in the SL glass specimens (Ca/Si = 1.00–1.50, (Na+K)/Si = 0.10–0.80) is similar to the one observed by Rajabipour et al. [142, 174] surrounding SL glass particles in mortar specimens made with recycled glass aggregates (Ca/Si = 1.34–1.51, Na/Si = 0.06–0.29). Rajabipour et al. referred to this product as 'Pozzolanic CSH', differentiating it from the products with lower calcium content (Ca/Si = 0.29–0.37, (Na+K)/Si = 0.38–0.42) formed within cracks in the glass particles, which were called 'ASR gel'. The Pozzolanic CSH was

TABLE 3.7: Summary of the observed reaction products in interfacial expansion tests via SEM images and EDS analysis.

Spec.	Cement. matrix	Reactive Aggregate	Description	Ca/Si	(Na+K)/Si
C01	Calcareous mortar	SL glass	Ordered product on glass side (zone III, profile A-A)	1.00–1.10	0.10
			Disordered product on glass side (zone II, profile A-A)	1.20–1.30	0.20–0.40
C08	Cement paste	SL glass	Ordered product on glass side (zone III, profile C-C)	1.00–1.10	0.10
			Disordered product on glass side (zone II, profile C-C)	1.20–1.40	0.10–0.25
			Layered product on the CP side (zone II, profile B-B)	1.10–1.40	0.20–0.30
			Layered product on the CP side (zone III, profile B-B)	1.10–1.50	0.25–0.80
			Layered product on the CP side (zone IV, profile B-B)	1.10–1.30	0.20–0.50
			Layered product on the CP side (zone V, profile B-B)	1.10–1.30	0.10–0.20
D07	Cement paste	SL glass	Massive product besides the CP	1.25	0.12–0.14
E44	Siliceous mortar	BS glass	Massive product besides the mortar	0.55–1.32	0.33–0.70
E34	Cement paste	BS glass	Layers of massive product between layers of spongy product	0.06–0.28	0.18–0.34

regarded by the authors as a non-expansive product, attributing the observed expansion of the mortar uniquely to the ASR gel. This distinction between calcium-rich products with low swelling capacity and calcium-poor products with high swelling capacity has been also made by other authors [e.g. 111, 112, 171].

Our results, however, clearly indicate that the so-called 'Pozzolanic CSH' is also capable of developing significant expansions. The cause of this apparent contradiction may be found in the different mechanical restraint in each case. In the case of glass particles in mortar, the Pozzolanic CSH needs to generate cracks in the cement matrix in order to induce measurable expansions in concrete. In contrast, in the case of the interfacial expansion tests the Pozzolanic CSH only needs to detach the cement matrix-glass interface in order to develop measurable expansions. In other words, in the first case the Pozzolanic CSH needs to develop a swelling-pressure[1] capable of propagating cracks in the cement matrix, while in the second case it only needs to develop a swelling-pressure capable of overcoming the tensile strength of the cement matrix-glass interface, which is expected to be significantly lower. Then, we may conjecture that the formation of Pozzolanic CSH is in nature an expansive reaction that can be inhibited by a superimposed pressure equal or greater than its maximum swelling-pressure. This conjecture is further discussed in the following chapters (Sections 4.4.5 and 6.2).

[1]Swelling pressure is defined as the pressure developed by the formation of ASR products under constant volume conditions.

Finally, the ASR products observed in the specimens made with BS glass had lower contents of calcium (Ca/Si = 0.06–1.32) than the specimens made with SL glass (Ca/Si = 1.00–1.50), which is consistent with the lack of calcium in the BS glass.

3.9 Concluding remarks to the chapter

- The proposed testing methodology meets the objective of measuring ASR expansions at the level of a single interface between a reactive aggregate and a cementitious matrix.
- The proposed methodology can provide valuable information about the ASR expansion mechanisms, being at the same time inexpensive and very easy to replicate.
- The simplicity of the geometry and of the boundary conditions of the tested specimens make the interfacial expansion tests ideal for the calibration of micro- and meso-scale numerical models for ASR expansion in concrete.
- Some aspects of the proposed methodology need to be improved in order to reduce the scatter of the measurements and to ensure the repeatability and reproducibility of the results.
- The results presented do not constitute a systematic parametric study, and therefore, more testing would be necessary to confirm the observed effect of parameters such as the type of cementitious matrix, the type of reactive aggregate or the amount of available alkalis.

Chapter 4

Triaxially confined expansion tests

4.1 Introduction

A literature review about the effect of mechanical restraints in the development of ASR expansion in concrete has been presented in Section 2.8. There, it can be noticed that there are relatively few experimental studies concerning the effect of applied stresses on the development of ASR expansion, and that only two of them [79, 157] were performed with concrete under triaxial stress states. Furthermore, as discussed in Section 2.8, the test setups used in these two studies made the interpretation of the results quite problematic. In spite of the lack of experimental studies, the topic of expansion under triaxial stress states is of special relevance for many large structures around the world suffering form ASR, such as dams and confinement vessels of nuclear power plants.

With this in mind, a new testing machine for performing ASR expansion tests with cubic concrete specimens under constant triaxial stress is presented in this chapter. This machine was originally designed and constructed by Prof. Victor E. Saouma at the U. of Colorado - Boulder. Later, it was transferred to UPC (Barcelona) where, in the framework of this doctoral thesis, a number of modifications were introduced to the original setup. The equipment has the advantage that constant stresses are applied by means of six loading plates that cover most of the surface of the specimen (Fig. 4.1). This creates a quasi-uniform stress state inside the material, which should facilitate the interpretation of the results.

The machine was used to obtain ASR expansion curves of glass concrete for three different stress states which are also presented and discussed in this chapter. As a result,

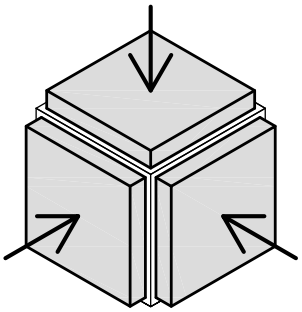

FIGURE 4.1: Schematic representation of ASR expansion tests under triaxial confinement.

a modification to the phenomenological model by Saouma and Perotti [183] is proposed in order to reproduce the obtained expansion rates. Complementarily, a number of mechanical tests were performed to characterize the concrete tested, both before and after the ASR expansion tests, as well as SEM/EDS analysis of the ASR products and the corresponding cracking pattern. Finally, based on this later analysis, an ASR expansion mechanism capable of explaining the obtained confined expansion rates (as well as the results obtained in Chapter 3), is also proposed.

This chapter is mainly a transcription of a journal article by the author and co-workers [117], enriched with some complementary experimental data included in Appendix A.5 and the above mentioned SEM/EDS analysis (Sections 4.3.5 and 4.4.5). Additional information about the testing machine, as well as the mounting and calibration processes, can be found in the in the bachelor's thesis by J. Stokes [201], I. Acosta [2] and E. Vacas [215], co-advised by the author.

4.2 AAR Triaxial Machine

With the aim of measuring ASR expansions in concrete under true triaxial confinement, i.e. under different constant stress along each of the main directions, an ad hoc testing machine, called 'Alkali-Aggregate Reaction Triaxial Machine' (AARTM), was originally designed and constructed by the Prof. Victor E. Saouma at the U. of Colorado - Boulder. Later, in 2010, it was transferred to UPC (Barcelona) where a number of modifications were introduced to the original set-up.

The AARTM consists of a triaxial load frame which can deliver 0 to 9 MPa confining stress on each axis of a $150 \times 150 \times 150$ mm cubical specimen. Specimen deformation is measured using three displacement sensors on each of the three axes. The apparatus is designed to be capable of raising and maintaining the specimen temperature at a pre-set value between 30 to 70 °C, and the faces of the loading plates in contact with

the specimens are crossed by grooves for a solution to circulate in order to keep the specimen wet and supply reactants (alkalis). A LabVIEW-based computer control and data acquisition system maintains the desired confining stress and specimen temperature while logging all relevant data points.

4.2.1 Loading frame

A three-piece steel assembly is used to provide reaction forces for the three hydraulic actuators. The frame is constructed of W12 × 24 I-beams and designed to deflect less than 0.25 mm under the full 220 kN confinement load. Each section of the frame is bolted together at the vertical axis to form a monolithic structure. Refer to Fig. 4.2 for a general view of the load frame assembly.

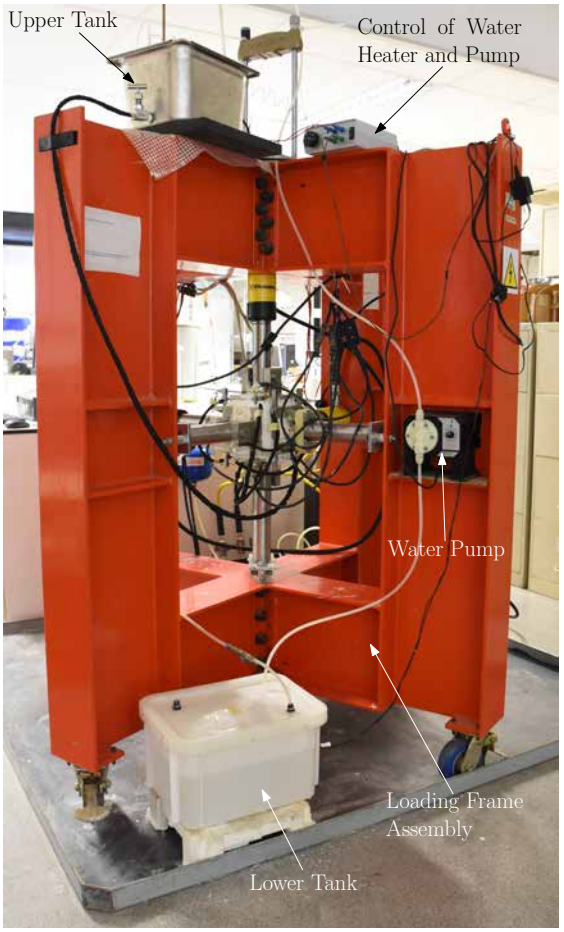

FIGURE 4.2: General view of the AARTM.

4.2.2 Triaxial confinement and measurement systems

The AARTM is equipped with three 220 kN hydraulic actuators and six 138.3×138.3 mm stainless steel loading plates used to apply the confining stress to the test specimen.

Actuators are connected to the three 'active' loading plates by means of cylindrical steel rods. Three additional steel rods of similar length connect the 'passive' plates to the loading frame. Each rod was drilled to accept a 32 mm pin used to transfer the confining load to the loading plates. Active rods were machined to thread into the hydraulic actuators, while the passive rods were threaded to accept a large nut. The nut provides an adjustment mechanism for aligning the non-active loading plates. Refer to Fig. 4.3 for a view of the load application system.

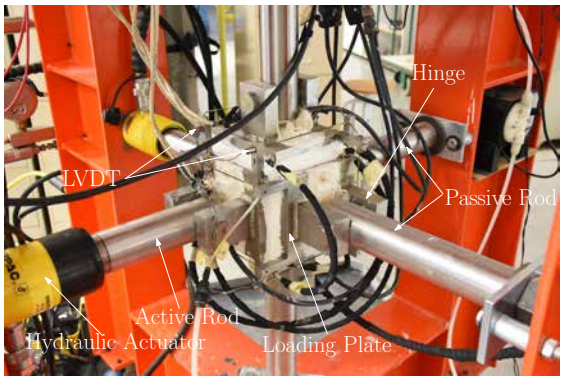

FIGURE 4.3: Detail view of the AARTM.

The nominal applied stress is calculated as the ratio between the applied load and the nominal surface area of a specimen (150 × 150 mm). It must be noted that the surface area of the plates is slightly smaller than that of the face of the specimens and, therefore, the stresses within the specimen are not completely uniform. However, numerical simulations of a specimen subjected to the same load in each direction indicate that 91% of the volume of the specimen has stresses within ±20% of the nominal ones.

Each of the three active loading plates connected to a hydraulic actuator is equipped with three Linearly Variable Differential Transformers (LVDTs), from Macro Sensors (model CD-375, range ±2.54 mm, linearity ±0.5%). Each LVDT senses the distance to the opposite plate by means of a threaded extension rod which is attached at the opposite plate end. Refer to Fig. 4.4 for the relative position of the LVDTs on the active loading plates. Strain in a given direction is then calculated as the ratio between the average relative displacements measured with the i- and j-LVDTs (see Fig. 4.4, left), and the initial specimen dimension in that direction (approx. 150 mm). The k-LVDT is used for monitoring the relative rotation between opposite plates.

4.2.3 Temperature control system

A closed-loop temperature control system is employed with the AARTM to accelerate the AAR. Each stainless steel loading plate is equipped with a 150 Watt flush-mounted heating element (Fig. 4.3 and Fig. 4.4). The three active loading plates are equipped

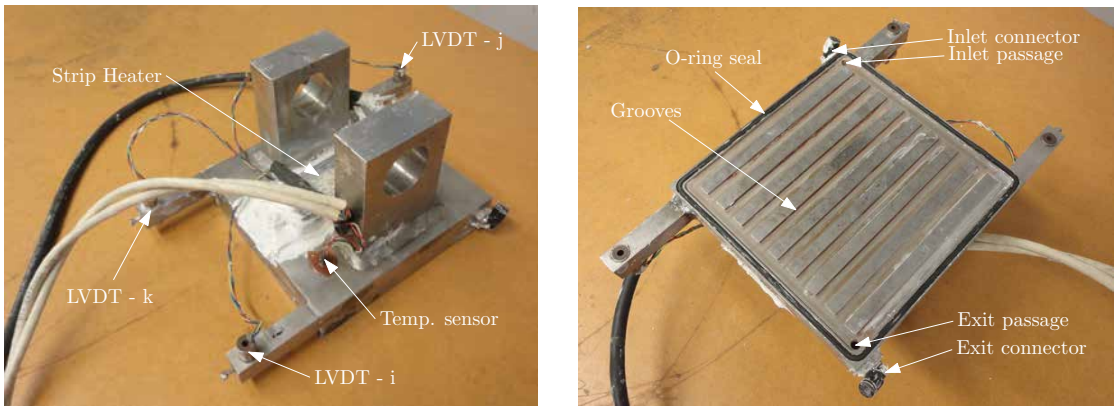

FIGURE 4.4: Detail views of an active loading plate of the AARTM.

with precision temperature sensors (Fig. 4.4, left). Averaged temperature feedback from the loading plates is used for the closed-loop control. This system has proven to be stable and effective, reliably holding the specimen temperature constant within ±1 °C.

4.2.4 Hydraulic load systems

Three independent high pressure hydraulic loading systems, one for each axis direction, are employed to provide specimen confining stress via the stainless steel loading plates. These systems utilize pneumatic energy delivered via the laboratory compressed air distribution system to drive three hydraulic pumps. The air flow to the hydraulic pumps is controlled by the computer using direct acting electric solenoid valves. Varying the duration and interval in which the solenoid valves are open allows for proportional control of the pressure rise in the system. Each hydraulic circuit includes a hydraulic manifold where a pressure transducer, an analogue pressure gauge and an adjustable pressure relief valve are installed. This pressure relief valve is set to a pressure slightly higher than the desired confining pressure and supplements the computer controlled hydraulic pump to provide tighter load regulation.

4.2.5 Liquid circulation system

As already mentioned, the face of the loading plates in contact with the specimen are crossed by grooves to allow the circulation of alkaline solution. Liquid leakage is prevented by means of Viton™ O-rings in between the plates and the specimen. Refer to Fig. 4.4 for detail views of a loading plate. The sealing offered by the O-ring is not completely effective and needs to be complemented by the application of silicon sealant covering the specimen-plate contours. The plates are connected to each other in a series circuit by means of polyamide 4×2.7 mm hoses thermally insulated with self-adhesive

tape of EPDM rubber foam. The alkaline solution circulates by gravity through the loading plates series circuit, from a stainless steel tank of 12 L, located at the top of the loading frame, to a polyethylene tank of 20 L located at floor level (Fig. 4.2). The liquid flow is regulated manually by means of a stainless steel needle valve. Finally, a diaphragm pump commanded by a float switch in the upper tank, recirculates the liquid from the lower tank to the upper one. In order to prevent that the circulating liquid cools down the specimen, the upper tank is equipped with a 400 W electric cartridge heater commanded by a mechanical thermostat which keeps the liquid temperature close to the test temperature.

4.3 Experimental procedures

4.3.1 Concrete specimens

Two different kinds of concrete were investigated. The first one, called 'control concrete', was made only with non-reactive (crushed limestone) aggregates. The second one, called 'reactive concrete', in contrast, was made using the same mixture but replacing the coarser fraction of aggregates with crushed colourless soda-lime glass as reactive aggregate. Control specimens were tested in the same conditions as the reactive specimens in order to assess creep and/or shrinkage deformations. The cement used was CEM I 42,5 N-SR 5 [3] with oxide composition given in Table A.1 of Appendix A.1, where cement PC01 was used for casting sets #1 and #2, cement CP04 was used for casting set #3, and cement CP05 was used for casting set #4. Both mixtures had a cement content of 420 kg/m^3 and a water/cement weight ratio of 0.45. The alkali level of the concrete was raised to 5.25 kg/m^3 Na_2O_{eq} by adding NaOH to the mixing water. The non-reactive aggregate was well graded and passed a 12.70 mm sieve. For the reactive concrete, the coarser 64 % of the non-reactive aggregate volume (particles between 2.50 and 12.70 mm) was replaced by crushed soda-lime glass particles. Detailed particle size distributions of the aggregates are given in Appendix A.5, Table A.2.

The specimens were cast at four different times. Control and reactive specimens cast on the same date constitute a 'casting set', which is indicated in Table 4.1 for each specimen tested. After casting, the specimens remained in moulds for 24 h at room temperature and with the exposed surface covered with a plastic film in order to prevent moisture loss. Once demoulded, specimens were put in 1 m NaOH solution (1 mol of NaOH per kg of water) at room temperature (21±2 °C) for at least three months. Before performing the expansion tests, the pouring face of each specimen was polished to remove excessive roughness.

TABLE 4.1: List of specimens tested. Note: Id. = Identifier.

Type	Id.	Casting set #	Curing period (weeks)	Test duration (weeks)
Load case 0-0-0				
Reactive	TM01	1	39	30
	TM10	2	14	36
	TM12	2	14	36
	TM13	2	14	36
Control	TM05	2	14	36
	TM06	2	14	36
	TM07	2	14	36
Load case 1-1-1				
Reactive	TM02	1	42	3
	TM21	3	39	5
Control	TM03	1	39	2
	TM19	3	35	3
Load case 9-9-1				
Reactive	TM11	2	44	3
	TM20	3	49	3
Control	TM08	2	34	3
	TM15	3	53	3
Load case 9-9-9				
Reactive	TM14	2	56	5
	TM22	3	67	3
Control	TM09	2	68	4
	TM16	3	63	3
Mechanical tests				
Reactive	TM24	3	47	none
	TM30	4	15	none
	TM31	4	15	none
Control	TM18	3	47	none
	TM25	4	15	none
	TM26	4	15	none

The curing solution, which was the same to be used for the subsequent expansion tests, was chosen to have a total alkali concentration similar to that of the specimen pore solution, preventing in that way the reduction of the pore solution alkalinity due to alkali leaching towards the curing bath. The minimum extent of the curing period has been adopted based on previous tests (see Appendix A.7) which indicated that for shorter curing periods the expansion rate measured in the testing conditions described below was dependent on the age of the specimen.

4.3.2 Free expansion test setup

To assess the effect of the applied stress state on the ASR expansion rate, it is essential to perform additional free expansion tests in parallel to the tests under loading. These additional tests cannot be carried out with the AARTM since a minimum pressure is needed in each direction to ensure full contact of the loading plates with the specimen, in order to guarantee the sealing effect of the O-rings. Therefore, a different procedure described below was used to perform free expansion tests with specimens of identical characteristics to those used in the AARTM, and under the same exposure conditions (1 m NaOH solution at 60 °C).

One week before starting the free expansion test, each specimen was removed from the alkaline curing bath and let air dry for 24 h. Then, stainless-steel datum discs were glued with epoxy resin to the specimen surface in the configuration indicated in Fig. 4.5. In all cases, the Z-direction was matched with the specimen casting direction. Each pair of datum discs allowed measuring the length change at the surface of the specimen in one main direction by means of a 100 mm DEMEC strain gage (Fig. 4.5). In some of the specimens, only one measurement in each direction (X1, Y1, Z1) was performed. After 24 h, once the epoxy resin was cured, each specimen was placed in a 19 L airtight plastic container filled with 1 m NaOH solution and kept at room temperature for another 5 days for rewetting. Afterwards, the containers with the specimens were introduced in an oven at 60 °C. After 24 h, the containers were removed from the oven in order to perform the first reading (zero-reading) between each pair of datum discs. Then, the containers with the specimens were returned to the oven and kept there at 60 °C until the next reading. The average temperature in the oven during the test was 59.95 °C with a standard deviation of 0.33 °C. Measurements were made for a total test duration of 30 weeks. For clarification, a schematic timeline of the testing procedure is given in Table 4.2.

4.3.3 Confined expansion test setup

The steps followed to perform a confined expansion test using the AARTM machine are schematically summarized in Table 4.3. First, the specimen was removed from the alkaline bath and let dry exposed to air for 24 h. Then, a thin layer of silicone sealant was applied at the rims of each face of the specimen (20 mm inwards) and was let cure for 48 h. This silicone layer improves the sealing function of the loading plates O-rings by providing them a smooth settlement surface. Afterwards, the specimen was placed in between of the loading plates of the AARTM and isotropically confined with a small pressure (0.30 MPa, approx.). Immediately, a thick layer of silicone sealant was

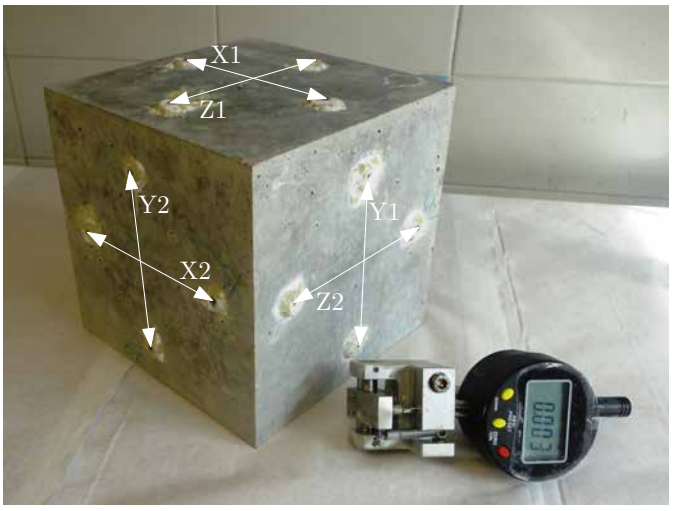

FIGURE 4.5: Specimen with datum discs and DEMEC strain gage used for strain measurement in free expansion tests. Z-direction was matched with the casting direction.

TABLE 4.2: Schematic timeline of the free expansion tests. 'x' denotes the age (in days) of the specimen when first removed from the alkaline bath.

day 0	• Concrete casting
day 1	• Unmolding
...	Curing in alkaline solution at room temperature (between 14 and 39 weeks)
day x	• Removal of the specimen from the alkaline bath
day x+1	• Gluing of the datum discs
day x+2	• Returning specimen to the alkaline bath
...	Curing in alkaline solution at room temperature (5 days)
day x+7	• Heating up to 60 °C
day x+8	• Zero-reading
...	Free ASR expansion (30 weeks)
day x+217	• End of test

applied covering the specimen-plate contours and was let cure for 72 h, while keeping the confining pressure. Once the silicone was cured, the LVDTs cores and the hoses for liquid circulation were put in position. The 1 m NaOH solution was allowed to circulate for 48 h at room temperature to re-saturate the specimen. In order to guarantee full contact between the specimen and the plates, previously to heating, the pressure in each direction was raised to 5 MPa and then lowered again to 0.30 MPa, while maintaining the other two at 1 MPa. Next, the pressure was set again to isotropic 0.30 MPa and the heating systems of the plates and alkaline solution tank were turned on. The target temperature of 60 °C was usually reached within an hour, moment in which the specimen was loaded to the desired stress state and the data acquisition started. These stress state and temperature were kept constant for at least 21 days. After that, in some cases, the load state was changed and the test continued for some additional time. The

average temperatures during the test periods were slightly below the nominal, with values ranging between 59.88 to 59.98 °C, and with standard deviation always below 0.45 °C. The average applied stresses during the test periods were within 5% of the nominal values, with standard deviations under 3%. Refer to Appendix A.5, Table A.3, for the average stresses and temperatures recorded in each test. In all cases, the total volume of circulating alkaline solution was over 25 L and the flow rate over 2 L/h.

TABLE 4.3: Schematic timeline of the confined expansion tests. 'x' denotes the age (in days) of the specimen when removed from the alkaline bath.

day 0	• Concrete casting
day 1	• Unmolding
...	Curing in alkaline solution at room temperature (between 34 and 68 weeks)
day x	• Removal of the specimen from the alkaline bath • Application of the silicone sealant layer at the rims of each face of the specimen.
day x+2	• Placing of the specimen in the AARTM • Sealing of the contours of plate-specimen contacts
day x+4	• Beginning of the circulation of the alkaline solution
day x+7	• Loading/unloading to 5 MPa in each direction • Heating up to 60 °C • Application of the desired loading state • Starting of data acquisition
...	Confined ASR expansion (21 days)
day x+28	• End of test

4.3.4 Mechanical test setups

In order to assess the mechanical properties of the control and reactive concretes, a number of uniaxial compression tests (UCTs) and wedge splitting tests (WSTs) were performed. The WST procedure is described in detail in Ref. [27].

For the UCTs, the original cubic specimens of 150 × 150 × 150 mm were cut with a diamond saw into four prismatic specimens of approximately 75 × 75 × 150 mm. The prismatic specimens were cut in such a way that two of them were aligned with the casting direction and the other two were normal to it. To one specimen of each pair, two LVDTs (RDP GT2500, range ±2.5 mm, linearity error $< \pm 0.1\%$ F.S.) were attached along the loading direction for measuring the material strain. The UCTs were performed with a controlled displacement rate of 0.25 mm/min. The specimens with attached LVDTs were subjected to two load/unload cycles up to 1/4 of the estimated compression strength before the final loading until failure. The other two specimens were directly loaded until failure. The compression strength (f_c) of the original cubical specimen is obtained as the average of the peak compressive stress of the four prismatic

specimens. The initial tangent modulus (E) is obtained as the average of the values obtained from the two prismatic specimen with attached LVDTs.

For the WSTs, the original cubical specimens were cut into two prismatic specimens of approximately $75 \times 150 \times 150$ mm. Then the grove and the notch were cut in such a way that the fracture path of one specimen was aligned with the casting direction, and in the other specimen was normal to it. The crack opening displacement (COD) was measured along the axis of the horizontal splitting force with two LVDTs (RDP GT2500, range ± 2.5 mm, linearity error $< \pm 0.1\%$ F.S.), one on each side of the specimen. The applied vertical load was measured with a 25 kN load cell (UtilCell 610, linearity error $< \pm 0.25\%$ F.S.). The COD rate was 0.125 mm/min. The specific fracture energy of the original cubical specimen in mode I (G_I^f) is obtained as the average of the values obtained from the two prismatic specimens tested. Additionally, the tensile strength (f_t) is estimated via numerical modelling according with the procedure described in Ref. [120].

4.3.5 SEM images and EDS analyses

SEM/EDS analysis were performed at the *Centres Cientifics i Tecnològics* of the *Universitat de Barcelona* (CCiTUB) with scanning electron microscope FEI Quanta 200 equipped with EDS-EDAX Genesis. The samples were prepared at the *Servei de Làmina Prima* of the *Facultat de Ciències de la Terra* of *Universitat de Barcelona*. The samples were cut with a diamond saw with a width of approximately 10 mm and then put in vacuum desiccator for two days. After drying, the samples were impregnated with a low viscosity epoxy resin. Once the epoxy set, the upper 1–2 mm were cut with a low speed precision diamond saw. The new exposed surfaces were ground and polished with abrasive grains successively finer, starting with 15 μm and finishing with 1 μm. In order to avoid leaching, all the grinding and polishing operations were done using polishing oil instead of water.

4.4 Results and discussion

4.4.1 Free expansion tests

Three control specimens and four reactive specimens were tested in free-expansion conditions. Refer to Table 4.1 for a list of the specimens tested with their respective curing and testing times. The strain measured for each specimen is depicted in Fig. 4.6 as the average of the strain measured along each of the three directions of the specimen. The dashed lines indicate the envelope of the measured strain curves.

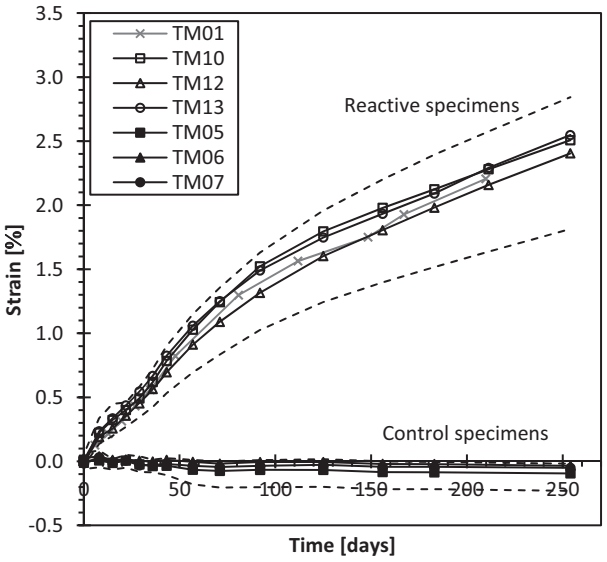

FIGURE 4.6: Averaged axial strain evolution in free-expansion conditions of both reactive and control specimens. Dashed lines indicate the envelope of all the measured strain curves in the three directions.

As it can be seen in the figure, the control specimens developed a slight contraction of around 0.05% over the first 75 days and then seemed to stabilize. Reactive specimens exhibited a roughly constant expansion rate for strains below 1%. Beyond that value, the expansion rate decreased until reaching an approximately constant value of about one fourth of the initial rate. Note that specimen TM01, which was 39 weeks-old when tested, showed a very similar behaviour to that of the remaining reactive specimens of only 14 weeks. This seems to indicate that, at least within 14 to 39 weeks, the extent of the curing period does not affect the subsequent development of the ASR expansions. However, a systematic study would be needed to confirm this particular aspect. This issue is of interest since the specimens tested with the AARTM were of different ages, as it is indicated in Table 4.1.

4.4.2 Confined expansion results

Three nominal load cases were studied with the AARTM:

- 'Case 1-1-1', $\sigma_x = \sigma_y = \sigma_z = -1$ MPa
- 'Case 9-9-9', $\sigma_x = \sigma_y = \sigma_z = -9$ MPa
- 'Case 9-9-1', $\sigma_x = \sigma_y = -9$ MPa, $\sigma_z = -1$ MPa

In all cases the casting direction of the specimens was matched with the Z-direction of the AARTM. Per each load case, two control and two reactive specimens were tested.

The list of specimens tested with their respective curing and testing times is given in Table 4.1.

The reason for the control specimens is because concrete subject to sustained load will inevitably show creep (and possibly cracking) deformations, and therefore the strains measured for reactive specimens under loading will be the combined effect of both actions. Additionally, one can expect that the principle of superposition will not be strictly satisfied, i.e. the effect of simultaneous loading and ASR will not be equal to the sum of ASR strains of unloaded specimens plus mechanical deformations of similar non-reactive specimens. In this context, the approach followed is to accept the following conventional definitions:

- Basic creep: time-dependent deformations measured on control (non-reactive) specimens under load.
- ASR strain: difference between total deformations measured on reactive specimens under load and basic creep.

With this convention, possible interaction effects of the simultaneous action of loading and ASR, are folded into the 'ASR strain', which will be also dependent on stress as shown in the following sections. Note that this approach has already been used in the literature [62, 109, 157] and it is conceptually similar for instance to the standardized procedure for the separation of creep and shrinkage strains.

4.4.2.1 Strain curves of control specimens

The axial strain curves obtained from control specimens are given in Fig. 4.7a to c. All the specimens experienced a monotonous contraction with decreasing rate throughout the test. Th test with specimen TM03 (Fig. 4.7a) ended prematurely due to a leak of alkaline solution.

In these plots we may distinguish two different kinds of scatter. On one hand, there are differences between curves of strain along different axes of the same specimen that should, in principle, be equal since they were subject to the same load. See for instance the curves of specimen TM19 (Fig. 4.7a), which was subject to the 1-1-1 loading and, nevertheless, the strain curves exhibit non-negligible differences. This scatter seems to be random and intrinsic to the creep phenomenon itself and/or to the testing procedure.

On the other hand, there are differences within the curves of the two specimens tested with the same load case. For instance, specimens from the casting set #3 (TM19 and

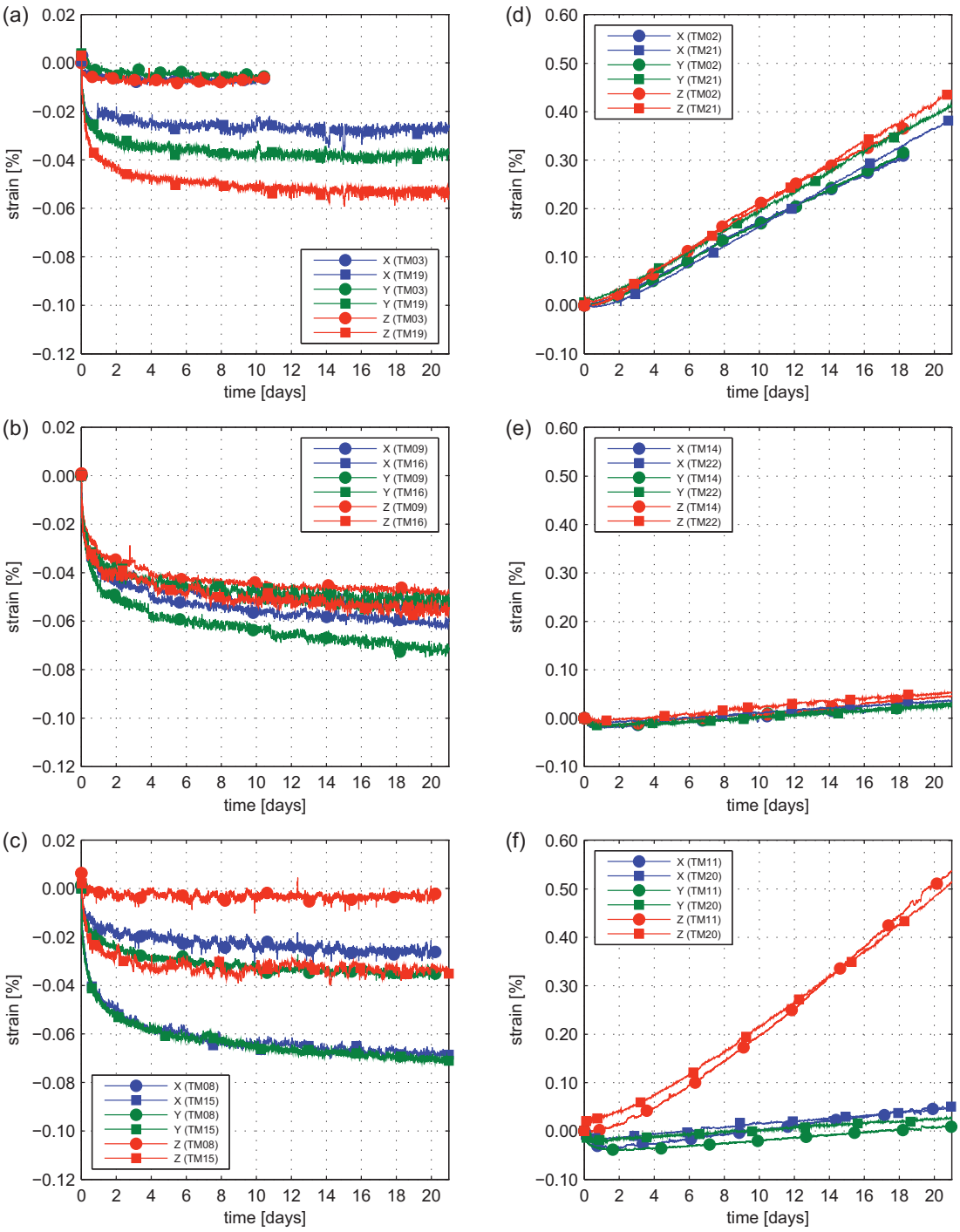

FIGURE 4.7: Axial strain curves of control specimens under (a) 1-1-1, (b) 9-9-9, and (c) 9-9-1 load cases; axial strain curves, after deducting creep, of reactive specimens under (d) 1-1-1, (e) 9-9-9, and (f) 9-9-1 load cases.

TM15) experienced higher contractions than specimens from casting sets #1 (TM03) and #2 (TM08). This seems to indicate that concrete from casting set #3 had different creep properties than the ones from casting sets #1 and #2. Based on this assumption, it was decided that the control specimen used for creep deduction of a given reactive specimen had to be from the same casting set. For instance, creep of reactive specimen TM02 was deducted considering the strain curves of control specimen TM03, because both belong to the same casting set (see Table 4.1).

4.4.2.2 Strain curves of reactive specimens

The axial strain curves of reactive specimens, after deducting creep, are plotted in Figs. 4.7d to 4.7f. (Additionally, the axial strain curves of reactive specimens without deducting any creep effects are presented in Appendix A.5, Fig. A.47.) As already explained, the creep deduction consisted in directly subtracting, for each load case, the strains measured in the corresponding control specimens. To do so, first the control specimen strain curves were fitted with a proposed logarithmic function. Then, the fitted creep function was used to estimate the creep strains to be deducted from the measured total strains in the reactive specimens. The creep function adopted and the procedure followed to fit the function parameters are described in detail in Appendix A.6. It must be noted that with the term creep we are denoting all the time dependent strains measured on control specimens, including concrete creep, but probably also the deformation of the silicone layers and the O-rings in between the specimen faces and the machine loading plates.

As shown in Figs. 4.7d to 4.7f, the differences between curves of specimens tested with the same load case are within the expected scatter for ASR expansion tests. In all cases, the maximum expansion rates required between 2 and 4 days to be reached. For applied stress of 9 MPa, the strain curves in the corresponding direction, exhibited a slight contraction during the first day, that was eventually overcome by expansions (Figs. 4.7e and 4.7f). This seems to indicate that the creep strains measured on control specimens were smaller than those occurring in the corresponding reactive ones. However, this difference cannot be attributed to ASR since it is observed at the very beginning of the tests when the effect of ASR may be regarded as insignificant. Then, it seems more likely to be the result of differences in the mechanical/creep parameters of control and reactive concretes, as it is discussed in Section 4.4.4.

In Fig. 4.8, the average of the volumetric strain curves obtained for each load case, after deducting creep, are plotted together, including the free expansion case (0-0-0). The

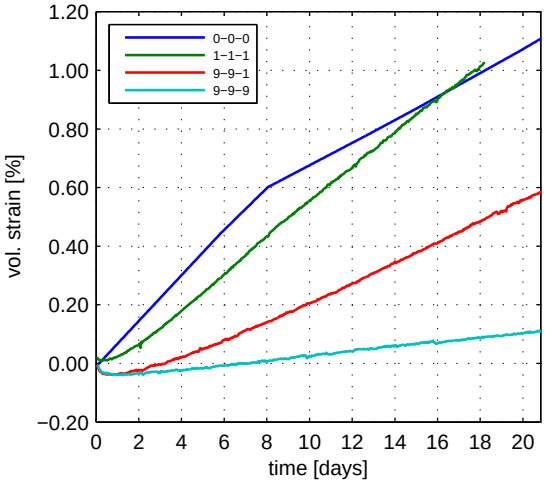

FIGURE 4.8: Comparison of average volumetric strain curves, after deducting creep, of reactive specimens under different triaxial confinement.

bi-linear shape of the free expansion curve is because the specimen deformations were measured only three times in the first 21 days.

For a quantitative analysis of the effect of stresses, axial and volumetric expansion rates obtained from the curves plotted in Figs. 4.7d to 4.7e are summarized in Table 4.4. The expansion rates were obtained by fitting the expansion curve points (t, ε_i^{asr}), with a straight line between $t = 4$ and $t = 21$ days for the specimens tested in the AARTM, and between $t = 0$ and $t = 21$ days for the free expansion tests. The volumetric expansion rate was obtained as the sum of the three axial expansion rates. In Fig. 4.9 (primary load states), volumetric expansion rates are plotted against the applied volumetric stress.

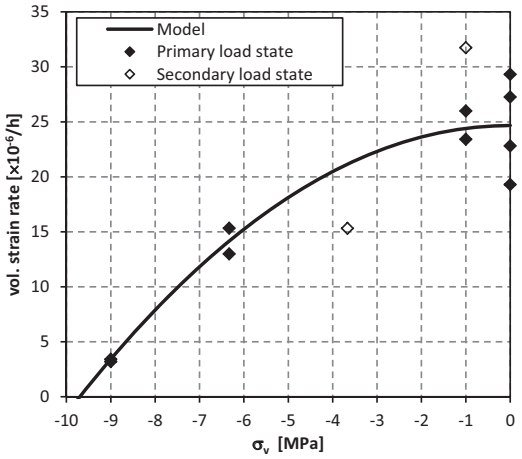

FIGURE 4.9: Volumetric strain rate of tested reactive specimen versus applied volumetric stress. Creep effects have only been deducted from the specimens under primary load states.

The volumetric expansion rate was practically the same for load cases 0-0-0 and 1-1-1. However, for load cases 9-9-1 and 9-9-9 the volumetric expansions rate was reduced

TABLE 4.4: Axial and volumetric ASR expansion rates expressed in $[10^{-6}\mathrm{h}^{-1}]$. Creep has been deducted for primary load cases but not for secondary load cases (marked with '*'). Values calculated with the proposed model are given in between brackets.

Id	$\dot{\varepsilon}_x^{asr}$	$\dot{\varepsilon}_y^{asr}$	$\dot{\varepsilon}_z^{asr}$	$\dot{\varepsilon}_v^{asr}$	$\dot{\varepsilon}_x^{asr}/\dot{\varepsilon}_v^{asr}$	$\dot{\varepsilon}_y^{asr}/\dot{\varepsilon}_v^{asr}$	$\dot{\varepsilon}_z^{asr}/\dot{\varepsilon}_v^{asr}$
Load Case 0-0-0							
TM01	5.48	7.21	6.61	19.29	0.28	0.37	0.34
TM10	9.17	6.99	11.10	27.26	0.34	0.26	0.41
TM12	7.42	5.88	9.52	22.82	0.33	0.26	0.42
TM13	9.45	9.94	9.93	29.32	0.32	0.34	0.34
Average	*7.88*	*7.50*	*9.29*	*24.67*	*0.32*	*0.31*	*0.38*
Model	*(8.22)*	*(8.22)*	*(8.22)*	*(24.67)*	*(0.33)*	*(0.33)*	*(0.33)*
Load Case 1-1-1							
TM02	7.27	7.54	8.61	23.41	0.31	0.32	0.37
TM21	8.47	8.43	9.09	26.00	0.33	0.32	0.35
Average	*7.87*	*7.99*	*8.85*	*24.71*	*0.32*	*0.32*	*0.36*
Model	*(8.14)*	*(8.14)*	*(8.14)*	*(24.41)*	*(0.33)*	*(0.33)*	*(0.33)*
Load Case 9-9-1							
TM11	1.88	1.16	12.29	15.33	0.12	0.08	0.80
TM20	1.27	0.93	10.80	13.00	0.10	0.07	0.83
Average	*1.58*	*1.04*	*11.55*	*14.17*	*0.11*	*0.07*	*0.82*
Model	*(1.13)*	*(1.13)*	*(11.89)*	*(14.15)*	*(0.08)*	*(0.08)*	*(0.84)*
Load Case 9-9-9							
TM14	1.04	1.06	1.32	3.41	0.30	0.31	0.39
TM22	1.00	0.95	1.26	3.20	0.31	0.30	0.39
Average	*1.02*	*1.00*	*1.29*	*3.31*	*0.31*	*0.30*	*0.39*
Model	*(1.14)*	*(1.14)*	*(1.14)*	*(3.43)*	*(0.33)*	*(0.33)*	*(0.33)*
Load Case 1-1-1 after 9-9-9 (*)							
TM14	10.70	9.94	11.10	31.74	0.34	0.31	0.35
Model	*(8.06)*	*(8.06)*	*(8.06)*	*(24.41)*	*(0.33)*	*(0.33)*	*(0.33)*
Load Case 1-9-1 after 1-1-1 (*)							
TM21	7.72	0.42	7.18	15.32	0.50	0.03	0.47
Model	*(10.15)*	*(0.85)*	*(10.15)*	*(21.15)*	*(0.48)*	*(0.04)*	*(0.48)*

significantly as the mean compression stress was increased.

Under isotropic stress states (0-0-0, 1-1-1 and 9-9-9) the axial expansion rate in the casting direction (Z-direction) was greater than that of the other two directions of the same specimen, therefore possibly revealing a constitutive anisotropy of the specimens. This phenomenon has been observed by many researchers [e.g 109, 157]. The rate of ASR expansion in Z-direction measured for the load case 9-9-1 was greater than the one measured for load case 1-1-1, while in the other two directions the expansion rates were similar to those obtained for load case 9-9-9. Somehow, the confinement applied on X- and Y-directions increased the expansion rate in the less stressed Z-direction.

Based on the same concepts as proposed in Saouma and Perotti [183], a new formula is proposed to predict the observed ASR volumetric expansion rate under compressive stresses ($\dot{\varepsilon}_v^{asr}$):

$$\dot{\varepsilon}_v^{asr} = \Gamma_c(\sigma_v)\dot{\varepsilon}_{v,free}^{asr} \tag{4.1}$$

where $\dot{\varepsilon}^{asr}_{v,free}$ is the rate of volumetric ASR expansion without applied stresses, and Γ_c is a dimensionless factor that accounts for the reduction of $\dot{\varepsilon}^{asr}_{v}$ under compressive stresses, which is assumed to be a function of the volumetric stress σ_v as follows

$$\Gamma_c = \begin{cases} 1 & \text{if} \quad \sigma_v \geq 0 \\ 1 - (\sigma_v/\bar{\sigma}_v)^2 & \text{if} \quad 0 > \sigma_v \geq \bar{\sigma}_v \\ 0 & \text{if} \quad \sigma_v < \bar{\sigma}_v \end{cases} \tag{4.2}$$

where $\bar{\sigma}_v$ is a parameter that stands for the volumetric stress under which ASR expansion would be totally suppressed. This value is taken as -9.7 MPa (in contrast with Saouma and Perotti expression in which $\bar{\sigma}_v$ was made equal to the characteristic compression strength of concrete). The volumetric stress is defined as $\sigma_v = (\sigma_1 + \sigma_2 + \sigma_3)/3$ where $(\sigma_1, \sigma_2, \sigma_3)$ are the principal stresses.

Then, the reduced volumetric rate is distributed in the three principal directions by means of the formula given in Saouma and Perotti [183] as follows:

$$\dot{\varepsilon}^{asr}_{i} = W_i\left(\sigma_1, \sigma_2, \sigma_3\right) \dot{\varepsilon}^{asr}_{v} \tag{4.3}$$

where $\dot{\varepsilon}^{asr}_{i}$ is the ASR expansion rate in principal axis i, and W_i is a weight factor for the principal axis i, which is a function of the three principal stresses and is calculated following the procedure proposed by Saouma and Perotti [183]. For comparison, the ASR expansion rates values obtained using these formulae are informed in between brackets in Table 4.4. As can be seen, a fairly good agreement is obtained. It is remarkable that the weight factors proposed by Saouma and Perotti based on the experimental results of Multon and Toutlemonde [157] are in very good agreement with the ones resulting from our tests, despite the fact that the constitutive anisotropy of the specimens in the casting direction (Z-direction) is not reproduced.

It has to be recognized that the model represented by Eqs. (4.1)–(4.3) is a drastic simplification of a complex phenomenon involving cracking, creep and chemo-transport processes at various levels of observation. Therefore, the curves and parameter values obtained have a phenomenological character and may change for different concretes, exposure conditions, etc. Nevertheless, it is remarkable that, as said before, this simple approach can fit data from at least two independent test series.

4.4.3 Effect of changing the stress state

In order to have some insight into the effect of changing the stress state on the ASR expansion rates, after the standard testing time (21 days) had been completed, the stress

state of two specimens (TM14 and TM21) were changed and the tests continued for an additional period of approximately 12 days.

After the 21 days under the 9-9-9 load case, the stresses on specimen TM14 were reduced to 1-1-1. As a result, the expansion rate increases significantly as it can be seen in Fig. 4.10a. Since the counterpart control specimen was not subject to the same change of the stress state, creep could not be measured, and the curves presented in Fig. 4.10a are the raw ones, i.e. without any creep deduction. The expansion rates were maximum immediately after the stress change, decreasing asymptotically to constant rate values in the following days. Interestingly, no instantaneous (elastic) expansions associated with the reduction of the compression stresses can be observed in the curves. The asymptotic expansion rates, presented in Table 4.4 and Fig. 4.9 (secondary load states), were obtained by fitting the expansion curve points (t, ε_i) with a straight line between $t = 25$ and $t = 32$ days. These values are 30% greater than the ASR expansion rates obtained for load case 1-1-1 (Table 4.4). Note that the expansion rates obtained for the secondary load cases are not attributable to ASR exclusively, since strains due to other causes have not been deducted. In this case, the decompression of the specimen may have originated a differed elastic creep expansion which could explain, at least in part, the initial variation of the expansion rates. Other causes related with the ASR expansion mechanisms may also play a role. For instance, the greater initial expansion rate may be related to the swelling of ASR gel formed under the 9-9-9 stress state due to water absorption when the confining stress decrease to 1-1-1. In any case, additional testing would be necessary to explain in more detail the behaviour observed.

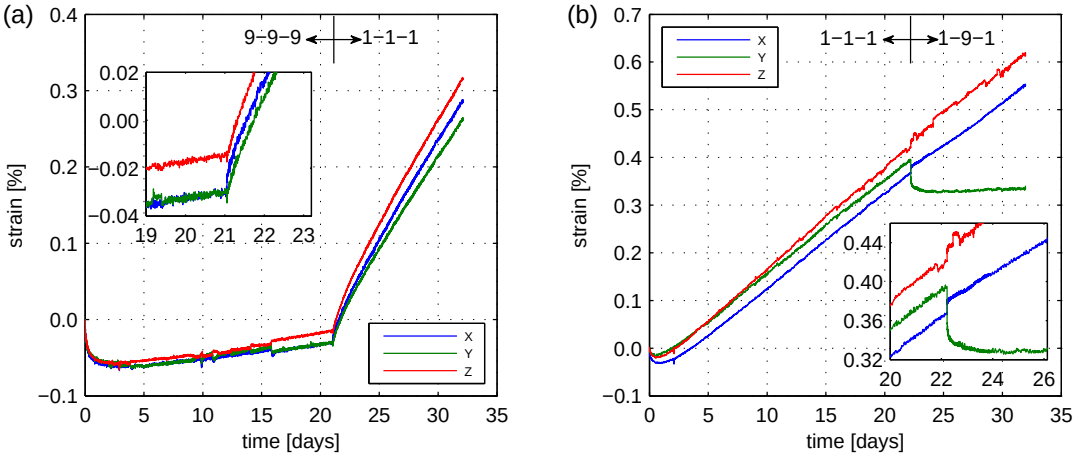

FIGURE 4.10: Axial strain curves (without deducting any creep effects) of: (a) reactive specimen TM14, first subjected to load case 9-9-9 for 21 days and then to load case 1-1-1 until the end of the test; (b) reactive specimen TM21, first subjected to load case 1-1-1 for 22 days and then to load case 1-9-1 until the end of the test.

For specimen TM21, the stress state was changed after 22 days from 1-1-1 to 1-9-1. The resulting raw expansion curves are presented in Fig. 4.10b. In this case, in contrast with the previous one, instantaneous strains are clearly appreciated: a negative strain jump in the Y-direction and smaller positive strain jumps, attributable to Poisson's effect, in the X- and Z-directions. After that, the expansion along the Y-direction practically stops, while it continues along the X- and Z-directions but with a rate 10 to 20% smaller than for the previous 1-1-1 stress state. In the same way as for the previous specimen, the expansion rates for the 1-9-1 stress state has been estimated and reported in Table 4.4. Again, the lack of a counterpart control specimen with the same stress history makes it impossible to deduct creep and therefore obtain the net ASR expansion rates. However, one can estimate that the deduction of the creep strains in this case would result in a slight increase of the expansion rate in the Y-direction and an even smaller, if any, reduction in the X- and Z-direction rates, due to Poisson's effect on creep strains. Therefore, the increase of the Y-stress seems not only to have reduced the Y-direction expansion rate but also the expansions on the other two axes. Again, additional testing would be needed to confirm these observations.

Finally, the expressions proposed in Eqs. (4.1) to (4.3) were used to estimate the ASR expansion rates under the secondary load cases. The values obtained are reported in between brackets in Table 4.4. As it can be seen, the weight factors are in good agreement with the experimental ones. However, the volumetric expansion rates are not very well predicted.

4.4.4 Mechanical test results

The results of the mechanical tests performed on some control and reactive specimens are summarized in Table 4.5. The initial elastic modulus (E) and the compression strength (f_c) were measured on control and reactive specimens subjected to four different histories of curing and ASR testing. The specific fracture energy in mode I (G_I^f) and the tensile strength (f_t) were obtained only from control and reactive specimens which had been cured for 15 weeks but had not been subject to ASR testing.

Lets first consider the results from the specimens cured for 15 weeks and not tested for ASR. The E and f_c measured for control concrete are significantly higher than those measured on reactive concrete. In contrast, the G_I^f measured on reactive concrete is practically twice the one measured on control concrete, while the estimated f_t values are similar. These differences can be attributed to the flaky shape and to the smoothness of the crushed glass particles. Since concrete creep in absolute terms is known to decrease with increasing elastic modulus, the creep strain experienced by control specimens during

TABLE 4.5: Results of the mechanical tests: initial tangent modulus (E), compression strength (f_c), tensile strength (f_t), and specific fracture energy in mode I (G_I^f).

Type	Id.	E [GPa]	f_c [MPa]	f_t [MPa]	G_I^f [J/m^2]
Cured for 15 weeks					
Control	TM25	41.5	42.5	-	-
Reactive	TM30	21.5	26.8	-	-
Control	TM26	-	-	2.8	74.6
Reactive	TM31	-	-	2.4	144.1
Cured for 47 weeks					
Control	TM18	40.0	60.5	-	-
Reactive	TM24	19.0	24.9	-	-
Cured for 63-67 weeks and tested 9-9-9 for 3 weeks					
Control	TM16	40.3	54.3	-	-
Reactive	TM22	25.5	34.4	-	-
Cured for 14 weeks and tested 0-0-0 for 36 weeks					
Control	TM07	41.7	52.6	-	-
Reactive	TM13	5.6	8.5	-	-

the confined expansion tests may have been lower than the ones experienced by reactive specimens. This may explain the initial contraction observed in the ASR expansion curves in the direction under -9 MPa stress (Fig. 4.7e and f), and indicate that the actual ASR expansion rates may have been slightly higher than those reported in Table 4.4. An effort shall be made in future tests in order to obtain similar mechanical parameters in control and reactive concretes.

When considering the remaining results, it seems that curing and testing history only have an influence on the measured values of f_c and E in reactive concrete, but not on control concrete. Comparison of results from specimens TM30 and TM24 (curing times of 15 and 47 weeks, respectively) suggests that ASR degradation occurring at curing conditions was not significant, even when some signals of occurring ASR (ASR gel spots, slight cracking) were detected on the specimen cured for 47 weeks. In contrast, E and f_c values from specimen TM13, which was previously tested in free expansion conditions for 36 weeks and experienced ASR expansions of about 2.5% (Fig. 4.6), showed important reductions in comparison with those measured on TM30. Finally, specimen TM22, which had a longer curing period and was tested for 3 weeks experiencing some ASR expansions (0.05%, Fig. 4.7e), not only did not degrade its mechanical parameters but actually improved them.

4.4.5 SEM images and EDS analyses

After testing (21 days under 1-1-1 load case), specimen TM02 was cut in two halves with a diamond saw. In Fig. 4.11, an enlarged view of the central cross section is presented. In

the image, the crushed SL glass particles can be distinguished surrounded by limestone mortar. Whitish ASR products, mainly within cracks in the glass particles, can also be distinguished. From this central section, two samples were taken for performing SEM/EDS analysis. One sample was taken from the centre and the other one from one lateral of the cross section. No influence of the original sample location was noticed in the results obtained, and, thus, henceforth no distinction between the two samples will be made in the analysis of the results.

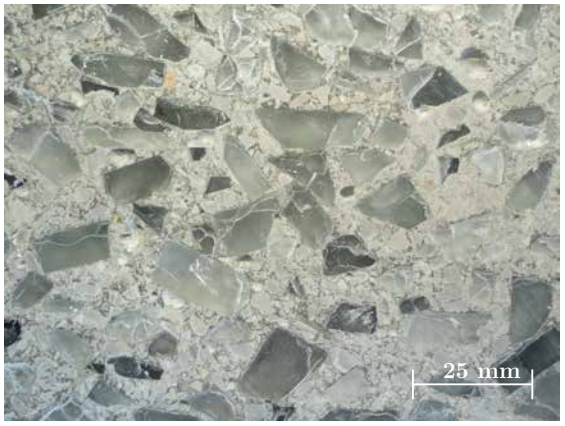

FIGURE 4.11: Detail view of a cross section of specimen TM02 after testing (21 days under 1-1-1 load case). Whitish ASR products can be appreciated within cracks in SL glass particles.

Some of the SEM images obtained are presented in Figs. 4.12 and 4.13. The points analysed via EDS are indicated on the images and the obtained chemical compositions (normalized to Si, Ca, Na and K) are given in Table 4.6. In those images, three types of ASR products have been identified:

Low-calcium product Mainly localized within cracks inside glass particles, with molar ratios Ca/Si≈0.22–0.35 and (Na+K)/Si≈0.14–0.28.

High-calcium product Localized within cracks in the limestone mortar, with molar ratios Ca/Si≈1.40–1.43 and (Na+K)/Si≈0.12–0.15.

Intermediate product Transitional product between the low- and high-calcium products, with calcium content ranging in between the two extreme values. Alkali content, in turn, tends to decrease with increasing calcium content.

It is not possible to reconstruct the sequence of formation of the different ASR products and the propagation of cracks from a set of SEM images at a single testing time. However, based on the experimental study performed by Rajabipour et al. [174], it is possible to infer that ASR expansion begun mainly due to the precipitation of low-calcium products within pre-existing cracks inside glass particles. These pre-existing cracks are the

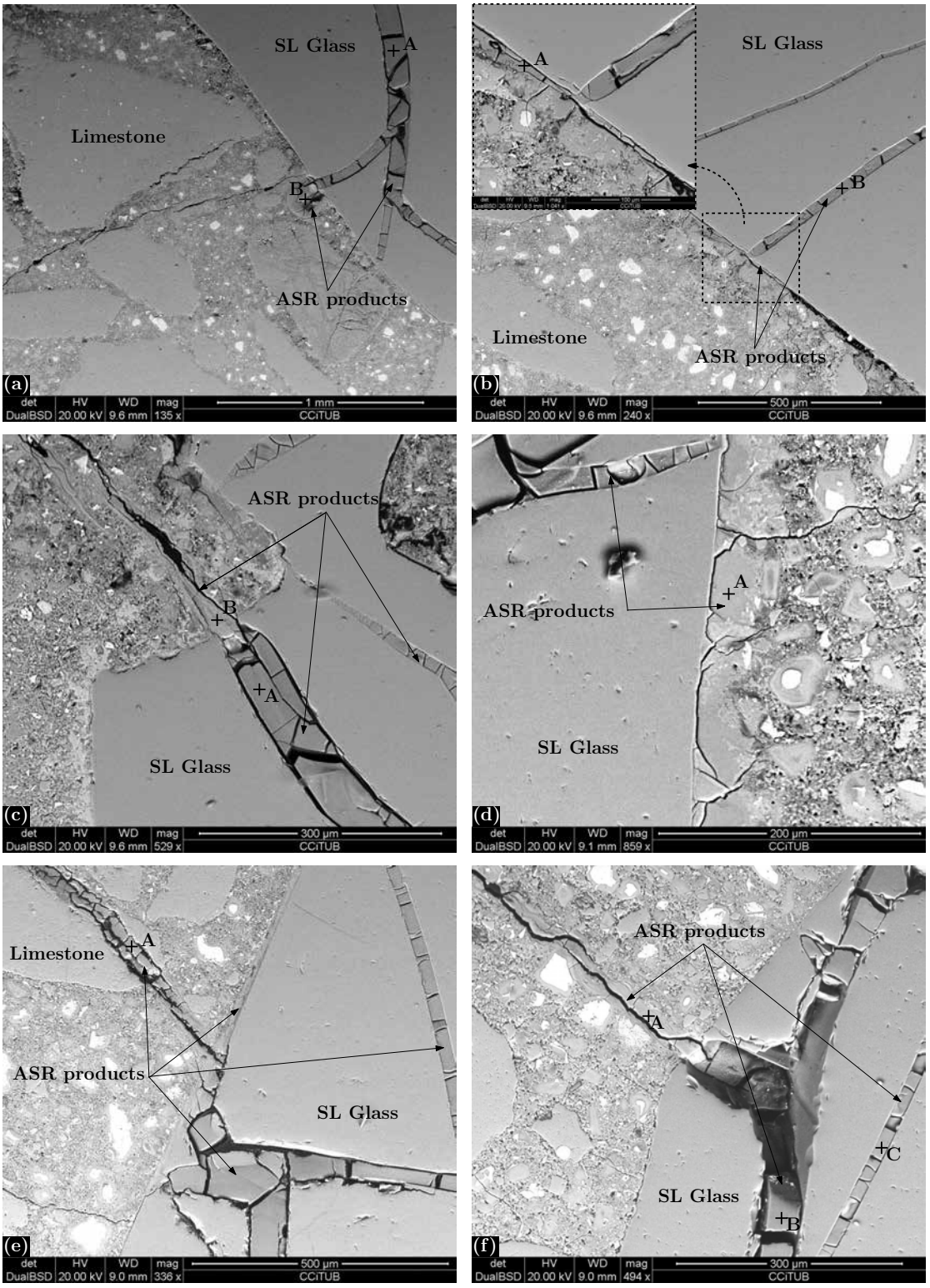

FIGURE 4.12: SEM images of a cross section of specimen TM02 after testing (21 days under 1-1-1 load case). EDS analysis were performed at the points indicated. Refer to Table 4.6 for the resulting chemical compositions.

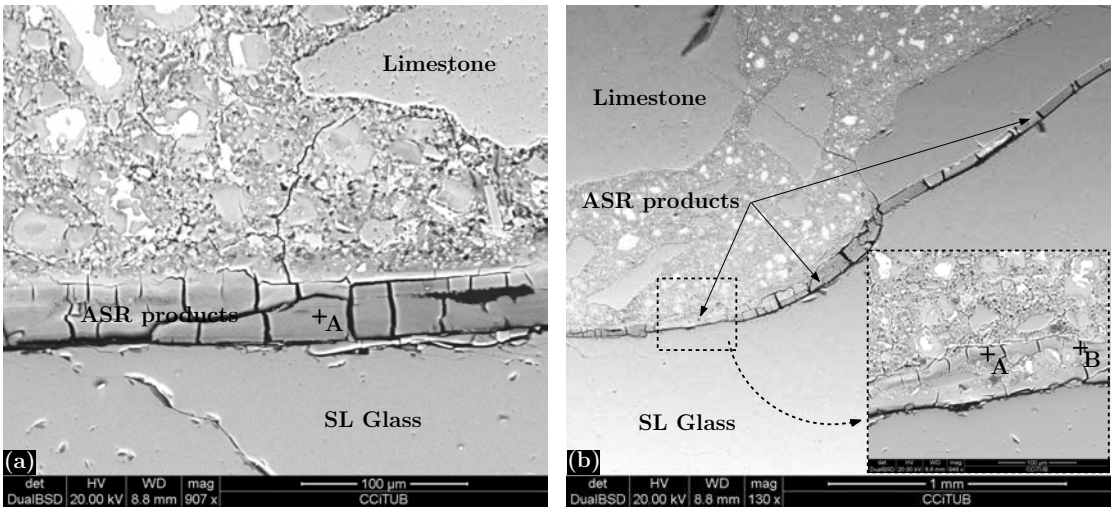

FIGURE 4.13: SEM images of a cross section of specimen TM02 after testing (21 days under 1-1-1 load case). EDS analysis were performed at the points indicated. Refer to Table 4.6 for the resulting chemical compositions.

TABLE 4.6: Chemical composition of ASR products (normalized to Si, Ca, Na and K) in specimen TM02 obtained via SEM images and EDS analysis.

Figure	Point	Location	Composition (at%)					
			Si	Na	K	Ca	Ca/Si	(Na+K)/Si
4.12a	A	Glass crack	73.3	10.4	0.0	16.3	0.22	0.14
4.12a	B	HCP macropore	56.9	13.8	8.5	20.8	0.37	0.39
4.12b	A	Glass-cement interface	55.6	8.6	9.4	26.4	0.48	0.32
4.12b	B	Glass crack	63.2	8.6	7.9	20.4	0.32	0.26
4.12c	A	Glass crack	61.4	10.3	7.1	21.3	0.35	0.28
4.12c	B	HCP crack	39.6	2.7	2.1	55.6	1.40	0.12
4.12d	A	Glass-cement interface	47.1	3.7	1.5	47.7	1.01	0.11
4.12e	A	Limestone crack	61.7	6.7	4.6	27.0	0.44	0.18
4.12f	A	HCP crack	48.5	4.6	2.9	43.9	0.91	0.16
4.12f	B	Glass crack	66.3	8.9	6.4	18.3	0.28	0.23
4.12f	C	Glass crack	65.8	9.6	6.9	17.7	0.27	0.25
4.13a	A	Glass-cement interface	60.3	6.7	8.9	24.0	0.40	0.26
4.13b	A	HCP crack	56.9	7.3	8.1	27.7	0.49	0.27
4.13b	B	HCP crack	48.8	6.2	5.2	39.8	0.82	0.23

residual result of the glass crushing process. The swelling of the low-calcium product within the residual cracks produced wedging stresses that propagate cracks towards the limestone mortar with the same orientation as the gel-filled residual cracks inside glass (Fig. 4.12a, c and f). In other cases, internal restrictions and differential mechanical properties of glass, ITZ and Hydrated Cement Paste (HCP) may have induced more intricate cracking paths (Fig. 4.12e and Fig. 4.13b). The induced cracks in the limestone mortar were not initially filled with ASR products, but they were filled with intermediate and/or high-calcium products as the ASR progressed. Surprisingly, in most SEM images the glass-HCP interface appears clean and does not show evidence of ASR products. In the few cases where a significant amount of ASR products was found at a glass-HCP

interface, it was usually connected to a glass crack (see for instance Figs. 4.12b, d and e, and 4.13b).

In glass concrete specimens tested according to ASTM C1260 (free expansion in 1 M NaOH solution at 80 °C) [9], Rajabipour et al. [174] found a diffuse layer of high-calcium product (up to about 20 μm thick) at the boundary between the glass and the HCP. This high-calcium product layer could not be identified in the samples taken from specimen TM02. In any case, the amount/morphology/location of the ASR products formed at the glass-HCP interfaces of glass concrete, if any, substantially differ from the well differentiated layers of reaction products obtained with Interfacial Expansion Tests reported in Chapter 3. Consider, for instance, the SEM images of a reactive specimen of Set #2 of Series C presented in Fig. 3.14. This specimen was prepared with the same glass, the same cement, the same w/c ratio, and the same initial alkali content as specimen TM02. Moreover, both specimens were tested with the same alkaline bath (1 m NaOH solution) and temperature (60 °C). Thus, it may be expected that the chemical and micro-structural (porosity, solid fractions, bonding strength, etc.) conditions for ASR at the glass-HCP interfaces had been similar in both cases, and, therefore, the differences in the resulting ASR products can not be explained by those factors.

As already proposed in Section 3.8.6, a possible explanation may be found in the different mechanical restraint in each case. In the case of the Interfacial Expansion Tests, the ASR products only need to overcome the tensile strength of the cement matrix-glass interface in order to develop measurable expansions and to make room for further precipitation of reaction products. In contrast, in the case of glass particles within a cementitious matrix, the ASR products not only need to overcome the tensile strength of the glass-cement interface, but also need to deform/crack the surrounding cementitious matrix (and even surpass superimposed external pressures, as in the case of specimen TM02). In other words, the swelling pressure needed for separating glass-cement interfaces is certainly much lower in the first case than in the second case. This observations lead us to conjecture, in contrast with the interpretation of Rajabipour et al. [174], that the formation of high-calcium ASR products is indeed an expansive reaction, but an expansive reaction which can be slowed down by an applied pressure, or even inhibited if the applied pressure is higher than the maximum swelling-pressure capable of being developed by this reaction product. The low-calcium product within cracks inside glass particles, in turn, would have a similar behaviour but with a maximum swelling-pressure significantly higher than the maximum swelling-pressure of the high-calcium product. Considering that under load case 9-9-9, the glass concrete specimen were still capable of developing expansions, 9 MPa (or 9.7 MPa accordingly with the model proposed in

Section 4.4.2.2) may be considered as a lower bound value of the swelling-pressure of low-calcium products. The real value has to be certainly higher, since, besides the external pressure, the low-calcium ASR products have also to overcome the internal restraints.

This discussion about the role of the mechanical restraints in the development of ASR expansion of SL glass concrete, which started in Section 3.8.6, is continued in the following Section 6.2, leading to the proposal of a reaction-expansion mechanism and the formulation of a chemo-mechanical numerical model.

4.5 Chapter concluding remarks

- Accelerated ASR expansion tests performed on cubical concrete specimens under free and triaxially-confined expansion conditions have been presented. Two different concrete mixtures were tested under the same conditions, one reactive, with crushed SL glass aggregate, and one non-reactive.
- For the triaxially-confined tests, an ad hoc testing machine was originally designed and constructed by Prof. V.E. Saouma at the U. of Colorado - Boulder, and later modified by the author at UPC-Barcelona. This machine has shown to be capable of accurately applying and maintaining targeted true-triaxial compressive stress states and temperatures on the specimen, while keeping it in contact with a highly alkaline solution.
- The results seem to indicate that the volumetric ASR expansion rate is reduced as the applied volumetric compressive stress is increased. Additionally, there seems to be an increase of the expansion rate in the less compressed direction in detriment of the expansion rates in the most compressed ones. These observations are in good agreement with the model previously proposed by Saouma and Perotti [183], although a correction is proposed for the dependency of total volumetric expansion with volumetric stress.
- SEM/EDS analyses of the reaction products and cracking of a specimen tested under isotropic pressure of 1 MPa, indicate the presence of ASR products with variable calcium content, from low-calcium products (molar Ca/Si≈0.30) inside cracks within glass particles to high-calcium products (molar Ca/Si≈1.40) formed in contact with the HCP. Most of the ASR expansion and cracking is attributed to the low-calcium product.
- Future work should be intended to use the testing methodology proposed for ASR confined expansion test also for studying concrete made with natural reactive aggregates.

Chapter 5

Modelling of diffusion-dominated durability problems in cement-based materials

5.1 Introduction

The diffusion of aqueous chemical species plays a role in most durability problems of cement-based materials. In the Hardened Cement Paste (HCP), the solid phases and the pore solution phase are in a dynamic chemical equilibrium. The solid phases that form the HCP are an assemblage of hydrated compounds that may be crystalline or gel-like in character. Any change in the composition of the solution caused by diffusion of aqueous species will affect the amount and composition of the cement hydration products or even give rise to the precipitation of new products. The exchange of aqueous species due to diffusion may occur between the cementitious matrix and the environment and/or between cementitious matrix and inclusions such as aggregates. Then, serviceability or even structural problems may arise due to: (i) dissolution of the cement hydration products, with consequent loss of bearing capacity and increase of permeability; or (ii) precipitation of solids at pores or interfaces within the cementitious material, eventually leading to internal pressures, expansions and cracking. The first case corresponds to durability problems such as Calcium Leaching and Acid Attack, while the second corresponds to problems such as Corrosion of Reinforcement Steel, External Sulphate Attack, and Alkali-Aggregate Reactions.

In all cases, complex interplays exist between chemical reactions, diffusion processes transporting the reactants inward or the products outward the reaction sites, and mechanical stresses leading to concrete expansion and cracking. For instance,

- the formation of expansive reaction products may induced internal pressures, which in turn may lead to concrete cracking.
- since cracks constitute preferential paths for the ingress of reactants from the surrounding medium, their presence may accelerate the deleterious process.
- the dissolution or precipitation of solid species may modify the pore structure and, hence, the effective diffusivity of the continuum porous material, with consequences for the kinetics of the degradation process.

A deep understanding of the mechanisms underlying the deterioration processes of cement-based materials is very much facilitated by the formulation of mathematical models. Such models allow us to identify the key factors which determine the kinetics and the extent of the degradation based on the material composition (chemical and mineralogical composition, microstructure, etc.) and the environmental conditions (temperature, humidity, presence of external reactant sources, etc.).

Along this line, a general framework for numerical modelling of diffusion-dominated durability problems in cement-based materials is proposed in this chapter. The model consists in two separate (decoupled) FEM formulations, one for the diffusion-reaction problem and the other for the mechanical problem. The model has the distinctive feature of explicitly considering discontinuities (cracks, cement paste-aggregate interfaces, etc.) which in both formulations are represented via zero-thickness interface elements. Coupling effects are introduced by implementing a staggered scheme in which each FE model interacts with the other. In order to facilitate the exchange of information both codes share the same FE mesh. In a first stage of development, the model is formulated assuming that the cement-based material is water-saturated but it can be readily extent for non-saturated conditions in the future.

This modelling framework is the continuation of the previous work developed within the group of Mechanics of Materials (MECMAT) of UPC by A. Idiart [97] for modelling External Sulphate Attack on concrete. However, substantial modifications are introduced in this thesis. In particular, the original diffusion-reaction theoretical formulation and the numerical implementation have been completely redone, in order to include features such as the chemical speciation in pore solution, the precipitation of compressible reaction products or the occurrence of chemical reactions at discontinuities.

In the following chapter (Chapter 6), the modelling framework proposed here is adapted for modelling ASR expansions in concrete. In a previous work, the author and coworkers used a similar framework for modelling acid attack of oilwell cement exposed to carbonated brine [128].

5.2 Diffusion-reaction problem

5.2.1 Generalities

The cement-based material under consideration is modelled as a continuum porous material completely saturated with water, i.e. the volume of pore solution in the material is equal to the total volume of pores. Within the total volume of pores, two different fractions are distinguished. On one hand, the volume of pores occupied by free water which constitutes the capillary pore fraction. On the other hand, the pores occupied by gel water which constitutes the gel pore fraction. 'The gel water', in contrast with the capillary water, 'is visualized as being within the influence of absorbing forces' [25] and is associated with gel-like constituents with high specific surface, such as C–S–H or ASR gel.

In the cement pore solution, a number of aqueous species relevant for the deleterious process to be modelled are considered. Between them, a distinction is made between primary and secondary aqueous species. The transport process of primary species is modelled explicitly, while the concentration of secondary species is obtained locally as function of the primary ones by means of equilibrium equations.

The solid skeleton is formed by a number of solid phases that can be stable or evolve with time depending on the deleterious process to be model. Additionally, solid phases may precipitate occupying capillary pore space or inducing expansions. The volume of gel pores is available as an aqueous reaction medium but it cannot be occupied by precipitated solids. The unstable solid phases evolve according to chemical kinetic laws which are functions of the concentration of both primary and secondary aqueous species.

Discontinuities (cracks or ITZ), when present, are modelled essentially with the same assumptions. When a crack occurs, two continuum domains are separated 'creating' a new volume, immediately filled with pore solution, and capable of allocating solid reaction products. In the case of ITZ, an initial volume may be assigned to the discontinuity even when there is no mechanical separation between the cementitious matrix and the aggregate, in order to account for its differentiated microstructure with regard to the bulk cementitious matrix.

The only transport process considered is the Fickian diffusion of aqueous species in the pore solution. The diffusion is assumed to occur through both capillary and gel pores. The effective diffusivity of the continuum porous medium and that of the discontinuities are determined by the volumetric fractions of the different constituents, which may be evolving with time.

5.2.2 Diffusion-reaction formulation

5.2.2.1 Solute mass balance

The solute mass balance equations are obtained under the following assumptions:

- Concrete pores and discontinuities are assumed to be completely saturated with water and remain in this condition.
- Water movement is not explicitly considered.
- Temperature is assumed to remain constant and uniform within the domain.
- The only transport process considered is the Fickian diffusion of aqueous species in the pore solution.

Therefore, the effects of electrical potential gradient, activity coefficient gradients, temperature gradient and advective water fluxes in the transport of the considered aqueous species are neglected. For a full formulation of the transport of ions in cement paste which includes all these effects, see Refs. [178, 179].

Solute mass balance equations are stated for both the continuum porous medium and the discontinuities. For the continuum porous medium, the approach proposed by Bear and Cheng for contaminant transport in groundwater [16, Ch. 7] has been followed, whereas for the discontinuities, the work of Segura and Carol [191] has been adapted making it consistent with the approach of Bear and Cheng.

Unless otherwise indicated, second order effects in diffusion and chemical kinetics due to geometry changes induced by the mechanical loads are neglected for the porous continuum medium, but explicitly considered for discontinuities in terms of the normal aperture of the zero-thickness interface elements.

The same formulation is used for simulating both types of discontinuities, cracks and ITZs. The only difference lies in the fact that cracks only appear when the mechanical strength of the material is overcome, while ITZ are always present in the HCP-aggregate interfaces. As developed below, from the formulation point of view that means that the discontinuity width (w) will be always be $w > 0$ in the case of ITZ, whereas in the case of a crack it will remain $w = 0$ while the mechanical strength is not been overcome.

Finally, sink/source terms are introduced in the balance equations of both continuum and interface elements to take into account the increase of the quantity of aqueous species due to the dissolution of solids, and, vice versa, the reduction of the quantity of aqueous species due to the precipitation of solids.

In the following paragraphs, the solute mass balance equations are written for only one, generic, aqueous β-species. These equations are later extended to n aqueous species in Section 5.2.3.3.

Continuum porous medium

Let us consider a 2D domain Ω of continuum water saturated porous medium (Fig. 5.1). The mass balance equation of the β-species in a Representative Elementary Volume (REV) $\mathcal{U} = dxdy$ may be written as:

$$\frac{\partial(\phi c^\beta)}{\partial t}dxdy = -\frac{\partial j_x^\beta}{\partial x}dxdy - \frac{\partial j_y^\beta}{\partial y}dxdy + q^\beta dxdy \tag{5.1}$$

where c^β [mol m_{ps}^{-3}] is the concentration of the β-species in the pore solution, expressed as quantity of solute per unit volume of pore solution; j_x^β and j_y^β [mol m^{-2} s^{-1}] are the fluxes per unit area of β-species in directions x and y, respectively; ϕ [m_{ps}^3 m^{-3}] is the total porosity of the porous medium; q^β [mol m^{-3} s^{-1}] is the chemical source rate expressed as the quantity of β-species produced/consumed per unit volume of porous medium, which is generally a function of concentration c^β. Note that the time derivatives of dx and dy have been neglected.

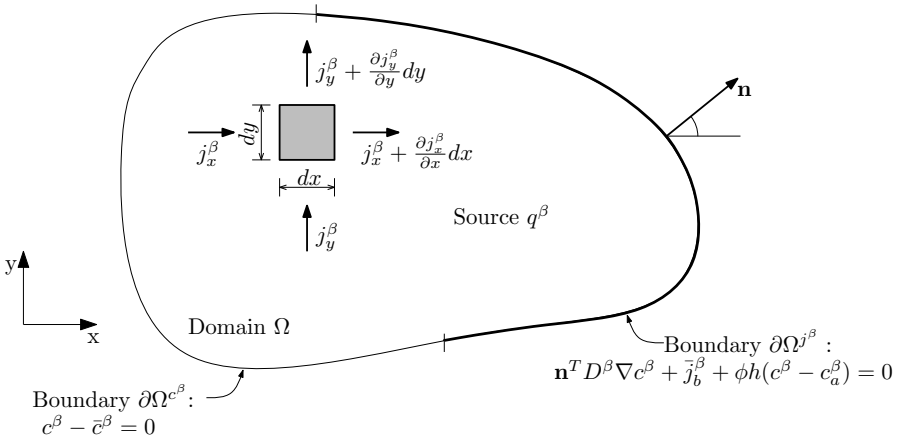

FIGURE 5.1: Problem definition for diffusion-reaction in a continuum 2D domain.

The fluxes j_x^β and j_y^β are calculated considering Fick's law and isotropic effective diffusivity D^β:

$$j_x^\beta = -D^\beta \frac{\partial c^\beta}{\partial x}; \qquad j_y^\beta = -D^\beta \frac{\partial c^\beta}{\partial y} \tag{5.2}$$

Effective diffusivity reflects the averaged macroscopic diffusive flux in the porous medium and may be evaluated with expression:

$$D^\beta = \phi\lambda D_w^\beta \tag{5.3}$$

where D_w^β [$m^2 s^{-1}$] is the diffusivity of the β-species in bulk water, and $0 < \lambda < 1$ is a dimensionless pore structure parameter that introduces the restrictive effects of tortuosity and constrictivity in the macroscopic diffusive flux. The units of D^β are [$(m^3_{ps} m^{-3})(m^2 s^{-1})$].

Replacing Eq. (5.2) in Eq. (5.1) and after some manipulation, we obtain the following expression of the solute mass balance in the porous medium over a domain Ω:

$$\frac{\partial(\phi c^\beta)}{\partial t} = \nabla \left(D^\beta \nabla c^\beta \right) + q^\beta \quad \text{in } \Omega \tag{5.4}$$

where $\nabla(\cdot) = \left[\frac{\partial(\cdot)}{\partial x} \quad \frac{\partial(\cdot)}{\partial y} \right]^T$.

Two possible boundary conditions are considered:

1. Prescribed concentartion condition (Dirichlet condition):
$$c^\beta = \bar{c}^\beta \qquad \text{on } \partial\Omega^{c^\beta} \tag{5.5a}$$
2. Prescribed flux condition (Neumann condition):
$$j_b^\beta = \bar{j}_b^\beta + \phi h (c^\beta - c_a^\beta) \qquad \text{on } \partial\Omega^{j^\beta} \tag{5.5b}$$

where $\bar{c}^\beta$ is the prescribed concentration at the domain boundary $\partial\Omega^{c^\beta}$ and $\bar{j}_b^\beta$ is the prescribed normal flow at the domain boundary $\partial\Omega^{j^\beta}$, with outer normal direction $\mathbf{n}$. The last term in Eq. (5.5b) expresses the solute diffusive flow through the border due to the concentration difference between the boundary (c^β) and the external media (c_a^β); h [m s^{-1}] is the 'convection' coefficient. The normal flux j_b^β is obtained by projecting the boundary flow over the boundary normal

$$j_b^\beta = -\mathbf{n}^T D^\beta \nabla c^\beta \tag{5.6}$$

Note that $\partial\Omega = \partial\Omega^{c^\beta} \cup \partial\Omega^{j^\beta}$. The boundary split in two zones is conceptual, because these conditions can appear in different zones along the boundary.

Discontinuities

Let us consider a 2D discontinuity of width w [m] surrounded by continuum porous medium, and a local orthogonal coordinate system (l, n) defined on the plane tangent to the discontinuity surface (Fig. 5.2). The continuum and the discontinuity are assumed to be fully saturated with water. Diffusion of aqueous β-species may occur both in the longitudinal and in the transversal directions to the discontinuity, in the latter case incoming into the discontinuity from the surrounding porous medium on one side and outgoing into the continuum medium on the other side. Additionally, the β-species may be consumed or produced locally due to chemical reactions.

For the sake of simplicity, it is assumed that the longitudinal diffusion along the discontinuity, as well as the chemical reaction rates, depend on the concentration of the β-species in pore solution at the centre of the discontinuity width w and that is equal to:

$$c^{\beta}_{mp} = \frac{c^{\beta}_{top} + c^{\beta}_{bot}}{2} \tag{5.7}$$

where c^{β}_{top} and c^{β}_{bot} [mol $\mathrm{m}^{-3}_{\mathrm{ps}}$] are the concentrations at both sides (top and bottom) of the discontinuity. Consistently, the remaining parameters/variables of the discontinuity are also computed at the mid-plane, but assumed to be valid across the discontinuity width w.

Then, considering a REV along the discontinuity with volume $\mathcal{U} = wdl$, and enforcing conservation of the solute mass we obtain:

$$\frac{\partial(w\phi_{mp}c^{\beta}_{mp})}{\partial t}dl = -\frac{\partial J^{\beta}_{l}}{\partial l}dl + q^{\beta}_{mp}dl \tag{5.8}$$

where J^{β}_{l} [mol m^{-1} s^{-1}] is the longitudinal local flow of β-species, w [m] is the discontinuity width, ϕ_{mp} [$\mathrm{m}^{3}_{\mathrm{ps}}$ m^{-3}] is the total porosity of the discontinuity, i.e. the ratio between the void volume (saturated with pore solution) and the total volume of the discontinuity, and q^{β}_{mp} [mol m^{-2} s^{-1}] is the chemical sink/source term of the β-species, which generally is a function of the concentration c^{β}_{mp}.

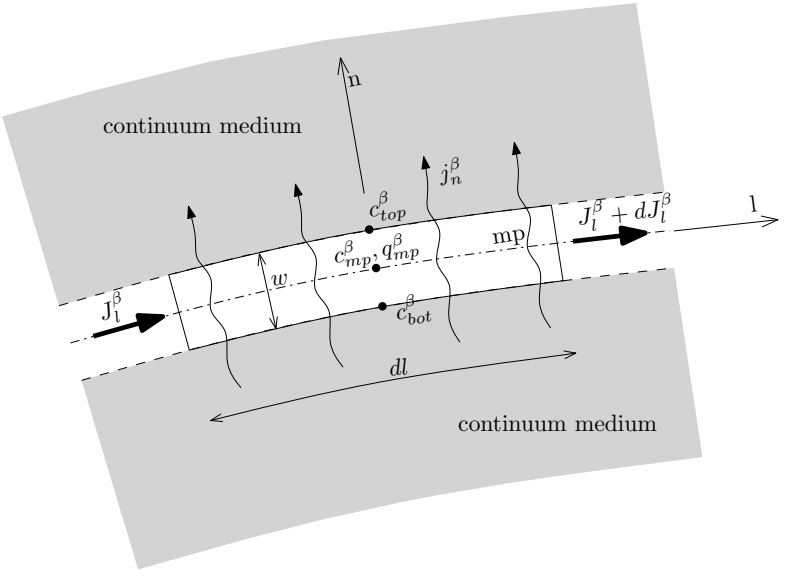

FIGURE 5.2: Problem definition for diffusion-reaction in a 2D discontinuity.

Generalized Fick's law relates the localized flow of β-species with the concentration gradient in the longitudinal direction:

$$J_l^\beta = -\left(wD_l^\beta\right)\frac{\partial c_{mp}^\beta}{\partial l} = -T_l^\beta\frac{\partial c_{mp}^\beta}{\partial l} \tag{5.9}$$

where D_l^β [$(\mathrm{m}_{\mathrm{ps}}^3\ \mathrm{m}^{-3})(\mathrm{m}^2\ \mathrm{s}^{-1})$] is the effective longitudinal diffusivity of the discontinuity.

Substitution of Eq. (5.9) into Eq. (5.8) leads to the partial differential equation that governs longitudinal flow along the mid-plane:

$$\frac{\partial(w\phi_{mp}c_{mp}^\beta)}{\partial t} = \frac{\partial}{\partial l}\left(T_l^\beta\frac{\partial c_{mp}^\beta}{\partial l}\right) + q_{mp}^\beta \tag{5.10}$$

which is analogous to the 1D partial differential equation governing the diffusion of solutes through continuum porous medium.

Besides the longitudinal transmissivity, the existence of a discontinuity may also represent an obstacle or resistance to solute flow in the transversal direction, for instance due to the transition from a pore system into an open channel and back into a pore system or due to the existence of infill material. This resistance may reduce the diffusive flow in the transversal direction and results in a localized concentration drop across the discontinuity. Similar potential drops are observed in other diffusion-like processes, as in the case of heat flow through interfaces between two distinct materials or voltage drops at the interface of an electrode and an electrolyte in electrochemical problems. In this thesis, a transversal concentration drop $\check{c}_{mp}^\beta$ [mol $\mathrm{m}_{\mathrm{ps}}^{-3}$] between the discontinuity boundaries is considered, which is related to a transversal flux j_n^β [mol $\mathrm{m}^{-2}\ \mathrm{s}^{-1}$] by a transversal diffusivity D_n^β [$(\mathrm{m}_{\mathrm{ps}}^3\ \mathrm{m}^{-3})(\mathrm{m}\ \mathrm{s}^{-1})$] coefficient:

$$j_n^\beta = D_n^\beta(c_{bot}^\beta - c_{top}^\beta) = D_n^\beta\check{c}_{mp}^\beta \tag{5.11}$$

where the subscripts *bot* and *top* stand for bottom and top discontinuity boundaries.

5.2.2.2 Source terms

General expressions of the net production rate of β-species per unit volume of the continuum (q^β) and per unit area of discontinuity (q_{mp}^β) are given in Eqs. (5.12) and (5.13), where x_α^β is the stoichiometric coefficient of the β-species in the formation reaction of solid α-species, $\bar{\Gamma}^\alpha$ [mol $\mathrm{m}^{-3}\ \mathrm{s}^{-1}$] is the net rate of formation of the solid α-species per unit volume of porous material, and $\bar{\Gamma}_{mp}^\alpha$ [mol $\mathrm{m}^{-2}\ \mathrm{s}^{-1}$] is the net rate of formation of solid α-species per unit area of discontinuity. Note that the number of solid α-species is

generically considered greater than one.

$$q^{\beta} = -\sum_{\alpha} x_{\alpha}^{\beta} \bar{\Gamma}^{\alpha} \tag{5.12}$$

$$q_{mp}^{\beta} = -\sum_{\alpha} x_{\alpha}^{\beta} \bar{\Gamma}_{mp}^{\alpha} \tag{5.13}$$

5.2.2.3 Mass balance of solid species

The mass balance equation of the solid α-species is given by

$$\frac{\partial M^{\alpha}}{\partial t} = \bar{\Gamma}^{\alpha} \tag{5.14}$$

$$\frac{\partial M_{mp}^{\alpha}}{\partial t} = \bar{\Gamma}_{mp}^{\alpha} \tag{5.15}$$

where M^{α} [mol m^{-3}] is the concentration of the solid α-species per unit volume of undeformed continuum porous medium, and M_{mp}^{α} [mol m^{-2}] is the concentration of the solid α-species per unit area of discontinuity.

The rates of formation ($\bar{\Gamma}^{\alpha}, \bar{\Gamma}_{mp}^{\alpha}$) will generally depend on the concentration of primary and secondary aqueous species but also on the concentration of solid species. The latter dependency may be justified because the solid species is intervening in the reaction (e.g. in a dissolution process), or may be due to the fact that the evolution of the solid species modifying the material microstructure (porosity, specific surface, etc.) with consequences on the kinetics of the reactions considered.

5.2.2.4 Water mass balance

The mass balance of (gel and capillary) water in the continuum medium is given by the following expression:

$$\frac{\partial M^{H}}{\partial t} = \bar{\Gamma}^{H} + J^{H} \tag{5.16}$$

where M^{H} [mol m^{-3}] is the concentration of water per unit volume of undeformed continuum medium, J^{H} [mol m^{-3} s^{-1}] is the net ingress of external water per unit volume of undeformed continuum medium, and $\bar{\Gamma}^{H}$ [mol m^{-3} s^{-1}] is the rate of water consumption/production by the chemical reactions per unit volume of undeformed continuum medium. Analogously, the mass balance of water in discontinuities is given by

$$\frac{\partial M_{mp}^{H}}{\partial t} = \bar{\Gamma}_{mp}^{H} + J_{mp}^{H} \tag{5.17}$$

where M^H_{mp} [mol m^{-2}] is the concentration of water per unit area of discontinuity, J^H_{mp} [mol m^{-2} s^{-1}] is the net ingress of external water per unit area of discontinuity, and $\bar{\Gamma}^H$ [mol m^{-2} s^{-1}] is the rate of water consumption/production by the chemical reactions per unit area of discontinuity.

In order to fulfil the above stated assumptions, J^H and J^H_{mp} are such that (gel and capillary) pores and cracks remain completely saturated with water, i.e. the volume of pore solution remains equal to the total volume of pores and cracks. Note that, since the volume of pores is determined by the solid skeleton, there is no need to explicitly consider the water content in order to solve Eq. (5.4) or (5.10).

The following general expression gives $\bar{\Gamma}^H$ as a function of the dissolution/precipitation reaction rates of solid the α-species ($\bar{\Gamma}^\alpha$) and the corresponding stoichiometric coefficients of water (x^H_α) and hydroxyl ions (x^{oh}_α):

$$\bar{\Gamma}^H = -\sum_\alpha \left(x^H_\alpha + x^{oh}_\alpha \right) \bar{\Gamma}^\alpha \tag{5.18}$$

5.2.2.5 Volumetric fraction balance

The updated total volume of continuum porous medium $\mathcal{U}$ [m^3 m$^{-3}_{\text{rv}}$] is given by

$$\mathcal{U} = \mathcal{U}^{cp} + \sum_\vartheta \mathcal{U}^\vartheta + \sum_\alpha \mathcal{U}^\alpha \tag{5.19}$$

where $\mathcal{U}^\vartheta$ [m^3 m$^{-3}_{\text{rv}}$] is the volume of inert solid ϑ-species, $\mathcal{U}^\alpha$ [m^3 m$^{-3}_{\text{rv}}$] is the volume of reactive solid α-species, and $\mathcal{U}^{cp}$ [m^3 m$^{-3}_{\text{rv}}$] is the volume of capillary pores. These volumes are given as fractions of the total volume in the initial (undeformed) configuration. That means that initially $\mathcal{U} = 1$.

Similarly, the updated total volume of a discontinuity $\mathcal{U}_{mp}$ [m^3 m$^{-2}_{\text{mp}}$] is given by

$$\mathcal{U}_{mp} = \mathcal{U}^{cp}_{mp} + \sum_\vartheta \mathcal{U}^\vartheta_{mp} + \sum_\alpha \mathcal{U}^\alpha_{mp} \tag{5.20}$$

where the volume fractions considered are the same as for the continuum medium but expressed per unit area of discontinuity mid-plane. Strictly speaking, $\mathcal{U}^{cp}$ [m^3 m$^{-2}_{\text{mp}}$] not only represents the volume of capillary pores, but also the empty volume crated by crack aperture, which is assumed to be filled with free water.

Since inert solid phases are not affected by the chemical reactions ($\partial \mathcal{U}^{\vartheta}/\partial t = 0$ and $\partial \mathcal{U}^{\vartheta}_{mp}/\partial t = 0$), the time rate of volume changes is given by

$$\frac{\partial \mathcal{U}}{\partial t} = \frac{\partial \mathcal{U}^{cp}}{\partial t} + \sum_{\alpha} \frac{\partial \mathcal{U}^{\alpha}}{\partial t} \tag{5.21}$$

$$\frac{\partial \mathcal{U}_{mp}}{\partial t} = \frac{\partial \mathcal{U}^{cp}_{mp}}{\partial t} + \sum_{\alpha} \frac{\partial \mathcal{U}^{\alpha}_{mp}}{\partial t} \tag{5.22}$$

The volumes of solid the α-species are obtained as follows:

$$\mathcal{U}^{\alpha} = \omega^{\alpha} M^{\alpha} \tag{5.23}$$

$$\mathcal{U}^{\alpha}_{mp} = \omega^{\alpha} M^{\alpha}_{mp} \tag{5.24}$$

where ω^{α} [$\mathrm{m}^3\ \mathrm{mol}^{-1}$] is the apparent molar volume which results from:

$$\omega^{\alpha} = \frac{\eta^{\alpha}}{1 - \phi^{\alpha}} \tag{5.25}$$

In Eq. (5.25), η^{α} [$\mathrm{m}^3\ \mathrm{mol}^{-1}$] is the 'specific' molar volume, and ϕ^{α} [$\mathrm{m}^3_{\mathrm{ps}}\ \mathrm{m}^{-3}$] is the gel porosity of the solid α-species. The apparent molar volume of solid the α-species is defined as the volume occupied the solid α-species itself (the specific volume) plus the volume occupied by the absorbed water (gel water volume). Then, 'gel porosity' is defined as the ratio between the gel water volume and the apparent volume of the solid α-species. Note that gel porosity is null for crystalline species such as portlandite or calcite.

The volumes of capillary pores in the continuum medium ($\mathcal{U}^{cp}$) and in discontinuities ($\mathcal{U}^{cp}_{mp}$) are calculated with expressions

$$\mathcal{U}^{cp} = \left\langle 1 - \sum_{\vartheta} \mathcal{U}^{\vartheta} - \sum_{\alpha} \mathcal{U}^{\alpha} \right\rangle_{+} \tag{5.26}$$

$$\mathcal{U}^{cp}_{mp} = \left\langle \mathcal{U}^{o}_{mp} + a^{cr}_{n} - \sum_{\vartheta} \mathcal{U}^{\vartheta}_{mp} - \sum_{\alpha} \mathcal{U}^{\alpha}_{mp} \right\rangle_{+} \tag{5.27}$$

where $\mathcal{U}^{o}_{mp}$ [$\mathrm{m}^3\ \mathrm{m}^{-2}$] is the initial volume of capillary pores of the ITZ, which is null for discontinuities in bulk aggregate or cementitious matrix, a^{cr}_{n} [m] is the normal aperture of the discontinuity, and the operator $\langle X \rangle_{+}$ stands for 'the positive part of X', i.e. if $X < 0$, $\langle X \rangle_{+} = 0$ otherwise $\langle X \rangle_{+} = X$. In a coupled analysis, a^{cr}_{n} is obtained by solving the mechanical problem stated in Section 5.3.

Since concrete is assumed to be fully saturated with water, the total volume of pore solution ($\mathcal{U}^{ps}$, $\mathcal{U}^{ps}_{mp}$) in the REV, which includes free and gel water, is equal to the total

volume of pores and/or clean crack aperture, i.e.

$$\mathcal{U}^{ps} = \mathcal{U}^{cp} + \sum_{\alpha} \phi^{\alpha} \mathcal{U}^{\alpha} + \sum_{\vartheta} \phi^{\vartheta} \mathcal{U}^{\vartheta} \tag{5.28}$$

$$\mathcal{U}^{ps}_{mp} = \mathcal{U}^{cp}_{mp} + \sum_{\alpha} \phi^{\alpha} \mathcal{U}^{\alpha}_{mp} + \sum_{\vartheta} \phi^{\vartheta} \mathcal{U}^{\vartheta}_{mp} \tag{5.29}$$

Finally, the total porosities ϕ and ϕ_{mp} are given by expressions:

$$\phi = \frac{\mathcal{U}^{ps}}{\mathcal{U}} \tag{5.30}$$

$$\phi_{mp} = \frac{\mathcal{U}^{ps}_{mp}}{\mathcal{U}_{mp}} \tag{5.31}$$

Eventually, the volume of reaction products may grow to a point in which the available space is exhausted, i.e. $\mathcal{U}^{cp} = 0$. From this point on, any additional volume of reaction products will impose a mechanical action at the reaction site. The nature of this action will depend on the mechanical constitutive laws adopted and may vary from one deleterious process to another.

5.2.2.6 Diffusion coefficients

The effective diffusivity D^{β} [m^2/s] of the aqueous β-species in the saturated porous medium depends on its microstructure, particularly on the capillary porosity ϕ^{cp}. As the reaction progresses the amount of solid phases may vary altering ϕ^{cp} and, consequently, the diffusivity D^{β}. Two extreme cases may be distinguished [159]. In the first one, there is no solid skeleton ($\phi^{cp} = 1$) and the diffusion occurs in free-water conditions. In the second one, there is no capillary porosity ($\phi^{cp} = 0$) and diffusion only occurs through gel- or nano-pores. For intermediate cases, effective diffusivity varies as a function of capillary porosity, depending on porous microstructural parameters such as tortuosity and constrictivity.

In Eq. (5.3), the effective diffusivity is conceptually related to the diffusivity in bulk water by means of the total porosity ϕ and a pore structure parameter λ. In order to consider the evolution of the diffusivity of the continuum porous medium with its microstructure, this relationship can be rewritten as:

$$D^{\beta} = D^{\beta}_{w} \cdot f(\phi^{cp}, D^{\beta}_{s}/D^{\beta}_{w}, k_1, k_2, \ldots, k_n) \tag{5.32}$$

where the function f is a dimensionless function of the capillary porosity ϕ^{cp}, the diffusivity of the β-species through the solid phases D^{β}_{s}, and a number of fitting parameters

$k_1, k_2, \ldots, k_n$ that account for microstructural features such as tortuosity and constrictivity. Note that different functions f may be considered depending on the deleterious process to be modelled.

The localized longitudinal and normal diffusivities of a discontinuity, T_l^β and D_n^β will be mainly determined by its width (w [m]), but also by the effective diffusivity of the filling material (D_f^β[m^2/s]), which in turn may depend on the same variables and parameters given for Eq. (5.32). Then,

$$T_l^\beta = f(w, D_f^\beta) \tag{5.33}$$

$$D_n^\beta = f(w, D_f^\beta) \tag{5.34}$$

5.2.2.7 Chemical kinetics

The calculation of reaction rates $\bar{\Gamma}^\alpha$ and $\bar{\Gamma}_{mp}^\alpha$ used in Eqs. (5.12) and (5.13), requires to establish the corresponding kinetic laws. It is assumed that the driving force of the dissolution/precipitation reaction of the reactive solid α-species is $(\psi^\alpha - 1)$, where ψ^α is the dimensionless saturation index of the pore solution with respect to the solid α-species. Dissolution and precipitation reactions are assumed not to occur simultaneously but alternately depending on ψ^α. If $\psi^\alpha > 1$, the solution is over-saturated with respect to the α-species and, consequently, the reaction progresses in the precipitation direction. If $\psi^\alpha < 1$, the solution is under-saturated and solid dissolution occurs. If $\psi^\alpha = 1$, the solid and the solution are in thermodynamical equilibrium. Generally, the formation rate is proportional to the volume of pore solution, while the dissolution rate, in contrast, is proportional to the surface of the α-species exposed to the pore solution.

The saturation indexes are assumed to be of the form

$$\psi^\alpha = \frac{1}{K_{sp}^\alpha} \prod_\beta \left(a^\beta\right)^{x_\alpha^\beta} \tag{5.35}$$

where K_{sp}^α is the saturation product constant of the α-species, and a^β [mol m^{-3}] is the thermodynamic activity of the aqueous β-species in pore solution. The product may include all the aqueous species intervening in the formation of the solid α-species, or only part of them.

5.2.2.8 Thermodynamic activity

In order to account for deviations from ideal behaviour of the aqueous β-species in pore solution due to the interactions with other aqueous species, activity a^β is considered in

chemical equilibrium equations instead of concentration c^β. Activity and concentration are related by means of a dimensionless factor γ^β (activity coefficient) as follows

$$a^\beta = \gamma^\beta c^\beta \tag{5.36}$$

In the present formulation, activity coefficients are calculated using Eq. (5.37), where z^β is the number of electric charges of the β-species considered, I [mol/L] is the ionic strength of the solution, and A_γ is the Debye-Hückel parameter. This equation is the well-known Davies Equation with the modification of the second term proposed by Samson and Lemaire [177], in order to extend its applicability to solutions at ionic strengths up to 1.20 mol/L. The expression of I is given in Eq. (5.38). The Debye-Hückel parameter is given as a function of temperature in Appendix B.2.

$$\log_{10}\gamma^\beta = -A_\gamma \left(z^\beta\right)^2 \left[\frac{\sqrt{I}}{1+\sqrt{I}} - \left(0.2I - \frac{I^2}{24}\right)\right] \tag{5.37}$$

$$I = \frac{1}{2}\sum_\beta \left(z^\beta\right)^2 c^\beta \tag{5.38}$$

5.2.2.9 Chemical speciation

The concentration of secondary species in pore solution is determined locally as a function of the concentration of primary species. This is achieved by simultaneously enforcing the following equations:

$$\sum_\beta z^\beta c^\beta = 0 \tag{5.39}$$

$$K_{eq}^w = a^h a^{oh} \tag{5.40}$$

$$K_{eq}^{AB} = \frac{a^A a^B}{a^{AB}} \tag{5.41}$$

The first equation enforces the electrical charge neutrality of the solution. The second one is the equilibrium equation of water self-dissociation, Reaction (5.42), where the superscripts *oh* and *h* stand for OH^- and H^+, and K_{eq}^w is the water self-ionization constant. The third equation above is the equilibrium equation of a generic ionic dissociation of the aqueous species AB (Reaction (5.43)), being K_{eq}^{AB} the corresponding equilibrium constant.

$$H_2O \longleftrightarrow H^+ + OH^- \tag{5.42}$$

$$AB \longleftrightarrow A^+ + B^- \tag{5.43}$$

The number of dissociation reactions to be considered will depend on the deleterious process considered. Considering previous Eqs. (5.39)–(5.41) plus Eqs. (5.36) and (5.37), it is possible to determine the equilibrium concentrations of any given secondary species as a function of the concentrations of the primary ones by solving the resultant nonlinear system of equations. This is achieved by a mix of analytical and numerical procedures, which is described in detail for the ASR model in the next chapter (Section 6.4.7).

5.2.3 Space discretization (FE formulation)

In this section, the above obtained governing equations are discretized in space by means of the FEM. For the continuum porous medium, this is achieved through the classical Galerkin's Weighted Residual (GWR) method and the Principle of Virtual Work (PVW). For discontinuities, the FE formulation of zero-thickness interface elements originally proposed by Segura and Carol for diffusion problems through clean discontinuities [191] has been adapted in order to consider diffusion-reaction processes through discontinuities filled with porous materials.

5.2.3.1 Continuum porous medium

The equivalent integral form of the governing differential equations given in Section 5.2.2.1 is obtained applying the GWR method. In this manner, multiplying Eqs. (5.4) and (5.5b) by the weighting functions W and $\bar{W}$, and integrating over the domain Ω and the boundary $\partial\Omega$, respectively, gives:

$$\int_\Omega W \left[\nabla^T D^\beta \nabla c^\beta - \frac{\partial(\phi c^\beta)}{\partial t} + q^\beta\right] d\Omega + \oint_{\partial\Omega^{j^\beta}} \bar{W}\left[\mathbf{n}^T D^\beta \nabla c^\beta + \bar{j}_b^\beta + \phi h(c^\beta - c_a^\beta)\right] d\partial\Omega = 0 \tag{5.44}$$

Integrating by parts the terms with second derivatives and adopting $W = -\bar{W}$ one obtains:

$$-\int_\Omega (\nabla^T W) D^\beta \nabla c^\beta d\Omega + \oint_{\partial\Omega^{c^\beta}+\underline{\partial\Omega^{j^\beta}}} W \mathbf{n}^T D^\beta \nabla c^\beta d\partial\Omega - \int_\Omega W \frac{\partial(\phi c^\beta)}{\partial t} d\Omega + \int_\Omega W q^\beta d\Omega - \oint_{\partial\Omega^{j^\beta}} W\left[\underline{\mathbf{n}^T D^\beta \nabla c^\beta} + \bar{j}_b^\beta + \phi h(c^\beta - c_a^\beta)\right] d\partial\Omega = 0 \tag{5.45}$$

where the terms underlined cancel each other. The resulting integral form is:

$$-\int_\Omega (\nabla^T W) D^\beta \nabla c^\beta d\Omega - \oint_{\partial\Omega^{c^\beta}} W j_b^\beta d\partial\Omega - \int_\Omega W \frac{\partial(\phi c^\beta)}{\partial t} d\Omega + \int_\Omega W q^\beta d\Omega - \oint_{\partial\Omega^{j^\beta}} W\left[\bar{j}_b^\beta + \phi h(c^\beta - c_a^\beta)\right] d\partial\Omega = 0 \tag{5.46}$$

where $j_b^\beta = -\mathbf{n}^T D^\beta \nabla c^\beta$ (eq. (5.6)) has been introduced in the second term. Selecting $W = \delta c^\beta$ as a virtual increment of the concentration and $\nabla W = \nabla \delta c^\beta$ as the corresponding virtual gradient vector, Eq. (5.46) may be rewritten as

$$-\int_\Omega (\nabla^T \delta c^\beta) D^\beta \nabla c^\beta d\Omega - \oint_{\partial\Omega^{c^\beta}} \delta c^\beta j_b^\beta d\partial\Omega - \int_\Omega \delta c^\beta \left(\dot{\phi} c^\beta + \phi \dot{c}^\beta\right) d\Omega + \int_\Omega \delta c^\beta q^\beta d\Omega - \oint_{\partial\Omega^{j^\beta}} \delta c^\beta \left[\bar{j}_b^\beta + \phi h (c^\beta - c_a^\beta)\right] d\partial\Omega = 0 \tag{5.47}$$

where the dot notation ($\dot{X} = \partial X/\partial t$) has been used and the derivative of the product has been developed in the third term.

Let us now assume a discretization of the domain Ω using 2D finite elements with n nodes. The real distribution of concentrations of the β-species within this element (c^β) is approximated by the interpolation of the nodal values $\tilde{c}^\beta$:

$$c^\beta(x,y,t) \approx \tilde{c}^\beta(x,y,t) = \sum_{i=1}^{n} N_i^\beta(x,y) c_i^\beta(t) = \mathbf{N}_\mathbf{e}^\beta \cdot \mathbf{c}_\mathbf{e}^\beta \tag{5.48}$$

where c_i^β and N_i^β are the concentration at node i and the corresponding shape function, respectively, x and y are the global spatial coordinates, and t stands for elapsed time. For a quadrilateral linear element, i.e. $n = 4$, the expressions for the shape function and nodal concentrations matrices are, respectively,

$$\mathbf{N}_\mathbf{e}^\beta = \begin{bmatrix} N_1^\beta & N_2^\beta & N_3^\beta & N_4^\beta \end{bmatrix}_{(x,y)} \tag{5.49}$$

$$\mathbf{c}_\mathbf{e}^{\beta T} = \begin{bmatrix} c_1^\beta & c_2^\beta & c_3^\beta & c_4^\beta \end{bmatrix}^T \tag{5.50}$$

Similarly, applying Eq. (5.48), virtual increments δc^β at any point within the element can be obtained as functions of the virtual increments at element nodes:

$$\delta c^\beta \approx \mathbf{N}_\mathbf{e}^\beta \cdot \delta \mathbf{c}_\mathbf{e}^\beta = \left(\mathbf{N}_\mathbf{e}^\beta \cdot \delta \mathbf{c}_\mathbf{e}^\beta\right)^T = \left(\delta \mathbf{c}_\mathbf{e}^\beta\right)^T \cdot \mathbf{N}_\mathbf{e}^{\beta T} \tag{5.51}$$

Substituting the approximations of c^β and δc^β (Eqs. (5.48) and (5.51)) into the weak form Eq. (5.47) we obtain:

$$-\int_\Omega \left(\delta \mathbf{c}_\mathbf{e}^\beta\right)^T \left(\nabla \mathbf{N}_\mathbf{e}^\beta\right)^T D^\beta \nabla \mathbf{N}_\mathbf{e}^\beta \mathbf{c}_\mathbf{e}^\beta d\Omega - \oint_{\partial\Omega^{c^\beta}} \left(\delta \mathbf{c}_\mathbf{e}^\beta\right)^T \mathbf{N}_\mathbf{e}^{\beta T} j_b^\beta d\partial\Omega - \int_\Omega \left(\delta \mathbf{c}_\mathbf{e}^\beta\right)^T \mathbf{N}_\mathbf{e}^{\beta T} \left(\dot{\phi} c^\beta + \phi \dot{c}^\beta\right) d\Omega + \int_\Omega \left(\delta \mathbf{c}_\mathbf{e}^\beta\right)^T \mathbf{N}_\mathbf{e}^{\beta T} q^\beta d\Omega - \oint_{\partial\Omega^{j^\beta}} \left(\delta \mathbf{c}_\mathbf{e}^\beta\right)^T \mathbf{N}_\mathbf{e}^{\beta T} \left[\bar{j}_b^\beta + \phi h (\mathbf{N}_\mathbf{e}^\beta \mathbf{c}_\mathbf{e}^\beta - c_a^\beta)\right] d\partial\Omega = 0 \tag{5.52}$$

Since virtual increments are arbitrary, the previous equation leads to

$$-\int_{\Omega}\left(\nabla\mathbf{N}_{\mathbf{e}}^{\beta}\right)^{T}D^{\beta}\nabla\mathbf{N}_{\mathbf{e}}^{\beta}\mathbf{c}_{\mathbf{e}}^{\beta}d\Omega-\oint_{\partial\Omega^{c^{\beta}}}\mathbf{N}_{\mathbf{e}}^{\beta T}j_{b}^{\beta}d\partial\Omega-\int_{\Omega}\mathbf{N}_{\mathbf{e}}^{\beta T}\left(\dot{\phi}c^{\beta}+\phi\dot{c}^{\beta}\right)d\Omega$$
$$+\int_{\Omega}\mathbf{N}_{\mathbf{e}}^{\beta T}q^{\beta}d\Omega-\oint_{\partial\Omega^{j^{\beta}}}\mathbf{N}_{\mathbf{e}}^{\beta T}\left[\bar{j}_{b}^{\beta}+\phi h(\mathbf{N}_{\mathbf{e}}^{\beta}\mathbf{c}_{\mathbf{e}}^{\beta}-c_{a}^{\beta})\right]d\partial\Omega=0 \tag{5.53}$$

which can be rearranged as

$$\mathbf{E}_{\mathbf{e}}^{\beta}\mathbf{c}_{\mathbf{e}}^{\beta}+\dot{\mathbf{S}}_{\mathbf{e}}^{\beta}\mathbf{c}_{\mathbf{e}}^{\beta}+\mathbf{S}_{\mathbf{e}}^{\beta}\dot{\mathbf{c}}_{\mathbf{e}}^{\beta}-\mathbf{Q}_{\mathbf{e}}^{\beta}+\mathbf{F}_{\mathbf{e}}^{\beta}=\mathbf{0} \tag{5.54}$$

where

$$\mathbf{E}_{\mathbf{e}}^{\beta}=\int_{\Omega_{e}}(\nabla\mathbf{N}_{\mathbf{e}}^{\beta})^{T}D^{\beta}\nabla\mathbf{N}_{\mathbf{e}}^{\beta}d\Omega+\int_{\partial\Omega_{e}^{j^{\beta}}}\mathbf{N}_{\mathbf{e}}^{\beta T}\phi h\mathbf{N}_{\mathbf{e}}^{\beta}d\partial\Omega \tag{5.55}$$

$$\mathbf{S}_{\mathbf{e}}^{\beta}=\int_{\Omega_{e}}\mathbf{N}_{\mathbf{e}}^{\beta T}\phi\mathbf{N}_{\mathbf{e}}^{\beta}d\Omega \tag{5.56}$$

$$\dot{\mathbf{S}}_{\mathbf{e}}^{\beta}=\int_{\Omega_{e}}\mathbf{N}_{\mathbf{e}}^{\beta T}\dot{\phi}\mathbf{N}_{\mathbf{e}}^{\beta}d\Omega \tag{5.57}$$

$$\mathbf{Q}_{\mathbf{e}}^{\beta}=\int_{\Omega_{e}}\mathbf{N}_{\mathbf{e}}^{\beta T}q^{\beta}d\Omega \tag{5.58}$$

$$\mathbf{F}_{\mathbf{e}}^{\beta}=\int_{\partial\Omega_{e}^{j^{\beta}}}\mathbf{N}_{\mathbf{e}}^{\beta T}(\bar{j}_{b}^{\beta}-\phi hc_{a}^{\beta})d\partial\Omega+\int_{\partial\Omega_{e}^{c^{\beta}}}\mathbf{N}_{\mathbf{e}}^{\beta T}j_{b}^{\beta}d\partial\Omega \tag{5.59}$$

$\mathbf{E}_{\mathbf{e}}^{\beta}$ [m^3 s^{-1}] is the diffusivity matrix; $\mathbf{S}_{\mathbf{e}}^{\beta}$ [m^3] is the capacity matrix; $\dot{\mathbf{S}}_{\mathbf{e}}^{\beta}$ [m^3 s^{-1}] is the capacity matrix rate; $\mathbf{Q}_{\mathbf{e}}^{\beta}$ [mol s^{-1}] is nodal 'force' vector corresponding to volumetric chemical source q^{β}; $\mathbf{F}_{\mathbf{e}}^{\beta}$ [mol s^{-1}] is the nodal flux vector corresponding to prescribed flux over boundary part $\partial\Omega_{e}^{j^{\beta}}$ and to the fluxes resulting from prescribed values of concentration over boundary part $\partial\Omega_{e}^{c^{\beta}}$.

Equation (5.54) reflects the mass balance of the β-species within the element, taking into account the nodal fluxes due to internal diffusion, internal chemical sources, and imposed boundary conditions. For the general case of an element sharing nodes with other neighbouring elements, Eq.(5.54) is modified as follows:

$$\mathbf{E}_{\mathbf{e}}^{\beta}\mathbf{c}_{\mathbf{e}}^{\beta}+\dot{\mathbf{S}}_{\mathbf{e}}^{\beta}\mathbf{c}_{\mathbf{e}}^{\beta}+\mathbf{S}_{\mathbf{e}}^{\beta}\dot{\mathbf{c}}_{\mathbf{e}}^{\beta}-\mathbf{Q}_{\mathbf{e}}^{\beta}+\mathbf{F}_{\mathbf{e}}^{\beta}=\mathbf{f}_{\mathbf{e}}^{\beta} \tag{5.60}$$

where $\mathbf{f}_{\mathbf{e}}^{\beta}$ [mol s^{-1}] is the vector of nodal fluxes coming from neighbouring elements at shared nodes.

5.2.3.2 Discontinuities

For the FE discretization of discontinuities, zero-thickness interface elements with 'double nodes' proposed by Segura and Carol [191] for diffusion problems are considered. These are interface elements with 4 or 6 nodes, depending on its linear or quadratic character respectively (see for instance the linear element sketched in Fig. 5.3).

In order to obtain the FE formulation for these elements, some auxiliary points are defined on the interface mid-plane and in between nodes facing each other (Fig. 5.3). Concentrations in these mid-plane points are considered only as auxiliary variables, which will be finally eliminated in terms of the 'external' node variables, and therefore will not appear in the final element formulation. In the following, the formulation will be developed for linear elements although an analogous procedure would be valid for quadratic order elements.

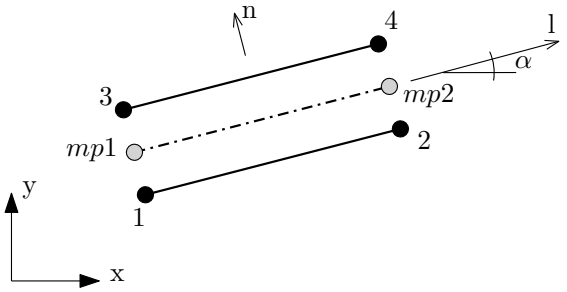

FIGURE 5.3: Linear double-nodded interface element.

The 'mid-plane points' define a 1D auxiliary element which is used to discretize the mid-plane of the discontinuity as sketched in Fig. 5.4a. The real distribution of concentration along the discontinuity axis (c^{β}_{mp}) is approximated through interpolation of the nodal concentration values ($\tilde{c}^{\beta}_{mp}$):

$$c^{\beta}_{mp}(x,y,t) \approx \tilde{c}^{\beta}_{mp}(x,y,t) = \sum_{i=1}^{n} N^{\beta}_{mp_i}(x,y) c^{\beta}_{mp_i}(t) = \mathbf{N}^{\beta}_{\mathbf{mp_e}} \cdot \mathbf{c}^{\beta}_{\mathbf{mp_e}} \tag{5.61}$$

where $c^{\beta}_{mp_i}$ and $N^{\beta}_{mp_i}$ are the concentration at node i and the corresponding shape function, respectively, x and y are the global spatial coordinates and t stands for elapsed time. For a linear element, i.e. $n = 2$, the expressions for the shape functions and nodal concentration vectors are, respectively:

$$\mathbf{N}^{\beta}_{\mathbf{mp_e}} = \begin{bmatrix} N^{\beta}_{mp_1} & N^{\beta}_{mp_2} \end{bmatrix}; \quad \mathbf{c}^{\beta}_{\mathbf{mp_e}} = \begin{bmatrix} c^{\beta}_{mp_1} & c^{\beta}_{mp_2} \end{bmatrix}^T \tag{5.62}$$

In order to express this formulation in terms of the main variables at the actual nodes, it is assumed that the concentration field along the mid-plane of the discontinuity is the

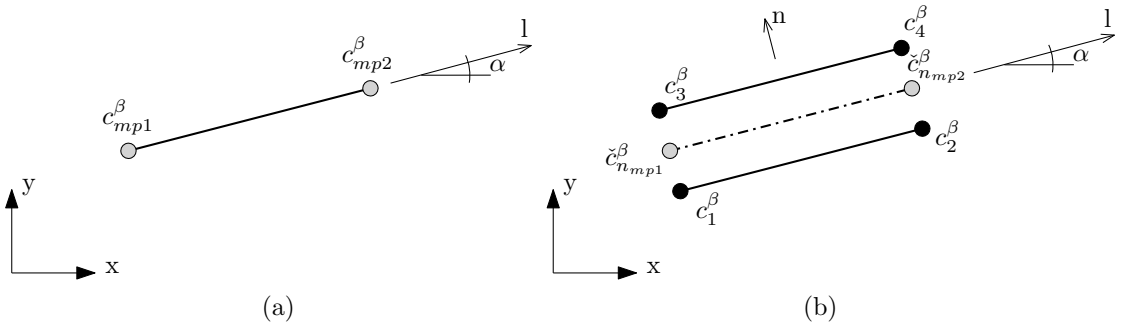

FIGURE 5.4: Interface elements used in the FE formulation with regard to (a) longitudinal flow and (b) transversal flow.

average of the concentration field on the upper and lower sides of the interface:

$$c^\beta_{mp} = \frac{c^\beta_{bot} + c^\beta_{top}}{2} \tag{5.63}$$

This assumption is supposed to be valid all along the mid-plane including the 'mid-plane points' and may be expressed as:

$$\mathbf{c^\beta_{mp_e}} = \begin{bmatrix} c^\beta_{mp_1} \\ c^\beta_{mp_1} \end{bmatrix} = \begin{bmatrix} \frac{c^\beta_1 + c^\beta_3}{2} \\ \frac{c^\beta_2 + c^\beta_4}{2} \end{bmatrix} = \frac{1}{2} \begin{bmatrix} \mathbf{I_2} & \mathbf{I_2} \end{bmatrix} \mathbf{c^\beta_{j_e}} \tag{5.64}$$

where $\mathbf{c^\beta_{j_e}} = \begin{bmatrix} c^\beta_1 & c^\beta_2 & c^\beta_3 & c^\beta_4 \end{bmatrix}^T$ are the nodal concentrations, and $\mathbf{I_2}$ is the 2×2 identity matrix. Introduction of Eq. (5.64) in Eq. (5.61) leads to the expression of concentration at any point of the mid-plane in terms of the nodal concentration values:

$$c^\beta_{mp} = \frac{1}{2} \mathbf{N^\beta_{mp_e}} \begin{bmatrix} \mathbf{I_2} & \mathbf{I_2} \end{bmatrix} \mathbf{c^\beta_{j_e}} \tag{5.65}$$

The zero-thickness interface element with double nodes is considered now, see Fig. 5.4b. The formulation is first developed in the local joint element axes, and later is extended to the real interface nodes. Each mid-plane auxiliary node is located 'in between' the two nodes facing each other, what in practice means the same coordinates for both if (as usual) the two nodes in the pair have same location. The transversal jump of the concentration ($\check{c}^\beta$) at each mid-point is interpolated between the corresponding pair of nodes:

$$\check{c}^\beta_{mp}(x, y, t) \approx \sum_{j=1}^{n} N^\beta_{mp_j}(x, y) \check{c}^\beta_{mp_j}(t) = \mathbf{N^\beta_{mp_e}} \cdot \check{\mathbf{c}}^\beta_{\mathbf{mp_e}} \tag{5.66}$$

where the shape function vector ($\mathbf{N}^{\beta}_{\mathbf{mp_e}}$) has the same expression as in Eq. (5.62), and the mid-plane nodal vector concentration drop is:

$$\check{\mathbf{c}}^{\beta}_{\mathbf{mp_e}} = \begin{bmatrix} \check{c}^{\beta}_{mp_1} & \check{c}^{\beta}_{mp_2} \end{bmatrix}^T \tag{5.67}$$

In order to relate the nodal flows to the nodal concentration values in terms of the real nodes, we define the concentration drop at the mid-plane node as the difference of concentration between the two surrounding real nodes:

$$\check{\mathbf{c}}^{\beta}_{\mathbf{mp_e}} = \begin{bmatrix} \check{c}^{\beta}_{mp_1} \\ \check{c}^{\beta}_{mp_2} \end{bmatrix} = \begin{bmatrix} c^{\beta}_1 - c^{\beta}_3 \\ c^{\beta}_2 - c^{\beta}_4 \end{bmatrix} = \begin{bmatrix} \mathbf{I_2} & -\mathbf{I_2} \end{bmatrix} \cdot \mathbf{c}^{\beta}_{\mathbf{j_e}} \tag{5.68}$$

Then, introducing Eq. (5.68) in Eq. (5.66) we can obtain:

$$\check{c}^{\beta}_{mp} = \mathbf{N}^{\beta}_{\mathbf{mp_e}} \begin{bmatrix} \mathbf{I_2} & -\mathbf{I_2} \end{bmatrix} \mathbf{c}^{\beta}_{\mathbf{j_e}} \tag{5.69}$$

The FE equation for interface elements is obtained now on the basis of the analogy between the mechanical and the diffusion problems and making use of the PVW, that in classical mechanical analyses reads as:

$$\delta \mathbf{u_e}^T \cdot \mathbf{f_e} = \int_{\Omega_e} (\delta \boldsymbol{\varepsilon})^T \cdot (\boldsymbol{\sigma} + \kappa \dot{\boldsymbol{\varepsilon}} + \rho \ddot{\boldsymbol{\varepsilon}})\, d\Omega_e \tag{5.70}$$

where $\delta \mathbf{u_e}$ is a nodal virtual displacement, $\delta \boldsymbol{\varepsilon}$ is the associated deformation, $\mathbf{f_e}$ is the nodal force vector, $\boldsymbol{\sigma}$ is the internal stress, κ is the damping parameter, ρ is the mass density, and Ω_e is the element domain. The analogy between mechanical and diffusion FEM based formulation is described next:

$$\mathbf{u} = (\mathbf{N^u})^T \mathbf{u_e} \quad \Longleftrightarrow \begin{cases} c^{\beta}_{mp} = \mathbf{N}^{\beta}_{\mathbf{mp_e}} \cdot \mathbf{c}^{\beta}_{\mathbf{mp_e}} \\ \check{c}^{\beta}_{mp} = \mathbf{N}^{\beta}_{\mathbf{mp_e}} \cdot \check{\mathbf{c}}_{\mathbf{mp_e}} \end{cases}$$

$$\boldsymbol{\varepsilon} = \mathbf{L^u u} = \mathbf{B^u_e u_e} \quad \Longleftrightarrow \begin{cases} \dfrac{\partial c^{\beta}_{mp}}{\partial l} = \dfrac{\partial \mathbf{N}^{\beta}_{\mathbf{mp_e}}}{\partial l} \mathbf{c}^{\beta}_{\mathbf{mp_e}} \\ \check{c}_{mp} = \mathbf{N}^{\beta}_{\mathbf{mp_e}} \cdot \check{\mathbf{c}}_{\mathbf{mp_e}} \end{cases}$$

$$\dot{\boldsymbol{\varepsilon}} = \mathbf{L^u \dot{u}} = \mathbf{B^u_e \dot{u}_e} \quad \Longleftrightarrow \begin{cases} \dfrac{\partial c^{\beta}_{mp}}{\partial t} = \mathbf{N}^{\beta}_{\mathbf{mp_e}} \cdot \dfrac{\partial \mathbf{c}^{\beta}_{\mathbf{mp_e}}}{\partial t} \end{cases}$$

$$\boldsymbol{\sigma} = \mathbf{D^u \varepsilon} = \mathbf{D^u B^u_e u_e} \quad \Longleftrightarrow \begin{cases} j^{\beta}_l = \dfrac{J^{\beta}_l}{w} = -\dfrac{T^{\beta}_l}{w} \dfrac{\partial c^{\beta}_{mp}}{\partial l} = -\dfrac{T^{\beta}_l}{w} \dfrac{\partial \mathbf{N}^{\beta}_{\mathbf{mp_e}}}{\partial l} \mathbf{c}^{\beta}_{\mathbf{mp_e}} \\ j^{\beta}_n = T^{\beta}_n \check{c}^{\beta}_{mp} = T^{\beta}_n \mathbf{N}^{\beta}_{\mathbf{mp_e}} \cdot \check{\mathbf{c}}_{\mathbf{mp_e}} \end{cases}$$

where $\mathbf{u}$ is the displacement field vector, $\mathbf{u_e}$ is the nodal displacement vector, $\mathbf{N^u}$ is the displacement shape function matrix, $\mathbf{L^u}$ is the differential operator, $\mathbf{B^u}$ is the strain operator, $\boldsymbol{\sigma}$ is the stress field vector, and $\mathbf{D^u}$ is the mechanical constitutive matrix.

In this way, the nodal concentrations ($\mathbf{c}^{\beta}_{\mathbf{mp_e}}$) and the nodal concentration jump ($\check{\mathbf{c}}_{\mathbf{mp_e}}$) play the role of the nodal displacement ($\mathbf{u_e}$), the longitudinal concentration gradient and transversal concentration jump fields ($\partial c^{\beta}_{mp}/\partial l$ and $\check{c}^{\beta}_{mp}$) play the role of the strain field ($\boldsymbol{\varepsilon}$), and the longitudinal and transverse flows (j_l and j_n) behave as the stress field ($\boldsymbol{\sigma}$). According to this analogy we may express the PVW adapted to the diffusion-reaction problem as:

$$(\delta\mathbf{c_{j_e}})^T\,\mathbf{f}^{\beta}_{\mathbf{j_e}} = \int_{l_{mp}} \delta c^{\beta}_{mp}\frac{\partial(w\phi_{mp}c^{\beta}_{mp})}{\partial t}dl - \int_{l_{mp}}\left(\frac{\partial\delta c^{\beta}_{mp}}{\partial l}\right)J_l dl - \int_{l_{mp}}\delta c^{\beta}_{mp}q^{\beta}_{mp}dl + \int_{l_{mp}}\delta\check{c}^{\beta}_{mp}j^{\beta}_{n}dl \tag{5.71}$$

where $\mathbf{f}^{\beta}_{\mathbf{j_e}}$ is the induced nodal flux of β-species, and $\delta\mathbf{c_{j_e}}$ is the nodal virtual variation of concentration. The first three right-hand terms correspond to governing equation (5.8) and the last one to Eq. (5.11). The second right-hand term results from applying Green's theorem.

The derivative of the product is developed in the first term of the right-hand side of Eq. (5.71), and Eq. (5.9) and (5.11) are introduced to obtain:

$$(\delta\mathbf{c_{j_e}})^T\,\mathbf{f}^{\beta}_{\mathbf{j_e}} = \int_{l_{mp}}\delta c^{\beta}_{mp}\phi_{mp}w\frac{\partial c^{\beta}_{mp}}{\partial t}dl + \int_{l_{mp}}\delta c^{\beta}_{mp}(\phi_{mp}\dot{w}+\dot{\phi}_{mp}w)c^{\beta}_{mp}dl + \int_{l_{mp}}\left(\frac{\partial\delta c^{\beta}_{mp}}{\partial l}\right)T^{\beta}_{l}\left(\frac{\partial c^{\beta}_{mp}}{\partial l}\right)dl - \int_{l_{mp}}\delta c^{\beta}_{mp}q^{\beta}_{mp}dl + \int_{l_{mp}}\delta\check{c}^{\beta}_{mp}D^{\beta}_{n}\check{c}^{\beta}_{mp}dl \tag{5.72}$$

Now, applying Eq. (5.61), (5.64), (5.66) and (5.68) we can write:

$$\delta c^{\beta}_{mp} = (\delta\mathbf{c_{j_e}})^T\frac{1}{2}\begin{bmatrix}\mathbf{I_2}\\ \mathbf{I_2}\end{bmatrix}\left(\mathbf{N}^{\beta}_{\mathbf{mp_e}}\right)^T \tag{5.73}$$

$$c^{\beta}_{mp} = \mathbf{N}^{\beta}_{\mathbf{mp_e}}\frac{1}{2}\begin{bmatrix}\mathbf{I_2} & \mathbf{I_2}\end{bmatrix}\mathbf{c}^{\beta}_{\mathbf{j_e}} \tag{5.74}$$

$$\frac{\partial c^{\beta}_{mp}}{\partial t} = \mathbf{N}^{\beta}_{\mathbf{mp_e}}\frac{1}{2}\begin{bmatrix}\mathbf{I_2} & \mathbf{I_2}\end{bmatrix}\dot{\mathbf{c}}^{\beta}_{\mathbf{j_e}} \tag{5.75}$$

$$\frac{\partial\delta c^{\beta}_{mp}}{\partial l} = \left(\delta\mathbf{c}^{\beta}_{\mathbf{j_e}}\right)^T\frac{1}{2}\begin{bmatrix}\mathbf{I_2}\\ \mathbf{I_2}\end{bmatrix}\left(\frac{\partial\mathbf{N}^{\beta}_{\mathbf{mp_e}}}{\partial l}\right)^T \tag{5.76}$$

$$\frac{\partial c^{\beta}_{mp}}{\partial l} = \frac{\partial\mathbf{N}^{\beta}_{\mathbf{mp_e}}}{\partial l}\frac{1}{2}\begin{bmatrix}\mathbf{I_2} & \mathbf{I_2}\end{bmatrix}\mathbf{c}^{\beta}_{\mathbf{j_e}} \tag{5.77}$$

$$\delta\check{c}^{\beta}_{mp} = (\delta\mathbf{c_{j_e}})^T\begin{bmatrix}\mathbf{I_2}\\ -\mathbf{I_2}\end{bmatrix}\left(\mathbf{N}^{\beta}_{\mathbf{mp_e}}\right)^T \tag{5.78}$$

$$\check{c}_{mp}^{\beta} = \mathbf{N}_{\mathbf{mp_e}}^{\beta} \begin{bmatrix} \mathbf{I_2} & -\mathbf{I_2} \end{bmatrix} \mathbf{c}_{\mathbf{j_e}} \tag{5.79}$$

Replacing these expressions in Eq. (5.72) and operating we get:

$$\begin{aligned} \left(\delta \mathbf{c}_{\mathbf{j_e}}^{\beta}\right)^T \mathbf{f}_{\mathbf{j_e}}^{\beta} = & \int_{l_{mp}} \left(\delta \mathbf{c}_{\mathbf{j_e}}^{\beta}\right)^T \frac{1}{2} \begin{bmatrix} \mathbf{I_2} \\ \mathbf{I_2} \end{bmatrix} \left(\mathbf{N}_{\mathbf{mp_e}}^{\beta}\right)^T (\phi_{mp}\dot{w} + \dot{\phi}_{mp} w) \mathbf{N}_{\mathbf{mp_e}}^{\beta} \frac{1}{2} \begin{bmatrix} \mathbf{I_2} & \mathbf{I_2} \end{bmatrix} \mathbf{c}_{\mathbf{j_e}} dl \\ & + \int_{l_{mp}} \left(\delta \mathbf{c}_{\mathbf{j_e}}^{\beta}\right)^T \frac{1}{2} \begin{bmatrix} \mathbf{I_2} \\ \mathbf{I_2} \end{bmatrix} \left(\mathbf{N}_{\mathbf{mp_e}}^{\beta}\right)^T (\phi_{mp} w) \mathbf{N}_{\mathbf{mp_e}}^{\beta} \frac{1}{2} \begin{bmatrix} \mathbf{I_2} & \mathbf{I_2} \end{bmatrix} \dot{\mathbf{c}}_{\mathbf{j_e}} dl \\ & + \int_{l_{mp}} \left(\delta \mathbf{c}_{\mathbf{j_e}}^{\beta}\right)^T \frac{1}{2} \begin{bmatrix} \mathbf{I_2} \\ \mathbf{I_2} \end{bmatrix} \left(\frac{\partial \mathbf{N}_{\mathbf{mp_e}}^{\beta}}{\partial l}\right)^T T_l^{\beta} \frac{\partial \mathbf{N}_{\mathbf{mp_e}}^{\beta}}{\partial l} \frac{1}{2} \begin{bmatrix} \mathbf{I_2} & \mathbf{I_2} \end{bmatrix} \mathbf{c}_{\mathbf{j_e}} dl \\ & - \int_{l_{mp}} \left(\delta \mathbf{c}_{\mathbf{j_e}}^{\beta}\right)^T \frac{1}{2} \begin{bmatrix} \mathbf{I_2} \\ \mathbf{I_2} \end{bmatrix} \left(\mathbf{N}_{\mathbf{mp_e}}^{\beta}\right)^T q_{mp}^{\beta} dl \\ & + \int_{l_{mp}} \left(\delta \mathbf{c}_{\mathbf{j_e}}^{\beta}\right)^T \begin{bmatrix} \mathbf{I_2} \\ -\mathbf{I_2} \end{bmatrix} \left(\mathbf{N}_{\mathbf{mp_e}}^{\beta}\right)^T D_n^{\beta} \mathbf{N}_{\mathbf{mp_e}}^{\beta} \begin{bmatrix} \mathbf{I_2} & -\mathbf{I_2} \end{bmatrix} \mathbf{c}_{\mathbf{j_e}} dl \end{aligned} \tag{5.80}$$

Since this equation must be fulfilled for any virtual concentration increment $\delta \mathbf{c}_{\mathbf{j_e}}^{\beta}$, it can be simplified as follows:

$$\begin{aligned} \mathbf{f}_{\mathbf{j_e}}^{\beta} = & \frac{1}{2} \begin{bmatrix} \mathbf{I_2} \\ \mathbf{I_2} \end{bmatrix} \left[\int_{l_{mp}} \left(\mathbf{N}_{\mathbf{mp_e}}^{\beta}\right)^T (\phi_{mp}\dot{w} + \dot{\phi}_{mp} w) \mathbf{N}_{\mathbf{mp_e}}^{\beta} dl \right] \frac{1}{2} \begin{bmatrix} \mathbf{I_2} & \mathbf{I_2} \end{bmatrix} \mathbf{c}_{\mathbf{j_e}} \\ & + \frac{1}{2} \begin{bmatrix} \mathbf{I_2} \\ \mathbf{I_2} \end{bmatrix} \left[\int_{l_{mp}} \left(\mathbf{N}_{\mathbf{mp_e}}^{\beta}\right)^T (\phi_{mp} w) \mathbf{N}_{\mathbf{mp_e}}^{\beta} dl \right] \frac{1}{2} \begin{bmatrix} \mathbf{I_2} & \mathbf{I_2} \end{bmatrix} \dot{\mathbf{c}}_{\mathbf{j_e}} \\ & + \frac{1}{2} \begin{bmatrix} \mathbf{I_2} \\ \mathbf{I_2} \end{bmatrix} \left[\int_{l_{mp}} \left(\frac{\partial \mathbf{N}_{\mathbf{mp_e}}^{\beta}}{\partial l}\right)^T T_l^{\beta} \frac{\partial \mathbf{N}_{\mathbf{mp_e}}^{\beta}}{\partial l} dl \right] \frac{1}{2} \begin{bmatrix} \mathbf{I_2} & \mathbf{I_2} \end{bmatrix} \mathbf{c}_{\mathbf{j_e}} \\ & - \frac{1}{2} \begin{bmatrix} \mathbf{I_2} \\ \mathbf{I_2} \end{bmatrix} \left[\int_{l_{mp}} \left(\mathbf{N}_{\mathbf{mp_e}}^{\beta}\right)^T q_{mp}^{\beta} dl \right] \\ & + \begin{bmatrix} \mathbf{I_2} \\ -\mathbf{I_2} \end{bmatrix} \left[\int_{l_{mp}} \left(\mathbf{N}_{\mathbf{mp_e}}^{\beta}\right)^T D_n^{\beta} \mathbf{N}_{\mathbf{mp_e}}^{\beta} dl \right] \begin{bmatrix} \mathbf{I_2} & -\mathbf{I_2} \end{bmatrix} \mathbf{c}_{\mathbf{j_e}} \end{aligned} \tag{5.81}$$

If the corresponding matricial products are performed:

$$\begin{aligned} \mathbf{f}_{\mathbf{j_e}}^{\beta} = & \frac{1}{2} \begin{bmatrix} \mathbf{I_2} \\ \mathbf{I_2} \end{bmatrix} \dot{\mathbf{S}}_{\mathbf{mp_e}}^{\beta} \frac{1}{2} \begin{bmatrix} \mathbf{I_2} & \mathbf{I_2} \end{bmatrix} \mathbf{c}_{\mathbf{j_e}}^{\beta} \\ & + \frac{1}{2} \begin{bmatrix} \mathbf{I_2} \\ \mathbf{I_2} \end{bmatrix} \mathbf{S}_{\mathbf{mp_e}}^{\beta} \frac{1}{2} \begin{bmatrix} \mathbf{I_2} & \mathbf{I_2} \end{bmatrix} \dot{\mathbf{c}}_{\mathbf{j_e}}^{\beta} + \frac{1}{2} \begin{bmatrix} \mathbf{I_2} \\ \mathbf{I_2} \end{bmatrix} \mathbf{E}_{\mathbf{Lmp_e}}^{\beta} \frac{1}{2} \begin{bmatrix} \mathbf{I_2} & \mathbf{I_2} \end{bmatrix} \mathbf{c}_{\mathbf{j_e}}^{\beta} \end{aligned}$$

$$-\frac{1}{2}\begin{bmatrix}\mathbf{I_2}\\ \mathbf{I_2}\end{bmatrix}\mathbf{Q}^{\beta}_{\mathbf{mp_e}}+\begin{bmatrix}\mathbf{I_2}\\ -\mathbf{I_2}\end{bmatrix}\mathbf{E}^{\beta}_{\mathbf{Nmp_e}}\begin{bmatrix}\mathbf{I_2} & -\mathbf{I_2}\end{bmatrix}\mathbf{c}^{\beta}_{\mathbf{j_e}} \tag{5.82}$$

$$\begin{aligned}\mathbf{f}^{\beta}_{\mathbf{j_e}}=&\frac{1}{4}\begin{bmatrix}\dot{\mathbf{S}}^{\beta}_{\mathbf{mp_e}} & \dot{\mathbf{S}}^{\beta}_{\mathbf{mp_e}}\\ \dot{\mathbf{S}}^{\beta}_{\mathbf{mp_e}} & \dot{\mathbf{S}}^{\beta}_{\mathbf{mp_e}}\end{bmatrix}\mathbf{c}^{\beta}_{\mathbf{j_e}}+\frac{1}{4}\begin{bmatrix}\mathbf{S}^{\beta}_{\mathbf{mp_e}} & \mathbf{S}^{\beta}_{\mathbf{mp_e}}\\ \mathbf{S}^{\beta}_{\mathbf{mp_e}} & \mathbf{S}^{\beta}_{\mathbf{mp_e}}\end{bmatrix}\dot{\mathbf{c}}^{\beta}_{\mathbf{j_e}}+\frac{1}{4}\begin{bmatrix}\mathbf{E}^{\beta}_{\mathbf{Lmp_e}} & \mathbf{E}^{\beta}_{\mathbf{Lmp_e}}\\ \mathbf{E}^{\beta}_{\mathbf{Lmp_e}} & \mathbf{E}^{\beta}_{\mathbf{Lmp_e}}\end{bmatrix}\mathbf{c}^{\beta}_{\mathbf{j_e}}\\ &-\frac{1}{2}\begin{bmatrix}\mathbf{Q}^{\beta}_{\mathbf{mp_e}}\\ \mathbf{Q}^{\beta}_{\mathbf{mp_e}}\end{bmatrix}+\begin{bmatrix}\mathbf{E}^{\beta}_{\mathbf{Nmp_e}} & -\mathbf{E}^{\beta}_{\mathbf{Nmp_e}}\\ -\mathbf{E}^{\beta}_{\mathbf{Nmp_e}} & \mathbf{E}^{\beta}_{\mathbf{Nmp_e}}\end{bmatrix}\mathbf{c}^{\beta}_{\mathbf{j_e}}\end{aligned} \tag{5.83}$$

Finally, collecting all the terms, the FE equation for the diffusion-reaction problem through the interface element is obtained as:

$$\mathbf{f}^{\beta}_{\mathbf{j_e}}=\mathbf{E}^{\beta}_{\mathbf{j_e}}\mathbf{c}^{\beta}_{\mathbf{j_e}}+\dot{\mathbf{S}}^{\beta}\mathbf{c}^{\beta}_{\mathbf{j_e}}+\mathbf{S}^{\beta}_{\mathbf{j_e}}\dot{\mathbf{c}}^{\beta}_{\mathbf{j_e}}-\mathbf{Q}^{\beta}_{\mathbf{j_e}} \tag{5.84}$$

where

$$\mathbf{E}^{\beta}_{\mathbf{j_e}}=\mathbf{E}^{\beta}_{\mathbf{Lj_e}}+\mathbf{E}^{\beta}_{\mathbf{Nj_e}} \tag{5.85}$$

$$\mathbf{E}^{\beta}_{\mathbf{Lj_e}}=\frac{1}{4}\begin{bmatrix}\mathbf{E}^{\beta}_{\mathbf{Lmp_e}} & \mathbf{E}^{\beta}_{\mathbf{Lmp_e}}\\ \mathbf{E}^{\beta}_{\mathbf{Lmp_e}} & \mathbf{E}^{\beta}_{\mathbf{Lmp_e}}\end{bmatrix} \tag{5.86}$$

$$\mathbf{E}^{\beta}_{\mathbf{Nj_e}}=\begin{bmatrix}\mathbf{E}^{\beta}_{\mathbf{Nmp_e}} & \mathbf{E}^{\beta}_{\mathbf{Nmp_e}}\\ \mathbf{E}^{\beta}_{\mathbf{Nmp_e}} & \mathbf{E}^{\beta}_{\mathbf{Nmp_e}}\end{bmatrix} \tag{5.87}$$

$$\mathbf{S}^{\beta}_{\mathbf{j_e}}=\frac{1}{4}\begin{bmatrix}\mathbf{S}^{\beta}_{\mathbf{mp_e}} & \mathbf{S}^{\beta}_{\mathbf{mp_e}}\\ \mathbf{S}^{\beta}_{\mathbf{mp_e}} & \mathbf{S}^{\beta}_{\mathbf{mp_e}}\end{bmatrix} \tag{5.88}$$

$$\dot{\mathbf{S}}^{\beta}_{\mathbf{j_e}}=\frac{1}{4}\begin{bmatrix}\dot{\mathbf{S}}^{\beta}_{\mathbf{mp_e}} & \dot{\mathbf{S}}^{\beta}_{\mathbf{mp_e}}\\ \dot{\mathbf{S}}^{\beta}_{\mathbf{mp_e}} & \dot{\mathbf{S}}^{\beta}_{\mathbf{mp_e}}\end{bmatrix} \tag{5.89}$$

$$\mathbf{Q}^{\beta}_{\mathbf{j_e}}=\frac{1}{2}\begin{bmatrix}\mathbf{Q}^{\beta}_{\mathbf{mp_e}}\\ \mathbf{Q}^{\beta}_{\mathbf{mp_e}}\end{bmatrix} \tag{5.90}$$

and

$$\mathbf{E}^{\beta}_{\mathbf{Nmp_e}}=\int_{l_{mp}}\left(\mathbf{N}^{\beta}_{\mathbf{mp_e}}\right)^{T}D^{\beta}_{n}\mathbf{N}^{\beta}_{\mathbf{mp_e}}dl \tag{5.91}$$

$$\mathbf{E}^{\beta}_{\mathbf{Lmp_e}}=\int_{l_{mp}}\left(\frac{\partial\mathbf{N}^{\beta}_{\mathbf{mp_e}}}{\partial l}\right)^{T}T^{\beta}_{l}\frac{\partial\mathbf{N}^{\beta}_{\mathbf{mp_e}}}{\partial l}dl \tag{5.92}$$

$$\dot{\mathbf{S}}^{\beta}_{\mathbf{mp_e}}=\int_{l_{mp}}\left(\mathbf{N}^{\beta}_{\mathbf{mp_e}}\right)^{T}(\phi_{mp}\dot{w}+\dot{\phi}_{mp}w)\mathbf{N}^{\beta}_{\mathbf{mp_e}}dl \tag{5.93}$$

$$\mathbf{S}^{\beta}_{\mathbf{mp_e}}=\int_{l_{mp}}\left(\mathbf{N}^{\beta}_{\mathbf{mp_e}}\right)^{T}(\phi_{mp}w)\mathbf{N}^{\beta}_{\mathbf{mp_e}}dl \tag{5.94}$$

$$\mathbf{Q}^{\beta}_{\mathbf{mp_e}}=\int_{l_{mp}}\left(\mathbf{N}^{\beta}_{\mathbf{mp_e}}\right)^{T}q^{\beta}_{mp}dl \tag{5.95}$$

$\mathbf{E}^{\beta}_{\mathbf{je}}$ [m^3 s^{-1}] is the diffusivity matrix; $\mathbf{S}^{\beta}_{\mathbf{je}}$ [m^3] is the capacity matrix; $\dot{\mathbf{S}}^{\beta}_{\mathbf{je}}$ [m^3 s^{-1}] is the capacity matrix rate; $\mathbf{Q}^{\beta}_{\mathbf{je}}$ [mol s^{-1}] is nodal 'force' vector corresponding to chemical source per unit area of discontinuity q^{β}_{mp}.

5.2.3.3 Extension to multiple aqueous species

The solute mass balance equation in the continuum porous medium Eq. (5.4) is extended to n aqueous β-species as

$$\begin{cases} \dfrac{\partial(\phi c^{\beta_1})}{\partial t} = \nabla^T \left(D^{\beta_1} \nabla c^{\beta_1}\right) + q^{\beta_1}\left(c^{\beta_1}, \ldots, c^{\beta_n}\right) \\ \vdots \qquad\qquad \vdots \qquad\qquad \vdots \\ \dfrac{\partial(\phi c^{\beta_n})}{\partial t} = \nabla^T \left(D^{\beta_n} \nabla c^{\beta_n}\right) + q^{\beta_n}\left(c^{\beta_1}, \ldots, c^{\beta_n}\right) \end{cases} \tag{5.96}$$

where the n equations are coupled through the source terms q^{β}. Similarly, the solute mass balance equations for a discontinuity, Eqs. (5.10) and (5.11), are extended to n aqueous β-species:

$$\begin{cases} \dfrac{\partial(w\phi_{mp} c^{\beta_1}_{mp})}{\partial t} = \dfrac{\partial}{\partial l}\left(T^{\beta_1}_{l} \dfrac{\partial c^{\beta_1}_{mp}}{\partial l}\right) + q^{\beta_1}_{mp}; \quad j^{\beta_1}_{n} = D^{\beta_1}_{n} \check{c}^{\beta_1}_{mp} \\ \vdots \qquad\qquad \vdots \qquad\qquad \vdots \qquad \vdots \qquad \vdots \\ \dfrac{\partial(w\phi_{mp} c^{\beta_n}_{mp})}{\partial t} = \dfrac{\partial}{\partial l}\left(T^{\beta_n}_{l} \dfrac{\partial c^{\beta_n}_{mp}}{\partial l}\right) + q^{\beta_n}_{mp}; \quad j^{\beta_n}_{n} = D^{\beta_n}_{n} \check{c}^{\beta_n}_{mp} \end{cases} \tag{5.97}$$

Again, the n equations are coupled through the source terms. Both systems of equations can be written in matrix notation as follows:

$$\phi \dot{\mathbb{c}} + \dot{\phi} \mathbb{c} = \mathbf{L}^T \left(\mathbf{D}\mathbf{L}\mathbb{c}\right) + \mathbf{q} \tag{5.98}$$

$$\dot{w}\phi_{mp}\mathbb{c} + w\dot{\phi}_{mp}\mathbb{c} + w\phi_{mp}\dot{\mathbb{c}} = \mathbf{L}^T_{l} \left(\mathbf{T}_{l}\mathbf{L}_{l}\mathbb{c}\right) + \mathbf{q} \tag{5.99}$$

$$\mathbf{j_n} = \mathbf{D}_n \check{\mathbb{c}} \tag{5.100}$$

with

$$\mathbb{c} = \begin{bmatrix} c^{\beta_1} & \cdots & c^{\beta_n} \end{bmatrix}^T \tag{5.101}$$

$$\check{\mathbb{c}} = \begin{bmatrix} \check{c}^{\beta_1} & \cdots & \check{c}^{\beta_n} \end{bmatrix}^T \tag{5.102}$$

$$\dot{\mathbb{c}} = \begin{bmatrix} \frac{\partial c^{\beta_1}}{\partial t} & \cdots & \frac{\partial c^{\beta_n}}{\partial t} \end{bmatrix}^T \tag{5.103}$$

$$\mathbf{L} = \left[\begin{array}{ccc|ccc} \frac{\partial}{\partial x} & & 0 & \frac{\partial}{\partial y} & & 0 \\ & \ddots & & & \ddots & \\ 0 & & \frac{\partial}{\partial x} & 0 & & \frac{\partial}{\partial y} \end{array}\right]^T \tag{5.104}$$

$$\mathbf{L}_l = \begin{bmatrix} \frac{\partial}{\partial l} & & 0 \\ & \ddots & \\ 0 & & \frac{\partial}{\partial l} \end{bmatrix}^T \tag{5.105}$$

$$\mathbf{D} = \left[\begin{array}{ccc|ccc} D_x^{\beta_1} & & 0 & & & \\ & \ddots & & & 0 & \\ 0 & & D_x^{\beta_n} & & & \\ \hline & & & D_y^{\beta_1} & & 0 \\ & 0 & & & \ddots & \\ & & & 0 & & D_y^{\beta_n} \end{array}\right] \tag{5.106}$$

$$\mathbf{T}_l = \begin{bmatrix} T_l^{\beta_1} & & 0 \\ & \ddots & \\ 0 & & T_l^{\beta_n} \end{bmatrix} \tag{5.107}$$

$$\mathbf{D}_n = \begin{bmatrix} D_n^{\beta_1} & & 0 \\ & \ddots & \\ 0 & & D_n^{\beta_n} \end{bmatrix} \tag{5.108}$$

$$\mathbf{q} = \begin{bmatrix} q^{\beta_1} & \cdots & q^{\beta_n} \end{bmatrix}^T \tag{5.109}$$

$$\mathbf{j_n} = \begin{bmatrix} j_n^{\beta_1} & \cdots & j_n^{\beta_n} \end{bmatrix}^T \tag{5.110}$$

In order to obtain the corresponding FE formulation, the interpolation Eqs. (5.48), (5.65) and (5.69) have to be rewritten as:

$$\mathbb{c} = \mathbf{N_e c_e} \tag{5.111}$$

$$\mathbb{c}_{mp} = \mathbf{N_{mp_e}} \begin{bmatrix} \mathbf{I_{2n}} & \mathbf{I_{2n}} \end{bmatrix} \mathbf{c_{j_e}} \tag{5.112}$$

$$\check{\mathbb{c}}_{mp} = \frac{1}{2} \mathbf{N_{mp_e}} \begin{bmatrix} \mathbf{I_{2n}} & -\mathbf{I_{2n}} \end{bmatrix} \mathbf{c_{j_e}} \tag{5.113}$$

which correspond to quadrangular linear elements and double nodded linear interface elements. There, $\mathbf{c_e}$ is the nodal concentration vector of a continuum element, $\mathbf{c_{e_j}}$ is the nodal concentration vector of an interface element, $\mathbf{I_{2n}}$ is the $2n \times 2n$ identity matrix, and

$$\mathbf{N_e} = \begin{bmatrix} \mathbf{N_{e1}} & \mathbf{N_{e2}} & \mathbf{N_{e3}} & \mathbf{N_{e4}} \end{bmatrix}; \quad \text{with } \mathbf{N_{ei}} = \begin{bmatrix} N_i^\beta & 0 & 0 \\ 0 & N_i^\beta & 0 \\ 0 & 0 & N_i^\beta \end{bmatrix} \tag{5.114}$$

$$\mathbf{N_{mp_e}} = \begin{bmatrix} \mathbf{N_{mp_{e1}}} & \mathbf{N_{mp_{e2}}} \end{bmatrix}; \quad \text{with } \mathbf{N_{mp_{ei}}} = \begin{bmatrix} N_{mpi}^\beta & 0 & 0 \\ 0 & N_{mpi}^\beta & 0 \\ 0 & 0 & N_{mpi} \end{bmatrix} \tag{5.115}$$

where N_i and N_{mpi} are linear shape functions.

Then, following analogous steps to those described in Section 5.2.3.1, the following FE equation is obtained for continuum elements:

$$\mathbf{E_e c_e} + \dot{\mathbf{S}}_\mathbf{e}\mathbf{c_e} + \mathbf{S_e}\dot{\mathbf{c}}_\mathbf{e} - \mathbf{Q_e} + \mathbf{F_e} = \mathbf{f_e} \tag{5.116}$$

where

$$\mathbf{E_e} = \int_{\Omega_e} (\mathbf{LN_e})^T \mathbf{D} \mathbf{LN_e} d\Omega + \int_{\partial\Omega_e^j} \mathbf{N_e}^T \phi h \mathbf{N_e} d\partial\Omega \tag{5.117}$$

$$\mathbf{S_e} = \int_{\Omega_e} \mathbf{N_e}^T \phi \mathbf{N_e} d\Omega \tag{5.118}$$

$$\dot{\mathbf{S}}_\mathbf{e} = \int_{\Omega_e} \mathbf{N_e}^T \dot{\phi} \mathbf{N_e} d\Omega \tag{5.119}$$

$$\mathbf{Q_e} = \int_{\Omega_e} \mathbf{N_e}^T \mathbf{q} d\Omega \tag{5.120}$$

$$\mathbf{F_e} = \int_{\partial\Omega_e^j} \mathbf{N_e}^T (\bar{\mathbf{j}}_b - \phi h \mathbb{c}_a) d\partial\Omega + \int_{\partial\Omega_e^c} \mathbf{N_e}^T \mathbf{j}_b d\partial\Omega \tag{5.121}$$

Similarly, following the steps of Section 5.2.3.2, the follow FE equation is obtained for interface elements:

$$\mathbf{E_{j_e}} \mathbf{c_{j_e}} + \dot{\mathbf{S}}\mathbf{c_{j_e}} + \mathbf{S_{j_e}}\dot{\mathbf{c}}_\mathbf{j_e} - \mathbf{Q_{j_e}} = \mathbf{f_{j_e}} \tag{5.122}$$

where

$$\mathbf{E_{j_e}} = \mathbf{E_{Lj_e}} + \mathbf{E_{Nj_e}} \tag{5.123}$$

$$\mathbf{E_{Lj_e}} = \frac{1}{4} \begin{bmatrix} \mathbf{E_{Lmp_e}} & \mathbf{E_{Lmp_e}} \\ \mathbf{E_{Lmp_e}} & \mathbf{E_{Lmp_e}} \end{bmatrix} \tag{5.124}$$

$$\mathbf{E_{Nj_e}} = \begin{bmatrix} \mathbf{E_{Nmp_e}} & \mathbf{E_{Nmp_e}} \\ \mathbf{E_{Nmp_e}} & \mathbf{E_{Nmp_e}} \end{bmatrix} \tag{5.125}$$

$$\mathbf{S_{j_e}} = \frac{1}{4} \begin{bmatrix} \mathbf{S_{mp_e}} & \mathbf{S_{mp_e}} \\ \mathbf{S_{mp_e}} & \mathbf{S_{mp_e}} \end{bmatrix} \tag{5.126}$$

$$\dot{\mathbf{S}}_\mathbf{j_e} = \frac{1}{4} \begin{bmatrix} \dot{\mathbf{S}}_\mathbf{mp_e} & \dot{\mathbf{S}}_\mathbf{mp_e} \\ \dot{\mathbf{S}}_\mathbf{mp_e} & \dot{\mathbf{S}}_\mathbf{mp_e} \end{bmatrix} \tag{5.127}$$

$$\mathbf{Q_{j_e}} = \frac{1}{2} \begin{bmatrix} \mathbf{Q_{mp_e}} \\ \mathbf{Q_{mp_e}} \end{bmatrix} \tag{5.128}$$

and

$$\mathbf{E_{Nmp_e}} = \int_{l_{mp}} (\mathbf{N_{mp_e}})^T \mathbf{D_n} \mathbf{N_{mp_e}} dl \tag{5.129}$$

$$\mathbf{E_{Lmp_e}} = \int_{l_{mp}} (\mathbf{L}_l \mathbf{N_{mp_e}})^T \mathbf{T}_l \mathbf{L}_l \mathbf{N_{mp_e}} dl \tag{5.130}$$

$$\dot{\mathbf{S}}_{\mathbf{mp_e}} = \int_{l_{mp}} (\mathbf{N_{mp_e}})^T (\phi_{mp} \dot{w} + \dot{\phi}_{mp} w) \mathbf{N_{mp_e}} dl \tag{5.131}$$

$$\mathbf{S_{mp_e}} = \int_{l_{mp}} (\mathbf{N_{mp_e}})^T (\phi_{mp} w) \mathbf{N_{mp_e}} dl \tag{5.132}$$

$$\mathbf{Q_{mp_e}} = \int_{l_{mp}} (\mathbf{N_{mp_e}})^T \mathbf{q_{mp}} dl \tag{5.133}$$

5.2.3.4 Discontinuous porous medium

After assembly of the continuum and zero-thickness interface elements, the nodal flows cancel and a single system of equations in terms of the concentration of aqueous β-species in pore solution at the nodes is reached for the whole problem domain. Assembly of Eq. (5.116) for the continuum elements and Eq. (5.122) for the interfaces gives the following system of equations for the boundary value problem under analysis after spatial discretization:

$$\mathbf{E}\mathbf{c} + \dot{\mathbf{S}}\mathbf{c} + \mathbf{S}\dot{\mathbf{c}} - \mathbf{Q} + \mathbf{F} = \mathbf{0} \tag{5.134}$$

5.2.4 Time discretization

The generalized trapezoidal rule is considered in order to discretize Eq. (5.134) in time. If the problem is to be solved between an initial time t_0 and a final time t_f, a partition of the time interval $[t_0, t_f]$ is considered, which results in a series of time increments $\Delta t_{n+1} = t_{n+1} - t_n$. During a given time step Δt_{n+1}, the variation of the nodal concentration vector $\mathbf{c}$ is linearly approximated by means of the the following expression:

$$\mathbf{c}_{n+\theta} = (1-\theta)\mathbf{c}_n + \theta \mathbf{c}_{n+1} = \mathbf{c}_n + \theta \Delta \mathbf{c}_{n+1} \tag{5.135a}$$

$$\dot{\mathbf{c}}_{n+\theta} = \left[\frac{d\mathbf{c}}{dt}\right]_{n+\theta} = \frac{1}{\Delta t_{n+1}} \Delta \mathbf{c}_{n+1} \tag{5.135b}$$

where $\Delta \mathbf{c}_{n+1} = \mathbf{c}_{n+1} - \mathbf{c}_n$. Similarly, the variations of the diffusivity matrix, the capacity matrix and the imposed flux vector in Δt_{n+1} are also linearly approximated:

$$\mathbf{E}_{n+\theta} = (1-\theta)\mathbf{E}_n + \theta \mathbf{E}_{n+1} \tag{5.136a}$$

$$\mathbf{S}_{n+\theta} = (1-\theta)\mathbf{S}_n + \theta \mathbf{S}_{n+1} \tag{5.136b}$$

$$\dot{\mathbf{S}}_{n+\theta} = \left[\frac{d\mathbf{S}}{dt}\right]_{n+\theta} = \frac{1}{\Delta t_{n+1}}\left(\mathbf{S}_{n+1} - \mathbf{S}_n\right) \tag{5.136c}$$

$$\mathbf{F}_{n+\theta} = (1-\theta)\mathbf{F}_n + \theta\mathbf{F}_{n+1} \tag{5.136d}$$

The chemical source vector, in contrast, is obtained at time $t_{n+\theta}$ as a function of the linearly interpolated concentration vector $\mathbf{c}_{n+\theta}$, i.e.

$$\mathbf{Q}_{n+\theta} = \mathbf{Q}\left(\mathbf{c}_{n+\theta}^{\beta_1}, \mathbf{c}_{n+\theta}^{\beta_2}, \ldots, \mathbf{c}_{n+\theta}^{\beta_n}\right) \tag{5.137}$$

The value of θ may vary between 0 and 1 depending on the time integration scheme considered, as shown in Table 5.1:

TABLE 5.1: Time-marching schemes according to the value of θ.

θ	**Time integration scheme**
0	forward finite differences (Euler)
1/2	central finite differences (Crank-Nicholson)
1	backward finite differences
2/3	Galerkin Method
7/8	Lambert Method

5.2.5 Numerical solution

Let us consider the function $\mathbf{c}(t)$ to be an approximation to the solution of Eq. (5.134) in the time interval Δt_{n+1}, then the corresponding residual vector is defined as:

$$\mathbb{I}_{n+1} = \int_{t_n}^{t_{n+1}} \left[\mathbf{E}(\tau)\mathbf{c}(\tau) + \dot{\mathbf{S}}(\tau)\mathbf{c}(\tau) + \mathbf{S}(\tau)\dot{\mathbf{c}}(\tau) + \mathbf{F}(\tau) - \mathbf{Q}(\tau)\right] d\tau \tag{5.138}$$

Then, using the time discretization proposed above, the terms of Eq. (5.138) can be rewritten as follow:

$$\int_{t_n}^{t_{n+1}} \mathbf{E}(\tau)\mathbf{c}(\tau)d\tau \approx \left[(1-\theta)\mathbf{E}_n + \theta\mathbf{E}_{n+1}\right]\left[(1-\theta)\mathbf{c}_n + \theta\mathbf{c}_{n+1}\right]\Delta t_{n+1} \tag{5.139a}$$

$$\int_{t_n}^{t_{n+1}} \dot{\mathbf{S}}(\tau)\mathbf{c}(\tau)d\tau \approx \left(\mathbf{S}_{n+1} - \mathbf{S}_n\right)\left[(1-\theta)\mathbf{c}_n + \theta\mathbf{c}_{n+1}\right] \tag{5.139b}$$

$$\int_{t_n}^{t_{n+1}} \mathbf{S}(\tau)\dot{\mathbf{c}}(\tau)d\tau \approx \left[(1-\theta)\mathbf{S}_n + \theta\mathbf{S}_{n+1}\right]\left(\mathbf{c}_{n+1} - \mathbf{c}_n\right) \tag{5.139c}$$

$$\int_{t_n}^{t_{n+1}} \mathbf{F}(\tau)d\tau \approx \left[(1-\theta)\mathbf{F}_n + \theta\mathbf{F}_{n+1}\right]\Delta t_{n+1} \tag{5.139d}$$

$$\int_{t_n}^{t_{n+1}} \mathbf{Q}(\tau)d\tau \approx \mathbf{I}_{\mathbf{Q}}(\mathbf{c}_n, \mathbf{c}_{n+1}) \tag{5.139e}$$

Since the variation of $\mathbf{E}$ with time is usually small, it has been found that the first term can be further simplified, without inducing significant error, by assuming a linear variation of the product $\mathbf{Ec}$, i.e.

$$\int_{t_n}^{t_{n+1}} \mathbf{E}(\tau)\mathbf{c}(\tau)d\tau \approx \left[(1-\theta)\mathbf{E}_n\mathbf{c}_n + \theta\mathbf{E}_{n+1}\mathbf{c}_{n+1}\right]\Delta t_{n+1} \tag{5.140}$$

The vector $\mathbf{I_Q}$ [mol] represents the nodal net production of aqueous species obtained by assuming linear variation of the nodal concentrations between $\mathbf{c}_n$ and $\mathbf{c}_{n+1}$. The procedure to obtain $\mathbf{I_Q}$ is discussed in the next Section.

Then, being known the values of $\mathbf{E}_n$, $\mathbf{S}_n$, $\mathbf{F}_n$ and $\mathbf{c}_n$, the residual vector ${}^i\mathbb{I}_{n+1}$ for given trial values ${}^i\mathbf{E}_{n+1}$, ${}^i\mathbf{S}_{n+1}$, ${}^i\mathbf{F}_{n+1}$ and ${}^i\mathbf{c}_{n+1}$ can be approximated by means of:

$$\begin{aligned} {}^i\mathbb{I}_{n+1} = {} & \overbrace{\left[(1-\theta)\Delta t\mathbf{E}_n - 2(1-\theta)\mathbf{S}_n\right]\mathbf{c}_n - (1-\theta)\Delta t\mathbf{F}_n}^{\text{fix}} \\ & + \left[\theta\Delta t\,{}^i\mathbf{E}_{n+1} + (1-2\theta)\mathbf{S}_n + 2\theta\,{}^i\mathbf{S}_{n+1}\right]{}^i\mathbf{c}_{n+1} \\ & + (1-2\theta)\,{}^i\mathbf{S}_{n+1}\mathbf{c}_n - \theta\Delta t\,{}^i\mathbf{F}_{n+1} - {}^i\mathbf{I_Q} \end{aligned} \tag{5.141}$$

In order to improve the initial approximation to the solution, a Taylor's series of the residual vector as a function of $\mathbf{c}_{n+1}$ is proposed:

$$\mathbb{I}({}^{i+1}\mathbf{c}_{n+1}) \approx \mathbb{I}({}^i\mathbf{c}_{n+1}) + \left.\frac{\partial\mathbb{I}}{\partial\mathbf{c}}\right|_{{}^i\mathbf{c}_{n+1}} {}^{i+1}\delta\mathbf{c}_{n+1} + \mathcal{O}_2 \tag{5.142}$$

Forcing $\mathbb{I}({}^{i+1}\mathbf{c}_{n+1}) = 0$ and neglecting the truncation error $\mathcal{O}_2$ we get:

$${}^i\mathbb{K}^{i+1}\delta\mathbf{c}_{n+1} = -\mathbb{I}({}^i\mathbf{c}_{n+1}) \tag{5.143}$$

where

$${}^i\mathbb{K} = \left.\frac{\partial\mathbb{I}}{\partial\mathbf{c}}\right|_{{}^i\mathbf{c}_{n+1}} = \theta\Delta t\,{}^i\mathbf{E}_{n+1} + (1-2\theta)\mathbf{S}_n + 2\theta\,{}^i\mathbf{S}_{n+1} - \theta\left.\frac{\partial\mathbf{I_Q}}{\partial\mathbf{c}}\right|_{{}^i\mathbf{c}_{n+1}} \tag{5.144}$$

is the tangent 'stiffness' matrix. Solving this linear system of equations we obtain an improvement ${}^{i+1}\delta\mathbf{c}_{n+1}$ of the initial approximation such as ${}^{i+1}\mathbf{c}_{n+1} = {}^i\mathbf{c}_{n+1} + {}^{i+1}\delta\mathbf{c}_{n+1}$. With ${}^{i+1}\mathbf{c}_{n+1}$ the corresponding ${}^{i+1}\mathbf{E}_{n+1}$, ${}^{i+1}\mathbf{S}_{n+1}$, ${}^{i+1}\mathbf{F}_{n+1}$ and ${}^{i+1}\mathbf{I_Q}$ are calculated and replaced in Eq. (5.141) to obtain the updated residual vector. This iterative procedure continues until the module of the residual vector reaches a pre-established tolerance. Note that the terms indicated as 'fix' in Eq. (5.141) remain constant along of the iterative process. The calculation of the derivative of vector $\mathbf{I_Q}$ with respect to the nodal concentration vector (last term of Eq. (5.144)) is described in detail in the following section.

5.2.6 Time integration of the chemical law

Equation (5.139e) can be rewritten for a single continuum element as

$$\mathbf{I_{Q_e}}(\mathbf{c}_{\mathbf{e}n}, \mathbf{c}_{\mathbf{e}n+1}) = \int_{t_n}^{t_{n+1}} \mathbf{Q_e}(\tau) d\tau \tag{5.145}$$

Introducing Eq. (5.120),

$$\mathbf{I_{Q_e}}(\mathbf{c}_{\mathbf{e}n}, \mathbf{c}_{\mathbf{e}n+1}) = \int_{t_n}^{t_{n+1}} \int_{\Omega_e} \mathbf{N_e}^T \mathbf{q}(\tau) d\Omega d\tau \tag{5.146}$$

This equation can be rearranged as

$$\mathbf{I_{Q_e}}(\mathbf{c}_{\mathbf{e}n}, \mathbf{c}_{\mathbf{e}n+1}) = \int_{\Omega_e} \mathbf{N_e}^T \underbrace{\left[\int_{t_n}^{t_{n+1}} \mathbf{q}(\tau) d\tau \right]}_{\mathbf{i_q}} d\Omega \tag{5.147}$$

where vector $\mathbf{i_q}$ is the time integral of the chemical source vector ($\mathbf{q}$) when a linear variation of the concentration vector $\mathbb{c}$ is assumed. The components of vector $\mathbf{i_q}$ are

$$\mathbf{i_q}(\mathbb{c}_n, \mathbb{c}_{n+1}) = \begin{bmatrix} \int_{t_n}^{t_{n+1}} q^{\beta_1}(\tau) d\tau \\ \vdots \\ \int_{t_n}^{t_{n+1}} q^{\beta_n}(\tau) d\tau \end{bmatrix} \tag{5.148}$$

By introducing Eq. (5.12), these integrals may be rewritten as

$$\int_{t_n}^{t_{n+1}} q^{\beta_i}(\tau) d\tau = -\sum_{\alpha} x_{\alpha_i}^{\beta_i} \int_{t_n}^{t_{n+1}} \bar{\Gamma}^{\alpha_i}(\mathbb{c}, \mathbb{M}) d\tau \tag{5.149}$$

where $\mathbb{M} = \begin{bmatrix} M^{\alpha_1} & \cdots & M^{\alpha_n} \end{bmatrix}^T$ is the vector of local solid concentrations. If we now integrate Eq. (5.14),

$$\int_{t_n}^{t_{n+1}} \bar{\Gamma}^{\alpha_i}(\mathbb{c}, \mathbb{M}) d\tau = M_{n+1}^{\alpha_i} - M_n^{\alpha_i} \tag{5.150}$$

and introduce it in Eq. (5.149), then Eq. (5.148) may be rewritten as:

$$\mathbf{i_q} = \begin{bmatrix} -\sum_{\alpha} x_{\alpha_i}^{\beta_1} (M_{n+1}^{\alpha_i} - M_n^{\alpha_i}) \\ \vdots \\ -\sum_{\alpha} x_{\alpha_i}^{\beta_n} (M_{n+1}^{\alpha_i} - M_n^{\alpha_i}) \end{bmatrix} \tag{5.151}$$

Finally, $\mathbf{i_q}$ is obtained by solving locally the following system of integral equations:

$$\begin{cases} M_{n+1}^{\alpha_1} = M_n^{\alpha_1} + \int_{t_n}^{t_{n+1}} \bar{\Gamma}^{\alpha_1}(\mathbb{c}, \mathbb{M}) d\tau \\ \vdots \qquad\quad \vdots \qquad\quad \vdots \\ M_{n+1}^{\alpha_n} = M_n^{\alpha_n} + \int_{t_n}^{t_{n+1}} \bar{\Gamma}^{\alpha_n}(\mathbb{c}, \mathbb{M}) d\tau \end{cases} \tag{5.152}$$

where $\mathbb{c}(\tau)$ and $\mathbb{M}_n$ are known. The best procedure for solving this system of equations depends on the chosen chemical kinetic laws. It can be solved analytically, numerically or with a mixed procedure as the one proposed in Section 6.4.8 for ASR.

The derivative of $\mathbf{I_{Q_e}}$ with respect to $\mathbf{c_e}$, is given by

$$\frac{\partial \mathbf{I_{Q_e}}}{\partial \mathbf{c_e}} = \frac{\partial}{\partial \mathbf{c_e}} \left[\int_{\Omega_e} \mathbf{N_e}^T \mathbf{i_q} d\Omega \right] \tag{5.153}$$

Applying Leibniz's rule,

$$\frac{\partial \mathbf{I_{Q_e}}}{\partial \mathbf{c_e}} = \int_{\Omega_e} \mathbf{N_e}^T \frac{\partial \mathbf{i_q}}{\partial \mathbf{c_e}} d\Omega \tag{5.154}$$

Applying the chain rule,

$$\frac{\partial \mathbf{I_{Q_e}}}{\partial \mathbf{c_e}} = \int_{\Omega_e} \mathbf{N_e}^T \frac{\partial \mathbf{i_q}}{\partial \mathbb{c}} \frac{\partial \mathbb{c}}{\partial \mathbf{c_e}} d\Omega \tag{5.155}$$

Introducing Eq. (5.112),

$$\frac{\partial \mathbf{I_{Q_e}}}{\partial \mathbf{c_e}} = \int_{\Omega_e} \mathbf{N_e}^T \frac{\partial \mathbf{i_q}}{\partial \mathbb{c}} \mathbf{N_e} d\Omega \tag{5.156}$$

Analogous equations can be obtained for interface elements using Eqs. (5.128) and (5.133),

$$\mathbf{I_{Q_{je}}}(\mathbf{c_{je}}_n, \mathbf{c_{je}}_{n+1}) = \frac{1}{2} \begin{bmatrix} \mathbf{I_6} \\ \mathbf{I_6} \end{bmatrix} \int_{l_{mp}} (\mathbf{N_{mp_e}})^T \underbrace{\left[\int_{t_n}^{t_{n+1}} \mathbf{q_{mp}}(\tau) d\tau \right]}_{\mathbf{i_{q_j}}} dl \tag{5.157}$$

$$\mathbf{i_{q_j}} = \begin{bmatrix} -\sum_{\alpha} x_{\alpha_i}^{\beta_1} (M_{mp_{n+1}}^{\alpha_i} - M_{mp_n}^{\alpha_i}) \\ \vdots \\ -\sum_{\alpha} x_{\alpha_i}^{\beta_n} (M_{mp_{n+1}}^{\alpha_i} - M_{mp_n}^{\alpha_i}) \end{bmatrix} \tag{5.158}$$

$$\begin{cases} M_{mp_{n+1}}^{\alpha_1} = M_{mp_n}^{\alpha_1} + \int_{t_n}^{t_{n+1}} \bar{\Gamma}_{mp}^{\alpha_1}(\mathbb{c}, \mathbb{M}_{mp}) d\tau \\ \vdots \qquad\quad \vdots \qquad\quad \vdots \\ M_{mp_{n+1}}^{\alpha_n} = M_{mp_n}^{\alpha_n} + \int_{t_n}^{t_{n+1}} \bar{\Gamma}_{mp}^{\alpha_n}(\mathbb{c}, \mathbb{M}_{mp}) d\tau \end{cases} \tag{5.159}$$

$$\frac{\partial \mathbf{I_{Q_{je}}}}{\partial \mathbf{c_{je}}} = \frac{1}{4} \begin{bmatrix} \mathbf{I_{2n}} \\ \mathbf{I_{2n}} \end{bmatrix} \left[\int_{l_{mp}} (\mathbf{N_{mp_e}})^T \frac{\partial \mathbf{i_{q_j}}}{\partial \mathbb{c}} \mathbf{N_{mp_e}} dl \right] \begin{bmatrix} \mathbf{I_{2n}} & \mathbf{I_{2n}} \end{bmatrix} \tag{5.160}$$

Finally, by assembling the element matrices $\frac{\partial \mathbf{I_{Q_e}}}{\partial \mathbf{c_e}}$ and $\frac{\partial \mathbf{I_{Q_{je}}}}{\partial \mathbf{c_{je}}}$, the global matrix $\frac{\partial \mathbf{I_Q}}{\partial \mathbf{c}}$ is obtained.

5.3 Mechanical problem

Similarly as for the diffusion-reaction problem, the material is considered to be formed by continuum zones separated by discontinuities (cracks and ITZs). In the proposed approach, non-linearity is restricted only to the behaviour of the discontinuities, while classical elasticity is assumed for the continuum porous material.

Even though the material is considered to be fully saturated with water, the pressure of the water in pores and discontinuities is assumed to be negligible, i.e. it is assumed that the total and the effective stresses in the material are the same. The present formulation also assumes that tension is positive and compression negative, small-strain theory, isothermal equilibrium and negligible inertial forces.

The FE formulation of the continuum medium is only briefly summarized here, since it is extensively treated in the literature [e.g. 225]. The discrete crack FE formulation, in contrast, is less common and, therefore, is described in more detail. The formulation is based on the use of zero-thickness interface elements with double nodes and well established mechanical formulations within the discrete crack approach [28, 32, 34, 80].

5.3.1 Formulation

5.3.1.1 Continuum medium

The mechanical behaviour of a continuum material for two-dimensional problems is described combining the linear momentum balance equation in a domain Ω, the constitutive relationship, and the compatibility equation that links strains to displacements. In matrix notation these equations can be written as:

$$\text{Momentum balance:} \qquad (\mathbf{L^u})^T \boldsymbol{\sigma} = 0 \qquad \text{in } \Omega \tag{5.161}$$

$$\text{Constitutive relationship:} \qquad d\boldsymbol{\sigma} = \mathbf{D^u} d\boldsymbol{\varepsilon} \tag{5.162}$$

Compatibility equation: $$\boldsymbol{\varepsilon} = \mathbf{L^u u} \tag{5.163}$$

with

$$\boldsymbol{\sigma} = \begin{bmatrix} \sigma_{xx} & \sigma_{yy} & \sigma_{zz} & \sigma_{xy} \end{bmatrix}^T \tag{5.164}$$

$$\boldsymbol{\varepsilon} = \begin{bmatrix} \varepsilon_{xx} & \varepsilon_{yy} & \varepsilon_{zz} & \varepsilon_{xy} \end{bmatrix}^T \tag{5.165}$$

$$\mathbf{u} = \begin{bmatrix} u_x & u_y \end{bmatrix}^T \tag{5.166}$$

$$\mathbf{L^u} = \begin{bmatrix} \dfrac{\partial}{\partial x} & 0 & 0 & \dfrac{\partial}{\partial y} \\ 0 & \dfrac{\partial}{\partial y} & 0 & \dfrac{\partial}{\partial x} \end{bmatrix}^T \tag{5.167}$$

where $\boldsymbol{\sigma}$ is the stress vector, $\boldsymbol{\varepsilon}$ is the strain vector, $\mathbf{u}$ is the displacements vector, $\mathbf{L^u}$ is the differential operator, and $\mathbf{D^u}$ is the 4×4 tangential constitutive matrix. Note that the ε_{zz} is either zero (plane strain problem) or determined from the material constitution by assuming σ_{zz} is zero (plane stress problem).

Two possible boundary conditions are considered:

1. Prescribed displacement condition (Dirichlet): $\mathbf{u} - \bar{\mathbf{u}} = 0 \quad$ on $\partial\Omega^u$ (5.168)
2. Prescribed tractions condition (Newmann): $\mathbf{G}^T\boldsymbol{\sigma} - \bar{\mathbf{t}} = 0 \quad$ on $\partial\Omega^t$ (5.169)

where $\bar{\mathbf{u}}$ is a prescribed displacement on the domain boundary $\partial\Omega^u$, $\bar{\mathbf{t}}$ is a distributed normal load on the domain boundary $\partial\Omega^t$, and

$$\mathbf{G}^T = \begin{bmatrix} n_x & 0 & 0 & n_y \\ 0 & n_y & 0 & n_x \end{bmatrix} \tag{5.170}$$

in which $\mathbf{n} = (n_x, n_y)$ are direction cosines of the normal to the boundary $\partial\Omega$.

5.3.1.2 Discontinuities

Stresses and relative displacements are defined in the discontinuity mid-plane. In the particular case of a one-dimensional discontinuity embedded in a 2D domain, both vectors are composed of a normal and a tangential components:

$$\boldsymbol{\sigma}_{\mathbf{mp}} = \begin{bmatrix} \sigma_n \\ \tau_l \end{bmatrix} \quad \mathbf{a}_{\mathbf{mp}} = \begin{bmatrix} a_n \\ a_l \end{bmatrix} \tag{5.171}$$

where $\boldsymbol{\sigma}_{\mathbf{mp}}$ is the mid-plane stress vector, σ_l and σ_n are the shear and tensile stresses at the mid-plane, $\mathbf{a}_{\mathbf{mp}}$ is the relative displacement vector and the subscripts l and n

stand for longitudinal (i.e. tangential) and normal respectively, and therefore a_l is the discontinuity sliding and a_n is the aperture.

The constitutive equation links the stresses in the mid-plane of the discontinuity to the relative displacements:

$$d\boldsymbol{\sigma}_{\mathbf{mp}} = \mathbf{D}^{\mathbf{u}}_{\mathbf{mp}} d\mathbf{a}_{\mathbf{mp}} \tag{5.172}$$

where $\mathbf{D}^{\mathbf{u}}_{\mathbf{mp}}$ is the tangential stiffness matrix. In a continuum medium, the constitutive model relates stresses to strains, and the strain field is related to the displacements field by a compatibility equation. Analogously, the present formulation for a discontinuity also requires a compatibility equation to relate the relative displacement field at the mid-plane to the displacement of the discontinuity walls:

$$d\mathbf{a}_{\mathbf{mp}} = d\mathbf{u}^{\mathbf{top}} - d\mathbf{u}^{\mathbf{bot}} = \mathbf{L}^{\mathbf{u}}_{\mathbf{mp}} d\mathbf{u} \tag{5.173}$$

where $\mathbf{L}^{\mathbf{u}}_{\mathbf{mp}}$ is an operator that relates the relative displacement vector to the displacement vector at both sides of the discontinuity ($\mathbf{u}^{\mathbf{top}}$ and $\mathbf{u}^{\mathbf{bot}}$).

5.3.2 Space discretization (FE formulation)

5.3.2.1 Continuum medium

A finite element approximation for displacements is given by

$$\mathbf{u} = \begin{bmatrix} u_x(x,y,t) \\ u_y(x,y,t) \end{bmatrix} \approx \begin{bmatrix} \sum_{i=1}^{n} N_i^u(x,y) u_{i_x}(t) \\ \sum_{i=1}^{n} N_i^u(x,y) u_{i_y}(t) \end{bmatrix} = \mathbf{N}^{\mathbf{u}}_{\mathbf{e}}\ \mathbf{u}_{\mathbf{e}} \tag{5.174}$$

where N_i^u are element shape functions, $\mathbf{u_e}$ are time dependent nodal displacements and the sum ranges over the number of nodes associated with an element. For a quadrilateral linear element ($n = 4$),

$$\mathbf{N}^{\mathbf{u}}_{\mathbf{e}} = \begin{bmatrix} N_1^u & 0 & N_2^u & 0 & N_3^u & 0 & N_4^u & 0 \\ 0 & N_1^u & 0 & N_2^u & 0 & N_3^u & 0 & N_4^u \end{bmatrix}_{(x,y)} \tag{5.175}$$

$$(\mathbf{u_e})^T = \begin{bmatrix} u_{1_x} & u_{1_y} & u_{2_x} & u_{2_y} & u_{3_x} & u_{3_y} & u_{4_x} & u_{4_y} \end{bmatrix}^T \tag{5.176}$$

By applying the PVW [225], the following expression is reached:

$$\int_{\Omega_e} (\mathbf{B}^{\mathbf{u}}_{\mathbf{e}})^T\, \boldsymbol{\sigma}\ d\Omega - \mathbf{F}^{\mathbf{u}}_{\mathbf{e}} = \mathbf{f}^{\mathbf{u}}_{\mathbf{e}} \tag{5.177}$$

where $\mathbf{B_e^u} = \mathbf{L^u N_e^u}$ is the strain operator, $\mathbf{f_e^u}$ is the vector of forces at nodes shared with neighbouring elements, and

$$\mathbf{F_e^u} = \int_{\partial\Omega_e^u} (\mathbf{N_e^u})^T \ \bar{\mathbf{t}} \ d\partial\Omega \tag{5.178}$$

is the right-hand side force vector. Considering linear elasticity ($\boldsymbol{\sigma} = \boldsymbol{D^u}\boldsymbol{\varepsilon}$) and replacing $\boldsymbol{\varepsilon} = \mathbf{B_e^u u_e}$ in Eq. (5.177):

$$\mathbf{K_e^u u_e} - \mathbf{F_e^u} = \mathbf{f_e^u} \tag{5.179}$$

in which

$$\mathbf{K_e^u} = \int_{\partial\Omega_e^u} (\mathbf{B_e^u})^T \, \mathbf{D_e^u B_e^u} d\Omega \tag{5.180}$$

is the linear stiffness matrix.

5.3.2.2 Discontinuities

The local orthonormal coordinate system on the mid-plane is related to the global coordinate system through a rotation matrix $\mathbf{r}$. This rotation matrix transforms the relative displacements in the local base ($\mathbf{a_{mp}}$) to the relative displacements in the global coordinate system ($\hat{\mathbf{a}}_{\mathbf{mp}}$).

$$\mathbf{a_{mp}} = \mathbf{r} \ \hat{\mathbf{a}}_{\mathbf{mp}} \tag{5.181}$$

For a two-dimensional interface element (Fig. 5.5),

$$\mathbf{r} = \begin{bmatrix} \cos\alpha & \sin\alpha \\ -\sin\alpha & \cos\alpha \end{bmatrix} \qquad \text{and} \qquad \hat{\mathbf{a}}_{\mathbf{mp}} = \begin{bmatrix} a_x \\ a_y \end{bmatrix}$$

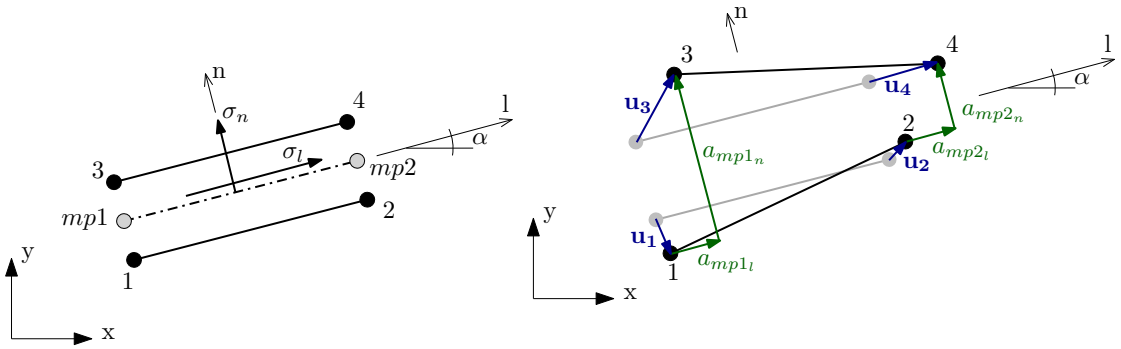

FIGURE 5.5: Stresses and relative nodal displacements at the mid-plane of a linear interface element.

The variables within the mid-plane ($\hat{\mathbf{a}}_{\mathbf{mp}}$) are interpolated from their values at the mid-plane nodes:

$$\hat{\mathbf{a}}_{\mathbf{mp}} = \begin{bmatrix} a_x(x,y,t) \\ a_y(x,y,t) \end{bmatrix} \approx \begin{bmatrix} \sum_{i=1}^{n} N^u_{mpi}(x,y) a_{mpi_x}(t) \\ \sum_{i=1}^{n} N^u_{mpi}(x,y) a_{mpi_y}(t) \end{bmatrix}$$

For the linear element in Fig. 5.5 ($n = 4$),

$$\hat{\mathbf{a}}_{\mathbf{mp}} \approx \begin{bmatrix} N^u_{mp1} & 0 & N^u_{mp2} & 0 \\ 0 & N^u_{mp1} & 0 & N^u_{mp2} \end{bmatrix}_{(x,y)} \begin{bmatrix} a_{mp1_x} \\ a_{mp1_y} \\ a_{mp2_x} \\ a_{mp2_x} \end{bmatrix}_t = \mathbf{N^u_{mp_e}} \cdot \hat{\mathbf{a}}_{\mathbf{mp_e}} \tag{5.182}$$

The relative displacement ($\hat{\mathbf{a}}_{\mathbf{mp}}$) is the difference of displacements between the continuum at each side of the discontinuity ('top' and 'bottom'):

$$\hat{\mathbf{a}}_{\mathbf{mp}} = \begin{bmatrix} a_x \\ a_y \end{bmatrix} = \begin{bmatrix} u_x^{top} - u_x^{bot} \\ u_y^{top} - u_y^{bot} \end{bmatrix} \tag{5.183}$$

Finally, the relative displacement of the mid-plane nodes ($\hat{\mathbf{a}}_{\mathbf{mp_e}}$) can be expressed in terms of the displacements at the real nodes:

$$\hat{\mathbf{a}}_{\mathbf{mp_e}} = \begin{bmatrix} a_{mp1_x} \\ a_{mp1_y} \\ a_{mp2_x} \\ a_{mp2_x} \end{bmatrix} = \begin{bmatrix} u_{3_x} - u_{1_x} \\ u_{3_y} - u_{1_y} \\ u_{4_x} - u_{2_x} \\ u_{4_y} - u_{2_y} \end{bmatrix} = \begin{bmatrix} -\mathbf{I_4} & \mathbf{I_4} \end{bmatrix} \begin{bmatrix} u_{1_x} \\ u_{1_y} \\ u_{2_x} \\ u_{2_y} \\ u_{3_x} \\ u_{3_y} \\ u_{4_x} \\ u_{4_y} \end{bmatrix} = \begin{bmatrix} -\mathbf{I_4} & \mathbf{I_4} \end{bmatrix} \mathbf{u_{j_e}} \tag{5.184}$$

Summarizing, $\mathbf{a_{mp}}$ can be expressed in the form of the compatibility Eq. (5.173) as

$$\mathbf{a_{mp}} = \mathbf{B^u_{mp_e}} \begin{bmatrix} -\mathbf{I_4} & \mathbf{I_4} \end{bmatrix} \mathbf{u_{j_e}} \tag{5.185}$$

with

$$\mathbf{B^u_{mp_e}} = \mathbf{r}\ \mathbf{N^u_{mp_e}} \tag{5.186}$$

The discretized equation governing the mechanical behaviour of the interface element is obtained through application of the PVW. A virtual displacement of the interface

element nodes ($\delta\mathbf{u_{j_e}}$) and the corresponding relative displacements developed on the mid-plane of the joint ($\delta\mathbf{a_{mp}}$) are considered:

$$\left(\delta\mathbf{u_{j_e}}\right)^T\mathbf{f}^{\mathbf{u}}_{\mathbf{j_e}} = \int_{l_{mp}} \left(\delta\mathbf{a_{mp}}\right)^T\boldsymbol{\sigma}_{\mathbf{mp}}dl \qquad \forall\delta\mathbf{u_{j_e}} \tag{5.187}$$

where $\mathbf{f}^{\mathbf{u}}_{\mathbf{j_e}}$ and $\boldsymbol{\sigma}_{\mathbf{mp}}$ are a set of equilibrated nodal forces and the mid-plane stresses, respectively. Equation (5.185) is then introduced in order to relate $\delta\mathbf{a_{mp}}$ to $\delta\mathbf{u_{j_e}}$:

$$\left(\delta\mathbf{u_{j_e}}\right)^T\mathbf{f}^{\mathbf{u}}_{\mathbf{j_e}} = \int_{l_{mp}} \left(\delta\mathbf{u_{j_e}}\right)^T\begin{bmatrix}-\mathbf{I_4} & \mathbf{I_4}\end{bmatrix}^T\left(\mathbf{N}^{\mathbf{u}}_{\mathbf{mp_e}}\right)^T\mathbf{r}^T\boldsymbol{\sigma}_{\mathbf{mp}}dl \qquad \forall\delta\mathbf{u_{j_e}} \tag{5.188}$$

Since this equation must be fulfilled for any virtual displacement $\delta\mathbf{u_{j_e}}$, it necessarily leads to the following one:

$$\mathbf{f}^{\mathbf{u}}_{\mathbf{j_e}} = \begin{bmatrix}-\mathbf{I_4} & \mathbf{I_4}\end{bmatrix}^T\int_{l_{mp}}\left(\mathbf{N}^{\mathbf{u}}_{\mathbf{mp_e}}\right)^T\mathbf{r}^T\boldsymbol{\sigma}_{\mathbf{mp}}dl \tag{5.189}$$

Which can be further synthesized introducing Eq. (5.186),

$$\mathbf{f}^{\mathbf{u}}_{\mathbf{j_e}} = \begin{bmatrix}-\mathbf{I_4} & \mathbf{I_4}\end{bmatrix}^T\int_{l_{mp}}\left(\mathbf{B}^{\mathbf{u}}_{\mathbf{mp_e}}\right)^T\boldsymbol{\sigma}_{\mathbf{mp}}dl = \begin{bmatrix}-\int_{l_{mp}}\left(\mathbf{B}^{\mathbf{u}}_{\mathbf{mp_e}}\right)^T\boldsymbol{\sigma}_{\mathbf{mp}}dl \\ \int_{l_{mp}}\left(\mathbf{B}^{\mathbf{u}}_{\mathbf{mp_e}}\right)^T\boldsymbol{\sigma}_{\mathbf{mp}}dl\end{bmatrix} \tag{5.190}$$

Therefore, collecting all previous equations we reach the mechanical FE equation for the zero thickness interface element in terms of the nodal displacements values:

$$\mathbf{f}^{\mathbf{u}}_{\mathbf{j_e}} = \int_{l_{mp}}\left(\mathbf{B}^{\mathbf{u}}_{\mathbf{j_e}}\right)^T\boldsymbol{\sigma}_{\mathbf{mp}}dl \tag{5.191}$$

where $\mathbf{B}^{\mathbf{u}}_{\mathbf{j_e}} = \begin{bmatrix}-\left(\mathbf{B}^{\mathbf{u}}_{\mathbf{mp_e}}\right)^T & \left(\mathbf{B}^{\mathbf{u}}_{\mathbf{mp_e}}\right)^T\end{bmatrix}$.

Considering now the incremental version of Eq. (5.191), assuming the incremental constitutive behaviour given in Eq. (5.172), and replacing with the compatibility equation (5.185), one obtains the final FE equation for interface elements:

$$d\mathbf{f}^{\mathbf{u}}_{\mathbf{j_e}} = \mathbf{K}^{\mathbf{u}}_{\mathbf{j_e}}d\mathbf{u_{j_e}} \tag{5.192}$$

in which

$$\mathbf{K}^{\mathbf{u}}_{\mathbf{j_e}} = \int_{l_{mp}}\left(\mathbf{B}^{\mathbf{u}}_{\mathbf{j_e}}\right)^T\mathbf{D}^{\mathbf{u}}_{\mathbf{mp}}\mathbf{B}^{\mathbf{u}}_{\mathbf{j_e}}dl \tag{5.193}$$

is the tangential stiffness matrix of the interface element.

5.3.2.3 Discontinuous porous medium

After assembly of the continuum and zero-thickness interface elements, the nodal forces cancel and a single system of equations in terms of the nodal displacements is reached for the whole problem domain. Assembly of Eq. (5.179) for the continuum elements and Eq. (5.191) for the interface elements gives the following system of equations for the boundary value after spatial discretization:

$$\int_{\Omega} (\mathbf{B}^{\mathbf{u}})^T \boldsymbol{\sigma} d\Omega = \mathbf{F}^{\mathbf{u}} \tag{5.194}$$

5.3.3 Numerical solution

Similarly as for the diffusion-reaction problem, a Newton-Raphson strategy is followed. Let us consider the vector $\mathbf{u}_{n+1}$ to be an approximation to the solution of Eq. (5.191) for boundary conditions given by $\mathbf{F}^{\mathbf{u}}_{n+1}$. Then, the corresponding residual vector is defined as:

$$\mathbb{R}_{n+1} = \mathbb{R}(\mathbf{u}_{n+1}) = -\int_{\Omega} (\mathbf{B}^{\mathbf{u}})^T \boldsymbol{\sigma}_{n+1} d\Omega + \mathbf{F}^{\mathbf{u}}_{n+1} \tag{5.195}$$

where $\boldsymbol{\sigma}_{n+1}$ is a function of $\mathbf{u}_{n+1}$ according to the constitutive equations of the material (Eqs. (5.162) and (5.172)). In order to improve the initial approximation to the solution, a Taylor's series of the residuals as a function of $\mathbf{u}_{n+1}$ is proposed:

$$\mathbb{R}({}^{i+1}\mathbf{u}_{n+1}) \approx \mathbb{R}({}^{i}\mathbf{u}_{n+1}) + \left.\frac{\partial \mathbb{R}}{\partial \mathbf{u}}\right|_{{}^{i}\mathbf{u}_{n+1}} {}^{i+1}\delta\mathbf{u}_{n+1} + \mathcal{O}_2 \tag{5.196}$$

Forcing $\mathbb{R}({}^{i+1}\mathbf{u}_{n+1}) = 0$ and neglecting the truncation error $\mathcal{O}_2$ we get:

$${}^{i}\mathbb{K}\ {}^{i+1}\delta\mathbf{u}_{n+1} = -\mathbb{R}({}^{i}\mathbf{u}_{n+1}) \tag{5.197}$$

where

$${}^{i}\mathbb{K} = \left.\frac{\partial \mathbb{R}}{\partial \mathbf{u}}\right|_{{}^{i}\mathbf{u}_{n+1}} \tag{5.198}$$

is the tangent stiffness matrix. Solving this linear system of equations, an improvement ${}^{i+1}\delta\mathbf{u}_{n+1}$ of the initial approximation ${}^{i}\mathbf{u}_{n+1}$ is obtained. Then,

$${}^{i+1}\mathbf{u}_{n+1} = {}^{i}\mathbf{u}_{n+1} + {}^{i+1}\delta\mathbf{u}_{n+1} \tag{5.199}$$

5.4 Chemo-Mechanical coupling

The mechanical formulation and the diffusion-reaction formulation are implemented in two different codes, called respectively `DRAC` and `DRACFLOW`. Both codes use the same FE mesh and the same integration points. This mesh includes zero-thickness interface elements in between continuum elements accounting for potential crack paths, and cement-aggregate interfaces. In order to introduce coupling effects, each code exchanges data with the other one, in the context of a 'staggered procedure'. The mechanical code, `DRAC`, passes the obtained nodal displacements to `DRACFLOW`, and, in turn, `DRACFLOW` passes to DRAC updated values of chemical history variables (e.g. porosity, moles of solid α-species, etc.) at integration points. Depending on the durability problem considered, one or more of the following coupling effects may be introduced:

Internal pressure

The precipitation of expansive reaction products may eventually exert internal pressures in the porous continuum medium and/or in the discontinuities, if the available space to allocate them is exhausted. The value of this pressure will depend on the amount of precipitated solids and on the mechanical constitutive laws of both the precipitated solid species and the surrounding solid skeleton. This mechanism is visualized in Fig. 5.6 in the form of a parallel 1D chemical pressure cell-spring device. In this figure, $d\sigma$ is a differential increment of the macroscopic total stress due to external forces, and $d\varepsilon$ is the corresponding overall differential strain. The left branch corresponds to the constitutive behaviour of the solid skeleton while the right branch corresponds to the constitutive behaviour of the precipitated reaction products. The springs generically stand for the mechanical laws of each part, which do not have to be necessarily elastic.

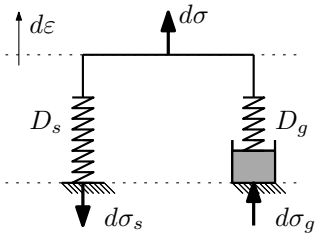

FIGURE 5.6: Chemical pressure cell-spring device for concrete expansions due to the formation of reaction products. Adapted from Ulm et al. [214].

In this way, the total stress increment is decomposed in two components:

$$d\sigma = d\sigma_s + d\sigma_g \tag{5.200}$$

where $d\sigma_s$ is the differential increment of effective stress and $d\sigma_g$ is the differential increment of internal pressure induced by the reaction products. The increment of effective stress is given as a function of the increment of the strains by means of the skeleton constitutive law (Eq. (5.162)). In contrast, the increment of internal pressure is not only a function of the strain but also of the amount of precipitated solid α-species, i.e.:

$$d\sigma_g = \left.\frac{\partial \sigma_g}{\partial \varepsilon}\right|_{\mathbb{M}^\alpha} d\varepsilon + \left.\frac{\partial \sigma_g}{\partial \mathbb{M}^\alpha}\right|_{\varepsilon} d\mathbb{M}^\alpha \tag{5.201}$$

This mechanisms are considered for modelling ASR expansions in concrete (Chapter 6) as it is discussed Section 6.5.2.

Pseudo-thermal strains/apertures

In the particular case that the reaction products are assumed to be incompressible, the mechanical effect of the reaction products are more easily treated as imposed volumetric strains ($\boldsymbol{\varepsilon}^{\mathbf{o}}$) in the continuum or imposed apertures ($\mathbf{a}^{\mathbf{o}}_{\mathbf{mp}}$) in discontinuities. For instance, treating $\boldsymbol{\varepsilon}^{\mathbf{o}}$ and $\mathbf{a}^{\mathbf{o}}_{\mathbf{mp}}$ as pseudo-thermal expansions and displacements, and modifying the corresponding constitutive laws (Eqs. (5.162) and (5.172)) as follows:

$$d\boldsymbol{\sigma} = \mathbf{D}^{\mathbf{u}}(d\boldsymbol{\varepsilon} - d\boldsymbol{\varepsilon}^{\mathbf{o}}) \tag{5.202}$$

$$d\boldsymbol{\sigma}_{\mathbf{mp}} = \mathbf{D}^{\mathbf{u}}_{\mathbf{mp}}(d\mathbf{a}_{\mathbf{mp}} - d\mathbf{a}^{\mathbf{o}}_{\mathbf{mp}}) \tag{5.203}$$

This approach has been followed in previous versions of the model for simulating External Sulphate Attack [98] and Drying Shrinkage [99].

Degradation of mechanical parameters

The dissolution of cement hydration products induces deterioration of its mechanical parameters (e.g. elastic modulus, tensile strength, specific fracture energy, etc.). This deterioration can be tracked by means of each variable M^α of the chemical model or by means of other representative history variables, such as the capillary porosity ϕ^{cp}. Then, the deterioration may be introduced in the mechanical model through a damage parameter d, which, for instance, could be of the form:

$$d = \frac{\phi^{cp} - \phi^{cp}_{ini}}{1 - \phi^{cp}_{ini}} \tag{5.204}$$

where ϕ^{cp}_{ini} is the reference (initial) porosity. This damage parameter can be then used for reducing a given mechanical parameter as follows:

$$X = (1 - d)^{\alpha_X} X_{ini} \tag{5.205}$$

where α_X is a fitting parameter.

Variation of transport properties of the continuum

The formation/dissolution of solid fractions in the continuum medium modifies the microstructural parameters (pore fractions, tortuosity, constrictivity, etc.) of the material with consequences in its transport properties. This phenomenon may be considered by relating evolution of solid fractions due to chemical reactions with the effective diffusivity coefficient, as it has been done, in a previous version of the model, for simulating External Sulphate Attack [98], and, already with the modelling framework proposed in this chapter, for simulating Acid Attack of oilwell cement [128].

Variation of transport properties of dicontinuities

Concrete cracks due to external loads or due to the internal pressures induced by the precipitation of expansive reaction products, constitute preferential paths for the ingress of reactants speeding up the deleterious process. This phenomenon may be considered in the model by calculating the diffusivities (D_n, D_l) of a given discontinuity as monotonic increasing functions of its normal aperture (a_n), as it has been done in a previous versions of the model for simulating External Sulphate Attack [98] and Drying Shrinkage [99]. The evolution of transport properties of discontinuities, for the particular case in which reaction products are formed within them, is discussed in Section 6.4.9.2 of this thesis.

Variation of chemical kinetics

Concrete cracking creates new surface areas exposed to alkaline pore solution which may eventually trigger dissolution processes. Another possibility is that the changes in concrete porosity or crack aperture modify the volume of pore solution in the material and, consequently, modify the absolute rates of formation of reaction products. The effects have been considered, for instance, for modelling Acid Attack of oilwell cement [128], and in Section 6.4.6 of this thesis for modelling ASR.

The staggered procedure, which is administrated by a third code named `STAG`, is schematically illustrated in Fig. 5.7. For each time step, `DRAC` and `DRACFLOW` are called alternatively in order to independently solve the mechanical problem and the diffusion-reaction problem. After each call, `DRAC` writes a file with the nodal displacements obtained at the end of the time step. This file is read by `DRACFLOW` and used to calculate the transport parameters of the material and, in some cases, also the sink/source terms (reaction rates). In turn, after each call, `DRACFLOW` writes two files, one containing the nodal concentrations and the other one containing history variable values at integration points, in

both cases at the end of the time step. The file with history variable values is then read by DRAC and used in its calculations in different manners depending on the specific durability problem being analysed. The nodal concentration file and the nodal displacement file are used by STAG to assess the convergence of the staggered procedure.

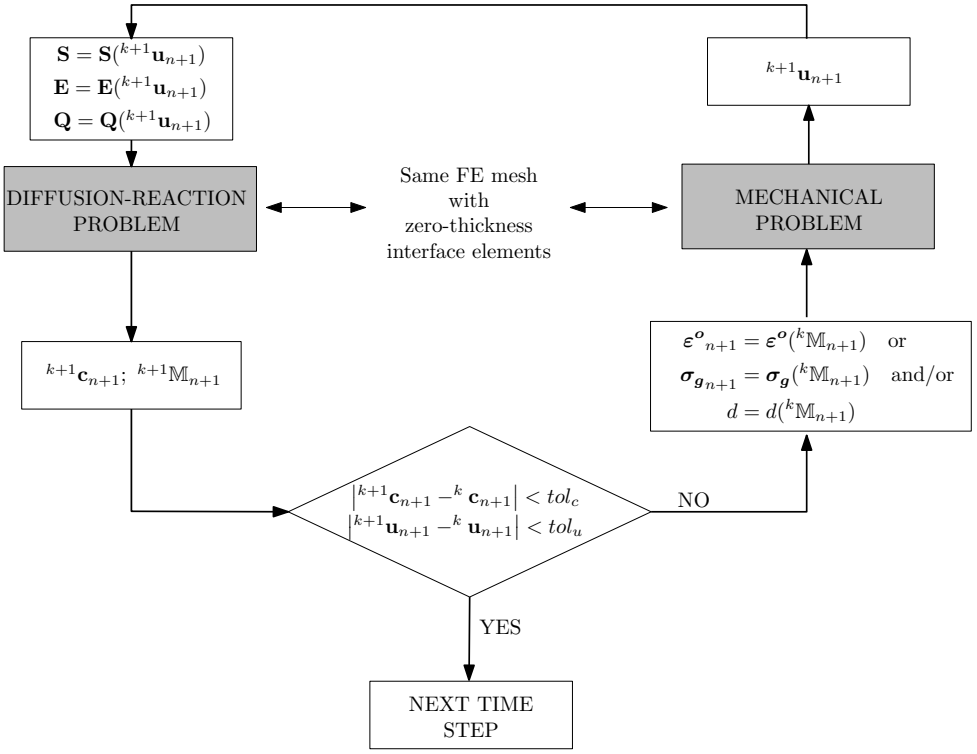

FIGURE 5.7: Staggered procedure scheme.

5.5 Chapter concluding remarks

- A general framework for modelling diffusion-dominated deleterious processes in cement-based materials has been theoretically and numerically formulated. The resulting formulation consists of two separated parts, one dealing with the mechanical problem and one dealing with the diffusion-reaction problem. A number of coupling terms links together both formulations. The spacial discretization of the theoretical formulation has been done with the Finite Element Method (FEM) and the time discretization has been done with the Finite Difference Method.

- The proposed model makes it possible to simulate the various observed interplays between the diffusion of aqueous species in pore solution, the precipitation or dissolution of solid species, and the stress-strain state of the material, with the distinctive feature of explicitly considering the role played by discontinuities (cracks or aggregate-cementitious matrix interfaces) within the material.

- The formulation has been implemented in two different codes, one dealing with the mechanical problem (`DRAC`) and one dealing with the diffusion-reaction problem (`DRACFLOW`). The coupling between the two codes is achieved by updating the coupling terms of each problem in an iterative process. To do so, each code exchanges data with the other one, in the context of a 'staggered procedure' which is administrated by a third code called `STAG`.

- The proposed model is based on previous developments within the research group of Mechanics of Materials (MECMAT) at UPC. However, substantial contributions are made, in particular with regard to the diffusion-reaction formulation.

Chapter 6

Modelling of ASR expansions in soda-lime glass concrete

6.1 Introduction

In this chapter, a chemo-mechanical mechanism is proposed for explaining the cracking and expansion patterns experimentally observed due to ASR in Soda-Lime (SL) glass concretes. This mechanism is based in part on the studies published by Rajabipour et al. [174] and Maraghechi et al. [142], but with substantial modifications in order to explain the results obtained with the Interfacial Expansion Tests presented in Chapter 3 and the Confined Expansion Tests presented in Chapter 4.

Later, assuming some simplifying hypotheses, the proposed mechanism is mathematically formulated in the modelling framework presented in Chapter 5. The most significant of those simplification consists of considering that the dissolution/precipitation processes associated with ASR only occur within zero-thickness interface elements representing cement-glass contacts and fractures.

SL glass has some peculiarities as concrete aggregate, and thus the model includes some assumptions that make it not strictly applicable for the more usual case of concrete made with natural reactive aggregates. However, it can be readily adapted for other types of reactive aggregates by introducing minor changes in the formulation.

Simulation results obtained with this model, in some cases contrasted with experimental results, are described in the following Chapter 7.

6.2 Chemo-mechanic mechanism for ASR expansions in SL glass concrete

SL glass is by far the most prevalent type of glass. Mainly used for windowpanes and food/beverage containers, it accounts for about 90% of the manufactured glass [219]. That means that every year, millions of tons of SL waste glass are produced worldwide. This has motivated, in recent years, many studies with the aim of giving a second use to SL glass by incorporating it to concrete in the form of crushed granular material as a replacement of natural aggregate or as a powdered material as a replacement of Portland cement.

SL glass is an amorphous material composed of silica tetrahedral units, connected to each other by bridging oxygens, or to other atoms, mainly Na, Ca and H, through non-bridging oxygens [141]. Typical compositions of SL glass range between 73 to 75 wt% of SiO_2, 9 to 14 wt% of Na_2O, 8 to 14 wt% of CaO, with minor contents of K_2O, MgO, Al_2O_3 and Fe_2O_3. In contact with highly alkaline solutions, as the cement pore solution, SL glass dissolves congruently into aqueous Si, Na and Ca species due to the nucleophilic attack of hydroxyl ions (OH^-), in a process similar to the one described in Section 2.3.1 for pure metastable silica. These aqueous species eventually react between themselves and with other aqueous species already present in the pore solution forming Calcium-Alkali-Silica-Hydrates (C–R–S–H) of variable composition. Depending on various factors, the formation of C–R–S–H may eventually lead to beneficial or harmful effects on concrete. For instance, several studies have demonstrated that if SL glass is ground to particle sizes similar to those of regular Portland cement (<100 μm), it exhibits pozzolanic behaviour [4, 100, 147, 161, 193]. That means that if it is used as partial replacement of Portland cement, the ground SL glass slowly reacts with the calcium hydroxide resulting from the clinker hydration gradually forming secondary hydration products (C–R–S–H) with Ca/Si molar ratios around 1.5, commonly referred in the literature as 'pozzolanic CSH'. These secondary products fill the large capillary voids around the SL glass particles with consequent reduction of porosity and refinement of the pore sizes, thus improving the strength and impermeability of the system. The formation of pozzolanic CSH has not been found to induce deleterious expansions in concrete. On the contrary, the use of ground glass as a partial replacement of cement has been found effective for reducing the potential of ASR expansions in concrete prepared with natural reactive aggregates [147], similarly to other pozzolans [1].

On the other hand, the use of crushed SL glass as replacement of natural aggregates (particle size >0.5 mm) has been demonstrated to be very pernicious for concrete due to the development of ASR expansions [4, 53, 174, 224]. Rajabipour and co-workers

[174] explain the different results obtained with ground and crushed SL glass particles based on the presence of microcracks in the latest ones. These authors found that the C–R–S–H formed at the interface between the crushed SL glass particles and the cement paste (Fig. 6.1a) has similar composition to the one formed in the pozzolanic reaction of ground SL glass (Ca/Si≈1.5), while the C–R–S–H formed within the glass microcracks (Fig. 6.1b) has lower Ca/Si ratios of around 0.3. In a subsequent work, Maraghechi et al. [142] found that this low-calcium C–R–S–H is only formed within pre-existing cracks wider than 2.5 μm. Moreover, they found that only crushed SL glass particles with sizes greater than 0.3 mm have cracks wider than 2.5 μm, i.e. they found no low-calcium C–R–S–H associated with ground glass particles.

These observations leaded them to conjecture that the high-calcium (pozzolanic) C–R–S–H is not expansive, and that the deleterious expansions found in concrete made with crushed SL glass is only due to the formation of highly expansive low-calcium C–R–S–H (referred as 'ASR gel') within pre-existing microcracks inside glass particles wider than 2.5 μm. In order to confirm this conjecture, the authors performed a second set of tests in which the microcracks of the crushed SL glass particles were healed by annealing at 650 °C [142]. As a result, the ASR expansions practically disappeared, thus confirming the determinant role of microcracks in the ASR expansions of crushed SL glass concrete. Similarly, when using crack-free SL glass beads in Portland cement mortars (Fig. 6.1c), no low-calcium C–R–S–H (ASR gel) was observed [141].

According to these authors, the presence of portlandite at the glass-cement paste interface prevents the formation of expansive low-calcium C–R–S–H and favours the formation of high-calcium C–R–S–H [142, 174]. This seems to be confirmed by the fact that when 'SL glass aggregates were used in alkali activated fly ash mortars, which do not form solid $Ca(OH)_2$', low-calcium C–R–S–H 'was observed both within the interior and at the surface of glass aggregates' (Fig. 6.1d)[141].

The absence of C–R–S–H within cracks thinner than 2.5 μm is explained by the fact that the diffusivity and permeability of cracks grow with the crack width [5, 58, 102]. Since the initiation and propagation of ASR depend on the diffusion of ionic reactants, as well as on the permeation of water inside the microcracks, the ASR rate within very thin cracks may be significantly slower, to the point that C–R–S–H did not form within the testing time in quantities that were detectable by SEM [142].

In this thesis, Section 4.4.5, similar observations have been made in a crushed SL glass concrete specimen after a confined expansion test (load case 1-1-1). Namely that low-calcium products (C–R–S–H with molar Ca/Si≈0.3) were formed within cracks inside glass particles while intermediate and high-calcium products (C–R–S–H with molar Ca/Si≈1.4) were formed in contact with the Hydrated Cement Paste (HCP). However,

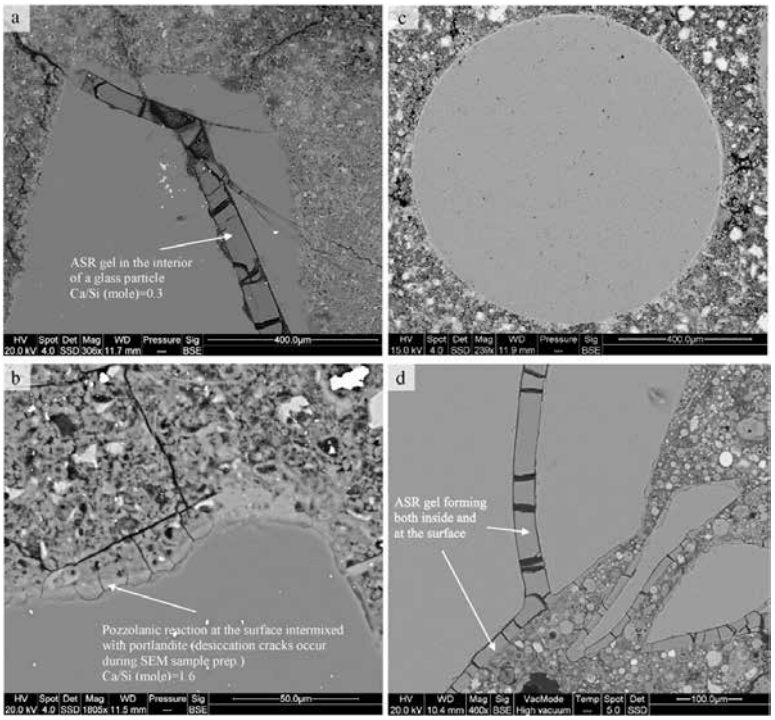

FIGURE 6.1: BSE images of mortars containing SL glass: (a) Low-calcium C–R–S–H (ASR gel) formation in the interior of a glass particle while the surface remains immune, (b) formation of high calcium C–R–S–H (pozzolanic reaction) at the glass-cement paste interface, (c) absence of ASR in crack-free glass beads, (d) Low-calcium C–R–S–H (ASR gel) in alkali activated fly ash mortar occurring both at the surface and interior of glass. Images taken from Ref. [141].

.

the diffuse layer of high-calcium product (up to about 20 μm thick) at the boundary between glass and the HCP reported by Rajabipour et al. [174] (Fig. 6.1b) could not be identified in our samples.

In the Interfacial Expansion Tests (Chapter 3) performed with specimens made with SL glass discs, in contrast, well differentiated layers of reaction products were observed at HCP- and mortar-glass interfaces (see for instance Figs. 3.14 and 3.15). The molar Ca/Si ratios measured in these products ranged from 1.0 to 1.5 (Table 3.7), which are somehow lower than the calcium content of the pozzolanic CSH reported by Rajabipour at al. [174], but, in any case, much higher than the calcium content of the reaction products within cracks. Moreover, the interfacial expansion curves obtained demonstrate that the reaction products rich in calcium are capable of developing significant expansions, in marked contradiction with the above mentioned proposition by Rajabipour et al. [174] that calcium-rich products are not expansive.

This contradiction can be solved if, instead of considering them as 'expensive' or 'not expansive', the low- and high-calcium products are differentiated in terms of the maximum swelling-pressure (MSP) that they can exert. In this sense, it can be conjectured

that the high-calcium products (the pozzolanic CSH) is capable of developing swelling-pressures high enough to separate the glass-cement interfaces in Interfacial Expansion Tests, but not high enough to separate the glass-cement interfaces of glass particles within concrete due to the additional resistance of the surrounding cementitious matrix. Consequently, in the first case the interfacial expansions continued 'indefinitely' while in the second case they are somehow inhibited by the mechanical restraint exerted by the cementitious matrix.

Analogous considerations can be done for the low-calcium product formed within cracks inside glass particles. As shown in Chapter 4, the ASR expansion rate of crushed SL glass concrete is reduced for increasing confining pressure. The maximum applied pressure of 9 MPa was not enough to totally inhibit the expansion, but it has been estimated by extrapolation of the results obtained (see Fig. 4.9) that a pressure of about 10 MPa would be capable of doing so. This inhibiting pressure is denoted by $\bar{\sigma}_v$ in Eq. (4.2). Therefore, it can be inferred that the low-calcium products have also a MSP which, according to our results, would have a lower bound of about 10 MPa. Note that this MSP has to be greater than $\bar{\sigma}_v$, because it has to simultaneously overcome $\bar{\sigma}_v$ and the tensile strength of the solid skeleton surrounding the reaction sites.

For given temperature and Relative Humidity (RH), the MSP has to be regarded as a property of each type of reaction product, while the $\bar{\sigma}_v$ has to be regarded as property of the particular reactive concrete considered. The MSP depends on the hydrophilic potential of the consider reaction product, and, consequently, it is expected to vary with its chemical composition (and probably also with temperature and RH). The $\bar{\sigma}_v$ of a given concrete, in turn, obviously depends on the MSP of the different ASR products formed within the concrete, but also on the concrete meso-structure itself (strength of the cementitious matrix, amount and size distribution of aggregates, etc.), since that determines the internal restraint to the expansion of the ASR products.

These concepts can also be used for explaining that the ASR expansion rates are progressively reduced as the applied external pressure is increased (see Fig. 4.9). Since the crushed glass particles used for preparing the specimens have different sizes, different shapes, and different residual cracks, and since these particles are randomly distributed within the limestone mortar, it can be expected that the internal mechanical restraint at each reaction site is different. Consequently, different external pressures are expected to be needed to inhibit the ASR expansions at each reaction site. Therefore, as the external pressure growths, the number of inhibited reaction sites increases, and the macroscopic expansion rate decreases.

For the proposed interpretation of the experimental evidence, the ASR products may be visualized as a space-filling gel composed by the aggregation of colloidal clusters of

C–R–S–H of variable composition (see Section 2.3.2). Two different fractions of water are distinguished in the ASR products: the water chemically bound in the C–R–S–H and the water within the influence of absorbing forces, referred as 'gel water'. These absorbing forces can be attributed to different mechanisms (e.g. osmotic pressure, double-layer repulsive forces, surface forces of solid C–R–S–H) but in any case they are expected to be dependent on the chemical composition of the C–R–S–H. The content of gel water determines the distance between the colloidal clusters and, consequently, the 'bulk' volume of the ASR product, i.e. increase as water is absorbed. If this swelling is prevented by the surrounding solid skeleton, a mechanical pressure will be exerted on the ASR gel (C–R–S–H + gel water) counteracting the absorption pressure and, consequently, the amount of gel water absorbed will be lower than in free swelling conditions. Conversely, if the mechanical restraint is removed the original potential of water absorption will be restored and the ASR products will swell. The gel water within the ASR products is regarded as part of the concrete pore solution, i.e. as an aqueous medium in which diffusion-reaction processes may occur. Then, changes in the amount of gel water are expected to have an effect on the reaction rates by locally reducing either the effective diffusion section, the 'wet' surface area of dissolving silica, or the volume of reacting medium.

In order to clarify the proposed expansion mechanism, in Fig. 6.2 the progressive formation of ASR products within a pre-existing crack inside a non-reactive aggregate is schematically represented. Additionally, the qualitative evolutions of some significant parameters as functions of the amount of formed ASR products (M^{RP}) are also presented, namely: the swelling-pressure σ_g, the gel porosity ϕ^{RP} (defined as the volume of gel water per unit volume of ASR products), the crack width w, and the total porosity ϕ (defined as the volume of pore solution — which includes free and gel water — per unit volume of crack). During the initial stages (Fig. 6.2, A–C), both sides of the crack are assumed to be fixed. Later, the upper side is released allowing it to move freely following the volume change of the ASR products.

The process starts with the diffusion of reactants into the crack, which eventually leads to the formation of colloidal C–R–S–H clusters aggregated in a gel structure (Fig. 6.2A). Since the crack and the ASR products within it are assumed to remain always completely saturated with water, these ASR products initially coexist with the free water that fills the remaining empty space in the crack. In this condition, the ASR products are unstressed and, thus, the gel porosity is the maximum possible (ϕ_o^{RP}) depending on the chemical composition of the C–R–S–H clusters.

As the reaction progresses (Fig. 6.2B), the free water volume is replaced by the ASR

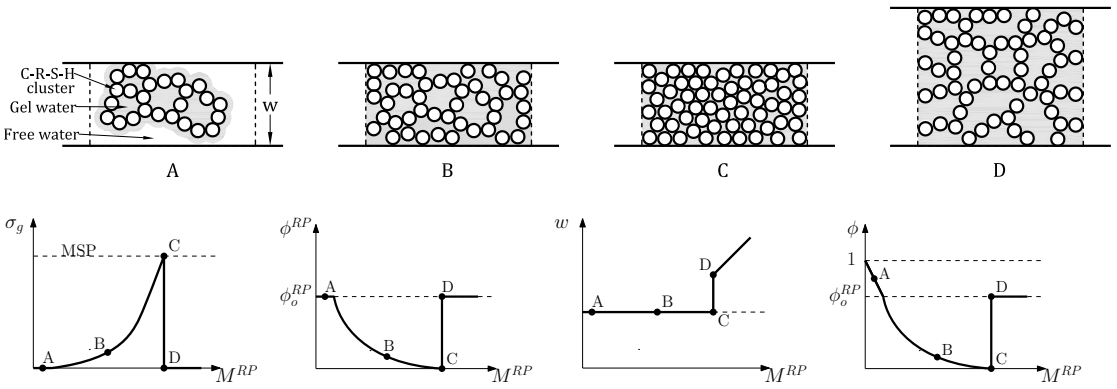

FIGURE 6.2: Schematic representation of progressive formation of ASR products within a pre-existing crack inside a non-reactive aggregate.

products and, consequently, the total porosity decreases linearly with M^{RP} until reaching the maximum gel porosity ϕ_o^{RP}. From this point on, the formation of C–R–S–H occurs at the expense of the gel water volume, i.e. the gel porosity of the ASR products is reduced. In this situation, the ASR products tend to swell in order to recover the maximum gel porosity. However, since both sides of the crack are fixed, this is not possible and a swelling-pressure (σ_g) is induced.

As more C–R–S–H is formed, the gel/total porosity decreases and the swelling-pressure increases. When the gel porosity is exhausted (Fig. 6.2C), the MSP is reached. At this point, since there is no remaining pore solution, the formation of C–R–S–H stops.

If now the upper side of the crack is released (Fig. 6.2D), the swelling-pressure disappears, and, thus, water is absorbed by the ASR products until recovering the maximum gel porosity. Consequently, the ASR products swell displacing the upper side of the crack. This swelling is expected to occur rapidly but not instantaneously since water would need some time to flow into the ASR products. Without any mechanical restraint, further formation of C–R–S–H implies a linear grow the crack width with M^{RP}, with constant gel/total porosity, and without inducing swelling-pressure.

It must be noted that the above-described mechanisms cannot explain by themselves the well-known fact that, when concrete is under anisotropic stress states, there is an increase of the ASR expansion rate(s) in the less compressed direction(s) that may be higher than in free expansion conditions (see the discussion in Section 2.8 of experimental results found in the literature, and our own experimental results presented in Chapter 4). In order to explain this phenomenon, the effect of the concrete stress state on the orientation of the cracks induced by the formation of ASR products has to be considered. When ASR expansions occur in unloaded concrete, the induced cracks are oriented randomly, in patterns known as 'map cracking' (Fig. 2.1). In contrast, when ASR expansions occur in loaded/restrained concrete, the induced cracks are aligned with the direction of the minor

principal stress (Fig. 2.2). Since cracks constitute preferential paths for the diffusion of reactants, the formation of reaction products within them is favoured in detriment of other locations, and, consequently, the expansion rate in the direction normal to the crack plane is accelerated. Additionally, the development of internal pressures due to the formation of reaction products, combined with the reduction of the material shear strength due to cracking, may result in an increase of the shear dilatancy in the less compressed directions (normal to the minor principal stress). These mechanisms are further discussed in Section 7.5.

6.3 Main modelling assumptions

With the aim of formulating the above-proposed reaction-expansion mechanisms within the modelling framework proposed in Chapter 5, a number of simplifying assumptions are adopted. These assumptions are listed and discussed in this section, always bearing in mind that the final goal of the model is to simulate the experimental tests presented in Chapters 3 and 4.

6.3.1 General

In the experimental tests presented in Chapters 3 and 4, two stages has been distinguished: the curing stage, at room temperature for a period of time greater than 28 days, and the exposure stage at 60 °C. Since the extent of the ASR developed during the curing stage is much smaller than one developed during the exposure stage, the simulations will only consider the ASR occurring during the exposure stage. It is also assumed that before starting the exposure stage, the Portland cement in the specimens had reached its maximum possible hydration degree, and, therefore, no changes in the HCP microstructure due to clinker hydration during the exposure stage are considered. Moreover, the specimen pores and cracks are assumed to be fully saturated with water at all times during the tests.

6.3.2 Concrete micro- and meso-structure

SL glass concrete is considered as formed by two homogeneous continuum components. On one hand, the SL glass aggregates, and, on the other, the 'cementitious matrix' (HCP or mortar). These components are modelled by means of continuum Finite Elements (FE), separated by means of zero-thickness interface elements which allow us to introduce the particular characteristics of the cement/glass contacts. Interface elements

are introduced also in between continuum elements of the same component in order to simulate the propagation of cracks.

The SL glass is considered to be non-porous, impervious, and constituted by a unique volume fraction. The cementitious matrix, in contrast, is considered to have three different volume fractions: capillary pores, portlandite, and Inert Cement Paste (ICP), the latter corresponding to cement hydration products which are considered to not have any chemical interaction with ASR, e.g. C–S–H, AFt, or AFm. The volume of ICP includes both the volume of solid hydration products and the volume of gel water absorbed by them. The volume of gel water is considered to be part of the volume cement pore solution, or, what is the same, given that the material is assumed to be fully saturated, the volume of gel pores are considered to be part of the total volume of pores. The remaining volume occupied by pore solution is referred as 'capillary pores' even when it may include other voids such as macro-pores or cracks. The diffusion-reaction processes are allowed to occur in the gel pores, but the reaction products are no allowed to precipitate within gel pores. Moreover, diffusivity through gel pores is assumed to be lower than through capillary pores. All these volume fractions, as well as the concentration of aqueous species in pore solution, are assumed to be known at the beginning of the exposure stage.

6.3.3 Transport processes

The only transport process considered is the Fickean diffusion of aqueous species due to concentration gradients. These diffusion processes are allowed through the continuum FE representing the cementitious matrix and along the interface elements representing glass/cement interfaces and opened cracks.

Bulk glass is assumed to be non-porous and impervious. Only if the glass is cracked, the pore solution can penetrate the glass particle boundaries in localized fluxes along the opened cracks. Otherwise, only the external surface of the glass particle, in contact with the cement paste, is exposed to the cement pore solution. The effective diffusivity and porosity of the cementitious matrix are assumed to remain constant during the simulations.

Local changes in the water content due to its production/consumption in the dissolution/formation of solid species, or due to changes in pore volume, are assumed to occur instantaneously and without any associated convective transport of aqueous species.

6.3.4 Chemical reactions

It is assumed that ASR in SL glass concrete can be suitably represented by considering the following chemical reactions:

i) Dissolution/formation of portlandite

$$\mathrm{Ca(OH)_2} \rightleftharpoons \mathrm{Ca^{2+}} + 2\ \mathrm{OH^-} \tag{6.1}$$

ii) Dissolution/formation of SL glass

$$\underbrace{(\mathrm{SiO_2})\,(\mathrm{CaO})_{c_1}\,(\mathrm{R_2O})_{c_2/2}}_{\text{SL glass}} + (2 + c_1 + \frac{c_2}{2})\ \mathrm{H_2O} \rightleftharpoons \mathrm{SiO_4H_3^-} + c_1\mathrm{Ca^{2+}} + c_2\mathrm{R^+} + (2c_1 + c_2)\mathrm{OH^-} + \mathrm{H^+} \tag{6.2}$$

iii) Dissolution/formation of high-calcium ASR product (RPA)

$$\underbrace{(\mathrm{SiO_2})(\mathrm{CaO})_{a_1}(\mathrm{R_2O})_{a_2/2}(\mathrm{H_2O})_{2-a_1-a_2/2+a_3+a_5}}_{\text{RPA}} \rightleftharpoons \mathrm{SiO_4H_3^-} + a_1\mathrm{Ca^{2+}} + a_2\mathrm{R^+} + a_3\mathrm{OH^-} + a_4\mathrm{H^+} + a_5\mathrm{H_2O} \tag{6.3}$$

iv) Dissolution/formation of low-calcium ASR product (RPB)

$$\underbrace{(\mathrm{SiO_2})(\mathrm{CaO})_{b_1}(\mathrm{R_2O})_{b_2/2}(\mathrm{H_2O})_{2-b_1-b_2/2+b_3+b_5}}_{\text{RPB}} \rightleftharpoons \mathrm{SiO_4H_3^-} + b_1\mathrm{Ca^{2+}} + b_2\mathrm{R^+} + b_3\mathrm{OH^-} + b_4\mathrm{H^+} + b_5\mathrm{H_2O} \tag{6.4}$$

v) Water self-dissociation

$$\mathrm{H_2O} \rightleftharpoons \mathrm{H^+} + \mathrm{OH^-} \tag{6.5}$$

vi) Dissociation of aqueous alkali hydroxides

$$\mathrm{ROH} \rightleftarrows \mathrm{R^+} + \mathrm{OH^-} \tag{6.6}$$

Note that in the above equations sodium (Na) and potassium (K) are treated indifferently as 'alkalis' (R). The effect of the remaining chemical species usually present in concrete on the development of ASR is neglected.

The SL glass is considered to be composed only by SiO_2, CaO, and R_2O. Other minor components are neglected. Since the composition of SL glass may vary, Reaction (6.2) is given generically in terms of stoichiometric coefficients c_1 and c_2. For this thesis, a typical glass composition of 76.7 wt% SiO_2, 14.1 wt% CaO, and 9.2 wt% R_2O, is adopted, resulting in $c_1 = 0.20$ and $c_2 = 0.24$. Then, Reaction (6.2) can be rewritten as follows

$$\underbrace{(SiO_2)\,(CaO)_{0.2}\,(R_2O)_{0.12}}_{\text{SL glass}} + 2.32\ H_2O \rightleftharpoons SiO_4H_3^- + 0.2\ Ca^{2+} + 0.24\ R^+ + 0.64\ OH^- + H^+ \quad (6.7)$$

It is assumed that, in contact with alkaline solutions, SiO_2 in SL glass dissolves according to the process described in Section 2.3.1 and that Ca^{2+} and R^+ are congruently released. Note that the whole dissolution process described in Section 2.3.1 is reduced to a single reaction with a fixed stoichiometry. Moreover, only one aqueous silica species is considered, a simplification that gives good results for solutions with pH 11 to 12 (see Fig. 2.7). Out of this range, other aqueous silica species ($SiO_4H_2^{2-}$ above, and $SiO_4H_4^0$ below this range) should be considered for an accurate estimate of silica solubility. Although the pH of concrete pore solution is generally close to 13, it seems reasonable to expect a lower pH at the reaction sites due to the consumption of alkalis and the pass of silicic acid to the solution. Because of this, it seems acceptable to consider only $SiO_4H_3^-$ as the result of SiO_2 dissolution.

The ASR gel is assumed to be a simple mixture of two components (the above-mentioned C–R–S–H clusters) of constant composition, as suggested by Helmut and Stark [88] (see Section 2.6). These two components, referred as Reaction product A (RPA) and Reaction Product B (RPB), are assumed to be the result of Reactions (6.3) and (6.4) (toward the left), where a_i and b_i, are fixed stoichiometric coefficients to determined. Note that a_1 and b_1 determine the Ca/Si molar ratios, while a_2 and b_2 determine the R/Si molar ratios of the reaction products. The coefficients $a_{3,4}$ and $b_{3,4}$ are alternatively used to fulfil the electro-neutrality condition of the reactions according to Eqs. (6.8) and (6.9). Coefficients a_5 and b_5, which can be negative, make it possible to adjust the content of nonevaporable water of the RP.

$$a_3 = \max[2a_1 + a_2 - 1, 0]; \quad a_4 = \max[1 - 2a_1 - a_2, 0] \quad (6.8)$$

$$b_3 = \max[2b_1 + b_2 - 1, 0]; \quad b_4 = \max[1 - 2b_1 - b_2, 0] \quad (6.9)$$

Suitable values of the stoichiometric coefficients $a_{1,2}$ and $b_{1,2}$ are obtained by fitting experimental measurements of the chemical composition of the ASR products. This is

done following a method similar to the one proposed by Helmuth et al. [89], as it is explained in Appendix B.1, resulting in $a_1 = 1.5$, $a_2 = 0.2$, $a_3 = 2.2$, $a_4 = 0$, $b_1 = 0.3$, $b_2 = 0.3$, $b_3 = 0$, $b_4 = 0.1$. That means that the RPA has higher content of calcium and lower content of alkalis than the RPB. In Fig. 6.3, the ASR product compositions, presented in Chapters 3 and 4, are plotted together with the range of compositions that can be reproduced by the model with the adopted set of stoichiometric coefficients. Replacing these stoichiometric coefficients in the generic Reactions (6.3) and (6.4), the following expressions are obtained:

$$\underbrace{(SiO_2)(CaO)_{1.5}(R_2O)_{0.1}(H_2O)_{2.6+a_5}}_{\text{RPA}} \rightleftharpoons SiO_4H_3^- + 1.5\ Ca^{2+} + 0.2\ R^+ + 2.2\ OH^- + a_5\ H_2O \tag{6.10}$$

$$\underbrace{(SiO_2)(CaO)_{0.3}(R_2O)_{0.15}(H_2O)_{1.55+b_5}}_{\text{RPB}} \rightleftharpoons SiO_4H_3^- + 0.3\ Ca^{2+} + 0.3\ R^+ + 0.1\ H^+ + b_5\ H_2O \tag{6.11}$$

Since in the current version of the model the water balance is not explicitly considered, the stoichiometric coefficients a_5 and b_5 do not need to be specified.

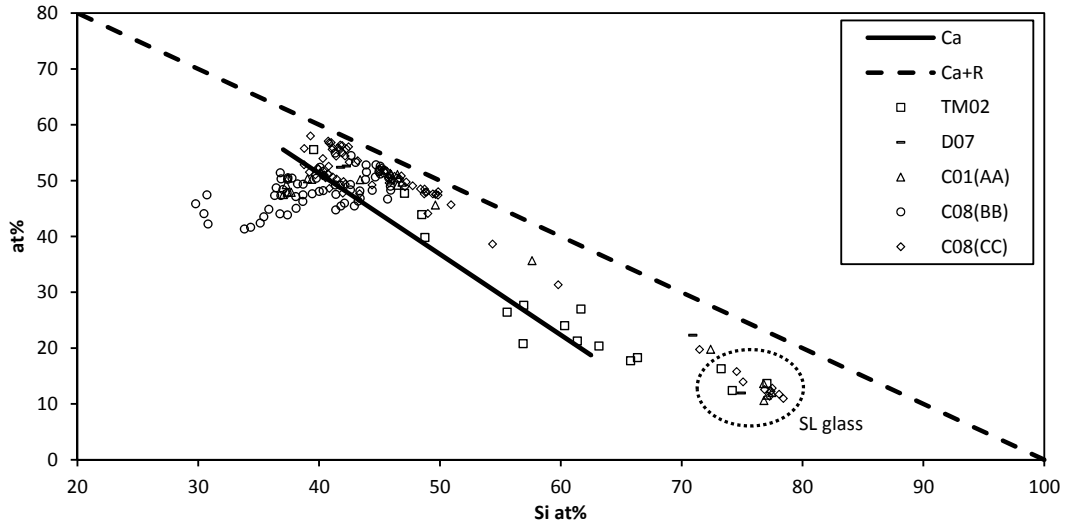

FIGURE 6.3: Composition of ASR products in SL glass concrete presented in Si, Ca, and R basis. Markers indicate compositions obtained with EDS analysis of specimens from Interfacial Expansion Tests (D07, C01 and C08) and from Confined Expansion Tests (TM02). The solid line indicate the range of compositions that can be reproduced by the model with the adopted set of stoichiometric coefficients ($a_1 = 1.5$, $a_2 = 0.2$, $b_1 = 0.3$, $b_2 = 0.3$). Note: at% = atomic percentage.

Being ROH (NaOH or KOH) a strong base, the dissociation Reaction (6.6) is not usually explicitly considered, since aqueous ROH is assumed to be completely dissociated. However, this simplification may lead to significant error for solutions with high pH (above

12), as may be found in concrete pore solution in some cases. The effects of explicitly considering Reaction (6.6) are discussed in Section 7.2.

6.3.5 Reactive-transport processes at cracks and interfaces

In the SEM images of glass concrete affected by ASR presented in Chapters 3 and 4, ASR products could only be found filling cracks, both inside glass particles and in the cementitious matrix, and in between the cementitious matrix and glass aggregate particles. This, of course, does not imply that the precipitation of ASR products could not have occurred dispersed in the porous cementitious matrix, since, in this case, it would be probably impossible to detect in the SEM images. In any case, it seems clear that the precipitation reactions occur mainly at these locations. Moreover, the glass zones which appear to be altered by dissolution processes are reduced to a few microns inside of the original glass surface. With this in mind, and with the aim of reducing the computational cost, in the proposed model Reactions (6.2)–(6.4) are assumed to occur only at the glass-cement interfaces and within opened cracks, i.e. dissolution/precipitation reactions are allowed within interface elements, but not in the continuum FEs.

The proposed reaction mechanism is schematically summarized in Fig. 6.4, where the interfacial zone between HCP and a cracked SL glass particle in concrete is represented. As already mentioned, material pores and cracks are assumed to be fully saturated with water at all times during the reaction. Moreover, the pore water of the HCP has a certain content of aqueous calcium and alkalis, which determine the highly alkaline character of the pore solution, and which eventually diffuse into the pre-existing glass cracks. The SL glass in contact with this highly alkaline solution, both at the glass-cement contact and within the pre-existing glass crack, dissolves into silicate, calcium, and alkali ions (Reaction (6.2)). Wherever (within cracks or in between glass and cement) the three reactants (aqueous calcium, alkali and silicate ions) are available in sufficient concentration, Reactions (6.3) and (6.4) may occur forming RPA and RPB. Simultaneously, at the glass-cement interfacial zone (and eventually at both sides HCP cracks), portlandite is dissolved (Reaction (6.1)) in order to restore equilibrium calcium concentration of the pore solution.

Both, glass and portlandite dissolutions are assumed to occur as dissolution fronts moving away from the discontinuity (crack or interface) mid-plane inward the glass and the HCP, respectively. At the glass-cement interface and at HCP cracks, where calcium ions resulting from portlandite dissolution are more readily available, the formation of RPA is favoured in detriment of the formation of RPB. Consequently, the resulting ASR

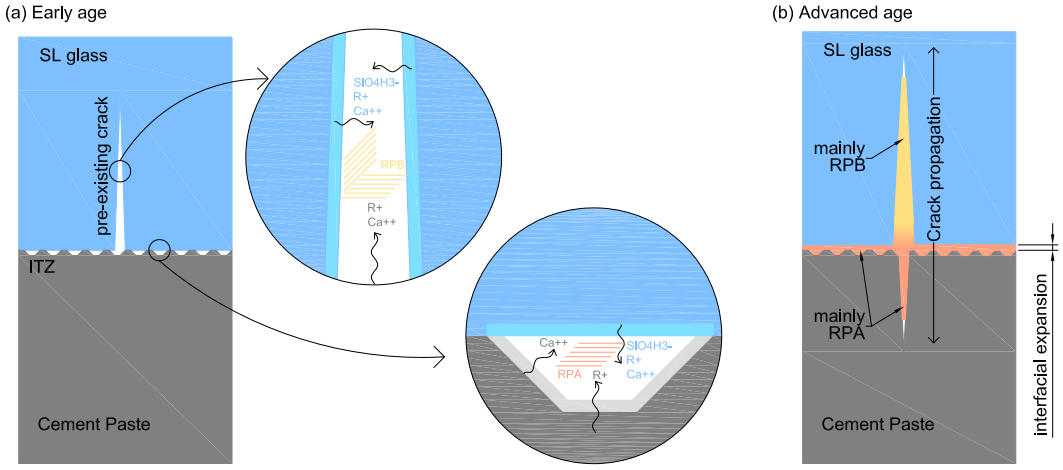

FIGURE 6.4: Schematic representation of ASR mechanism in SL glass concrete.

product has higher calcium content than the ASR products formed within the glass crack.

At a given location, if the volume of precipitated reaction products is greater than the available space within the crack/interface (plus the additional space liberated by silica and portlandite dissolution), a localized internal pressure is induced, which eventually may lead to the propagation of cracks. Additionally, the volume balance of the solid constituents plus the crack aperture, determines the transport properties of the crack/interface.

6.3.6 Mechanical properties of ASR products

The ASR products are assumed to precipitate at the reaction site (where Reactions (6.3) and (6.4) occur) and remain there. That is, no flow of the ASR products due to applied stress is considered.

The volume occupied by a mole of solid ASR product 'α' (where 'α' may refer to either RPA or RPB) is referred as 'specific molar volume' (η^{α}). The 'apparent molar volume' (ω^{α}) is defined as the sum of the volume of the solid ASR product plus the volume occupied by the absorbed water (gel water). The ratio between the volume of gel water and the apparent volume of ASR products is referred as 'gel porosity' (ϕ^{α}). In unstressed condition, the gel porosity and, consequently, the apparent molar volume have their maximum values ϕ_o^{α} and ω_o^{α}, respectively.

If a progressively increasing compressive stress is applied to the ASR product, the gel porosity is assumed to monotonically decrease from ϕ_o^{α} until zero for stresses beyond a certain threshold value σ_{th}^{α} (Fig. 6.5, left). As the result, the apparent molar volume is monotonically reduced from ω_o^{α} until reaching (if the solid strains are neglected) the solid

volume η^{α} (Fig. 6.5, right). Note that σ^{α}_{th} is the Maximum Swelling-Pressure (MSP) defined in Section 6.2. In comparison with the volume changes induced by the variation of gel water content, the volume change of the solid clusters due to applied stresses is regarded as negligible. The values of η^{α}, ϕ^{α}_{o}, and σ^{α}_{th} are assumed to depend on the composition of the RP, in such a way that low-calcium products (RPB) have much higher values of ϕ^{α}_{o}, and σ^{α}_{th} than high-calcium products (RPA). Finally, the properties of the mixture of RPA and RPB will result of the weighted average of the properties of each component.

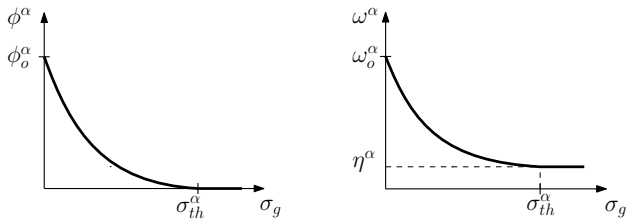

FIGURE 6.5: Schematic representation of the evolution of gel porosity (ϕ^{α}) and apparent molar volume (ω^{α}) of the ASR product 'α' (RPA or RPB) for increasing compressive stress (σ_g).

6.4 Diffusion-reaction formulation

In this section, the previously discussed modelling assumptions are formulated within the generic modelling framework proposed in Chapter (5). In order to facilitate the comparison, the chemical species intervening in Reactions (6.2)–(6.6) are summarized in Table 6.1 in the same 'categories' used in Chapter (5). Additionally, the identifiers (Id.) adopted for each species are also indicated.

TABLE 6.1: Chemical species considered in the model for ASR expansions in SL glass concrete.

State	Character	Species	Chemical notation	Id.
Solid	Reactive (α-species)	SL Glass	$SiO_2(CaO)_{0.2}(R_2O)_{0.12}$	S
		Portlandite	$Ca(OH)_2$	C
		Reaction Product A	$(SiO_2)(CaO)_{1.5}(R_2O)_{0.1}(H_2O)_{2.6+a_5}$	A
		Reaction Product B	$(SiO_2)(CaO)_{0.3}(R_2O)_{0.15}(H_2O)_{1.55+b_5}$	B
	Inert (ϑ-species)	Inert Cement Paste	n/a	ICP
Aqueous	Primary (β-species)	Monovalent silicate ion	$SiO_4H_3^-$	s
		Calcium ion	Ca^{2+}	c
		Total alkalis	ROH and R^+	r
	Secondary (β-species)	Alkali Hydroxide	ROH	$r0$
		Alkali ion	R^+	$r1$
		Hydroxyl ion	OH^-	oh
		Hydronium ion	H^+	h
Liquid		Water	H_2O	H

6.4.1 Solute mass balance

The mass balance equations of the three primary aqueous species in pore solution are obtained for the continuum porous medium by rewriting Eq. (5.96) as follows:

$$\begin{cases} \dfrac{\partial(\phi c^s)}{\partial t} = \nabla^T \left(D^s \nabla c^s\right) \\ \dfrac{\partial(\phi c^c)}{\partial t} = \nabla^T \left(D^c \nabla c^c\right) \\ \dfrac{\partial(\phi c^r)}{\partial t} = \nabla^T \left(D^r \nabla c^r\right) \end{cases} \tag{6.12}$$

where

the superscripts s, c and r stand for aqueous silicate, calcium and alkali species,

c^β [mol $\mathrm{m}_{\mathrm{ps}}^{-3}$] is the molar concentration of the β-species per unit volume of pore solution,

ϕ [$\mathrm{m}_{\mathrm{ps}}^3\mathrm{m}^{-3}$] is the total porosity of the porous medium, calculated as the ratio between the volume of pore solution and the volume of the porous medium,

D^β [$(\mathrm{m}_{\mathrm{ps}}^3\mathrm{m}^{-3})\mathrm{m}^2\ \mathrm{s}^{-1}$] is the effective diffusivity of the aqueous β-species in the porous medium (assumed isotropic $D_x^\beta = D_y^\beta = D^\beta$), and

$\nabla = \left[\frac{\partial}{\partial x} \quad \frac{\partial}{\partial y}\right]^T$.

Note that the source terms (q^β) have been omitted since no dissolution/precipitation reactions are considered to take place in the continuum medium. The variable c^r represents the summation of the molar concentrations of both alkali aqueous species in pore solution as it is given by Eq. (6.13), where the superscript $r0$ and $r1$ stand for ROH and R^+ respectively.

$$c^r = c^{r0} + c^{r1} \tag{6.13}$$

The mass balance equations along a discontinuity (crack or interface) mid-plane is obtained by rewriting Eq. (5.97) as:

$$\begin{cases} \dfrac{\partial(w\phi_{mp} c^s_{mp})}{\partial t} = \dfrac{\partial}{\partial l}\left(T_l^s \dfrac{\partial c^s_{mp}}{\partial l}\right) + q^s_{mp} \\ \dfrac{\partial(w\phi_{mp} c^c_{mp})}{\partial t} = \dfrac{\partial}{\partial l}\left(T_l^c \dfrac{\partial c^c_{mp}}{\partial l}\right) + q^c_{mp} \\ \dfrac{\partial(w\phi_{mp} c^r_{mp})}{\partial t} = \dfrac{\partial}{\partial l}\left(T_l^r \dfrac{\partial c^r_{mp}}{\partial l}\right) + q^r_{mp} \end{cases} \tag{6.14}$$

with transversal passing fluxes given by

$$j_n^s = D_n^s \check{c}_{mp}^s; \quad j_n^c = D_n^c \check{c}_{mp}^c; \quad j_n^r = D_n^r \check{c}_{mp}^r \tag{6.15}$$

where

c_{mp}^β [mol $\mathrm{m}_{\mathrm{ps}}^{-3}$] is the molar concentration of the β-species evaluated at the discontinuity mid-plane,

$\check{c}_{mp}^\beta$ [mol $\mathrm{m}_{\mathrm{ps}}^{-3}$] is the difference of concentration of the β-species in pore solution between the two surfaces of the discontinuity,

w [m] is the width of the discontinuity,

ϕ_{mp} [$\mathrm{m}_{\mathrm{ps}}^3$ m^{-3}] is the total porosity of the discontinuity filling ($\phi_{mp} = 1$ for a clean discontinuity),

q_{mp}^β [mol m^{-2} s^{-1}] is the rate of net production β-species per unit of mid-plane surface area,

T_l^β [($\mathrm{m}_{\mathrm{ps}}^3\mathrm{m}^{-3}$)($\mathrm{m}^3$ s^{-1})] is the longitudinal 'transmissivity' of the β-species in the discontinuity, and

D_n^β [($\mathrm{m}_{\mathrm{ps}}^3\mathrm{m}^{-3}$)(m s^{-1})] is the transversal diffusivity of the β-species in the discontinuity.

6.4.2 Source terms

The net production rates at of primary aqueous species in the discontinuities are obtained by rewriting the generic Equation (5.13) according to the stoichiometry of Reactions (6.2)–(6.4) as follows:

$$q_{mp}^s = -\bar{\Gamma}_{mp}^S - \bar{\Gamma}_{mp}^A - \bar{\Gamma}_{mp}^B \tag{6.16a}$$

$$q_{mp}^c = -0.2\ \bar{\Gamma}_{mp}^S - \bar{\Gamma}_{mp}^C - 1.5\ \bar{\Gamma}_{mp}^A - 0.3\ \bar{\Gamma}_{mp}^B \tag{6.16b}$$

$$q_{mp}^r = -0.24\ \bar{\Gamma}_{mp}^S - 0.2\ \bar{\Gamma}_{mp}^A - 0.3\ \bar{\Gamma}_{mp}^B \tag{6.16c}$$

where S, C, A and B indicate SL glass, portlandite, RPA and RPB, respectively; $\bar{\Gamma}_{mp}^\alpha$ [mol m^{-2} s^{-1}] is the net rate of formation of solid α-species per unit area of discontinuity; and the dimensionless stoichiometric coefficients (x_α^β) have been replaced by the values adopted in Section 6.3.4.

6.4.3 Mass balance of solid species

The mass balance equations for solid species in a discontinuity are obtained by rewriting the general Eq. (5.15) for each solid species considered:

$$\frac{\partial M_{mp}^{S}}{\partial t} = \bar{\Gamma}_{mp}^{S} \tag{6.17a}$$

$$\frac{\partial M_{mp}^{C}}{\partial t} = \bar{\Gamma}_{mp}^{C} \tag{6.17b}$$

$$\frac{\partial M_{mp}^{A}}{\partial t} = \bar{\Gamma}_{mp}^{A} \tag{6.17c}$$

$$\frac{\partial M_{mp}^{B}}{\partial t} = \bar{\Gamma}_{mp}^{B} \tag{6.17d}$$

where M_{mp}^{α} [mol m^{-2}] is the amount of solid α-species per unit area of discontinuity. The initial content of α-species in the interface elements is always null, i.e. $M_{mp}^{\alpha}(t=0)=0$. However, depending on the type of discontinuity being represented, dissolution of SL glass and/or portlandite is allowed leading to negative contents. A negative M_{mp}^{S} or M_{mp}^{C} indicates the amount of SL glass/portlandite dissolved at one or both sides of the interface. Therefore, M_{mp}^{S} can only be negative if at least one side of the interface element is shared with a continuum element representing SL glass. Similarly, M_{mp}^{C} can only be negative if at least one side of the interface element is shared with a continuum element representing cementitious matrix (mortar or HCP).

6.4.4 Water balance

As a post-processing result, the net rate of water production/consumption in a discontinuity ($\bar{\Gamma}_{mp}^{H}$) can be obtained from the following expression:

$$\bar{\Gamma}_{mp}^{H} = -2.0\ \bar{\Gamma}_{mp}^{C} - (2.2 + a_5)\,\bar{\Gamma}_{mp}^{A} - b_5\ \bar{\Gamma}_{mp}^{B} \tag{6.18}$$

where the dimensionless stoichiometric coefficients adopted in Section 6.3.4 have been introduced. Note that $\bar{\Gamma}_{mp}^{H}$ is positive if water is produced and negative otherwise. As discussed in Section 5.2.2.4, assuming that the material remains fully saturated with water implies that there is no need of explicitly considering the water balance in order to solve the diffusion-reaction problem.

6.4.5 Volumetric balance

Since precipitation/dissolution reactions are not allowed to occur in the continuum medium, the initial volumetric fractions of solid species will remain constant. In contrast,

the precipitation/dissolution of solid species is allowed at discontinuities (glass-cement contacts or cracks) and consequently the volumetric fractions assigned to them may change.

The volumes of solid species considered for discontinuities are obtained, from Eq. (5.24), as functions of their molar concentration as follow:

$$\mathcal{U}^S_{mp} = \frac{\eta^S}{1-\phi^S} M^S_{mp} \tag{6.19a}$$

$$\mathcal{U}^C_{mp} = \frac{\eta^C}{1-\phi^S} M^C_{mp} \tag{6.19b}$$

$$\mathcal{U}^A_{mp} = \frac{\eta^A}{1-\phi^A} M^A_{mp} \tag{6.19c}$$

$$\mathcal{U}^B_{mp} = \frac{\eta^B}{1-\phi^B} M^B_{mp} \tag{6.19d}$$

where η^α [m^3 mol^{-1}] and ϕ^α [$\mathrm{m}^3_{\mathrm{ps}}$ m^{-3}] are the 'specific' molar volume and the gel porosity of the solid α-species, respectively.

The gel porosity is generically assumed to depend on the applied stress σ_g, according to

$$\phi^\alpha = \phi^\alpha_o \; f^\alpha_\phi(\sigma_g) \tag{6.20}$$

where ϕ^α_o is the gel porosity value for the unstressed state. $f^\alpha_\phi(\sigma_g)$ is a continuous, non-negative function defined for $\sigma_g \in (-\infty, 0]$ as follows

$$f^\alpha_\phi(\sigma_g) = 1 - \frac{\exp\left[-k\left(1-\bar{\sigma}_g\right)^p\right] - \exp(-k)}{1-\exp(-k)} \tag{6.21}$$

$$\text{with } \bar{\sigma}_g = \begin{cases} \sigma_g/\sigma_{th} & \text{if} \quad \sigma_{th} < \sigma_g \leq 0 \\ 1 & \text{if} \quad \sigma_g < \sigma_{th} \end{cases}$$

where $p > 1$ and $k \neq 0$ are dimensionless shape parameters, and σ_{th} [Pa] is the threshold stress below which the gel porosity becomes null. Note that $f^\alpha_\phi(\sigma_g)$ is an interpolation function ranging from 1, for $\sigma_g = 0$, to 0, for $\sigma_g \leq \sigma_{th}$. Since SL glass and portlandite have no gel porosity, the function f^α_ϕ is only applicable for Reaction Products A and B. The same threshold stress is used in functions f^A_ϕ and f^B_ϕ, which is obtained as follows:

$$\sigma_{th} = \frac{M^A_{mp}\tilde{\sigma}^A_{th} + M^B_{mp}\tilde{\sigma}^B_{th}}{M^A_{mp} + M^B_{mp}} \tag{6.22}$$

where $\tilde{\sigma}^A_{th}$ and $\tilde{\sigma}^B_{th}$ are the threshold stresses of pure Reaction Products A and B, respectively.

The 'specific' molar volume η^{α} is treated differently in the diffusion-reaction formulation than in the mechanical one. In the first case, it is considered to remain constant, being unaffected by σ_g, i.e. SL glass, portlandite and the RP clusters are treated as incompressible solids. This is justified because the volume change of these solids due to the applied stress is expected to be much smaller than the overall volume changes induced by the reduction of the gel water content. Therefore, neglecting the change of specific molar volume is not expected to significantly modify the chemo-transport results.

In the case of the mechanical formulation, in contrast, considering the RPs filling a discontinuity as incompressible solids is a very restrictive condition which hinder the numerical solution of the problem. This problem is avoided by assigning, in the mechanical formulation, the following stress dependence to the specific molar volume of Reaction Products A and B:

$$\eta^{\alpha} = \eta_o^{\alpha}\ f_{\eta}^{\alpha}\left(\sigma_g\right) \tag{6.23}$$

where η_o^{α} is the specific molar volume in unstressed state and $f_{\eta}^{\alpha}(\sigma_g)$ is a continuous, non-negative function defined for $\sigma_g \in (-\infty, 0]$ as follows

$$f_{\eta}^{\alpha} = \exp\left(k_{\eta}\sigma_g\right) \tag{6.24}$$

where k_{η} [Pa^{-1}] is a positive (very small) compliance constant. Since $\sigma_g \leq 0$, the smaller k_{η}, the higher the stiffness of the RP clusters. Note that f_{η}^{α} ranges from 1, for $\sigma_g = 0$, to 0, for $\sigma_g \to -\infty$. k_{η} plays the role of a 'penalty coefficient' that needs to be sufficiently small to induce negligible volume changes from the chemo-transport point of view, but sufficiently high to facilitate the converge to the numerical solution of the mechanical problem. This issue is further discussed in Section 6.5.2.2.

As explained above (Section 6.4.3), M^S and M^C (and consequently $\mathcal{U}_{mp}^S$ and $\mathcal{U}_{mp}^C$) can be negative, indicating the amount of SL glass/portlandite dissolved at one or both sides of the discontinuity. Portlandite is finely dispersed in the HCP and, consequently, its dissolution leaves behind a solid skeleton of inert cement paste which continues delimiting the discontinuity. In contrast, SL glass dissolution, being a congruent dissolution process, moves forward the border of the discontinuity. In a simplified approach, these observations lead us to consider the volume of dissolved SL glass (but not the volume of dissolved portlandite) as part of the total volume of discontinuity. Then, the total volume ($\mathcal{U}_{mp}$ [$\mathrm{m}^3\ \mathrm{m}_{\mathrm{mp}}^{-2}$]) and the volume of capillary pores ($\mathcal{U}_{\mathrm{mp}}^{cp}$ [$\mathrm{m}_{\mathrm{ps}}^3\ \mathrm{m}_{\mathrm{mp}}^{-2}$]) assigned to a discontinuity, can be obtained by adapting Eqs. (5.20) and (5.27) as follow:

$$\mathcal{U}_{mp} = \mathcal{U}_{mp}^{o} + a_n^{cr} - \left\langle \mathcal{U}_{mp}^{S} \right\rangle_{-} \tag{6.25}$$

$$\mathcal{U}^{cp}_{mp} = \mathcal{U}_{mp} - \langle \mathcal{U}^{S}_{mp} \rangle_{+} - \langle \mathcal{U}^{C}_{mp} \rangle_{+} - \mathcal{U}^{A}_{mp} - \mathcal{U}^{B}_{mp} \tag{6.26}$$

where $\mathcal{U}^{o}_{mp}$ is an initial volume of 'capillary pores' (volume filled with free water), a^{cr}_{n} [m] is the cracking normal aperture (see Section 6.5.2.1), and $\langle X \rangle_{-}$ and $\langle X \rangle_{+}$ are Macaulay brackets standing for 'the negative part of X' and 'the positive part of X', respectively.

The total volume of pore solution ($\mathcal{U}^{ps}_{mp}$ [$\mathrm{m^3_{ps}\ m^{-2}_{mp}}$]) results from the sum of the solution in capillary pores and the solution in gel pores:

$$\mathcal{U}^{ps}_{mp} = \mathcal{U}^{cp}_{mp} + \phi^{A}\mathcal{U}^{A}_{mp} + \phi^{B}\mathcal{U}^{B}_{mp} \tag{6.27}$$

Finally, the expression of the total porosity ϕ_{mp} is the same as given in Eq. (5.31), i.e.

$$\phi_{mp} = \frac{\mathcal{U}^{ps}_{mp}}{\mathcal{U}_{mp}} \tag{6.28}$$

In order to facilitate the interpretation of previous equations, Fig. 6.6 depicts a schematic representation of a SL glass-HCP interface under different conditions. The first case (Fig. 6.6a) represents a sound (not cracked) interface before any dissolution/precipitation reaction occurs. In the proposed modelling framework, reactions in discontinuities can occur only if they contain certain amount of pore solution ($\phi_{mp} > 0$). Therefore, in order to simulate the ASR occurring at a glass-cement interface, an initial volume of pore solution needs to be considered in the corresponding interface elements. This is done by assigning an initial volume of 'capillary pores' (volume filled with free water) $\mathcal{U}^{o}_{mp}$. This initial volume is only considered in the diffusion-reaction problem, i.e. for the mechanical problem the interface is considered closed ($a^{cr}_{n} = 0$). Note that $\mathcal{U}^{o}_{mp}$ will be null for interface elements inside bulk glass or cementitious matrix.

The second case (Fig. 6.6b) represents the same interface with its faces separated a distance a^{cr}_{n} [m] (cracking normal aperture) after a fracturing process. The cracking normal aperture is obtained by solving the mechanical problem. The total volume of the interface in this condition is $\mathcal{U}_{mp} = a^{cr}_{n} + \mathcal{U}^{o}_{mp}$ which coincides with the volume of 'capillary pores' $\mathcal{U}^{cp}_{mp}$ since the solid fractions are null.

The third case (Fig. 6.6c) represents a sound (not cracked) interface where dissolution of glass and portlandite, as well of precipitation of reaction products, have occurred. Dissolution fronts of glass and portlandite are indicated with dotted lines in the figure. Since glass is assumed to dissolve congruently, the advancement of the dissolution creates a volume of 'capillary pores' which is incorporated to the interface volume. In contrast, the dissolution of portlandite in the adjacent HCP increases the porosity but leaves a residual solid skeleton which continues delimiting the discontinuity. Therefore,

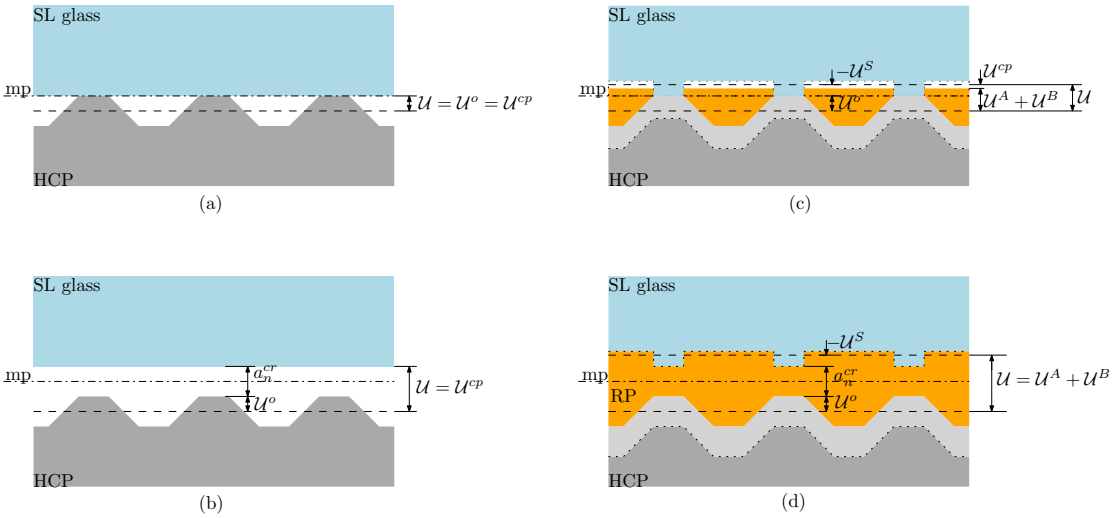

FIGURE 6.6: Schematic representation of a SL glass-HCP interface under different conditions: (a) sound interface before any reaction has started, (b) cracked interface before any reaction has started, (c) sound interface after dissolution/precipitation reactions, and (d) cracked interface due to the internal pressure exerted by reaction products. Dotted lines indicate glass and portlandite dissolution fronts. Dashed lines indicate top and bottom limits of the interface (for diffusion-reaction processes). The subscripts *mp* have been removed from the volumetric fraction symbols for the sake of clarity.

the volume of the dissolved portlandite is not incorporated to the interface volume. Simultaneously to the dissolution of glass and portlandite, reaction products have been formed filling in part the 'capillary pores'.

As the reaction progresses, eventually the volume of 'capillary pores' is exhausted and the precipitation of any additional amounts of reaction products will exert an internal pressure at both sides of the interface. The mechanical reaction to this pressure (σ_g) will reduce the gel porosity and, consequently, the apparent volume of the reaction products. If the internal internal (gel) pressure is high enough (Fig. 6.6d), the tensile strength of the interface may be overcome, and the interface is cracked developing a normal aperture a_n^{cr}. The volume created by the crack aperture is incorporated to the total interface volume as capillary pore volume. The crack aperture decompresses the reaction products in such a way that the newly created capillary pore space is immediately filled by them.

6.4.6 Reaction rates

The calculation of the sink/source terms q_{mp}^{β} according with Eqs. (6.16a)–(6.16c) requires establishing the kinetic laws of Reactions (6.2)–(6.4) in order to obtain the corresponding reaction rates $\bar{\Gamma}_{mp}^{\alpha}$ [mol m^{-2} s^{-1}]. For later convenience, $\bar{\Gamma}_{mp}^{\alpha}$ is given as

$$\bar{\Gamma}_{mp}^{\alpha} = \mathcal{U}_{mp}^{ps} \Gamma_{mp}^{\alpha} \tag{6.29}$$

where Γ^{α}_{mp} [mol m^{-3}_{ps} s^{-1}] is the net formation rate of α-species per unit volume of pore solution in the discontinuity.

It is assumed that the driving force of the dissolution/precipitation reactions of reactive α-species is the distance from equilibrium expressed as $(\psi^{\alpha} - 1)$, where ψ^{α} is the dimensionless saturation index of the pore solution with respect to the solid α-species. Dissolution and precipitation reactions are assumed not to occur simultaneously but alternately depending on ψ^{α}. If $\psi^{\alpha} > 1$, the solution is over-saturated with respect to the α-species and, consequently, the reaction progresses in the precipitation direction. If $\psi^{\alpha} < 1$, the solution is under-saturated and solid dissolution occurs. If $\psi^{\alpha} = 1$, the solid and the solution are in thermodynamical equilibrium.

The saturation indexes adopted for Reactions (6.2)–(6.4) are

$$\text{SL Glass :} \qquad \psi^{S} = \frac{a^{s} a^{h}}{K^{S}_{sp}} \tag{6.30a}$$

$$\text{Portlandite :} \qquad \psi^{C} = \frac{a^{c} \left(a^{oh}\right)^{2}}{K^{C}_{sp}} \tag{6.30b}$$

$$\text{Reaction Product A :} \qquad \psi^{A} = \frac{a^{s} \left(a^{c}\right)^{1.5} \left(a^{r1}\right)^{0.2} \left(a^{oh}\right)^{2.2}}{K^{A}_{sp}} \tag{6.30c}$$

$$\text{Reaction Product B :} \qquad \psi^{B} = \frac{a^{s} \left(a^{c}\right)^{0.3} \left(a^{r1}\right)^{0.3} \left(a^{h}\right)^{0.1}}{K^{B}_{sp}} \tag{6.30d}$$

where a^{β} [mol m^{-3}] is the thermodynamic activity of the aqueous β-species in pore solution, and K^{α}_{sp} is the saturation product constant of α-species dissolution. Note that the saturation index of SL glass has been made to depend only on the activity of silicate ions and the pH of the solution, as it has been proposed by Maraghechi et al. [141]. The saturation product constants of portlandite (K^{C}_{sp}) and of SL glass (K^{S}_{sp}) as functions of temperature are obtained from the literature as it is detailed in Appendix B.4. The saturation product constants of RPA and RPB (K^{A}_{sp} and K^{B}_{sp}), in contrast, need to be calibrated by fitting ASR experimental results.

The adopted kinetic laws are:

$$\Gamma^{S}_{mp} = f_{\psi}(\psi^{S}) \times \begin{cases} k^{S}_{f} & \text{if} \quad \psi^{S} \geq 1 \\ \left(\mathcal{U}^{ps}_{mp}\right)^{-1} \mathcal{S}_{mp} f^{S}_{1} f^{S}_{2} k^{S}_{d} \left(a^{oh}\right)^{p} & \text{if} \quad \psi^{S} < 1 \end{cases} \tag{6.31}$$

$$\Gamma^{C}_{mp} = f_{\psi}(\psi^{C}) \times \begin{cases} k^{C}_{f} & \text{if} \quad \psi^{C} \geq 1 \\ \left(\mathcal{U}^{ps}_{mp}\right)^{-1} \mathcal{S}_{mp} f^{C}_{1} k^{C}_{d} & \text{if} \quad \psi^{S} < 1 \end{cases} \tag{6.32}$$

$$\Gamma^{A}_{mp} = f_{\psi}(\psi^{S}) \times \begin{cases} k^{A}_{f} & \text{if} \quad \psi^{A} \geq 1 \\ k^{A}_{d} & \text{if} \quad \psi^{A} < 1 \end{cases} \tag{6.33}$$

$$\Gamma^B_{mp} = f_\psi(\psi^S) \times \begin{cases} k^B_f & \text{if} \quad \psi^B \geq 1 \\ k^B_d & \text{if} \quad \psi^B < 1 \end{cases} \tag{6.34}$$

where k^α_f and k^α_d are kinetic constants for the α-species formation and dissolution, respectively.

The kinetic laws are usually considered to be proportional to the distance $(\psi^\alpha - 1)$ [e.g. 74, 95, 141]. However, from the numerical point of view, this has the disadvantage that the maximum precipitation rate is not bounded. It has been found that in some cases this may lead to divergence of the Newton-Raphson iterative procedure described in Section 5.2.5. In order to avoid this problem, the reaction rates $\bar{\Gamma}^\alpha_{mp}$ have been adopted which are proportional to the following exponential function of the saturation index ψ^α:

$$f_\psi(\psi^\alpha) = \left[1 - 2\exp\left(\psi^\alpha \ln\frac{1}{2}\right)\right] \tag{6.35}$$

This function varies monotonically from $f_\psi = -1$, for $\psi^\alpha = 0$, to $f_\psi = 0$, for $\psi^\alpha = 0$, and asymptotically $f_\psi \to 1$ for $\psi^\alpha \to +\infty$.

In all cases, the formation reactions are considered to occur uniformly in the pore solution within the interface FE and, therefore, the kinetics of the α-species formation has been made proportional to $\mathcal{U}^{ps}_{mp}$. Having no experimental data on the specific surface of ASR products and for the sake of simplicity, the dissolution reactions of RPA and RPB are also considered to be proportional to $\mathcal{U}^{ps}_{mp}$. In contrast, as mentioned above (Section 6.3), the dissolution reactions of SL glass and portlandite are considered to occur in dissolution fronts, and, therefore, to have dissolution rates proportional to the surface area of the corresponding dissolution front. This surface area changes depending on the location of the interface FE (at the cementitious matrix, inside a glass particle, or at a glass-cement contact) and is not constant but evolves with the cracking of the interface and the precipitation of solids within it. These effects have been introduced in the kinetic laws of glass and portlandite dissolution by means of the functions f^S_1, f^C_1, and $\mathcal{S}_{mp}$ which return the surface area estimated of dissolution front per unit area of discontinuity mid-plane according to the following expressions:

$$f^S_1 = \begin{cases} 0 & \text{if it is a cement-cement interface} \\ 1 & \text{if it is a cement-glass interface} \\ 2 & \text{if it is a glass-glass interface} \end{cases} \tag{6.36a}$$

$$f^C_1 = \begin{cases} 2 & \text{if it is a cement-cement interface} \\ 1 & \text{if it is a cement-glass interface} \\ 0 & \text{if it is a glass-glass interface} \end{cases} \tag{6.36b}$$

$$\mathcal{S}_{mp} = \phi_{mp}\mathcal{S}^o_{mp} + \phi_{mp}\left(1 - \mathcal{S}^o_{mp}\right)\frac{W^{cr}}{G^I_f} \tag{6.37}$$

where $\mathcal{S}^o_{mp}$ is the initial surface area of dissolution front corresponding to interfaces with $\mathcal{U}^o_{mp} > 0$, G^I_f is the specific fracture energy in mode I, and W^{cr} is a history variable of the mechanical constitutive law of the interface which saves the amount of work spent in fracture processes during the formation of the crack. W^{cr} is a coupling variable that in the current implementation is obtained indirectly as a closed form expression of the normal aperture of the FE interface (see Eq. (6.95) in the following Section 6.5.2.1). This expression is exact only if the fracture is developed in pure tension (mode I), which is not necessarily always the case. In future implementations, W^{cr} will be obtained directly from the mechanical code by means of an additional exchange file.

Finally, the dissolution rate of SL glass is penalized by a reduction factor f^S_2 which asymptotically tends to 0 for growing amounts of dissolved glass (M^S_{mp}):

$$f^S_2 = \exp\left(A^S \left\langle M^S_{mp} \right\rangle_-\right) \tag{6.38}$$

where A^S [m^2 mol^{-1}] is a fitting parameter. This factor accounts for the increasing distance of the glass dissolution front to the mid-plane of the discontinuity.

6.4.7 Chemical speciation

The calculation of the reaction rates according to the equations presented in the previous section requires to determine the concentration of secondary aqueous species as a function of the concentration of the primary ones. This is achieved by simultaneously enforcing the following equations:

$$-c^s + 2c^c + c^{r1} + c^h - c^{oh} = 0 \tag{6.39}$$

$$c^r = c^{r0} + c^{r1}$$

$$\gamma^h c^h \gamma^{oh} c^{oh} = K_w \tag{6.40}$$

$$\frac{\gamma^{oh} c^{oh} \gamma^{r1} c^{r1}}{\gamma^{r0} c^{r0}} = K^r_e \tag{6.41}$$

$$\log_{10}\gamma^{oh} = \log_{10}\gamma^h = \log_{10}\gamma^{r1} = A_\gamma\left[\frac{\sqrt{I}}{1+\sqrt{I}} - \left(0.2I - \frac{I^2}{24}\right)\right] \tag{6.42}$$

$$I = \frac{1}{2}\left(c^s + 4c^c + c^{r1} + c^h + c^{oh}\right)\,[\text{mol/L}] \tag{6.43}$$

The first equation is the electric charge balance equation given in Eq. (5.39), rewritten for the aqueous species considered in this model. The second equation is the definition of the total alkali concentration previously given in Eq. (6.13). The third equation is the equilibrium equation of water self-ionization previously given in Eq. (5.40), rewritten in terms of concentrations and activity coefficients. The fourth equation is the equilibrium equation of the dissociation of aqueous ROH (Reaction (6.6)), where K_e^r is the corresponding equilibrium constant. The fifth equation is the modified Davies equation previously given in Eq. (5.37), rewritten for $z^\beta = 1$. Finally, the sixth equation is the expression of the ionic strength previously given in Eq. (5.38), rewritten for the aqueous species considered in this model.

The effect of temperature on the chemical speciation is introduced through the Debye-Hückel parameter (A_γ) and the dissociation equilibrium constants (K_w and K_e^r). The expression of A_γ as a function of temperature is given in Appendix B.2, while the expressions of K_w and K_e^r as functions of temperature are given in Appendix B.3.

Finally, as a post-processing result, the pH of the pore solution, defined as the decimal logarithm of the reciprocal of the hydrogen ion activity (a^h) [48], can be obtained from

$$\mathrm{pH} = -\log_{10}(a^h) = -\log_{10}(\gamma^h c^h) \tag{6.44}$$

6.4.8 Time integration of the chemical law

The time integration of the chemical law is done according to the procedure described in Section 5.2.6. To do so, the generic system of equations (5.159) is rewritten for this model as

$$\begin{cases} M_N^S = M_0^S + \int_{t_0}^{t_N} \bar{\Gamma}^S(\tau) d\tau \\ M_N^C = M_0^C + \int_{t_0}^{t_N} \bar{\Gamma}^C(\tau) d\tau \\ M_N^A = M_0^A + \int_{t_0}^{t_N} \bar{\Gamma}^A(\tau) d\tau \\ M_N^B = M_0^B + \int_{t_0}^{t_N} \bar{\Gamma}^B(\tau) d\tau \end{cases} \tag{6.45}$$

where the subscripts mp have been removed for clarity, and $M_0^\alpha = M^\alpha(t_0)$ and $M_N^\alpha = M^\alpha(t_N)$, being t_0 and t_N the time at the beginning and at the end of the time increment Δt. For the adopted kinetic laws (Section 6.4.6) the system of equations (6.45) has no analytical solution and, therefore, it is necessary to use to a numerical procedure. With this purpose, the time increment Δt, corresponding to the global time discretization described in Section 5.135, is subdivided in N sub-increments $\delta t_{i+1} = t_{i+1} - t_i$, such

that

$$\sum_{i=0}^{N-1} \delta t_{i+1} = \Delta t \tag{6.46}$$

Then, the variation of M^α in a time sub-increment δt_{i+1} is $\delta M^\alpha_{i+1} = M^\alpha_{i+1} - M^\alpha_i$, in such a way that

$$M^\alpha_N = M^\alpha_0 + \sum_{i=0}^{N-1} \delta M^\alpha_{i+1} \tag{6.47}$$

Now the system of equations (6.45) can be rewritten in differential form and for a time t in the sub-increment δt_{i+1} as

$$\begin{cases} \dot{M}^S = \bar{\Gamma}^S_i \\ \dot{M}^C = \bar{\Gamma}^C_i \\ \dot{M}^A = \mathcal{U}^{ps}(t)\Gamma^A_i \\ \dot{M}^B = \mathcal{U}^{ps}(t)\Gamma^B_i \end{cases} \tag{6.48}$$

In the first two equations, the reaction rates have been replaced by a explicit (forward) Euler approximation, i.e. $\bar{\Gamma}^S(t)$ and $\bar{\Gamma}^C(t)$ are considered to remain constant and equal to their respective values at the beginning of the sub-increment ($\bar{\Gamma}^S_i$ and $\bar{\Gamma}^C_i$). In the last two equations, in contrast, the expressions of the reaction rates have been decomposed according to Eq. (6.35), and Γ^A and Γ^B are considered to remain constant and equal to their respective values at the beginning of the sub-increment ($\bar{\Gamma}^A_i$ and $\bar{\Gamma}^B_i$). In turn, the volume of pore solution $\mathcal{U}^{ps}(t)$ can be replaced by the following expression obtained by introducing Eqs. (6.19), (6.25) and (6.26) in Eq. (6.27),

$$\mathcal{U}^{ps}(t) = \left\langle \mathcal{U}^o + a^{cr}_n(t) - M^S(t)\eta^S - \left\langle M^C(t) \right\rangle_+ \eta^C - M^A(t)\eta^A - M^B(t)\eta^B \right\rangle_+ \tag{6.49}$$

where the crack aperture $a^{cr}_n(t)$ is obtained, in turn, as a linear interpolation of the known value at the beginning of the time increment and the trial value at the end of time increment:

$$a^{cr}_n(t) = a^{cr}_n(t_0) + \frac{a^{cr}_n(t_N) - a^{cr}_n(t_0)}{\Delta t}(t - t_N) \tag{6.50}$$

Note that for the diffusion-reaction code, at a given iteration of the staggered coupling procedure, $a^{cr}_n(t_N)$ is a known constant value.

Then, assuming that the $\mathcal{U}^{ps}$ remains greater than zero in the time interval (t_i, t), we obtain the following system of four differential equations with four unknowns:

$$\begin{cases} \dot{M}^S = \bar{\Gamma}_i^S \\ \dot{M}^C = \bar{\Gamma}_i^C \\ \dot{M}^A + \mathsf{a}_1 M^A = \mathsf{b}_1^A + \mathsf{a}_2 \Gamma_i^A \left(t - t_i\right) \\ \dot{M}^B + \mathsf{a}_1 M^B = \mathsf{b}_1^B + \mathsf{a}_2 \Gamma_i^B \left(t - t_i\right) \end{cases} \tag{6.51}$$

where

$$\begin{aligned} \mathsf{a}_1 &= \eta^A \Gamma_i^A + \eta^B \Gamma_i^B \\ \mathsf{a}_2 &= \left[\frac{a_n^{cr}(t_N) - a_n^{cr}(t_0)}{\Delta t} - \left(\eta^S \bar{\Gamma}_i{}^S + \eta^C \bar{\Gamma}_i{}^C \right) \right] \\ \mathsf{b}_1^A &= \eta^B \Gamma_i^B M_i^A - \left(\eta^S M_i^S + \eta^C M_i^C + \eta^B M_i^B \right) \Gamma_i^A + (\mathcal{U}^o + a_n^{cr}(t_i)) \Gamma_i^A \\ \mathsf{b}_1^B &= \eta^A \Gamma_i^A M_i^B - \left(\eta^S M_i^S + \eta^C M_i^C + \eta^A M_i^A \right) \Gamma_i^B + (\mathcal{U}^o + a_n^{cr}(t_i)) \Gamma_i^B \end{aligned}$$

After some algebra, the following expressions of $M^S(t)$ and $M^C(t)$ are obtained:

$$M^S(t) = M_i^S + \bar{\Gamma}_i^S \left(t - t_i\right) \tag{6.52}$$

$$M^C(t) = M_i^C + \bar{\Gamma}_i^C \left(t - t_i\right) \tag{6.53}$$

Concerning $M^A(t)$ and $M^B(t)$, for $\mathsf{a}_1 \neq 0$ the expressions obtained are:

$$M^A(t) = \frac{\mathsf{b}_1^A}{\mathsf{a}_1} + \frac{\mathsf{a}_2}{\mathsf{a}_1} \Gamma_i^A \left[\left(t - t_i\right) - \frac{1}{\mathsf{a}_1} \right] + \left(M_i^A - \frac{\mathsf{b}_1^A}{\mathsf{a}_1} + \frac{\mathsf{a}_2}{\mathsf{a}_1^2} \Gamma_i^A \right) \exp\left[-\mathsf{a}_1 \left(t - t_i\right) \right] \tag{6.54}$$

$$M^B(t) = \frac{\mathsf{b}_1^B}{\mathsf{a}_1} + \frac{\mathsf{a}_2}{\mathsf{a}_1} \Gamma_i^B \left[\left(t - t_i\right) - \frac{1}{\mathsf{a}_1} \right] + \left(M_i^B - \frac{\mathsf{b}_1^B}{\mathsf{a}_1} + \frac{\mathsf{a}_2}{\mathsf{a}_1^2} \Gamma_i^B \right) \exp\left[-\mathsf{a}_1 \left(t - t_i\right) \right] \tag{6.55}$$

while for $\mathsf{a}_1 = 0$, the expressions are:

$$M^A(t) = M_i^A + \mathsf{b}_1^A \left(t - t_i\right) + \frac{1}{2} \mathsf{a}_2 \Gamma_i^A \left(t - t_i\right)^2 \tag{6.56}$$

$$M^B(t) = M_i^B + \mathsf{b}_1^B \left(t - t_i\right) + \frac{1}{2} \mathsf{a}_2 \Gamma_i^B \left(t - t_i\right)^2 \tag{6.57}$$

If the above-mentioned condition ($\mathcal{U}^{ps} > 0$ in the time interval (t_i, t)) is not satisfied, analytical solutions can also be found. These solutions are not presented here for the sake of brevity but are given in Appendix B.6.

As usual in numerical methods, the greater the number of time sub-divisions, the greater the accuracy of the solution and the greater the computational cost. Therefore, it is necessary to establish a criterion for the number of sub-divisions to be used based on the resulting integration error. Since estimating the error analytically is not straight

forward, an algorithm has been implemented that, at each integration point, performs the time integration several times with increasing number of sub-divisions, until the difference of the result in two subsequent calculations is lower than a certain tolerance.

6.4.9 Effective diffusion coefficients

6.4.9.1 Continuum porous medium

As stated above (Section 6.3.3), the effective diffusivity of primary aqueous species in the continuum medium (D^β), as well as its porosity ϕ, are assumed to remain constant. The procedure adopted for estimating these values for the cementitious matrix, as well as the special treatment given to glass elements, are discussed in the following paragraphs.

Cementitious matrix

The effective diffusivity of the cementitious matrix (cement paste or mortar) is estimated by means of the following analytical expression proposed by Oh and Jang [159]:

$$D^\beta = D_w^\beta \Delta_\phi \Delta_a \tag{6.58}$$

In this expression, similar to Eq. (5.3), the diffusivity of the β-species in bulk water (D_w^β [$\mathrm{m^2 s^{-1}}$]) is reduced by means of two dimensionless factors, Δ_ϕ and Δ_a, ranging between 1 and 0. The first reduction factor accounts for effects of the solid skeleton of the HCP (reduction of the effective diffusion section, tortuosity, constrictivity, etc.) by means of the following expression:

$$\Delta_\phi = \left(m_\phi + \sqrt{m_\phi^2 + \frac{\phi^{per}}{1-\phi^{per}} \left(\frac{D_s^\beta}{D_w^\beta} \right)} \right)^n \tag{6.59}$$

$$\text{with} \quad m_\phi = \frac{1}{2} \left[\left(\frac{D_s^\beta}{D_w^\beta} \right)^{1/n} + \frac{\phi^{cp}}{1-\phi^{per}} \left(1 - \left(\frac{D_s^\beta}{D_w^\beta} \right)^{1/n} \right) - \frac{\phi^{per}}{1-\phi^{per}} \right]$$

where D_s^β is the average effective diffusivity of the β-species through the solid skeleton, ϕ^{per} is the percolation threshold (if $\phi^{cp} < \phi^{per}$, the capillary pores are not connected), and n is the percolation exponent. According to Oh and Jang, realistic values of these parameters are $D_s^\beta / D_w^\beta \approx 2 \times 10^{-4}$ and $n \approx 2.7$ for Portland cement pastes, and $D_s^\beta / D_w^\beta \approx 5 \times 10^{-5}$ and $n \approx 4.5$ for silica fume pastes; ϕ^{per} falls between 0.16–0.18 in both cases. The capillary porosity of the HCP can be estimated based on w/c ratio and the cement composition using cement hydration models from the literature, e.g. the classical model by Powers and Brownyard [167].

The second reduction factor, applicable for mortars, accounts for the effects of aggregates dispersed in the cementitious matrix by means of the following expression:

$$\Delta_a = 1 + \frac{V_a}{\dfrac{1}{2\,(D_i/D_p)\,\varepsilon - 1} + \dfrac{1 - V_a}{3}} \tag{6.60}$$

where V_a is the volume fraction of aggregate particle inclusions, ε is the ratio of the ITZ thickness to the mean radius of aggregate particle inclusions, and D_i/D_p is the ratio of the effective diffusivity in the ITZ to the effective diffusivity in the bulk HCP. The thickness of ITZ is assumed to be approximately 20 μm based on Scrivener and Nemati's observations [190]. The ratio D_i/D_p may range between 6 and 12. In this expression, two opposite effects are considered. On one hand, the presence of aggregates (assumed to be impervious) reduces the effective diffusion section. On the other, the interfacial transition zones surrounding these aggregates have higher porosity than the bulk HCP and, thus, these zones have also higher effective diffusivity.

SL glass

The effective diffusivity and the porosity in SL glass particles is assumed to be null. If in the FE analysis these conditions were directly introduced as $D^\beta = 0$ and $\phi = 0$ in Eqs. (5.55) and (5.56), when the global diffusivity and capacity matrices are assembled, the degrees of freedom (DOFs) corresponding to nodes that only belong to SL glass FE would not be linked to other DOFs nor to imposed source terms, and, consequently, the equations corresponding to these nodes would be indeterminate.

This problem has been solved by means of an internal algorithm implemented in the diffusion-reaction code (`DRACFLOW`) that, besides assigning $D^\beta = 0$ and $\phi = 0$ to the SL glass elements, identifies the problematic nodes and imposes to them null concentrations ($\mathbb{c} = \mathbf{0}$). In that way, the DOFs corresponding to these nodes are 'excluded' from the solution of the system equations corresponding to the diffusion-reaction problem.

Another possible way of dealing with this problem would have been assigning a very small diffusivity to SL glass elements. However, this solution was ruled out because it had the inconvenient of being very restrictive for the mesh size both inside glass particles and at the neighbouring cementitious matrix.

6.4.9.2 Discontinuities

The longitudinal (T_l^β) and transversal (D_n^β) diffusivities of discontinuities will vary as ASR progresses, due to dissolution/precipitation of the solid species assigned to them, as well as due to the possible changes in the mechanical aperture due to fracturing processes.

In the following paragraphs, the relations adopted between the volume fractions in the discontinuity and longitudinal and transversal diffusivities are presented.

Longitudinal diffusivity

The total longitudinal flow J_l^β [mol s^{-1}] of the β-species along the discontinuity may be decomposed in:

$$J_l^\beta = J_{l1}^\beta + J_{l2}^\beta \tag{6.61}$$

where J_{l1}^β [mol s^{-1}] is the localized flux through the discontinuity filling and J_{l2}^β [mol s^{-1}] is the localized flux through the 'clean' discontinuity width (see Fig. 6.7). Assuming that both fluxes are proportional to the longitudinal concentration gradient in the mid-plane of the discontinuity, Eq. (6.61) can be rewritten as

$$J_l^\beta = -T_l^\beta \frac{\partial c_{mp}^\beta}{\partial l} \tag{6.62}$$

$$\text{with} \quad T_l^\beta = \left(\mathcal{U}_{mp} - \mathcal{U}_{mp}^{cp}\right) D_1^\beta + \mathcal{U}_{mp}^{cp} D_2^\beta \tag{6.63}$$

where D_1^β and D_2^β [m^{2}s^{-1}] are the diffusivities of the filled and non-filled sectors of the discontinuity, respectively.

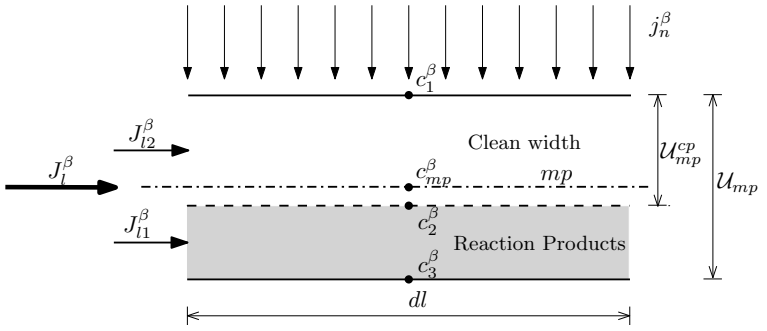

FIGURE 6.7: Schematic representations of diffusion in a discontinuity.

D_1^β is assumed to be the average effective diffusivity of the β-species through the ASR products filling the discontinuity (analogous to D_s^β in Eq. (6.59)). The diffusion in the non-filled sector is treated as a clean crack using Eq. (6.64) for calculating D_2^β as a function of the clean width $\mathcal{U}_{mp}^{cp}$. It is assumed there that D_2^β increases linearly with $\mathcal{U}^{cp}$, for $\mathcal{U}_{mp}^{cp}$ between zero and a critical crack aperture ($w^{crit} \approx 1 \times 10^{-4}$ m). For larger crack openings, the diffusivity is considered to be constant and equal to the diffusion coefficient in bulk water D_w^β. This law has been proposed by Idiart et al. [98], based on

the experimental work of Djerbi et al. [58].

$$D_2^\beta = \begin{cases} \dfrac{\mathcal{U}_{mp}^{cp}}{w^{crit}} D_w^\beta & \text{if} \quad \mathcal{U}_{mp}^{cp} < w^{crit} \\ D_w^\beta & \text{if} \quad \mathcal{U}_{mp}^{cp} \geq w^{crit} \end{cases} \tag{6.64}$$

Finally,

$$\frac{T_l^\beta}{D_w^\beta} = \left(\mathcal{U}_{mp} - \mathcal{U}_{mp}^{cp}\right) \frac{D_1^\beta}{D_w^\beta} + \mathcal{U}_{mp}^{cp} \begin{cases} \dfrac{\mathcal{U}_{mp}^{cp}}{w^{crit}} & \text{if} \quad \mathcal{U}_{mp}^{cp} < w^{crit} \\ 1 & \text{if} \quad \mathcal{U}_{mp}^{cp} \geq w^{crit} \end{cases} \tag{6.65}$$

Transversal diffusivity

For continuity, the transversal flux through the discontinuity has to be the same in clean and filled sectors, i.e.

$$j_n^\beta = j_{n1}^\beta = j_{n2}^\beta \tag{6.66}$$

Assuming that the fluxes in both sectors follow Fick's law and that the concentration gradient within each sector is constant, j_{n1}^β and j_{n2}^β [mol m^{-1} s^{-1}] are given by

$$j_{n1}^\beta = D_1^\beta \frac{\partial c^\beta}{\partial n} = D_1^\beta \frac{\left(c_3^\beta - c_2^\beta\right)}{\mathcal{U}_{mp} - \mathcal{U}_{mp}^{cp}} \tag{6.67}$$

$$j_{n2}^\beta = D_w^\beta \frac{\partial c^\beta}{\partial n} = D_w^\beta \frac{\left(c_2^\beta - c_1^\beta\right)}{\mathcal{U}_{mp}^{cp}} \tag{6.68}$$

where c_1^β, c_2^β and c_3^β are the concentrations of the β-species at both sides of the discontinuity and in the interface between filled and at non-filled sectors (see Fig. 6.7). Introducing Eq. (6.68) and (6.67) in Eq. (6.66) leads to

$$\check{c}^\beta = c_3^\beta - c_1^\beta = j_n^\beta \left(\frac{\mathcal{U}_{mp}^{cp}}{D_w^\beta} + \frac{\mathcal{U}_{mp} - \mathcal{U}_{mp}^{cp}}{D_1^\beta} \right) \tag{6.69}$$

Finally, by comparing Eq. (6.69) with Eq. (5.11), the expression of the transversal diffusivity of the discontinuity D_n^β [m s^{-1}] is obtained:

$$D_n^\beta = \frac{1}{\dfrac{\mathcal{U}_{mp}^{cp}}{D_w^\beta} + \dfrac{\left(\mathcal{U}_{mp} - \mathcal{U}_{mp}^{cp}\right)}{D_1^\beta}} \tag{6.70}$$

Since $D_n^\beta \to +\infty$ when $\mathcal{U}_{mp} \to 0$, an upper bound is established in calculations in order to avoid ill-conditioning of the diffusion matrix.

Correction for interface elements representing interfacial transition zones
The cement paste within the interfacial transition zone (ITZ) around aggregate particles has a significantly higher porosity than bulk cement paste [160, 189]. Consequently, this zone exhibits higher effective diffusivity than the bulk cement paste [24]. Even though the ITZ has a width of only a few tens of microns [189], to consider the localized increase of effective diffusivity may have a significant effect on the results because of the proximity to the reaction site. To do so, when an interface element is in between SL glass and the cementitious matrix, Eqs. (6.65) and (6.70) are modified as follow:

$$\frac{T_l^\beta}{D_w^\beta} = w_{ITZ}\frac{D_{ITZ}^\beta}{D_w^\beta} + \left(\mathcal{U}_{mp} - \mathcal{U}_{mp}^{cp}\right)\frac{D_1^\beta}{D_w^\beta} + \mathcal{U}_{mp}^{cp}\begin{cases} \dfrac{\mathcal{U}_{mp}^{cp}}{w^{crit}} & \text{if} \quad \mathcal{U}_{mp}^{cp} < w^{crit} \\ 1 & \text{if} \quad \mathcal{U}_{mp}^{cp} \geq w^{crit} \end{cases} \tag{6.71}$$

$$D_n^\beta = \frac{1}{\dfrac{\mathcal{U}_{mp}^{cp}}{D_w^\beta} + \dfrac{\left(\mathcal{U}_{mp} - \mathcal{U}_{mp}^{cp}\right)}{D_1^\beta} + \dfrac{w_{ITZ}}{D_{ITZ}^\beta}} \tag{6.72}$$

where w_{ITZ} [m] is the width of the ITZ, and D_{ITZ}^β is the effective diffusivity of the β-species in the ITZ. These modifications are based on considering the ITZ in a similar way to the layer of reaction products.

6.4.9.3 Extrapolation to other temperatures

Samson and Marchand [178] found that the ratio between the effective diffusivity in porous materials and the diffusivity in free water (D^β/D_w^β) remains almost constant for temperatures between 4 to 40 °C, indicating that an increase in temperature only contributes to increase the thermal agitation of ions in solution without affecting the microstructure of the HCP. In this work, it is assumed that these observation are still valid for temperatures up to 60 °C, and that are also valid for diffusion processes along/across discontinuities. In terms of Eqs. (6.58), (6.65), and (6.70), this means that, in the range between 4 to 60 °C, the only parameter dependent on temperature is the diffusion coefficients of the β-species in bulk water (D_w^β).

The values of D_w^β at standard conditions (25 °C, 0.1 MPa) can be easily found in physics handbooks (e.g. in [131]). These coefficients can be extrapolated to other conditions by means of the Stokes-Einstein relation given in Eq. (6.73), where μ_w [Pa s] is the viscosity of the bulk water and T [°K] is the absolute temperature [223]. The values of D_w^β at standard conditions for the aqueous species considered in the model are given in Table 6.2, as well as the diffusion coefficients in bulk water at 60 °C calculated using

Eq. (6.73) with water viscosities obtained from Kestin et al. [106].

$$\left(\frac{D_w^\beta \mu_w}{T}\right)_{T1} = \left(\frac{D_w^\beta \mu_w}{T}\right)_{T2} \tag{6.73}$$

TABLE 6.2: Diffusion coefficients in $[10^{-9}\ m^2/s]$ for aqueous species in bulk water at different temperatures. Diffusivities in bulk water at 25 °C are from Lide [131, p. 5-95] with the exception of the diffusivity of silicate ions which is from Yokoyama [222]. Diffusivities at 60 °C have been extrapolated using Stoke-Einstein relation with water viscosities given in Kestin et al. [106]. In the last column, diffusivities are normalized with respect to chloride ion diffusivity.

β-species	25 °C	60 °C	D_w^β/D_w^{cl}
Cl^-	2.032	4.328	1.000
$SiO_4H_3^-$	1.195	2.545	0.588
Ca^{2+}	0.792	1.687	0.390
Na^+	1.334	2.841	0.656
K^+	1.957	3.280	0.963

6.4.9.4 Extrapolation to other aqueous species

It is assumed that the ratio between the diffusivities of two different aqueous species β_1 and β_2 is the same, no matter if the diffusion occurs in bulk water, porous medium or discontinuities, i.e.

$$\frac{D_w^{\beta_1}}{D_w^{\beta_2}} = \frac{D^{\beta_1}}{D^{\beta_2}} = \frac{T_l^{\beta_1}}{T_l^{\beta_2}} = \frac{D_n^{\beta_1}}{D_n^{\beta_2}} \tag{6.74}$$

In terms of Eqs. (6.58), (6.65), and (6.70), this means that parameters ϕ^{per}, n, D_s^β/D_w, D_1^β/D_w, w_{crit}, and D_i^β/D_p are the same whatever the aqueous β-species considered. Therefore, these parameters can be fitted with the available experimental measurements of the effective diffusivity of one species, namely chloride ions, and, then, used for estimating the diffusivity of other aqueous β-species by means of the ratios D_w^β/D_w^{cl} given in Table 6.2.

6.5 Mechanical formulation

6.5.1 Constitutive law for continuum elements

The continuum medium is assumed to have a linear elastic behaviour. Non-linearity and internal pressure due to the precipitation of reaction products are considered only for the interface elements representing discontinuities.

6.5.2 Constitutive law for interface elements

The mechanism of ASR expansion of a discontinuity is schematically represented in Fig. 6.8a. The precipitation of reaction products within the discontinuity once the volume of 'capillary pores' ($\mathcal{U}_{mp}^{cp}$) has been filled up induces a local pressure $\bar{\boldsymbol{\sigma}}_{\boldsymbol{g}}$ that tends to separate the discontinuity sides. As a reaction, the solid bridges that keep both sides of discontinuity together are tensioned developing local stress $\bar{\boldsymbol{\sigma}}_{\boldsymbol{s}}$. The average of these local pressure/stress in the discontinuity surface area are referred as $\boldsymbol{\sigma}_{\boldsymbol{g}}$ and $\boldsymbol{\sigma}_{\boldsymbol{s}}$, respectively. The conjugate variable for both stresses is the relative displacement of both sides of the discontinuity $\mathbf{a_{mp}}$. That means that the reaction products and the discontinuity interact in a parallel scheme and, therefore, the constitutive stress vector of the discontinuity filled with reaction products $\boldsymbol{\sigma}_{\mathbf{mp}}$ is given by

$$\boldsymbol{\sigma}_{\mathbf{mp}} = \boldsymbol{\sigma}_{\boldsymbol{s}} + \boldsymbol{\sigma}_{\boldsymbol{g}} \tag{6.75}$$

or, in its corresponding differential form, by

$$d\boldsymbol{\sigma}_{\mathbf{mp}} = d\boldsymbol{\sigma}_{\boldsymbol{s}} + d\boldsymbol{\sigma}_{\boldsymbol{g}} = \frac{\partial \boldsymbol{\sigma}_{\boldsymbol{s}}}{\partial \mathbf{a_{mp}}} d\mathbf{a_{mp}} + \left.\frac{\partial \boldsymbol{\sigma}_{\boldsymbol{g}}}{\partial \mathbf{a_{mp}}}\right|_{\mathbb{M}_{mp}} d\mathbf{a_{mp}} + \left.\frac{\partial \boldsymbol{\sigma}_{\boldsymbol{g}}}{\partial \mathbb{M}_{mp}}\right|_{\mathbf{a_{mp}}} d\mathbb{M}_{mp} \tag{6.76}$$

where $\mathbb{M}_{mp} = \begin{bmatrix} M_{mp}^{S} & M_{mp}^{C} & M_{mp}^{A} & M_{mp}^{B} \end{bmatrix}^{T}$ is the vector of local solid concentrations.

The mechanical constitutive model considered for a discontinuity filled with reaction products is schematically represented by the parallel device shown in Fig. 6.8b. The left branch represents the constitutive law of the discontinuity, while the right branch represents the constitutive law of the reaction products within it. The constitutive law considered for the discontinuity, originally proposed by Carol and Prat [35, 36], was formulated in the framework of the elasto-plasticity theory but including concepts and parameters of fracture mechanics. This law, briefly described in the following Section 6.5.2.1, is used in the version developed by Caballero et al. [29] without introducing any modification. The constitutive law of the reaction products within the discontinuity (Section 6.5.2.2), in contrast, is derived from the balance of volumetric fractions proposed in Section 6.4.5, and, consequently, it is an original contribution of this thesis.

6.5.2.1 Constitutive law for cracks

This section briefly describes the mechanical constitutive model considered for the discontinuities. This constitutive model was originally proposed by Carol and Prat [35, 36] and subsequently modified by Carol et al. [34, 37], López [135], and Caballero et al. [29].

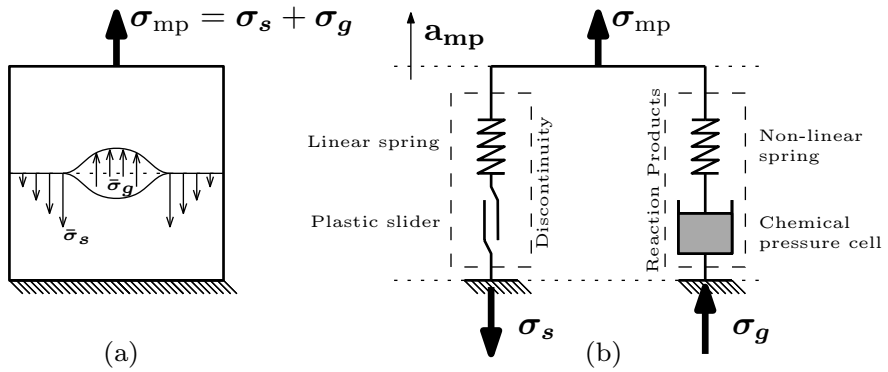

FIGURE 6.8: (a) Mechanism of ASR expansion of a discontinuity. (b) Schematic representation of the constitutive model for ASR expansion of a discontinuity. The left branch represents the constitutive law of the discontinuity and the right branch represents the constitutive law of the reaction products within it. Inspired in Fig. 1 of Ref. [214].

The model, based on the theory of elasto-plasticity, includes concepts of fracture mechanics and fracture energy parameters. Extensive description of the model, numerical implementation details, and validation tests can be found in the cited references.

Basic variables and elastic behaviour

The 3D constitutive model for interface elements is formulated in terms of one normal and two tangential surface tractions, $\boldsymbol{\sigma_s} = \begin{bmatrix}\sigma_n & \tau_{l_1} & \tau_{l_2}\end{bmatrix}^T$, and the conjugate relative separation displacements $\mathbf{a_{mp}} = \begin{bmatrix}a_n & a_{l_1} & a_{l_2}\end{bmatrix}^T$ (Fig. 6.9). Before cracking starts, the interface FE is considered to behave elastically, assuming decoupling of the normal and tangential stiffness properties:

$$\boldsymbol{\sigma_s} = \mathbf{D}_s^{el}\mathbf{a_{mp}} \Rightarrow \begin{bmatrix}\sigma_n \\ \tau_{l_1} \\ \tau_{l_2}\end{bmatrix} = \begin{bmatrix}K_n & 0 & 0 \\ 0 & K_l & 0 \\ 0 & 0 & K_l\end{bmatrix} \begin{bmatrix}a_n \\ a_{l_1} \\ a_{l_2}\end{bmatrix} \tag{6.77}$$

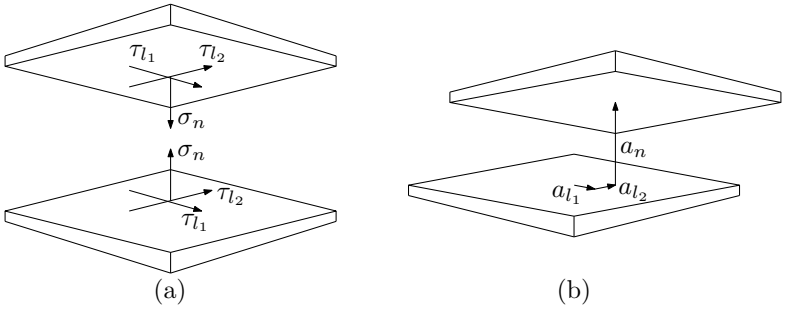

FIGURE 6.9: Definition of (a) stress variables and (b) conjugated relative displacements for interface elements.

The meaning of K_n and K_l [Pa/m] is explained as follows by Caballero et al. [29]:

> 'Although in some cases the elastic interface stiffness may be related to actual physical behaviour of some "mortar" material, in fracture analysis the interface is nothing but a surface representing the fracture process zone. Therefore the elastic deformations of the interface should remain sufficiently small (ideally zero) in order to minimize interpenetration and prevent sliding before cracking initiates. According to this idealization, the elastic normal and shear stiffness should have properties as high as possible. However, excessively high values may create ill-conditioning due to very different orders of magnitude of the stiffness properties in the global stiffness matrix. Moreover, the elastic trial stress prediction may be too far away from the loading surface to assure stable plastic return. Therefore, in general the elastic stiffness values need to provide a compromise between finite thickness interface layers which asymptotically diminish to zero thickness.'

Failure surface

Cracking begins when the stress on the interface plane reaches the condition $F = 0$, where F is the plastic or fracture surface defined in the space of normal and shear stresses. As in the classical theory of plasticity, the yield surface or plastic loading surface is defined in terms of the stress components and some strength parameters:

$$F = F(\boldsymbol{\sigma_s}, \kappa) \tag{6.78}$$

For this model, a three-parameter hyperbolic fracture surface [29] has been adopted:

$$F\left(\boldsymbol{\sigma_s}, \mathbf{p}\left(W^{cr}\right)\right) = \sqrt{\tau_l^2 + (c - \chi \tan\varphi)^2} - (c - \sigma_n \tan\varphi) \tag{6.79}$$

where τ_l [Pa] is the modulus of the shear stresses $\left(\tau_l = \sqrt{\tau_{l_1}^2 + \tau_{l_2}^2}\right)$, σ_n [Pa] is the normal stress, χ [Pa] is the vertex of the hyperbola representing the tensile strength, c [Pa] is the cohesion, and $\tan\varphi$ is the tangent of friction angle. The last two parameters define the asymptote to the hyperbola, as shown in Fig. 6.10.

Once the crack begins to open, the fracture surface begins to contract and the stress decreases, so that the updated stress point always remains on the cracking surface. Given an initial fracture surface, represented by curve '0' in Fig. 6.10c, its final configuration will depend on the specific mode of fracture taking place. For pure tension (Mode I), a fully developed crack requires, as the only kinematic condition, that the normal separation of the sides of the interface is allowed (Fig. 6.10b). Due to the heterogeneity of the material, the cracking surface is usually rough and, consequently, tangential stress

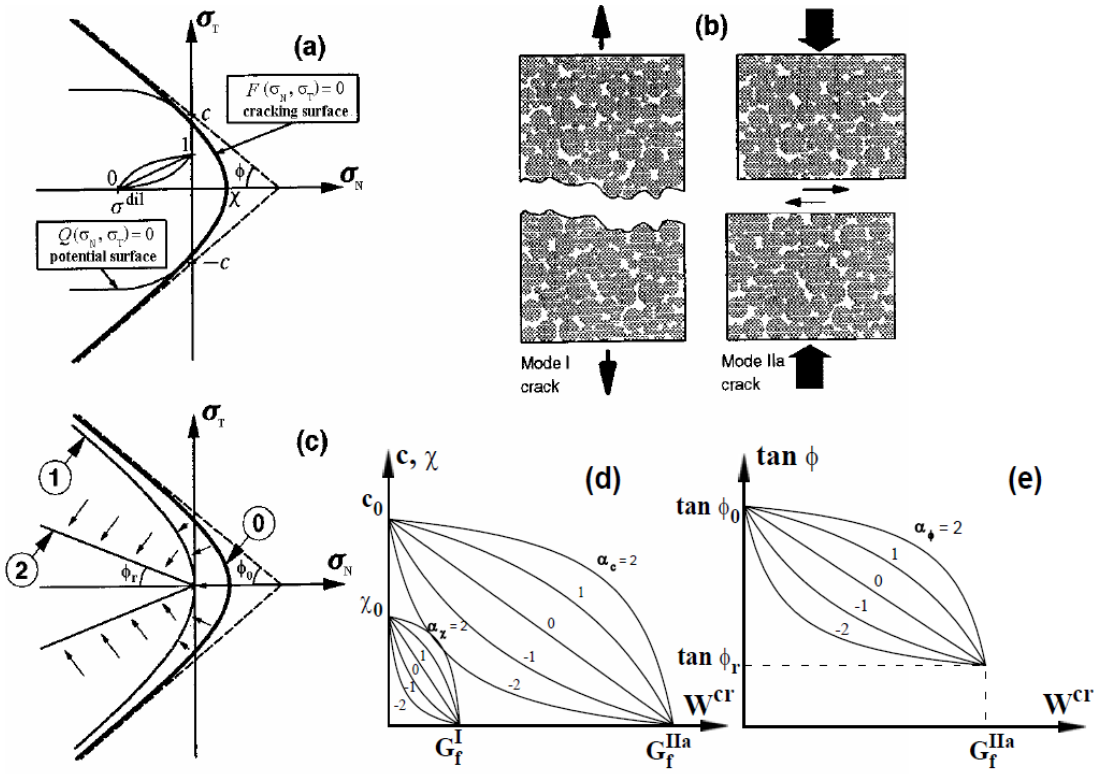

FIGURE 6.10: Crack laws: (a) hyperbolic cracking surface F and plastic potential Q; (b) fundamental modes of fracture; (c) evolution of cracking surface; (d) softening laws for χ and c; (e) softening law for $\tan\phi$. Image taken from Ref. [136]. Note: σ_N, σ_T, ϕ in the figure correspond to $\sigma_n, \tau_l, \varphi$ in the notation used in this thesis.

is not purely frictional but also accounts for the 'saw tooth effect. This is reflected in the non-linearity of the final fracture surface, which is a hyperbola with vertex at the origin (curve '1' in Fig. 6.10c).

The other limit situation corresponds to cracking under shear and very high compression with no dilatancy, which is called 'asymptotic mixed mode' or 'Mode IIa' [35]. In this second fracture mode, slip occurs in the tangential direction without normal dilatancy (Fig. 6.10b), and the final fracture surface is defined by a pair of straight lines representing pure frictional behaviour (curve '2' in Fig. 6.10c).

The parameters that control the two fracture modes described above are the specific fracture energy in Mode I, G_f^I [J/m^2], and the specific fracture energy in Mode IIa , G_f^{IIa} [J/m^2].

Flow rule (dilatancy)

The definition of the flow rule in this model is similar to the flow rule in classical continuum plasticity. The plastic potential is referred as fracture potential Q, and it is formulated in terms of the relative displacements and stresses on the interface plane.

The relative displacement vector, $d\mathbf{a_{mp}}$, contains an elastic part ($d\mathbf{a^{e}_{mp}}$), and a non-recoverable part, the fracture ('crack') component ($d\mathbf{a^{cr}_{mp}}$):

$$d\mathbf{a_{mp}} = d\mathbf{a^{e}_{mp}} + d\mathbf{a^{cr}_{mp}} \tag{6.80}$$

The fracture component is given by:

$$d\mathbf{a^{cr}_{mp}} = d\lambda \, \frac{\partial Q}{\boldsymbol{\sigma_s}} = d\lambda \, \boldsymbol{m}_Q \tag{6.81}$$

where, $d\lambda$ is the fracture multiplier and $\boldsymbol{m}_Q$ is the gradient of Q.

The corresponding fracture work is defined in the following incremental form:

$$dW^{cr} = \begin{cases} \boldsymbol{\sigma_s} \cdot d\mathbf{a^{cr}_{mp}} = d\lambda \, \boldsymbol{\sigma_s} \cdot \boldsymbol{m}_Q & \text{if } \sigma_n \geq 0 \\ \\ (|\tau_l| + \sigma_n \tan\varphi) \, |da_l^{cr}| & \text{if } \sigma_n < 0 \end{cases} \tag{6.82}$$

where $da_l^{cr} = \sqrt{\left(da_{l_1}^{cr}\right)^2 + \left(da_{l_2}^{cr}\right)^2}$ represents the increment of relative crack opening displacements in the tangential direction.

The preceding equations (Eq. (6.82)) imply that, for pure tension ($\sigma_n > 0$), all the work dissipated is used for crack formation. In contrast, in compression, the work dissipated includes also some frictional work (heat) and, therefore, the work spent in the fracture processes (crack formation) is only a part of the total work dissipated.

In heterogeneous materials, fracture planes show some roughness due to the propensity of the cracks to propagate along the weakest areas (particle contacts, particle-matrix boundary, etc.). In these conditions, shear slip will, in general, produce also dilatancy (crack opening) due to the 'saw tooth effect'. The direction of dilatancy can be determined by the methods of the theory of plasticity, in which the direction of the fracture deformation vector at each point is perpendicular to the plastic (or fracture) potential (flow rule). Then, the dilatancy angle can be interpreted as the angle between the gradient of Q and the shear axis. That means that a direction parallel to the shear axis indicates no dilatancy, while a direction parallel to the normal stress axis indicates a fracture opening without tangential displacement, such as in a pure tension case. The fracture potential ($\boldsymbol{m}_Q$) is defined as function of the fracture surface through a transformation matrix $\mathbf{A}$ as follows:

$$\boldsymbol{m}_Q = \frac{\partial Q}{\partial \boldsymbol{\sigma_s}} = \mathbf{An} \tag{6.83}$$

$$\boldsymbol{n} = \frac{\partial F}{\partial \boldsymbol{\sigma_s}} = \begin{bmatrix} \frac{\partial F}{\partial \sigma_n} \\ \frac{\partial F}{\sigma_{l_1}} \\ \frac{\partial F}{\sigma_{l_2}} \end{bmatrix} = \begin{bmatrix} \tan\phi \\ \dfrac{\sigma_{l_1}}{\sqrt{|\sigma_l|^2 + (c + \chi \tan\phi)^2}} \\ \dfrac{\sigma_{l_2}}{\sqrt{|\sigma_l|^2 + (c + \chi \tan\phi)^2}} \end{bmatrix} \tag{6.84}$$

$$\mathbf{A} = \begin{bmatrix} f_c^{dil} f_\sigma^{dil} & 0 & 0 \\ 0 & 1 & 0 \\ 0 & 0 & 1 \end{bmatrix} \tag{6.85}$$

If $\mathbf{A}$ is equal to identity tensor ($\mathbf{A} = \mathbf{I}$), then the flow rule is associated; otherwise ($\mathbf{A} \neq \mathbf{I}$), it is non-associated. In this model, an evolutionary approach has been followed, such that flow rule evolves from an initially associated flow rule to non-associated flow rule as the normal stress is increased and the joint is degraded.

This approach is based on experimental results for quasi-brittle materials with dilatant behaviour [7] which show that the higher the value of the compressive stress, the smaller the effect of dilatancy. Furthermore, the variation of dilatancy decreases with the increase of joint degradation. For example, in a constant compression shear test, the dilatancy angle decreases with the increase of total tangential relative displacement [163]. These effects on dilatancy are taken into account by reducing the normal component of the $\mathbf{A}$ matrix using the f_c^{dil} and f_σ^{dil} factors:

- Reduction with stress level. To account for the effect of stress level, the dilatancy varies with the intensity of the compressive stress, in such a way that dilatancy is totally suppressed when compression reaches a pre-defined value σ_{dil} [Pa] (see Fig. 6.10a).

$$f_\sigma^{dil} = 1 - S\left(\frac{\sigma_n}{\sigma_{dil}}, \alpha_{\sigma_{dil}}\right) \tag{6.86}$$

- Reduction with degradation. Dilatancy decreases as the fracture surface is degraded, and it vanishes completely when the surface F reaches the state of residual friction (curve '2' in Fig. 6.10b):

$$f_c^{dil} = 1 - S\left(\frac{W^{cr}}{G_F^{IIa}}, \alpha_{c_{dil}}\right) \tag{6.87}$$

In these expressions, function S is given by

$$S(\xi, \alpha) = \left(\frac{e^{-\alpha}\xi}{1 + (e^{-\alpha} - 1)\xi}\right) \tag{6.88}$$

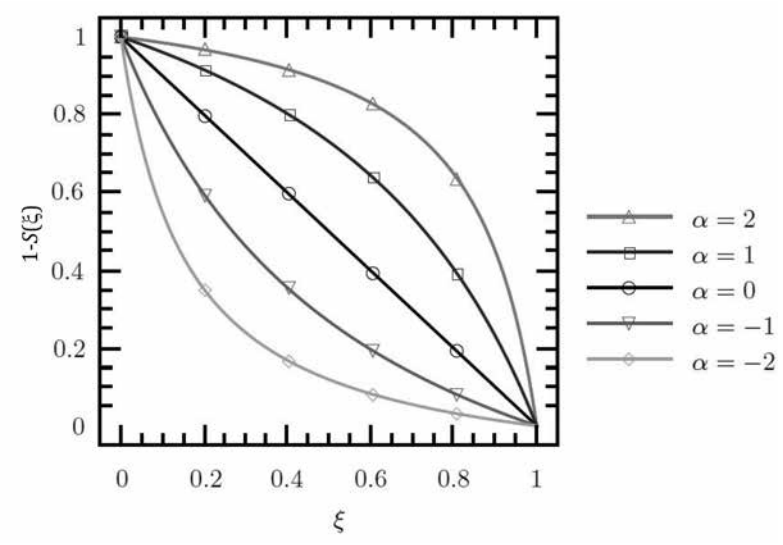

FIGURE 6.11: Evolution law. Taken from Ref. [77].

where ξ is the generic (normalized) property to be scaled and α is the scaling factor. The effect of α in the evolution factor can be appreciated in Fig. 6.11. Note that, for $\alpha = 0$, the linear relation $S(\xi, 0) = \xi$ is recovered.

Evolution laws

The evolution of the fracture surface is given by the reduction of the parameters of Eq. (6.79), namely: tensile strength (χ), cohesion (c), and friction angle ($\tan\varphi$), as functions of the work spent in the crack formation (W^{cr}, Eq. (6.82)).

Tensile strength (χ) decreases from its initial value χ_o as W^{cr} increases, becoming zero when $W^{cr} = G_f^I$. The scaling function $S(\xi_\chi, \alpha_\chi)$ is applied considering $\xi_\chi = W^{cr}/G_f^I$ and $\alpha = \alpha_\chi$ (Fig. 6.10d), resulting in the following expression:

$$\chi = \begin{cases} \chi_o \left[1 - S\left(\xi_\chi, \alpha_\chi\right)\right] & \text{if } W^{cr} < G_f^I \\ 0 & \text{if } W^{cr} \geq G_f^I \end{cases} \tag{6.89}$$

The reduction of cohesion (c) is given indirectly through χ, $\tan\phi$ and an auxiliary variable a representing the horizontal distance between the vertex of the hyperbola and the intersection point of the asymptotes with the horizontal axis, i.e.:

$$c = (\chi + a)\tan\phi \tag{6.90}$$

Assuming that this auxiliary variable a changes from its initial value a_0 (obtained from Eq. (6.90) with the initial values of χ, c, and $\tan\phi$) to zero when $W^{cr} = G_f^{IIa}$, the parameters of the scaling function $S(\xi_a, \alpha_a)$ are given by $\xi_a = W^{cr}/G_f^{IIa}$ and $\alpha = \alpha_a$.

The reduction function of c is then expressed as follows:

$$c = \begin{cases} c_o \left[1 - S(\xi_a, \alpha_a) - \dfrac{\chi_o}{c_o} \tan\phi \left(S\left(\xi_\chi, \alpha_\chi\right) - S\left(\xi_a, \alpha_a\right)\right)\right] & \text{if } W^{cr} < G_f^{IIa} \\ 0 & \text{if } W^{cr} \geq G_f^{IIa} \end{cases} \tag{6.91}$$

This equation allows splitting the evolution of the fracture surface F into a translation plus a contraction, which in the context of the theory of plasticity can be interpreted as a combined kinematic plus isotropic softening [135].

Finally, the internal friction angle varies from an initial value φ_o, which includes the 'saw tooth effect', to a purely frictional residual value φ_{res} when $W^{cr} \geq G_f^{IIa}$ (see Fig. 6.10e):

$$\tan\varphi = \begin{cases} \tan\varphi_0 - (\tan\varphi_0 - \tan\varphi_{res})\, S(\xi_\varphi, \alpha_\varphi) & \text{if } W^{cr} < G_f^{IIa} \\ \tan\varphi_{res} & \text{if } W^{cr} \geq G_f^{IIa} \end{cases} \tag{6.92}$$

Note that, in order to allow a purely tensile fracture (Mode I), the following relation must be fulfilled [135, p.55]:

$$c_o \geq \chi_o \left(\frac{1}{2\ \tan\varphi_o} + \tan\varphi_o\right) \tag{6.93}$$

Exact solution for fracture in Mode I

For pure tensile stress state (fracture in Mode I) with normal crack aperture a_n^{cr} growing monotonously, and adopting a lineal softening law ($\alpha_\chi = 0$), the following expressions can be derived [135, Ch. 3]:

$$\sigma_n = \chi_o \exp\left(-\frac{\chi_o}{G_f^I} a_n^{cr}\right) \tag{6.94}$$

$$\frac{W^{cr}}{G_f^I} = 1 - \exp\left(-\frac{\chi_o}{G_f^I} a_n^{cr}\right) \tag{6.95}$$

This latter expression may be used in the diffusion-reaction formulation for evaluating the factor $\mathcal{S}_{mp}$ (Eq. (6.37)) of the proposed kinetic laws as function of the normal crack aperture.

6.5.2.2 Constitutive law of the reaction products

A mechanical constitutive law for the reaction products filling a discontinuity is derived in this section from the balance of volumetric fractions proposed in Section 6.4.5.

The precipitated reaction products are assumed not to exhibit any Poisson's effect ($\nu = 0$) and to have null tangential stiffness ($G = 0$). Then, of the six components of the general strain/stress vector in the interface local axis (n, l_1, l_2), only the component in the normal direction can be non-null. In this way, the stress state of the reaction products can be suitably presented in the same stress space used for the formulation of zero-thickness interface elements with the vector $\boldsymbol{\sigma_g} = \begin{bmatrix}\sigma_g & 0 & 0\end{bmatrix}^T$. Moreover, the precipitation of the reaction products is assumed to occur homogeneously in the normal direction of the discontinuity, and, therefore, the reaction products stress σ_g and the conjugated reaction products strain ε_g are assumed to be uniform in this direction. These assumptions have two main consequences:

- the strain in the normal direction ε_g and the volumetric strain are the same thing.
- for a given content of reaction products, ε_g can be univocally determined by the relative normal displacement of the interface a_n^{cr}.

To stablish this last relation, it is convenient to define the auxiliary variable $\mathcal{U}_{max}$ [m^3 $\mathrm{m}_{\mathrm{mp}}^{-2}$] as follows:

$$\mathcal{U}_{max} = \sum_{\alpha} \frac{\eta_o^{\alpha}}{1 - \phi_o^{\alpha}} \left\langle M_{mp}^{\alpha} \right\rangle_+ \tag{6.96}$$

Obtained from Eq. (6.19), $\mathcal{U}_{max}$ is the volume occupied by the reaction products filling the discontinuity in unstressed state, and, therefore, it is the reference volume from which the strain of the reaction products ε_g has to be computed, i.e.

$$\varepsilon_g = \left\langle \frac{\mathcal{U}}{\mathcal{U}_{max}} - 1 \right\rangle_- \tag{6.97}$$

The Macaulay Brackets are used here for considering the case in which the volume $\mathcal{U}$ of the discontinuity is greater than $\mathcal{U}_{max}$. Since the reaction products are assumed not capable of developing tensile strain/stress, $\mathcal{U} > \mathcal{U}_{max}$ implies that $\mathcal{U}^{cp} > 0$ and, therefore, that the reaction products are unstrained. Otherwise, if $\mathcal{U} \leq \mathcal{U}_{max}$, then $\mathcal{U}^{cp} = 0$ and the reaction products have been compressed ($\varepsilon_g < 0$ and $\sigma_g < 0$) until the volume of reaction products and the volume of discontinuity were equal. In this last condition and based on Eqs. (6.25) and (6.19), the volume $\mathcal{U}$ can be expressed either as

$$\mathcal{U} = \mathcal{U}^o - \eta_o^S \left\langle M_{mp}^S \right\rangle_- + \left\langle a_n \right\rangle_+ \tag{6.98}$$

or

$$\mathcal{U} = \sum_{\alpha} \frac{\eta^{\alpha}(\sigma_g)}{1 - \phi^{\alpha}(\sigma^{\alpha})} \left\langle M_{mp}^{\alpha} \right\rangle_+ \tag{6.99}$$

Note that in Eq. (6.98) it has been assumed that the elastic relative displacements are negligible and, consequently, $a_n^{cr} \approx \langle a_n \rangle_+$. Replacing these latter equations in Eq. (6.97) and for a given set of values M_{mp}^{α}, the strain of the reaction products can be obtained indistinctly as a function of a_n,

$$\varepsilon_g = \frac{\mathcal{U}^o - \eta_o^S \left\langle M_{mp}^S \right\rangle_- + \langle a_n \rangle_+}{\mathcal{U}_{max}} - 1 \tag{6.100}$$

or as function of σ_g,

$$\varepsilon_g = \frac{1}{\mathcal{U}_{max}} \sum_{\alpha} \frac{\eta^{\alpha}(\sigma_g)}{1 - \phi^{\alpha}(\sigma_g)} \left\langle M_{mp}^{\alpha} \right\rangle_+ - 1 \tag{6.101}$$

The first equation establishes a 'compatibility condition' by relating the reaction products strain to the relative normal displacement of the interface element and, indirectly via Eq. (5.185), to its nodal displacements. The second equation, in contrast, establishes the mechanical 'constitutive relation' between strain and stress of the reaction products.

In order to combine the mechanical response of the discontinuity and the reaction products in the above-proposed parallel scheme (Fig. 6.8), it is convenient to obtain an expression to calculate σ_g as a function of a_n. This is achieved by combining Eqs. (6.100) and (6.101) as follows

$$\mathcal{U}^o - \eta^S \left\langle M_{mp}^S \right\rangle_- + a_n - \sum_{\alpha} \frac{\eta_o^{\alpha} f_{\eta}^{\alpha}(\sigma_g)}{1 - \phi_o^{\alpha} f_{\phi}^{\alpha}(\sigma_g)} \left\langle M_{mp}^{\alpha} \right\rangle_+ = 0 \tag{6.102}$$

From this explicit equation, depending on the adopted functions f_{ϕ}^{α} and f_{η}^{α}, the calculation of σ_g for a given a_n may be done analytically or may require to use numerical methods.

The tangential stiffness matrix of the constitutive equation of the reaction products within the discontinuity is defined as follows:

$$\mathbf{D_g} = \frac{d\boldsymbol{\sigma_g}}{d\mathbf{a}_{\mathrm{mp}}} = \begin{bmatrix} D_g & 0 & 0 \\ 0 & 0 & 0 \\ 0 & 0 & 0 \end{bmatrix} \tag{6.103}$$

where

$$D_g = \frac{\partial \sigma_g}{\partial a_n} \tag{6.104}$$

Applying the chain rule, this latter equation can be rewritten as

$$D_g = \frac{\partial \sigma_g}{\partial \varepsilon_g}\frac{\partial \varepsilon_g}{\partial a_n} = \left(\frac{\partial \varepsilon_g}{\partial \sigma_g}\right)^{-1}\frac{\partial \varepsilon_g}{\partial a_n} \tag{6.105}$$

The derivatives on the right-hand side of this equation are obtained by differentiating Eqs. (6.100) and (6.101) as follow:

$$\frac{\partial \varepsilon_g}{\partial a_n} = \frac{1}{\mathcal{U}_{max}} \tag{6.106}$$

$$\frac{\partial \varepsilon_g}{\partial \sigma_g} = \frac{1}{\mathcal{U}_{max}}\sum_{\alpha}\frac{\left\langle M^{\alpha}_{mp}\right\rangle_+}{\left[1-\phi^{\alpha}_o f^{\alpha}_{\phi}(\sigma_g)\right]^2}\left\{\left[1-\phi^{\alpha}_o f^{\alpha}_{\phi}(\sigma_g)\right]\,\eta^{\alpha}_o\frac{\partial f^{\alpha}_{\eta}}{\partial \sigma_g}\bigg|_{\sigma_g} + \eta^{\alpha}_o f^{\alpha}_{\eta}(\sigma_g)\,\phi^{\alpha}_o\frac{\partial f^{\alpha}_{\phi}}{\partial \sigma_g}\bigg|_{\sigma_g}\right\} \tag{6.107}$$

Finally, introducing Eqs. (6.106) and (6.107) in Eq. (6.105), one obtains the final expression of the tangential stiffness:

$$D_g = \sum_{\alpha}\frac{\left[1-\phi^{\alpha}_o f^{\alpha}_{\phi}(\sigma_g)\right]^2}{\left\langle M^{\alpha}_{mp}\right\rangle_+}\left\{\left[1-\phi^{\alpha}_o f^{\alpha}_{\phi}(\sigma_g)\right]\,\eta^{\alpha}_o\frac{\partial f^{\alpha}_{\eta}}{\partial \sigma_g}\bigg|_{\sigma_g} + \eta^{\alpha}_o f^{\alpha}_{\eta}(\sigma_g)\,\phi^{\alpha}_o\frac{\partial f^{\alpha}_{\phi}}{\partial \sigma_g}\bigg|_{\sigma_g}\right\}^{-1} \tag{6.108}$$

On the effect of some parameters

In order to clarify the effect of some of the parameters involved in the mechanical model just described, Fig. 6.12 depicts the curves σ_g-ε_g and σ_g-a^{cr}_n, corresponding to a crack without initial volume ($\mathcal{U}^o_{mp} = 0$) and a certain content of Reaction Product B (RPB) ($M^B_{mp} > 0$). At point ①, crack aperture is greater than U_{max}, and, consequently, the RPB is unstrained/unstressed. At point ②, crack aperture is smaller than $\mathcal{U}_{max}$ but greater than the 'specific' volume of RPB. Since the strain of solid clusters is negligible ($k_\eta \approx 0$), this volume reduction is due to the reduction of gel water content, reflected in the change of gel porosity from ϕ^B_o to a smaller value ϕ^B. Finally, at point ③, stress is higher that the maximum swelling pressure of RPB ($\sigma_g > \tilde{\sigma}^B_{th}$) and, consequently, the gel water has been completely driven out ($\phi^B = 0$). The tangential stiffness at this point is very high, since any further reduction of the RPB volume will occur at the expense of deforming of solid clusters.

In Fig. 6.13a, the σ_g-a^{cr}_n curve of the same discontinuity but with the amount of RPB reduced to a half is presented. The volume of solid clusters and $\mathcal{U}_{max}$ are reduced in same proportion as M^B_{mp}, but the maximum swelling pressure is not altered.

In Fig. 6.13b, the effect of assuming a non-zero initial volume $\mathcal{U}^o_{mp}$ for the discontinuity can be appreciated. The constitutive curve is shifted to the left and, if the volume of

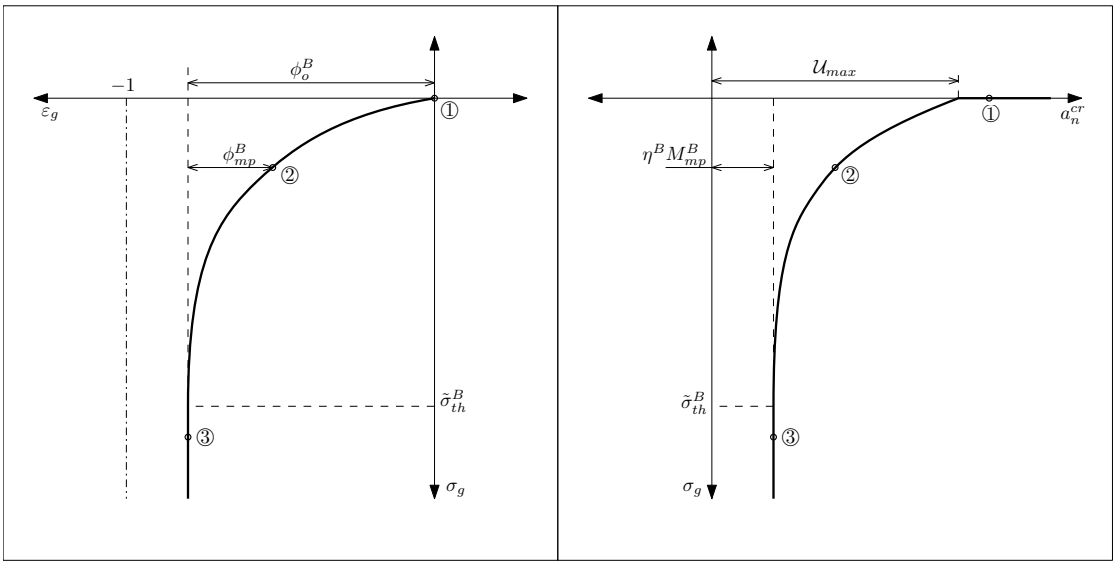

FIGURE 6.12: Mechanical constitutive curves of Reaction Product B filling a crack.

solid clusters is smaller than $\mathcal{U}_{mp}^o$, the maximum pressure σ_g that can be exerted by the RPB on the discontinuity sides is reduced to a certain value (coincident with $a_n^{cr} = 0$) smaller than $\tilde{\sigma}_{th}^B$. It must be noted that in none of the two cases presented in Fig. 6.13, the σ_g-ε_g constitutive curve given in Fig. 6.12 is modified.

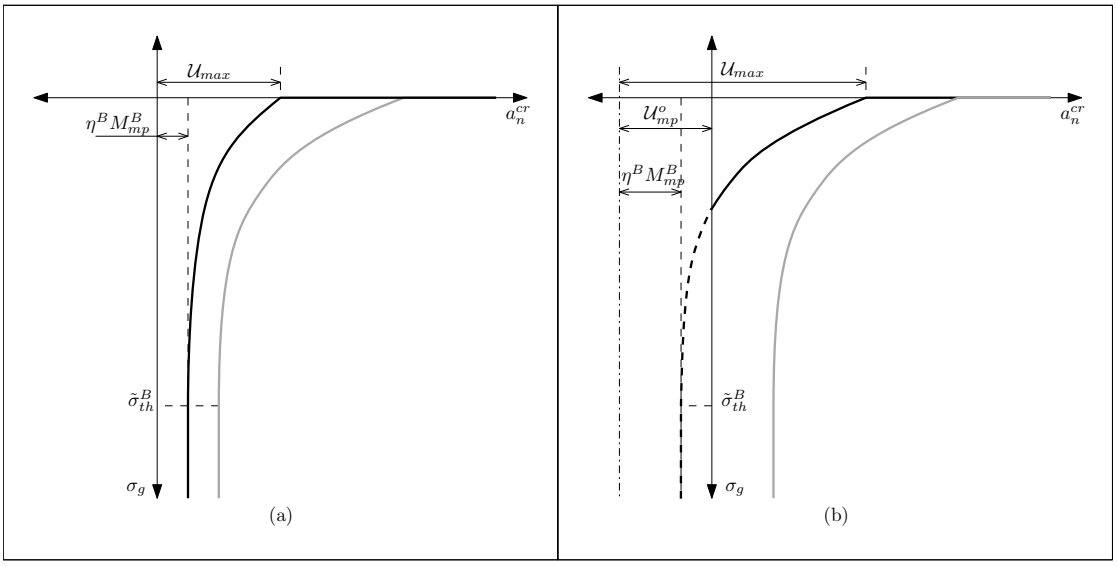

FIGURE 6.13: Mechanical constitutive curves of Reaction Product B (RPB) filling a crack. (a) Effect of reducing the amount of RPB. (b) Effect of assigning an initial volume $\mathcal{U}_{mp}^o$ to the discontinuity. In grey, reference curve presented in Fig. 6.12.

In Fig. 6.14, the effect of reducing the unstressed gel porosity (ϕ_o^B) without altering the volume of solid clusters is shown. $\mathcal{U}_{max}$ is reduced and the stiffness of RPB is increased. In contrast, the increase of the compliance of the solid clusters (k_η) to an unrealistic high value, presented in Fig. 6.15, significantly reduces the overall stiffness.

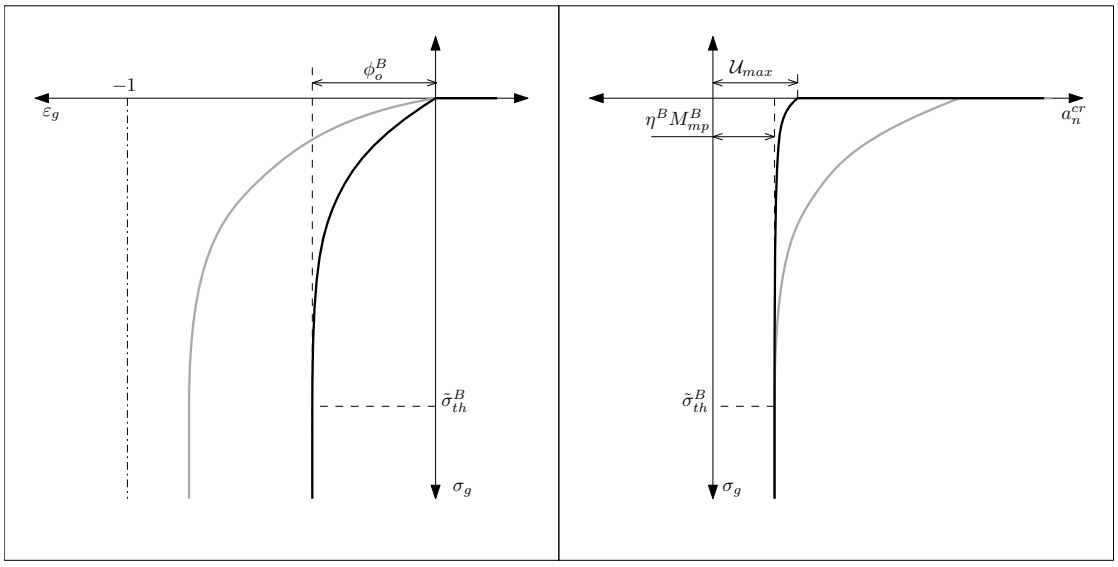

FIGURE 6.14: Mechanical constitutive curves of Reaction Product B filling a crack. Effect of reducing the unstressed gel porosity (ϕ_o^B). In grey, reference curves presented in Fig. 6.12.

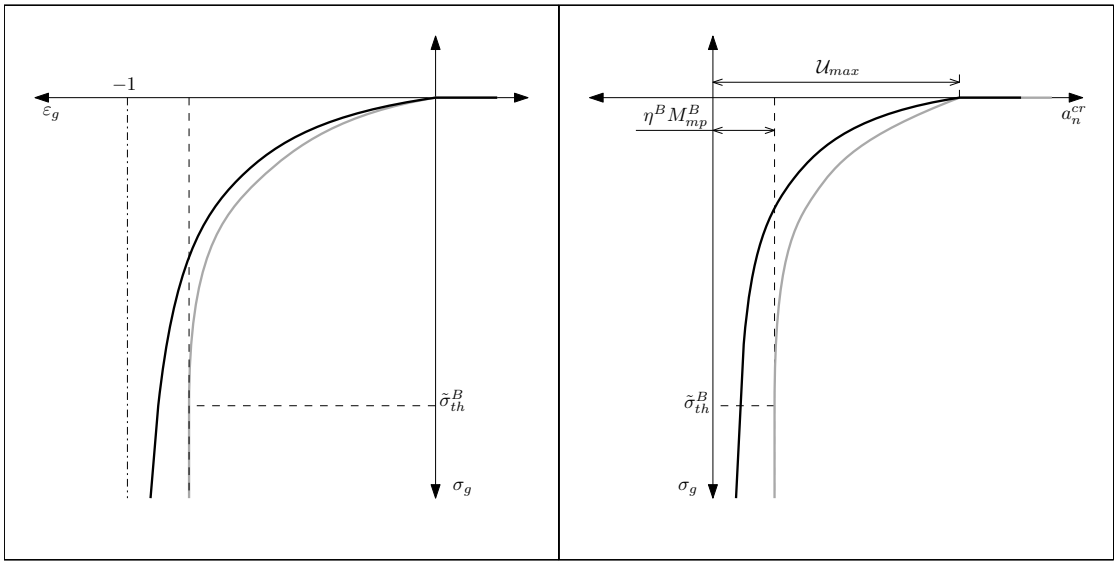

FIGURE 6.15: Mechanical constitutive curves of Reaction Product B filling a crack. Effect of increasing the compliance (k_η) of solid clusters. In grey, reference curves presented in Fig. 6.12.

Finally, the effect of adding to the amount of RPB the same amount of RPA ($M_{mp}^A = M_{mp}^B$) is shown in Fig. 6.16, assuming that $\eta^A \approx \eta^B$, $\phi_o^A = 2\phi_o^B$, and $\tilde{\sigma}_{th}^A = \frac{3}{10}\tilde{\sigma}_{th}^B$. It can be seen that both $\mathcal{U}_{max}$ and the volume of solid clusters increase, even though not in the same proportion. The absolute volume of gel water is also increased but the gel porosity of the mixed RP is smaller than the gel porosity of RPB. The threshold pressure of the mixed reaction product (σ_{th}) is the average of $\tilde{\sigma}_{th}^A$ and $\tilde{\sigma}_{th}^B$.

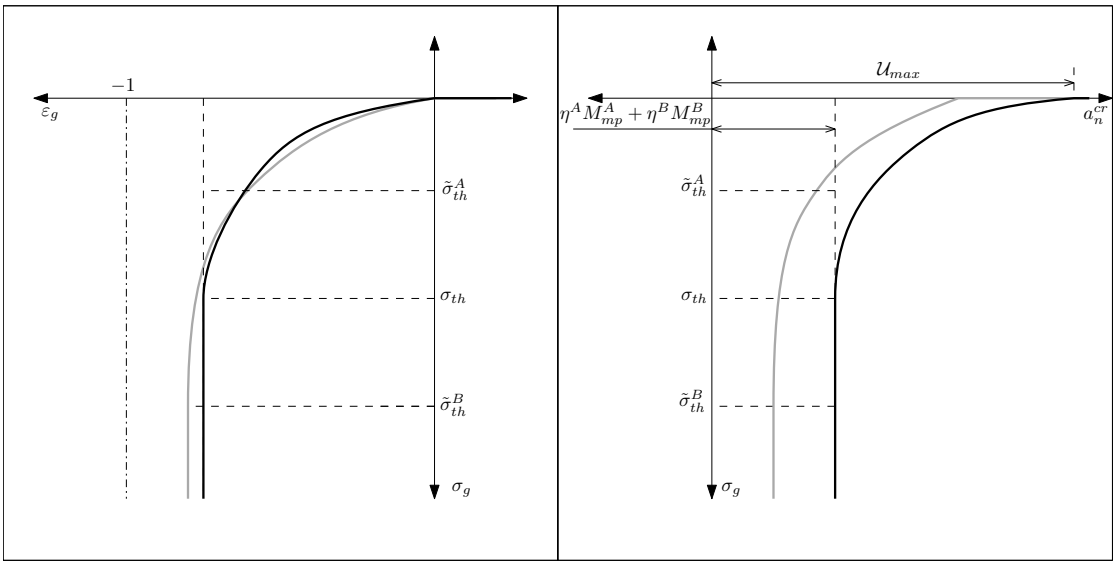

FIGURE 6.16: Mechanical constitutive curves of mixed Reaction Products A and B filling a crack. In grey, reference curves presented in Fig. 6.12.

6.6 Chemo-Mechanical coupling

As explained in Section 5.4, the mechanical formulation and the diffusion-reaction formulation are implemented in two different codes, called `DRAC` and `DRACFLOW`, respectively. Both codes use the same FE mesh and the same integration points. This mesh includes zero-thickness interface elements in between continuum elements accounting for potential crack paths and cement-aggregate contacts.

Moreover, both codes have the same time discretization scheme consisting in time 'steps' composed by a number of (at least one) time 'increments'. In order to stablish the coupling staggered scheme, the time steps in `DRAC` and `DRACFLOW` have to match each other (see Fig. 6.17). However, the number of increments within the time steps may be different for each code, depending on the requirements of the problem.

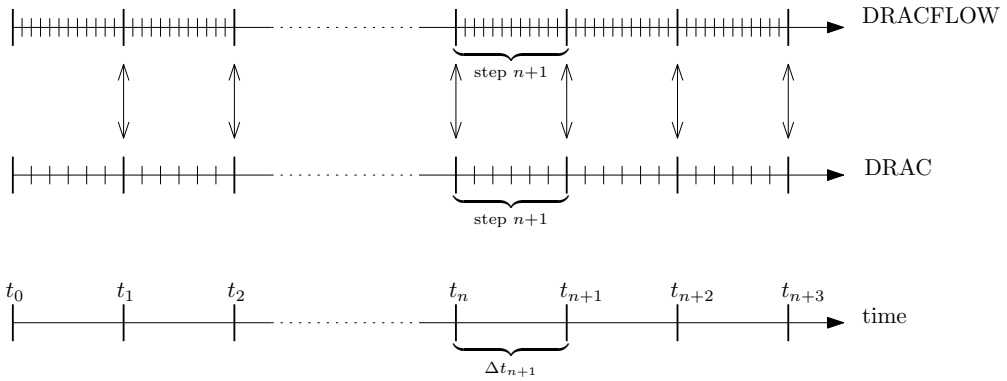

FIGURE 6.17: Schematic representation of the time discretization. Vertical arrows indicate exchange of information between `DRAC` and `DRACFLOW`.

The staggered procedure, which is administrated by a third code named STAG, is schematically illustrated in Fig. 6.18. For the calculation of each time step, `DRAC` and `DRACFLOW` are called alternatively in order to independently solve the mechanical problem and the diffusion-reaction problem, respectively.

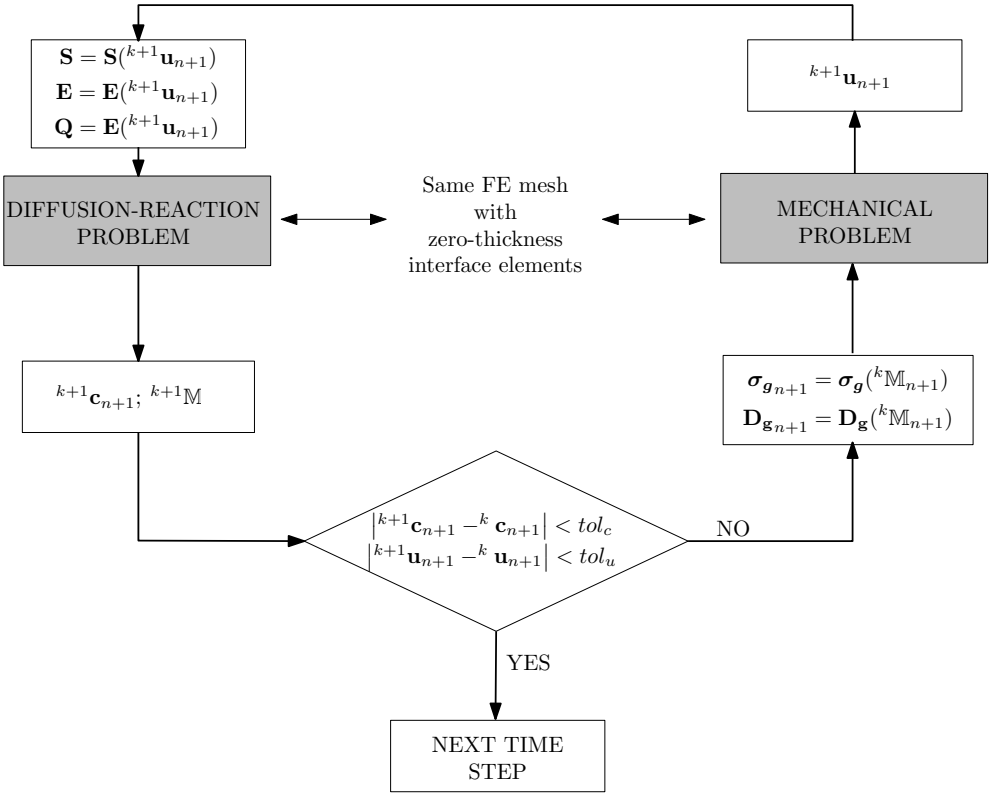

FIGURE 6.18: Staggered procedure scheme for the ASR model.

On one hand, after each call, `DRAC` writes a file with the obtained nodal displacements at the end of the time step. This file is read by `DRACFLOW` and used to calculate the total normal aperture a_n of the interface elements at each integration point via the transformation equation (5.185). The value of a_n at each increment within the time step is linearly interpolated between the known values at the beginning and the end of the step. Then, the crack normal aperture (a_n^{cr}), which is the actual coupling variable, is approximated via the following equation:

$$a_n^{cr} \approx \begin{cases} 0 & \text{if } a_n \leq \chi_o/K_n \\ a_n & \text{if } a_n > \chi_o/K_n \end{cases} \tag{6.109}$$

This approximation is based on the fact that the elastic aperture (a_n^e) of the interface elements is always very small and, consequently, the difference between the plastic (fracture) and total aperture is negligible. Additionally, a distinction needs to be made between cracked and uncracked discontinuities. This is done by assuming that the predominant cracking mode is mode I and, consequently, that if $a_n > \chi_o/K_n$, the interface

is cracked. Otherwise ($a_n \leq \chi_o/K_n$), the crack is uncracked or closed ($a_n \leq 0$). This distinction is particularly important in order to identify newly created surfaces ($\mathcal{S}_{mp} > 0$), which can be subject to dissolution processes, and empty volumes ($\mathcal{U}^{cp}_{mp} > 0$), which can allocate reaction processes. Alternatively, a^{cr}_n could have been obtained directly from `DRAC`, but this would have implied to write for each time step an additional coupling file.

Once the time variation of a^{cr}_n within the time step and at each integration point has been determined, it is used for calculating the evolution of each of the α-species via Eqs. (6.37) and (6.51). Simultaneously, the evolution of volume fractions $\mathcal{U}_{mp}$, $\mathcal{U}^{cp}_{mp}$, and $\mathcal{U}^{ps}_{mp}$ is tracked via Eqs. (6.25), (6.26), and (6.49). Finally, allowing us to update the transport properties of the interface elements (ϕ_{mp}, T_l, and D_n) at the end of each time increment, via Eqs. (5.31), (6.65), and (6.70).

On the other hand, after each call, `DRACFLOW` writes two files with results at the end of the time step, one containing the nodal concentrations of aqueous primary species and the other containing the amount (positive or negative) of all solid α-species ($\mathbb{M}_{mp} = \begin{bmatrix} M^S_{mp} & M^C_{mp} & M^A_{mp} & M^B_{mp} \end{bmatrix}$) at each integration point. This second file is read by `DRAC` and used for calculating the stress of the reaction products within the interface element σ_g and their tangential stiffness D_g, as explained in Section 6.5.2.2. To do so, the value of $\mathbb{M}$ at each time increment within the time step is obtained by linear interpolation of the known values at the beginning and the end of the time step.

The nodal concentration files and the nodal displacement files are used by STAG to assess the convergence of the staggered procedure by comparing their values in two successive iterations of the staggered procedure (Fig. 6.18).

6.7 Chapter concluding remarks

- A new reaction-expansion mechanism for ASR in SL glass concrete is proposed based on the experimental results presented in Chapters 3 and 4, as well as on other results found in the literature.
- This reaction mechanism has been formulated within the general modelling framework for diffusion-dominated durability in cement-based materials, which has been proposed in Chapter 5.
- In the resulting model, the dissolution/precipitation reactions involved in ASR expansions are considered to occur only within the zero-thickness interface elements representing fractures and cement-glass contacts, while diffusion of primary aqueous species may occur within interface as well as continuum finite elements.

- The reaction products precipitated in the interface elements may eventually induce internal pressures which may lead to fracture processes. These internal pressures are related to the amount of gel water absorbed by the reaction products which, in turn, depends on their chemical composition.
- SL glass has some peculiarities as concrete aggregate, and, thus, the model includes some assumptions that make it not strictly applicable for the more usual case of concrete made with natural reactive aggregates. However, it can be readily adapted for other types of reactive aggregates, such as natural reactive aggregates, by introducing minor changes in the formulation.
- In the following Chapter 7, results obtained with the model are presented and, in some cases, contrasted with experimental results.

Chapter 7

Modelling results

7.1 Introduction

The model proposed in previous Chapter 6 for simulating expansions due to Alkali-Silica Reaction (ASR) in concrete made with soda-lime glass (SL glass), is used in this chapter for analysing a number of real and ideal cases of increasing complexity, namely:

i) Chemical speciation

Simulation of the chemical speciation of the pore solution for different concentrations of primary aqueous species. The results are partially contrasted with experimental results from the literature.

ii) Expansion of an isolated interface element

Ideal case intended to demonstrate the mechanical response of an isolated interface element to the formation of reaction products. Different mechanical boundary conditions and different combinations of mechanical parameters are studied in order to asses their influence on the results.

iii) Interfacial Expansion Tests

Simulation of some of the experimental Interfacial Expansion Tests presented in Chapter 3.

iv) One-aggregate specimen

Ideal case consisting of one SL glass aggregate in a matrix of non-reactive mortar. Different mechanical boundary conditions are studied in order to asses their influence on the results.

The cases presented here are considered as necessary steps in the process of validating the proposed model. This process is part of an ongoing project, not completed in this

thesis, that must include additional cases. In particular, the simulation of specimens with multiple SL glass particles, essential to complete the validation of the model is left out of this thesis and listed in the 'Future work' section in Chapter 8.

7.2 Chemical speciation

In this section, the capabilities of the formulation proposed in Section 6.4.7 for obtaining the chemical speciation of the pore solution as a function of the three primary aqueous species (Si, Ca, and R) are demonstrated and partially contrasted with experimental results from the literature.

In the first set of simulations, the chemical speciation of a solution at 60 °C was performed for a range of aqueous alkali and silicate concentrations ($0 \leq c^s \leq 500$, $0 \leq c^r \leq 1000$) under two different conditions: (1) portlandite saturated, i.e. $\psi^C = 1$, and (2) without calcium, i.e. $\psi^C = 0$. The results obtained are given in Figs. 7.1 and 7.2. These figures include contour plots of: concentration of aqueous ROH (c^{r0}), concentration of R^+ (c^{r1}), concentration of OH^- (c^{oh}), concentration of Ca^{2+} (c^c), concentration of H^+ (c^h), pH, and activity coefficients for silicate[1] and calcium ions.

It can be appreciated that, for both calcium conditions, pH increased with c^r and, inversely, pH decreased with larger c^s. However, for the first condition ($\psi^C = 1$), portlandite acts as an alkaline buffer keeping the solution pH well above 10 in the whole range of concentrations studied, while for the second condition there was an abrupt change of pH, from alkaline (for $c^r > c^s$), to acidic (for $c^r < c^s$). Note that the concentration of ROH_{aq} was significant only for pH above 12.

The contour plots of the saturation indexes of Reaction Product A (ψ^A) and Reaction Product B (ψ^B) for the first condition (portlandite saturated) are presented in Fig. 7.3. The assumed saturation product constants were $K^A_{sp} = 964.5$ and $K^B_{sp} = 0.06116$. Note that the scales of the c^r and c^s axes were changed with respect to the previous figure in order to highlight the transition zones from unsaturated ($\psi^\alpha < 1$) to saturated ($\psi^\alpha > 1$).

The second set of simulations includes two cases in which the speciation model was used to reproduce experimental results from the literature. In the first case (Fig. 7.4), the experimental curve obtained by Duchesne and Reardon [60] of portlandite solubility in NaOH solution at 25 °C as a function of the total NaOH concentration was reproduced. Similarly, in the second case (Fig. 7.5), the curve of pH of NaOH solutions as a function

[1] Note that according to Eq. 5.37 the rest of monovalent ionic species (R^+, OH^-,H^+) have the same activity coefficient.

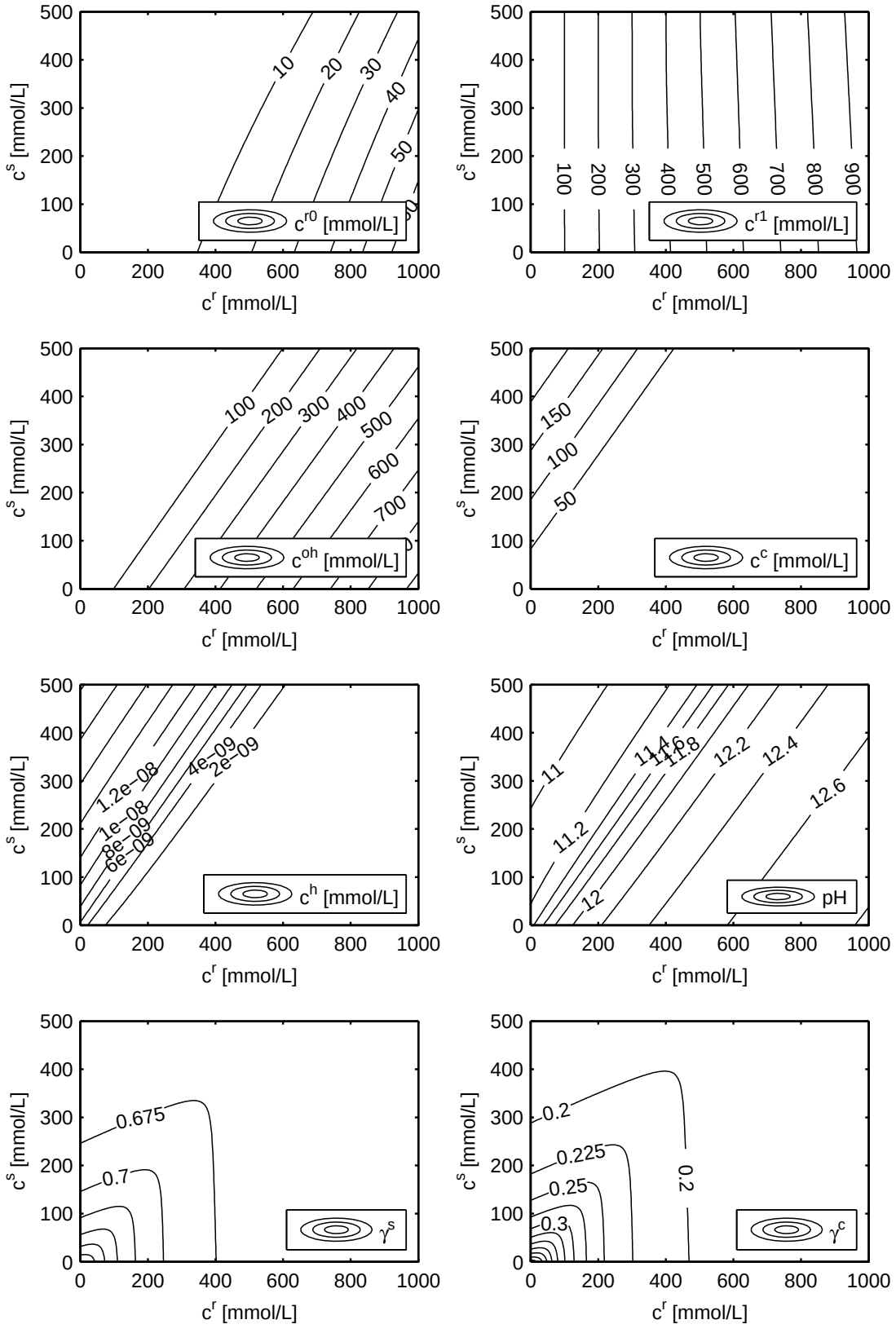

FIGURE 7.1: Chemical speciation of a portlandite saturated solution as a function of the concentrations of aqueous alkalis and silicate ions.

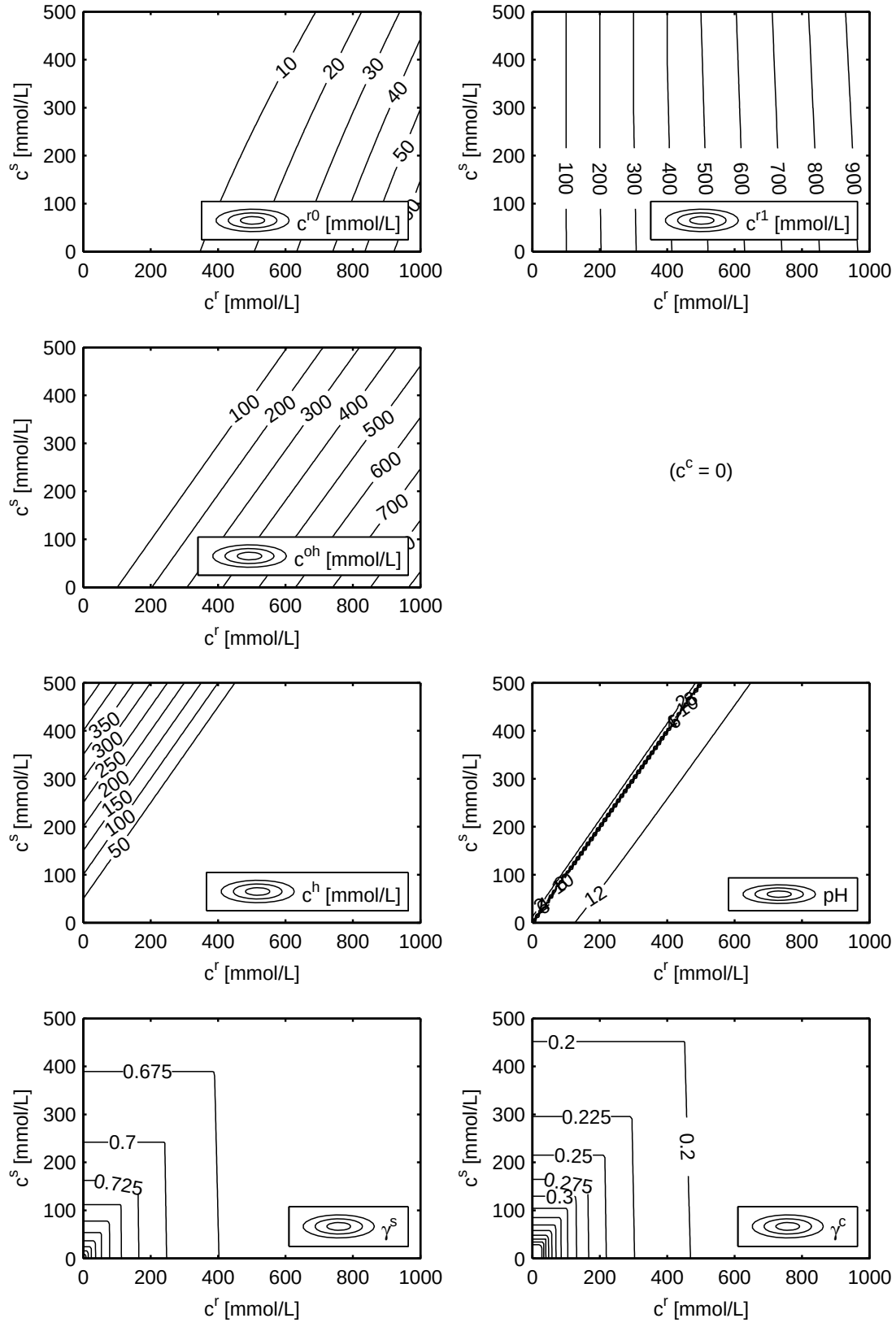

Activity coeff.: **Davies mod.** / Aqueous ROH: **YES** / Ψ^C = **0** / T=60ºC

FIGURE 7.2: Chemical speciation of a solution (without calcium) as a function of the concentrations of aqueous alkalis and silicate ions.

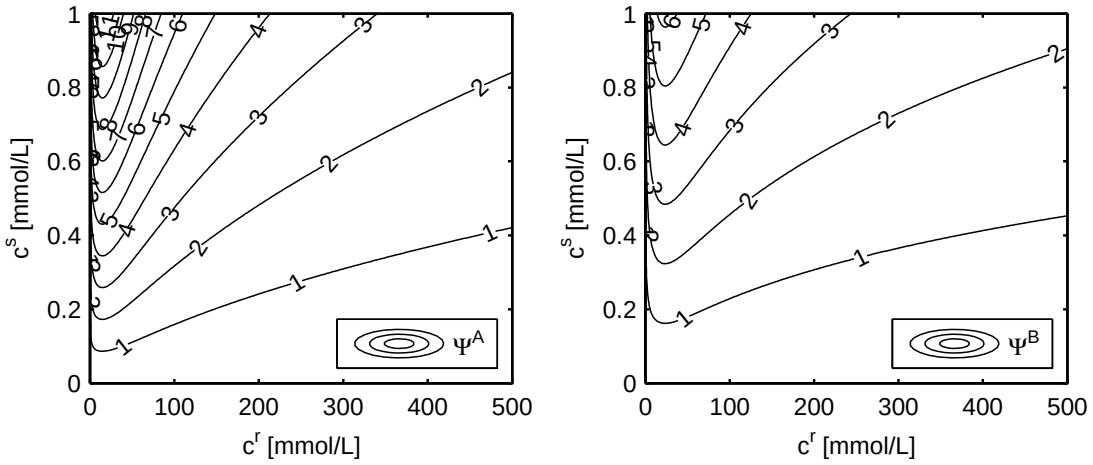

FIGURE 7.3: Saturation indexes of Reaction Product A (ψ^A) and Reaction Product B (ψ^B) as functions of the concentrations of aqueous alkalis and silicate ions in a portlandite saturated solution at 60 °C.

of total NaOH concentration was obtained with the model and contrasted with the experimental measurements reported in Ref. [59].

In the first case, the simulated portlandite solubilities were slightly below the experimental ones, with increasing relative error as the ionic strength of the solution was increased. In the second case, the simulated pH was below the experimental measurements for $c^r < 80$ mol/m^3, and above them for higher sodium concentrations. However, despite the simplicity of the model, in both cases the experimental measurements were fairly well reproduced by the simulations.

Better fitting of the experimental curves would probably require a more accurate calculation of the activity coefficients by means of more complex ion interaction models, e.g. Pitzer's Model [164]. An improvement of this kind could be implemented in the future, however, it would certainly increase the coding and calculation cost while it is not certain that it would significantly improve the simulation results of ASR expansions in concrete given the remaining uncertainties and necessary approximations in other aspects of the overall formulation.

Complementarily, additional simulations of the two last cases, performed with simplified versions of the speciation model, are presented in Appendix B.7, in order to assess the influence of the activity coefficients γ^β and of the dissociation of aqueous ROH on the results obtained.

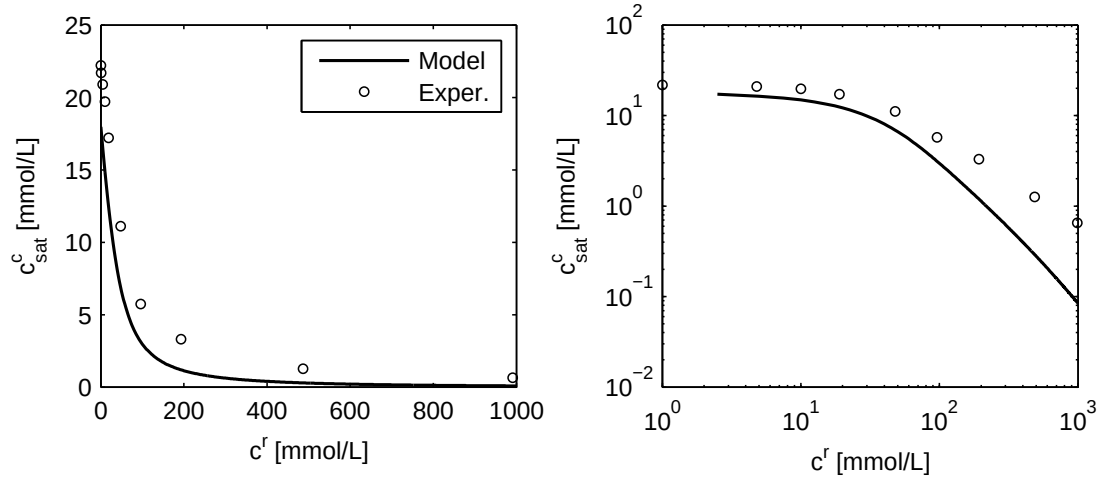

FIGURE 7.4: Comparison of model-calculated and experimental measurements of portlandite solubility in NaOH solution at 25 °C. Left and right figures represent the same data but at two different scales. Experimental data from Ref. [60].

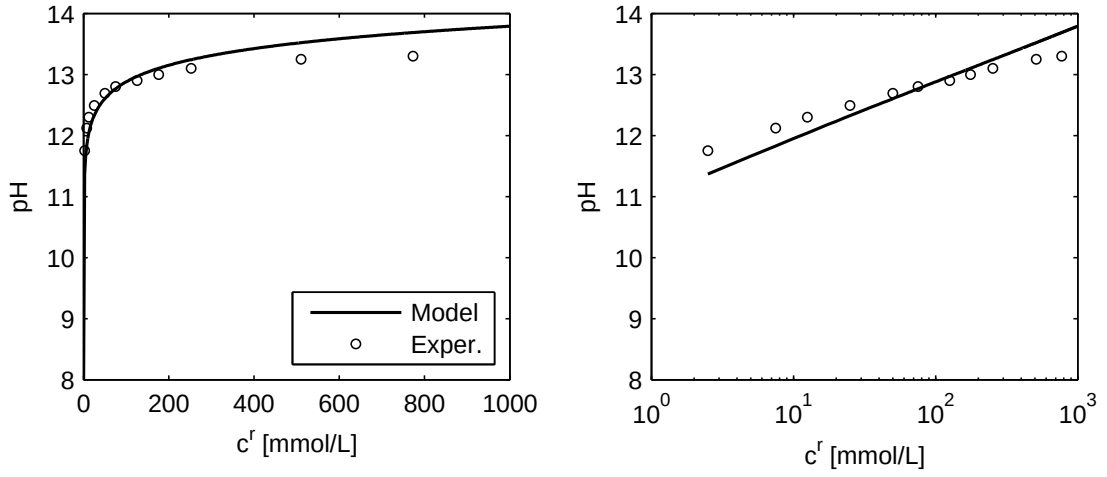

FIGURE 7.5: Comparison of model-calculated and experimental measurements of pH of NaOH solution at 25 °C. Left and right figures represent the same data but at two different scales. Experimental data from Ref. [59].

7.3 Mechanical response of an isolated interface element to the formation of reaction products

This section is aimed at demonstrating the mechanical response of an interface element when reaction products are formed within it, according to the mechanical constitutive law described in Section 6.5.2. With this purpose, the simplest possible model geometry and discretization were adopted, consisting of two square continuum elements of 1 m side with a zero-thickness interface element in between (Fig. 7.6). This model was considered under three different boundary conditions schematically represented in Fig. 7.6. The first scheme (Fig. 7.6a) does not introduce any external restriction to the expansion of the

interface element, and, thus, it is referred as 'free expansion' condition. In the second scheme (Fig. 7.6b), a uniform vertical pressure q [MPa] is applied on the top side of the model. In this scheme, the internal pressure exerted by the reaction products needs to overcome the applied pressure q in order to induce an interfacial expansion. Finally, in the third scheme (Fig. 7.6c), the vertical displacement of the top side of the model is prevented, and, therefore, the expansion of the interface element can only occur at the expense of deforming the continuum elements. For each type of boundary conditions, a number of cases were simulated varying relevant parameters in order to assess their influence on the results.

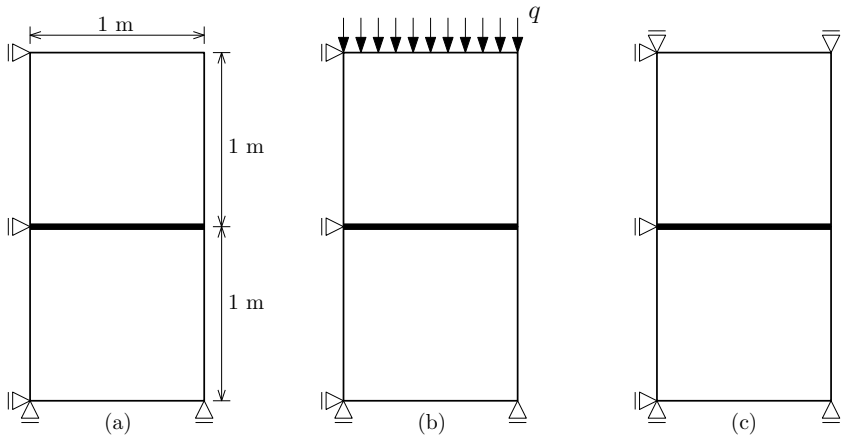

FIGURE 7.6: Modelling of an isolated interface element. Model geometry and boundary conditions: (a) free expansion, (b) expansion under normal loading, (c) expansion under passive restraint. The thick line represents the zero-thickness interface element.

With the intention of facilitating the interpretation of the results, the diffusion-reaction model was simplified by cancelling the kinetics laws proposed in Eqs. (6.31)–(6.34) and imposing constant reactions rates per unit volume of pore solution: $\Gamma^S_{mp} = \Gamma^C_{mp} = \Gamma^A_{mp} = 0$ and $\Gamma^B_{mp} = 75$ mol $\mathrm{m}^{-3}_{\mathrm{ps}}$ h^{-1}. That means that, of the whole set of dissolution/formation reactions considered by the model (Reactions (6.1)–(6.4)), only the formation of Reaction Product B (RPB) was allowed. Note that by imposing constant reaction rates the mechanical response was decoupled from the diffusion and chemical speciation analyses, and, therefore, they are omitted from the discussion of the results obtained. The chemo-mechanical coupling, however, was not completely deactivated, since the reaction rate $\bar{\Gamma}^B_{mp}$ [mol m^{-2} s^{-1}] per unit area of discontinuity is proportional to the volume of pore solution $\mathcal{U}^{ps}_{mp}$ (Eq. (6.29)), which in turn depends on the cracking normal aperture a^{cr}_n (Eq. (6.49)).

For all the simulations, the following parameters of the chemo-transport formulation were considered: $\eta^B_o = 50.01 \times 10^{-6}$ m^3/mol, $\phi^B_o = 0.796$, $\sigma^B_{th} = -10$ MPa, $k_\eta = 1 \times 10^{-6}$ MPa^{-1}, $\mathcal{U}^o_{mp} = 1 \times 10^{-6}$ $\mathrm{m}^3/\mathrm{m}^2$; the dimensionless shape parameters of the f^B_ϕ function (Eq. (6.21)) were $k = 1$ and $p = 2$. The remaining chemical and diffusion

parameters had no effect on the results obtained and, thus, they are omitted for the sake of brevity.

With regard to the mechanical parameters, the same, very high, normal and tangential elastic stiffnesses of the interface element, $K_n = K_l = 1 \times 10^9$ MPa/m, were adopted for all cases. With the geometry and boundary conditions considered, the interface element will only develop normal stresses. Consequently, the shear parameters (c_o, $\tan\varphi_o$, G_f^{IIa}, σ_{dil}, α_a, α_φ, $\alpha_{\sigma_{dil}}$, $\alpha_{c_{dil}}$) had no effect on the results. The initial tensile strength (χ_o) and the specific fracture energy in Mode I (G_f^I), which had a major influence on the results, are given below for each simulated case. The scaling factor of the evolution law of the tensile strength, was taken as $\alpha_\chi = 0$ for all cases.

For the continuum elements, a linear elastic law under the hypothesis of plane stresses was adopted for all cases. The mechanical properties of the continuum elements are only relevant for the development of the expansions of the interface element for the cases with the third scheme of boundary conditions (Fig. 7.6c), as it is discussed below.

Finally, the time discretization of the staggered scheme consisted of 480 steps of 1.5 h. These time steps were further subdivided in 12 and 100 equal increments per time steps in `DRACFLOW` and `DRAC`, respectively. For the cases with external loading, the pressure q was applied (or removed) in one additional step, in which the time increments in `DRACFLOW` were null. In that way, the external loading of the specimens may be regarded as 'instantaneous'.

7.3.1 Free expansion

Five cases with different combinations of χ_o and G_f^I were simulated with the first boundary conditions (Fig. 7.6a), in order to assess the effect of the tensile strength on the development of the expansion of the interface element.

Effect of initial tensile strength

The first set of results are given in Fig. 7.7. These results correspond to three cases with the same specific fracture energy in Mode I, $G_f^I = 10$ J/m^2, but with different initial tensile strength χ_o, as it is indicated in the legend of the plots.

Let us first consider the evolution curves corresponding to the case with $\chi_o = 2.5$ MPa. Before day 2, the formation of RPB progressively filled the initial volume of the discontinuity ($\mathcal{U}_{mp}^o$), without inducing any stress on the discontinuity nor on the RPB itself. At day 2, approximately, the volume of 'capillary pores' was exhausted and, consequently, the subsequent progressive formation of RPB induced a growing internal pressure (σ_g)

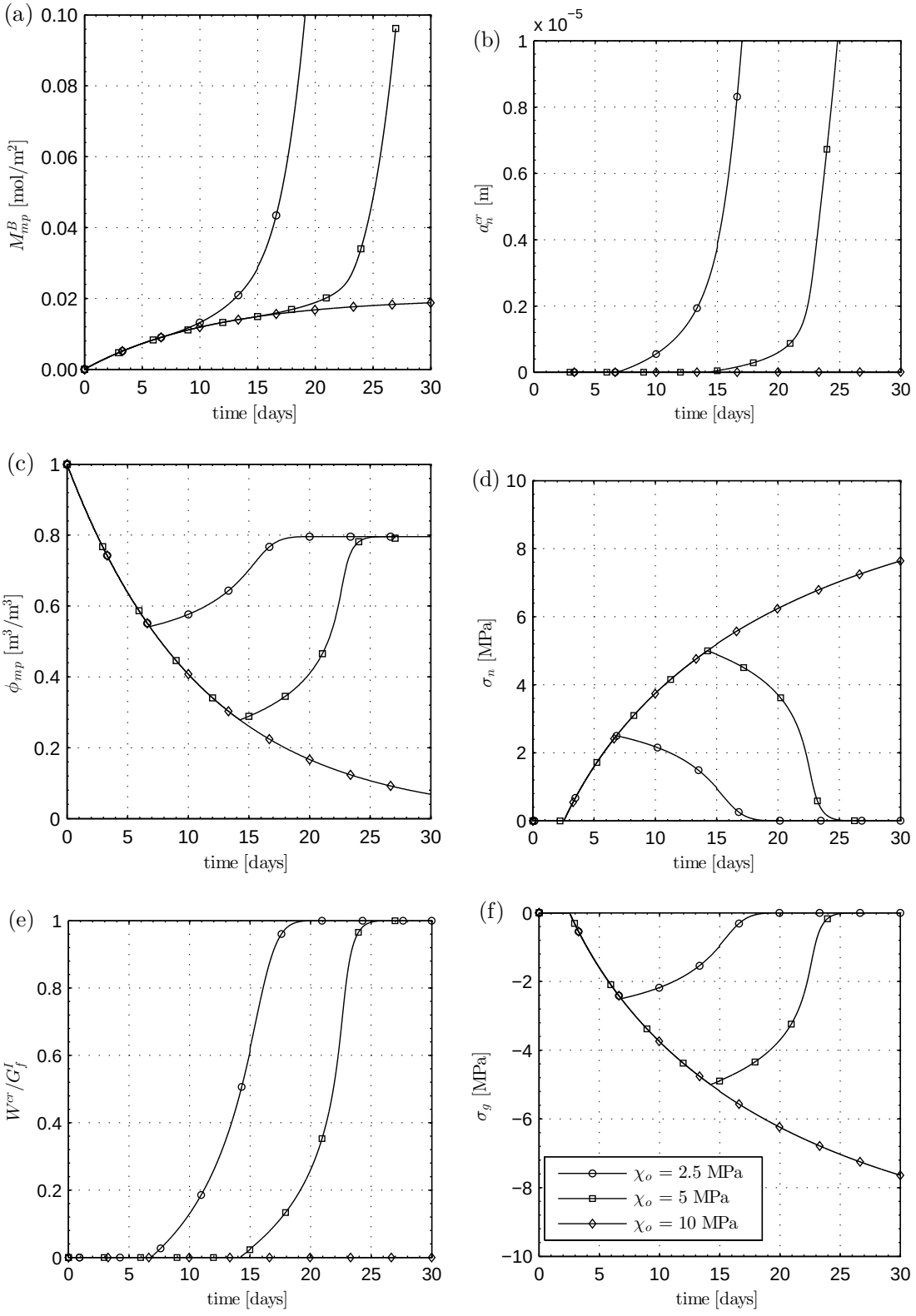

FIGURE 7.7: Free expansion of an isolated interface element. Effect of the initial tensile strength (χ_o) of the discontinuity on the evolution of the amount of RPB (M^B_{mp}), the normal cracking aperture (a^{cr}_n), the total porosity (ϕ_{mp}), the normalized fracture work (W^{cr}/G^I_f), the normal stress of the discontinuity (σ_n), and the stress of the reaction products (σ_g).

(Fig. 7.7f), which eventually reached the tensile strength of the discontinuity (day 7), starting the cracking process. Note that the equilibrium condition in the normal direction of the discontinuity required that $\sigma_n + \sigma_g = 0$ at all times, as it can be observed in the mirrored evolution curves of σ_n and σ_g (Figs. 7.7d and f). From this point on, the cracking normal aperture (a_n^{cr}) started growing (Fig. 7.7b) and σ_g decreased due to the softening of the tensile strength of the discontinuity. The evolution of the fracturing work dissipated is given in Fig. 7.7e, normalized by G_f^I. For $W^{cr} = 0$, the discontinuity was not cracked; for $0 < W^{cr} < G_f^I$, the discontinuity was partially cracked (it had still some residual tensile strength, i.e. $0 < \chi < \chi_o$); for $W^{cr} = G_f^I$, the discontinuity was completely cracked ($\chi = 0$).

Before cracking, the total porosity (Fig. 7.7c) was progressively reduced, first (until day 2) due to the filling of $\mathcal{U}_{mp}^o$, and then, as the RPB was getting compressed, due to the reduction of the gel porosity (ϕ^B). After cracking, the softening of the discontinuity progressively decompressed the RPB and, consequently, the gel porosity (and the total porosity, which at this point was the same) progressively grew up. Note that once the internal pressure became null, the total porosity became constant and equal to ϕ_o^B. Since, for this simplified version of the model, $\mathcal{U}_{mp}^{ps} = (a_n^{cr} + \mathcal{U}_{mp}^o)\phi_{mp}$ and $\dot{M}_{mp}^B = \mathcal{U}_{mp}^{ps}\Gamma_{mp}^B$, the changes in the gel porosity explain why the formation of RPB was progressively slowed down until reaching day 7, the moment in which the discontinuity started to get cracked and the trend changed with an acceleration of the formation rate of RPB (Fig. 7.7a).

Increasing the tensile strength to 5 MPa had the effect of delaying the cracking of the discontinuity, but, qualitatively, the evolution curves were similar to those obtained with $\chi_o = 2.5$ MPa. In contrast, with $\chi_o = 10$ MPa the discontinuity was not cracked during the simulated time and, what is more, it would not reach cracking for any simulation time, since $|\sigma_g|$ may grow tending asymptotically to $|\sigma_{th}^B| = 10$ MPa, but never overcome that value.

Effect of the specific fracture energy in mode I

The second set of results is given in Fig. 7.8. These evolution curves correspond to three cases with the same tensile strength $\chi_o = 2.5$ MPa, but with different specific fracture energy in Mode I, as it is indicated in the legend of the plots. Note that the case with $G_f^I = 10$ J/m^2 is the one previously described in detail, and that the other two cases have qualitatively similar evolution curves. Changing G_f^I only had an effect once σ_g had reached the χ_o, and the cracking softening started ($W^{cr} > 0$). From this point on, the higher the G_f^I, the slower the rate of formation of RPB (Fig. 7.8a) and, thus, the slower the expansion rate of the interface (Fig. 7.8b). This is explained by the increase of ductility associated to the increase of G_f^I, which implies that higher a_n^{cr} is needed

to obtain the same reduction in the tensile strength, which in turn determines the gel porosity of the RPB, the volume of pore solution, and the rate of formation of RPB.

7.3.2 Expansion under normal loading

Two cases with different constant load q of 1.5 and 3 MPa were simulated with the boundary conditions schematically represented in Fig. 7.6b. Additionally, two cases were simulated in which the applied constant loads of 1.5 and 3 MPa were removed after 15 days (half of the simulated time). In all cases, the same values of $\chi_o = 2.5$ MPa and $G_f^I = 5$ J/m^2 were adopted. For comparison, the evolution curves of the free expansion case ($q = 0$) discussed in the previous section, which used the same values of χ_o and G_f^I, are also plotted in the figures.

Constant loading

As RPB was formed, first the initial volume of capillary pores ($\mathcal{U}_{mp}^o$) was filled without exerting any internal pressure. Once $\mathcal{U}_{mp}^o$ was exhausted (approximately at day 2), the formation of RPB started to exert a growing internal pressure (σ_g), tending to separate both sides of the interface element. However, the separation (the cracking of the interface element) did not start until the growing $|\sigma_g|$ reached a value equal to the initial tensile strength (χ_o) plus the applied load (q), i.e. until $\sigma_g = \chi_o + q$. Comparing with the case without loading, the cracking time was delayed from day 7 to day 16, for $q = 3$ MPa (Figs. 7.9b and e). Furthermore, the higher the applied load q, the higher the σ_g at the starting of the cracking process (Figs. 7.9f), and, consequently, the smaller the gel porosity of RPB (Figs. 7.9c), the smaller the volume of pore solution, and the smaller the rate of formation of RPB (Figs. 7.9a). Note that if $\chi_o + q$ would have been greater or equal to $\left|\sigma_{th}^B\right|$, the separation would not have occurred at any time and the rate of formation of RPB would have asymptotically decreased to zero.

Loading and unloading

Two additional cases were simulated in which, instead of keeping the applied load q until the end of the simulation, the load was removed after the first 15 days. The evolution curves obtained are given in Fig. 7.10. As explained above, the load q was applied and removed 'instantaneously', that is, in calculation steps in which the simulated time was stopped, with no formation of RPB.

As q was removed, the vertical equilibrium was restored either by increasing σ_n, if χ_o had not been reached yet, either by reducing σ_g via increasing the normal cracking aperture (a_n^{cr}), if the discontinuity was already in the softening stage. In the case of

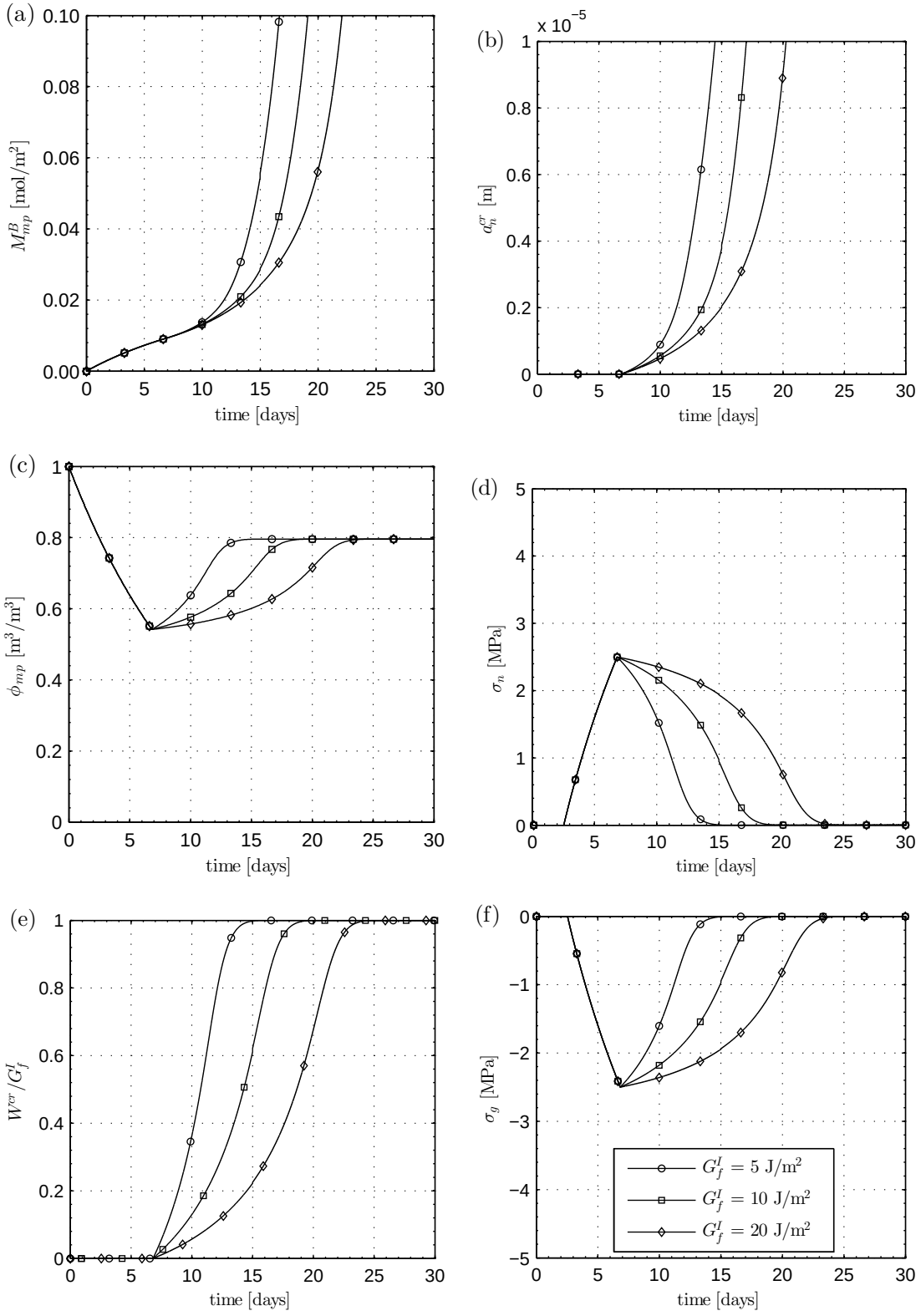

FIGURE 7.8: Free expansion of an isolated interface element. Effect of the specific fracture energy (G^I_f) of the discontinuity on the evolution of the amount of RPB (M^B_{mp}), the normal cracking aperture (a^{cr}_n), the total porosity (ϕ_{mp}), the normalized fracture work (W^{cr}/G^I_f), the normal stress of the discontinuity (σ_n), and the stress of the reaction products (σ_g).

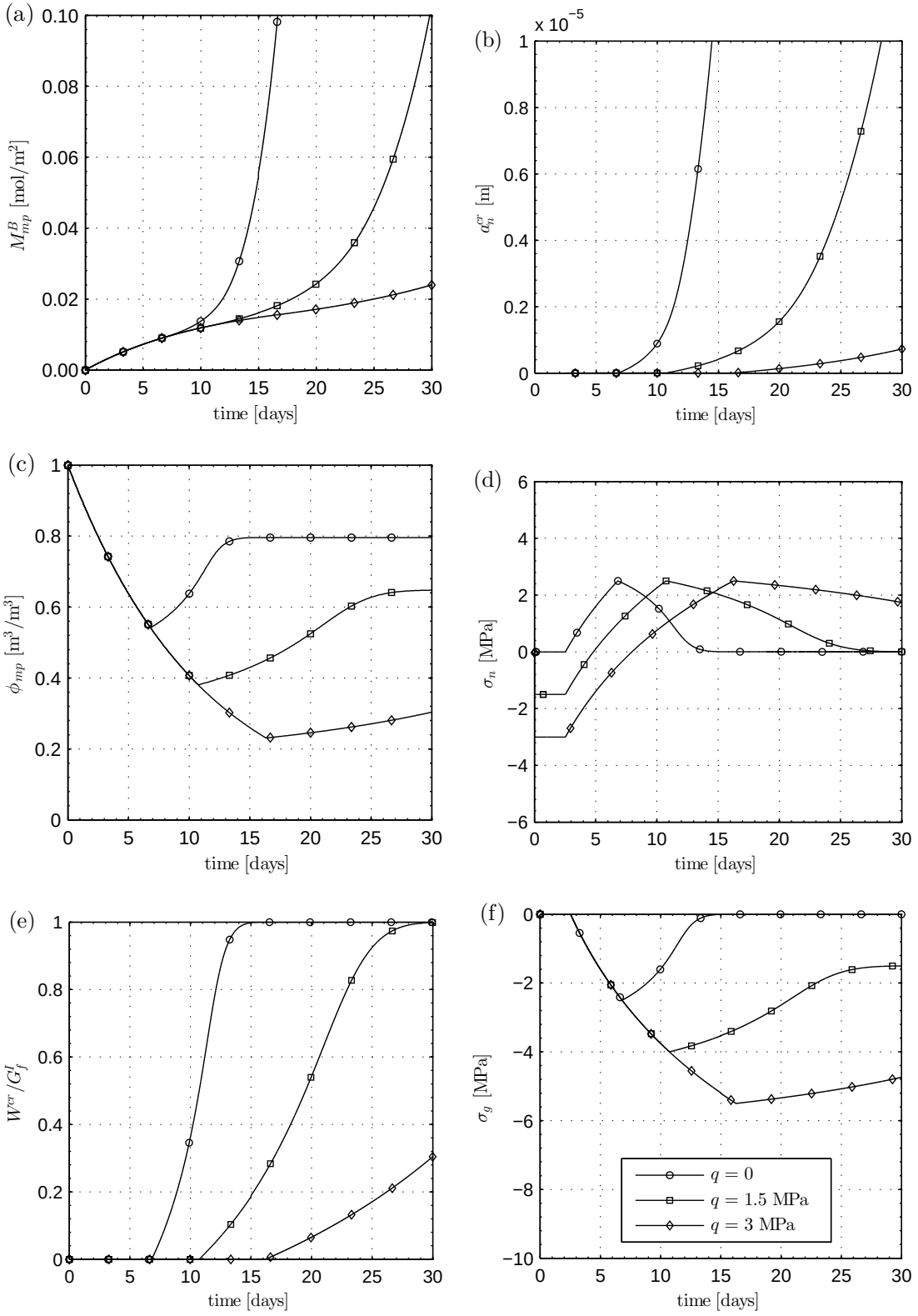

FIGURE 7.9: Expansion of an isolated interface element under constant normal loading. Effect of the magnitude of the applied load q on the evolution of the amount of RPB (M^B_{mp}), the normal cracking aperture (a^{cr}_n), the total porosity (ϕ_{mp}), the normalized fracture work (W^{cr}/G^I_f), the normal stress of the discontinuity (σ_n), and the stress of the reaction products (σ_g).

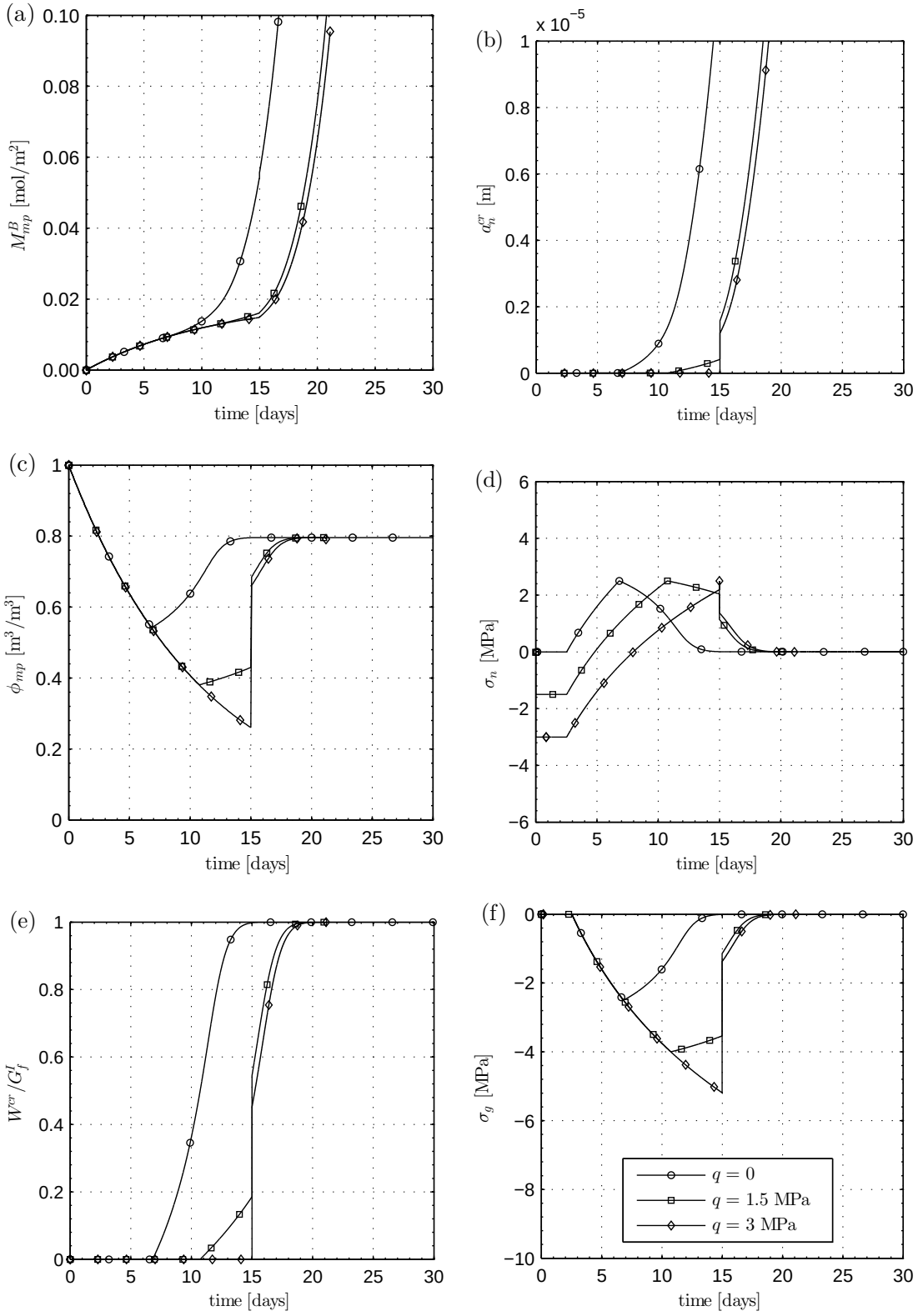

FIGURE 7.10: Expansion of an isolated interface element under loading-unloading conditions. Effect of the magnitude of the applied load q on the evolution of the amount of RPB (M^B_{mp}), the normal aperture (a^{cr}_n), the total porosity (ϕ_{mp}), the normalized fracture work (W^{cr}/G^I_f), the normal stress of the discontinuity (σ_n), and the stress of the reaction products (σ_g).

$q = 1.5$ MPa, in which the cracking had started before day 15 (Fig. 7.10e), removing q directly increased a_n^{cr} (Fig. 7.10b). In the case of $q = 3$ MPa, in contrast, which had not been cracked at day 15 (Fig. 7.10e), the progressive removal of q first increased σ_n ($W^{cr} > 0$,Fig. 7.10d), and then, once χ_o had been reached, tensile crack opening was induced ($a_n^{cr} > 0$) while σ_n decreased due to the softening of the discontinuity ($W^{cr} > 0$, Fig. 7.10e)). The net effect on the evolution curves of a_n^{cr} (Fig. 7.10b) was an instantaneous positive 'jump' at day 15 when q was removed. After this jump, the aperture rates were similar to those developed by the case with $q = 0$ for the same a_n^{cr}, i.e. it was as if the a_n^{cr} curves of the loaded cases were displaced towards the right.

7.3.3 Expansion under passive restraint

The mechanical boundary conditions indicated in Fig. 7.6c prevent any vertical displacement of the top side of the model. Therefore, the expansion of the interface element due to the formation of RPB can only occur at the expense of deforming the continuum elements at both sides of the interface element. Moreover, since the continuum elements are linear elastic, their vertical deformation induces a vertical stress σ_y, which is proportional to the normal aperture of the interface element. Since the simulations were performed under plane stress, the proportionality factor was $E/(2L)$, where E [MPa] is the elastic modulus of the continuum material and $L = 1$ m is the side length of the continuum elements. Note that the Poisson's coefficient had no influence on σ_y.

In order to asses the effect of the passive restraint exerted by the continuum elements on the development of the interface expansions, three cases were simulated with different elastic modulus E of 100, 1000, and 10000 GPa. The same parameters $\chi_o = 2.5$ MPa and $G_f^I = 5$ J/m^2 were adopted for the three cases. The evolution curves obtained are given in Fig. 7.11.

These evolution curves show that the elastic modulus E only had an effect on the results once the initial tensile strength (χ_o) had been reached (Fig. 7.11d) and the normal cracking aperture (a_n^{cr}) had started to grow, approximately at day 7 (Fig. 7.11b). Before this point, the evolution curves of the three cases were coincident and the internal pressure (σ_g) was equilibrated by the discontinuity stress, i.e. $\sigma_n + \sigma_g = 0$. From this point on, a vertical stress σ_y was induced (Fig. 7.11d), and the vertical equilibrium equation became $\sigma_n + \sigma_g = \sigma_y$.

It can be observed that the higher the elastic modulus, the slower the expansion rate of the interface element (Fig. 7.11b). In the cases with $E = 100$ GPa and $E = 1000$ GPa, the softening of the discontinuity, indicated by $W^{cr} > 0$ in Fig. 7.11e, allowed a partial

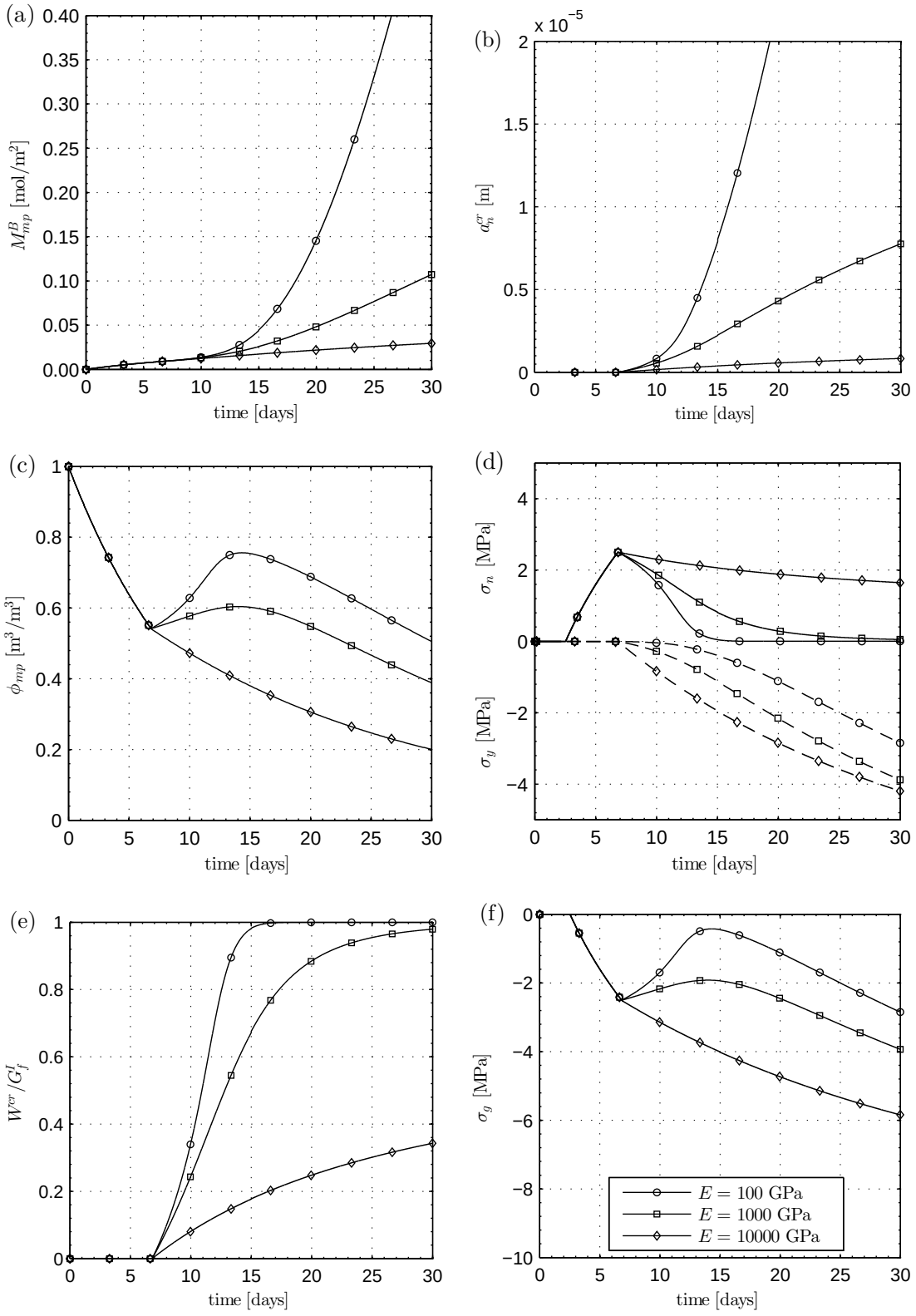

FIGURE 7.11: Expansion of an isolated interface element under passive restraint. Effect of the stiffness of the restraint (E) on the evolution of the amount of RPB (M^B_{mp}), the normal aperture (a^{cr}_n), the total porosity (ϕ_{mp}), the normalized fracture work (W^{cr}/G^I_f), the normal stress of the discontinuity (σ_n), and the stress of the reaction products (σ_g). Dashed lines in plot (d) indicate the induced vertical stress in the continuum elements (σ_y).

decompression of the reaction products and a consequent increase of the gel porosity (Fig. 7.11c), which resulted in a rapid increase of the expansion rate (Fig. 7.11b). However, as a_n^{cr} became larger, $|\sigma_g|$ eventually started to grow again, progressively reducing the gel porosity (Fig. 7.11c) and, consequently, the rate of formation of RPB (Fig. 7.11a). Furthermore, if the simulation time would have been sufficiently extended, the rate of formation of RPB would have tended asymptotically to zero. In the case with $E = 10000$ GPa, the behaviour was similar, but with the difference that the induced σ_y grew faster with a_n^{cr} than the softening reduction of σ_n, and, therefore, there was no decompression of the RPB.

7.4 Interfacial Expansion Tests

In this section, the complete version of the model is used for simulating the Series F of the experimental Interfacial Expansion Tests presented in Chapter 3. This series was intended to assess the role played by the mass exchange between the alkaline bath and the specimens on the development of the interfacial expansions. With this purpose, three sets of specimens with different lateral sealing were tested (Fig. 3.35). The specimens were prepared with plain cement paste and SL glass discs, and exposed to an alkaline solution (40 g NaOH and 2 g of $Ca(OH)_2$ per kg of water) at 60 °C after a curing period of 28 days at room temperature. Details of the preparation of the specimens, as well as of the curing and exposure conditions are given in Section 3.7.1.

As previously discussed in Section 6.3.1, the model was formulated under the assumptions that no significant ASR occurs during the curing of the cementitious matrix, and that the Hydrated Cement Paste (HCP) had reached its maximum possible hydration degree before starting the exposure stage. Consequently, the simulation results presented here only comprise the exposure stage of the considered Interfacial Expansion Tests.

7.4.1 Model description

The model geometry is schematically represented in Fig. 7.12a. The geometry considered takes advantage of the symmetries of the specimens: an horizontal symmetry plane normal to the axis of the specimen, and a vertical symmetry axis coincident with the specimen axis. The latter assumption allows us to reduce the 3D problem to a 2D axisymmetric problem. (The FE formulation of the model for axisymmetric problems is not explained in this thesis, but it can be readily obtained by analogy with axisymmetric formulations from the literature [e.g. 226]). This geometry was discretized with 378 quadratic continuum elements and 14 quadratic interface elements (Fig. 7.12b), giving

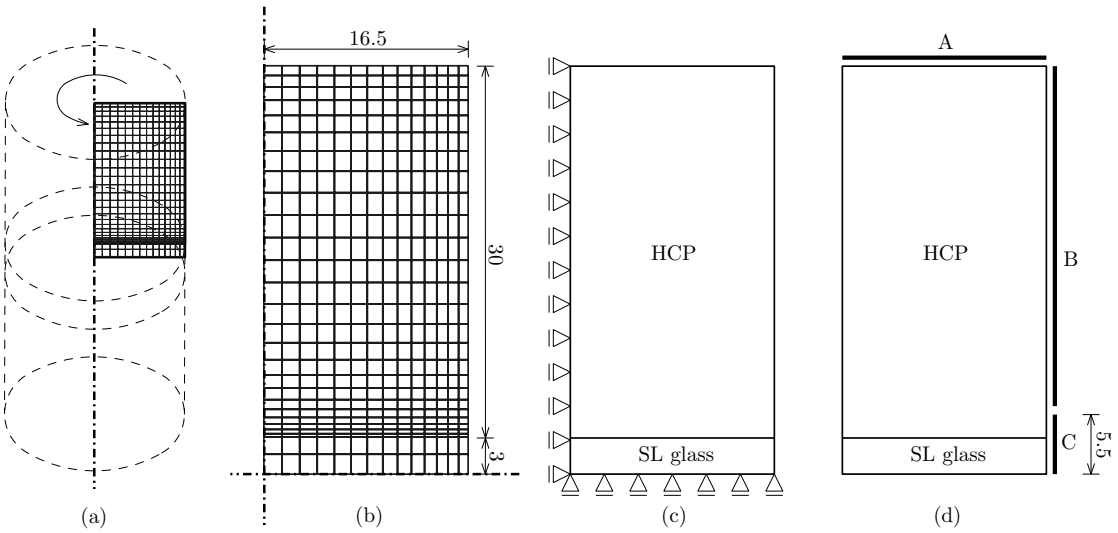

FIGURE 7.12: Modelling of Interfacial Expansion Tests. (a) Location of the modelled sector within a complete specimen. (b) Model geometry and FE mesh. Zero-thickness interface elements were introduced in between the continuum elements representing SL glass and those representing HCP. Dimensions are given in mm. (c) Mechanical boundary conditions. (d) Diffusion boundary conditions. Thick lines indicate the sectors of the boundary exposed to the alkaline solution, with imposed $c^s = 0$, $c^c = 0.034$ mol/m^3 and $c^r = 1000$ mol/m^3. For specimens of Set #2, concentrations are imposed only at sector A; for Set #3, at sectors A and B; and for Set #1, at sectors A, B, and C.

a total of 1246 nodes. The interface elements were placed in between the continuum elements representing the HCP and those representing SL glass.

The time discretization of the staggered scheme consisted in 896 steps of 1.5 h each. These steps were further subdivided in 12 and 100 equal increments for the diffusion-reaction analysis with `DRACFLOW` and for the mechanical analysis in `DRAC`, respectively.

The boundary conditions for the mechanical problem, intended to materialize the vertical symmetry axis and the horizontal symmetry plane, are schematically represented in Fig. 7.12c.

The mechanical behaviour of the SL glass-HCP interface was simulated with the mechanical elasto-plastic constitutive law for interface elements described in Section 6.5.2.1. Part of the parameters of this constitutive law are given in Table 7.1. The rest of the parameters were: $G_f^{IIa} = 10 \times G_f^I$, $\tan\varphi_r = \tan\varphi_o$, $\sigma_{dil} = 40$ MPa, $\alpha_a = \alpha_\varphi = \alpha_{\sigma_{dil}} = \alpha_{c_{dil}} = 0$. The continuum elements were assumed to be linear elastic, with elastic modulus E and Poisson's coefficient ν given in Table 7.2.

The boundary conditions for the diffusion problem are schematically represented in Fig. 7.12d, were the thick lines indicate the zones of the surface area of the specimen exposed to the alkaline solution. At these zones, the concentration of primary aqueous species in pore solution was imposed to be the same as in the alkaline bath. These

TABLE 7.1: Modelling of Interfacial Expansion Tests. Parameters of the SL glass-HPC interface elements.

Material	$\mathcal{U}^o_{mp}$ [m^3/m^2]	$\mathcal{S}^o_{mp}$ [m^2/m^2]	K_n [MN/m]	K_l [MN/m]	χ_o [MPa]	c_o [MPa]	$\tan\varphi_o$	G^I_f [J/m^2]
SL glass-HCP	1E−6	0.7	1E+9	1E+9	1.5	3	0.7	5

TABLE 7.2: Modelling of Interfacial Expansion Tests. Parameters of the continuum elements representing HCP and SL glass.

Material	E [GPa]	ν	ϕ	D^s [m^2/h]	D^c [m^2/h]	D^r [m^2/h]
HCP	25	0.2	0.421	4.70E−9	3.12E−9	5.25E−9
SL glass	70	0.2	0	0	0	0

concentrations were estimated by means of a speciation calculation similar to the ones performed in Section 7.2, resulting in $c^s = 0$, $c^c = 0.034$ mol/m^3, and $c^r = 1000$ mol/m^3. Depending on the lateral sealing applied (Fig. 3.35), the zones exposed to the alkaline bath change from one set of specimens to the other. For simulating the specimens with complete lateral sealing (Set #2), concentrations were imposed only at zone A; for specimens without any lateral sealing (Set #1), at zones A, B, and C; and for the specimens of Set #3, at zones A and B.

The concentration of aqueous silica in the pore solution of mature HCP is usually very low (< 0.1 mol/m^3) [17, 138], and, it is not expected to play a significant role in the development of ASR. Therefore, the initial concentration of silicate ions in the pore solution of the HCP was assumed $c^s = 0$. The initial concentration of aqueous alkalis was fixed by trial and error in order to best fit the experimental results. The value finally used was $c^r = 600$ mol/m^3. However, this value is fairly low for HCP with an alkali content of 1.1 wt% of Na_2O_e. Based on experimental results reported in the literature [e.g. 55, 133], this value is estimated to be close to 1000 mol/m^3, Possible reasons of this discrepancy are discussed below. The initial concentration of calcium ions was assumed to be the equilibrium calcium concentration of portlandite in a 0.6 M NaOH solution, estimated to be $c^c = 0.08354$ mol/m^3 by means of a speciation calculation similar to the ones performed in Section 7.2.

The effective diffusivity (D^β) and the total porosity (ϕ) considered for the continuum elements are given in Table 7.2. Note that the SL glass was assumed to be non-porous and impervious, as proposed in Section 6.3.3. The porosity of the HCP was obtained by estimating the amount of cement hydration products using the expressions given by Brouwers [25, 26], which are based on the work of Powers and Brownyard [167]. By introducing the mineral composition of the (nonhydrated) cement and the w/c ratio of the paste, these expressions allowed us to estimate the amount of the different cement

hydration products as well as the different porosity fractions (gel and capillary porosity). To do so, a maturity factor (degree of hydration) of 1.00 was assumed, and the mineral composition of cement was estimated from the oxide composition given in Table A.1 (PC02), Appendix A.1, by means of Bogue's method [10, Annex A1]. With the resulting capillary porosity ($\phi^{cp} = 0.117$), the effective diffusivities of the primary aqueous species (Table 7.2) were estimated as explained in Section 6.4.9.1, with parameters $D_s^\beta/D_w^\beta = 8 \times 10^{-5}$, $n = 2.7$, $\phi^{per} = 0.18$.

In contrast with the continuum elements, the longitudinal and transversal diffusivities of the interface elements evolve with the dissolution/precipitation of solid species and with the cracking processes (see Section 6.4.9.2). The parameters adopted for the evolution law were: $D_1^\beta/D_w^\beta = 10$, $D_{ITZ}^\beta/D_w^\beta = 7.64 \times 10^{-3}$, $w_{ITZ} = 2 \times 10^{-5}$ m, and $w^{crit} = 1 \times 10^{-4}$ m. The diffusivities of the primary species in bulk water at 60 °C are given in Table 6.2. For the aqueous alkali, the diffusivity of Na^+ was adopted. The initial volume of the interface elements ($\mathcal{U}_{mp}^o$) and the corresponding initial surface area of dissolution fronts ($\mathcal{S}_{mp}^o$) are given in Table 7.1.

The specific molar volume (η_o^α), the unstressed gel porosity (ϕ_o^α), and threshold stress ($\tilde{\sigma}_{th}^\alpha$) of the solid α-species (SL glass, portlandite, RPA, and RPB) are given in Table 7.3. The dimensionless shape parameters of the f_ϕ^α functions (Eq. (6.21)) were the same for RPA and RPB: $k = 1$ and $p = 2$. The compliance constant was the same for the four solid species: $k_\eta = 1 \times 10^{-6}$ MPa^{-1}.

TABLE 7.3: Parameters of the reactive solidα-species.

α-species	K_{sp}^α	k_f^α	k_d^α	η_o^α [cm^3/mol]	ϕ_o^α	$\tilde{\sigma}_{th}^\alpha$ [MPa]
S	2.010E−6	n/a	1E−10	30.00	0	n/a
C	2.278E+3	2E−2	2E−2	33.05	0	n/a
A	9.645E+2	2E+3	2E+3	60.42	0.402	−3
B	6.116E−2	1E+2	1E+2	50.01	0.796	−10

The saturation product constants (K_{sp}^α), and the formation (k_f^α) and dissolution (k_d^α) kinetic constants of the solid species are given in Table 7.3. K_{sp}^S and K_{sp}^C were obtained with the expressions given in Appendix B.4 for a temperature of 60 °C. The saturation index of SL glass was well under 1 in all the simulations, and, consequently, k_f^S had no effect on the results. The remaining saturation product constants and kinetic constants in Table 7.3 were adopted to fit the experimental results. Finally, the value taken for the exponent of the activity of the hydroxyl ions in the kinetic law of SL glass dissolution (Eq. (6.31)) was $p = 3$, and for the fitting parameter of the reduction factor f_2^S (Eq. 6.38) was $A^S = 13$ m^2/mol.

7.4.2 Modelling results

Expansion curves

Figure 7.13 shows the experimental interfacial expansion curves obtained for the three different lateral sealing cases together with the corresponding numerical curves obtained with the model. The experimental curves here are the same already presented in Figs. 3.36–3.38, but considering as the zero-reading the length change measuring after the first 24 h of the exposure stage. That means that the length changes during the first 29 days, corresponding to the curing stage and the first day of the exposure stage, are not considered in agreement with the modelling assumptions stated in Section 6.3.1. The net effect of the lateral sealing on the experimental expansion curves was a reduction of the expansion rate as the degree lateral sealing was increased (see the discussion in Section 3.8.5). As it can be appreciated in Fig. 7.13, the model seems capable of reproducing this effect.

Diffusion of aqueous species

Figures 7.14–7.16 show the concentration of aqueous alkali, calcium, and silicates in pore solution for the three boundary conditions considered and at different times. In the three cases, a diffusion front of alkalis moved inward the specimen from the boundaries exposed to the alkaline solution (Fig. 7.14). In Set #2, at day 20, the diffusion front of alkalis was still far from the ITZ. Moreover, the alkali concentration along the ITZ did not change significantly from its initial value. This seems to indicate that the amount of alkalis consumed in the formation of reaction products was approximately the same as the amount of alkalis released in the dissolution of SL glass. In contrast, for Sets #1 and #3, after 10 days the alkali concentration along the ITZ was not uniform any more, with higher values close to the end exposed to the alkaline solution.

The calcium concentration (Fig. 7.15) shows an inverse diffusion pattern, with calcium diffusing from the HCP towards the borders exposed to the alkaline bath. Superposed to this diffusion pattern, the chemical reactions in the interface elements resulted in a net (slight) consumption of calcium which induced a diffusion flux towards the ITZ. This is more clearly appreciated in Set #2, but it also occurred in Sets #1 and #3. It must be noted that, although the formation of reaction products consumed significant amounts of calcium, the high rate of dissolution of portlandite in the interface elements kept the calcium concentration close to the saturation concentration, i.e. with ψ^C close to 1. Consequently, the concentration of calcium at the interface elements was mainly determined by the variations of the pH associated with the diffusion of alkalis, rather than by the diffusion of calcium itself.

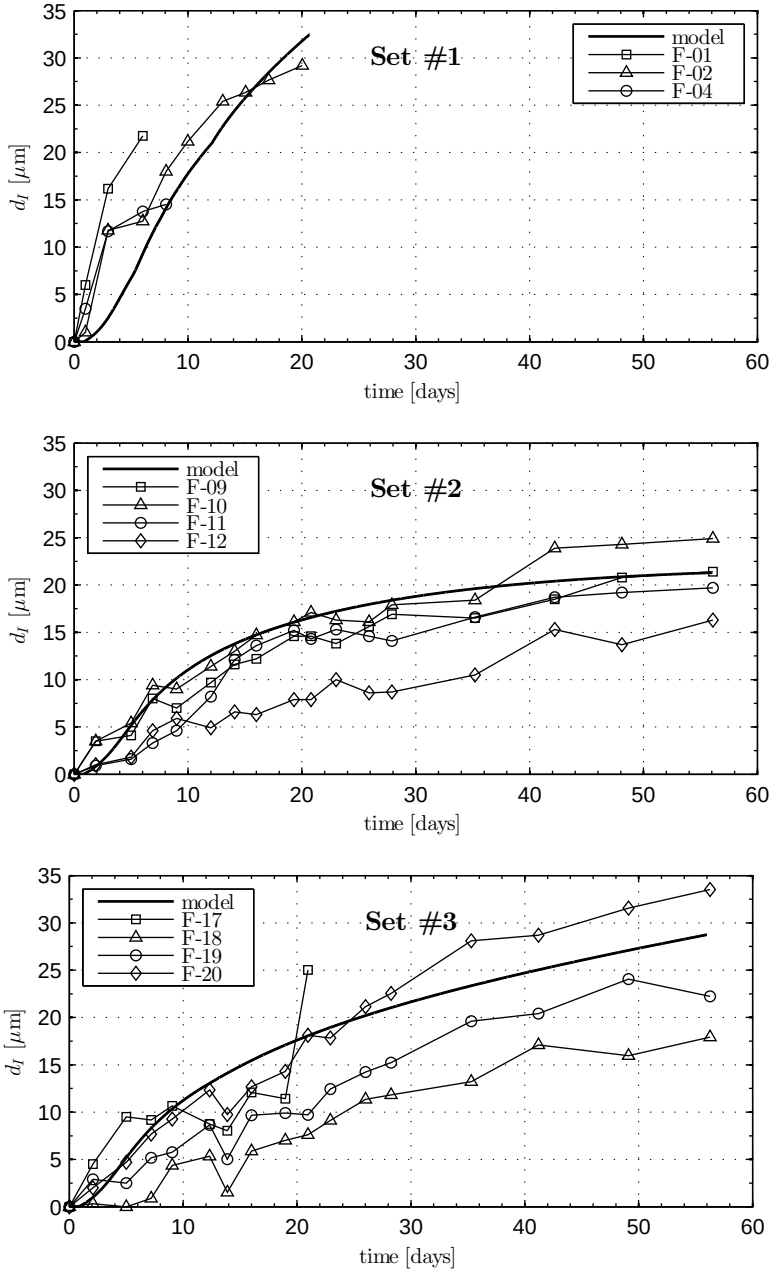

FIGURE 7.13: Modelling of Interfacial Expansion Tests. Comparison of experimental and numerical expansion curves of specimens with different lateral sealing. Set #1: without lateral sealing; Set #2: complete lateral sealing; Set #3: lateral sealing covering the interfacial zone.

The concentration patterns of silicates in pore solution are given in Fig. 7.16. Since the initial concentration in pore solution and the imposed concentration at the exposed borders were zero, the only source of the silicates in pore solution was the SL glass dissolution. At the beginning of the simulations, the rate of SL glass dissolution was very high and the amount of silicate ions produced was higher than the amount consumed in the formation of RPA and RPB. Consequently, the surplus silicates diffused towards the bulk HCP. As time passed, the rate of SL glass dissolution was reduced due both

to the formation of reaction products which reduced the surface area of the dissolution front and to the increasing distance of the dissolution front to the mid-plane of the discontinuity (see Section 6.4.6). This progressive reduction of the dissolution rate of SL glass eventually led to an inversion of the direction of the silicate diffusion flux, as it can be deduced from the reduction of the concentrations from day 10 to day 20. In other words, the silicate ions originated in the dissolution of SL glass at the interface and that had diffused towards the HCP, diffused back to the interface. In any case, the amount of silicate ions that diffuse out or into the interface elements was a very minor part of the silicate ions produced by the SL glass dissolution which were in their greater part immediately consumed in the formation of RPA and RPB.

Profiles of reaction products and internal pressure

The effect of the different boundary conditions can also be seen in the radial profiles of reactions products at the HCP-SL glass interface (Fig. 7.17). In Set #2, which, as discussed above, had uniform profiles of concentrations in pore solution in the radial direction, the volume of reaction products ($\mathcal{U}_{mp}^{RPA} + \mathcal{U}_{mp}^{RPB}$) along the HCP-SL glass interface was uniform at all times. In contrast, the volume of reaction products at the HCP-SL glass interface in Sets #1 and #3 was higher close to the right face exposed to the alkaline solution. This occurred more markedly for Set #1, but it can also be appreciated for Set #3. Moreover, in Set #1 the boundary condition prescribed of $c^s = 0$ at the nodes of the interface elements located at the right boundary implied that no reaction products could be formed there, since silicate anions are needed to form RPA and RPB (see Reactions (6.10) and (6.11)).

The profiles of induced internal pressure are given in Fig. 7.18. Note that the time sequence showed (0, 2.5 and 5 days) is different from the one in the previous figures (0, 10, and 20 days). This is because at day 10 the cracking process of the interface element was already very advanced ($W^{cr}/G_f^I \approx 1$) and, therefore, the internal pressure was practically zero. The profiles in Fig. 7.18 reflect the non-uniformity of the formation of reaction products along the interface in Sets #1 and #3. It is remarkable that, despite this lack of uniformity of σ_g, the profiles of normal stress σ_n (not presented here) were uniform. This is explained by the fact that the continuum elements above and below the interface elements behaved practically as two rigid bodies in relation to the compressibility of the reaction products. Bacuse of symmetry these 'rigid bodies' cannot rotate, and the mechanical aperture of the HCP-SL glass interfaces in Sets #1 and #3 were practically uniform, despite the non-uniform formation of reactions products. Consequently, the profiles of σ_n, which are determined by the normal aperture, were also uniform.

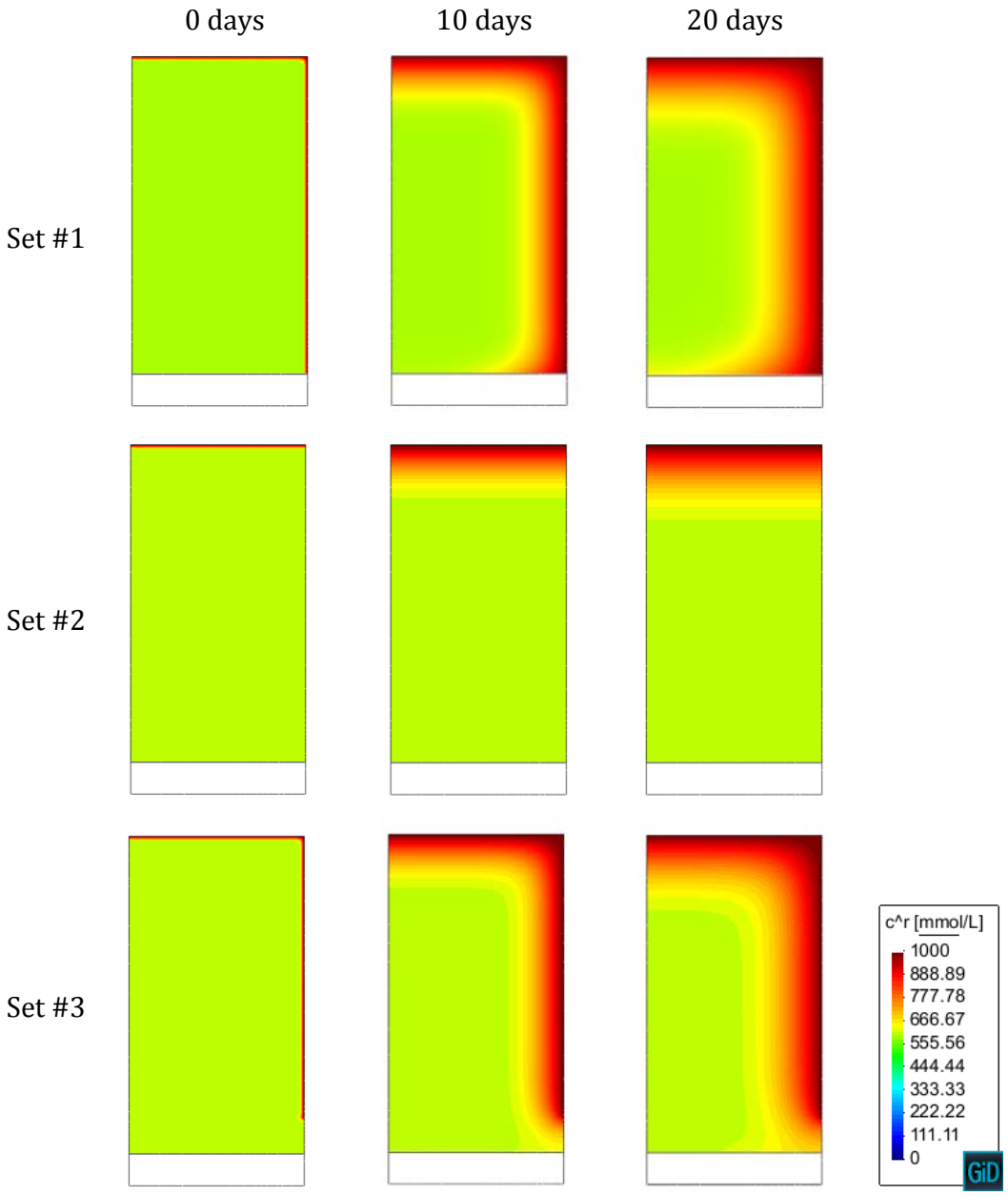

FIGURE 7.14: Modelling of Interfacial Expansion Tests. Concentration of alkalis in pore solution (c^r) at different times.

Chemical and mechanical evolution of the interface

To conclude, let us consider the time evolution of chemical and mechanical variables at a single integration point within an interface element of Set #2[2]. The time evolution of the three primary aqueous species is shown in Fig. 7.19a–c. The concentration of silicate ions (Fig. 7.19a) developed a sharp rise reaching $c^s = 30$ mol/m^3 within the first hour. Most of this rise was rapidly reverted in the following two days leading to $c^s < 1$ mol/m^3. Thereafter, c^s slowly decreased reaching 0.48 mol/m^3 at day 56. This behaviour was

[2]Since the concentration profiles of the primary aqueous species remained uniform in the radial direction, all the integration points of the interface elements in Set #2 have the same evolution curves.

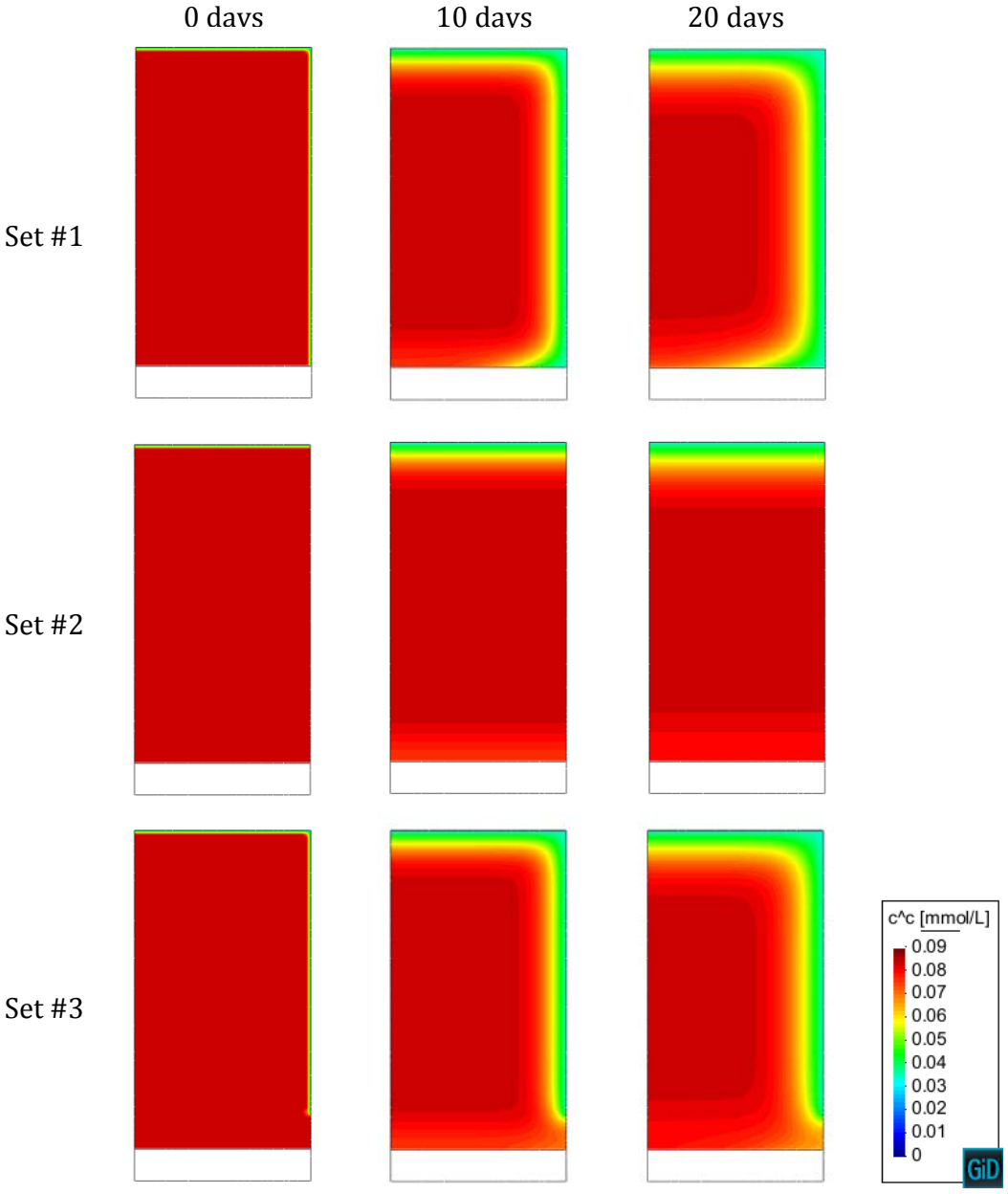

FIGURE 7.15: Modelling of Interfacial Expansion Tests. Concentration of calcium in pore solution (c^c) at different times.

associated with competing mechanisms. On one hand, the production of silicate ions due to the dissolution of SL glass, and, on the other, both the diffusion of the formed silicate ions towards the HCP and the consumption of silicate ions in the formation of RPA and (to a lesser extent) RPB. Additionally, the formation of reaction products reduces the total porosity (Fig. 7.19e) with consequent decrease of the dissolution rate of SL glass. The alkali concentration (Fig. 7.19c) also showed a sharp peak at the beginning of the simulation due to the same reasons as silicate ions, but in this case the peak had less importance in relation to the initial and final concentrations. It is significant that the final alkali concentration was higher than the initial one, mainly due to the production

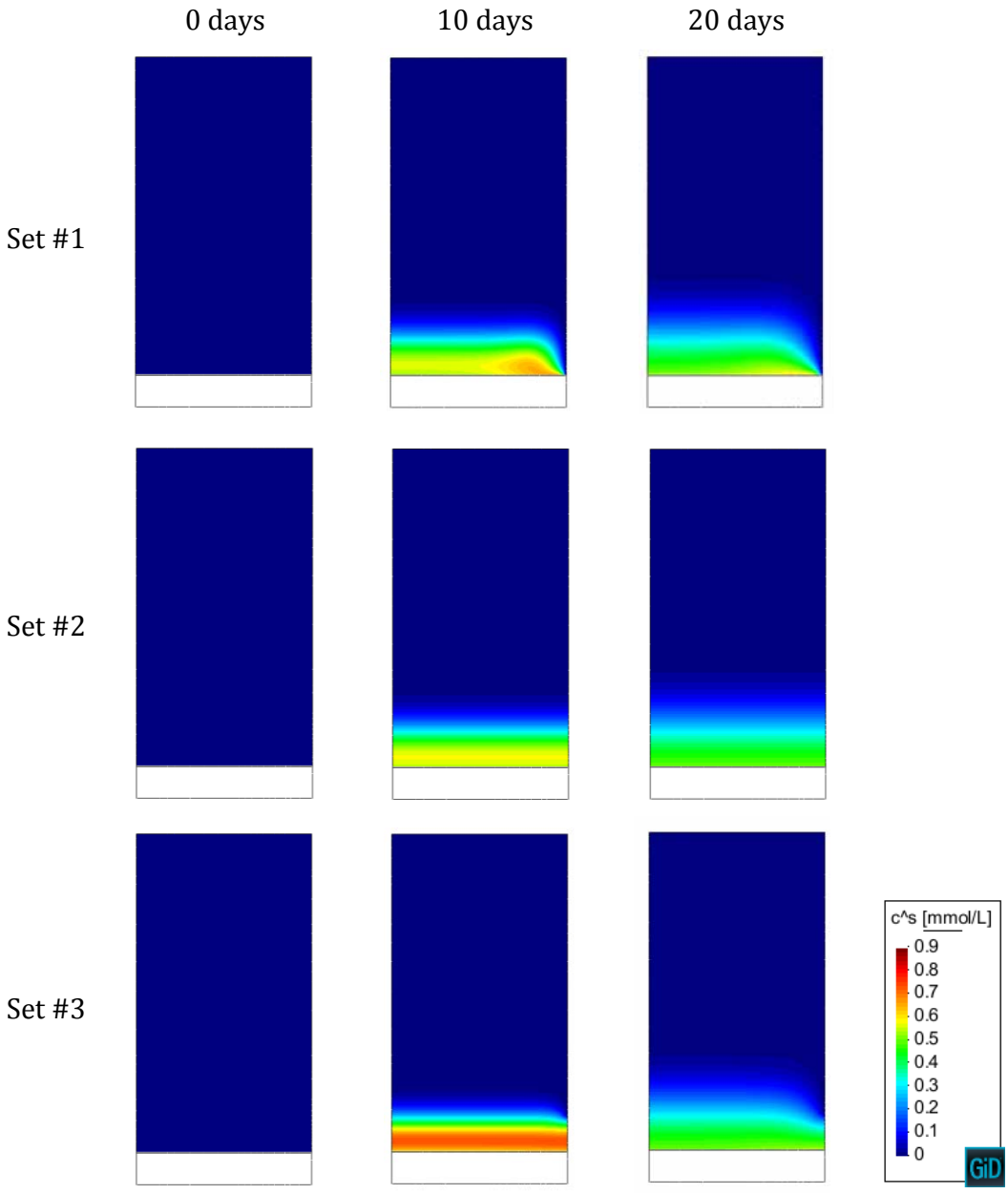

FIGURE 7.16: Modelling of Interfacial Expansion Tests. Concentration of silicates in pore solution (c^s) at different times.

of alkalis in the dissolution of SL glass. The initial calcium concentration (Fig. 7.19b), in contrast, showed a sudden but small drop in the first hour from 0.083 to 0.060, which was slowly reverted in the following days reaching 0.080 at day 56.

The evolution pH (Fig. 7.19d) reflects the evolution of the alkali and silicate concentrations, with a small drop from 12.61 to 12.60 within the first hour which was rapidly reverted reaching a value of 12.616, slightly over the initial pH. Note that with this pH the modelling assumption that the only aqueous silica species in pore solution is $H_3SiO_4^-$ might not be acceptable, and the concentration of $H_2SiO_4^{2-}$ might need to be considered

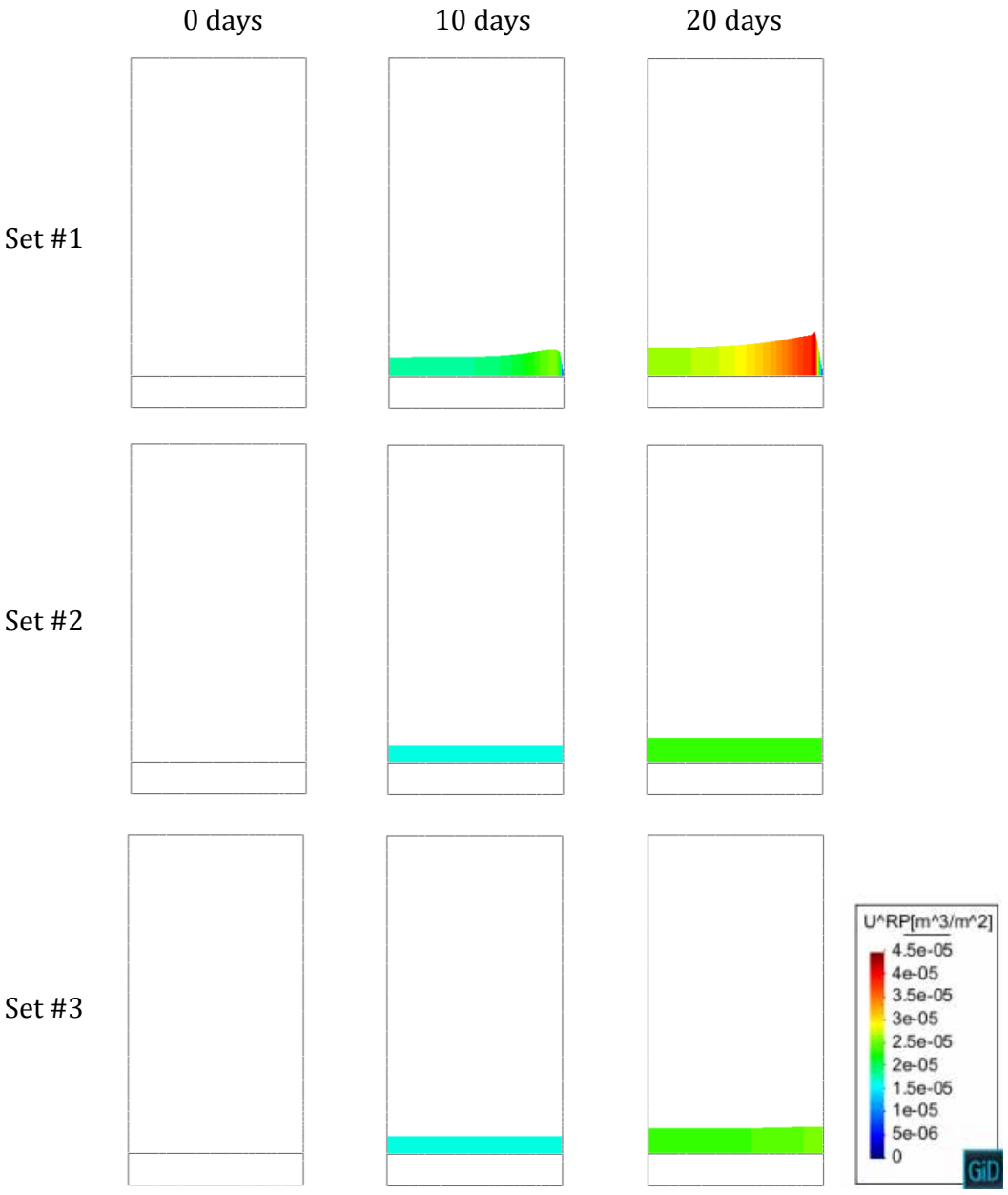

FIGURE 7.17: Modelling of Interfacial Expansion Tests. Volume of reactions products ($\mathcal{U}_{mp}^{RPA} + \mathcal{U}_{mp}^{RPB}$) within the HCP-SL glass interface at different times.

in the speciation analysis in order to obtain an accurate prediction of the pH of the pore solution. See Sections 2.3.1 and 6.3.4 for a detailed discussion of this issue.

The evolution of the saturation indexes of the four solid species is given in Fig. 7.19g, in a semi-logarithmic graph. Note that $\log_{10} \psi^{\alpha} = 0$ implies that the pore solution and the α-species are in chemical equilibrium. The saturation indexes of SL glass, RPA, and RPB (ψ^S, ψ^A, and ψ^B, respectively) roughly followed the evolution of the concentration of silicates ions. At the beginning of the simulation (day 0), $c^s = 0$, and, consequently, $\psi^S = \psi^A = \psi^B = 0$. (Note that these points are not plotted in the graph, since

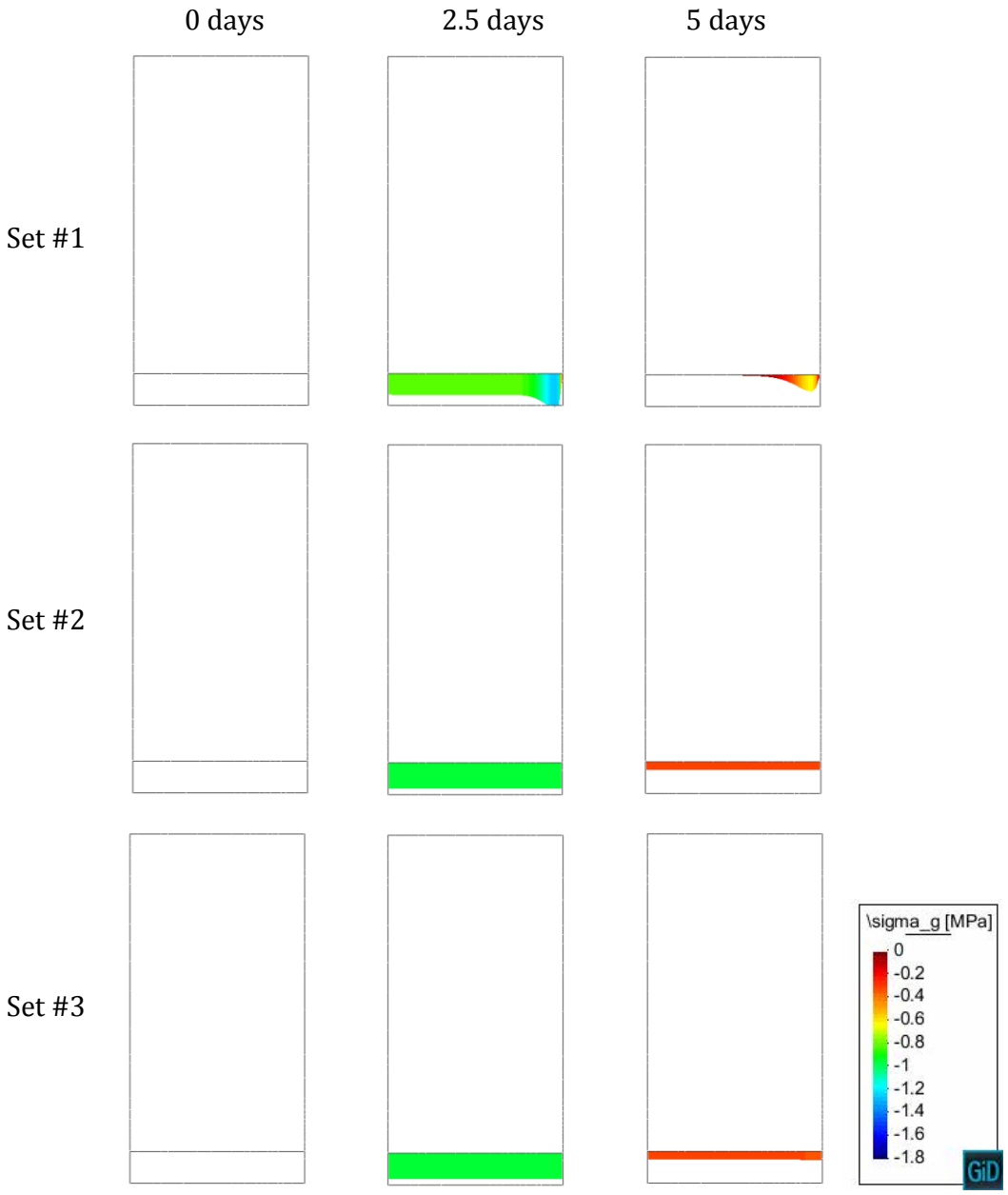

FIGURE 7.18: Modelling of Interfacial Expansion Tests. Internal pressure (σ_g) exerted by the reaction products within the HCP-SL glass interface at different times.

$\log_{10}(0) \rightarrow -\infty$.) When c^s reached its initial peak, ψ^S, ψ^A, and ψ^B reached also their own peaks, but in the case of RPA and RPB the peaks were in the over-saturated region, while in the case of SL glass it was in the under-saturated region. Consequently, as c^s decreased, ψ^S moved away from the equilibrium while ψ^A and ψ^B moved closer to it. Eventually, ψ^B passed to the under-saturated region (at day 27), but ψ^A remained over it at all times. This is not clearly visualized in Fig. 7.19g, but it can be inferred from the change of the slope sign of the evolution curve of M^B_{mp} (Fig. 7.19h). The saturation index of portlandite (ψ^C) started at equilibrium, reached a minimum of 0.72 for the

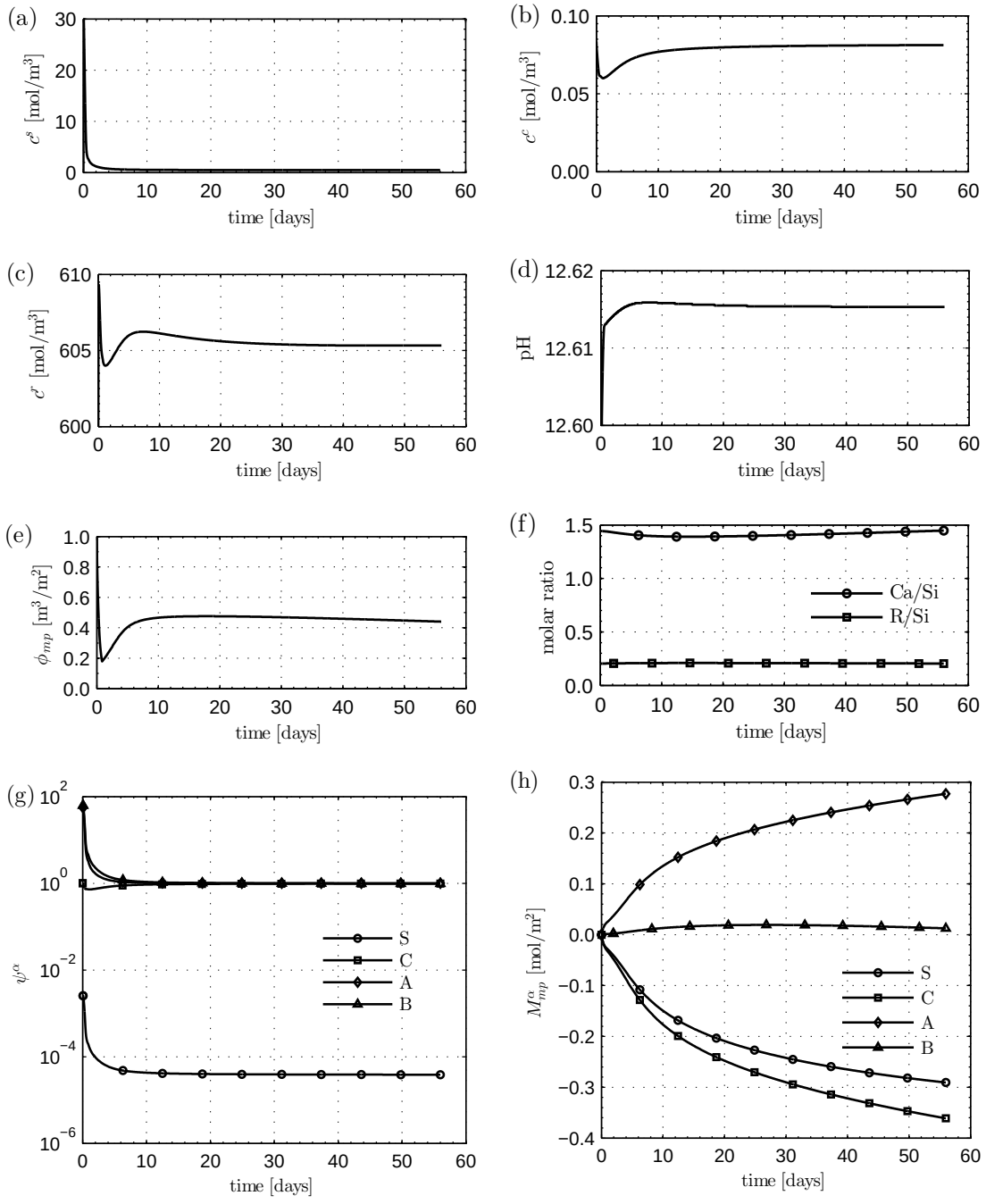

FIGURE 7.19: Modelling of Interfacial Expansion Tests. Chemical evolution within the HCP-SL glass interface elements (Set #2): (a–c) concentration of primary aqueous species in pore solution, (d) pH of the pore solution, (e) total porosity, (f) Ca/Si and R/Si molar ratios of the ASR product, (g) saturation indexes, and (h) molar concentration of solid species.

minimum value of pH (coincident with the peak value of c^s), and then slowly moved back towards the equilibrium condition.

The evolution of the concentration of solid species is given Fig. 7.19h. The amounts of SL glass and portlandite dissolved at their respective dissolution fronts are indicated by means of negative values (see Section 6.4.3). The rate of SL glass dissolution steadily decreased with time, mainly as a result of the f_2^S factor intervening in the dissolution rate equation (see Section 6.4.6). The M_{mp}^C and M_{mp}^A curves were roughly proportional to the M_{mp}^S curve. The M_{mp}^B curve had initially the same tendency as the M_{mp}^A curve, but, eventually, the saturation index of RPB became lower than 1, the reaction rate became negative, and part of the previously formed RPB was dissolved.

The evolution curves of the Ca/Si and R/Si molar ratios of the mixed reaction product (RPA and RPB) are given in Fig. 7.19f. The values obtained are similar to those measured by means of SEM/EDS analysis on reaction products in HCP-SL glass specimens (Table 3.7). Note that Ca/Si slightly increased with time as RPB was dissolved. In the terms discussed in Section 6.2, the mixed reaction product obtained can be characterized as a high-calcium product.

The evolution of the volume fractions of RPA and RPB is given as an area graph in Fig. 7.20a. The negative values of the bottom curve indicate the volume of dissolved SL glass. In the detail view of this graph, the initial volume of the interface ($\mathcal{U}_{mp}^o = 1 \times 10^{-6}$ m^3/m^2) can be appreciated. This initial volume was progressively increased due to the dissolution of SL glass and the cracking aperture (a_n^{cr}), as it results from Eq. 6.25. The SL glass dissolution started at day 0, but the crack aperture occurred only once the internal pressure (σ_g) developed by the RPA and RPB formed within the interface overcame its initial tensile strength (χ_o). This can be clearly visualized in Fig. 7.20b, where the evolution of the normal stress (σ_n), the internal pressure exerted by the reaction products (σ_g), and the work spent in fracture processes (W^{cr}/G_f^I) are plotted together. Until day 0.37, the volume of the unstressed RPA and RPB remained smaller than the total volume of the interface, i.e. $\mathcal{U}_{mp}^{cp} > 0$, and therefore no stress was developed. Between day 0.37 and day 0.85, σ_g and the equilibrating σ_n grew rapidly until reaching the initial tensile strength ($\chi_o = 1.5$ MPa). At this point, the fracturing process started ($a_n^{cr} > 0$ and $W^{cr} > 0$) and the total porosity had its minimum (Fig. 7.19e). As the tensile strength of the interface decreased due to the contraction of the fracture surface (see Section 6.5.2.1), the reaction products decompressed and the total porosity grew back tending to the unstressed gel porosity of the mixed reaction product as σ_g tended to 0.

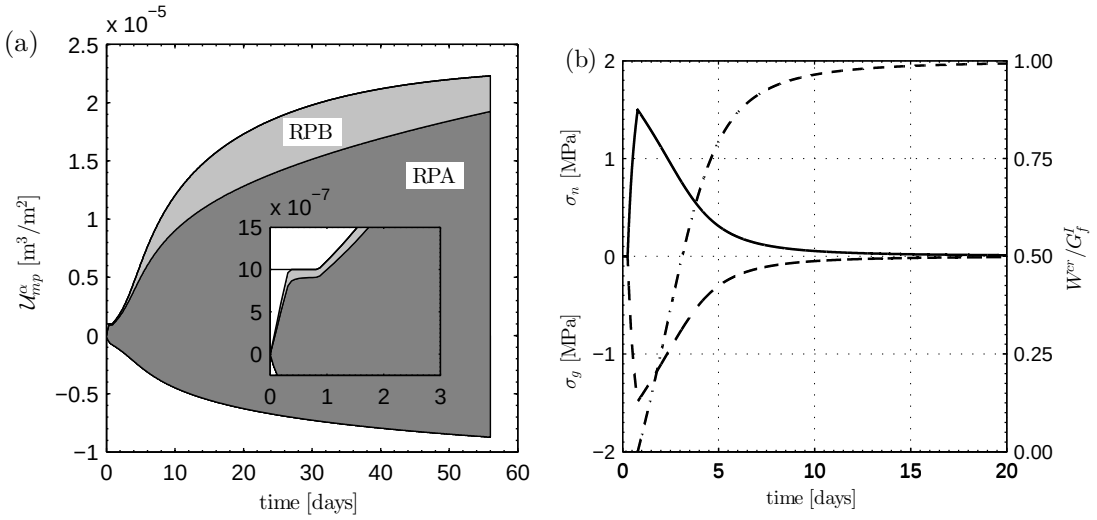

FIGURE 7.20: Modelling of Interfacial Expansion Tests. (a) Evolution of the volume fraction of reaction products. (b) Evolution of the normal stress (σ_n, continuous line), the internal pressure exerted by the reaction products (σ_g, dashed line), and the work spent in fracture processes (W^{cr}/G_f^I, dot-dashed line).

On the role of water transport

The interfacial expansion curves of series F indicate that as the degree of lateral sealing was increased, the expansion rate decreased. It has been argued (Section 3.8.5) that this effect may be attributed to the restriction imposed to the access of alkali and/or water from the alkaline bath into the reaction site. However, since the present modelling framework does not consider the mass balance of water explicitly (see Sections 5.2.2.4 and 6.3.3), the second of those effects, i.e. the potential influence of (the lack of) water availability on the kinetics of the ASR expansions cannot be represented directly. This simplification does not seem to affect the ability of the model to reproduce the experimental expansion curves, as it can be appreciated in Fig. 7.13. Nonetheless, the fact that two of the fitted parameters had to be given values a little out of the expected range of values might be the consequence of this simplification. Indeed, the value of the initial concentration of alkalis ($c^r = 600$ mol/m^3) required to fit the experimental expansion curves turns out a little low for HCP with an alkali content of 1.1 wt% of Na_2O_e. Based on experimental correlations reported in the literature [55, 133] of alkalis in the unhydrated cement and alkalis in pore solution of HCP, the initial concentration of alkalis in pore solution is estimated to had been close to 1000 mol/m^3. Also, the exponent of the activity of the hydroxyl ions in the kinetic law of SL glass dissolution (Eq. (6.31)) was adopted $p = 3$, when the available experimental data indicates that $p \approx 0.2$ [141]. Note that both, reducing the initial concentration of alkalis and increasing the effect of the activity of hydroxyl ions on the SL glass dissolution rate, have the net effect of increasing the influence of the alkalis coming from the exposure baths on the

expansion rate. Clearly, further analyses are needed in order to elucidate the role played by water transport on the kinetics of the interfacial expansion curves.

7.5 One-aggregate specimen

In this section, the complete version of the model is used to simulate an ideal case consisting of one circular SL glass aggregate with a pre-existing crack which is embedded in a square matrix of mortar. This case is intended to reproduce all the features of the ASR expansion mechanism proposed in Section 6.2, and do it with the simplest possible model geometry in order facilitate the interpretation of the results. These simulations are conceived as a necessary first step before addressing more realistic cases with several SL glass particles.

The mortar in this example is assumed to be the same as the mortar surrounding the SL glass particles in the reactive specimens used for the Confined Expansion Tests presented in Chapter 4. Moreover, whenever possible, the same model parameters calibrated for the simulations of Interfacial Expansion Tests in the previous section have been also used in this case.

The set of simulations performed includes five different mechanical boundary conditions: (i) without mechanical restraint (free expansion), (ii) compressive loading in the vertical direction, (iii) compressive loading in both vertical and horizontal direction, (iv) prevented length change in the vertical direction, and (v) prevented length changes in both the vertical and horizontal directions. Additionally, a number of simulations were performed under free expansion conditions for different configurations of the pre-existing crack.

7.5.1 Model description

The model geometry is schematically represented in Fig. 7.21a. The dimensions are all given in relative terms to the side length L of the specimen. This geometry consists of a circular SL glass aggregate embedded at the centre of a square matrix of mortar. In addition, a stiff loading plate is placed on each side of the specimen in order to prescribe suitable boundary conditions for the mechanical analyses. The model was discretized by means of 1112 quadratic triangular elements and 268 zero-thickness interface elements (Fig. 7.21b), giving a total of 2876 nodes. The locations of the interface elements are indicated with thick lines in Fig. 7.21b. These interface elements are intended to simulate five different types of discontinuities: (1) cracks inside the SL glass particle (glass-glass

interface), (2) cracks within the mortar matrix (mortar-mortar interface), (3) SL glass-mortar interface, (4) pre-existing cracks inside the SL glass particle, and (5) 'frictionless contacts' between the loading plates and the mortar specimen.

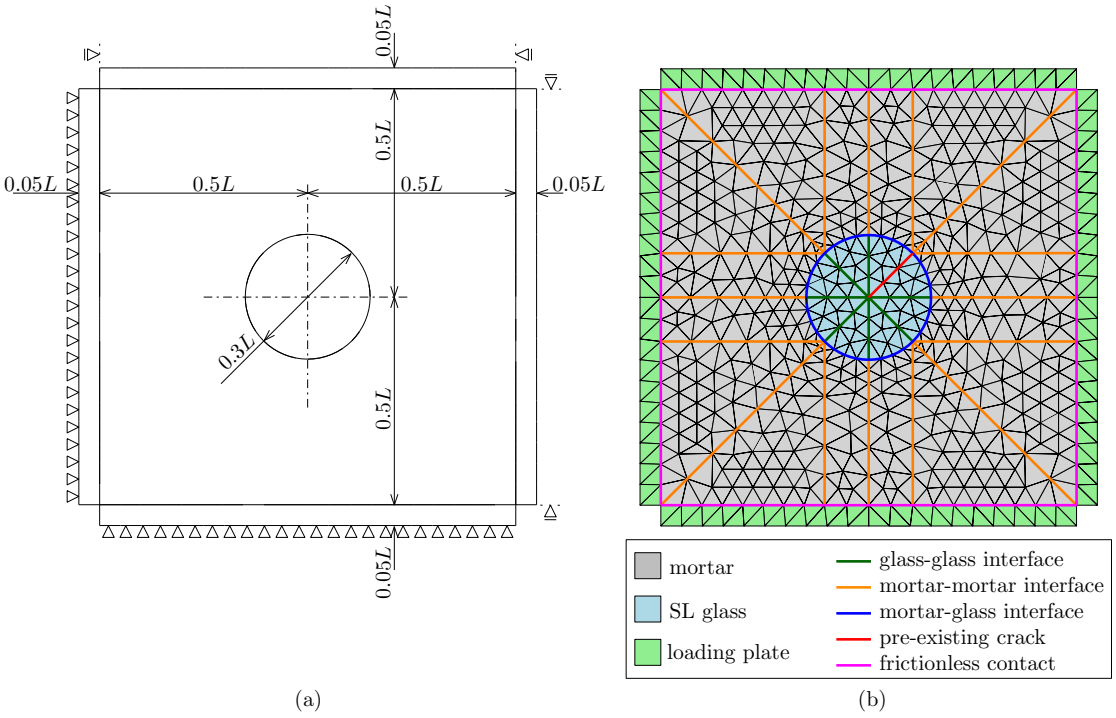

FIGURE 7.21: Modelling of a one-aggregate specimen. (a) Model geometry and boundary conditions for the 'free expansion' case. (b) Finite Element mesh. Thick lines indicate zero-thickness interface elements.

The interface elements representing the frictionless contacts between the loading plates and the specimen were equipped with a linear elastic mechanical constitutive law, with high normal stiffness and very low tangential stiffness. For the rest of the interface elements, the mechanical elasto-plastic constitutive law for interface elements described in Section 6.5.2.1 was considered. Part of the parameters used for this constitutive law are given in Table 7.4 for each type of discontinuity. The rest of the parameters were the same for all types: $G_f^{IIa} = 10 \times G_f^I$, $\tan\varphi_r = \tan\varphi_o$, $\sigma_{dil} = 40$ MPa, $\alpha_a = \alpha_\varphi = \alpha_{\sigma_{dil}} = \alpha_{c_{dil}} = 0$. The continuum elements were assumed to be linear elastic, with elastic modulus E and Poisson's coefficient ν given in Table 7.5.

The value of the specific fracture energy in mode I for the glass-glass interface elements was adopted based on values reported in the literature ranging between 2 and 3.8 J/m^2 [134, 218]. In order to make easier the convergence of the numerical calculations, the brittleness of SL glass was reduced by adopting a rather low value of initial tensile strength for the glass-glass elements (values reported in the literature range between 19 and 180 MPa [139, 216]). The values taken for the elastic modulus and Poisson's coefficient of bulk SL glass were adopted based on values reported in the literature [139, 216].

The values of initial tensile strength and specific fracture energy in mode I of the mortar-mortar interface elements and the elastic modulus of mortar were fixed on the basis of the values reported in Table 4.5 for control concrete, taking into consideration the different mixture proportions and the particle size distribution of the limestone aggregates. The values of initial tensile strength and specific fracture energy in mode I of the mortar-glass interface elements were assumed to be one half of their respective values adopted for the mortar-mortar interface elements, based on previous simulations of concrete at the meso-scale with the mechanical model [e.g. 98, 136, 137]. The parameters adopted for the interface elements representing the pre-existing cracks guarantee that they offer very low (practically zero) resistance to normal opening, very high stiffness upon closure, and a (practically) purely frictional behaviour under tangential relative displacements in compression.

TABLE 7.4: Modelling of a one-aggregate specimen. Parameters of the interface elements.

Material	$\mathcal{U}^o_{mp}$ [m^3/m^2]	$\mathcal{S}^o_{mp}$ [m^2/m^2]	K_n [MN/m]	K_l [MN/m]	χ_o [MPa]	c_o [MPa]	$\tan\varphi_o$	G^I_f [J/m^2]
glass-glass	0	1	1E+9	1E+9	3	6	0.7	2.5
mortar-mortar	0	1	1E+9	1E+9	3	6	0.7	10
mortar-glass	1E−6	0.7	1E+9	1E+9	1.5	3	0.7	5
pre-existing crack	1E−6	1	1E+9	1E+9	1E−2	1.5E−2	0.7	500
frictionless contact	0	n/a	1E+9	1	n/a	n/a	n/a	n/a

TABLE 7.5: Modelling of a one-aggregate specimen. Parameters of the continuum elements.

Material	E [GPa]	ν	ϕ	D^s [m^2/h]	D^c [m^2/h]	D^r [m^2/h]
mortar	35	0.2	0.24	1.35E−8	8.97E−9	1.51E−9
SL glass	70	0.2	0	0	0	0
loading plate	1E+9	0	0	0	0	0

For the diffusion problem, the boundaries were considered to be impervious, i.e. no fixed concentration nor diffusive flux were imposed to the problem. The initial concentrations of primary aqueous species in pore solution were assumed to be the same as the ones adopted for the simulation of Interfacial Expansion Tests (Section 7.4): $c^s = 0$, $c^c = 0.08354$ mol/m^3, $c^r = 600$ mol/m^3.

The effective diffusivities (D^β) and the total porosity (ϕ) considered for the continuum elements are given in Table 7.5. The SL glass and the loading plates were assumed to be non-porous and impervious. The porosity of the mortar was estimated on the basis of its mix composition. To do so, first the mortar mix composition was obtained from the overall mix composition of the SL glass concrete given in Section 4.3.1, resulting in a water-to-cement ratio of 0.45 and a volume fraction of aggregates of 0.43. Second, the pore fractions of the bulk HCP were estimated with the same procedure described

in Section 7.4.1, assuming the oxide composition of cement PC03 given in Table A.1 (Appendix A.1), and a maturity factor of 1.00, resulting in a capillary porosity of 0.204 and a total porosity of 0.408. Third, the volume of ITZ was estimated considering the limestone aggregates as spherical particles with an average diameter of aggregates of 1.4 mm, surrounded by a layer of ITZ with constant width of 20 μm. Then, it was assumed that the pore fractions in this volume of ITZs were 50% greater than in the bulk HCP. Finally, the limestone particles were assumed to be non-porous.

The effective diffusivities in the mortar were estimated with the procedure described in Section 6.4.9.1, with the volume capillary porosity of bulk HCP and the volume fraction of aggregates indicated in the previous paragraph ($\phi^{cp} = 0.204$, $V_a = 0.43$), and assuming the following parameters: $D_s^\beta / D_w^\beta = 5 \times 10^{-5}$, $n = 2.7$, $\phi^{per} = 0.18$, $\varepsilon = 0.029$, and $D_i / D_p = 5.85$. The diffusivities in bulk water (D_w^β) at 60 °C are given in Table 6.2. For the aqueous alkalis, the diffusivity of Na^+ was adopted.

For the interface elements representing frictionless constants the diffusivities were assumed constant, with small values in the longitudinal direction ($D_l^\beta / D_w^\beta = 1 \times 10^{-10}$) and very high values in the transversal direction ($D_n^\beta / D_w^\beta = 1 \times 10^6$ m^{-1}). For the rest of the interface elements, the longitudinal and transversal diffusivities evolved according to the evolution law proposed in Section 6.4.9.2. In all cases the parameter values $w^{crit} = 1 \times 10^{-4}$ m and $D_1^\beta / D_w^\beta = 10$ were used. For the mortar-glass interface elements $D_{ITZ}^\beta / D_w^\beta = 7.64 \times 10^{-3}$ and $w_{ITZ} = 2 \times 10^{-5}$ m were adopted. For the other interface elements, $w_{ITZ} = 0$ and, consequently, $D_{ITZ}^\beta / D_w^\beta = 0$. The initial volume of the interface elements ($\mathcal{U}_{mp}^o$) and the corresponding initial surface area of dissolution fronts ($\mathcal{S}_{mp}^o$) are given in Table 7.4. The value taken for the fitting parameter of the reduction factor f_2^S (Eq. 6.38) was $A^S = 13$ m^2/mol for mortar-glass interfaces and $A^S = 6.5$ m^2/mol for glass-glass interfaces.

The remaining parameters, namely η_o^α, ϕ_o^α, k_η, σ_{th}^α, K_{sp}^α, k_f^α, k_d^α, k_η, the shape parameters k and p of functions f_ϕ^α, and the exponent of the hydroxyl ions activity in the kinetic law of SL glass dissolution, were the same as used for simulating Interface Expansion Tests in the previous section.

As mentioned above, five different boundary conditions were considered for the mechanical problem: (i) without mechanical restraint (free expansion) (Fig. 7.21a), (ii) compressive loading in the vertical direction (Fig. 7.22a), (iii) compressive loading in both vertical and horizontal direction (Fig. 7.22b), (iv) zero length change in the vertical direction (Fig. 7.23a), and (v) zero length changes in both the vertical and horizontal directions (Fig. 7.23b). Note that the combination of very stiff loading plates, frictionless contacts, and the imposed boundary conditions guarantees that the sides of the

specimen do not bend nor rotate due to the applied loads and/or the development of internal pressures.

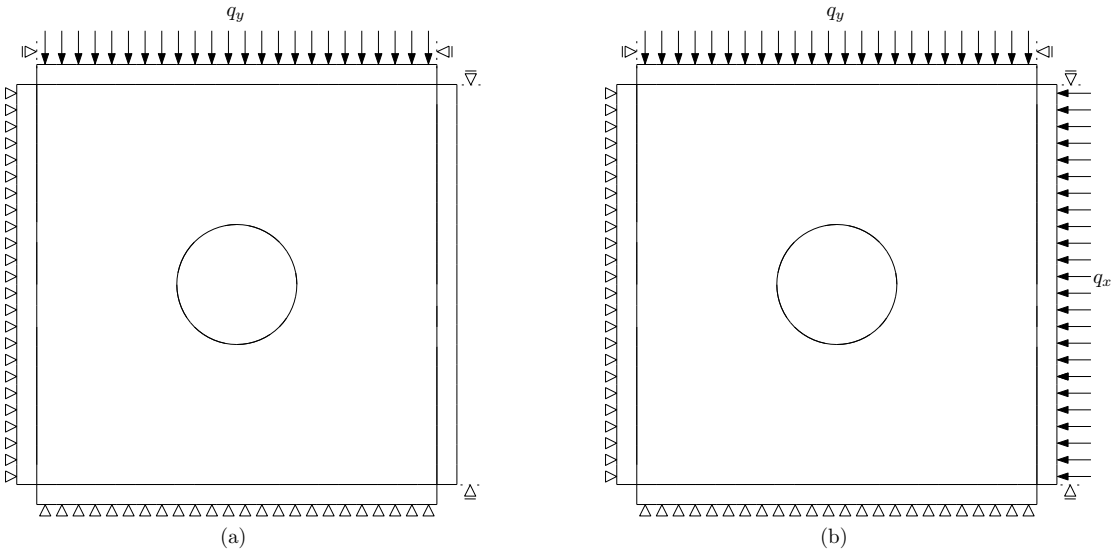

FIGURE 7.22: Modelling of a one-aggregate specimen. Mechanical boundary conditions for simulating ASR expansions (a) under vertical compression and (b) under vertical and horizontal compression.

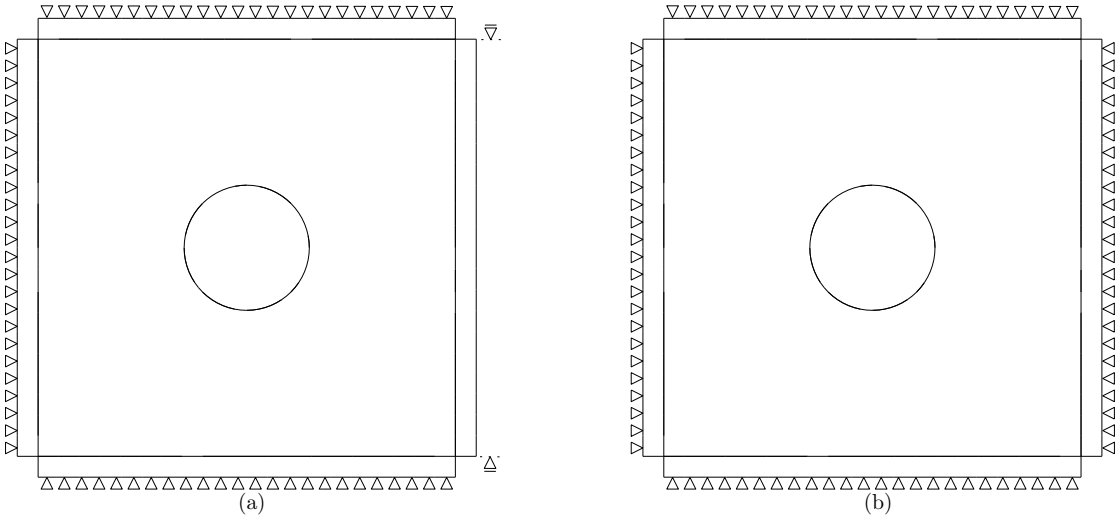

FIGURE 7.23: Modelling of a one-aggregate specimen.Mechanical boundary conditions for simulating ASR expansions with (a) zero length change in the vertical direction, and (b) zero length changes in both the vertical and horizontal directions.

The time discretization of the staggered scheme consisted in time steps of 3 h. Each of these steps was further subdivided in 12 and 50 equal increments in `DRACFLOW` and `DRAC`, respectively. For the cases with external loading, the q_x and/or q_y were applied in one additional step at the beginning of the simulations, in which the time increments in `DRACFLOW` were null. In that way, the external loading of the specimens may be regarded as 'instantaneous'.

7.5.2 Modelling results

7.5.2.1 Free expansion

Let us first consider the case with the mechanical boundary conditions given in Fig. 7.21a. Under these conditions, the upper and right loading plates are allowed to move freely in the vertical and horizontal directions, respectively, and, therefore, these conditions are referred to as 'free expansion conditions'.

The axial expansion curve obtained is given Fig. 7.24 in terms of the homogenized strain u_x/L, where u_x [m] is the length change in the horizontal direction and $L = 10$ mm is the side length of the mortar square. Note that, in this case, the model has a symmetry axis in the direction of the pre-existing crack, and, consequently, the expansions in the horizontal and vertical directions were the same. The points marked on the expansion curve (Fig. 7.24) indicate significant moments on the development of the ASR expansion, namely:

(A) The mortar-glass interface elements surrounding the circular aggregate started to crack.

(B) The pre-existing crack started to propagate into the mortar.

(C) The pre-existing crack started to propagate within the SL glass.

(D) Cracks started to grow from the mortar-glass interface into the mortar in direction to the left side, the bottom side, and left-bottom corner of the specimen.

(E) The cracking process reached the top-right corner of the specimen.

(F) The cracking process reached the left and bottom sides of the specimen.

For each of these moments, the deformed geometry, the spatial distribution of the reaction products ($\mathcal{U}^A_{mp} + \mathcal{U}^B_{mp}$), the Ca/Si molar ratio of the mixed reaction products, the internal pressure (σ_g), and the work spent in fracture processes (W^{cr}/G^I_f) are given in Figs. 7.25–7.29.

Between the beginning of the simulation and day 0.875 (point A on the expansion curve in Fig. 7.24), practically no expansion was developed. During this time, the reaction products formed in the mortar-glass interface elements progressively filled the available initial volume ($\mathcal{U}^o_{mp}$), eventually exerting a growing internal pressure (σ_g) once the initial volume was exhausted (Figs. 7.26 and 7.28). Point A coincides with the moment in which σ_g reached a value slightly over the initial tensile strength ($\chi_o = 1.5$ MPa) of the

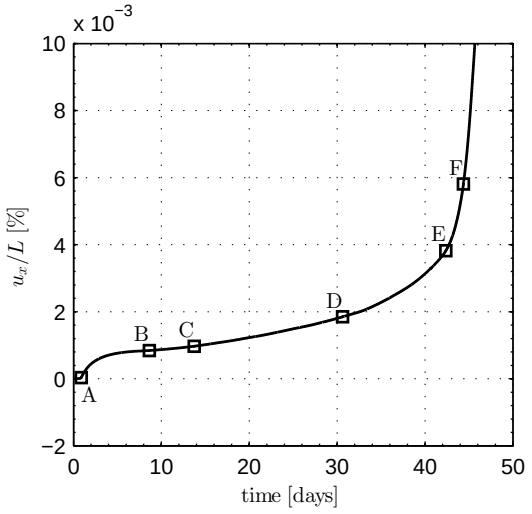

FIGURE 7.24: Modelling of a one-aggregate specimen in free expansion conditions. Axial strain in the horizontal direction. The points marked on the curve correspond to significant moments of the ASR expansion. Note: L=10 mm.

mortar-glass interface elements and the cracking process started (Fig. 7.28). Note that the cracking of the mortar-glass interface took practically the same time as the cracking of the HCP-glass interface in the simulation of Interfacial Expansion Tests (Section 7.4). Simultaneously, reaction products were also formed within the pre-existing crack but without exhausting its initial volume, i.e. without exerting any internal pressure. The profiles of Ca/Si molar ratio (Fig. 7.27) indicate that the reaction products at the mortar-glass interface were mainly RPA and that the reaction products within the pre-existing crack were mainly RPB.

After point A, reaction products continued to be formed both at the mortar-glass interface and within the pre-existing crack (Fig. 7.26). As the normal cracking aperture (a_n^{cr}) of the mortar-glass interface elements grew, the reactive stress exerted by the mortar matrix increased, and the local rate of formation of reaction products decreased due to a mechanism similar to the one described in Section 7.3.3. Eventually, the formation of reaction products at the mortar-glass interface elements stopped altogether at day 5.5, when σ_g became equal to the threshold stress of the mixed reaction product (σ_{th}).[3] Meanwhile, the formation of reaction products within the pre-existing crack continued (Figs. 7.26 and 7.27), exhausting the initial volume at day 2, and from there on exerting a growing internal pressure that eventually propagated the pre-existing crack both into the glass aggregate and into the mortar (Fig. 7.28). The crack propagation into the mortar occurred first (point B), because the previous formation of reaction products at the mortar-glass interface had tensioned the mortar but compressed the glass. The

[3]Even though the reaction products at the mortar-glass interface were mainly RPA, some RPB was also formed. Therefore, according to Eq. (6.22), σ_{th} at this location was (slightly) below $\tilde{\sigma}_{th}^{A} = -3$ MPa.

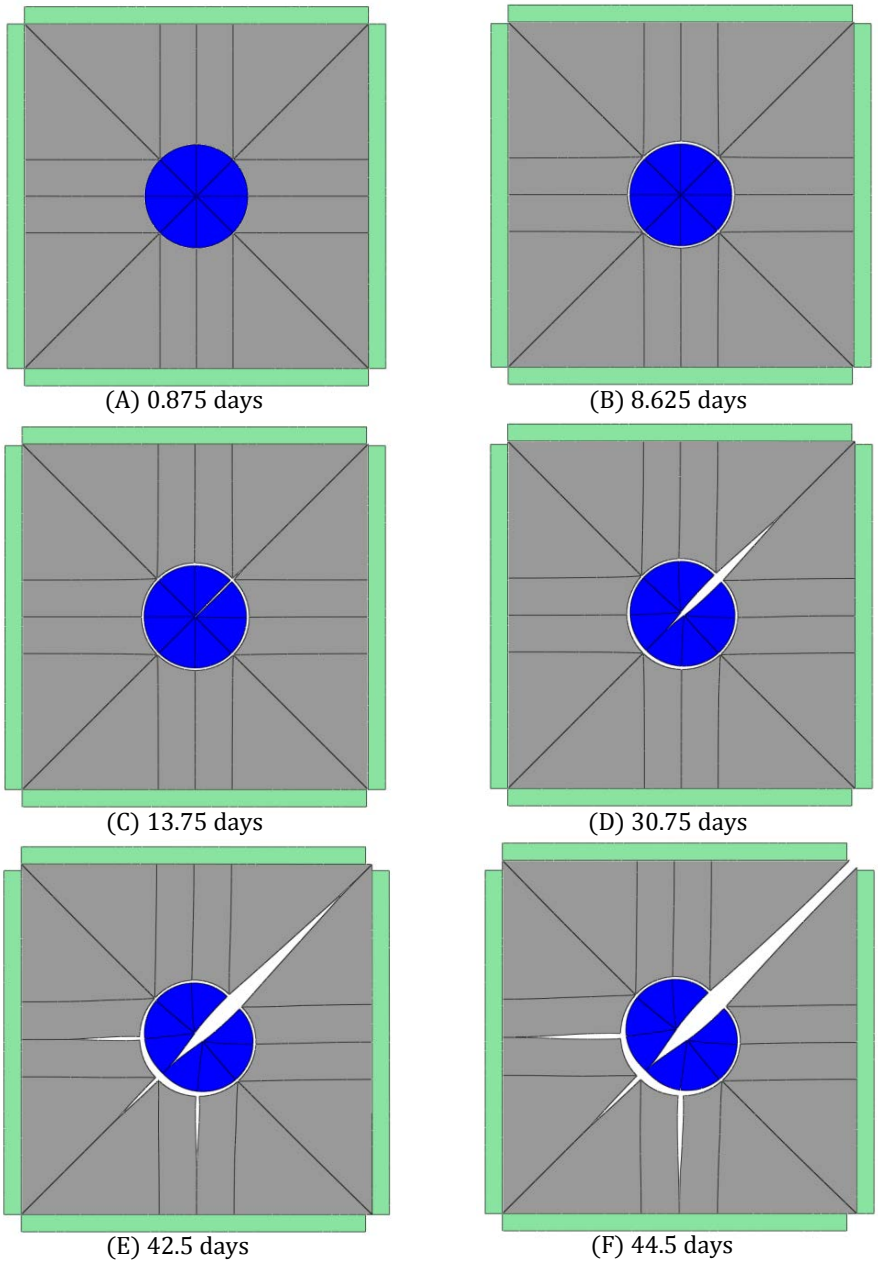

FIGURE 7.25: Modelling of a one-aggregate specimen in free expansion conditions. Deformed geometry (×500) at different times.

propagation into the SL glass occurred five days later at day 13.75 (point C). The resulting cracking apertures gave the mortar-mortar and glass-glass interface elements a volume of pore solution ($\mathcal{U}_{mp}^{ps} > 0$), enabling in that way the dissolution of portlandite in mortar-mortar interfaces, the dissolution of SL glass in glass-glass interfaces, and the formation of RPA and RPB in both types of interfaces.

It can be seen in Fig. 7.28 that from day 13.75 (point C) until the end of the simulation, there was a progressive increase of σ_g at the mortar-glass interface elements at both sides of the pre-existing crack, reaching values over σ_{th}. This increase of σ_g occurred

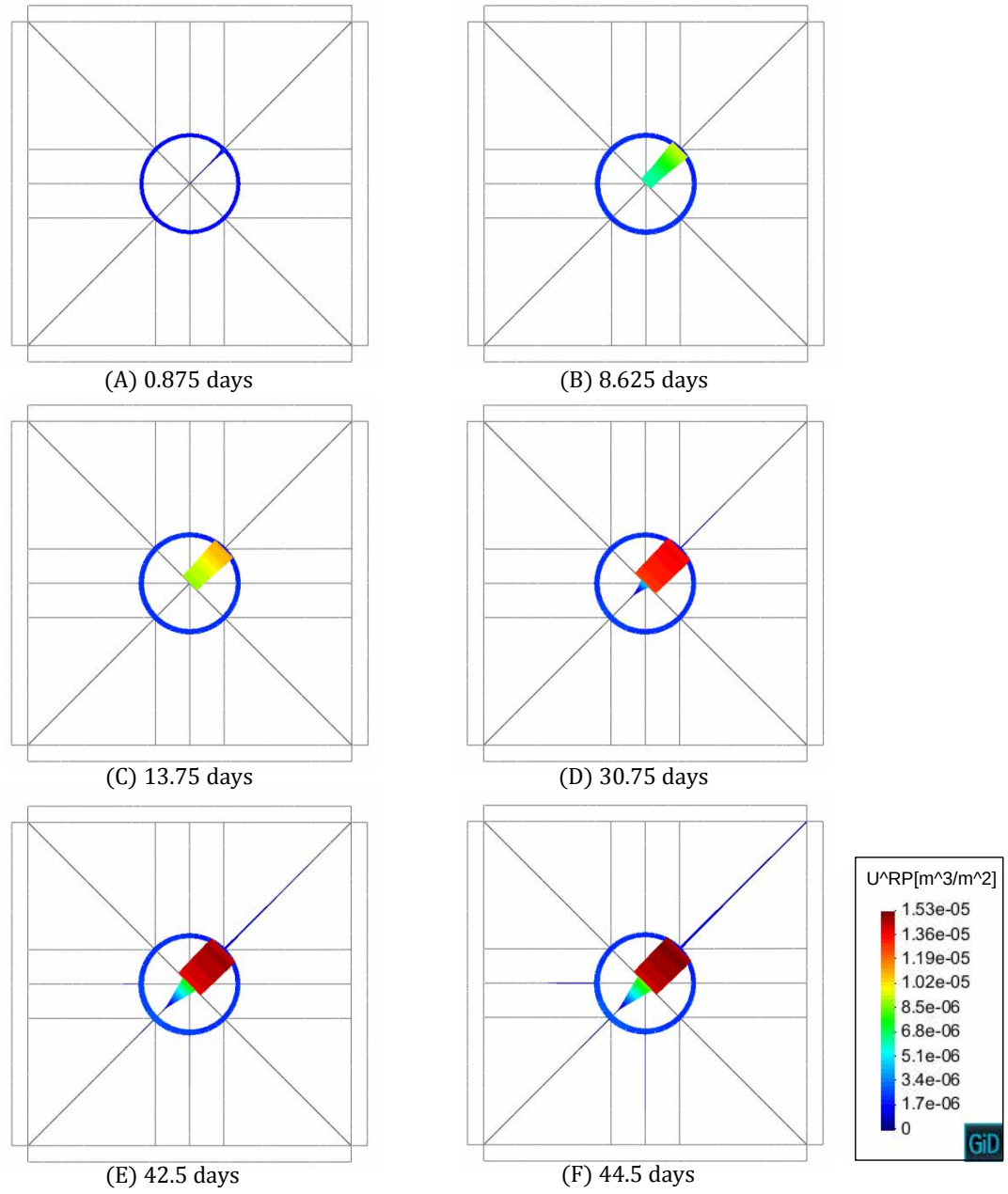

FIGURE 7.26: Modelling of a one-aggregate specimen in free expansion conditions. Volume of reaction products ($\mathcal{U}^A_{mp} + \mathcal{U}^B_{mp}$) along interface elements at different times.

as a consequence of the compression of the previously formed reaction products, via reduction of the normal cracking aperture ($da^{cr}_n/dt < 0$), and not to the formation of an additional amount of reaction products. The reduction of the crack aperture at the mortar-glass interface was the result of the propagation of the pre-existing crack in the framework of the kinematic restrictions imposed by the loading plates. Because of the same reasons, the normal stress (σ_n) of the mortar-mortar interfaces at the left-bottom quadrant of the specimen progressively increased as the pre-existing crack propagated. At day 30.75 (point D), σ_n reached in these locations the initial tensile strength of the mortar-mortar interfaces ($\chi_o = 3$ MPa), giving rise to three new cracks growing radially

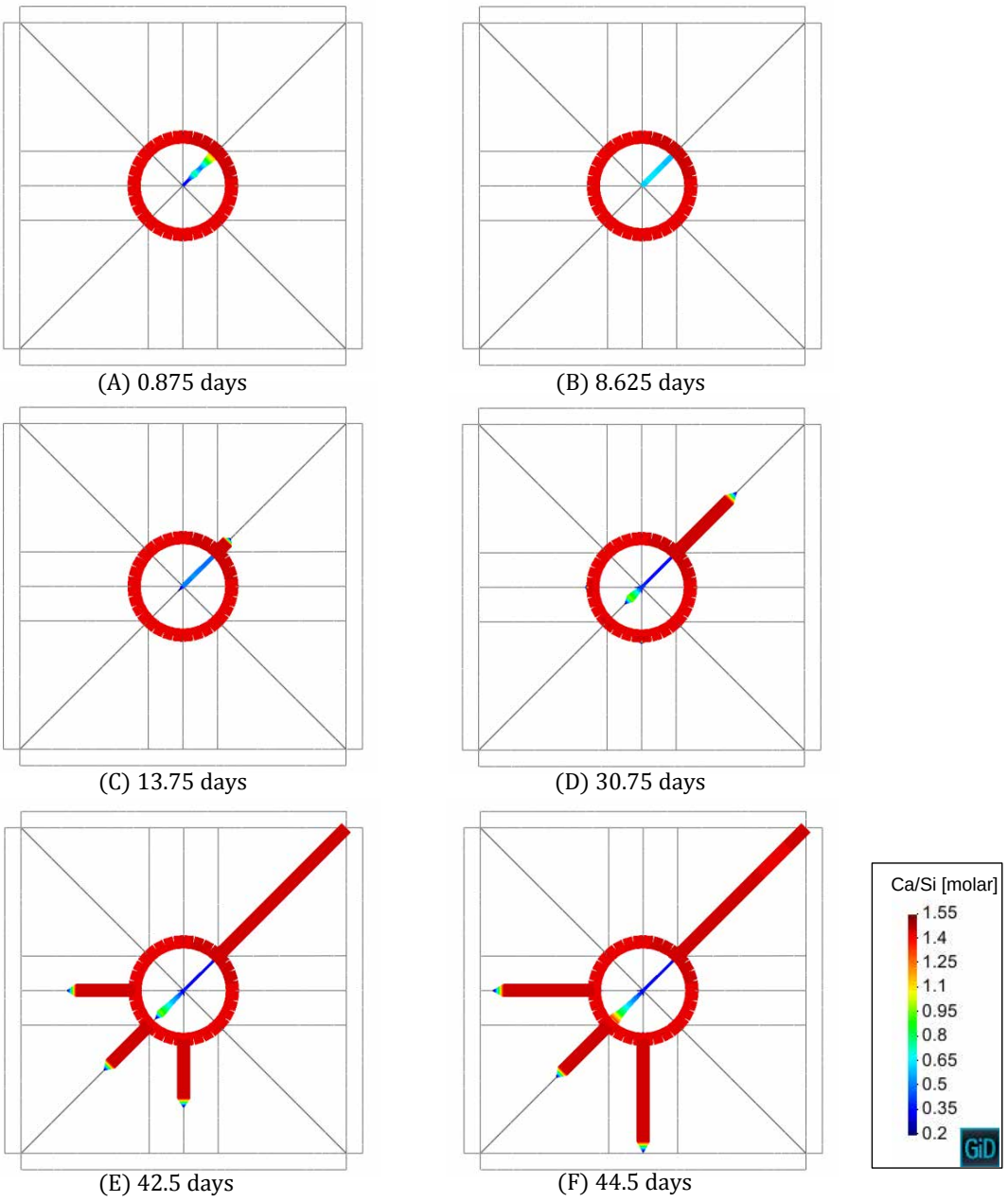

FIGURE 7.27: Modelling of a one-aggregate specimen in free expansion conditions. Ca/Si molar ratio of the mixed reaction products (RPA and RPB) at different times.

from the SL glass aggregate (Fig. 7.29). Again, the cracking aperture of mortar-mortar elements enabled the dissolution of portlandite and the formation of RPA and RPB.

From day 30.75 until the end of the simulation, the propagation of the cracks previously initiated continued, in some cases reaching the borders of the specimen (points E and F). The sudden rise of the expansion rate after point E (Fig. 7.24) indicates the configuration of a failure mechanism (separation of the right-bottom part of the specimen) that eventually led to the end of the simulation due to lack of convergence of the numerical solution. Note that in a more realistic concrete specimen with multiple coarse aggregate

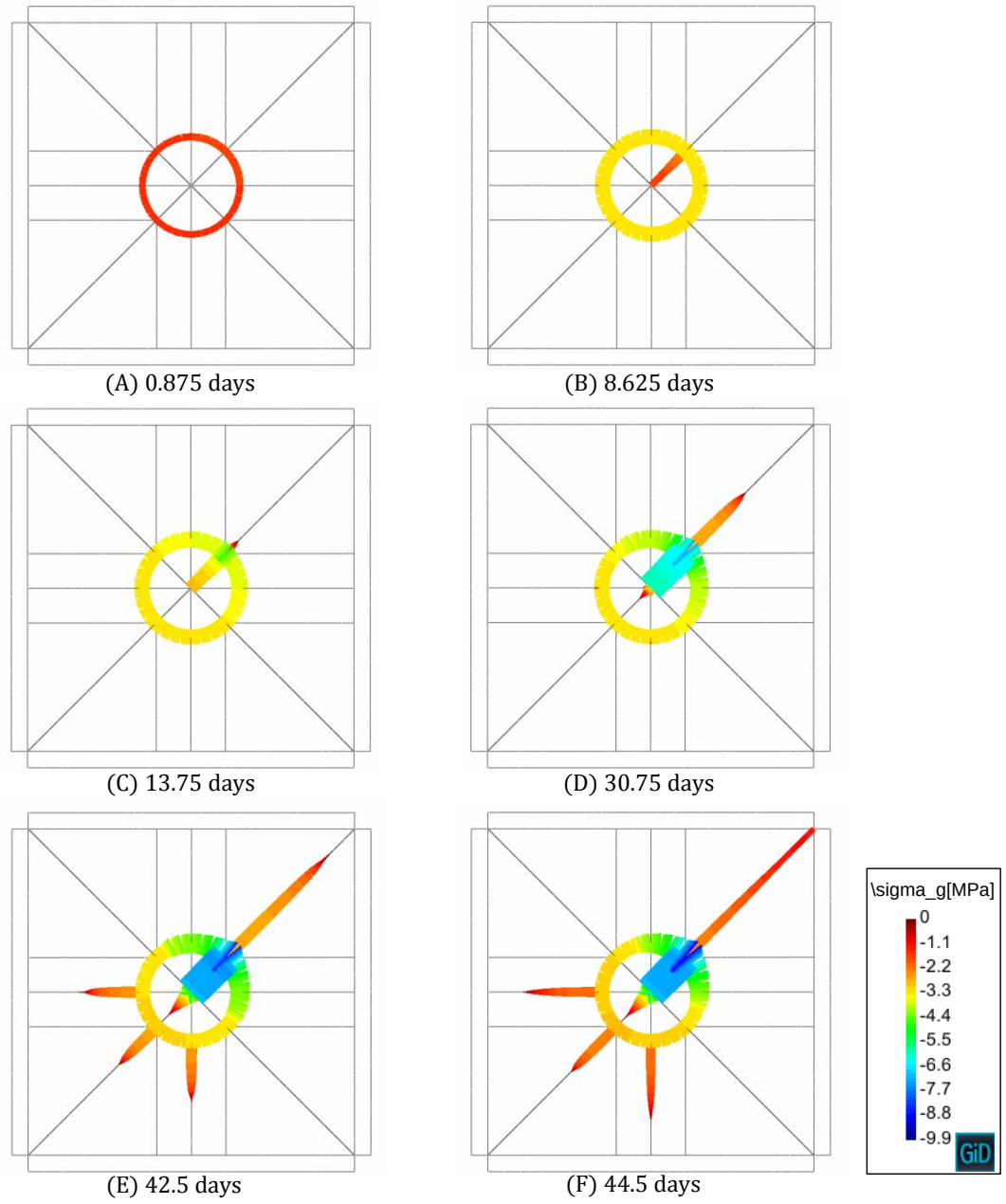

FIGURE 7.28: Modelling of a one-aggregate specimen in free expansion conditions. Internal pressure (σ_g) at different times.

particles this kind of 'brittle' failure mechanism would not have occurred, since the crack propagation would have had to go over more tortuous paths before configuring a failure mechanism. Therefore, the development of ASR strain curves after point E cannot be considered as representative of the behaviour of real SL glass concrete.

On the effect of the pre-existing crack

Some additional cases were simulated in free expansion conditions in order to assess the influence of the pre-existing crack on the ASR expansions. First, three cases were

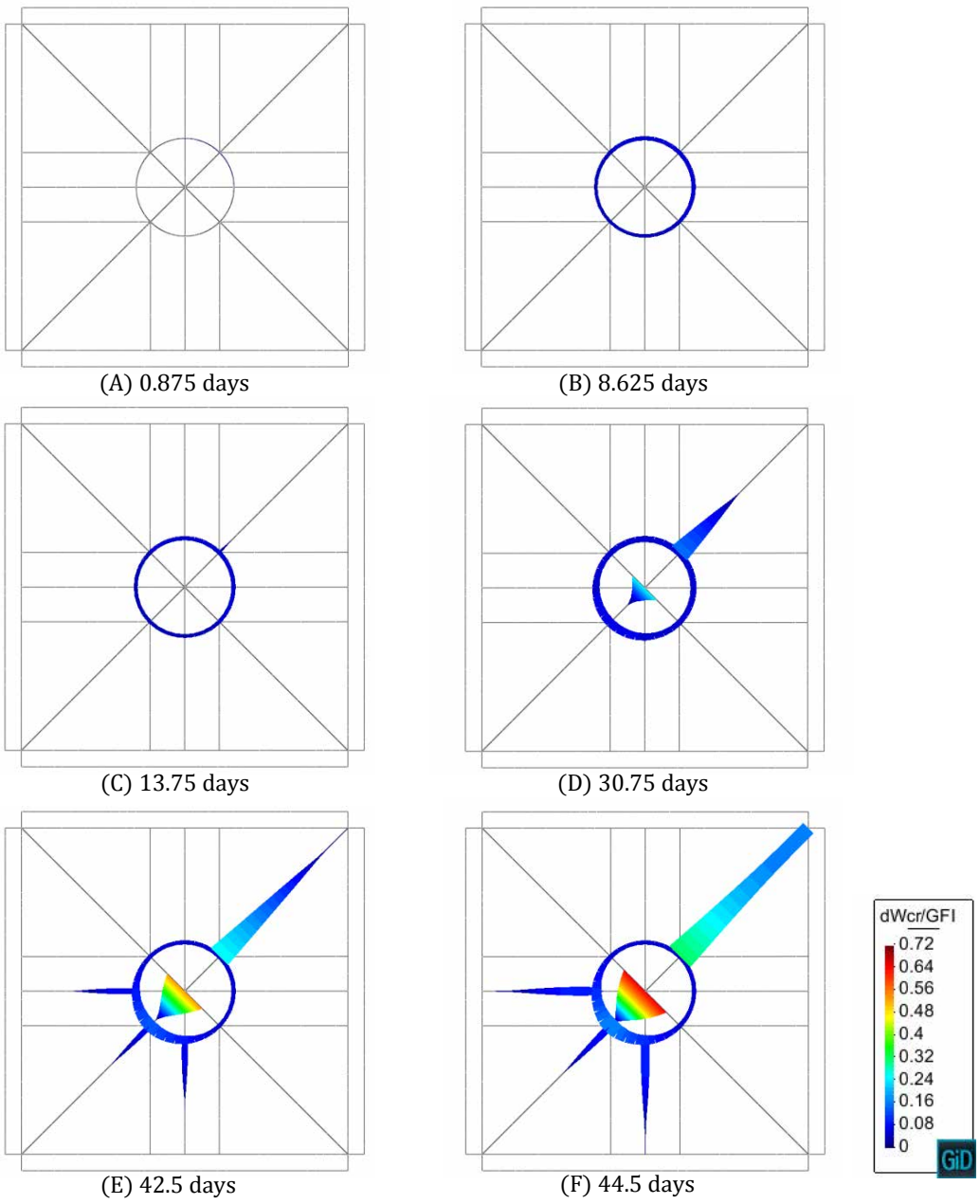

FIGURE 7.29: Modelling of a one-aggregate specimen in free expansion conditions. Work spent in fracture processes (W^{cr}/G_f^I) at different times.

considered in which the length of the pre-existing crack was progressively reduced from the original 1.5 mm to zero. The axial expansion curves obtained are given in Fig. 7.30. It can be observed that as the length of the pre-existing crack was reduced, the rate of expansion decreased, particularly after the moment (approximately at day 10) in which formation of reaction products at the mortar-glass interface was inhibited by the reactive normal stress exerted by the mortar matrix. Indeed, in the case without pre-exiting crack, the axial expansion rate was completely suppressed after this point, and no cracks were developed in the SL glass particle nor in the mortar matrix. Note that this result is qualitatively similar to the experimental results obtained by Maraghechi et

al. [141] using crack-free SL glass beads in Portland cement mortars (Fig. 6.1c), which was discussed in Section 6.2.

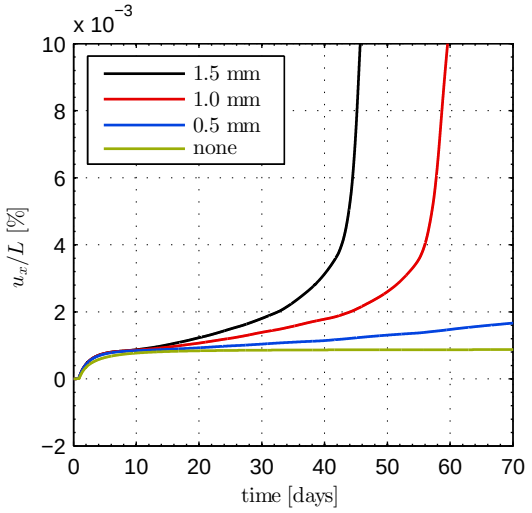

FIGURE 7.30: Modelling of a one-aggregate specimen in free expansion conditions. Axial strain for different values of the pre-existing crack length in the aggregate. The legend indicates the length of the pre-existing crack in each case.

Second, two cases were also simulated in which the direction of the pre-existing crack was changed from 45° with respect to the horizontal direction to 0° and 90°. The axial strain curves obtained are given in Fig. 7.31. The first consequence of rotating the pre-existing crack was that the symmetry of the model was lost. Consequently, the axial strains were different in the horizontal and vertical directions. It can be observed that before the moment in which the formation of reaction products at the mortar-glass interface was inhibited (approximately at day 10), the expansion curves of the three cases were very similar. After this point, the case with the pre-existing crack oriented vertically (90°) had a slower expansion rate in the vertical direction and a higher expansion rate in the horizontal direction than the reference case. Inversely, the case with the pre-existing crack oriented horizontally (0°) had a slower expansion rate in the horizontal direction and a higher expansion rate in the vertical direction than the reference case.

7.5.2.2 Expansion under uniaxial and biaxial compression

Let us now consider the mechanical boundary conditions schematically represented in Fig. 7.22a (uniaxial compression) and Fig. 7.22b (biaxial compression). For the first case, a uniform pressure $q_y = 10$ MPa was applied on the top-side loading plate, while the right-side loading plate was allowed to move freely in the horizontal direction. For the second case, uniform pressures $q_x = q_y = 10$ MPa were applied on both the top-side and right-side loading plates.

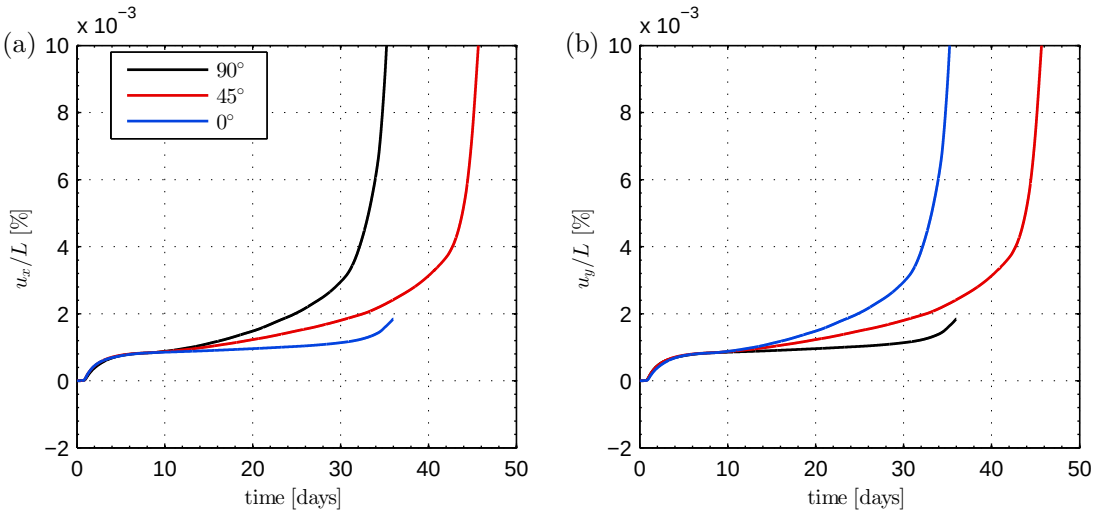

FIGURE 7.31: Modelling of a one-aggregate specimen in free expansion conditions. Axial strain in the (a) horizontal and (b) vertical directions for different orientations of the pre-existing crack in the aggregate. The legend indicates the angle formed by the pre-existing crack with respect to the horizontal direction.

The axial strain curves obtained are given Fig. 7.32, together with the expansion curves of the 'free expansion' case previously discussed ($q_x = q_y = 0$). The axial strain curves are represented in terms of the homogenized strains u_x/L and u_y/L, where u_x and u_y [m] are the length changes of the specimen in the horizontal and vertical directions, and $L = 10$ mm is the side length of the specimen. As already mentioned, the external pressures q_y and/or q_x were applied in one additional step at the beginning of the simulation, in which the time increments in `DRACFLOW` were null, i.e. the application of the q_y and/or q_x may be regarded as instantaneous. Moreover, the initial strains generated by the application of q_y and/or q_x were deducted from the strain curves, in order to facilitate the comparison of the ASR-induced strains obtained under different loading cases. The corresponding volumetric strain curves, considered as the sum of the horizontal and vertical strains, are given in Fig. 7.33. Finally, the deformed geometry and the spatial distributions of the reaction products ($\mathcal{U}^A_{mp} + \mathcal{U}^A_{mp}$), the internal pressure (σ_g), and the work spent in fracture processes (W^{cr}_{mp}/G^I_f), are given for one modelling time (day 34) in Figs. 7.34 and 7.35. The time chosen (day 34), corresponds to the moment just before a crack reached the upper border of the specimen in the uniaxial loading case.

Under uniaxial (vertical) loading, the specimen developed a progressive expansion in the horizontal direction and an associated contraction in the vertical direction (Figs. 7.32a and b). Moreover, the rate of expansion in the horizontal direction was higher than in the free expansion case ($q_x = q_y = 0$). However, the increase in the rate of horizontal expansion was not sufficient to compensate the contraction in the vertical direction, and,

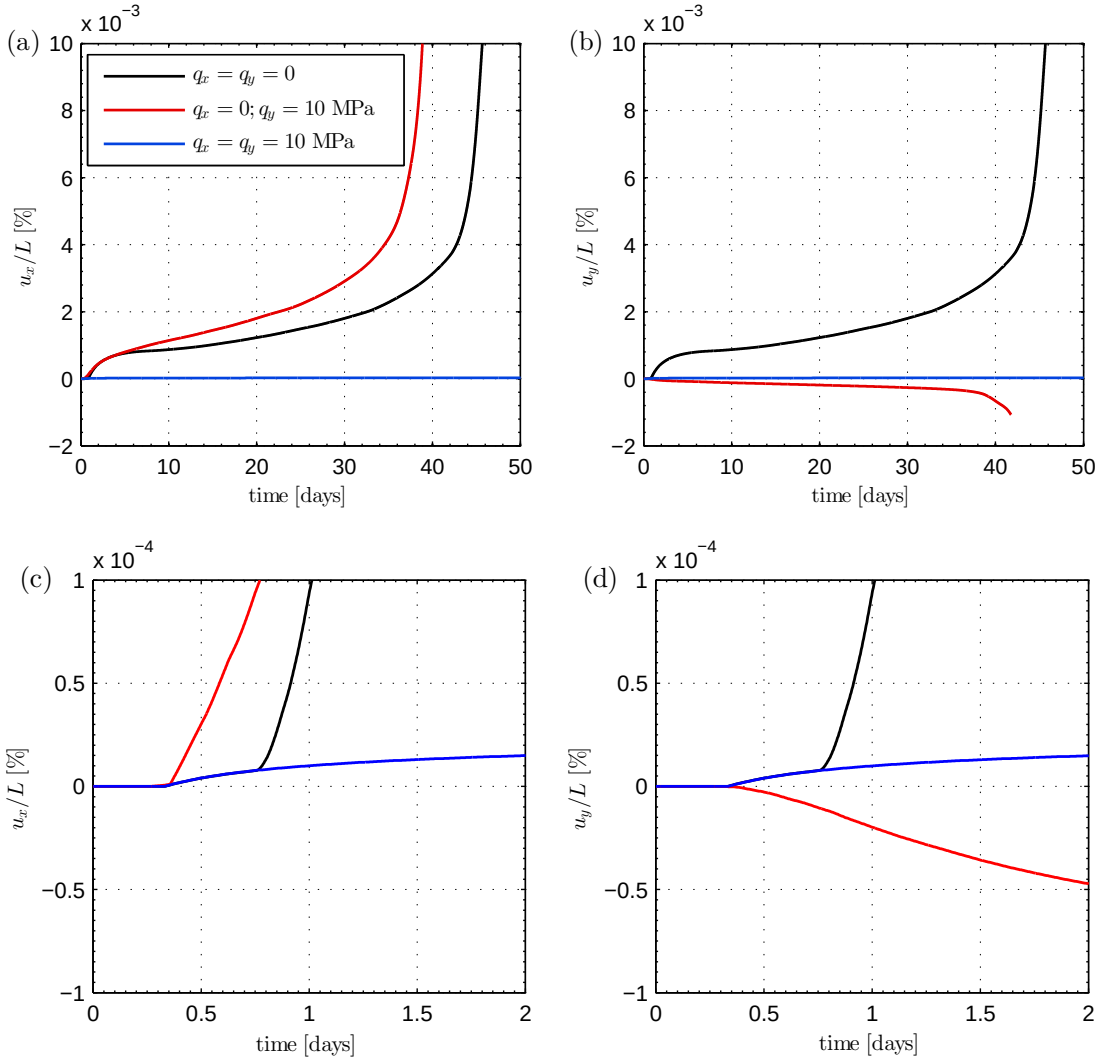

FIGURE 7.32: Modelling of a one-aggregate specimen under horizontal (q_x) and vertical (q_y) uniform external pressure. Axial strains in the (a) horizontal and (b) vertical directions. Plots (c) and (d) are detail views of plots (a) and (b), respectively. The initial strains generated by the application of q_y and/or q_x were deducted from the strain curves.

therefore, the volumetric expansion rate of the uniaxial case before the cracks reached the specimen border (day 34), was lower than in the free expansion case (Fig. 7.33) As in the free expansion case, the sudden rise of the expansion rate in the uniaxial case after day 34 was due to the configuration of a failure mechanism (separation of the right side part of the specimen) when cracks reached the borders of the specimen. The development of ASR strains after this point cannot be considered as representative of the behaviour of real SL glass concrete.

The effect of uniaxial loading on the development of the ASR expansions can be also appreciated in the cracking patterns. While in the free expansion case the cracking pattern was symmetric with the pre-existing crack propagating in the diagonal direction

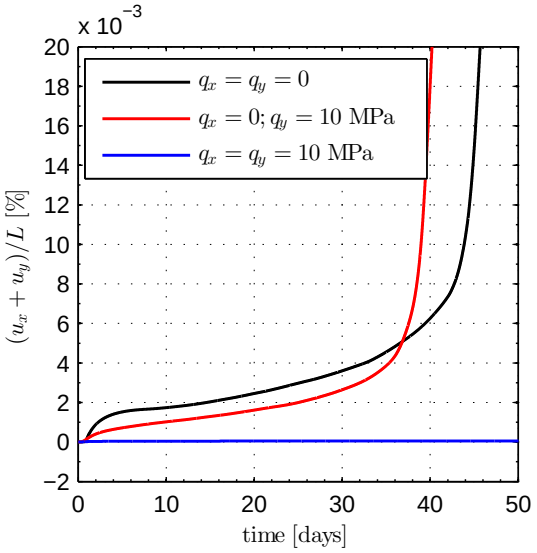

FIGURE 7.33: Modelling of a one-aggregate specimen under horizontal (q_x) and vertical (q_y) uniform external pressure. Time evolution of the volumetric strain.

(Figs. 7.25 and 7.29), in the case of uniaxial loading the propagation of cracks was vertically oriented (Figs. 7.34a and d).

In the biaxial case, the applied loads practically inhibited the ASR expansions (Figs. 7.32a and b). Only very small, symmetrical, strains can be appreciated in the detail views of Figs. 7.32c and d). The inhibition of the ASR expansions is confirmed by the absence of cracks in the specimen after 34 days (Figs. 7.35a and d).

It can be observed in the detail views (Figs. 7.32c and d) that until day 0.33 no strains were developed in none of the three cases. This period of 0.33 days was the time needed by the ASRs to fill the initial volume ($\mathcal{U}^o_{mp}$) of the mortar-glass interfaces. Since $\mathcal{U}^o_{mp}$ does not depend on the stress state and no internal pressure (σ_g) was developed during this period, the stress state had no effect on the development of the ASRs.

From day 0.33 onwards, σ_g at the mortar-glass elements started to grow inducing strains in the mortar specimen, with different characteristics depending on the initial stress state. In the free expansion and biaxial load cases, the expansion curves remained identical until day 0.875, when the expansion rate of the free expansion case suddenly rose as the mortar-glass elements cracked. In the case under biaxial loading, the isotropic compression, which was well over the threshold stress of the calcium-rich reaction product, prevented the cracking of the mortar-glass elements and, consequently, the rate of formation of reaction products asymptotically tended to zero as $\sigma_g \to \sigma_{th}$. It must be noted that the small expansions developed without cracking of the mortar-glass interface in the free expansion and biaxial cases, which are only appreciated in the detail views Figs. 7.32c and d, occurred with the interface elements in elastic regime ($a^{cr}_n = 0$). In

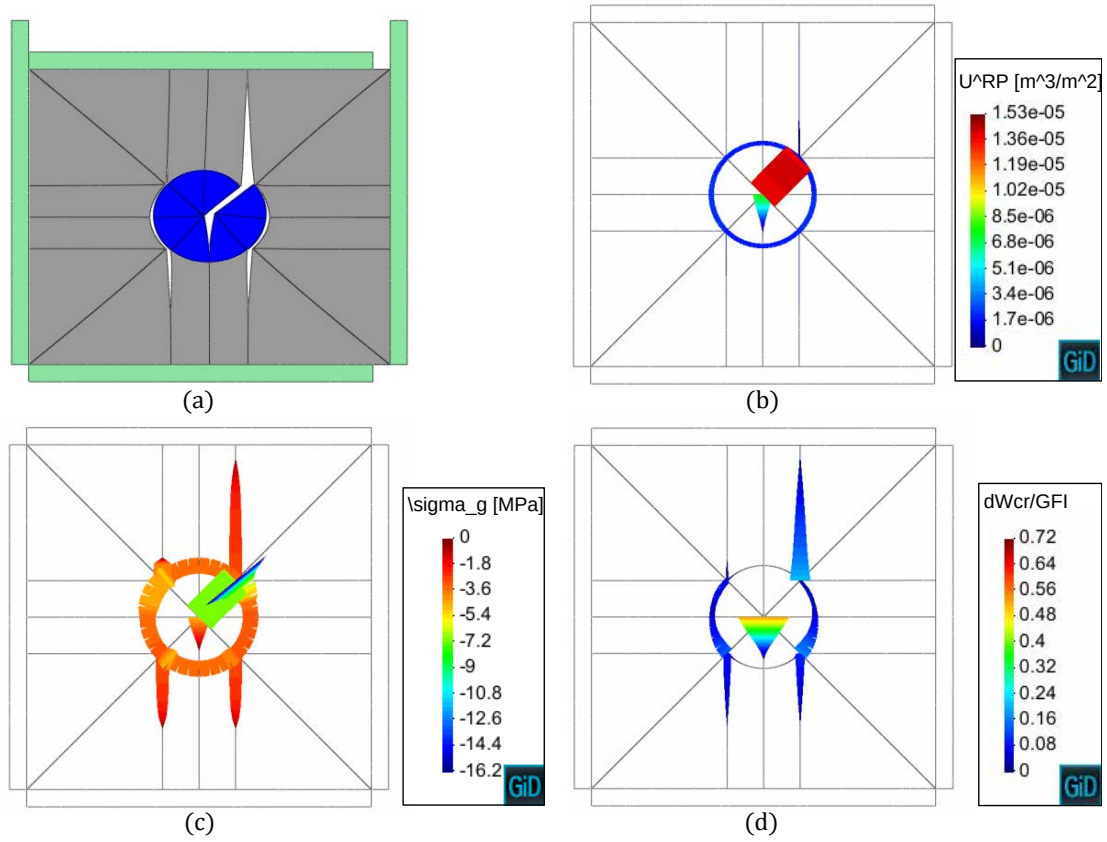

FIGURE 7.34: Modelling of a one-aggregate specimen under uniaxial compression (10 MPa). Modelling results at day 34: (a) deformed geometry (×500), (b) volume of reaction products, ($\mathcal{U}^A_{mp} + \mathcal{U}^B_{mp}$) (c) internal pressure (σ_g), (d) work spent in fracture processes (W^{cr}/G^I_f).

the case under uniaxial loading, the cracking of mortar-glass elements occurred slightly earlier than the free expansion case, with different consequences for the vertical and horizontal strains. In contrast with the free expansion case, where the cracking of the mortar-glass elements occurred in pure tensile mode (mode I), in the case under uniaxial loading the cracking occurred in mixed shear-compression mode, due to the initial stress state around the SL glass aggregate. This initial shear-compression stress state was determined by the higher stiffness of the glass aggregate in relation to the mortar matrix. Under these initial conditions and in the context of the adopted constitutive law (Section 6.5.2.1), the growing σ_g at the mortar-glass elements had the effect of progressively reducing the effective compressive normal stress (σ_n) and the shear strength determined by it. Eventually, if σ_g was sufficiently high, the hyperbolic failure surface was reached and the cracking process started (Section 6.5.2.1). As the mortar-glass elements cracked, the tangential relative displacement (a^{cr}_l) associated to the mixed craking mode allowed the mortar to 'slip' around the aggregate under the effect of the vertical load, with consequent descent of the top-side loading plate. This mechanism is behind the contractions developed at the very beginning of the simulation (Fig. 7.32b) but also

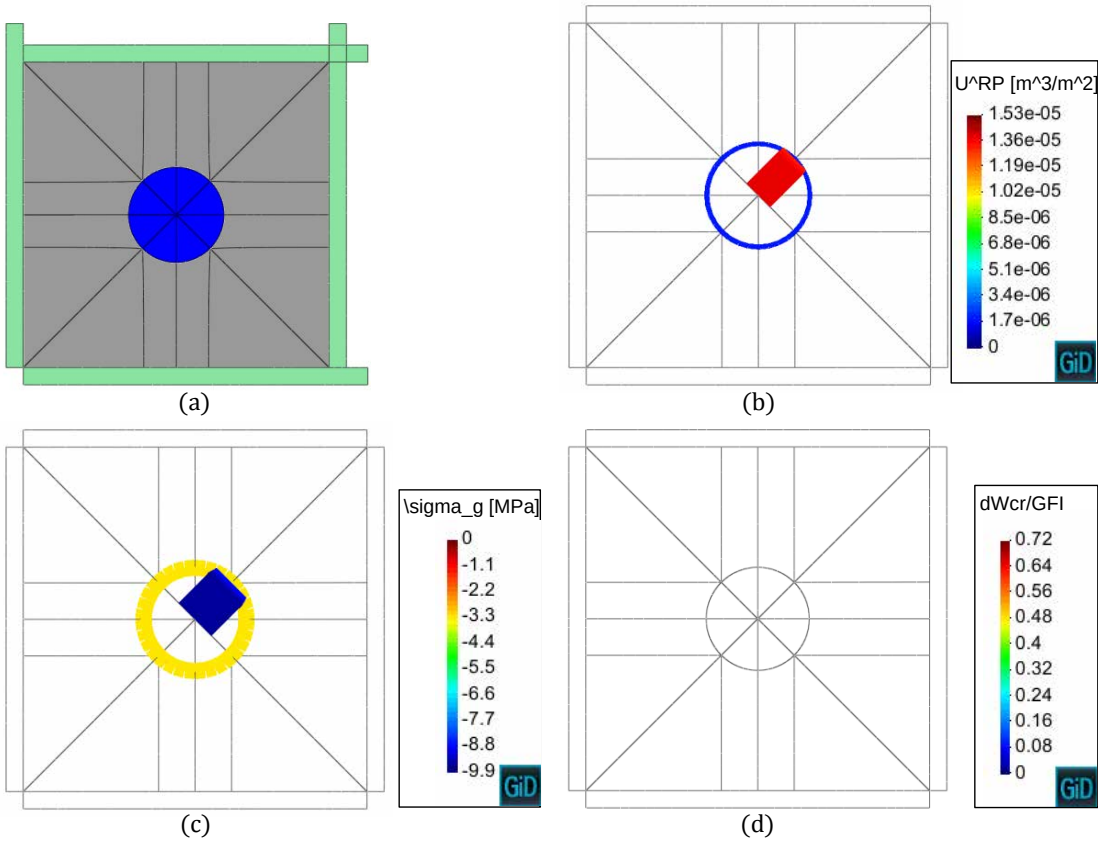

FIGURE 7.35: Modelling of a one-aggregate specimen under biaxial compression (10 MPa). Modelling results at day 34: (a) deformed geometry (×500), (b) volume of reaction products, ($\mathcal{U}^A_{mp} + \mathcal{U}^B_{mp}$) (c) internal pressure (σ_g), (d) work spent in fracture processes (W^{cr}/G^I_f).

of those developed later (Fig. 7.32a).

During the first five days, the horizontal expansion curve of the uniaxial load case was very similar to the horizontal expansion curve of the free expansion case. But approximately at day 5, the cracks in the uniaxial loading case started to propagate vertically both into the mortar matrix an inside the aggregate and, consequently, the horizontal expansion curve grew faster than in the free expansion case. It is good to bear in mind that in the free expansion case the propagation of cracks into the mortar and the SL glass aggregate did not occur until days 8.625 and 13.75, respectively, and in both cases in the diagonal direction (Section 7.5.2.1). The vertical orientation of the propagation of cracks in the case under uniaxial loading was determined by the vertical direction of the minimum principal stress in the mortar matrix. It may be argued that the cracking paths were limited to those defined by the location of the interface elements, and, therefore, that the direction of the crack propagation was also determined by the FE mesh. However, the evolution of the stress state of the continuum elements (not presented here) indicates that the minimum principal stress remained predominantly vertical at all locations during the simulation. Therefore, one may expect that, even if additional

crack paths were allowed, the crack propagation would still have been predominantly vertical.

As cracks propagated vertically in the mortar, the passive restraint exerted by the mortar on the expansion of the mortar-glass interfaces in the horizontal direction, was reduced, allowing further interfacial expansions with the subsequent degradation of the shear strength. This reduction of the shear strength, as explained above, caused further descent of the top-side plate under the effect of the vertical load.

Note that the effect of loading on the development of the ASR strains in the one-aggregate model is qualitatively similar to the effects observed in the experimental Confined Expansion Tests presented in Chapter 4. That is,

- **Reduction of the volumetric expansion rate for increasing volumetric stress.** Compare for instance the volumetric strain curves obtained with the model given in Fig. 7.33 (before day 34) and the experimental volumetric strain curves given in Fig. 4.9.
- **Increase of the expansion rate in one direction when compressive stress is applied perpendicularly to this direction.** Consider for instance the increase on the expansion rate in the Z-direction for the 9-9-1 load case in relation to the 1-1-1 load case (Figs. 4.7e and f), and compare it with the increase of the expansion rate in the horizontal direction developed by the model for the uniaxial loading case (Fig. 7.32a).
- **Contraction in a loaded direction when expansions are developed in the perpendicular direction.** This effect is clearly observed in the model results (Fig. 7.32b) because the expansion in the loaded direction was completely inhibited. In the results of the Confined Expansion Test it cannot be so clearly appreciated but it can be inferred from the curves depicted in the figures. Consider, for instance, Figs. 4.7e and f corresponding to the axial strain curves of load cases 9-9-9 and 9-9-1. The axial strain curves in the X- and Y-directions of load case 9-9-1 developed contractions in the first three days that were not observed in the axial strain curves of the 9-9-9 load case. Moreover, the expansion rates in the X- and Y-directions of load case 9-9-1 were (slightly) slower than the expansion rates observed in the axial strain curves of the 9-9-9 load case (Table 4.4). This differences may be attributed to the development in the 9-9-1 load case of contractions in the X- and Y-directions superposed to the ASR expansions in these directions. These contractions would be the consequence of the strength reduction of the concrete due to the cracking induced by the expansion in the Z-direction.

7.5.2.3 Swelling pressure

As a final example, let us consider the results obtained with the mechanical boundary conditions schematically represented in Fig. 7.23a (length change prevented in the vertical direction) and Fig. 7.23b (length change prevented both in the vertical and horizontal directions). For the sake of brevity, these boundary conditions are referred here on as 'uniaxial restraint' and 'biaxial restraint'. In the first case, the top-side loading plate was fixed, while the right-side loading plate was allowed to move freely in the horizontal direction. In the second case, both the top-side and the right-side loading plates were fixed. These cases were intended to assess the evolution of the pressure exerted by the one-aggregate specimen on the fixed loading plates as ASR progressed. Note that the first case (uniaxial restraint) is conceptually similar to the experimental setups discussed in Section 2.8 in which the longitudinal expansion of mortar or concrete bars is prevented via very stiff loading frames [e.g. 21, 67, 68, 105]. In those setups, the stress developed in the specimen in the restraint direction is usually called 'expansive' or 'swelling pressure'

For the case with uniaxial restraint, the time evolution of the horizontal axial strain and the vertical swelling pressure are given in Fig. 7.36. For the case with biaxial restraint, time evolution of the horizontal/vertical swelling pressure is given in Fig. 7.37. Note that in this case the model has a symmetry axis in the direction of the pre-existing crack, and, consequently, the swelling pressures in the horizontal and vertical directions had the same evolution. The swelling pressure r_y [MPa] is defined as the sum of all the vertical reaction forces on the fixed nodes of the top-side loading plate divided by the specimen side length $L = 10$ mm (unitary 1 m depth is assumed in the 2D formulation). Similarly, the swelling pressure r_x is defined as the sum of all the horizontal reaction forces on the fixed nodes of the right-side loading plate divided by the specimen side length L.

The deformed geometry and the spatial distribution of the reaction products ($\mathcal{U}^A_{mp}$+$\mathcal{U}^B_{mp}$), the internal pressure (σ_g), and the work spent in fracture processes (W^{cr}/G^I_f) of both cases, are given in Figs. 7.38 and 7.39. The time chosen to represent the results of the case under uniaxial restraint (day 54), corresponds to the moment just before a crack reached the bottom border of the specimen. The time chosen to represent the case under biaxial restraint (day 180), corresponds to a moment in which the swelling pressure had reached a plateau and was growing at a very small rate (Fig. 7.37).

Before reaching the aforementioned plateau, the swelling pressure of the case with biaxial restraint was growing monotonically since the moment in which the reaction products formed at the mortar-glass got pressurized at day 0.33 (Fig. 7.37). The mortar-glass interface elements were the first to be cracked (as in all the previous cases) and their

expansion was the main responsible for the growth of the swelling pressure until day 9, when the pre-existing crack started to propagate into the mortar. At this moment, the formation of reaction products at the mortar-glass interface (mainly RPA) was practically stopped due to the confining pressure exerted by the surrounding mortar matrix. The propagation of the pre-existing crack occurred in the diagonal direction. First (day 9) towards the top-right corner through the mortar. Then (day 14) it started to propagate also towards the bottom-left corner through the aggregate. At day 77 the diagonal

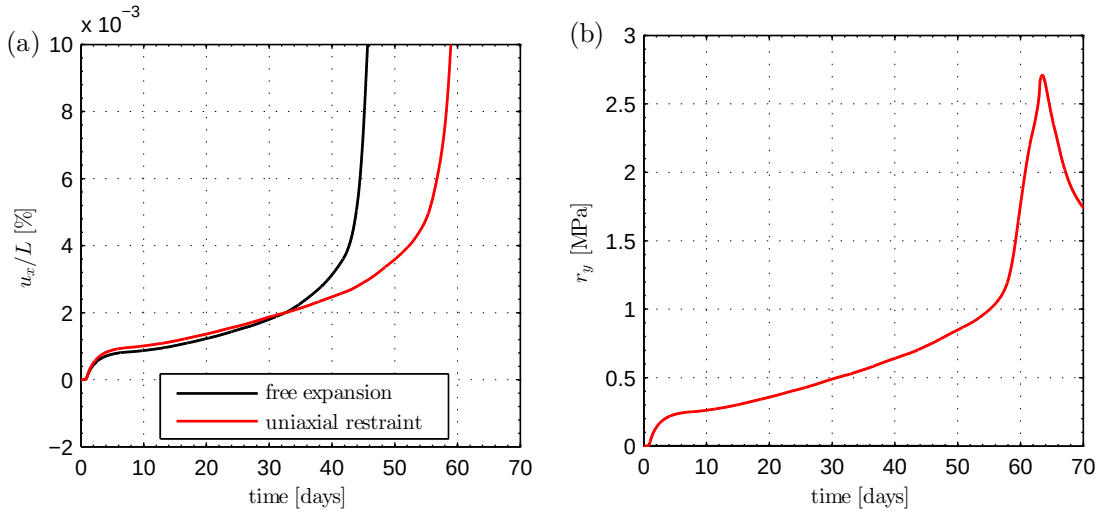

FIGURE 7.36: Modelling of a one-aggregate specimen with prevented vertical length change. (a) Axial strains in the horizontal direction. The axial strains of the free expansion case are also plotted for comparison. (b) Swelling pressure in the vertical direction.

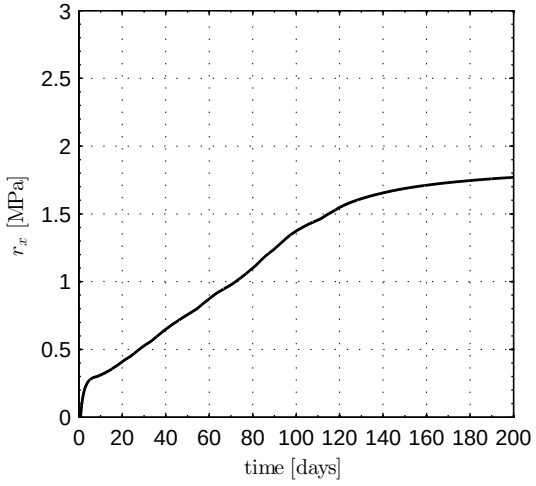

FIGURE 7.37: Modelling of a one-aggregate specimen with length changes prevented in the horizontal and vertical directions. Swelling pressure in the horizontal/vertical direction.

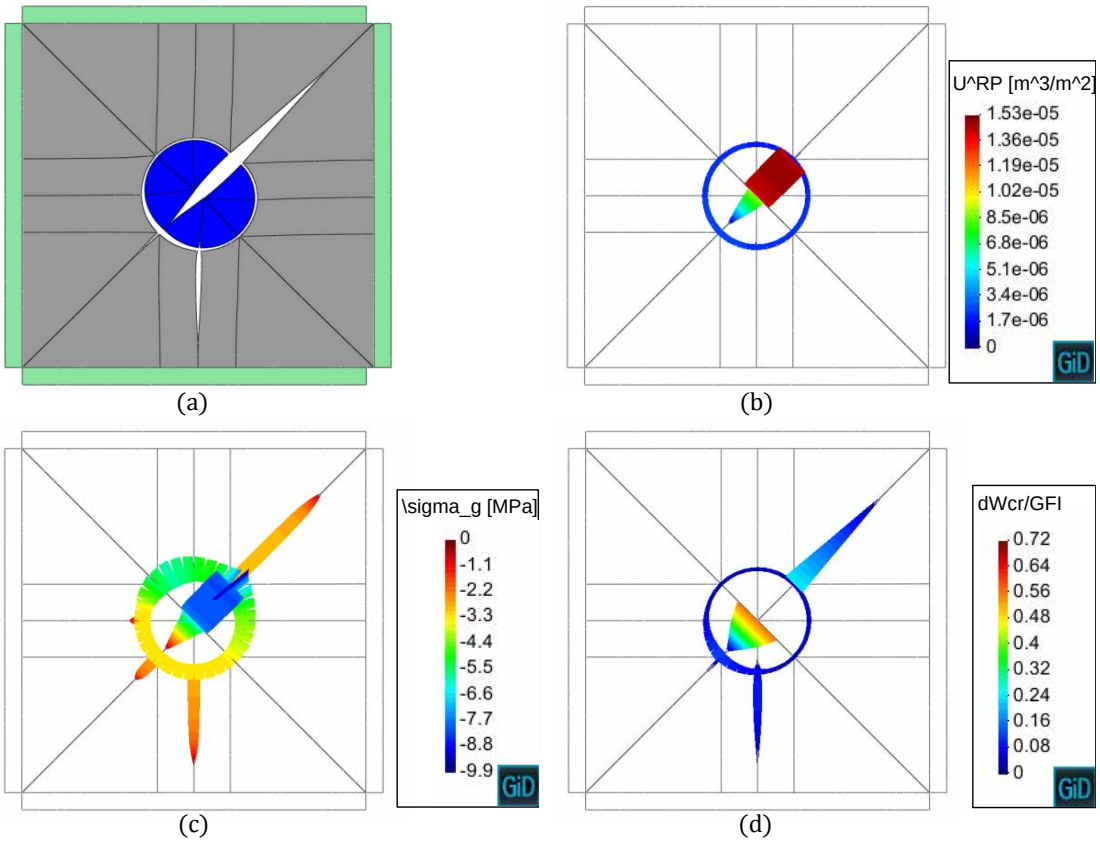

FIGURE 7.38: Modelling of a one-aggregate specimen with prevented vertical expansion. Modelling results at day 54: (a) deformed geometry (×500), (b) volume of reaction products, $(\mathcal{U}^A_{mp} + \mathcal{U}^B_{mp})$ (c) internal pressure (σ_g), (d) work spent in fracture processes (W^{cr}/G^I_f).

crack crossed the aggregate propagating trough the mortar towards the bottom-left corner. As the growing σ_g along the diagonal crack approached the threshold stress of the mixed reaction products (σ_{th}), the gel porosity decreased, the rate of production of reaction products decreased, and the growth rate of the swelling pressure steadily decreased. The small growth rate of the swelling pressure at day 180 (Fig. 7.37) and the corresponding distribution of σ_g (Fig. 7.39c) are consistent with this mechanism. Inside the SL glass aggregate, where the predominant reaction product was RPB, σ_g was approximately equal to the threshold stress of RPB ($\sigma_g \approx \tilde{\sigma}^B_{th} = -10$ MPa). In contrast, within cracks in the mortar matrix and at the mortar-glass interface, where the predominant reaction product was RPA, the stress values were $\sigma_g \approx \tilde{\sigma}^A_{th} = -3$ MPa.

In the case of uniaxial restraint, the cracking sequence was initially similar to the free expansion case: cracking of mortar-glass interface at day 0.875, propagation of the pre-existing crack into the mortar at day 9, and propagation of the pre-existing crack into the glass aggregate at day 13.75. Moreover, the horizontal strain curves were also similar before day 30, with a small difference that may be attributed to Poisson strains of the continuum elements as the specimen was vertically compressed. However, as

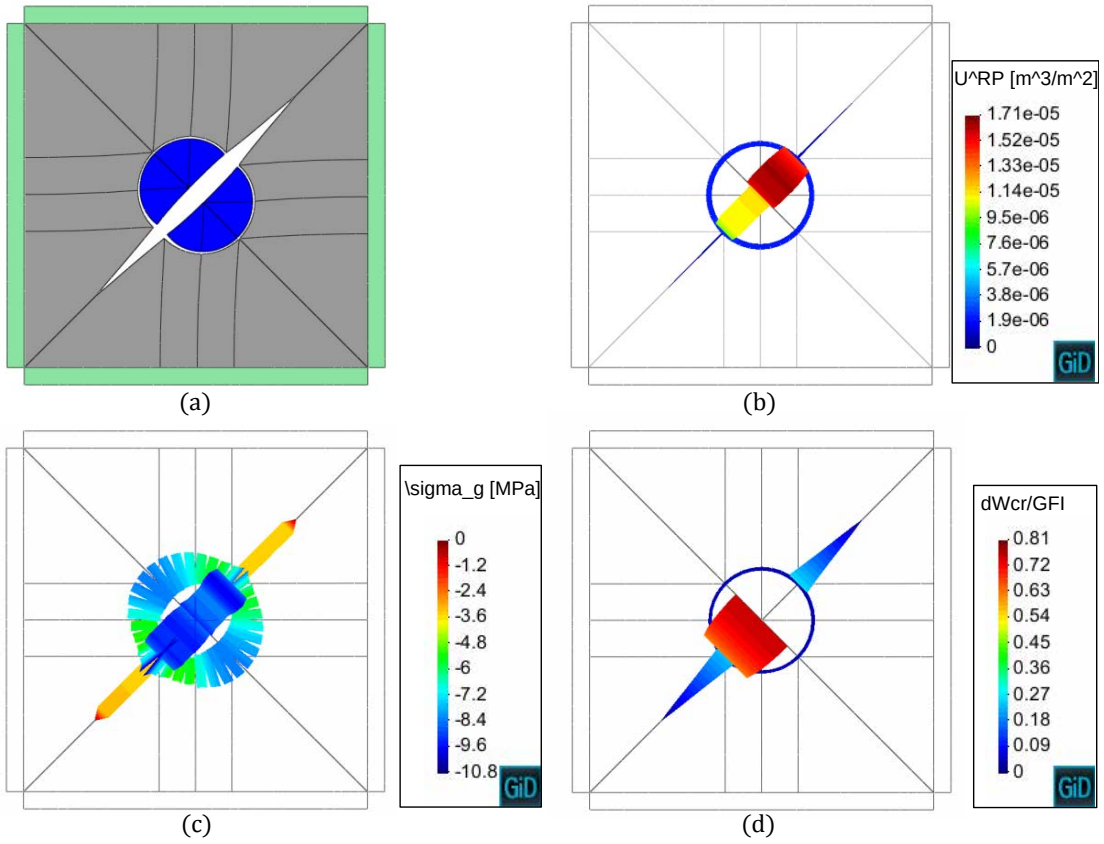

FIGURE 7.39: Modelling of a one-aggregate specimen with expansion prevented in the horizontal and vertical directions. Modelling results at day 180: (a) deformed geometry (×500), (b) volume of reaction products, $(\mathcal{U}^A_{mp} + \mathcal{U}^B_{mp})$ (c) internal pressure (σ_g), (d) work spent in fracture processes (W^{cr}/G^I_f).

the vertical pressure increased, the cracking sequence/pattern changed, and new cracks were mainly aligned with the minimum principal stress, i.e. in the vertical direction. This can be clearly appreciated by comparing the deformed geometry in Fig. 7.39a and the deformed geometry of the free expansion case in Fig. 7.25. It must be noted that at this time the minimum principal stress at the tip of the diagonal crack was also vertically oriented. However, lacking of alternative crack paths, the cracking continued propagating in the diagonal direction. In other words, from the day 30 onwards, the results obtained became mesh dependent. When the vertical crack growing from the mortar-glass interface reached the bottom side of the specimen (day 55) and when the crack growing from the pre-existing crack reached the top-right corner (day 57), the horizontal expansion rate (Fig. 7.36a) and vertical swelling pressure rates (Fig. 7.36b) were accelerated. Eventually, the vertical crack also propagated into the aggregate and got connected with the pre-existing crack around day 63, determining the swelling pressure peak (Fig. 7.36b). From there on, the swelling pressure diminished as the sector of the specimen configured by the vertical and diagonal crack started to move horizontally pushed by the formation of reaction products.

7.6 Chapter concluding remarks

- The model proposed in previous Chapter 6 for simulating expansions due to ASR in concrete made with SL glass, has been used in this chapter for analysing a number of cases of increasing complexity.
- The model has been able of qualitative and quantitatively reproducing experimental results from the Interfacial Expansion Test presented in Chapter 3. However, a point remains to be verified with further study regarding the applicability of the implicit assumption of unlimited availability of water at the reaction site.
- The effects of external loading on the development of ASR expansions in concrete, experimentally studied in Chapter 4, has been qualitatively reproduced with the simulation of one-aggregate specimens. Namely, the reduction of the volumetric expansion rate for increasing volumetric stress, and the increase of the expansion rate in one direction when a compressive stress is applied in the perpendicular direction.
- The basic application cases that have been presented in this chapter are considered as necessary steps in the process of validating the proposed model. This process is an ongoing work, not completed in this thesis, that must include additional cases, particularly, specimens with multiple SL glass particles (as suggested in the following Chapter 8).

Chapter 8

Summary, conclusions and future work

8.1 Summary and conclusions

The main contributions of this thesis may be summarized as follows:

i. A new experimental setup and the associated testing methodology for measuring Alkali-Silica Reaction (ASR) expansions at the level of a single aggregate-cementitious matrix interface has been developed and verified in an extensive testing campaign.

ii. Expansions occurring at the level of a single aggregate-cementitious matrix interface due to the formation of ASR products have been measured for the first time, in specimens made with different types of reactive aggregates, different cementitious matrices, and different alkali contents. Additionally, the effect of the mass transport of water and/or aqueous alkalis on the ASR interfacial expansion rate has been assessed.

iii. A testing methodology has been developed and verified on the basis of an existing testing machine for measuring ASR expansions in concrete specimens under triaxial confinement, which has been improved and updated for the new experimental campaign.

iv. ASR confined expansion curves of cubical concrete specimens have been obtained for three different triaxial stress states. For comparison, ASR free expansion curves of specimens of the same type have been also obtained.

v. The cracking patterns and the ASR products formed within the specimens tested have been characterized by means of Scanning Electron Microscopy (SEM) and Energy Dispersive Spectroscopy (EDS).

vi. A reaction-expansion mechanisms for ASR expansion in concrete has been proposed based on experimental observations. This mechanism is capable of explaining the effect of the stress state on the kinetics and distribution of ASR concrete expansions.

vii. A coupled Chemo-Mechanical (C-M) modelling framework for diffusion-dominated durability problems in cement-based materials has been formulated and implemented.

viii. A meso-scale coupled C-M model for simulating ASR expansions in concrete has been formulated and implemented. This model has been used for simulating a number of real and ideal cases, demonstrating its ability to reproduce experimental observations regarding the effect of concrete stress state on the development of ASR expansions.

These contributions have been presented in Chapters 3–7. Although interrelated, each of these chapters has dealt with a particular aspect of the thesis. A series of conclusions and main achievements can be extracted from each one of them:

8.1.1 On the Interfacial Expansion Tests

- The proposed testing methodology meets the objective of measuring ASR expansions at the level of a single interface between a reactive aggregate and a cementitious matrix.
- The proposed methodology can provide valuable information about the ASR expansion mechanisms, being at the same time inexpensive and very easy to replicate.
- The simplicity of the geometry and of the boundary conditions of the tested specimens make these tests ideal for the calibration of micro- and meso-scale numerical models for ASR expansion in concrete.
- The experimental results obtained seem to indicate that:
  - The ASR products formed in between SL glass and cement paste or mortar have relatively high calcium contents (molar Ca/Si = 1.0–1.5).
  - The mass exchange of alkali and/or water between the specimens and the alkaline bath determines the kinetics of the interfacial expansions.

  - The interfacial expansions are limited by the separation of the reactive aggregate (SL glass of Borosilicate glass) disc from the cementitious matrix occurring for interfacial expansions ranging between 30 μm and 50 μm.
  - The type of cementitious matrix has an influence on the interfacial expansion rates. The fastest expansions were measured on specimens with matrix made of cement and Micro Silica (MS) paste, followed by the specimens made with plain cement paste, and the specimens made with mortar, in this order.

- The results presented do not constitute a systematic parametric study, and therefore, more testing would be necessary to confirm the observed effect of parameters such as the type of cementitious matrix, the type of reactive aggregate or the amount of available alkalis.

- Some concern has been expressed regarding the scatter of the measured expansion curves and on the reproducibility of the results, indicating the need of establishing more strict methodologies for the specimen casting and measurement steps, as well as a better control of the environmental conditions of the laboratory.

- The SEM images performed gave interesting insights into the nature of the ASR products. However, the fact that most of the ASR products were lost and replaced by epoxy resin during the preparation process of the samples, made it difficult to interpret the images. For future tests, attention should be paid to improving the sample preparation procedure.

8.1.2 On the Confined Expansion Tests

- Accelerated ASR expansion tests performed on cubical concrete specimens under free and triaxially-confined expansion conditions have been presented. Two different concrete mixtures were tested under the same conditions, one reactive, with crushed SL glass aggregate, and one non-reactive.

- For the triaxially-confined tests, an ad hoc testing machine was originally designed and constructed by Prof. V.E. Saouma at the U. of Colorado - Boulder, and later modified by the author at UPC-Barcelona. This machine has shown to be capable of accurately applying and maintaining targeted true-triaxial compressive stress states and temperatures on the specimen, while keeping it in contact with a highly alkaline solution.

- The strains measured on non-reactive specimens were used to conventionally distinguish 'ASR strains' from 'basic creep' strains due to the applied loads.

- The results seem to indicate that the volumetric ASR expansion rate is reduced as the applied volumetric compressive stress is increased. Additionally, there seems to be an increase of the expansion rate in the less compressed direction in detriment of the expansion rates in the most compressed ones. These observations are in good agreement with the model previously proposed by Saouma and Perotti [183], although a correction is proposed for the dependency of total volumetric expansion with volumetric stress.

- SEM/EDS analyses of the reaction products and cracking of a specimen tested under isotropic pressure of 1 MPa, indicate the presence of ASR products with variable calcium content, from low-calcium products (molar Ca/Si≈0.30) inside cracks within glass particles to high-calcium products (molar Ca/Si≈1.40) formed in contact with the HCP. Most of the ASR expansion and cracking is attributed to the low-calcium product.

8.1.3 On the proposed modelling framework

- A general framework for modelling diffusion-dominated deleterious processes in cement-based materials has been theoretically and numerically formulated. The resulting formulation consists of two separated parts, one dealing with the mechanical problem and one dealing with the diffusion-reaction problem. A number of coupling terms links together both formulations. The spacial discretization of the theoretical formulation has been done with the Finite Element Method (FEM) and the time discretization has been done with the Finite Difference Method.

- The formulation has been implemented in two different codes, one dealing with the mechanical problem (`DRAC`) and one dealing with the diffusion-reaction problem (`DRACFLOW`). The coupling between the two codes is achieved by updating the coupling terms of each problem in an iterative process. To do so, each code exchanges data with the other one, in the context of a 'staggered procedure' which is administrated by a third code called `STAG`.

- The proposed model makes it possible to simulate the various observed interplays between the diffusion of aqueous species in pore solution, the precipitation or dissolution of solid species, and the stress-strain state of the material, with the distinctive feature of explicitly considering the role played by discontinuities (cracks or aggregate-cementitious matrix interface) within the material. The discontinuities are represented via zero-thickness interface elements introduced a priori in between the continuum elements.

- The main features of the diffusion-reaction formulation are:

  - It is possible to consider the Fickean diffusion of an arbitrary number of primary aqueous chemical species in pore solution.
  - From the concentration of the primary aqueous species, the concentration of secondary aqueous species (e.g. OH^- and H^+) is calculated locally based on chemical equilibrium equations.
  - An arbitrary number of reactive and non-reactive solid species can be considered.
  - The amount of reactive species evolve according to dissolution/formation reactions, with kinetic laws determined by the concentration of primary and secondary aqueous species in the pore solution.
  - Dissolution/formation of solid species can occur both in the continuum elements representing bulk porous material (aggregates or HCP/mortar) and within the interface elements representing discontinuities.
  - The volume balance of the solid species determines the evolution of the material porosity and, thus, of the effective diffusivity of the aqueous species.
  - Depending on the durability problem considered, the volume balance of the solid species may also affect the mechanical analysis determining the development of internal pressures or the degradation/improvement of the material mechanical properties.
  - Concrete pores and cracks are assumed to remain fully saturated with water at all times. Therefore, the water mass balance is not explicitly considered in the formulation.

- The mechanical formulation includes different mechanical constitutive laws available for both the continuum elements and the interface elements. In the context of this study, for the interface elements the selected option is an elasto-plastic constitutive law based on concepts and parameters of the non-linear fracture mechanics theory. The continuum elements are normally considered elastic or visco-elastic, the latter allowing the simulation of creep strains.

- The coupling between the diffusion-reaction and the mechanical formulations can be unidirectional or bidirectional, depending on the particular durability problem considered.

- The proposed model is based on previous developments within the research group of Mechanics of Materials (MECMAT) at UPC. However, substantial contributions has been made, in particular with regard to the diffusion-reaction formulation.

- This modelling framework can be used for modelling durability problems other than ASR, as it has been shown by the author and co-workers by modelling Acid Attack of oilwell cement exposed to carbonated brine [128].

8.1.4 On the proposed model for ASR expansions in concrete

- A new reaction-expansion mechanism for ASR in SL glass concrete has been proposed based on the experimental results presented in this thesis, as well as on other experimental results found in the literature. The distinctive features of this mechanism are:
  - The ASR products are visualized as a space-filling gel composed by the aggregation of colloidal clusters of calcium alkali silicate hydrates (C–R–S–H) of variable composition.
  - C–R–S–H with high calcium content is mainly formed at reaction sites close to HCP, while C–R–S–H with low calcium content is mainly formed in cracks inside the SL glass particles.
  - Two different fractions of water are distinguished in the ASR products: the water chemically bound in the C–R–S–H and the water within the influence of absorbing forces, referred as 'gel water'. These absorbing forces are dependent on the chemical composition of the C–R–S–H. Higher absorbing forces are attributed to low-calcium C–R–S–H in comparison with high-calcium C–R–S–H.
  - The content of gel water determines the distance between the colloidal clusters and, consequently, the 'bulk' volume of the ASR product, i.e. increase as water is absorbed.
  - If this swelling is prevented by the surrounding solid skeleton, a mechanical pressure will be exerted on the ASR gel (C–R–S–H + gel water) counteracting the absorption pressure and, consequently, the amount of gel water absorbed will be lower than in free swelling conditions. Beyond a certain value of mechanical pressure, referred as threshold stress or Maximum Swelling Pressure (MSP), the amount of gel water in the ASR products vanishes. Conversely, if the mechanical restraint is removed the original potential of water absorption will be restored and the ASR products will swell.
  - The gel water within the ASR products is regarded as part of the concrete pore solution, i.e. as an aqueous medium in which diffusion-reaction processes may occur. Then, changes in the amount of gel water have an effect on the reaction rates by locally reducing either the effective diffusion section, the 'wet' surface area of dissolving silica, or the volume of reacting medium.

- This reaction mechanism has been formulated within the general modelling framework for diffusion-dominated durability in cement-based materials, which has also been proposed in this thesis.

- The resulting model considers three primary aqueous species (silicate anions, calcium cations, and total alkalis) and four secondary aqueous species (hydroxyl anion, Hydronium cation, alkali hydroxide, and alkali cation).

- The model considers four reactive solid species: SL glass, portlandite, and two reaction products of fixed stoichiometry, one with low calcium content (RPA) and one with high calcium content (RPB). Then, the variable composition of the ASR products is obtained as the mixture of RPA and RPB.

- The dissolution/precipitation reactions involved in ASR expansions are considered to occur only within the zero-thickness interface elements representing fractures and cement-glass contacts, while diffusion of primary species may occur within interface as well as continuum finite elements.

- The reaction products precipitated in the interface elements may eventually induce internal pressures which may lead to fracture processes. These internal pressures are related to the amount of gel water absorbed by the reaction products which, in turn, depends on their chemical composition.

- SL glass has some peculiarities as concrete aggregate, and, thus, the model includes some assumptions that made it not strictly applicable for the more usual case of concrete make with natural reactive aggregates. However, it can be readily adapted for other types of reactive aggregates, such as natural reactive aggregates, by introducing minor changes in the formulation.

8.1.5 On the simulations results

- The model proposed for simulating expansions due to ASR in concrete made with SL glass, has been used for analysing a number of real and ideal cases of increasing complexity.

- The model has been able of qualitative and quantitatively reproducing experimental results from the Interfacial Expansion Tests presented in this thesis. However, some aspects of the formulation remain to be verified in further studies, in particular the assumption of infinite water availability implied by the fact of not considering explicitly the water mass balance at the reaction sites.

- The effects of external loading on the development of ASR expansions in concrete, observed in the Confined Expansion Tests reported in this thesis, has been qualitatively reproduced with the simulation of one-aggregate specimens. Namely, the reduction of the volumetric expansion rate for increasing volumetric stress, and the increase of the expansion rate in one direction when a compressive stress is applied in the perpendicular direction.
- The numerical simulations performed are considered as necessary steps in the process of validating the proposed model. This is an ongoing process, not totally completed in this thesis, that will include additional cases, particularly, the simulation of specimens with multiple SL glass particles as suggested in the next section.

8.2 Future work

In the course of the work developed, a number of possibilities of new research have been identified, some of them to further develop and improve the experimental methodologies and the numerical models presented in this thesis, and some of them to tackle new, although related, areas of research. Some of these research topics are listed below:

Enhancement of Interfacial Expansion Tests

The experimental interfacial expansion curves showed big scatters that have been attributed among other possible causes to certain specific aspects of the testing methodology. With a view on future experiments of this type, both the repeatability and reproducibility of the test results could perhaps be improved by establishing more strict methodologies for the specimen casting and measurement steps, as well as a better control of the environmental conditions of the laboratory.

Testing natural reactive aggregates

SL glass has some peculiarities as concrete aggregate that made the obtained experimental results not directly applicable for concrete made with natural reactive aggregates. For instance, the whole volume of SL glass is reactive, while in natural aggregates the reactive silica is usually present as veins or finely dispersed in a matrix of non-reactive minerals. Therefore, a new experimental campaign using natural reactive aggregates would be required in order to identify similarities or differences and, if necessary, reformulate the proposed ASR reaction-expansion mechanism.

Interfacial Expansion Tests at different temperatures

In the proposed ASR model, the effect of temperature on the kinetics of ASR expansions is expected to result automatically from the expressions of the variation of chemical/diffusion parameters as functions of temperature. Some of these dependencies can be directly found in the literature or obtained indirectly by fitting tabulated values of the parameter for different temperatures. Other, however, may need to be determined by fitting experimental results at different temperatures, such as the parameters of RPA and RPB, which are not real chemical species but simple substitutes of the complex ASR gel. A campaign of Interfacial Expansion Tests at different temperatures would be the best option for this purpose, given the simplicity of the geometry and of the boundary conditions of the tested specimens.

Interfacial Expansion Tests under uniaxial loading

The proposed ASR model predicts that if a normal compression pressure is applied to a discontinuity in which ASR products are being formed, the expansion rate of this discontinuity will be reduced or even inhibited if the applied normal stress is higher than the sum of the threshold stress of reaction products (σ_{th}) and the tensile strength of the discontinuity (χ) (see Section 7.3.2).

This prediction and the underlying assumptions regarding the nature of the reaction products can be experimentally verified by performing Interfacial Expansion Tests under uniaxial compression. Implementing a test setup of this kind, however, is not trivial. It would require to apply a constant axial load on the specimen while immersed in the alkaline solution at 60 °C. Moreover, the specimen length change would have to be measured under load and in the alkaline bath at 60 °C. Note that by complementing these tests with direct measurements of the tensile strength of the aggregate-matrix interface, the threshold stress of the formed ASR products might also be determined.

Confined Expansion Tests under additional load cases

The phenomenological model proposed by Saouma and Perotti [183], with the modification introduced in this thesis, seems capable of reproducing the confined expansion rates obtained under the three load cases studied (1-1-1, 9-9-9, and 9-9-1). However, the tested load cases do not prove the main underlying assumption of this model. That is, that the ASR volumetric expansion rates of two specimens under different imposed deviatoric stress tensor but equal hydrostatic stress will be the same. This assumption can be verified by testing additional load cases with the same volumetric stress as the load case 9-9-1, but different deviatoric stress tensor, for instance 6-6-7, 7-7-5 or 8-8-3.

Additionally, other load cases may be tested in order to prove the weight factors proposed in Saouma and Perotti's model for the distribution of the ASR volumetric expansions. In particular, anisotropic load cases with small deviatoric stresses would be of interest. This is suggested by preliminary modelling results (not presented in this thesis) with the one-aggregate specimen geometry (see Section 7.5) which indicate that under small deviatoric stresses the weight factors proposed by Saouma and Perotti may not be correct. Saouma and Perotti fitted these weight factors with the experimental results of Multon and Toutlemonde [157] in which the (initial) deviatoric stresses were 1/4 and 1/2 of the compressive strength of the tested concrete. In our Confined Expansion Test with loads 9-9-1 the deviatoric stress was about 1/5 of the compressive strength of the tested concrete. These values of deviatoric stresses are close or above the onset of compression nonlinearity, usually reported at about 1/3 of the compression strength. Therefore, load cases with lower deviatoric stress, say 1/10 of the compressive strength, would seem appropriate for new Confined Expansion Tests.

Enhancement of the ASR model

Many improvements can be proposed for the ASR model. The most significant of them would be:

- Considering more chemical species. In particular, considering sulphate species (aqueous SO_4^{2-} and solid ettringite) would be relevant for a more accurate calculation of the pH of the pore solution at high temperature. Note that each new primary aqueous species added implies a an additional degree of freedom (DOF) at each node of the FE model with the corresponding increase of the calculation cost and time. Therefore, any additional primary aqueous species to be considered should be chosen carefully.

- Explicit consideration of the water mass balance. The model assumes that concrete pores remain fully saturated with water at all times. This assumption may only be approximate for specimens kept under water at all times, as it has been discussed in Section 7.4.2, and surely it does not allow us to consider the effect of relative humidity in the kinetics and extension of ASR concrete expansions, which may be very relevant for structures in field conditions. Note that considering the water mass balance would require to introduce an additional field variable, i.e an additional DOF per each node of the FE mesh.

- Use of equilibrium equations for dissolution/precipitation reactions. Some of the dissolution/precipitation reactions considered by the model may be regarded as instantaneous in relation to the times required for the diffusive fluxes of aqueous

species (e.g. portlandite dissolution). Therefore, from the numerical point of view, it may be more convenient to consider these reactions by means of equilibrium equations rather than by means of chemical kinetic equations.

- Considering more complex ion interaction models for the calculation of the activity coefficients e.g. Pitzer's Model [164]. This would lead to more accurate calculations of the speciation of aqueous species and of the saturation indexes of reactive solid species, although at the expense of increasing the coding and calculation costs.

Enhancement of the mechanical constitutive law for interface elements

The mechanical constitutive law for interface elements (Section 6.5.2.1) does not allow the closure of open cracks, since once the interface element has plastified the unloading occurs with the initial (very high) elastic stiffness. This implies that the model cannot reproduce effects such as, for instance, a crack that is filled with ASR products and due to an applied external load tends to close exerting additional pressure on the ASR products. Such effect would be of interest for simulating the Confined Expansion Test of specimen TM21 in which the load case was changed during the test from 1-1-1 to 1-9-1 (Section 4.4.3)

With respect to this, the development of a new constitutive model based on a damage-plasticity formulation which at the same time retains the essential features of the present model, would be an important contribution. This challenging topic has been recently undertaken within the MECMAT group and is at present under development.

Parallelization of the codes

The proposed model requires fine FE meshes and small time increments/steps in order to reach stable numerical solutions. This is mainly due to the modelling scale used (micro or mesoscopic), the fast chemical kinetics of some reactions, the sharp concentration gradients due to localized chemical sink/source terms, and the staggered coupling scheme. Under these conditions, even small cases with simple geometries require large computational times. For instance, each of the one-specimen simulations presented in Section 7.5 required more than a week of computing time, using a processor Intel® Xeon® E5-1650, 3.20 GHz.

Even though some improvements can be made in the numerical formulation and on the structure of the current FE codes to reduce the calculation cost, simulating ASR expansions of real concrete specimens with hundreds or thousands of reactive aggregates, or the three-dimensional (3D) geometries, seem out of reach at the current level of development. The only way to potentially undertake large-scale ASR computation may

be resorting to MPI parallelization of the codes `DRAC` and `DRACFLOW`, in such a way that the computational load is divided among many processors with consequent reduction of the computational time. A parallel version of `DRAC` has been recently implemented [77] through public domain libraries PETSc [13], and could be readily adapted for the ASR model. The parallelization of `DRACFLOW`, in contrast, would require a major coding effort, although, with the accumulated experience within the group MECMAT, the task could be probably accomplished within a reasonable period of time.

8.3 Dissemination

At the time of submitting this document, this thesis and the related research work has already lead to the publication of two articles in international journals [117, 128], two more in preparation, and a series of thirteen publications in international conference proceedings [33, 118–127, 129, 145]. Additionally, the author has co-advised seven Bachelor Thesis [2, 38, 84, 143, 158, 201, 215] and one Master Thesis [144] on topics related with his doctoral thesis.

Appendix A

Experimental appendices

A.1 Oxide composition of cements and MS used in experiments

The Portland cement used was type CEM I 42,5 N-SR5 according to the Spanish standard UNE-EN 197-1 [3]. The microsilica was BASF Meyco® MS610.

The oxide composition was measured by X-Ray Fluorescence (XRF) analysis. The results are presented in Table A.1.

TABLE A.1: Oxide composition (in wt%) of Portland cements and microsilica used in experiments. n/m: not measured.

	Portland Cement					**Microsilica**
	PC01	**PC02**	**PC03**	**PC04**	**PC05**	**MS01**
CaO	61.72	62.64	66.03	63.71	63.35	0.66
SiO_2	17.64	19.53	20.11	20.78	20.47	92.72
Al_2O_3	4.55	4.56	3.60	3.62	3.99	0.53
Fe_2O_3	3.08	4.00	3.51	3.53	3.25	0.13
MgO	1.75	1.92	1.53	1.36	1.52	0.30
K_2O	0.83	0.87	0.76	0.91	0.91	0.42
Na_2O	0.07	0.11	0.13	0.20	0.16	0.20
TiO_2	0.23	0.24	0.17	0.16	0.18	0.01
P_2O_5	0.05	0.10	0.16	0.16	0.15	0.06
MnO	0.04	0.04	0.03	0.03	0.04	0.01
SO_3	n/m	n/m	n/m	n/m	n/m	n/m
Lost on Ignition	n/m	2.33	3.15	2.77	2.73	3.99
SUM	89.94	96.34	99.16	97.24	96.75	99.03
Na_2O_e	0.61	0.68	0.63	0.80	0.76	0.48

A.2 Interfacial Expansion Tests - Strain curves of control specimens

A.2.1 Series C

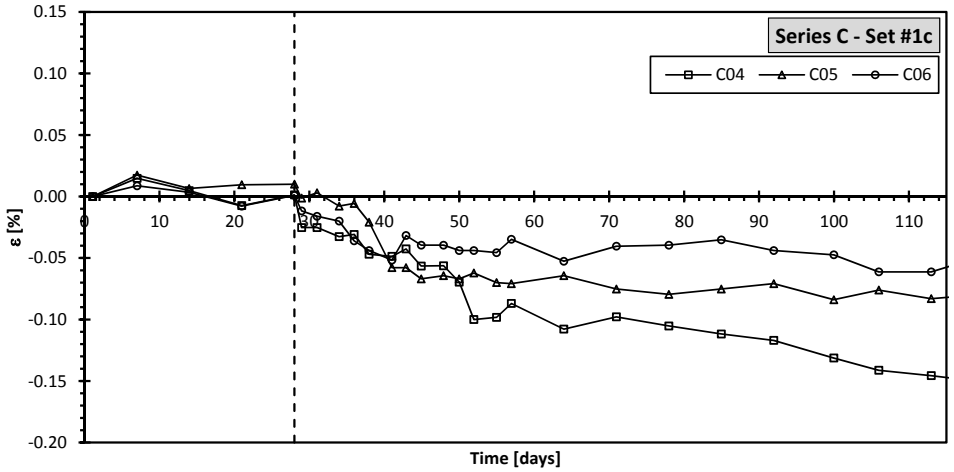

FIGURE A.1: Strain curves corresponding to Series C - Set #1c.

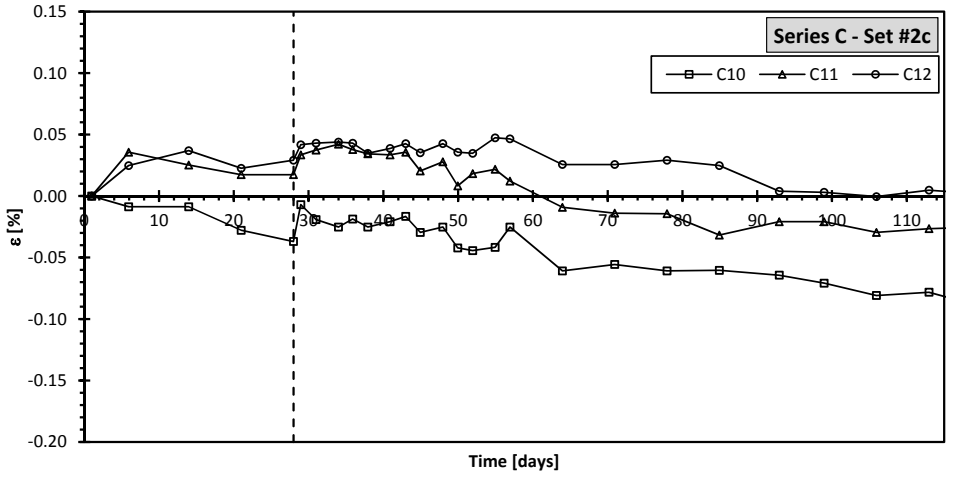

FIGURE A.2: Strain curves corresponding to Series C - Set #2c.

A.2.2 Series D

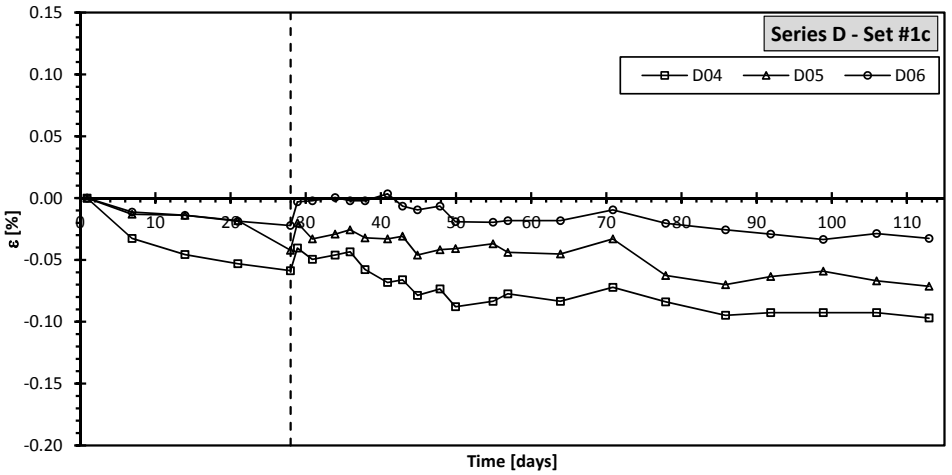

FIGURE A.3: Strain curves corresponding to Series D - Set #1c.

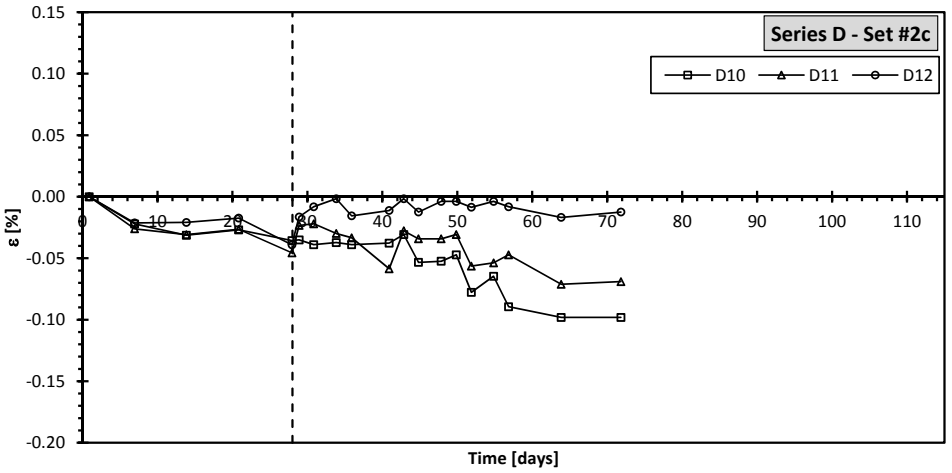

FIGURE A.4: Strain curves corresponding to Series D - Set #2c.

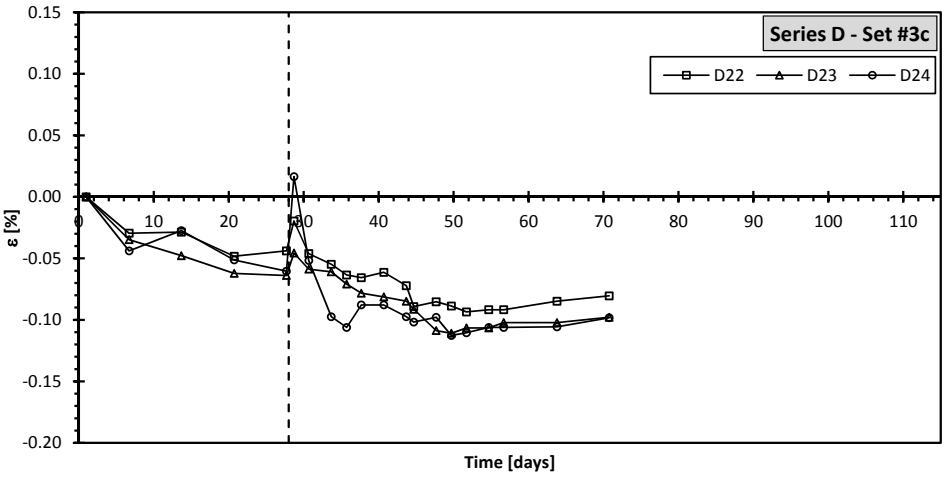

FIGURE A.5: Strain curves corresponding to Series D - Set #3c.

A.2.3 Series E

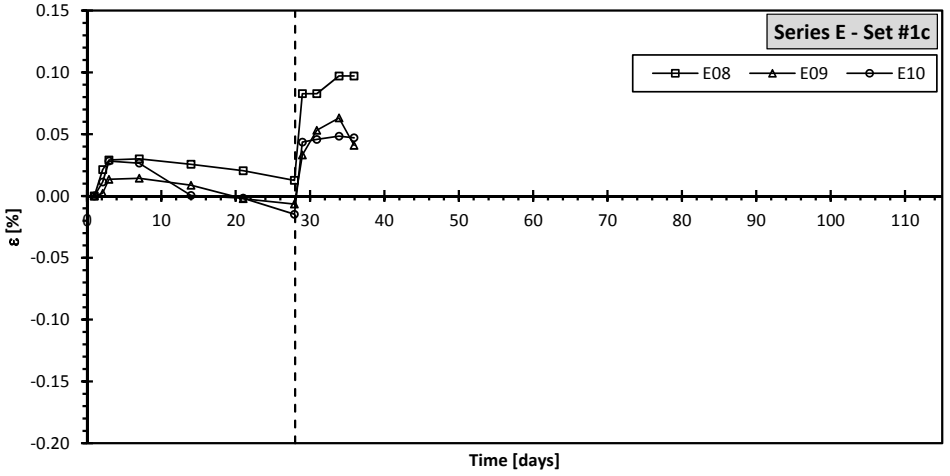

FIGURE A.6: Strain curves corresponding to Series E - Set #1c.

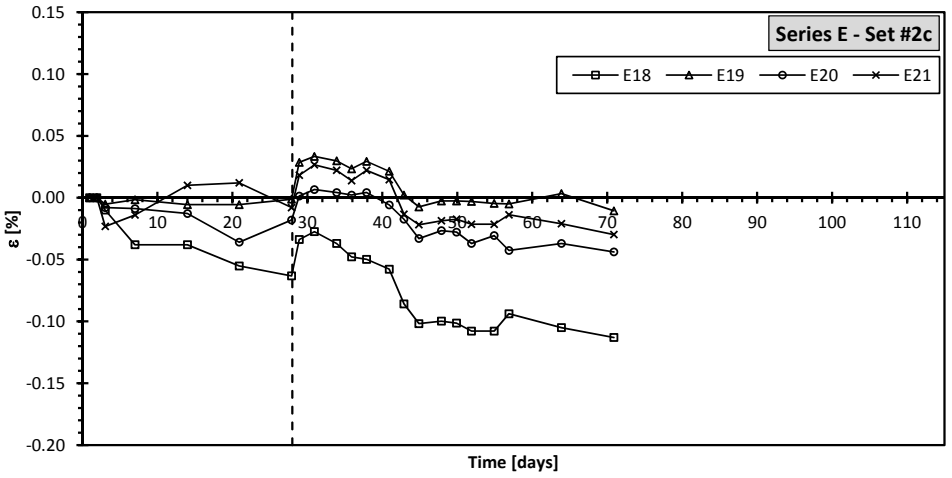

FIGURE A.7: Strain curves corresponding to Series E - Set #2c.

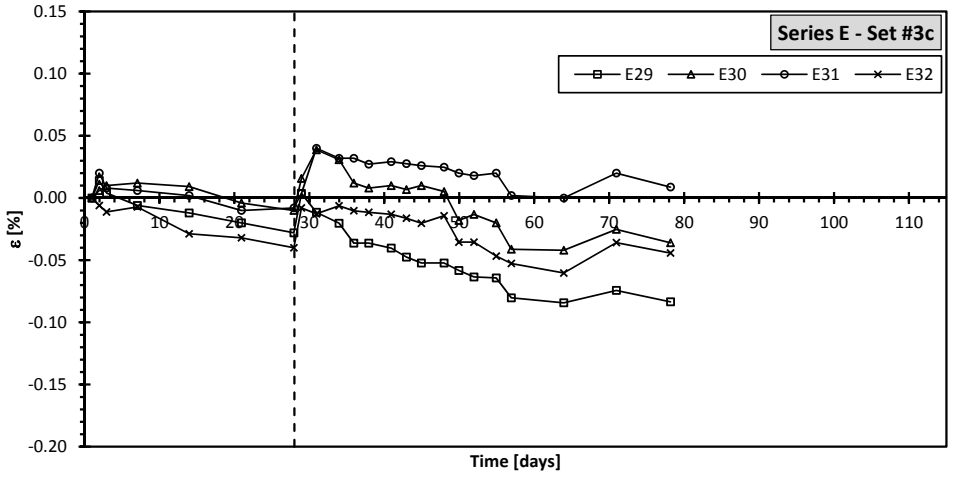

FIGURE A.8: Strain curves corresponding to Series E - Set #3c.

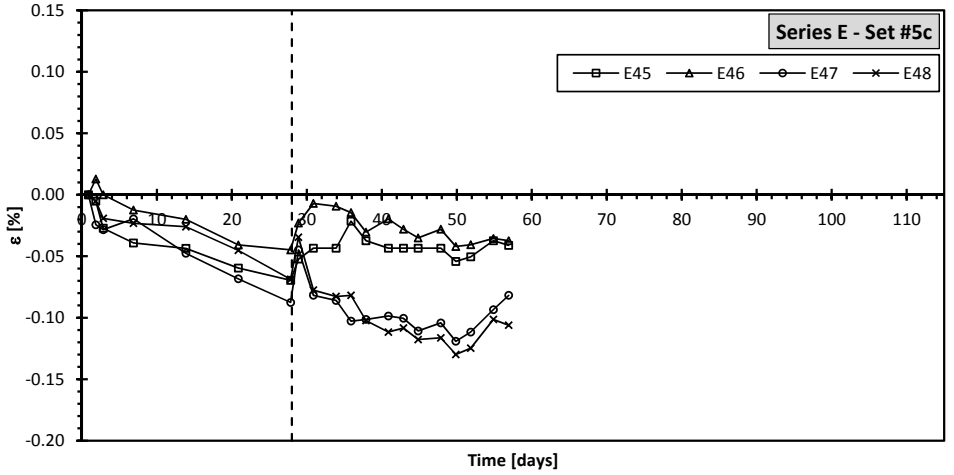

FIGURE A.9: Strain curves corresponding to Series E - Set #5c.

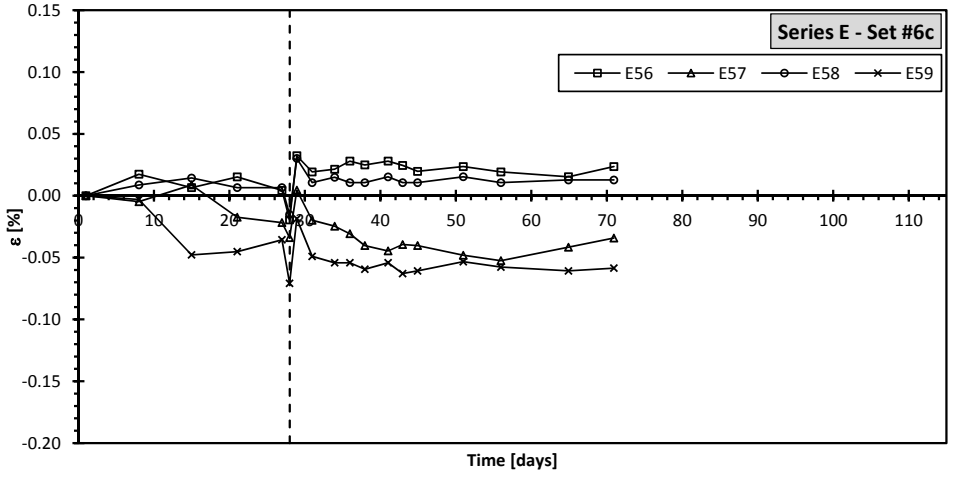

FIGURE A.10: Strain curves corresponding to Series E - Set #6c.

A.2.4 Series F

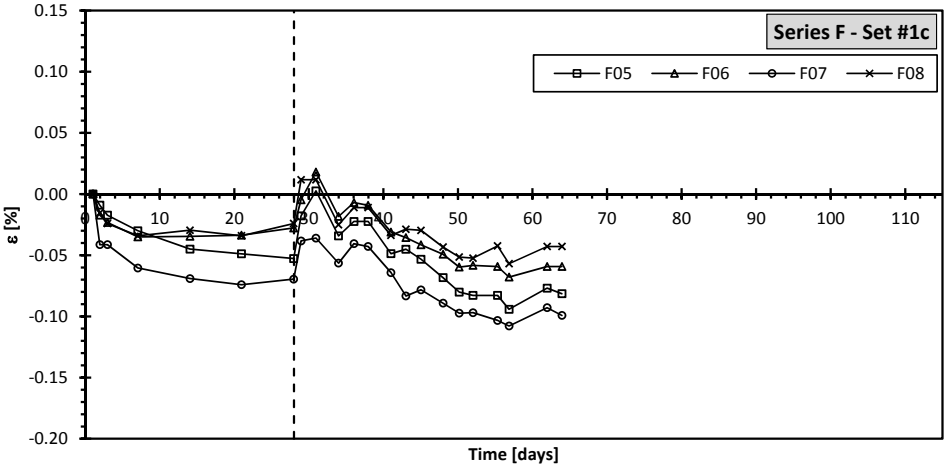

FIGURE A.11: Strain curves corresponding to Series F - Set #1c.

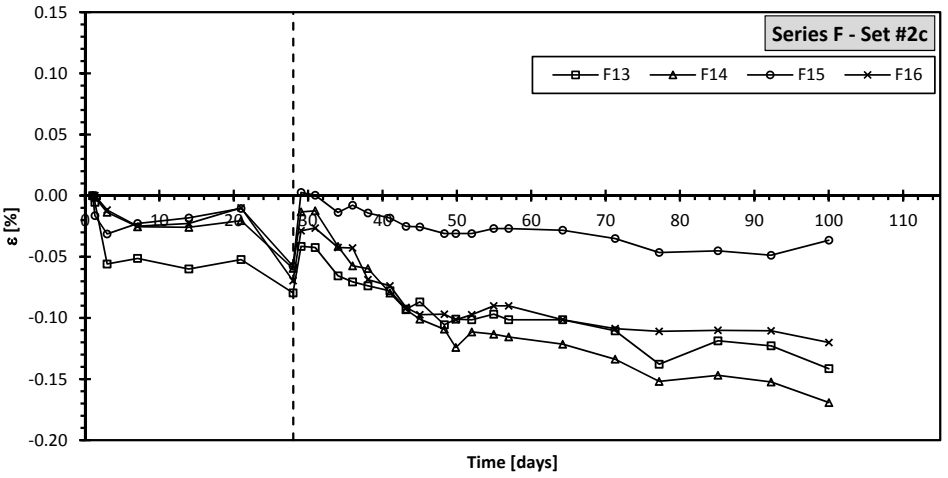

FIGURE A.12: Strain curves corresponding to Series F - Set #2c.

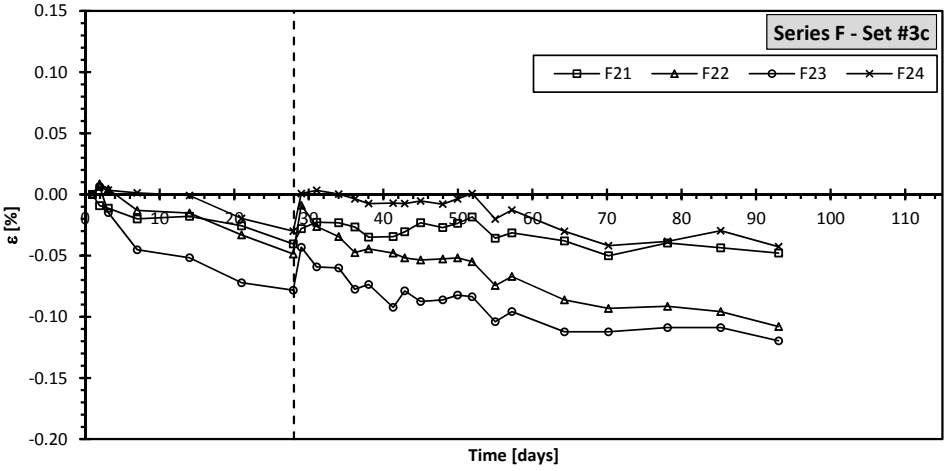

FIGURE A.13: Strain curves corresponding to Series F - Set #3c.

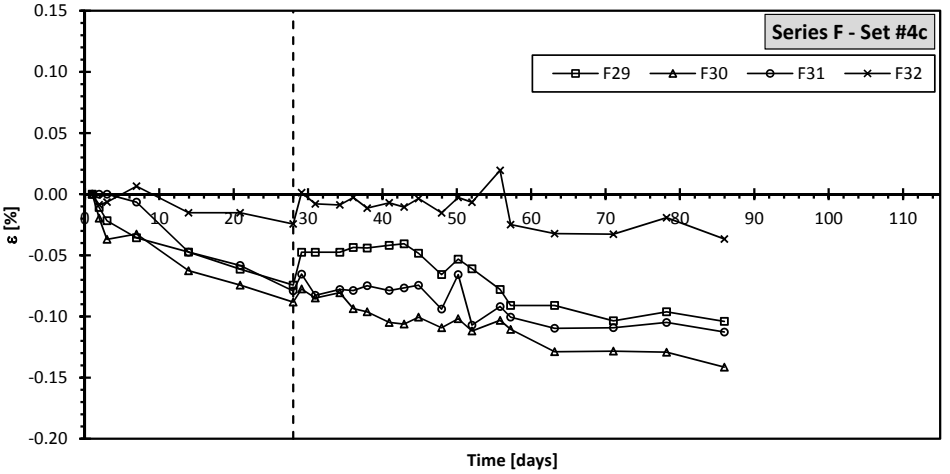

FIGURE A.14: Strain curves corresponding to Series F - Set #4c.

A.3 Interfacial Expansion Tests - Relative mass change curves

A.3.1 Series C

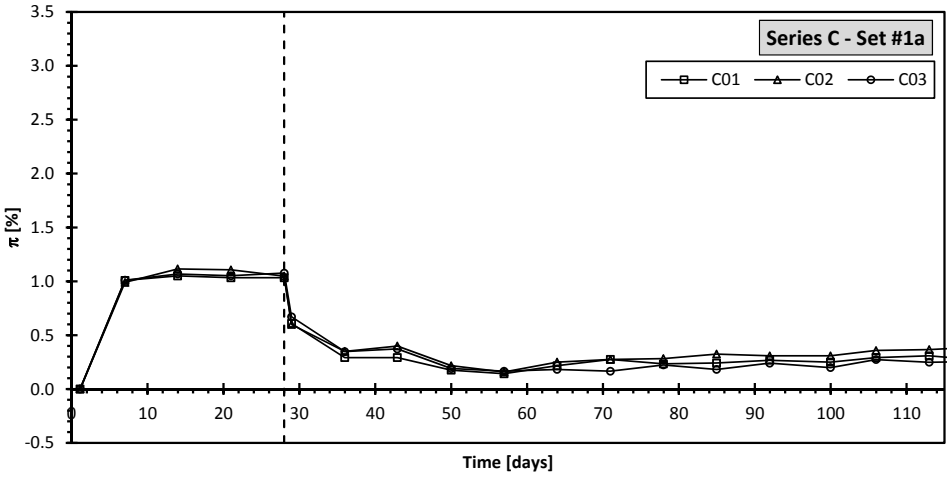

FIGURE A.15: Relative mass change curves corresponding to Series C - Set #1a.

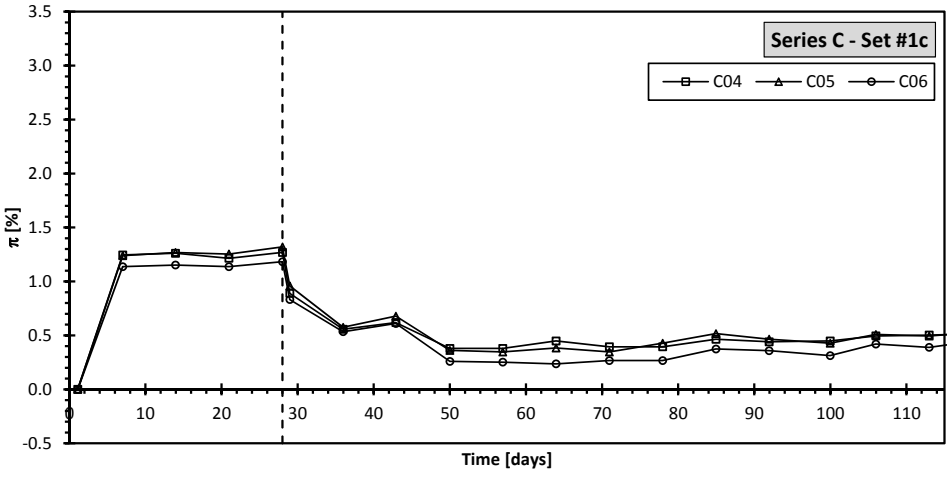

FIGURE A.16: Relative mass change curves corresponding to Series C - Set #1c.

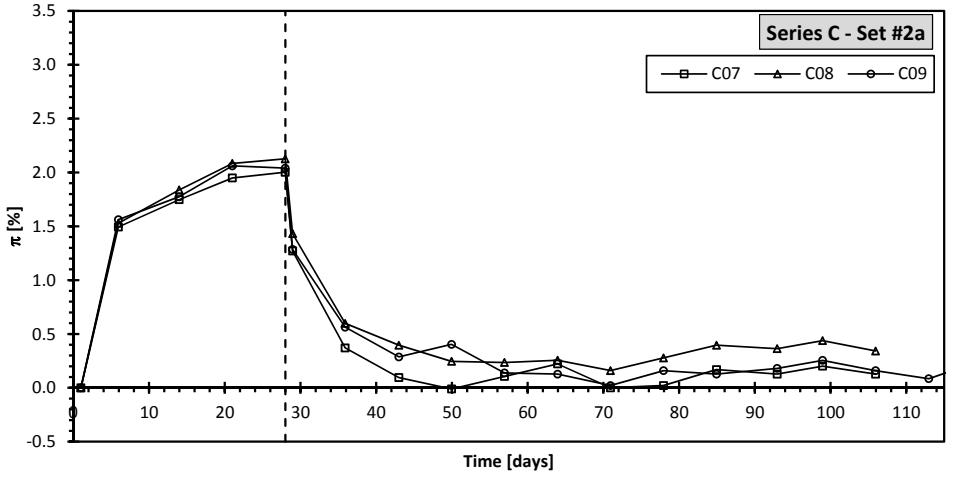

FIGURE A.17: Relative mass change curves corresponding to Series C - Set #2a.

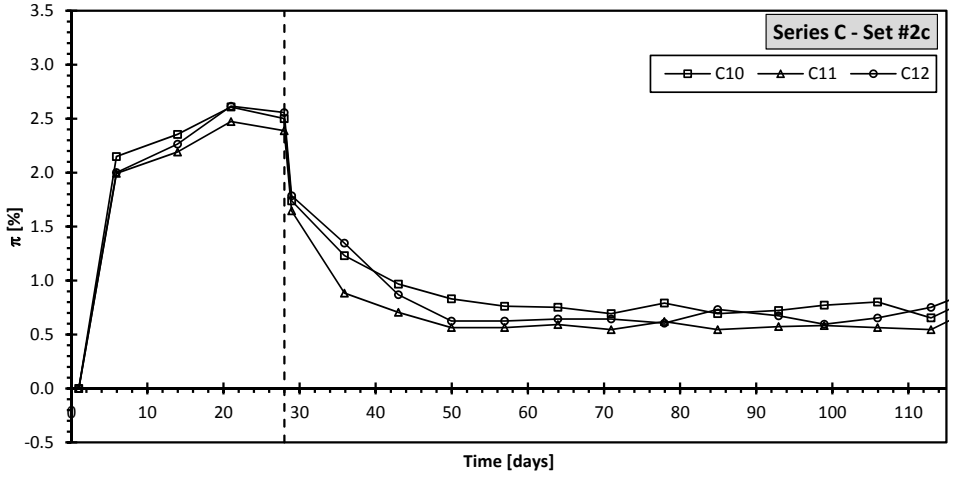

FIGURE A.18: Relative mass change curves corresponding to Series C - Set #2c.

A.3.2 Series D

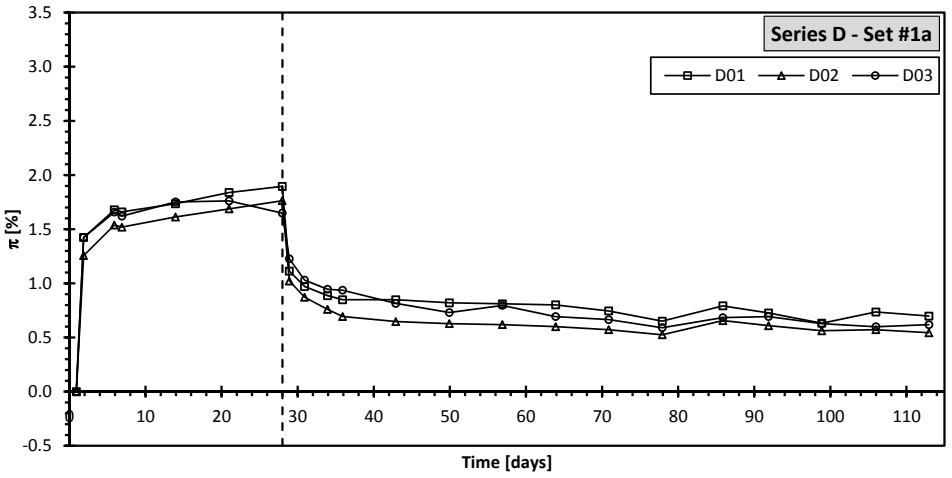

FIGURE A.19: Relative mass change curves corresponding to Series D - Set #1a.

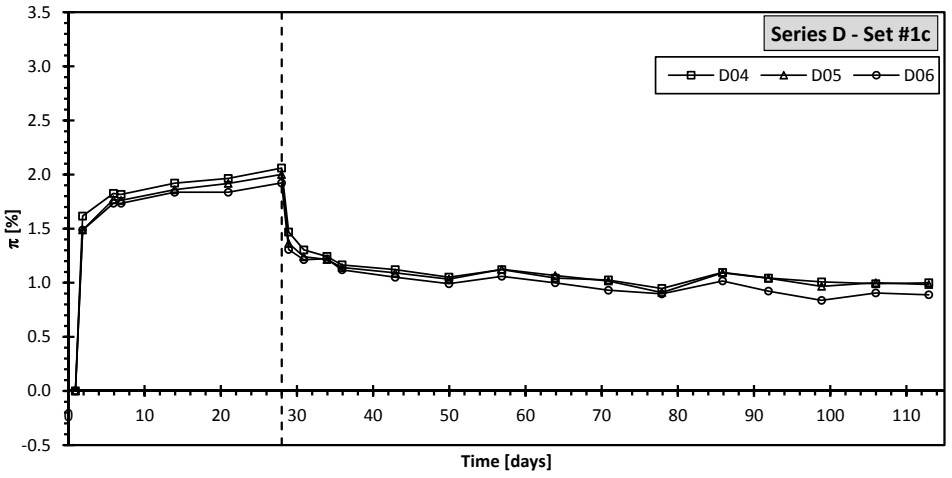

FIGURE A.20: Relative mass change curves corresponding to Series D - Set #1c.

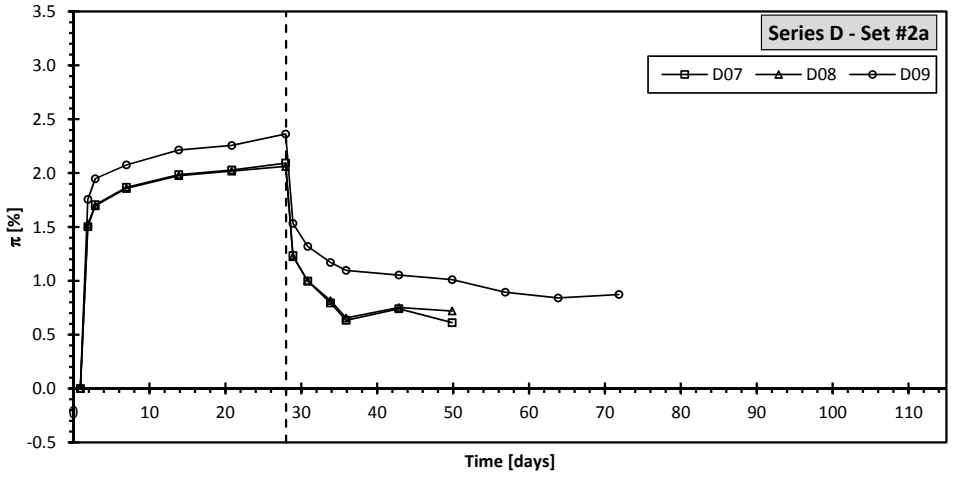

FIGURE A.21: Relative mass change curves corresponding to Series D - Set #2a.

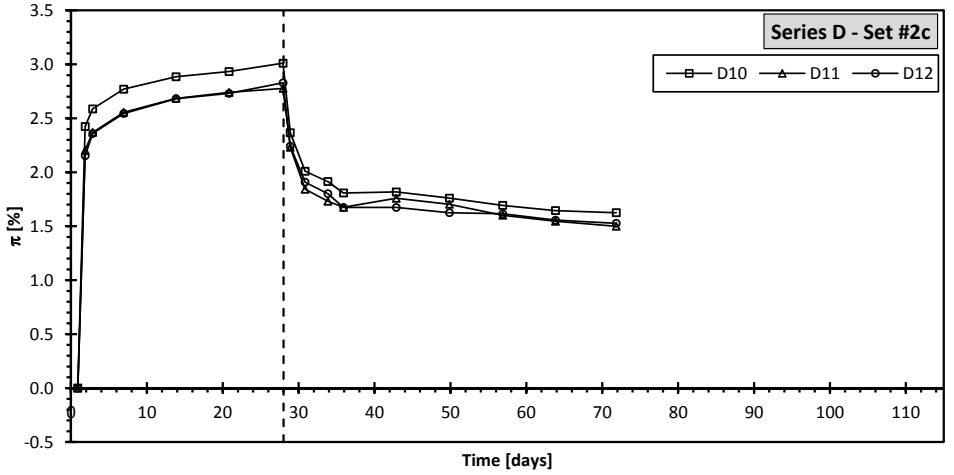

FIGURE A.22: Relative mass change curves corresponding to Series D - Set #2c.

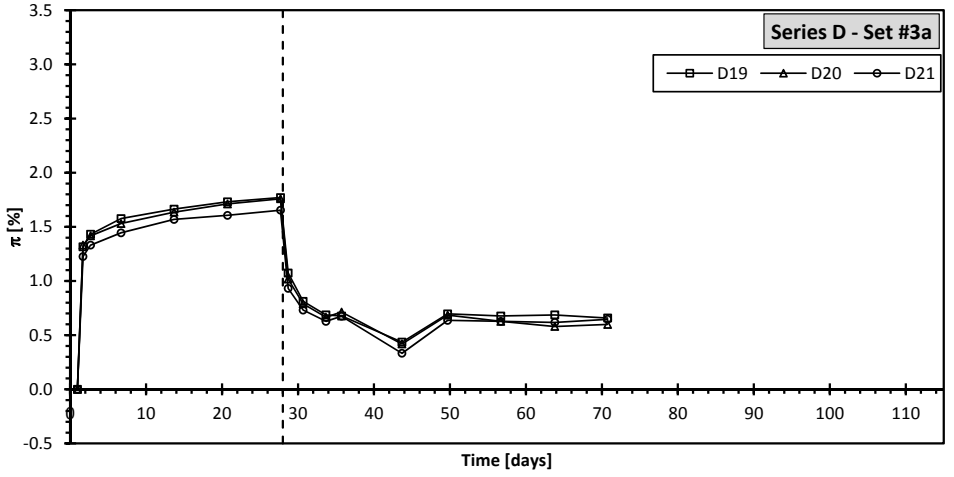

FIGURE A.23: Relative mass change curves corresponding to Series D - Set #3a.

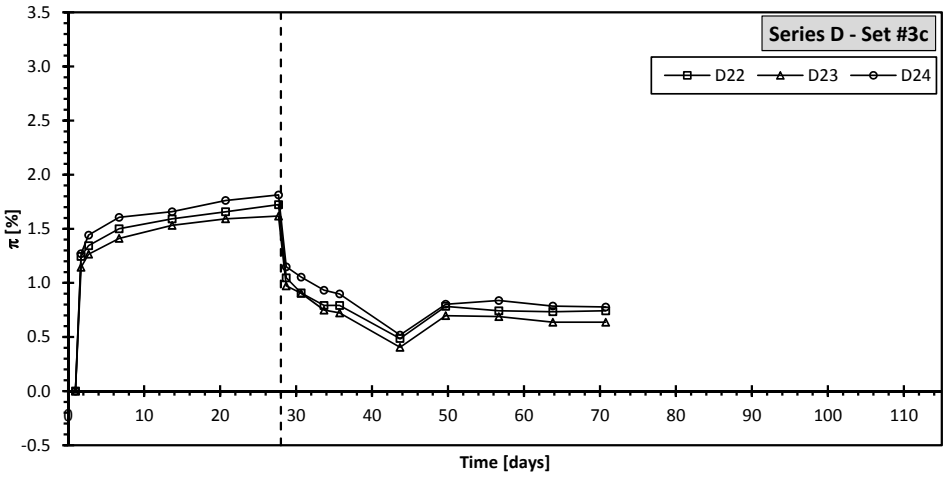

FIGURE A.24: Relative mass change curves corresponding to Series D - Set #3c.

A.3.3 Series E

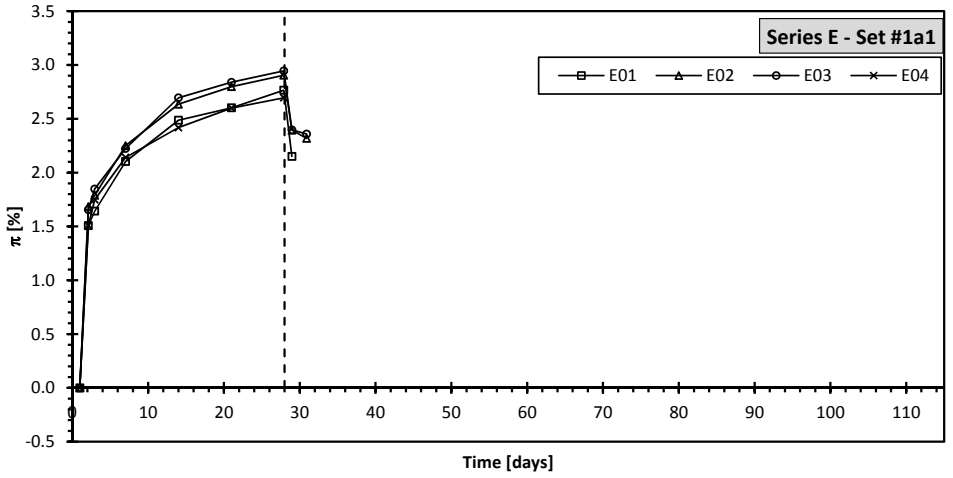

FIGURE A.25: Relative mass change curves corresponding to Series E - Set #1a1.

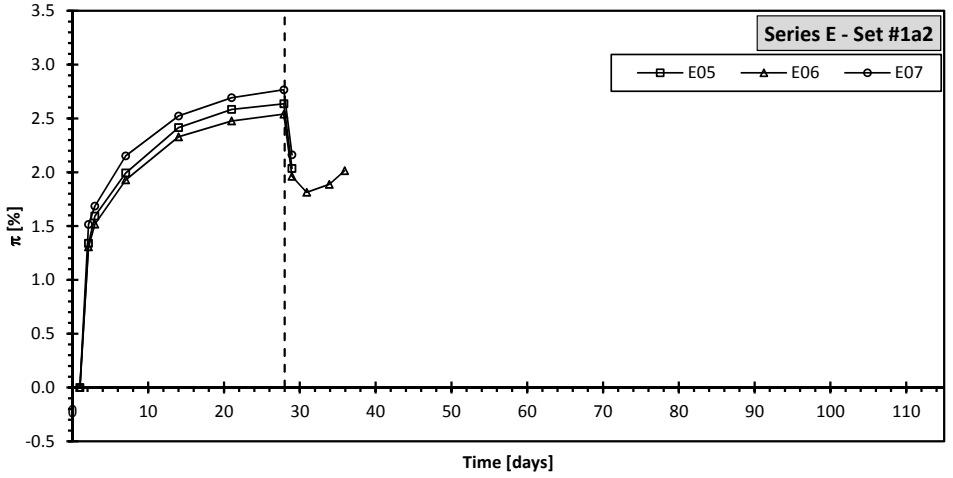

FIGURE A.26: Relative mass change curves corresponding to Series E - Set #1a2.

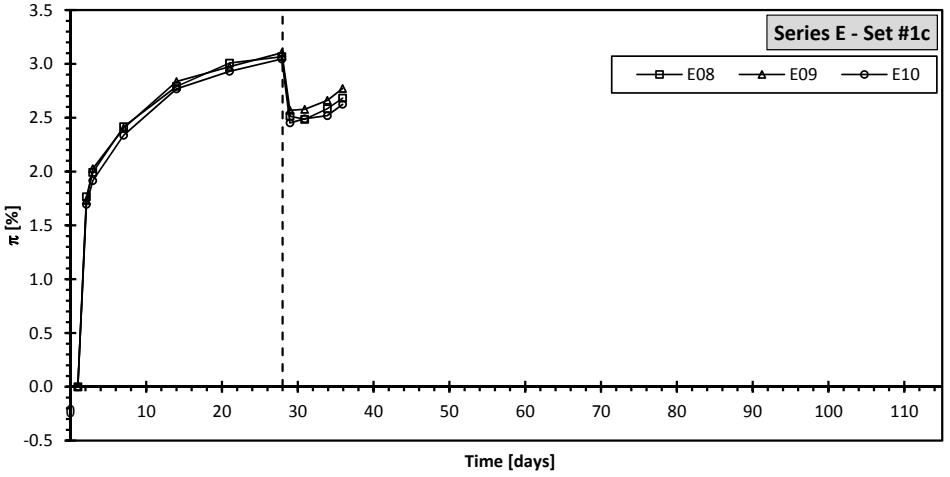

FIGURE A.27: Relative mass change curves corresponding to Series E - Set #1c.

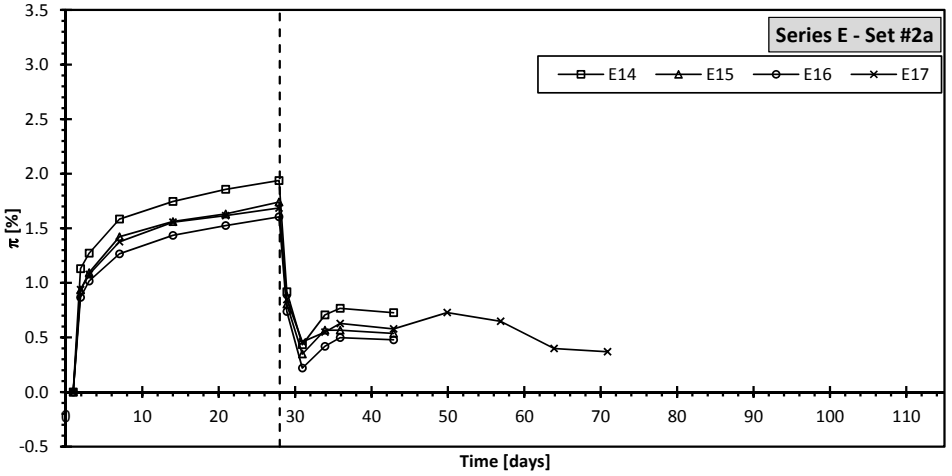

FIGURE A.28: Relative mass change curves corresponding to Series E - Set #2a.

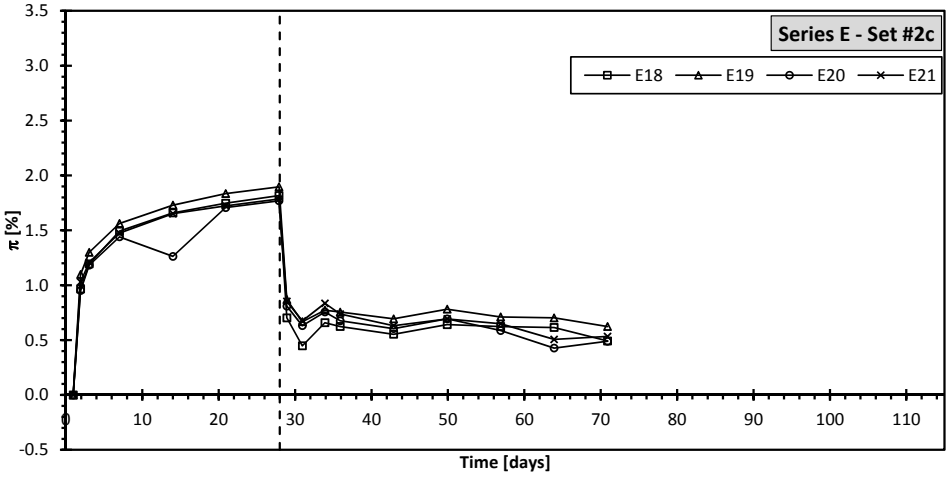

FIGURE A.29: Relative mass change curves corresponding to Series E - Set #2c.

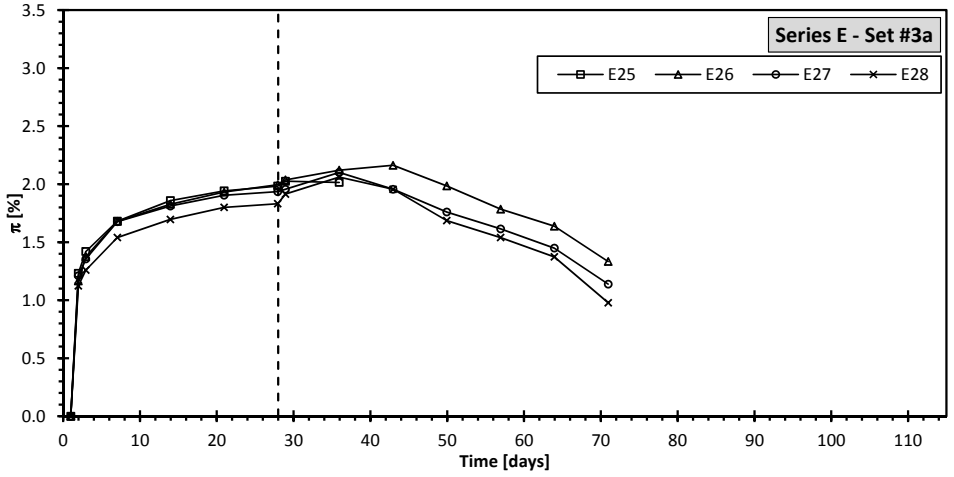

FIGURE A.30: Relative mass change curves corresponding to Series E - Set #3a.

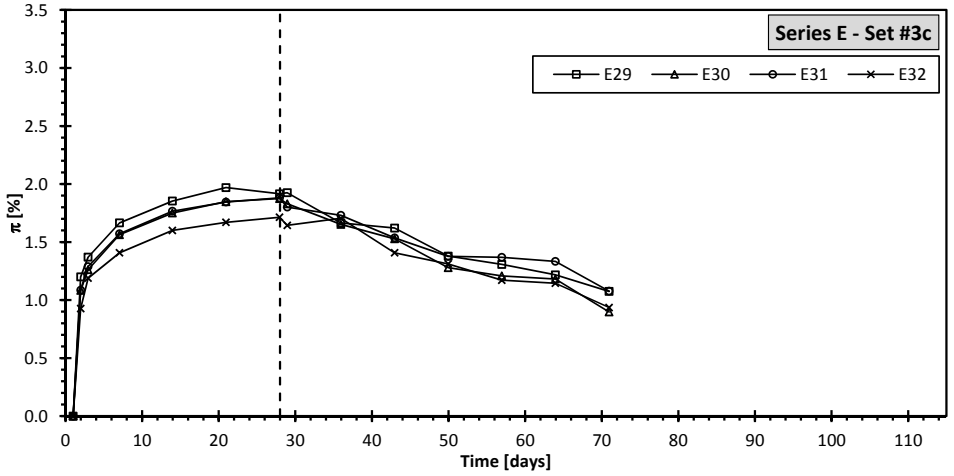

FIGURE A.31: Relative mass change curves corresponding to Series E - Set #3c.

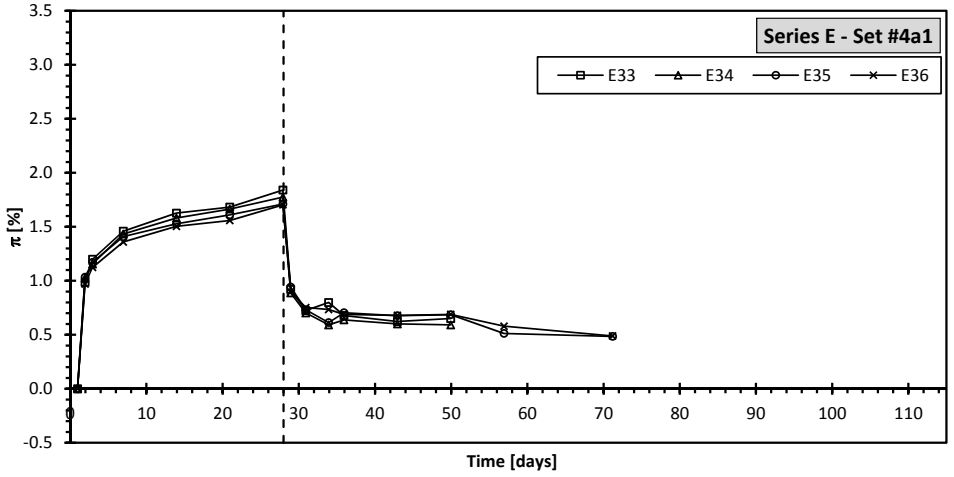

FIGURE A.32: Relative mass change curves corresponding to Series E - Set #4a1.

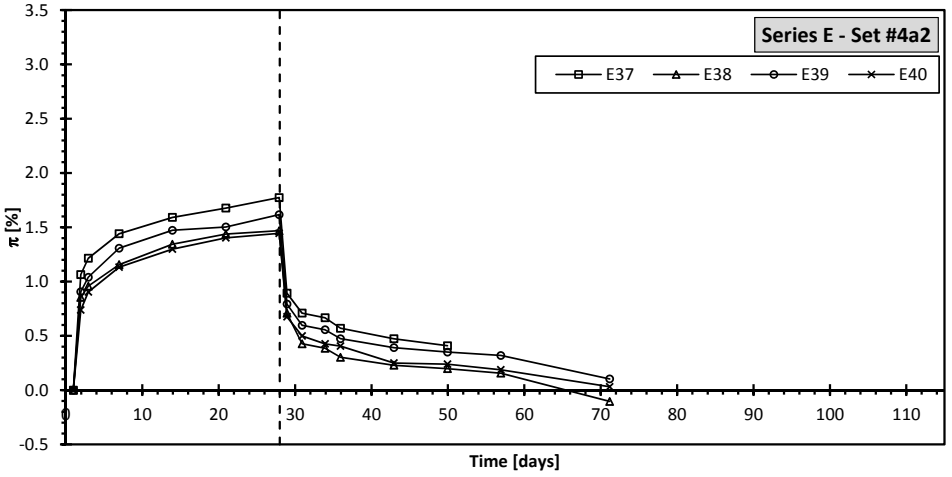

FIGURE A.33: Relative mass change curves corresponding to Series E - Set #4a2.

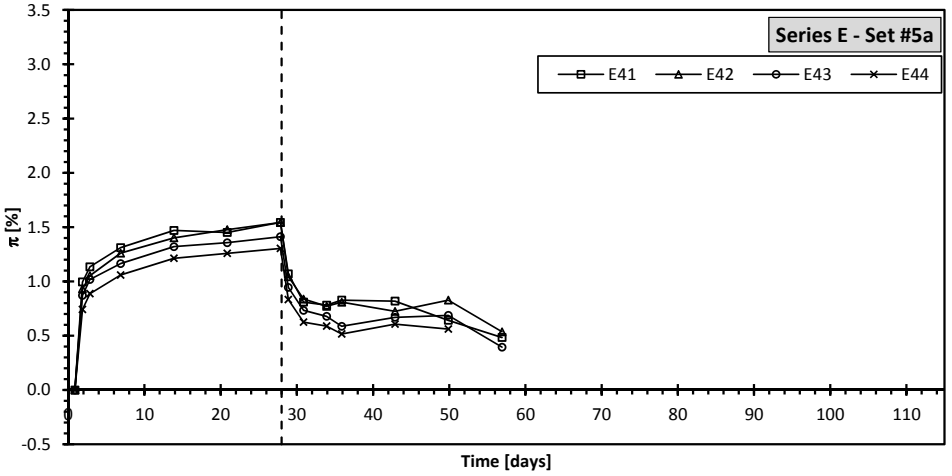

FIGURE A.34: Relative mass change curves corresponding to Series E - Set #5a.

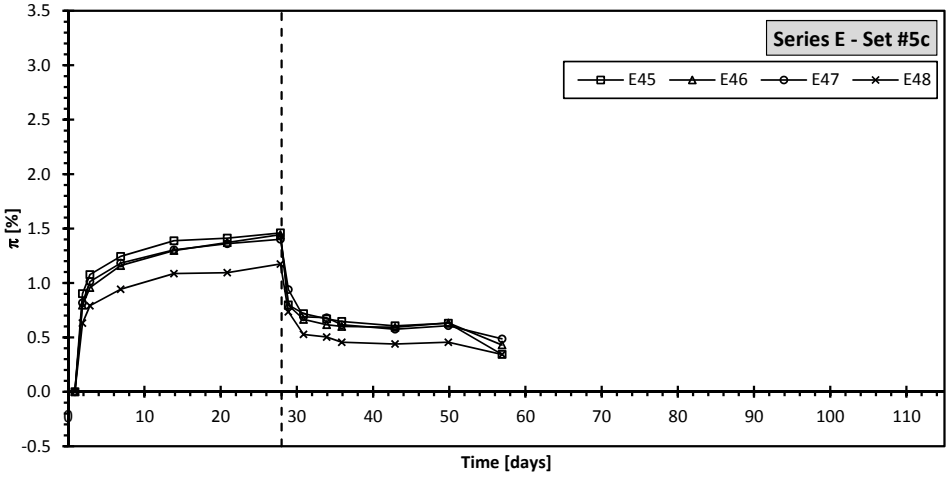

FIGURE A.35: Relative mass change curves corresponding to Series E - Set #5c.

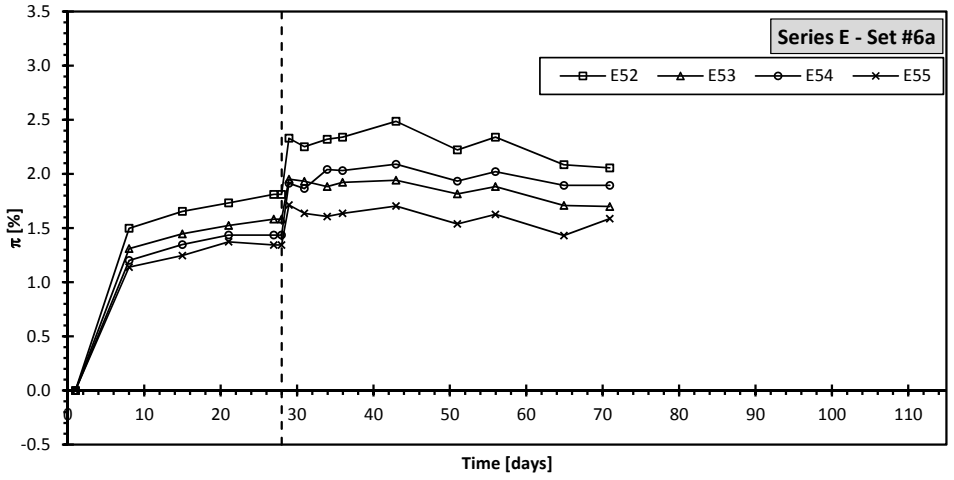

FIGURE A.36: Relative mass change curves corresponding to Series E - Set #6a.

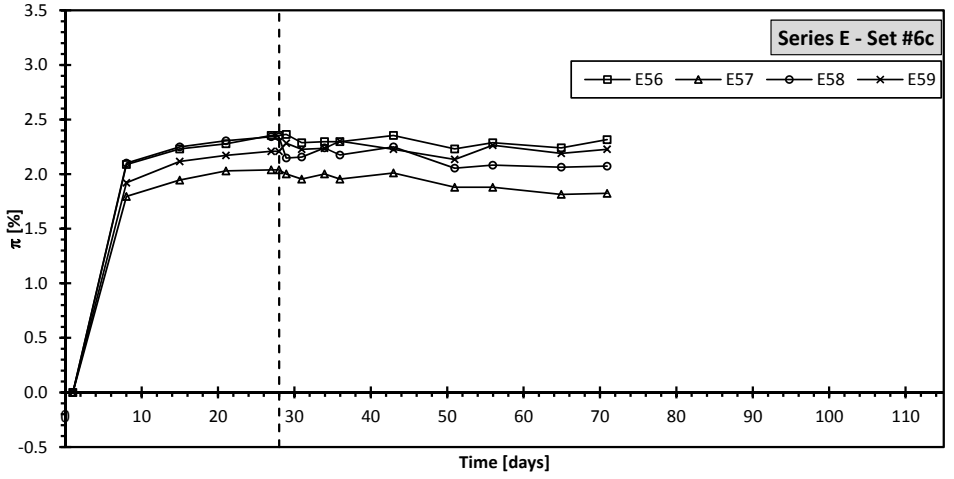

FIGURE A.37: Relative mass change curves corresponding to Series E - Set #6c.

A.3.4 Series F

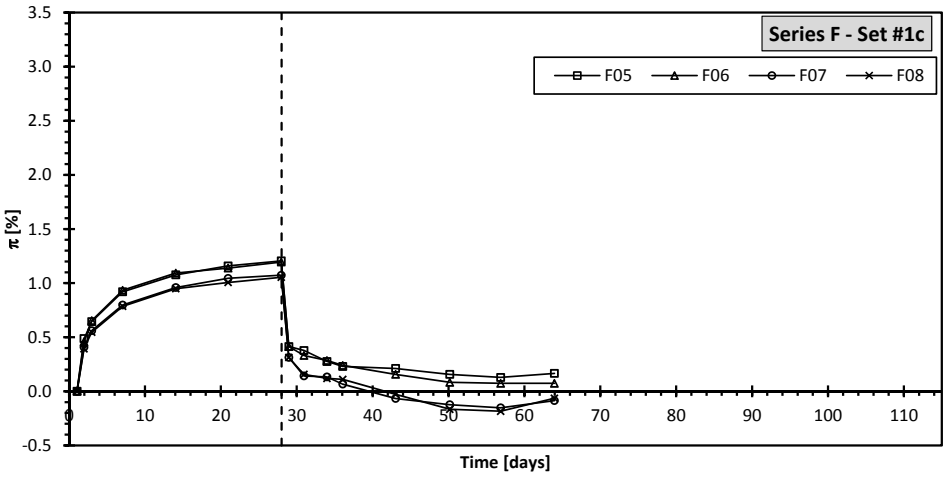

FIGURE A.38: Relative mass change curves corresponding to Series F - Set #1c.

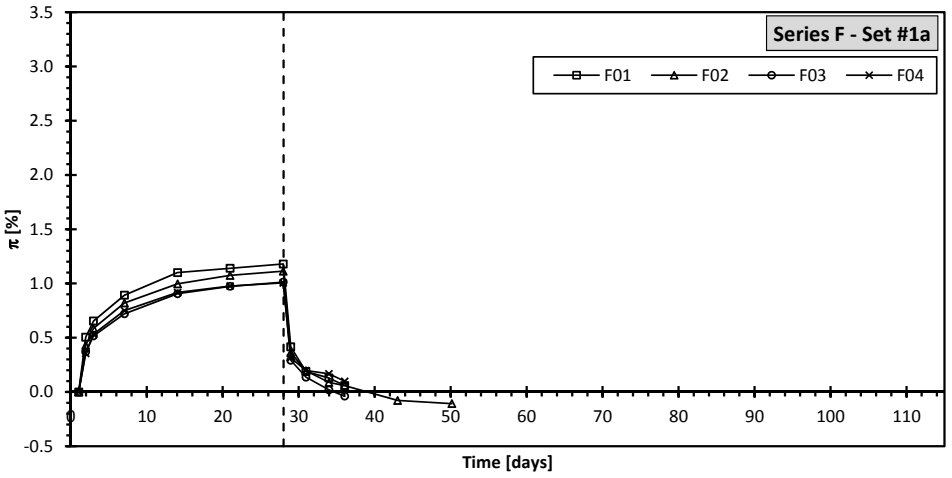

FIGURE A.39: Relative mass change curves corresponding to Series F - Set #1a.

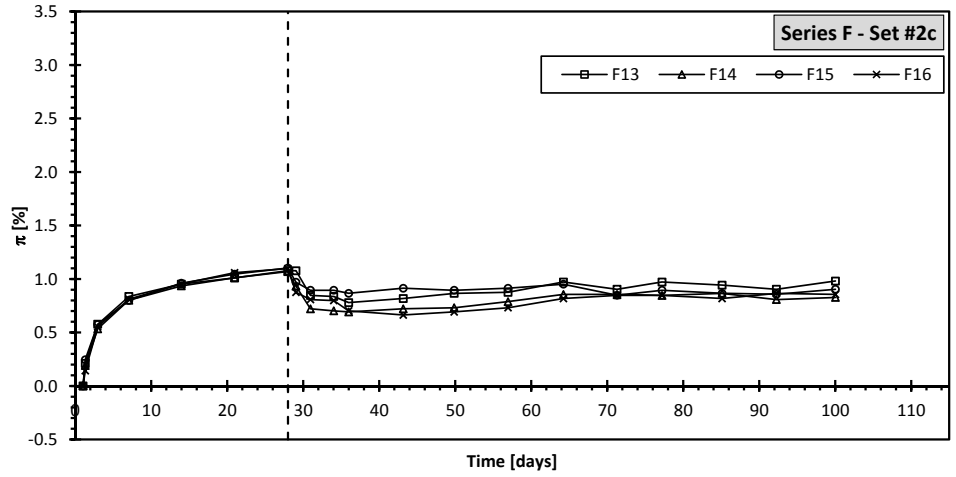

FIGURE A.40: Relative mass change curves corresponding to Series F - Set #2c.

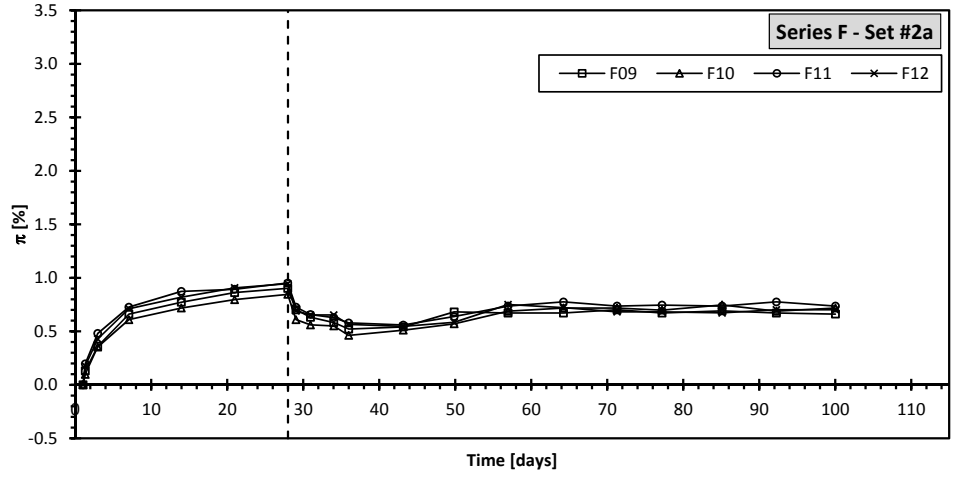

FIGURE A.41: Relative mass change curves corresponding to Series F - Set #2a.

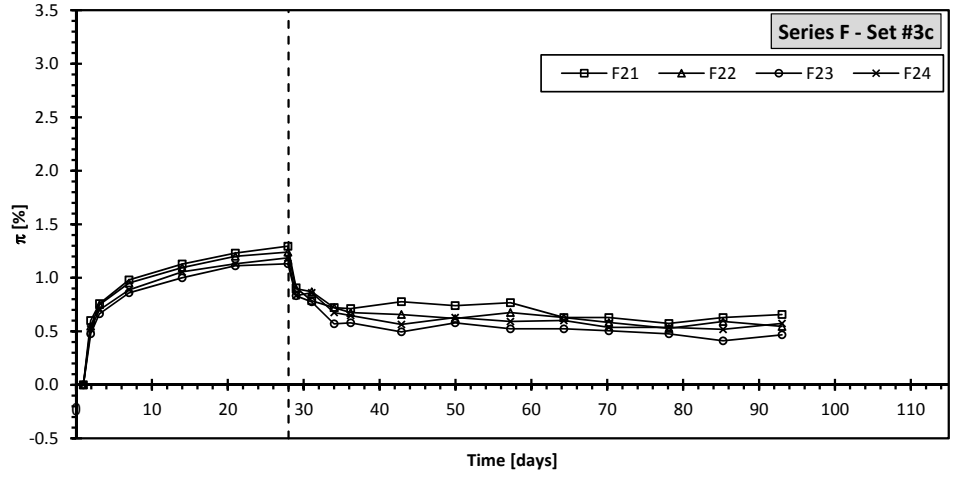

FIGURE A.42: Relative mass change curves corresponding to Series F - Set #3c.

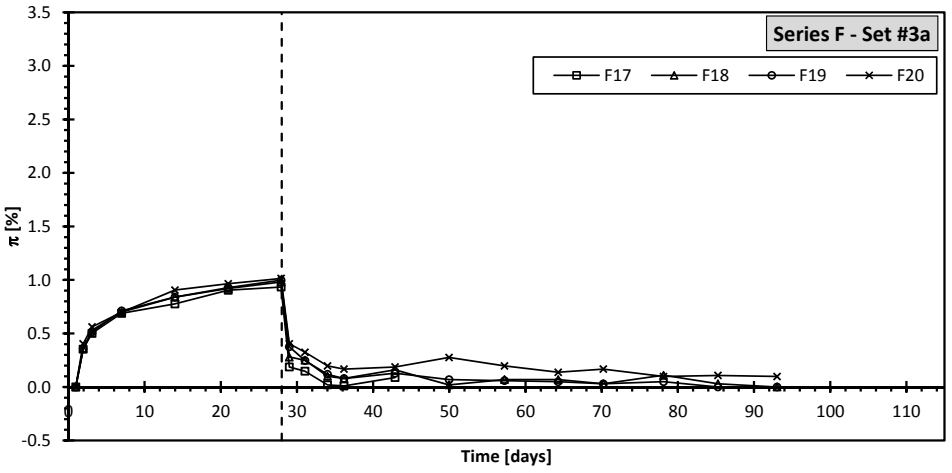

FIGURE A.43: Relative mass change curves corresponding to Series F - Set #3a.

A.4 Interfacial Expansion Tests - SEM/EDS analyses

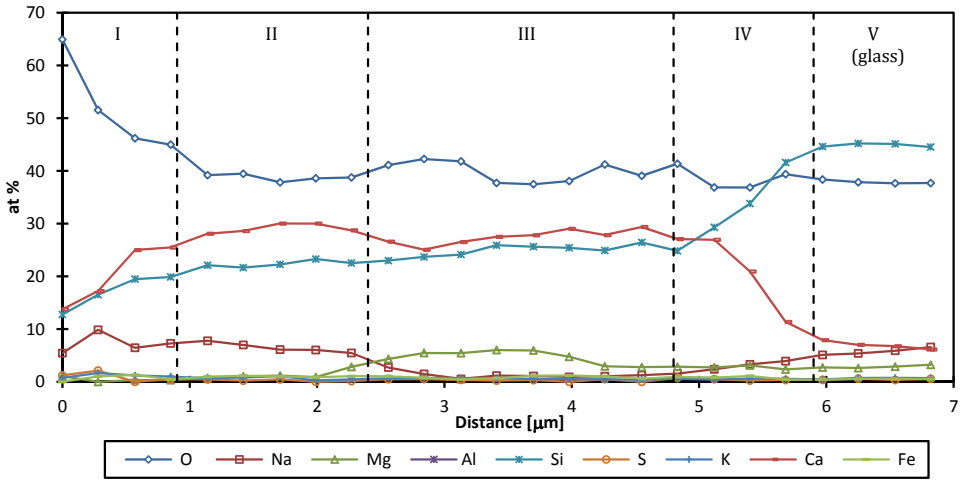

FIGURE A.44: Profile of the atomic composition along line AA of Fig. 3.15.

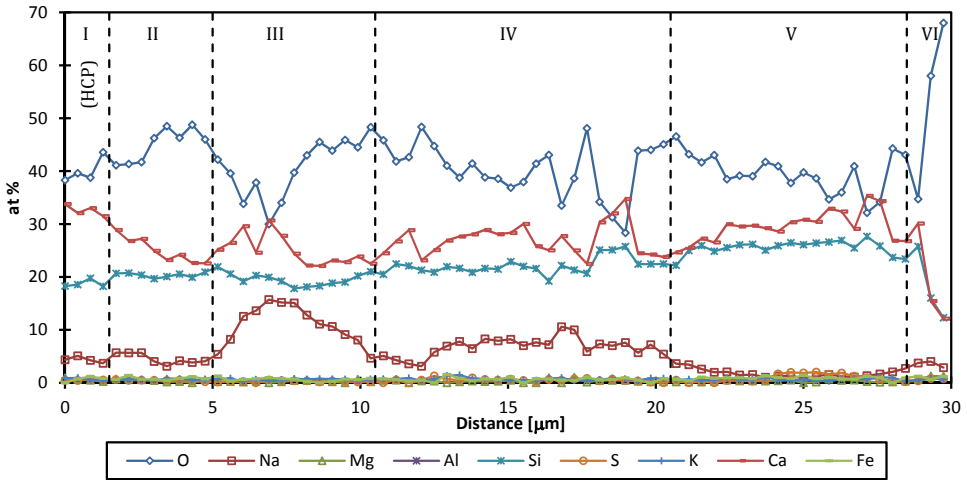

FIGURE A.45: Profile of the atomic composition along line AA of Fig. 3.14.

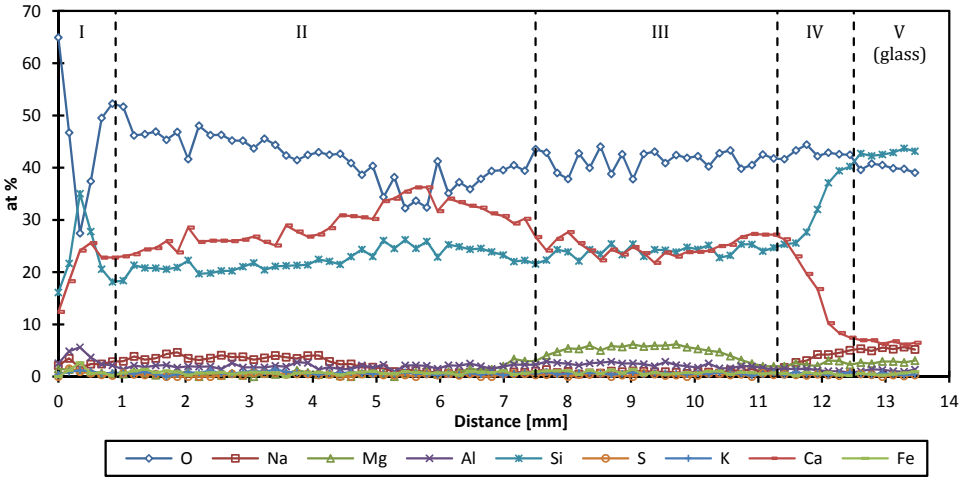

FIGURE A.46: Profile of the atomic composition along line CC of Fig. 3.14.

A.5 Confined Expansion Tests - Complementary tables and figures

Table A.2: Aggregate gradation and composition.

Sieve size (mm)		**Reactive Concrete**		**Control Concrete**	
Passing	Retained	wt%	Material	wt%	Material
12.70	9.52	29.3	glass	30.3	limestone
9.52	4.55	29.3	glass	30.3	limestone
4.55	2.50	4.1	glass	n/a	n/a
4.55	2.50	4.4	limestone	4.7	limestone
2.50	1.20	15.6	limestone	16.5	limestone
1.20	0.60	9.0	limestone	9.6	limestone
0.60	0.30	3.7	limestone	3.9	limestone
0.30	0.15	3.0	limestone	3.1	limestone
0.15	bottom	1.5	limestone	1.6	limestone

Table A.3: Average stresses and temperature during the ASR confined expansion tests. av = average; sd = standard deviation.

Specimen	σ_x [MPa]		σ_y [MPa]		σ_z [MPa]		T [°C]	
	av	sd	av	sd	av	sd	av	sd
Free Exp.	0.00	n/a	0.00	n/a	0.00	n/a	59.95	0.33
TM-02	-0.99	0.01	-1.00	0.02	-1.00	0.01	59.94	0.16
TM-21	-1.04	0.01	-1.05	0.02	-1.04	0.01	59.94	0.23
TM-03	-0.99	0.01	-1.00	0.02	-1.00	0.01	59.84	0.13
TM-19	-1.02	0.01	-1.04	0.02	-1.03	0.01	59.92	0.27
TM-11	-9.01	0.04	-9.06	0.04	-1.02	0.02	59.88	0.22
TM-20	-9.04	0.03	-9.09	0.03	-1.04	0.03	59.91	0.21
TM-08	-9.12	0.11	-9.17	0.11	-1.01	0.03	59.98	0.19
TM-15	-9.04	0.03	-9.09	0.03	-1.04	0.03	59.95	0.21
TM-14	-9.10	0.09	-9.15	0.09	-9.12	0.09	59.96	0.45
TM-22	-9.06	0.04	-9.10	0.04	-9.08	0.04	59.94	0.21
TM-09	-9.02	0.06	-9.07	0.06	-9.04	0.06	59.94	0.33
TM-16	-9.06	0.03	-9.10	0.03	-9.08	0.03	59.96	0.18

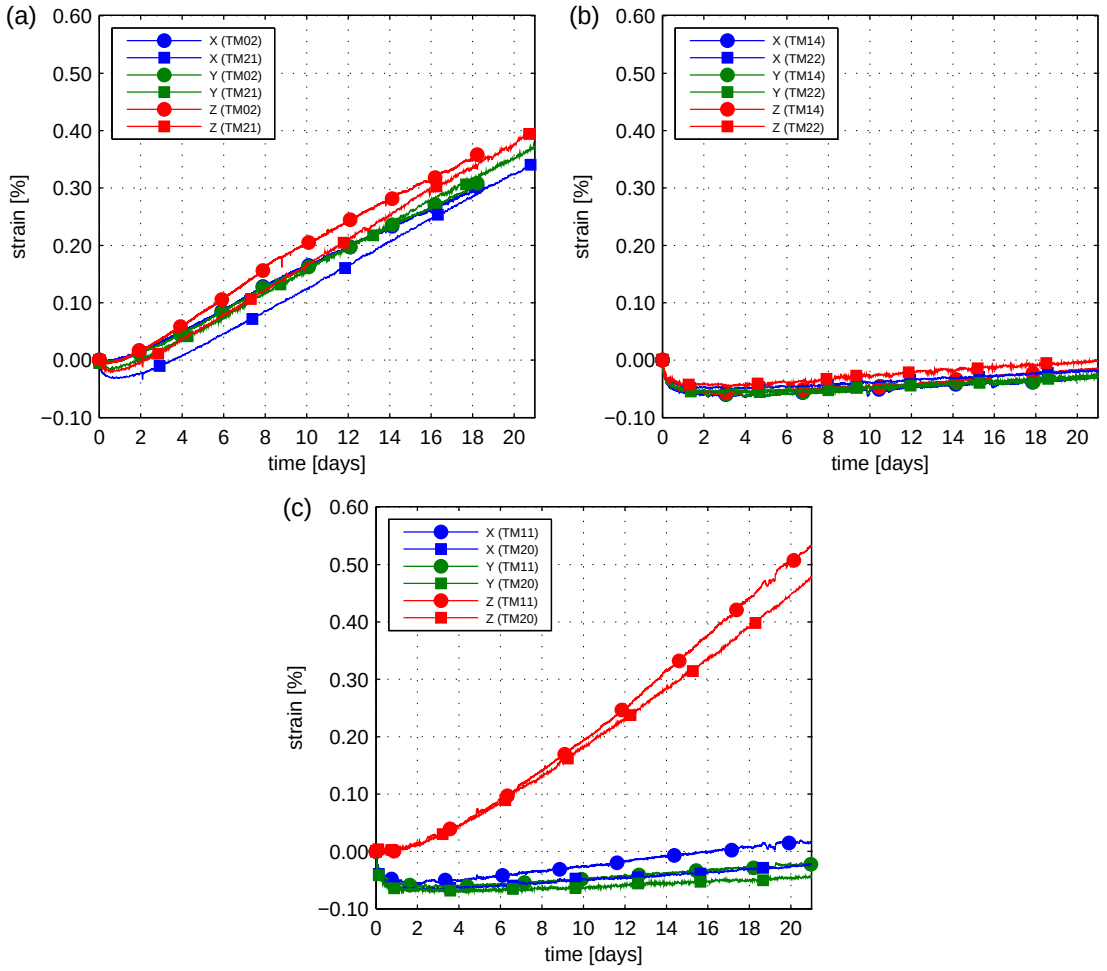

FIGURE A.47: Axial strain curves without deducting any creep effects of reactive specimens under (a) 1-1-1, (b) 9-9-9, and (c) 9-9-1 load cases.

A.6 Confined Expansion Tests - Creep deduction in confined expansion tests

The simplest possible creep deduction procedure was based in three assumptions. The first one was that the measured strains of the reactive specimens $\mathbf{e}^{rea} = \begin{bmatrix} \varepsilon_x^{rea} & \varepsilon_y^{rea} & \varepsilon_z^{rea} \end{bmatrix}$ were the addition of two independent terms, on one hand the ASR expansion term ($\mathbf{e}^{asr}$) and on the other the 'creep' strain term $\mathbf{e}^{cr}$, i.e.

$$\mathbf{e}^{rea} = \mathbf{e}^{asr} + \mathbf{e}^{cr} \tag{A.1}$$

The second assumption was that the creep strains in the reactive specimens were the same as those measured in the control specimens ($\mathbf{e}^{con}$) under the same conditions, i.e.

$$\mathbf{e}^{cr} = \mathbf{e}^{con} \tag{A.2}$$

Finally, the third assumption was that the strains developed by the control specimens subject to a constant stress state can be properly approximated with a function $C_i(t)$ which is fitted independently for each axis of loading i,

$$C_i(t) = \begin{cases} 0 & \text{if} \quad t \leq t_i \\ m_i \ln t + b_i & \text{if} \quad t > t_i \end{cases} \tag{A.3}$$

where t is the time elapsed since the moment when the specimen is loaded (beginning of the test), $t_i = \exp(-b_i/m_i)$, b_i and m_i are fitting parameters. Best fitting values of m_i and b_i were obtained for each tested control specimen by applying the least squares method (see Table A.4).

Under these three assumptions, the ASR expansion curves for a given stress state was readily obtained as:

$$\mathbf{e}^{asr} = \mathbf{e}^{rea} - \mathbf{C}(t) \tag{A.4}$$

TABLE A.4: Best fitting parameters m_i and b_i of function A.3 for each tested control specimen obtained applying the least square method (R^2 is the coefficient of determination). Valid for time t expressed in [h] and strains e_i expressed in [%].

Load case	**Specimen**	i	m_i [$\times 10^{-3}$]	b_i [$\times 10^{-3}$]	R^2
1-1-1	TM-03	X	-0.857	-2.666	0.53
		Y	-0.999	0.172	0.66
		Z	-0.699	-4.012	0.46
	TM-19	X	-2.070	-15.385	0.56
		Y	-3.607	-17.340	0.81
		Z	-5.502	-20.825	0.89
9-9-9	TM-09	X	-7.433	-14.826	0.97
		Y	-8.993	-15.062	0.97
		Z	-5.867	-12.389	0.96
	TM-16	X	-5.831	-18.033	0.94
		Y	-5.899	-16.776	0.90
		Z	-6.228	-16.751	0.94
9-9-1	TM-08	X	-3.543	-4.268	0.89
		Y	-4.815	-5.984	0.96
		Z	-0.706	0.667	0.27
	TM-15	X	-8.203	-18.506	0.96
		Y	-8.457	-18.698	0.98
		Z	-3.371	-14.193	0.65

A.7 Confined Expansion Tests - Preliminary free expansion tests

Previous to the confined expansion tests presented in Chapter 4, some preliminary free expansion tests were performed in order to adopt the most suitable concrete mixtures.

A.7.1 Description

The tested specimens are listed in Table A.5. The specimen were prismatic (75 × 75 × 295 mm) with stainless steel gauge inserts disposed in the main axis for length change measuring. Three different concretes were tested. The first one called 'Control Concrete' was made only with non-reactive (crushed limestone) aggregates. The other two concretes, called 'Reactive Concrete A' and 'Reactive Concrete B', in contrast, were made using the same mixture but replacing the coarser fractions of aggregates with crushed colorless soda-lime glass as reactive aggregates, as indicated in Table A.6. The Portland cement was type CEM I 42,5 N-SR5 according to the Spanish standard UNE-EN 197-1 [3]. The oxide composition of the cement is given in Table A.1, cement PC03, of the Appendix A.1. The three mixtures had a cement content of 420 kg/m^3 and water/cement weight ratio of 0.45. The alkali level of the concrete was raised to 5.25 kg/m^3 Na_2O_{eq} by adding NaOH to the mixing water.

TABLE A.5: List of tested specimens

Concrete	**Specimens**	**Curing period**
Control	A05 to A07	27 days
Reactive A	A01 to A03	28 days
Reactive A	A04	77 days
Reactive B	B01 to B03	28 days

TABLE A.6: Aggregate gradation and composition.

Sieve size (mm)		**Control Concrete**		**Reactive Concrete A**		**Reactive Concrete B**	
Pass.	Ret.	wt%	Material	wt%	Material	wt%	Material
12.70	9.52	29.3	limestone	30.3	glass	29.3	glass
9.52	4.55	29.3	limestone	30.3	glass	29.3	glass
4.55	2.50	4.1	limestone	3.9	limestone	4.1	glass
2.50	1.20	10.4	limestone	9.9	limestone	10.3	limestone
1.20	0.52	10.4	limestone	9.9	limestone	10.3	limestone
0.52	0.30	10.4	limestone	9.9	limestone	10.3	limestone
0.30	0.15	6.2	limestone	5.9	limestone	6.2	limestone

After casting, the specimens remained in moulds for 24 h at room temperature and with the exposed surface covered with a plastic film in order to prevent moisture loss.

Once demolded, specimens were put in 19 L airtight plastic containers (maximum 3 per container) filled with 1 m NaOH solution at room temperature (21±2 °C) for the periods indicated in Table A.6. After curing, the containers were placed in an oven at 60 °C until the end of the tests. During both stages, specimens were regularly removed for measuring length and weight changes, and immediately returned to the alkaline bath. Measuring procedure was similar to the one described in Section 3.3.4.

A.7.2 Results

Axial strain curves and weight change curves of the specimens listed in Table A.6 are presented in Figs. A.48 and A.49, respectively.

During the curing stage there were practically no length changes in both control and reactive specimens. When the bath temperature was changed from 22 to 60 °C, all the specimens experienced a sudden thermal expansion (≈0.10%). After that, control specimen remained without length changes, but the reactive specimens started to expand. For similar curing periods, specimens made with Reactive Concrete B developed higher initial expansion rates than the specimens made with Reactive Concrete A. However, after 20 days at 60 °C both sets of specimens showed similar expansion rates. Significantly, specimen A04 (Fig. A.48, middle) which was cured for an extended period of 77 days developed much higher expansion rate than the other reactive specimens cured for 28 days.

With regard to the weight changes, all the specimens gained weight (0.20-0.40 %) during the curing stage. When heated from 22 to 60 °C, all the specimen experienced sudden weight drops. After that, the weight of control specimens continued decreasing during the following 20 days, and then slowly started to increase again. The weight of the reactive specimens, in contrast, started to growth after the sudden drops in close correlation with the measured axial expansions (see Fig. A.50). The reason why the weight growths with the ASR expansions is not clear, but it may be due to the fixation of water coming from the alkaline bath both in the ASR products and in the induced microcracks.

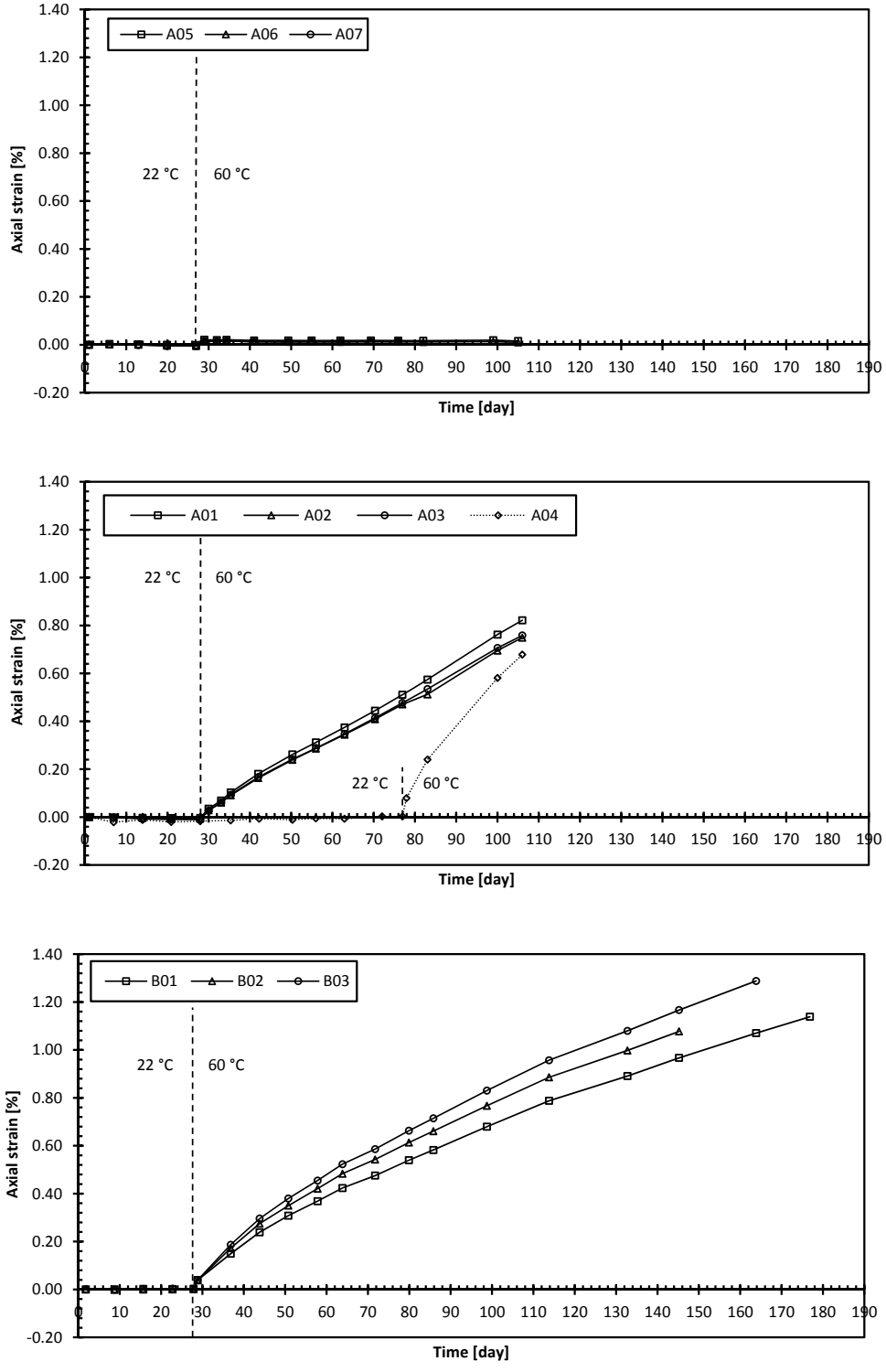

FIGURE A.48: Axial strain curves of specimens made with Control Concrete (top), Reactive Concrete A (middle), and Reactive Concrete B (bottom).

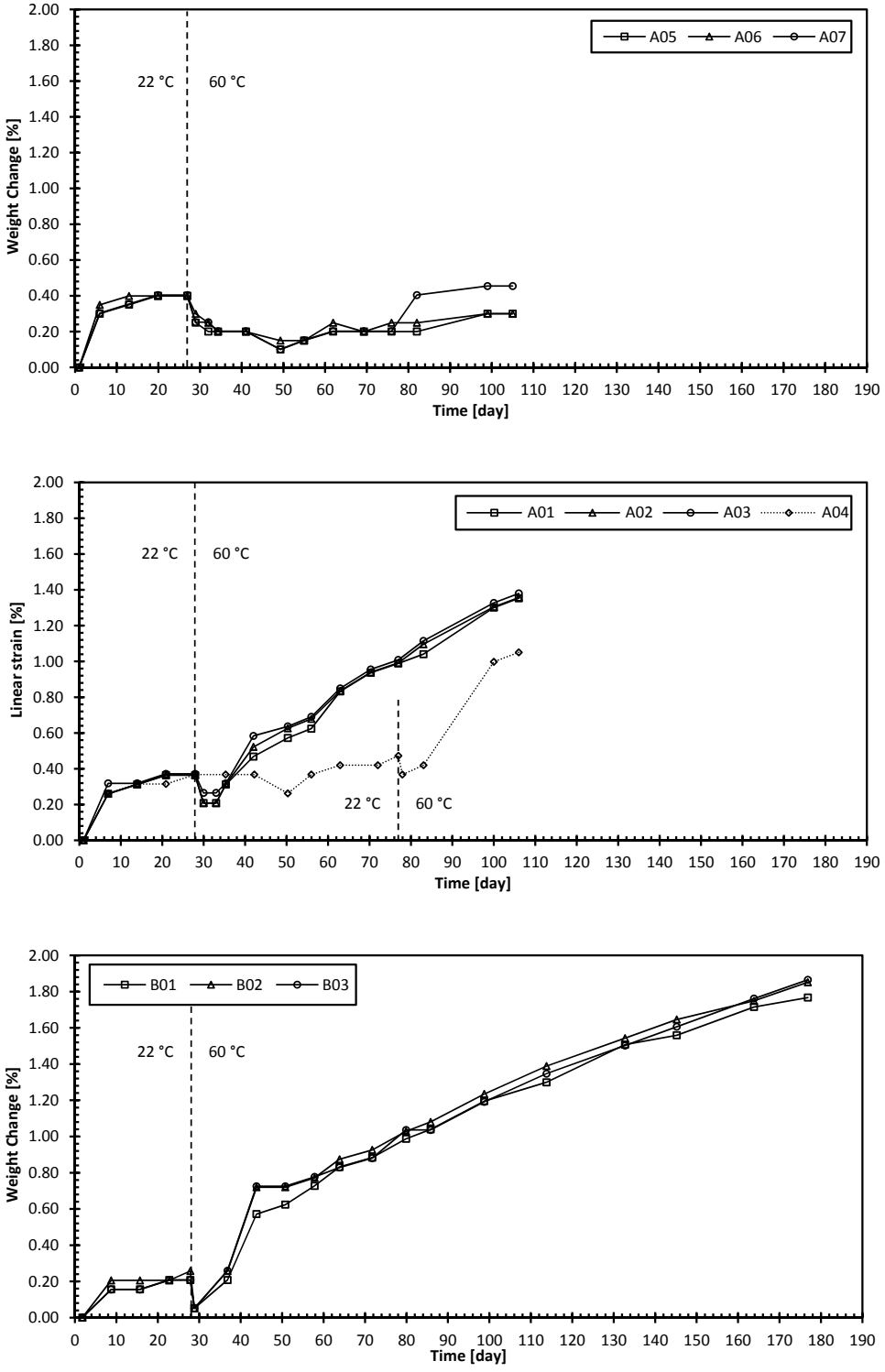

FIGURE A.49: Weight change of prismatic specimens made with Control Concrete (top), Reactive Concrete A (middle), and Reactive Concrete B (bottom).

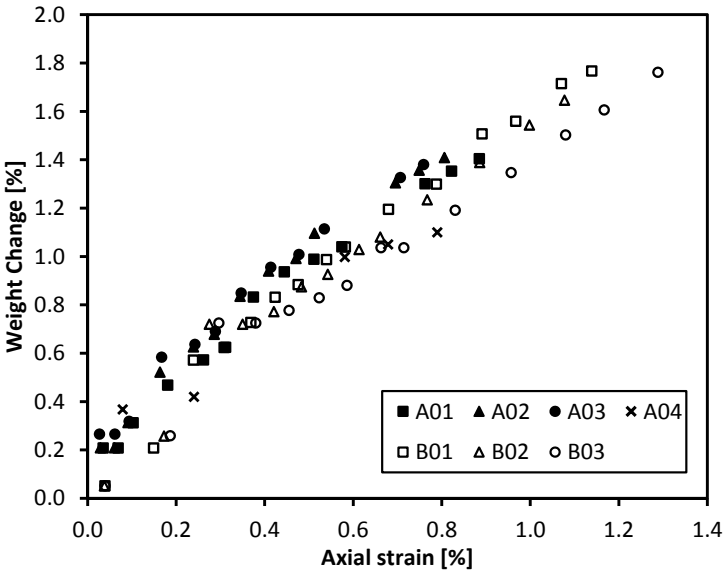

FIGURE A.50: Weight change versus Axial Strain of prismatic specimens made with reactive concretes A and B. Points corresponding to the curing stage are not plotted.

Appendix B

Numerical modelling appendices

B.1 Calcium and alkali stoichiometric coefficients of RPA and RPB

The overall composition of the reaction product (RP) at a given location is given as a mixture of two components (RPA and RPB) in a proportion given by a weighting factor x, as follows

$$x\text{RPA} + (1-x)\text{RPB} \longrightarrow \text{RP}; \quad 0 \leq x \leq 1 \tag{B.1}$$

The compositions of RPA and RPB in terms of generic stoichiometric coefficients a_i and b_i are given in Eqs. (6.3) and (6.4), respectively. From there, the anhydrous composition of RP as function of the weighting factor x is obtained:

$$\text{RP} \equiv (\text{SiO}_2)(\text{CaO})_{xa_1+(1-x)b_1}(\text{R}_2\text{O})_{xa_2/2+(1-x)b_2/2} \tag{B.2}$$

Lets now define the atomic percentage (at%) of silica, calcium and alkalis in the anhydrous RP as

$$\text{Si at\%} = \frac{nSi}{nSi + nCa + nR} \times 100 \tag{B.3}$$

$$\text{Ca at\%} = \frac{nCa}{nSi + nCa + nR} \times 100 \tag{B.4}$$

$$\text{R at\%} = \frac{nR}{nSi + nCa + nR} \times 100 \tag{B.5}$$

where the atoms of oxygen have not been considered, and nSi, nCa and nR are the number of moles of Si, Ca, and R, per mole of RP. Replacing nSi, nCa and nR with

the stoichiometric coefficients of Eq. (B.2), leads to:

$$\text{Si at\%} = \frac{1}{1 + x(a_1 + a_2) + (1-x)(b_1 + b_2)} \times 100 \tag{B.6}$$

$$\text{Ca at\%} = \frac{xa_1 + (1-x)b_1}{1 + x(a_1 + a_2) + (1-x)(b_1 + b_2)} \times 100 \tag{B.7}$$

$$\text{R at\%} = \frac{xa_2 + (1-x)b_2}{1 + x(a_1 + a_2) + (1-x)(b_1 + b_2)} \times 100 \tag{B.8}$$

After combining Eqs. (B.6) and (B.7), the linear relation given in Eq. (B.9) is found, with dimensionless constants m and b given by Eqs. (B.10) and (B.11).

$$\text{Ca at\%} = m\ \text{Si at\%} + b \tag{B.9}$$

$$m = b_1 - \frac{a_1 - b_1}{a_1 + a_2 - b_1 - b_2}(1 + b_1 + b_2) \tag{B.10}$$

$$b = \frac{a_1 - b_1}{a_1 + a_2 - b_1 - b_2} \times 100 \tag{B.11}$$

Note that Eq. (B.9) is only defined between the limit values of Si at% given by the compositions of RPA and RPB, i.e.

$$\text{Si at\%} \in \left[\frac{100}{1 + a_1 + a_2}, \frac{100}{1 + b_1 + b_2}\right] \tag{B.12}$$

Constants m and b can be obtained by plotting measured compositions of ASR products (typically obtained from EDS analysis) in terms of Ca at% versus Si at%, and making a linear regression. Suitable sets of stoichiometric coefficients (a_1, a_2, b_1,b_2) are those which return the fitted values of m and b when replaced in Eqs. (B.10) and (B.11), making it possible at the same time to represent the whole range of compositions experimentally measured.

To illustrate the procedure, in Fig. B.1, experimental composition of ASR reaction products reported by Rajabipour et al. [174] are plotted, in terms of the above-defined Ca at% versus Si at%, together with their linear regression and the linear function given in Eq. (B.9). The resulting values of the stoichiometric coefficients are $a_1 = 1.6$, $a_2 = 0.14$, $b_1 = 0.25$, $b_2 = 0.40$.

Note that there is no unique set of suitable stoichiometric coefficients. This procedure imposes a restriction to the values of a_1, a_2, b_1, and b_2 to be used in the simulations, but their final value will depend also on their effect on the ASR kinetics.

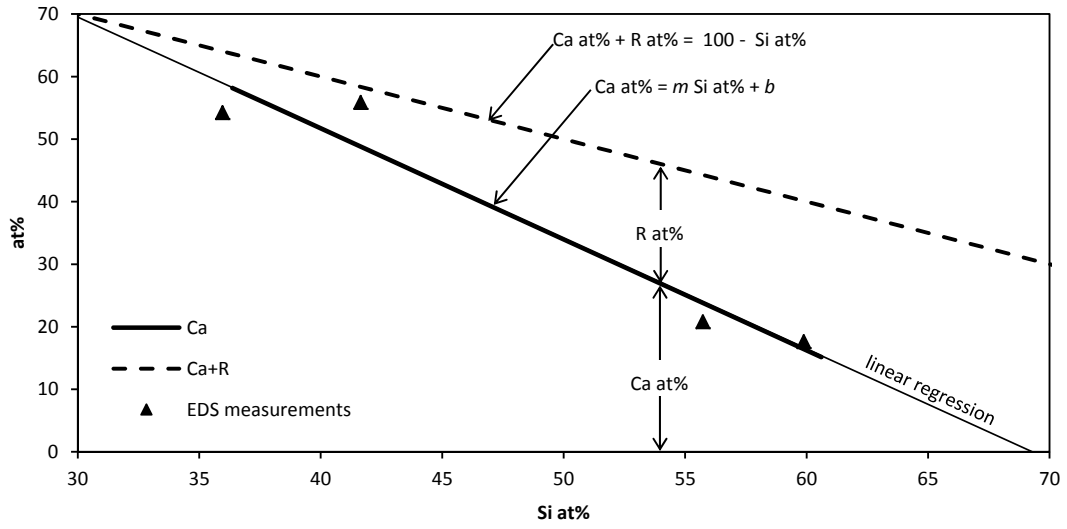

FIGURE B.1: Composition of ASR products in Si, Ca, and R basis. The measured compositions of ASR products [174] were fitted with the proposed Eq. (B.9), resulting in the following stoichiometric coefficients: $a_1 = 1.60$, $a_2 = 0.14$, $b_1 = 0.25$ and $b_2 = 0.40$. Note: at% = atomic percentage.

B.2 Debye-Hückel parameter as a function of temperature

The Debye-Hückel parameter is calculated as a function of absolute temperature with the approximate Eq. (B.13) proposed by Pitzer [164, p. 297]. Values of A_γ at 20 and 50 °C are 0.506 and 0.535, respectively. The effect of pressure on A_γ has been neglected.

$$A_\gamma = 0.17487 \times \left(4.1725332 - 0.1481291T^{0.5} + 1.5188505 \times 10^{-5}T^2 - 1.8016317 \times 10^{-8}T^3 + 9.3816144 \times 10^{-10}T^{3.5}\right) \quad \text{for } 273 \leq T \leq 373 \tag{B.13}$$

B.3 Equilibrium constants as functions of temperature

Water self-ionization

The water self-ionizations constant K_w, consistent with the activities of OH^- and H^+ given in mol/L, is obtained as a function of the absolute temperature T [°K] of the pore solution with the following equation:

$$\log_{10} K_w = A + C \cdot T^{-1} - E \cdot T^{-2} \tag{B.14}$$

where A, C, and E are fitting parameters given in Table B.1. This equation was obtained by fitting experimental values of K_w reported in the literature [130] for water temperatures in the range of 0 to 60 °C.

TABLE B.1: Fitting parameters for the estimate of K_w and K_e^r equilibrium constants using Eqs. (B.14) and (B.15).

	A	B	C	D	E
H_2O	-1.0085E+1	n/a	5.7855E+2	n/a	-5.20065E+5
$NaOH_{aq}$	5.63351337E+2	8.50758895E-2	-3.41076919E+4	-2.05919826E+2	1.81922307E+6
KOH_{aq}	1.42391301E+2	1.63613678E-2	-1.13134542E+4	-5.17821802E+1	3.86391389E+5

Dissociation of aqueous alkali hydroxides

The equilibrium constant K_e^r of the dissociation reaction of aqueous ROH (Reaction (6.6)) is obtained as a function of absolute temperature of the solution with the following expression

$$\log_{10} K_w - \log_{10} K_e^r = A + B \cdot T + C \cdot T^{-1} + D \cdot \log_{10}(T) + E \cdot T^{-2} \tag{B.15}$$

where A, B, C, D, and E are fitting parameters which depend on the type of alkali considered. The values of these parameters for NaOH and KOH, obtained from the thermodynamic data base THERMODDEM [208, 209], are given in Table B.1. Since in the model sodium and potassium are treated indistinctly, the set of fitting parameters to be used will be those of the most prevailing species. The resulting value of K_e^r is regarded as valid for activities expressed in mol/L, assuming for simplicity that molality is approximately equal to molarity.

B.4 Saturation products as functions of temperature

Portlandite

Assuming that the activity of solid portlandite is equal to 1, the equilibrium equation (saturation product) of Reaction (6.1) is given by:

$$\left\{Ca^{2+}\right\}\left\{OH^-\right\}^2 = K_{sp}^C \tag{B.16}$$

The saturation product constant K_{sp}^C is estimated as a function of the absolute temperature T [°K] by means of the following equation:

$$\log_{10} K_{sp}^C - 2\log_{10} K_w = A + B \cdot T + C \cdot T^{-1} + D \cdot \log_{10}(T) + E \cdot T^{-2} \tag{B.17}$$

where A, B, C, D, and E are fitting parameters given in Table B.2, and K_w is the water self-ionization constant, which is given as a function of temperature T in Appendix B.3. This expression has been adapted from the one given in the geochemical database THERMODDEM [210]. The resulting value of K_{sp}^C is regarded as valid for

activities expressed in mol/L, assuming for simplicity that molality is approximately equal to molarity.

TABLE B.2: Fitting parameters for the estimate of the solubility products of portlandite (K_{sp}^{C}) and SL glass (K_{sp}^{S}), according to the equations indicated in the first column.

Eq.	*A*	*B*	*C*	*D*	*E*
(B.17)	-2.84930557E+2	-4.4711E-2	2.1380182091E+4	1.04205027E+2	-7.54252616584E+5
(B.25)	-1.9987746E+1	-2.169E-3	5.53572306E+2	6.880739E+0	-8.4503400742E+4
(B.26)	-6.496E-01	n/a	1.479E+03	n/a	n/a
(B.27)	-3.0722346E+1	-2.169E-3	2.611122306E+3	6.880739E+0	-6.04568400742E+5

SL glass

It is assumed that, in contact with alkaline solutions, SiO_2 in SL glass dissolves according to the process described in Section 2.3.1 and that Ca^{2+} and R^{+} are congruently released to the solution together with the silicate ions. In the proposed ASR model, only two reactions are considered from the whole dissolution process presented in Section 2.3.1:

$$x(SiO_2)_s + 2H_2O \longleftrightarrow (x-1)(SiO_2)_s + (Si(OH)_4)_{aq} \tag{B.18}$$

$$(Si(OH)_4)_{aq} \longleftrightarrow (H_3SiO_4^-)_{aq} + H^+ \tag{B.19}$$

The process is further simplified by condensing these two reactions in the following single one:

$$x(SiO_2)_s + 2H_2O \longleftrightarrow (x-1)(SiO_2)_s + SiO_4H_3^- + H^+ \tag{B.20}$$

Assuming that the activity of water and solid SiO_2 are equal to 1, the equilibrium equations of Reactions (B.18)–(B.20) are given as follow:

$$\left\{H_3SiO_4^-\right\} = K' \tag{B.21}$$

$$\frac{\left\{H_3SiO_4^-\right\}\left\{H^+\right\}}{\left\{Si(OH)_4\right\}} = K'' \tag{B.22}$$

$$\left\{H_3SiO_4^-\right\}\left\{H^+\right\} = K_{sp}^{S} \tag{B.23}$$

where K' is the saturation product constant of Reaction (B.18), K'' the dissociation equilibrium constant of Reaction (B.19), and K_{sp}^{S} is the saturation product constant of Reaction (B.20) (and also of Reaction (6.2)). Combining these equations one obtains:

$$K_{sp}^{S} = K'K'' \tag{B.24}$$

Assuming that SiO_2 in SL glass behaves similarly to amorphous silica, K' is given as a function of absolute temperature T [°K] by the following best fitting expression obtained

from the geochemical data base THERMODDEM [207]:

$$\log_{10} K' = A + B \cdot T + C \cdot T^{-1} + D \cdot \log_{10}(T) + E \cdot T^{-2} \tag{B.25}$$

where A, B, C, D, and E are fitting parameters given in Table B.2.

In turn, the following best fitting expression of the dissociation constant K'' as function of temperature T is adapted from the one proposed by Fleming and Crerar [69]:

$$\log_{10} K'' - \log_{10} K_w = A + C \cdot T^{-1} \tag{B.26}$$

where A, B, C, D, and E are fitting parameters given in Table B.2, and K_w is the water self-ionization constant (given as function of temperature T in Appendix B.3).

Finally, combining Eqs. (B.24), (B.25), (B.26) and (B.14), the following expression of K_{sp} as a function of temperature T is obtained:

$$\log_{10} K^S_{sp} = A + B \cdot T + C \cdot T^{-1} + D \cdot \log_{10}(T) + E \cdot T^{-2} \tag{B.27}$$

where the resulting fitting parameters A, B, C, D, and E are given in Table B.2. The resulting value of K^S_{sp} is regarded as valid for activities in mol/L, assuming for simplicity that molality is approximately equal to molarity.

B.5 Chemical speciation of pore solution

Given the concentration of primary species in pore solution (c^s, c^c, c^r), the concentrations of secondary species (c^{oh}, c^h, c^{r0} and c^{r1}) are obtained by solving the following system of equations:

$$\begin{cases} c^{r1} + 2c^c + c^h - c^s - c^{oh} = 0 \\ \gamma^{oh} c^{oh} \gamma^h c^h - K_w = 0 \\ \gamma^{r1} c^{r1} \gamma^{oh} c^{oh} - K^r_e c^{r0} = 0 \\ c^r - c^{r0} - c^{r1} = 0 \end{cases} \tag{B.28}$$

where the activity coefficients γ^β are given by Eq. (5.37) with $z^\beta = 1$, i.e.

$$\log_{10} \gamma^{oh} = \log_{10} \gamma^h = \log_{10} \gamma^{r1} = A_\gamma \left[\frac{\sqrt{I}}{1+\sqrt{I}} - \left(0.2I - \frac{I^2}{24} \right) \right] \tag{B.29}$$

$$\text{with} \quad I = \frac{1}{2} \left(c^s + 4c^c + c^{r1} + c^h + c^{oh} \right) \text{[mol/l]}$$

Assuming that the activity coefficients are known and after combing appropriately the system of equations (B.28), the following cubic polynomial equation in terms of c^{oh} is reached:

$$A_0 + A_1 c^{oh} + A_2 \left(c^{oh}\right)^2 + A_3 \left(c^{oh}\right)^3 = 0 \tag{B.30}$$

with

$$\begin{aligned}
A_0 =& - K_e^r K_w \\
A_1 =& \left(c^s - 2c^c - c^r\right) K_e^r \gamma^h \gamma^{oh} - K_w \gamma^{oh} \gamma^{r1} \\
A_2 =& \left(c^s - 2c^c\right) \gamma^h \gamma^{r1} \left(\gamma^{oh}\right)^2 + K_e^r \gamma^h \gamma^{oh} \\
A_3 =& \gamma^{r1} \gamma^h \left(\gamma^{oh}\right)^2
\end{aligned}$$

If there is no alkalis in the solution ($c^r = 0$), the last two equations of the system (B.28) are no longer valid and have to be removed. In this case, a quadratic polynomial equation is obtain instead of a cubic one,

$$B_0 + B_1 c^{oh} + B_2 \left(c^{oh}\right)^2 = 0 \tag{B.31}$$

with

$$\begin{aligned}
B_0 =& - K_w \\
B_1 =& \left(c^s - 2c^c\right) \gamma^h \gamma^{oh} \\
B_2 =& \gamma^h \gamma^{oh}
\end{aligned}$$

For usual sets of values of c^s, c^c, and c^r, these polynomials have a unique suitable root, i.e. for Eq. (B.31), a unique root such as $c^{oh} > 0$, and for Eq. (B.30), a unique root such as $c^{oh} > 0$, $c^{r0} > 0$, and $c^{r1} > 0$.

Finally, to solve the system of equations (B.28) including the activity coefficients as functions of the unknowns (Eq. (B.29)) the following algorithm is used:

1. Make activity coefficients equal to 1.
2. Solve the polynomial equation (B.30) (or (B.31), if $c^r = 0$), and save the suitable root.
3. Replace the obtained value of c^{oh} in (B.28) to obtain c^h, c^{r1} and c^{r0}.
4. Calculate activity coefficients using Eq. (B.29).

5. Repeat from step 2 until the differences between the roots obtained in two successive iterations is within a certain tolerance.

This procedure usually converges in a few iterations.

B.6 Supplementary expressions for the time integration of the chemical law

In Section 6.4.8, an analytical solution of the system of differential equations (6.51) has been found under the assumption that $\mathcal{U}^{ps} > 0$ in the analysed time interval (t_i, t_{i+1}). In this appendix, analytical solutions are given for the three different possibles cases in which this condition is not fulfilled.

In the first possible case, the volume of pore solution at the beginning of the time interval is null and remains null until the end of the time interval. In such conditions, no reaction can occur between time t_i and t_{i+1}, and, consequently, $M^{\alpha}_{i+1} = M^{\alpha}_{i}$.

In the second possible case, the volume of pore solution at time t_i is positive, but at some time t_Ω between t_i and t_{i+1} it becomes null. Note that this can only occur if the constant a_2, defined for the system of equations (6.51), is negative. In such case, the analytical solution obtained in Section 6.4.8 (Eqs.(6.52)–(6.57)) can be used between t_i and t_Ω. But, since the volume of pore solution is null, between t_Ω and t_i all the reactions are stopped and, consequently, $M^{\alpha}_{i+1} = M^{\alpha}_{\Omega}$. In order to find the time t_Ω, $\mathcal{U}^{ps}(t_\Omega) = 0$ is imposed in Eq. (6.49), obtaining:

$$\mathcal{U}^{o} + a_n^{cr}(t_\Omega) - M^{S}(t_\Omega)\eta^{S} - \left\langle M^{C}(t)\right\rangle_{+}\eta^{C} - M^{A}(t_\Omega)\eta^{A} - M^{B}(t_\Omega)\eta^{B} = 0 \tag{B.32}$$

Then, introducing the expressions of $M^{\alpha}(t)$ given in Eqs. (6.52)–(6.57), and after some algebra, one obtains, for $\mathsf{a}_1 = 0$, that:

$$t_\Omega = t_i - \frac{\mathcal{U}^{ps}_i}{\mathsf{a}_2} \tag{B.33}$$

and for $\mathsf{a}_1 \neq 0$:

$$t_\Omega = t_i - \frac{1}{\mathsf{a}_1}\ln\left(-\frac{A}{B}\right) \tag{B.34}$$

where

$$A = \mathcal{U}^{o} + a_n^{cr}(t_i) - \frac{1}{\mathsf{a}_1}\left(\eta^{A}\mathsf{b}_1^{A} + \eta^{B}\mathsf{b}_1^{B}\right) + \frac{\mathsf{a}_2}{\mathsf{a}_1} - \left(\eta^{S}M_i^{S} + \eta^{C}M_i^{C}\right)$$

$$B = \eta^A M_i^A + \eta^B M_i^B - \frac{1}{\mathsf{a}_1}\left(\eta^A \mathsf{b}_1^A + \eta^B \mathsf{b}_1^B\right) + \frac{\mathsf{a}_2}{\mathsf{a}_1}$$

In the third possible case, the volume of pore solution is null at time t_i, but becomes positive at a certain time t_Ω between t_i and t_{i+1}. This can only occur if the rate of cracking aperture in the time interval is positive, i.e. $a_n^{cr}(t_N) > a_n^{cr}(t_0)$. Between t_i and t_Ω, no reaction can occur and, consequently, $M_\Omega^\alpha = M_i^\alpha =$. Between t_Ω and t_{i+1}, the analytical solution obtained in Section 6.4.8 can be used. In order to find the time t_Ω, $\mathcal{U}^{ps}(t_\Omega) = 0$ is imposed in Eq. (6.49). Additionally, Eq. (6.50) and $M_\Omega^\alpha = M_i^\alpha$ are introduced, leading to:

$$a_n^{cr}(t_i) + \frac{a_n^{cr}(t_N) - a_n^{cr}(t_0)}{\Delta t}(t_\Omega - t_i) + \mathcal{U}^o - M_i^S \eta^S - \left\langle M_i^C \right\rangle_+ \eta^C - M_i^A \eta^A - M_i^B \eta^B = 0 \tag{B.35}$$

Then, after little algebra, one obtains:

$$t_\Omega = t_i + \frac{A}{B} \tag{B.36}$$

where

$$A = M_i^S \eta^S + \left\langle M_i^C \right\rangle_+ \eta^C + M_i^A \eta^A + M_i^B \eta^B - \mathcal{U}^o - a_n^{cr}(t_i)$$
$$B = \frac{a_n^{cr}(t_N) - a_n^{cr}(t_0)}{\Delta t}$$

B.7 Speciation results with simplified versions of the chemical model

Three simplified versions of the chemical speciation model can be obtained by:

(i) considering activity coefficients constant and equal to one for every aqueous species, i.e. $\gamma^\beta = 1$, for all aqueous β-species.

(ii) considering ROH_{aq} completely dissociated, i.e. making $c^r = c^{r1}$ and omitting the last equation of the system (B.28).

(iii) considering both simplifications together.

With these versions of the model, additional simulations of the two last cases presented Section 7.2 were performed using the same chemical parameters in order to assess the influence of the activity coefficients γ^β and of the dissociation of ROH_{aq} on the results.

Figures B.3 and B.2 show the obtained results with the three simplified versions of the speciation model together with the results obtained with the full version of the model and the experimental measurements. Considering the non-ideal behaviour of aqueous β-species in pore solution through the activity coefficients calculated with Davies equations significantly improves the simulation results in the two cases analysed. In contrast, considering the dissociation of aqueous ROH has a small influence on the results, and this only for high concentrations of NaOH.

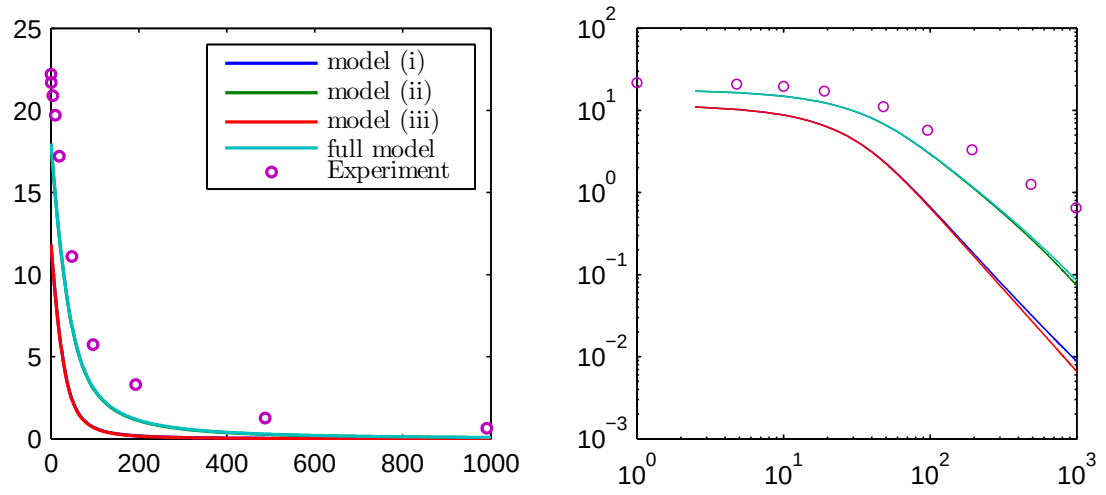

FIGURE B.2: Comparison of model-calculated and experimental measurements of portlandite solubility in NaOH solution at 25 °C for different versions of the chemical speciation model. Left and right figures present the same data but at two different scales. Experimental data from Ref. [60].

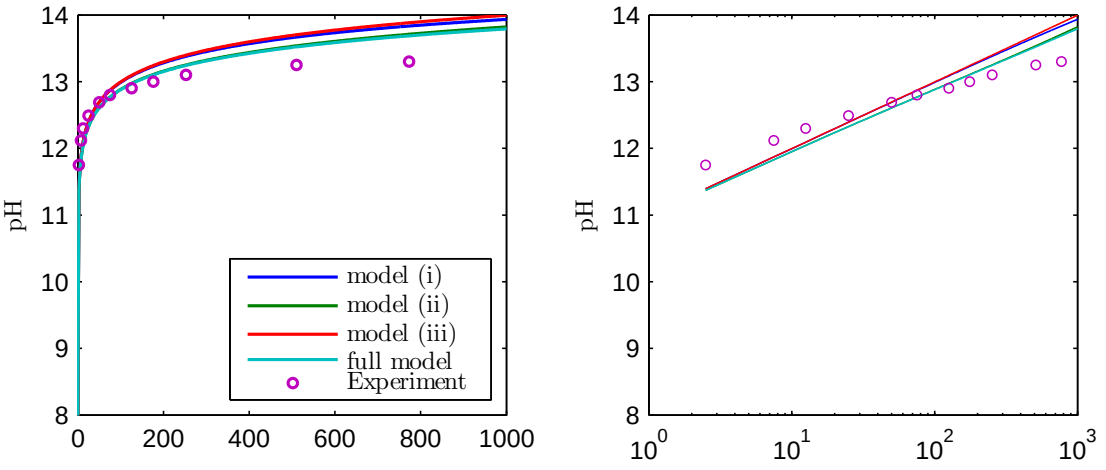

FIGURE B.3: Comparison of model-calculated and experimental measurements of pH of NaOH solution at 25 °C for different versions of the chemical speciation model. Left and right figures present the same data but at two different horizontal scales. Experimental data from Ref. [59].

Bibliography

[1] ACI. State-of-the-Art Report on Alkali-Aggregate Reactivity Reported by ACI Committee 221. Technical report, American Concrete Institute, 1998.

[2] I. Acosta. *Calibración y puesta en marcha de una nueva máquina de ensayo para hormigón afectado por la reacción álcali-árido.* Bachelor thesis (in spanish), Universitat Politècnica de Catalunya, 2012.

[3] AENOR. Cement-Part 1: Composition, specifications and conformity criteria for common cements UNE-EN 197-1, 2011.

[4] K. Afshinnia and P. R. Rangaraju. Influence of fineness of ground recycled glass on mitigation of alkali-bsilica reaction in mortars. *Construction and Building Materials*, 81:257–267, 2015.

[5] A. Akhavan, S.-M.-H. Shafaatian, and F. Rajabipour. Quantifying the effects of crack width , tortuosity , and roughness on water permeability of cracked mortars. *Cement and Concrete Research*, 42(2):313–320, 2012.

[6] M. Alnaggar, G. Cusatis, and G. D. Luzio. Lattice Discrete Particle Modeling (LDPM) of Alkali Silica Reaction (ASR) deterioration of concrete structures. *Cement and Concrete Composites*, 41:45–59, aug 2013.

[7] B. Amadei, S. Sture, S. Saeb, and R. Atkinson. Report to NSF: An evaluation of masonry joint shear strength in existing buildings. Technical report, Deot. of Civil, Environmental and Architectural Engrg., U. of Colorado, Boulder, 1989.

[8] K. Andersson and B. Allard. Chemical composition of cement pore solutions. *Cement and Concrete Research*, 19:327–332, 1989.

[9] ASTM. ASTM C1260-07 Standard Test Method for Potential Alkali Reactivity of Aggregate (Mortar-Bar Method). In *Annual Book of ASTM Standards*. ASTM International, 2007.

[10] ASTM. ASTM C150-07 Standard Specification for Portland Cement. In *Annual Book of ASTM Standards*, volume 552. ASTM International, 2007.

[11] ASTM. ASTM C289-07 Standard Tets Method for Potential Alkali-Silica Reactivity of Aggregates (Chemical Method). In *Annual Book of ASTM Standards*. ASTM International, 2007.

[12] ASTM. ASTM C227-10 Standard Test Method for Potential Alkali Reactivity of Cement-Aggregate Combinations (Mortar-Bar Method). In *Annual Book of ASTM Standards*. ASTM International, 2010.

[13] S. Balay, S. Abhyankar, M. F. Adams, J. Brown, P. Brune, K. Buschelman, L. Dalcin, V. Eijkhout, W. D. Gropp, D. Kaushik, M. G. Knepley, D. A. May, L. C. McInnes, R. T. Mills, T. Munson, K. Rupp, P. Sanan, B. F. Smith, S. Zampini, H. Zhang, and H. Zhang. PETSc Web page. http://www.mcs.anl.gov/petsc, 2018.

[14] Z. P. Bažant and A. Steffens. Mathematical model for kinetics of alkali-silica reaction in concrete. *Cement and Concrete Research*, 30(3):419–428, 2000.

[15] Z. P. Bažant, G. Zi, and C. Meyer. Fracture Mechanics of ASR in concretes with waste glass. *Journal of Engineering Mechanics*, 126(3):226–232, 2000.

[16] J. Bear and A. H.-D. Cheng. *Modeling Groundwater Flow and Contaminant Transport*. Springer Science & Business Media, 2010.

[17] U. Berner. Evolution of pore water chemistry during degradation of cement in a radioactive waste repository environment. *Waste Management*, 12(2-3):201–219, jan 1992.

[18] M.-A. Bérubé, J. Duchesne, J. F. Dorion, and M. Rivest. Laboratory assessment of alkali contribution by aggregates to concrete and application to concrete structures affected by alkali-silica reactivity. *Cement and Concrete Research*, 32(8):1215–1227, 2002.

[19] M.-A. Bérubé and B. Fournier. Alkali Releasable Aggregates in Concrete - Significance and Test Methods. In *12th Conference on Alkali-Aggregate Reaction*, pages 17–30, Beijing, China, 2004.

[20] A. Binal. Investigation of mixing ratio and restraint condition effects on alkali-silica gel pressure in mortar by using a uniaxial alkali-silica gel pressure measuring device (ASGPM-D). *Construction and Building Materials*, 21(6):1218–1228, jun 2007.

[21] A. Binal. The determination of gel swelling pressure of reactive aggregates by ASGPM device and a new reactive-innocuous aggregate decision chart. *Construction and Building Materials*, 22(1):1–13, jan 2008.

[22] R. F. Blanks. Concrete deterioration at Parker Dam. *Engineering News-Record*, 126:462–465, 1941.

[23] R. F. Bleszynski and M. D. A. Thomas. Microstructural Studies of Alkali-Silica Reaction in Fly Ash Concrete Immersed in Alkaline Solutions. *Advanced Cement Based Materials*, 7(2):66–78, 1998.

[24] D. Breton, J. Ollivier, and G. Ballivy. Diffusivité des ions chlore dans la zone de transition entre pâte de ciment et roche granitique. In *RILEM International Conference on Interface and Cementitious Composites*, pages 269–278, 1992.

[25] H. Brouwers. The work of Powers and Brownyard revisited: Part 1. *Cement and Concrete Research*, 34(9):1697–1716, sep 2004.

[26] H. Brouwers. The work of Powers and Brownyard revisited: Part 2. *Cement and Concrete Research*, 35(10):1922–1936, oct 2005.

[27] E. Brühwiler and F. Wittmann. The wedge splitting test, a new method of performing stable fracture mechanics tests. *Engineering Fracture Mechanics*, 35(1):117–125, 1990.

[28] A. Caballero, C. M. López, and I. Carol. 3D meso-structural analysis of concrete specimens under uniaxial tension. *Computer Methods in Applied Mechanics and Engineering*, 195(52):7182–7195, 2006.

[29] A. Caballero, K. J. Willam, and I. Carol. Consistent tangent formulation for 3D interface modeling of cracking/fracture in quasi-brittle materials. *Computer Methods in Applied Mechanics and Engineering*, 197(33-40):2804–2822, 2008.

[30] B. Capra and A. Sellier. Orthotropic modelling of alkali-aggregate reaction in concrete structures: numerical simulations. *Mechanics of Materials*, 35(8):817–830, aug 2003.

[31] A. Carles-Gibergues, J. P. Ollivier, B. Fournier, and M.-A. Bérubé. A new approach to the study of alkali-aggregate reaction mechanisms. In *8th ICAAR*, pages 161–166, Kyoto, 1989.

[32] I. Carol, A. Gens, and E. E. Alonso. A three dimensional elastoplastic joint element. In O. Stephanson, editor, *International Symposium on Fundamentals of Rock Joints*, pages 441–451. Centek Publishers, Bjorkliden, Sweden, 1985.

[33] I. Carol, J. Liaudat, and C. M. López. Modeling Concrete Expansions via Coupled C-M Mesoscale Analysis with Zero-Thickness Interface Elements, and Lab Experiments. In A. Sellier, É. Grimal, S. Multon, and É. Boudarot, editors, *Swelling*

Concrete in Dams and Hydraulic Structures (DSC 2017), pages 248–260. Wiley-ISTE, 2017.

[34] I. Carol, C. M. López, and O. Roa. Micromechanical analysis of quasi brittle materials using fracture based interface elements. *International Journal for Numerical Methods in Engineering*, 52:193–215, 2001.

[35] I. Carol and P. C. Prat. A statically constrained microplane model for the smeared analysis of concrete cracking. *Computer aided analysis and design of concrete structures*, 2:919–930, 1990.

[36] I. Carol and P. C. Prat. A multicrack model based on the theory of multisurface plasticity and two fracture energies. In *Computational Plasticity IV*, volume 2, pages 1583–1594. Pineridge Press, 1995.

[37] I. Carol, P. C. Prat, and C. M. López. Normal/Shear Cracking Model: Application to Discrete Crack Analysis. *Journal of Engineering Mechanics*, 123(8):765–773, 1997.

[38] J. Casellas. *Ensayos triaxials de rocas en celula de gran capacidad*. Bachelor thesis (in spanish), Universitat Politècnica de Catalunya, 2013.

[39] R. G. Charlwood, R. Steele, S. V. Solymar, and D. D. Curtis. A review of alkali aggregate reactions in hydroelectric plants and dams. In *International Conference of Alkali-Aggregate Reactions in Hydroelectric Plants and Dams.*, pages 1–29, Fredericton, Canada, 1992.

[40] S. Chatterji and N. Thaulow. Some fundamental aspects of alkali-silica reaction. *11th Conference on Alkali-Aggregate Reaction.*, pages 21–29, 2000.

[41] S. Chatterji, N. Thaulow, and A. D. Jensen. Studies of alkali-silica recation. Part 5. Verification of a newly proposed reaction mechanism. *Cement and Concrete Research*, 1989.

[42] CMI Multidisciplinary Design Project. Materials data book. *Cambridge University Engineering Department*, http://www-mdp.eng.cam.ac.uk/web/library/enginfo/cueddatabooks/materials.pdf. Accessed: 2017-03-21.

[43] I. Comby-Peyrot, F. Bernard, P.-O. Bouchard, F. Bay, and E. Garcia-Diaz. Development and validation of a 3D computational tool to describe concrete behaviour at mesoscale. Application to the alkali-silica reaction. *Computational Materials Science*, 46(4):1163–1177, oct 2009.

[44] C. Comi, R. Fedele, and U. Perego. A chemo-thermo-damage model for the analysis of concrete dams affected by alkali-silica reaction. *Mechanics of Materials*, 41(3):210–230, 2009.

[45] C. Comi, B. Kirchmayr, and R. Pignatelli. Two-phase damage modeling of concrete affected by alkali-silica reaction under variable temperature and humidity conditions. *International Journal of Solids and Structures*, 49(23-24):3367–3380, nov 2012.

[46] C. Comi and U. Perego. Anisotropic Damage Model for Concrete Affected by Alkali-Aggregate Reaction. *International Journal of Damage Mechanics*, 20(4):598–617, 2011.

[47] D. Constantiner and S. Diamond. Alkali release from feldspars into pore solutions. *Cement and Concrete Research*, 33(4):549–554, 2003.

[48] A. K. Covington, R. G. Bates, and R. A. Durst. Definition of pH scales, standard reference values, measurement of pH and related terminology. *Pure and Applied Chemistry*, 57(3):531–542, 1985.

[49] G. Cusatis, A. Mencarelli, D. Pelessone, and J. Baylot. Lattice Discrete Particle Model (LDPM) for failure behavior of concrete. II: Calibration and validation. *Cement and Concrete Composites*, 33(9):891–905, 2011.

[50] G. Cusatis, D. Pelessone, and A. Mencarelli. Lattice Discrete Particle Model (LDPM) for failure behavior of concrete. I: Theory. *Cement and Concrete Composites*, 33(9):881–890, 2011.

[51] A. Delagrave, J. P. Bigas, J. P. Ollivier, J. Marchand, and M. Pigeon. Influence of the interfacial zone on the chloride diffusivity of mortars. *Advanced Cement Based Materials*, 5(3-4):86–92, 1997.

[52] A. Delagrave, J. Marchand, and M. Pigeon. Influence of microstructure on the tritiated water diffusivity of mortars. *Advanced Cement Based Materials*, 7(2):60–65, 1998.

[53] R. K. Dhir, T. D. Dyer, and M. C. Tang. Alkali-silica reaction in concrete containing glass. *Materials and Structures*, 42(10):1451–1462, 2009.

[54] S. Diamond. Effects of Microsilica (Silica Fume) on Pore-Solution Chemistry of Cement Pastes. *Communications of the American Ceramic Society*, pages 82–84, 1983.

[55] S. Diamond. ASR - another look at mechanisms. In *8th International Conference on Alkali-Aggregate reaction*, pages 83–94, Kyoto, 1989.

[56] S. Diamond, R. S. J. Barneyback, and L. J. Struble. On the Physics and Chemistry of Alkali-Silica Reactions. In *5th Conference on Alkali-Aggregate Reaction in Concrete*, pages 1–11, Cape Town - South Africa, 1981.

[57] S. Diamond and N. Thaulow. A study of expansion due to alkali - silica reaction as conditioned by the grain size of the reactive aggregate. *Cement and Concrete Research*, 4(4):591–607, 1974.

[58] A. Djerbi, S. Bonnet, A. Khelidj, and V. Baroghel-bouny. Influence of traversing crack on chloride diffusion into concrete. *Cement and Concrete Research*, 38(6):877–883, jun 2008.

[59] Dow Chemical Company. pH versus concentration table for caustic soda. *Technical Information*, http://dowac.custhelp.com/ci/fattach/get/51535/0/filename/pH_Versus_Concentration_Table_For_Caustic_Soda.pdf. Accessed: 2015-11-03.

[60] J. Duchesne and E. Reardon. Measurement and prediction of portlandite solubility in alkali solutions. *Cement and Concrete Research*, 25(5):1043–1053, 1995.

[61] C. F. Dunant and K. L. Scrivener. Micro-mechanical modelling of alkali-silica-reaction-induced degradation using the AMIE framework. *Cement and Concrete Research*, 40(4):517–525, apr 2010.

[62] C. F. Dunant and K. L. Scrivener. Effects of aggregate size on alkali-silica-reaction induced expansion. *Cement and Concrete Research*, 42(6):745–751, jun 2012.

[63] C. F. Dunant and K. L. Scrivener. Effects of uniaxial stress on alkali-silica reaction induced expansion of concrete. *Cement and Concrete Research*, 42(3):567–576, mar 2012.

[64] E. M. R. Fairbairn, F. L. B. Ribeiro, L. E. Lopes, R. D. Toledo-Filho, and M. M. Silvoso. Modelling the structural behaviour of a dam affected by alkali-silica reaction. *Communications in Numerical Methods in Engineering*, 22(1):1–12, 2006.

[65] M. Farage, J. Alves, and E. Fairbairn. Macroscopic model of concrete subjected to alkaliaggregate reaction. *Cement and Concrete Research*, 34(3):495–505, mar 2004.

[66] I. Fernandes. Composition of alkali-silica reaction products at different locations within concrete structures. *Materials Characterization*, 60(7):655–668, jul 2009.

[67] C. F. Ferraris, J. R. Clifton, E. J. Garboczi, and F. L. Davis. Stress Due to Alkali-Silica Reaction in Mortars. In K. L. Scrivener and J. F. Young, editors,

Mechanisms of Chemical Degradation of Cement-based Systems, chapter 9, pages 75–82. E & FN Spon, London, 1995.

[68] C. F. Ferraris, E. J. Garboczi, F. L. Davis, and J. R. Clifton. The effect of stress relaxation, self-desiccation, and water absorption on the alkali-silica reaction in low water/cement ratio mortars. *Cement and Concrete Research*, 27(10):1553–1560, 1997.

[69] B. Fleming and D. Crerar. Silicic acid ionization and calculation of silica solubility at elevated temperature and pH application to geothermal fluid processing and reinjection. *Geothermics*, 1982.

[70] K. J. Folliard, R. Barborak, T. Drimalas, L. Du, S. Garber, J. H. Ideker, T. Ley, S. Williams, M. C. G. Juenger, B. Fournier, and M. D. A. Thomas. FHWA/TX-06/0-4085-5 Preventing ASR/DEF in New Concrete: Final Report. Technical report, The University of Texas at Austin, Center for Transportation Research (CTR), Austin, Texas, 2006.

[71] K. J. Folliard, M. D. A. Thomas, and K. E. Kurtis. FHWA-RD-03-047 Guidelines for the Use of Lithium to Mitigate or Prevent Alkali-Silica Reaction (ASR). Technical report, Federal Highway Administration, Washington, DC, USA, 2003.

[72] R. O. Fournier and J. J. Rowe. The solubility of amorphous and high pressures silica in water at high temperatures. *American Mineralogist*, 62:1052–1056, 1977.

[73] F. Gaboriaud, A. Nonat, D. Chaumont, and A. Craievich. Aggregation and Gel Formation in Basic SilicoCalcoAlkaline Solutions Studied: A SAXS, SANS, and ELS Study. *The Journal of Physical Chemistry B*, 103(28):5775–5781, 1999.

[74] S. Galí, C. Ayora, P. Alfonso, E. Tauler, and M. Labrador. Kinetics of dolomite-portlandite reaction: application to portland cement concrete. *Cement and Concrete Research*, 31:933–939, 2001.

[75] E. Garcia-Diaz, D. Bulteel, Y. Monnin, P. Degrugilliers, and P. Fasseu. ASR pessimum behaviour of siliceous limestone aggregates. *Cement and Concrete Research*, 40(4):546–549, 2010.

[76] E. Garcia-Diaz, J. Riche, D. Bulteel, and C. Vernet. Mechanism of damage for the alkali-silica reaction. *Cement and Concrete Research*, 36(2):395–400, feb 2006.

[77] D. Garolera. *Zero-thickness interface elements in petroleum geomechanics: sand production and hydraulic fracture.* Doctoral thesis, Universitat Politècnica de Catalunya, 2017.

[78] B. P. Gautam and D. K. Panesar. A new method of applying long-term multiaxial stresses in concrete specimens undergoing ASR, and their triaxial expansions. *Materials and Structures*, 49(9):3495–3508, 2016.

[79] B. P. Gautam, D. K. Panesar, S. A. Sheikh, and F. J. Vecchio. Multiaxial Expansion-Stress Relationship for Alkali Silica Reaction-Affected Concrete. *ACI Materials Journal*, 114(1):171–184, 2017.

[80] A. Gens, I. Carol, and E. E. Alonso. A constitutive model for rock joints; formulation and numerical implementation. *Computers and Geotechnics*, 9:3–20, 1990.

[81] G. Giaccio, R. Zerbino, J. Ponce, and O. Batic. Mechanical behavior of concretes damaged by alkali-silica reaction. *Cement and Concrete Research*, 38(7):993–1004, jul 2008.

[82] F. Glasser. Chemistry of the alkali-aggregate reaction. In R. Swamy, editor, *The alkali-silica reaction in concrete*, chapter 2, pages 30–53. Blackie and Son Ltd., Glasgow, 1992.

[83] L. D. Glasser and N. Kataoka. The chemistry of 'alkali-aggregate' reaction. *Cement and Concrete Research*, 1981.

[84] A. González. *Estudio experimental de las interfases árido-pasta afectadas por la reacción álcali-sílice.* Bachelor thesis (in spanish), Universitat Politècnica de Catalunya, 2012.

[85] E. Grimal, A. Sellier, Y. Le Pape, and E. Bourdarot. Creep, shrinkage, and anisotropic damage in alkali-aggregate reaction swelling mechanism-Part I: A constitutive model. *ACI Materials Journal*, 105(3):227–235, 2008.

[86] E. Grimal, A. Sellier, Y. L. Pape, and E. Bourdarot. Creep, shrinkage, and anisotropic damage in alkali-aggregate reaction swelling mechanism: part 2: identification of model parameters and application. *ACI Materials Journal*, 105(3):236–242, 2008.

[87] W. Hansen. Studies Relating to the Mechanism by Which the Alkali-Silica Reaction Proceeds in Concrete. In *ACI Journal Proceedings*, volume 15, pages 213–227, 1944.

[88] R. Helmuth and D. Stark. Alkali-silica reactivity mechanisms. *Materials Science of Concrete, The American Ceramic Society*, pages 131–208, 1992.

[89] R. Helmuth, D. Stark, S. Diamond, and M. Moranville-Regourd. Alkali-silica reactivity: an overview of research. Technical report, Startegic Highway Research Program, Washington, DC, USA, 1993.

[90] M. F. Herrador, F. Martínez-Abella, and R. Hoyo Fernández-Gago. Mechanical behavior model for ASR-affected dam concrete under service load: formulation and verification. *Materials and Structures*, 42(2):201–212, may 2009.

[91] D. W. Hobbs. The alkali-silica reaction - a model for predicting expansion in mortar. *Magazine of Concrete Research*, 33(117):208–220, 1981.

[92] D. W. Hobbs. *Alkali-silica reaction in concrete*. Telford, London, 1988.

[93] S. Hong and F. Glasser. Alkali binding in cement pastes: Part I. The CSH phase. *Cement and Concrete Research*, 29(1999):1893–1903, 1999.

[94] X. Hou and R. Kirkpatrick. Structural investigations of alkali silicate gels. *Journal of the American Ceramic Society*, 88(4):943–949, apr 2005.

[95] J. Icenhower and P. Dove. The dissolution kinetics of amorphous silica into sodium chloride solutions: effects of temperature and ionic strength. *Geochimica et Cosmochimica Acta*, 64(24):4193–4203, 2000.

[96] T. Ichikawa and M. Miura. Modified model of alkali-silica reaction. *Cement and Concrete Research*, 37(9):1291–1297, sep 2007.

[97] A. E. Idiart. *Coupled analysis of degradation processes in concrete specimens at the meso-level*. Doctoral thesis, Universitat Politècnica de Catalunya, 2009.

[98] A. E. Idiart, C. M. López, and I. Carol. Chemo-mechanical analysis of concrete cracking and degradation due to external sulfate attack: A meso-scale model. *Cement and Concrete Composites*, 33(3):411–423, mar 2011.

[99] A. E. Idiart, C. M. López, and I. Carol. Modeling of drying shrinkage of concrete specimens at the meso-level. *Materials and Structures*, 44(2):415–435, jun 2011.

[100] R. Idir, M. Cyr, and A. Tagnit-Hamou. Use of fine glass as ASR inhibitor in glass aggregate mortars. *Construction and Building Materials*, 24(7):1309–1312, 2010.

[101] R. K. Iler. *The chemistry of silica: solubility, polymerization, colloid and surface properties, and biochemistry*. Wiley Interscience, New York, 1979.

[102] S. Y. Jang, B. S. Kim, and B. H. Oh. Effect of crack width on chloride diffusion coefficients of concrete by steady-state migration tests. *Cement and Concrete Research*, 41(1):9–19, jan 2011.

[103] H. Kagimoto, Y. Yasuda, and M. Kawamura. ASR expansion, expansive pressure and cracking in concrete prisms under various degrees of restraint. *Cement and Concrete Research*, 59:1–15, 2014.

[104] G. Kalousek. Studies of portions of the quaternary system soda-lime-silica-water at 25 degrees C. *Journal of Research of the National Bureau of Standards*, 32(6):285, jun 1944.

[105] M. Kawamura and K. Iwahori. ASR gel composition and expansive pressure in mortars under restraint. *Cement and concrete composites*, 26(1):47–56, jan 2004.

[106] J. Kestin, H. E. Khalifa, and R. J. Correia. Tables of the dynamic and kinematic viscosity of aqueous NaCl solutions in the temperature range 20-150 C and the pressure range 0.1-35 MPa, 1981.

[107] R. J. Kirkpatrick, A. G. Kalinichev, X. Hou, and L. J. Struble. Experimental and molecular dynamics modeling studies of interlayer swelling: water incorporation in kanemite and ASR gel. *Materials and Structures*, 38(278):449–458, 2005.

[108] T. Knudsen and N. Thaulow. Quantitative microanalyses of alkali-silica gel in concrete. *Cement and Concrete Research*, 5(5):443–454, 1975.

[109] C. Larive. *Apports combinés de l'expérimentation et de la modélisation à la compréhension de l'alcali-réaction et de ses effets mécaniques.* Doctoral thesis (in french), École Nationale des Ponts et Chaussées, 1997.

[110] C. Larive, A. Laplaud, and O. Coussy. The role of water in alkali-silica reaction. In *11th Conference on Alkali-Aggregate Reaction*, pages 61–69, Québec., 2000.

[111] A. Leemann. Alkali-Silica Reaction autogenous deformations and pressure development in a model system. In B. Drimalas, T, Ideker, JH, Fournier, editor, *14th International Conference on Alkali-Aggregate Reactions in Concrete*, Austin, Texas, USA, 2012.

[112] A. Leemann, G. Le Saout, F. Winnefeld, D. Rentsch, and B. Lothenbach. Alkali-Silica Reaction: the influence of calcium on silica dissolution and the formation of reaction products. *Journal of the American Ceramic Society*, 94(4):1243–1249, apr 2011.

[113] A. Leemann and B. Lothenbach. The influence of potassium-sodium ratio in cement on concrete expansion due to alkali-aggregate reaction. *Cement and Concrete Research*, 38(10):1162–1168, oct 2008.

[114] A. Leemann and P. Lura. E-modulus of the alkali-silica-reaction product determined by micro-indentation. *Construction and Building Materials*, 44:221–227, 2013.

[115] P. Leger, P. Cote, and R. Tinawi. Finite element analysis of concrete swelling due to alkali-aggregate reactions in dams. *Computers and Structures*, 60(4):601–611, 1996.

[116] K. Li and O. Coussy. Concrete ASR degradation: from material modeling to structure assessment. *Concrete Science and Engineering*, 4(March):35–46, 2002.

[117] J. Liaudat, I. Carol, C. M. López, and V. E. Saouma. ASR Expansions in Concrete under Triaxial Confinement. *Cement and Concrete Composites*, 86:160–170, 2018.

[118] J. Liaudat, D. Garolera, I. Carol, M. R. Lakshmikantha, and J. Alvarellos. Avoiding fracture instability in Wedge Splitting Tests by means of numerical simulations. In E. Oñate, D. Owen, D. Peric, and M. Chiumenti, editors, *Computational Plasticity XIVFundamentals and Applications*, pages 514–521. International Center for Numerical Methods in Engineering (CIMNE), Barcelona, Spain, 2017.

[119] J. Liaudat, D. Garolera, C. M. López, and I. Carol. Numerical modeling of micro-indentation tests in Portland cement paste, using finite elements with fracture-based zero-thickness interfaces. In C. M. Guang Ye, K. Van Breugel, Wei Sun, editor, *2nd International conference on Microstructural-related Durability of Cementitious Composites*, pages 910–917. RILEM Publications, 2012.

[120] J. Liaudat, D. Garolera, A. Martínez, I. Carol, M. R. Lakshmikantha, and J. Alvarellos. Numerical modelling of the Wedge Splitting Test in rock specimens, using fracture-based zero-thickness interface elements. In E. Oñate, D. R. J. Owen, D. Peric, and M. Chiumeti, editors, *XIII International Conference on Computational Plasticity - Fundamentals and Applications*, pages 974–981. International Center for Numerical Methods in Engineering (CIMNE), Barcelona, Spain, first edition, 2015.

[121] J. Liaudat, C. M. López, and I. Carol. ASR free expansion tests at the level of a single aggregate-matrix interface: experimental results and numerical modelling. In C. Andrade, J. Gulikers, and R. Polder, editors, *Durability of Reinforced Concrete from Composition to Protection.*, pages 189–195. Springer, Cham, 2013.

[122] J. Liaudat, C. M. López, and I. Carol. Diffusion-reaction model for Alkali-Silica Reaction in concrete. In E. Oñate, D. Owen, D. Peric, and B. Suárez, editors, *Computational Plasticity XII - Fundamentals and Applications*, pages 479–489. International Center for Numerical Methods in Engineering (CIMNE), Barcelona, 2013.

[123] J. Liaudat, C. M. López, and I. Carol. Diffusion-reaction model for ASR: formulation and 1D numerical implementation. In N. Bicanic, H. Mang, G. Meschke,

and R. de Borst, editors, *Computational Modelling of Concrete Structures: Proceedings of the Conference on Computational Modelling of Concrete and Concrete Structures (EURO-C 2014), March 24-27, 2014, St. Anton am Arlberg, Austria*, number 2, pages 639–648. CRC Press, 2014.

[124] J. Liaudat, C. M. López, and I. Carol. Free expansion tests for ASR at the level of a single aggregate- matrix interface: experimental results and numerical modelling. In C. Andrade, J. Gulikers, and R. Polder, editors, *Durability of Reinforced Concrete from Composition to Protection*, pages 189–195. Springer International Publishing, Delft, The Netherlands, 2015.

[125] J. Liaudat, C. M. López, and I. Carol. Numerical and experimental study of ASR in concrete at the meso-level. In V. Saouma, J. Bolander, and E. Landis, editors, *The 9th International Conference on Fracture Mechanics of Concrete and Concrete Structures (FraMCoS 9)*. International Association of Fracture Mechanics for Concrete and Concrete Structures, 2016.

[126] J. Liaudat, C. M. López, and I. Carol. Coupled C-M meso-scale model for ASR expansion in concrete. In G. Meschke, B. Pichler, and J. G. Rots, editors, *Computational Modelling of Concrete Structures: Proceedings of the Conference on Computational Modelling of Concrete and Concrete Structures (EURO-C 2018), February 26-March 1, 2018, Bad Hofgastein, Austria*, pages 363–370. CRC Press, 2018.

[127] J. Liaudat, A. Martínez, C. M. López, and I. Carol. Numerical Modelling of ASR Expansions in Concrete. In C. Hellmich, B. Pichler, and J. Kollegger, editors, *10th International Conference on Mechanics and Physics of Creep, Shrinkage, and Durability of Concrete and Concrete Structures (CONCREEP 10)*, pages 445–454. American Society of Civil Engineers, Vienna, Austria, 2015.

[128] J. Liaudat, A. Martínez, C. M. López, and I. Carol. Modelling acid attack of oilwell cement exposed to carbonated brine. *International Journal of Greenhouse Gas Control*, 68C:191–202, 2018.

[129] J. Liaudat, M. Rodriguez, C. M. Lopez, and I. Carol. Recent developments in durability mesomechanics of concrete, including cracking via interface elements. In F.-J. Ulm, H. M. Jennings, and R. J. Pellenq, editors, *Ninth International Conference on Creep, Shrinkage, and Durability Mechanics (CONCREEP-9)*, pages 174–181. American Society of Civil Engineers, Cambridge, Massachusetts, United States, 2013.

[130] D. Lide, editor. *CRC Handbook of Chemistry and Physics (70th Edn.)*. CRC Press, Boca Raton (FL), 1990.

[131] D. R. Lide, editor. *CRC Handbook of Chemistry and Physics*. CRC Press, Boca Raton (FL), 85th edition, 2004.

[132] J. Lier, P. Bruyn, and J. Overbeek. The solubility of quartz. *The Journal of Physical Chemistry*, 64(11):1675–1682, 1960.

[133] J. Lindgård, Ö. Andiç-Çakr, I. Fernandes, T. F. Rønning, and M. D. A. Thomas. Alkali-silica reactions (ASR): Literature review on parameters influencing laboratory performance testing. *Cement and Concrete Research*, 42(2):223–243, feb 2012.

[134] K. R. Linger and D. G. Holloway. The fracture energy of glass. *Philosophical Magazine*, 18:1269–1280, 1968.

[135] C. M. Lopez. *Análisis microestructural de la fractura del hormigón utilizando elementos finitos tipo junta. Aplicación a diferentes hormigones.* Doctoral thesis (in spanish), Universitat Politècnica de Catalunya, 1999.

[136] C. M. López, I. Carol, and A. Aguado. Meso-structural study of concrete fracture using interface elements. I: numerical model and tensile behavior. *Materials and Structures*, 41:583–599, 2008.

[137] C. M. López, I. Carol, and A. Aguado. Meso-structural study of concrete fracture using interface elements.II: compression, biaxial and Brazilian test. *Materials and Structures*, 41:601–620, 2008.

[138] B. Lothenbach, F. Winnefeld, C. Alder, E. Wieland, and P. Lunk. Effect of temperature on the pore solution, microstructure and hydration products of Portland cement pastes. *Cement and Concrete Research*, 37(4):483–491, apr 2007.

[139] MakeItFrom. Material Properties Database — Soda-Lime (Float) Glass. *MakeItFrom.com*, http://www.makeitfrom.com/material-properties/Soda-Lime-Float-Glass. Accessed 2018-03-30.

[140] H. Maraghechi. *Development and assessment of alkali activated recycled glass-based concretes for civil infrastructure.* PhD thesis, The Pennsylvania State University, 2014.

[141] H. Maraghechi, F. Rajabipour, C. G. Pantano, and W. D. Burgos. Effect of calcium on dissolution and precipitation reactions of amorphous silica at high alkalinity. *Cement and Concrete Research*, 87:1–13, 2016.

[142] H. Maraghechi, S.-M.-H. Shafaatian, G. Fischer, and F. Rajabipour. The role of residual cracks on alkali silica reactivity of recycled glass aggregates. *Cement and Concrete Research*, 34(1):41–47, jan 2012.

[143] A. Martínez. *Estudio experimental de las expansiones por reacción álcali-sílice a nivel de la interfase pasta de cemento-agregado.* Bachelor thesis (in spanish), Universitat Politècnica de Catalunya, 2014.

[144] A. Martínez. *Ataque ácido en cementos de antiguos pozos en repositorios de CO2.* Master thesis (in spanish), Universitat Politècnica de Catalunya, 2016.

[145] A. Martínez, J. Liaudat, C. M. López, and I. Carol. Diffusion-reaction modelling of the degradation of oil-well cement exposed to carbonated brine. In E. Oñate, D. Owen, D. Peric, and M. Chiumenti, editors, *Computational Plasticity XIV Fundamentals and Applications*, pages 625–635. International Center for Numerical Methods in Engineering (CIMNE), Barcelona, Spain, 2017.

[146] H. Marzouk and S. Langdon. The effect of alkali-aggregate reactivity on the mechanical properties of high and normal strength concrete. *Cement and Concrete Composites*, 25(4-5 SPEC):549–556, 2003.

[147] A. M. Matos and J. Sousa-Coutinho. Durability of mortar using waste glass powder as cement replacement. *Construction and Building Materials*, 36:205–215, 2012.

[148] J. K. McGowan and H. E. Vivian. The Effect of Superincumbent Load on Mortar Bar Expansion. *Australian Journal of Applied Science*, 6:94–99, 1955.

[149] P. K. Mehta and P. J. M. Monteiro. *Concrete. Microstructure, properties and Materials.* McGraw-Hill, 3rd edition, 2006.

[150] H. S. Meissner. Cracking in Concrete Due to Expansive Reaction Between Aggregate and High-Alkali Cement as Evidenced in Parker Dam. *Engineering*, 37(549):549–568, 1941.

[151] R. C. Mielenz, K. T. Greene, and E. J. Bentont. Chemical Test for Reactivity of Aggregates with Cement Alkalies; Chemical Processes in Cement-Aggregate Reaction. *Journal of the American Concrete Institute*, 19(3):193–221, 1947.

[152] T. U. Mohammed, H. Hamada, and T. Yamaji. Alkali-silica reaction-induced strains over concrete surface and steel bars in concrete. *ACI Materials Journal*, 100(2):133–142, 2003.

[153] S. Multon. *Evaluation expérimentale et théorique des effets mécaniques de l'alcali-réaction sur des structures modèles.* Doctoral thesis (in french), Université de Marne-la-Vallée, France, 2004.

[154] S. Multon, M. Cyr, A. Sellier, P. Diederich, and L. Petit. Effects of aggregate size and alkali content on ASR expansion. *Cement and Concrete Research*, 40(4):508–516, 2010.

[155] S. Multon, J. Seignol, and F. Toutlemonde. Structural Behavior of Concrete Beams Affected by Alkali-Silica Reaction. *ACI Materials Journal*, 102(2):67–76, 2005.

[156] S. Multon, A. Sellier, and M. Cyr. Chemomechanical modeling for prediction of alkali silica reaction (ASR) expansion. *Cement and Concrete Research*, 39(6):490–500, jun 2009.

[157] S. Multon and F. Toutlemonde. Effect of applied stresses on alkali-silica reaction-induced expansions. *Cement and Concrete Research*, 36(5):912–920, may 2006.

[158] D. Navarro. *Comportamiento triaxial de rocas de sondeos profundos.* Bachelor thesis (in spanish), Universitat Politècnica de Catalunya, 2015.

[159] B. H. Oh and S. Y. Jang. Prediction of diffusivity of concrete based on simple analytic equations. *Cement and Concrete Research*, 34(3):463–480, mar 2004.

[160] J. Ollivier, J. Maso, and B. Bourdette. Interfacial transition zone in concrete. *Advanced Cement Based Materials*, 7355(94), 1995.

[161] A. Omran and A. Tagnit-Hamou. Performance of glass-powder concrete in field applications. *Construction and Building Materials*, 109:84–95, 2016.

[162] J. W. Pan, Y. T. Feng, J. T. Wang, Q. C. Sun, C. H. Zhang, and D. R. J. Owen. Modeling of alkali-silica reaction in concrete: a review. *Front. Struct. Civ. Eng*, 6(1):1–18, 2012.

[163] G. N. Pande, G. G. Beer, and J. R. Williams. *Numerical methods in rock mechanics.* John Wiley & Sons, 1990.

[164] K. S. Pitzer, editor. *Activiy coefficients in electrolyte solutions.* CRC Press, Boca Raton (FL), 2nd edition, 1991.

[165] J. Ponce and O. Batic. Different manifestations of the alkali-silica reaction in concrete according to the reaction kinetics of the reactive aggregate. *Cement and Concrete Research*, 36(6):1148–1156, jun 2006.

[166] A. B. Poole. Introduction to alkali-aggregate reaction in concrete. In R. N. Swamy, editor, *The Alkali-Silica Reaction in Concrete*, chapter 1, pages 1–29. Blackie and Son Ltd., Glasgow, 1992.

[167] T. Powers and T. Brownyard. Studies of the physical properties of hardened Portland cement paste. *ACI Journal Proceedings*, 43(9):101–132, 249–336, 469–505, 549–602, 669–712, 845–8, 1946.

[168] T. Powers and H. H. Steinour. An Interpretation of Published Researches on the Alkali-Aggregate Reaction. In *ACI Journal Proceedings*, volume 51, pages 497–516 and 785–812, 1955.

[169] S. Poyet, A. Sellier, B. Capra, G. Foray, J.-M. Torrenti, H. Cognon, and E. Bourdarot. Chemical modelling of Alkali Silica reaction: Influence of the reactive aggregate size distribution. *Materials and Structures*, 40(2):229–239, jul 2006.

[170] S. Poyet, A. Sellier, B. Capra, G. Thèvenin-Foray, J.-M. Torrenti, H. Tournier-Cognon, and E. Bourdarot. Influence of Water on Alkali-Silica Reaction: Experimental Study and Numerical Simulations. *Journal of Materials in Civil Engineering*, 18(4):588–596, 2006.

[171] M. Prezzi, P. J. M. Monteiro, and G. Sposito. The alkali-silica reaction, Part I: use of the double-layer theory to explain the behavior of reaction-product gels. *ACI Materials Journal*, 1(94):10–16, 1997.

[172] W. Puatatsananon and V. E. Saouma. Chemo-Mechanical Micromodel for Alkali-Silica Reaction. *ACI Materials Journal*, 110(1):67–77, 2013.

[173] F. Rajabipour, E. Giannini, C. F. Dunant, J. H. Ideker, and M. D. A. Thomas. Alkali-silica reaction: Current understanding of the reaction mechanisms and the knowledge gaps. *Cement and Concrete Research*, 76:130–146, 2015.

[174] F. Rajabipour, H. Maraghechi, and G. Fischer. Investigating the alkali-silica reaction of recycled glass aggregates in concrete materials. *Journal of Materials in Civil Engineering*, 22(12):1201–1208, 2010.

[175] E. Reardon. An ion interaction model for the determination of chemical equilibria in cement/water systems. *Cement and Concrete Research*, 20:175–192, 1990.

[176] H. Reinhardt and O. Mielich. A fracture mechanics approach to the crack formation in alkali-sensitive grains. *Cement and Concrete Research*, 41(3):255–262, mar 2011.

[177] E. Samson and G. Lemaire. Modeling chemical activity effects in strong ionic solutions. *Computational Materials Science*, 15:285–294, 1999.

[178] E. Samson and J. Marchand. Modeling the effect of temperature on ionic transport in cementitious materials. *Cement and Concrete Research*, 37(3):455–468, mar 2007.

[179] E. Samson and J. Marchand. Modeling the transport of ions in unsaturated cement-based materials. *Computers & Structures*, 85(23-24):1740–1756, dec 2007.

[180] E. Samson, J. Marchand, and J. J. Beaudoin. Describing ion diffusion mechanisms in cement-based materials using the homogenization technique. *Cement and Concrete Research*, 29(8):1341–1345, aug 1999.

[181] V. E. Saouma. *Numerical modeling of AAR*. CRC Press/Balkema, Leiden, The Netherlands, 2014.

[182] V. E. Saouma and L. Perotti. Alkali Aggregate Reactions in Dams; Stress Analysis and Long Term Predictions. In *ASDSO Dam Safety Conference*, page 19, New Orleans (USA), 2005.

[183] V. E. Saouma and L. Perotti. Constitutive Model for Alkali-Aggregate Reactions. *ACI Materials Journal*, 103(3):194–202, 2006.

[184] V. E. Saouma, L. Perotti, and T. Shimpo. Stress Analysis of Concrete Structures Subjected to Alkali-Aggregate Reactions. *ACI Structural Journal*, 104(5):532–541, 2007.

[185] V. E. Saouma and Y. Xi. CU/SA-XI-2004/001 Literature Review of Alkali Aggregate Reactions in Concrete Dams. Technical report, Swiss Federal Office for Water and Geology, 2004.

[186] G. W. Scherer. Structure and properties of gels. *Cement and Concrete Research*, 29(8):1149–1157, 1999.

[187] E. Schlangen and O. Çopurolu. Concrete damage due to Alkali-Silica reaction: a new method to determine the properties of the expansive gel. In et al. Carpinteri, editor, *Fracture Mechanics of Concrete and Concrete Structures - High-Performance Concrete and Evironmental Aspects*. 2007.

[188] K. Schmidt, L. Urbonas, A. Dressler, and D. Heinz. AKR-Performance-Prüfung von flugaschehaltigen Betonen Einfluss der Temperatur auf die Porenlösung und Möglichkeiten zur zielsicheren Bewertung. In J. Stark, editor, *17 Internationale BaustofftagungInternationale Baustofftagung*, pages 2 0267 – 2 0276, Weimar, 2009. F. A. Finger Institut für Baustoffkunde , Bauhaus Universität Weimar.

[189] K. L. Scrivener, A. K. Crumbie, and P. Laugesen. The Interfacial Transition Zone (ITZ) Between Cement Paste and Aggregate in Concrete. *Interface Science*, 12(4):411–421, 2004.

[190] K. L. Scrivener and K. M. Nemati. The percolation of pore space in the cement paste/aggregate interfacial zone of concrete. *Cement and Concrete Research*, 26(1):35–40, 1996.

[191] J. M. Segura and I. Carol. On zero-thickness interface elements for diffusion problems. *International Journal for Numerical and Analytical Methods in Geomechanics*, 28(9):947–962, aug 2004.

[192] A. Sellier, E. Bourdarot, S. Multon, M. Cyr, and E. Grimal. Combination of structural monitoring and laboratory tests for assessment of alkali-aggregate reaction swelling: Application to gate structure dam. *ACI Materials Journal*, 106(3):281–290, 2009.

[193] Y. Shao, T. Lefort, S. Moras, and D. Rodriguez. Studies on concrete containing ground waste glass. *Cement and Concrete Research*, 30(1):91–100, 2000.

[194] J. E. Shelby. *Introduction to glass science and technology*. The Royal Society of Chemistry, Cambridge, 1997.

[195] S. Sjöberg. Silica in aqueous environments. *Journal of Non-Crystalline Solids*, 196:51–57, 1996.

[196] J. M. Soler. Thermodynamic description of the solubility of CSH gels in hydrated Portland cement. Literature review. Technical report, Posiva Oy, Olkiluoto, Finland, 2007.

[197] H. Song, K. Cheng, and C. P. Ostertag. Influence of matrix properties on alkali silica reaction rates, jan 2007.

[198] T. Stanton. Expansion of concrete through reaction between cement and aggregate. In *Proceedings of American Society of Civil Engineers 66*, pages 1781–1811, 1940.

[199] T. Stanton, O. Porter, L. Meder, and A. Nicol. California experience with the expansion of concrete through reaction between cement and aggregate. In *ACI Journal Proceedings*, volume 38, pages 209–236, 1942.

[200] A. Steffens, K. Li, and O. Coussy. Aging approach to water effect on alkali-silica reaction degradation of structures. *Journal of engineering mechanics*, 129(1):50–59, 2003.

[201] J. Stokes. *An analysis of the design and assembly of the AAR tri-axial machine*. Bachelor thesis, Universitat Politècnica de Catalunya, 2011.

[202] L. J. Struble and S. Diamond. Swelling properties of synthetic alkali silica gels. *Journal of the American Ceramic Society*, 64(11):652–655, 1981.

[203] L. J. Struble and S. Diamond. Unstable swelling behaviour of alkali silica gels. *Cement and Concrete Research*, 11:611–617, 1981.

[204] A. Suwito, W. Jin, Y. Xi, and C. Meyer. A Mathematical Model for the Pessimum Size Effect of ASR in Concrete. *Concrete Science and Engineering*, 4(13):23–34, 2002.

[205] E. G. Swenson. A reactive aggregate undetected by ASTM tests. *ASTM Bulletin*, 226:48–51, 1957.

[206] N. Thaulow, U. Jakobsen, and B. Clark. Composition of alkali silica gel and ettringite in concrete railroad ties: SEM-EDX and X-ray diffraction analyses. *Cement and Concrete Research*, 26(2):309–318, 1996.

[207] THERMODDEM. Thermochemical and Mineralogical Tables for Geochemical Modeling — Amorphous Silica. *Bureau de Recherches Géologiques et Minières*, http://thermoddem.brgm.fr/species/amorphoussilica, 2018. Accessed 2018-02-12.

[208] THERMODDEM. Thermochemical and Mineralogical Tables for Geochemical Modeling — Aqueous KOH. *Bureau de Recherches Géologiques et Minières*, http://thermoddem.brgm.fr/species/koh, 2018. Accessed 2018-02-12.

[209] THERMODDEM. Thermochemical and Mineralogical Tables for Geochemical Modeling — Aqueous NaOH. *Bureau de Recherches Géologiques et Minières*, http://thermoddem.brgm.fr/species/naoh, 2018. Accessed 2018-02-12.

[210] THERMODDEM. Thermochemical and Mineralogical Tables for Geochemical Modeling — Portlandite. *Bureau de Recherches Géologiques et Minières*, http://thermoddem.brgm.fr/species/portlandite, 2018. Accessed 2018-02-12.

[211] M. D. A. Thomas. The effect of supplementary cementing materials on alkali-silica reaction: A review. *Cement and Concrete Research*, 41(12):1224–1231, dec 2011.

[212] M. D. A. Thomas, B. Fournier, K. Folliard, and Y. Resendez. FHWA-HIF-12-046 Alkali-Silica Reactivity Surveying and Tracking Guidelines. Technical report, Federal Highway Administration, Washington, DC, USA, 2012.

[213] G. A. Thompson, R. G. Charlwood, R. R. Steele, and D. D. Curtis. Mactaquac generating station intake and spillway remedial measure. In *18th International Congress on Large Dams*, pages Vol. 1, 347–368, Durban, South Africa, 1994.

[214] F.-J. Ulm, O. Coussy, L. Kefei, and C. Larive. Thermo-chemo-mechanics of ASR expansion in concrete structures. *Journal of Engineering Mechanics*, 126(3):233–242, 2000.

[215] E. Vacas. *Estudio experimental de la influencia del estado tensional en las expansiones por Reacción Álcali-Sílice en hormigón.* Bachelor thesis (in spanish), Universitat Politècnica de Catalunya, 2016.

[216] Viridian Glass. Glass physical properties. http://www.viridianglass.com/-/media/viridian-glass/files/downloads/brochures/glass-physical-properties.pdf. Accessed 2018-04-02.

[217] H. E. Vivian. The effect on mortar expansion of the particle size of reactive component in the aggregate. *Australian Journal of Applied Science*, 2:488–494, 1951.

[218] S. M. Wiederhorn. Fracture Surface Energy of Glass. *Journal of the American Ceramic Society*, 52(2):99–105, 1969.

[219] Wikipedia. Soda-lime glass — Wikipedia, The Free Encyclopedia. https://en.wikipedia.org/w/index.php?title=Soda-lime_glass&oldid=807782221. Accessed 2017-11-17.

[220] G. Xotta, K. Willam, E. Bombasaro, V. Salomoni, and C. Majorana. Coupled Effects of Creep and Alkali-Silica Reaction in Concrete at the Meso-Scale. In *CONCREEP 10*, pages 466–476, Vienna, 2015.

[221] C. Yi and C. Ostertag. Mechanical approach in mitigating alkali-silica reaction. *Cement and concrete research*, 35(1):67–75, jan 2005.

[222] T. Yokoyama. Diffusivity of dissolved silica in rock pore water at 25 ^{o}C as characterized by through-diffusion experiments. *Water Resources Research*, 49(12):8299–8309, dec 2013.

[223] L. Yuan-Hui and S. Gregory. Diffusion of ions in sea water and in deep-sea sediments. *Geochimica et cosmochimica acta*, 38:703–714, 1974.

[224] H. Zhu, W. Chen, W. Zhou, and E. A. Byars. Expansion behaviour of glass aggregates in different testing for alkali-silica reactivity. *Materials and Structures*, 42(4):485–494, jul 2008.

[225] O. Zienkiewicz and R. Taylor. *The Finite Element Method for Solid and Structural Mechanics.* Elsevier Butterworth-Heinemann, 6th edition, 2005.

[226] O. Zienkiewicz, R. Taylor, and J. Zhu. *The Finite Element Method: Its Basis and Fundamentals.* Butterworth-Heinemann, 7th edition, 2013.